

PREDICTING COMPLEX DRUG INTERACTIONS
OF CYP₃A₄, CYP₃A₅, AND CYP₂D₆ SUBSTRATES:
PHYSIOLOGICALLY BASED PHARMACOKINETIC MODELING
FOR INDIVIDUALIZED THERAPY

DISSERTATION

zur Erlangung des Grades des Doktors der Naturwissenschaften
der Naturwissenschaftlich-Technischen Fakultät
der Universität des Saarlandes

von
Helena Leonie Hanae Loer
Apothekerin, M.Sc.

Saarbrücken
2025

Tag des Kolloquiums:	30.10.2025
Dekan:	Prof. Dr.-Ing. Dirk Bähre
Berichterstatter:	Prof. Dr. Thorsten Lehr Prof. Dr. Marc Schneider
Akad. Mitglied:	Priv.-Doz. Dr. Matthias Engel
Vorsitz:	Prof. Dr. Claus Jacob

PUBLICATIONS

PUBLICATIONS INCLUDED IN THIS THESIS

This thesis comprises the following publications [1–4] related to projects I–IV:

- I Loer, H. L. H.; Feick, D.; Rüdesheim, S.; Selzer, D.; Schwab, M.; Teutonico, D.; Frechen, S.; van der Lee, M.; Moes, D. J. A. R.; Swen, J. J.; Lehr, T. Physiologically based pharmacokinetic modeling of tacrolimus for food–drug and CYP3A drug–drug–gene interaction predictions. *CPT: Pharmacometrics and Systems Pharmacology* **2023**, *12*, 724–738, DOI: [10.1002/psp4.12946](https://doi.org/10.1002/psp4.12946).
- II Loer, H. L. H.; Kovar, C.; Rüdesheim, S.; Marok, F. Z.; Fuhr, L. M.; Selzer, D.; Schwab, M.; Lehr, T. Physiologically based pharmacokinetic modeling of imatinib and N-desmethyl imatinib for drug–drug interaction predictions. *CPT: Pharmacometrics and Systems Pharmacology* **2024**, *13*, 926–940, DOI: [10.1002/psp4.13127](https://doi.org/10.1002/psp4.13127).
- III Kovar, C.; Loer, H. L. H.; Rüdesheim, S.; Fuhr, L. M.; Marok, F. Z.; Selzer, D.; Schwab, M.; Lehr, T. A physiologically-based pharmacokinetic precision dosing approach to manage dasatinib drug–drug interactions. *CPT: Pharmacometrics and Systems Pharmacology* **2024**, *13*, 1144–1159, DOI: [10.1002/psp4.13146](https://doi.org/10.1002/psp4.13146).
- IV Rüdesheim, S.*; Loer, H. L. H.*; Feick, D.; Marok, F. Z.; Fuhr, L. M.; Selzer, D.; Teutonico, D.; Schneider, A. R. P.; Solodenko, J.; Frechen, S.; van der Lee, M.; Moes, D. J. A. R.; Swen, J. J.; Schwab, M.; Lehr, T. A comprehensive CYP2D6 drug–drug–gene interaction network for application in precision dosing and drug development. *Clinical Pharmacology & Therapeutics* **2025**, *117*, 1718–1731, DOI: [10.1002/cpt.3604](https://doi.org/10.1002/cpt.3604).

* Authors contributed equally

CONTRIBUTION REPORT

The author of this thesis, Helena Leonie Hanae Loer, would like to declare her contributions to the listed publications according to the contributor roles taxonomy (CRediT) [5] as follows:

- I Conceptualization, Investigation, Visualization,
Writing – Original Draft, Writing – Review & Editing
- II Conceptualization, Investigation, Visualization,
Writing – Original Draft, Writing – Review & Editing
- III Conceptualization, Investigation, Writing – Review & Editing
- IV Conceptualization, Investigation, Visualization,
Writing – Original Draft, Writing – Review & Editing

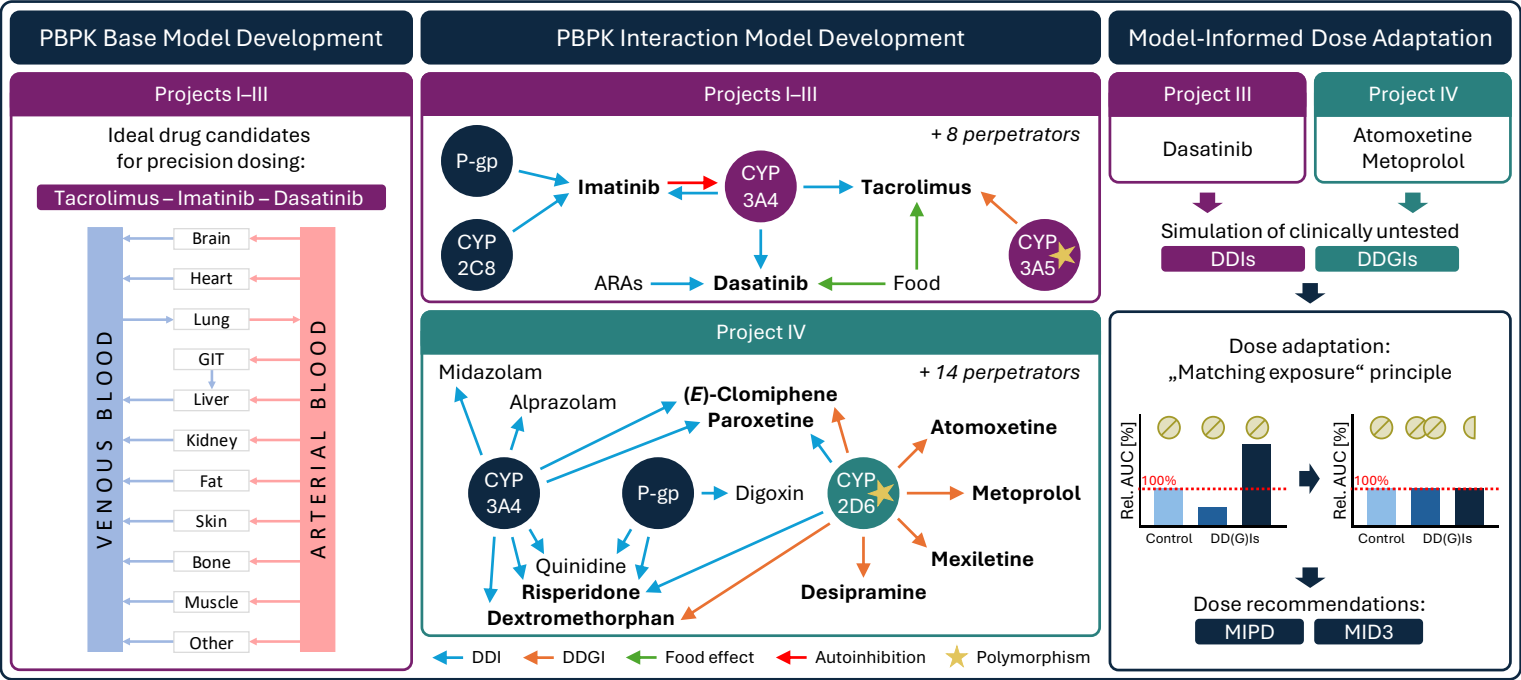
ABSTRACT

Personalized medicine and precision dosing strive to maximize therapeutic efficacy and safety by considering inter-patient variability in treatment decisions. Drug-gene (DGIs) and drug-drug interactions (DDIs) are leading causes of variability in drug response and adverse drug reactions. Clinical practice is complicated by their frequent co-occurrence, resulting in complex drug-drug-gene interactions (DDGIs). Due to the vast number of potential interactions, it is impossible to investigate all scenarios in clinical DD(G)I studies. Physiologically based pharmacokinetic (PBPK) modeling enables mechanistic predictions of clinically untested DD(G)Is and supports model-informed dose adaptations. In this thesis, new whole-body PBPK models are presented for the cytochrome P450 (CYP) 3A substrates tacrolimus, imatinib, and dasatinib. In addition, a comprehensive PBPK model network centered around CYP2D6 was built. The models' and network's predictive performance was evaluated across numerous complex DD(G)I scenarios. Beyond this, simulation of multiple clinically untested DD(G)Is and model-informed dose adaptations were conducted. Overall, this thesis showcases PBPK modeling as a promising framework to advance individualized therapy by bridging critical knowledge gaps between interaction study results and complex real-world scenarios.

ZUSAMMENFASSUNG

Die personalisierte Medizin und Präzisionsdosierung zielen darauf ab, die therapeutische Wirksamkeit und Sicherheit zu maximieren, indem sie interindividuelle Variabilität bei Behandlungsentscheidungen berücksichtigen. Arzneimittel-Gen- (DGIs) und Arzneimittel-Arzneimittel-Interaktionen (DDIs) sind Hauptursachen für ein variables Arzneimittelansprechen und unerwünschte Arzneimittelwirkungen. Ihr häufiges gemeinsames Auftreten als komplexe Arzneimittel-Arzneimittel-Gen-Interaktionen (DDGIs) erschwert die klinische Praxis. Die Vielzahl potenzieller Interaktionen macht es unmöglich, alle Szenarien in klinischen DD(G)I-Studien zu untersuchen. Die Physiologie-basierte Pharmakokinetik (PBPK) Modellierung ermöglicht mechanistische Vorhersagen klinisch ungetesteter DD(G)Is und unterstützt modellbasierte Dosisanpassungen. In dieser Arbeit werden neue Ganzkörper-PBPK-Modelle für die Cytochrom P450 (CYP) 3A-Substrate Tacrolimus, Imatinib und Dasatinib vorgestellt. Zudem wurde ein umfassendes PBPK-Modellnetzwerk rund um CYP2D6 gebaut. Die Vorhersageleistung der Modelle und des Netzwerks wurde in komplexen DD(G)I-Szenarien evaluiert. Darüber hinaus wurden mehrere klinisch ungetestete DD(G)Is und modellgestützte Dosisanpassungen simuliert. Insgesamt zeigt die Arbeit die PBPK-Modellierung als vielversprechenden Rahmen zur Weiterentwicklung der individualisierten Therapie durch die Überbrückung kritischer Wissenslücken zwischen Interaktionsstudienresultaten und komplexen realen Szenarien.

GRAPHICAL ABSTRACT



Graphical abstract. ARA: acid-reducing agent, AUC: area under the concentration-time curve, CYP: cytochrome P₄₅₀, DDI: drug-drug interaction, DDGI: drug-drug-gene interaction, GIT: gastrointestinal tract, MID₃: model-informed drug discovery and development, MIPD: model-informed precision dosing, PBPK: physiologically based pharmacokinetic, P-gp: P-glycoprotein, Rel.: relative.

CONTENTS

1	Introduction	1
1.1	Motivation	1
1.2	Identifying Ideal Drug Candidates for Precision Dosing	3
1.3	Drug-Gene Interactions and Clinical Implications	4
1.3.1	Overview	4
1.3.2	CYP3A5	5
1.3.3	CYP3A4	7
1.3.4	CYP2D6	7
1.4	Drug-Drug Interactions and Clinical Implications	9
1.4.1	Overview	9
1.4.2	Induction	10
1.4.3	Inhibition	12
1.5	Drug-Drug-Gene Interactions and Clinical Implications	12
1.6	Physiologically Based Pharmacokinetic Modeling	14
2	Objectives	17
2.1	Project I: PBPK Modeling of Tacrolimus	17
2.2	Project II: PBPK Modeling of Imatinib	17
2.3	Project III: PBPK Modeling of Dasatinib	18
2.4	Project IV: CYP2D6 DDGI Network Modeling	18
3	Methods	19
3.1	Compounds Selected for PBPK Base Modeling	19
3.1.1	Tacrolimus	19
3.1.2	Imatinib	20
3.1.3	Dasatinib	20
3.2	Software	21
3.3	PBPK Base Model Development	21
3.3.1	Base Model Building	22
3.3.2	Base Model Evaluation	23
3.4	PBPK Interaction Model Development	24
3.4.1	DGI Model Building	24
3.4.2	DDI Model Building	25
3.4.3	DDGI Model Building	26
3.4.4	Food-Effect Model Building	26
3.4.5	Interaction Model Evaluation	26
3.5	PBPK Model-Informed Dose Adaptation	27
4	Results	29
4.1	Project I: PBPK Modeling of Tacrolimus	29
4.2	Project II: PBPK Modeling of Imatinib	46
4.3	Project III: PBPK Modeling of Dasatinib	63
4.4	Project IV: CYP2D6 DDGI Network Modeling	81
5	Discussion and Future Directions	97
5.1	PBPK Modeling of Complex Drug Interactions	97

5.2	PBPK Modeling in MIPD	99
5.2.1	Current Status of MIPD	99
5.2.2	Potential and Limitations of PBPK-MIPD	100
5.2.3	Clinical Implementation of PBPK-MIPD	102
5.3	PBPK Modeling in MID3	105
6	Conclusion	109
	Bibliography	111
A	Publications	133
A.1	Original Research Articles	133
A.2	Conference Abstracts and Posters	134
B	Supplementary Materials	135
B.1	Project I: PBPK Modeling of Tacrolimus	136
B.2	Project II: PBPK Modeling of Imatinib	184
B.3	Project III: PBPK Modeling of Dasatinib	230
B.4	Project IV: CYP2D6 DDGI Network Modeling	285
	Acknowledgments	411

LIST OF FIGURES

Figure 1.1	“One-size-fits-all” versus precision dosing in drug therapy	1
Figure 1.2	Characteristics considered in the selection of drug candidates for precision dosing	3
Figure 1.3	<i>CYP3A5</i> polymorphism overview	6
Figure 1.4	<i>CYP2D6</i> polymorphism overview	8
Figure 1.5	Percentage-based classification of FDA-listed substrates, inducers, and inhibitors by CYP enzyme	10
Figure 1.6	DDI mechanisms and clinical examples	11
Figure 1.7	DDGI mechanisms and clinical examples	13
Figure 1.8	PBPK modeling overview	15
Figure 5.1	“Individualized Prediction” function integrated in the developed CDSS	103
Figure 5.2	“Dose Adaptation” function integrated in the developed CDSS	104

ACRONYMS

ADME	Absorption, distribution, metabolism, and excretion
ADR	Adverse drug reaction
ALL	Acute lymphoblastic leukemia
AS	Activity score
AUC _{last,pl}	Area under the plasma concentration-time curve determined between first and last concentration measurements
AUC _{last,wb}	Area under the whole blood concentration-time curve determined between first and last concentration measurements
AUC _{pl}	Area under the plasma concentration-time curve
AUC _{wb}	Area under the whole blood concentration-time curve
CAR	Constitutive androstane receptor
CDSS	Clinical decision support system
C _{max,pl}	Maximum plasma concentration
C _{max,wb}	Maximum whole blood concentration
CML	Chronic myeloid leukemia
CNV	Copy number variation
CPIC	Clinical Pharmacogenetics Implementation Consortium
CRediT	Contributor roles taxonomy
CYP	Cytochrome P450
DDGI	Drug-drug-gene interaction
DDI	Drug-drug interaction
DGI	Drug-gene interaction
DNA	Deoxyribonucleic acid
DPWG	Dutch Pharmacogenetics Working Group
EHR	Electronic health record
EMA	European Medicines Agency
FDA	US Food and Drug Administration

GMFE	Geometric mean fold error
IATDMCT	International Association of Therapeutic Drug Monitoring and Clinical Toxicology
IM	Intermediate metabolizer
k_{cat}	Catalytic rate constant
K_M	Michaelis–Menten constant
MID ₃	Model-informed drug discovery and development
MIPD	Model-informed precision dosing
MRD	Mean relative deviation
NDMI	N-desmethyl imatinib
NM	Normal metabolizer
NTI	Narrow therapeutic index
OATP	Organic-anion-transporting polypeptide
OSP	Open Systems Pharmacology
PBPK	Physiologically based pharmacokinetic
PDUFA	Prescription Drug User Fee Act
P-gp	P-glycoprotein
PharmGKB	Pharmacogenomics Knowledge Base
PharmVar	Pharmacogene Variation
PK	Pharmacokinetics
PM	Poor metabolizer
PopPK	Population pharmacokinetic
PXR	Pregnane X receptor
QSAR	Quantitative structure-activity relationship
QSP	Quantitative systems pharmacology
RM	Rapid metabolizer
SNP	Single nucleotide polymorphism
TDM	Therapeutic drug monitoring
TKI	Tyrosine kinase inhibitor
$T_{\text{max,pl}}$	Time to peak plasma concentration
UM	Ultrarapid metabolizer

INTRODUCTION

1.1 MOTIVATION

Even though the “one-size-fits-all” principle in treatment and dosing decisions has long been recognized as not applicable to all patients, it remains the predominant approach adopted by healthcare systems [6, 7]. Consequently, certain patients exhibit considerably reduced treatment response rates since only limited or no account is taken of inter-individual variability [7, 8]. To address this obstacle, clinicians have been striving for decades to establish the contrasting concept of personalized medicine, aimed at ensuring maximum therapeutic efficacy for each patient by considering individual characteristics based on clinical, genetic, genomic, and environmental information as well as lifestyle factors [6, 9].

Personalized medicine begins as early as the individual health risk prediction stage and continues to encompass disease diagnosis, classification of disease state, disease prognosis, and monitoring therapy response [6]. Here, precision dosing represents an important area aimed at determining optimal treatment regimens for each patient based on individual demographic factors, such as age, gender, and ethnicity (Figure 1.1) [10, 11].

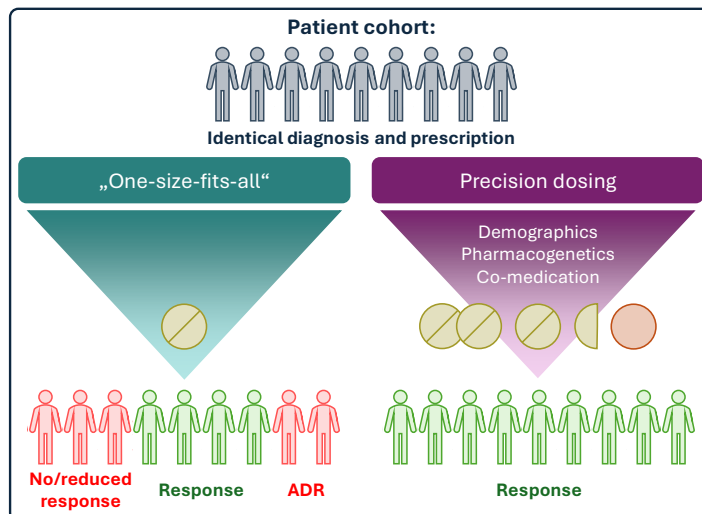


Figure 1.1: Schematic comparison between the traditional “one-size-fits-all” principle and the emerging precision dosing approach in drug therapy. According to the “one-size-fits-all” concept, patients with the same diagnosis and prescription are given a standardized dose without accounting for inter-individual factors. As a result, patient outcomes vary, ranging from no/reduced response to the occurrence of ADRs. In contrast, precision dosing considers demographic influences and factors such as pharmacogenetics and co-medication. Here, doses are adjusted individually or another, more suitable therapy option is selected to ensure a good response for all patients. ADR: adverse drug reaction.

Moreover, considerable variability in drug exposure can arise when the activity of key enzymes and transporters varies greatly, e.g. due to genetic polymorphisms or concomitant medication [12]. The resulting drug-gene (DGIs) and drug-drug interactions (DDIs) pose a significant challenge in clinical practice. One review article concludes that pharmacogenetic polymorphisms may impact drug efficacy and safety in about 60%–80% of patients. In addition, more than 60% of adverse drug reactions (ADRs) are reported to be linked to DGIs [13]. Similarly, studies of hospitalized patients established a prevalence for potential DDIs of around 50% and identified DDIs as a statistically significant risk factor for ADR occurrence [14, 15].

Given the great impact on treatment efficacy and safety, DGIs and DDIs are important factors to be considered in precision dosing (Figure 1.1). Complicating clinical practice further, 19% of potential interactions have been shown to involve a cumulative form of DGI and DDI effects, referred to as drug-drug-gene interactions (DDGIs) [12].

Dedicated clinical interaction studies are conducted to qualitatively and quantitatively determine the potential effects of DGIs, DDIs, and occasionally DDGIs, with the aim of facilitating treatment and dosing decisions. However, since interaction trials are usually performed with a small, homogeneous group of mostly healthy young men, the generalizability of study results to individual patients is limited [16, 17]. Even more challenging is the enormous quantity of potential interactions, making it impossible to investigate all scenarios in appropriate clinical studies. For example, the number of possible DDGI scenarios was calculated to reach 100 in a theoretical case of three therapy-relevant polymorphisms and five co-administered drugs, even increasing to over 10,000 with additional polymorphisms and medications [18]. Considering prescription of typically several drugs per patient, for instance five to eight on average in oncology, this poses a major challenge for individualized therapy [19]. Thus, data from clinical trials alone often cannot provide sufficient information to tailor a patient's treatment to their specific genotypes and entire medication – a crucial bottleneck that needs to be overcome on the road to implementing precision dosing in clinical practice.

Here, physiologically based pharmacokinetic (PBPK) modeling comes into play, offering not only a mechanistic framework for the investigation and prediction of a drug's pharmacokinetics (PK), but also enabling the detailed integration of DD(G)I processes [20]. Moreover, PBPK modeling allows the prediction of clinically untested DD(G)I scenarios and calculation of dose adjustments in the context of model-informed drug discovery and development (MID3) as well as model-informed precision dosing (MIPD) [10, 21–24].

The present thesis aims to illustrate and advance PBPK modeling as a basis for individualized therapy by developing PBPK models for selected clinically relevant drug candidates, investigating interaction effects, and demonstrating the general applicability of PBPK modeling to bridge the critical knowledge gap between interaction study results and complex real-world interaction scenarios.

In the following chapters, criteria for identifying drug candidates for precision dosing, the underlying mechanisms and clinical implications of DGIs, DDIs, and DDGIs, as well as concept and application areas of PBPK modeling are presented in more detail.

1.2 IDENTIFYING IDEAL DRUG CANDIDATES FOR PRECISION DOSING

When selecting drug candidates for precision dosing, characteristics of the drug, the disease, and the target patient group are assessed (Figure 1.2) [10, 25, 26].

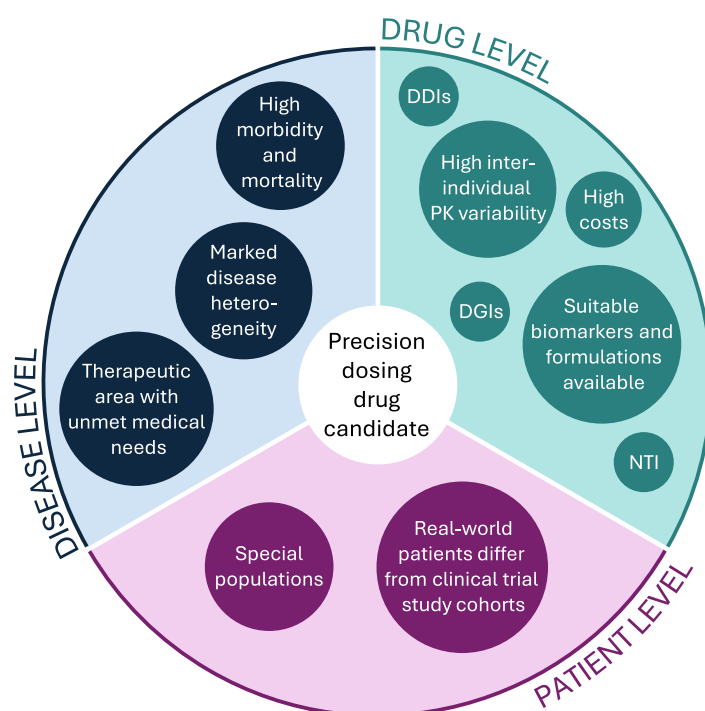


Figure 1.2: Drug-, disease-, and patient-specific characteristics considered in the selection of drug candidates for precision dosing [10, 25, 26]. DDI: drug-drug interaction, DGI: drug-gene interaction, NTI: narrow therapeutic index, PK: pharmacokinetics.

At the drug level, one of the most relevant parameters to consider is the therapeutic index, i.e. the ratio between lethal and effective drug dose in 50% of subjects [27]. Drugs with a therapeutic index of less than 2 are referred to as narrow therapeutic index (NTI) drugs. Since even small changes in systemic exposure are sufficient to cause subtherapeutic or toxic effects, NTI drugs are classic candidates for precision dosing [25, 27]. In addition, precision dosing is advisable for drugs exhibiting high inter-individual PK variability due to factors such as age, weight, and organ function, as well as drugs whose transport/metabolism is susceptible to pharmacogenetic or co-medication influences in the form of DGIs, DDIs, and DDGIs [25, 28].

Moreover, the successful implementation of precision dosing for a specific drug requires suitable biomarkers and formulations allowing flexible dosing [25]. Lastly, from a pharmacoeconomic perspective, it is most beneficial to improve the efficiency of expensive drug therapy thus saving healthcare expenditure [10, 25].

At the disease level, therapeutic areas with unmet medical needs, such as oncology, immunology and transplantation, and neurology, are of specific interest [26, 29]. Furthermore, precision dosing is particularly relevant for diseases linked to substantial morbidity or mortality as well as diseases exhibiting a high degree of heterogeneity [25], for example in relation to disease progression or response to treatment [30].

At the patient level, precision dosing is especially important when real-world patients differ greatly from the population studied in clinical trials regarding their physiology [10, 25]. In geriatric patients, for example, absorption, distribution, metabolism, and excretion (ADME) processes may vary compared to younger individuals due to typically lower glomerular filtration rates and altered body composition, among other factors [31]. Generally, special populations such as children, the elderly, and pregnant women are often excluded from clinical studies, reducing the transferability of trial results to these groups [32].

1.3 DRUG-GENE INTERACTIONS AND CLINICAL IMPLICATIONS

1.3.1 Overview

Research has shown that virtually all human genes exhibit excessive genetic polymorphism, i.e. different alleles occur at one locus within a population, with some leading to increased or decreased expression/activity of the respective gene product [33]. The present thesis focuses on the analysis of PK-related polymorphisms and their effect on drug metabolism and thus exposure.

In this context, the cytochrome P450 (CYP) enzyme family is of particular importance, as it is responsible for the main degradation of three out of four drugs, with 74% of metabolic reactions attributable to CYP3A4, CYP2D6, CYP2C9, CYP2C19, CYP1A2, and CYP3A5 in descending order [34, 35]. Genetic variability has been studied most extensively for the CYP2D6 isotype, characterized by a broad spectrum of more than 160 genetic variants [36, 37]. Besides CYP2D6, the Pharmacogene Variation (PharmVar) database, which catalogs allelic variations of genes affecting drug PK and pharmacodynamics, classifies CYP2C19, CYP2C9, CYP3A5, and CYP2B6 as high priority genes [37].

In general, the occurrence of allelic variants can be caused by different types of genetic variation: In addition to the well-researched single nucleotide polymorphisms (SNPs; variation of a single base pair in a complementary deoxyribonucleic acid (DNA) double strand), insertion and/or deletion events of nucleotides in genomic DNA (indels; 1 bp to 1 kb in length) have been identified [38, 39]. Furthermore, in recent years research

has discovered and investigated the influence of copy number variations (CNVs; duplications or deletions of DNA segments ranging from 1 kb to 3 Mb) on pharmacogenetic variability [38, 40, 41].

Depending on the level of function and/or number of alleles encoding a particular enzyme carried by an individual, i.e. the genotype, different phenotypes – typically considered for dose selection – are classified according to the Clinical Pharmacogenetics Implementation Consortium (CPIC) consensus terms, namely ultrarapid (UM), rapid (RM), normal (NM), intermediate (IM), and poor metabolizer (PM) [42–45].

While the number of pharmacogenetic studies being conducted is steadily increasing, implementation of pharmacogenetic information in clinical practice is progressing only slowly. To facilitate this translation of DGI study findings into clinical practice, several interdisciplinary research groups, such as the Dutch Pharmacogenetics Working Group (DPWG) and CPIC, are continuously working on the development and update of guidelines on pharmacogenetics-based therapeutic (dose) recommendations [42, 46, 47]. Moreover, in 2000, the Pharmacogenomics Knowledge Base (PharmGKB) was launched to provide researchers, clinicians, and the public with condensed pharmacogenomic knowledge, including summaries of the above-mentioned guidelines [48, 49].

However, an important prerequisite for the clinical application of such guidelines is knowing a patient's genotype/phenotype for relevant enzymes and transporters. Although drug-specific genotyping in the form of single-gene tests has been available for some time, cost and time factors prevent its frequent use in clinical practice. A more recent approach to overcome these challenges is the preemptive panel-based testing of several genes in parallel, with the resulting genotypes/phenotypes documented in patient records [50].

In the following sections, the CYP enzymes most relevant to this work – CYP3A4, CYP3A5, and CYP2D6 – are presented in more detail with regard to DGIs, illustrating the range and varying prevalence of genetic polymorphisms as well as their clinical implications.

1.3.2 CYP3A5

A quantitative study of adult human liver tissue showed that, in relation to the total protein amount of CYP3A enzymes, CYP3A5 only accounts for an average of 5.5%, while CYP3A4 constitutes 85.4% [51]. However, the contribution of CYP3A5 can increase to at least 50% due to the polymorphic nature of its expression, thus representing an important source of inter-individual heterogeneity in CYP3A-dependent drug clearance [52].

In contrast to CYP2D6, only nine allelic variants are currently known for CYP3A5, of which the alleles *1 (wild type), *3, *6, and *7 are most prevalent. Globally, CYP3A5 *3, resulting from an SNP at position 6986 (6986A>G) within intron 3, is the most relevant and best-studied allele, while CYP3A5 *6 (14690C>T) and *7 (27131_27132insA) play only a minor role. Each of these three alleles leads to the formation of a nonfunctional protein, either

by incorrect splicing (*3 and *6) or by frameshift mutation (*7) [43, 53]. Hence, *1/*1 carriers are classified as NMs, carriers of only one *1 allele as IMs, and individuals without any *1 allele as PMs [43].

Studies on the frequency distribution of the different *CYP3A5* alleles revealed a distinct trend (Figure 1.3.a): While in Caucasians *CYP3A5* *3 is the predominant variant and *CYP3A5* *1 only accounts for about 8% of alleles, in many African countries *CYP3A5* *1 is the main variant with an average prevalence of around 56% [43]. Interestingly, a trend can also be recognized within Africa: while *CYP3A5* *1 is the most common form in South and Southwest Africa, its proportion in East Africa averages less than 45%, while in North Africa only about 20% of *CYP3A5* alleles are of the *1 type [43, 54].

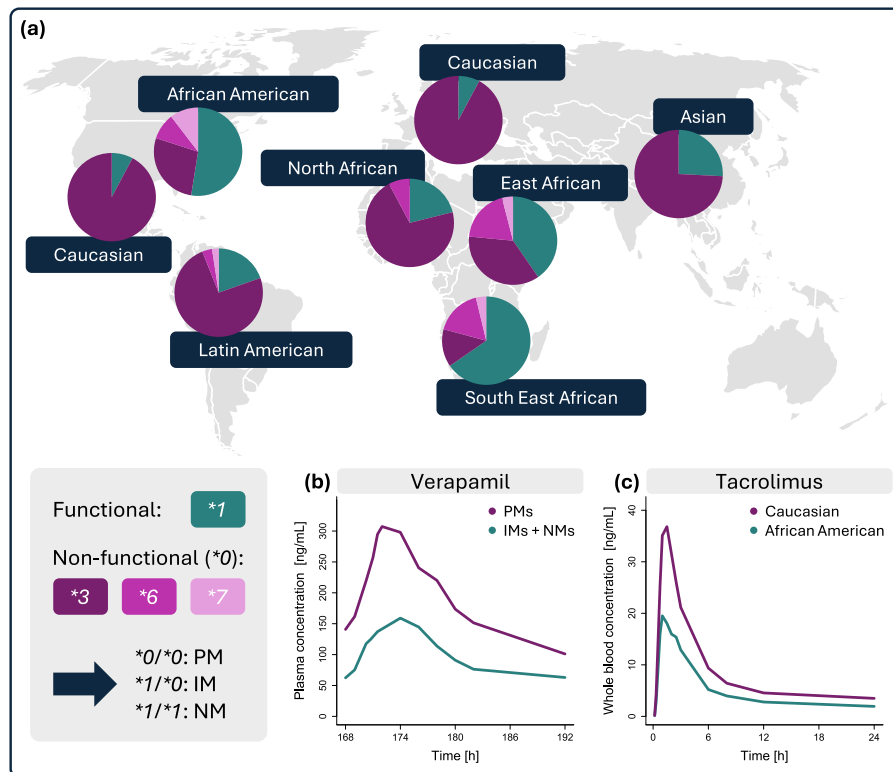


Figure 1.3: (a) Global frequency distribution of the different *CYP3A5* alleles and translation into phenotypes according to Birdwell et al. [43]. (b–c) Plasma / whole blood concentration-time profiles of the *CYP3A5* substrates (b) verapamil and (c) tacrolimus observed *in vivo*, stratified by *CYP3A5* phenotype and ethnicity, respectively [55, 56]. CYP: cytochrome P450, IM: intermediate metabolizer, NM: normal metabolizer, PM: poor metabolizer.

Given the potential *CYP3A5* activity range of no (PMs) to normal activity (NMs), the exposure of substrates mainly metabolized via *CYP3A5*, such as the immunosuppressant tacrolimus or the calcium channel blocker verapamil, can vary considerably, compromising treatment efficacy and safety. In the case of verapamil, for example, the area under the plasma concentration-time curve (AUC_{pl}) of R- and S-verapamil at steady state was reported to be 61% and 88% higher, respectively, in *CYP3A5* PMs compared

to a mixed study cohort of NMs and IMs (Figure 1.3.b, shown as racemic verapamil) [55]. Another study on oral administration of tacrolimus demonstrated the mentioned strong correlation between ethnicity and *CYP3A5* genotype, with a 61% higher area under the whole blood concentration-time curve (AUC_{wb}) measured in Caucasians versus African American study participants (Figure 1.3.c) [56]. Moreover, *CYP3A5* phenotype-dependency was observed not only for tacrolimus exposure but also urinary excretion. In *CYP3A5* PMs, a 2.4-fold higher amount of unchanged tacrolimus was measured in urine relative to a population of NMs and IMs, potentially increasing the risk of tacrolimus-induced nephrotoxicity in PMs [57].

1.3.3 *CYP3A4*

Although numerous polymorphic variants of the *CYP3A4* gene have been described in the literature, their general clinical relevance appears to be minor. In a global prevalence analysis of alleles across 12 CYP enzymes, Zhou et al. identified *CYP3A4* as the most conserved gene, with over 90% of alleles corresponding to the wild-type *1 allele [58]. Among the less common alleles, *CYP3A4* *22, characterized by reduced enzymatic activity, has attracted increasing scientific interest since its discovery in 2011 due to its demonstrated impact on the PK of several *CYP3A4* substrates [59, 60]. Overall, however, nongenetic factors are considered major contributors to the variability in *CYP3A4* metabolism, including perpetrator effects associated with DDIs, outlined in more detail in Section 1.4 [60, 61].

1.3.4 *CYP2D6*

As previously mentioned, the pharmacogenetic variability of the *CYP2D6* isotype has already been extensively studied and more than 160 different alleles have been documented to date (excluding subvariants) [36, 37]. This large quantity of alleles results in an even higher number of possible allele combinations, complicating genotype-phenotype translation and thus dose selection. Therefore, the so-called activity score (AS) system was introduced, according to which each *CYP2D6* allele is assigned a semiquantitative activity value of 0, 0.25, 0.5, 1 (corresponding to the reference activity of a *CYP2D6* *1 wild-type allele), or 2, which in total represents the AS value of the respective genotype [62, 63]. Based on this AS value, the phenotype is determined, where 0 corresponds to PM, 0.25–1 to IM, 1.25–2.25 to NM and anything over 2.25 to UM [63].

In contrast to *CYP3A5*, *CYP2D6* does not exhibit marked geographical and ethnic variability. Instead, a distribution study by Sistonen et al. showed the variation within a population to be greater than between populations (Figure 1.4.a) [64]. The most common variants identified were the functional alleles *CYP2D6* *1 (38%) and *2 (25%), the non-functional allele *4 (7%), as well as the reduced activity alleles *10 (11%) and *41 (7%). Interestingly, *CYP2D6* *10 only ranks this high because of its very pronounced prevalence

in East Asia (39%). It is also worth noting that gene duplications showed a relatively low frequency in all groups studied, except for the North African population, where a prevalence of 28% for the CNV *CYP2D6* *2xN was observed. This reflects the global distribution of phenotypes: NMs predominate across all populations analyzed, with a considerably higher frequency of UMs in North Africa and IMs in East Asia compared to the other regions [64].

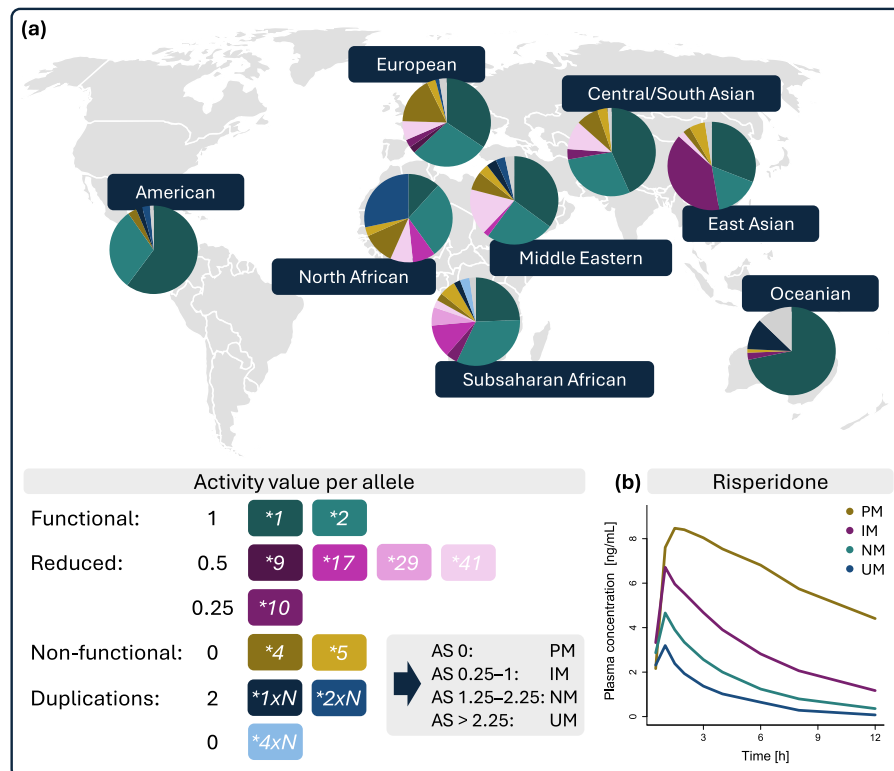


Figure 1.4: (a) Global frequency distribution of the different *CYP2D6* alleles according to Sistonen et al. [64] and translation into phenotypes [63]. Alleles with a frequency of less than 1% are summarized in gray. (b) Plasma concentration-time profiles of the *CYP2D6* substrate risperidone observed *in vivo*, stratified by *CYP2D6* phenotype [65]. AS: activity score, CYP: cytochrome P450, IM: intermediate metabolizer, NM: normal metabolizer, PM: poor metabolizer, UM: ultrarapid metabolizer.

The substantial effect of *CYP2D6* polymorphisms on the clearance of *CYP2D6* substrates and the resulting wide variation in exposure, necessitating activity-based dose adjustments, has been demonstrated in numerous studies investigating a broad range of AS values and phenotypes. In the case of the antihypertensive drug metoprolol, for instance, 13.8-fold and 9.5-fold higher AUC_{pl} values were observed for R- and S-metoprolol, respectively, in *CYP2D6* PMs compared to UMs [66]. Another example is the neuroleptic agent risperidone. Here, *CYP2D6* PMs were shown to exhibit a 14.7-fold higher exposure in relation to UMs (Figure 1.4.b) [65].

1.4 DRUG-DRUG INTERACTIONS AND CLINICAL IMPLICATIONS

1.4.1 *Overview*

DDIs, both adverse and intended, can arise whenever two or more drugs are administered concurrently [67]. The present thesis focuses on the assessment of PK-related interactions, where “victim” refers to the drug whose PK is influenced, and “perpetrator” indicates the drug affecting the victim’s PK.

Depending on the mechanism of interaction, perpetrators can interfere with different ADME processes. For instance, a victim’s absorption can be altered by a change in gastric pH following concomitant administration of pH-increasing agents, among other factors. In the context of distribution, a victim can be displaced from the plasma protein binding by drugs possessing a higher affinity for the same binding site, thereby increasing the victim’s passive diffusion [68]. Metabolic DDIs constitute the largest and best-studied subgroup of DDIs, with the CYP enzyme family being particularly relevant [35, 69]. Also of clinical importance, but less well understood, are transporter-mediated DDIs [70]. Depending on the transporter location, i.e. intestinal, hepatic, or renal transporter, a victim’s absorption, distribution, and/or excretion can be affected [68, 71]. Key transporters associated with DDIs include the efflux transporter P-glycoprotein (P-gp) and uptake transporters of the organic-anion-transporting polypeptide (OATP) family [72, 73].

In addition to active ingredients, food components can also influence a drug’s ADME processes, commonly referred to as “food effect”, for example by prolonging the gastric emptying time or increasing the gastrointestinal pH value. The underlying mechanisms are diverse and depend on both the food category, e.g. high-fat versus high-protein foods, and the properties of the drug, e.g. specific versus non-specific absorption window in the gastrointestinal tract [74].

The present work mainly examines metabolism- and transport-related DDIs resulting from a perpetrator inducing or inhibiting an enzyme or transporter. While induction processes cause an increase in enzyme or transporter levels, leading to accelerated metabolism or transport of the respective victim drug [68], inhibition processes reduce enzyme or transporter activity and thus the metabolism or transport rate [69].

As most drugs possess a certain interaction potential, whether as a substrate, inducer, and/or inhibitor, so-called index DDI studies are conducted during drug development to analyze the role of an investigational drug in DDI scenarios. For this, the US Food and Drug Administration (FDA) curates a list of official index victim and perpetrator drugs [23, 75]. In addition, the FDA maintains a registry of clinical CYP enzyme and transporter substrates, inducers, and inhibitors serving as a resource for healthcare professionals to evaluate the DDI potential of drugs in clinical practice [76].

The more than 200 substances listed illustrate specifically the CYP_{3A4} isozyme as an important source of DDIs, as it is not only involved in the metabolism of more than 50% of drugs but is also targeted by 37% of inducers and 42% of inhibitors (Figure 1.5) [76].

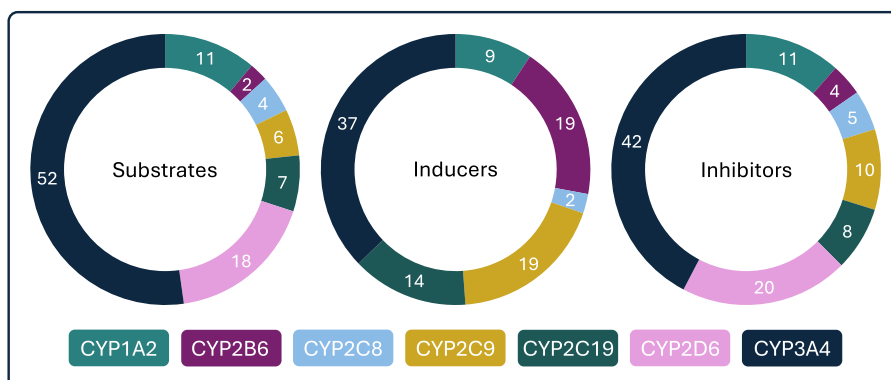


Figure 1.5: Percentage-based classification of FDA-listed substrates, inducers, and inhibitors by CYP enzyme [76]. CYP: cytochrome P450, FDA: US Food and Drug Administration.

In the following sections, the different types of metabolic and transport interactions are described in more detail, with selected interaction scenarios illustrating their critical effects on clinical efficacy and toxicity.

1.4.2 Induction

Most induction processes are mediated by the binding of perpetrators to specific ligand-activated transcription factors such as the pregnane X receptor (PXR) or constitutive androstane receptor (CAR) [77]. In the human body, PXR and CAR regulate the transcription of numerous target genes, thus when activated by an inducer, an increased *de novo* synthesis of the enzyme or transporter encoded by the respective gene is triggered (Figure 1.6.a) [77–79]. In the case of PXR, the regulation of CYP_{3A4} is best studied, while the primary target gene of CAR is CYP_{2B6} [77, 80].

The clinical relevance of induction processes can be exemplified by the effect of the potent CYP_{3A4} inducer rifampicin on the clearance of the CYP_{3A4} substrate and anticancer agent imatinib [81, 82]. Pretreatment with rifampicin was shown to reduce the AUC_{pl} of imatinib by 74%, increasing the risk of nonresponse to therapy and hence disease progression (Figure 1.6.b) [81].

However, induction-mediated DDIs pose a considerable challenge in clinical practice not only due to the decreasing effect on drug exposure, but also because the increase in enzymatic activity only slowly returns to normal levels after discontinuation of the inducer, as has been illustrated for the CYP_{3A4} substrate midazolam. After an initial reduction of 88%, the AUC_{pl} of midazolam was still decreased by 62% one week after ending rifampicin pretreatment, and even after two weeks only 82% of the control exposure was reported [83].

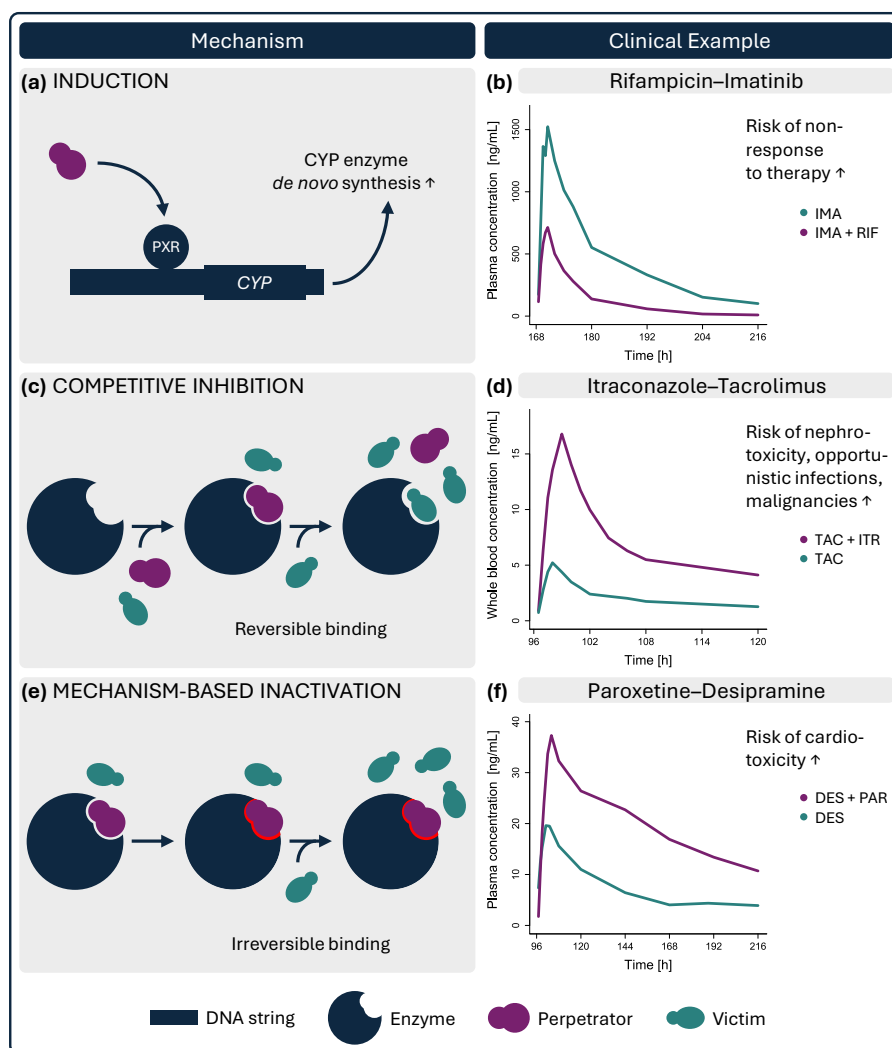


Figure 1.6: Schematic description of different drug-drug interaction mechanisms (adapted from Deodhar et al. [69] and Willson and Kliever [84]) and effects observed *in vivo*, exemplified by enzymatic interactions. (a) Induction: A perpetrator binds to and activates specific ligand-activated transcription factors such as the PXR, thereby increasing the *de novo* synthesis of corresponding enzymes: (b) Effect of pretreatment with the CYP_{3A4}/CYP_{2C8} inducer rifampicin on the exposure of imatinib [81]. (c) Competitive inhibition: A perpetrator competes reversibly with the victim for the active site of an enzyme: (d) Effect of pretreatment with the CYP_{3A} competitive inhibitor itraconazole on the exposure of tacrolimus [85]. (e) Mechanism-based inactivation: A perpetrator binds reversibly to the active site of an enzyme and is subsequently converted into a reactive intermediate species which irreversibly forms a stable covalent complex with the enzyme: (f) Effect of pretreatment with the CYP_{2D6} mechanism-based inactivator paroxetine on the exposure of desipramine [86]. CYP: cytochrome P₄₅₀, DES: desipramine, DNA: deoxyribonucleic acid, IMA: imatinib, ITR: itraconazole, PAR: paroxetine, PXR: pregnane X receptor, RIF: rifampicin, TAC: tacrolimus.

1.4.3 Inhibition

Based on the underlying mechanism, inhibition processes can be subdivided into reversible inhibition processes such as competitive and non-competitive inhibition, and irreversible inhibition processes, for example mechanism-based inactivation [69].

Competitive inhibition involves two substrates competing for the active site of an enzyme or transporter, i.e. the site where a compound binds to be metabolized or transported, typically resulting in the substrate with the higher binding affinity acting as perpetrator displacing the victim [69]. However, since the perpetrator's binding is reversible, competitive inhibition can be overcome by a sufficiently large increase in the victim's concentration (Figure 1.6.c) [68, 69].

In the case of the less frequent non-competitive inhibition, victim and perpetrator do not compete for the same binding site. Rather, the perpetrator causes a conformational change in the active site of the enzyme or transporter by binding to the allosteric site, thereby lowering the affinity for the victim, which cannot be reversed by increasing the victim's concentration [69].

Mechanism-based inactivation on the other hand is characterized by an initial reversible binding of a perpetrator to the active site, followed by its conversion to a reactive intermediate species which irreversibly forms a stable covalent complex with the respective target thus preventing further enzymatic activity (Figure 1.6.e). The intrinsic activity level can only be restored through *de novo* synthesis of the affected protein [69]. In contrast to reversible inhibition, the activity therefore remains reduced for a certain time even after discontinuation of the inactivator [87, 88].

Inhibition processes can severely impair treatment safety due to a potentially toxic increase in victim exposure. For instance, pretreatment with the competitive CYP3A inhibitor itraconazole led to a 3.3-fold higher AUC_{wb} of tacrolimus, elevating the risk of nephrotoxicity, opportunistic infections, and malignancies (Figure 1.6.d) [85, 89]. Another example is the mechanism-based CYP2D6 inactivator paroxetine, which was shown to increase the exposure of the antidepressant desipramine by 3.8-fold, resulting in an enhanced likelihood of desipramine-induced cardiotoxicity (Figure 1.6.f) [86, 90].

Furthermore, drugs can influence their own metabolism via autoinhibition, potentially altering enzymatic contributions to the overall metabolism and thus complicating assessment of perpetrator effects, as seen in the case of imatinib [91]. Here, mechanism-based inactivation of CYP3A4 leads to an increased role of CYP2C8 upon multiple dose administration [92].

1.5 DRUG-DRUG-GENE INTERACTIONS AND CLINICAL IMPLICATIONS

DDGIs are characterized by the combined effect of co-medication and genetic influences on a drug's exposure [12] due to a variety of underlying mechanisms (Figure 1.7).

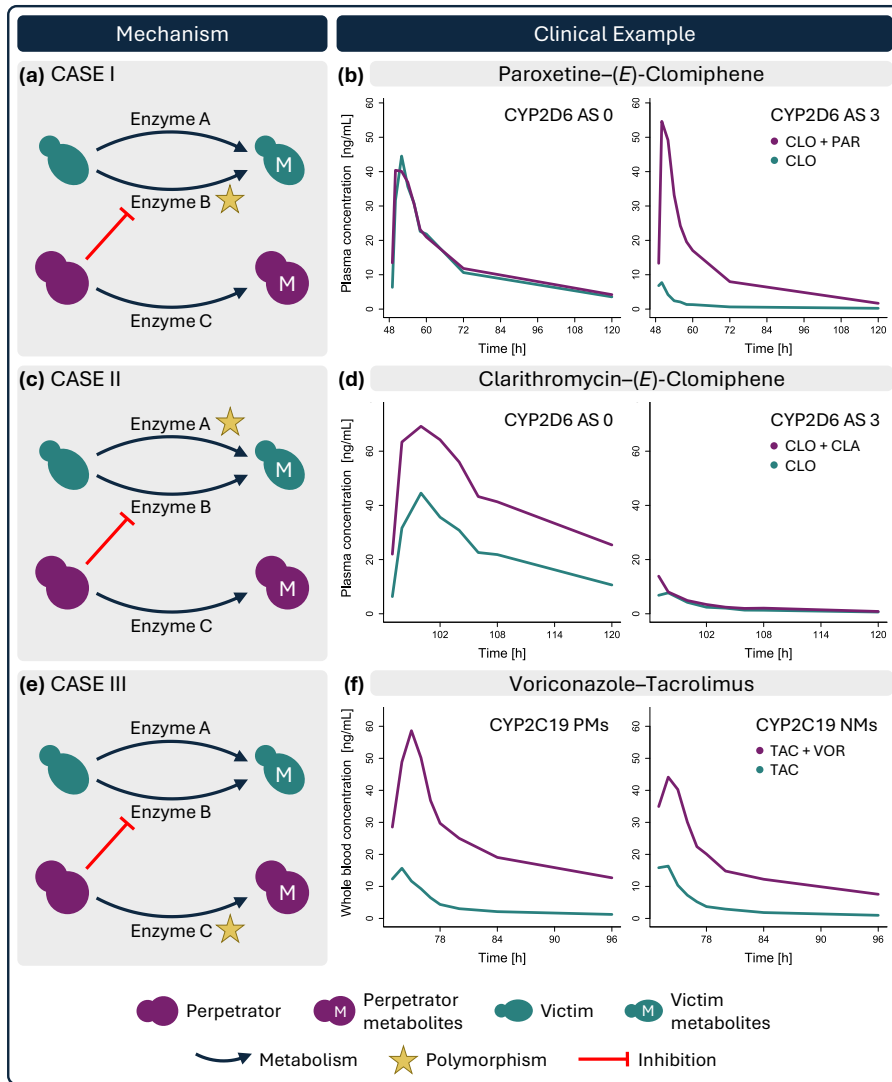


Figure 1.7: Schematic description of different drug-drug-gene interaction mechanisms and effects observed *in vivo*, using the example of inhibitors. (a) Case I: A perpetrator inhibits a polymorphically expressed enzyme involved in the victim's metabolism: (b) Effect of pretreatment with the CYP2D6 inhibitor paroxetine on the exposure of the CYP2D6/CYP3A4 substrate (E)-clomiphene depending on the CYP2D6 AS value [93]. (c) Case II: A polymorphically expressed enzyme contributes to the victim's metabolism, while a perpetrator inhibits another enzyme involved in the victim's degradation: (d) Effect of pretreatment with the CYP3A4 inhibitor clarithromycin on the exposure of (E)-clomiphene depending on the CYP2D6 AS value [93]. (e) Case III: A polymorphically expressed enzyme is involved in the perpetrator's metabolism: (f) Effect of pretreatment with the CYP3A inhibitor and CYP2C19 substrate voriconazole on the exposure of the CYP3A substrate tacrolimus depending on the CYP2C19 phenotype [94]. AS: activity score, CLA: clarithromycin, CLO: (E)-clomiphene, CYP: cytochrome P450, NM: normal metabolizer, PAR: paroxetine, PM: poor metabolizer, TAC: tacrolimus, VOR: voriconazole.

Perhaps the most straightforward case involves a perpetrator of a particular enzyme exerting different effects on a victim's PK, depending on the activity level of said enzyme (Figure 1.7.a). For example, following pretreatment with the CYP2D6 inhibitor paroxetine, only a 1.1-fold higher AUC_{pl} of the CYP2D6 substrate (*E*)-clomiphenes was observed in CYP2D6 PMs compared to a substantial increase of up to 12.5-fold in UMs (Figure 1.7.b) [93]. A temporary shift in phenotype, known as phenoconversion, occurs when the influence of a perpetrator drug overrides the effect of the individual's genotype [95].

However, DDGIs also arise when a polymorphically expressed enzyme contributes to the metabolism of a victim, while a co-administered perpetrator targets another enzyme also involved in the victim's degradation (Figure 1.7.c). For instance, (*E*)-clomiphenes is metabolized by CYP3A4 in addition to CYP2D6, with reduced CYP2D6 activity leading to an increased contribution of CYP3A4 to the overall metabolism. Accordingly, pretreatment with the CYP3A4 inhibitor clarithromycin led to a 2.1-fold higher exposure of (*E*)-clomiphenes in CYP2D6 PMs, whereas only a 1.1-fold increase was reported in CYP2D6 UMs (Figure 1.7.d) [93].

Furthermore, the inducing/inhibiting influence of a perpetrator may vary due to polymorphism-related differences in perpetrator exposure (Figure 1.7.e). For example, the effect of the CYP3A inhibitor and CYP2C19 substrate voriconazole on the AUC_{wb} of tacrolimus was observed to be more pronounced in CYP2C19 PMs relative to NMs, with a 6.0-fold versus 4.4-fold increase in tacrolimus exposure, respectively (Figure 1.7.f) [94].

In clinical practice, the diverse DDGI mechanisms often occur in complex combinations, as multiple therapy-relevant polymorphisms are involved, and concurrently administered drugs may mutually affect each other's PK.

1.6 PHYSIOLOGICALLY BASED PHARMACOKINETIC MODELING

In PBPK modeling, physiological organs/tissues of a body are represented by compartments connected via the circulating blood system (Figure 1.8) [96, 97]. Based on ordinary differential equations, describing the mass balance between the individual compartments, the impact of passive and active ADME processes on a drug's PK can be described and predicted [97].

The complexity of PBPK models necessitates a vast number of input parameters (Figure 1.8): System-dependent characteristics, such as organ volumes, tissue composition, blood flow rates, and protein abundance, are used to establish the physiological framework [98]. Commercial PBPK platforms usually provide corresponding data for an "average individual" [96, 97]. Drug-dependent parameters describe the physicochemical properties of a drug, such as molecular weight, lipophilicity, and acid dissociation constants [97, 98]. Process-related parameters, such as plasma protein binding or transport/metabolism-related measures, depend on both the organism and the drug. Lastly, clinical study data are required for model development, including demographic data of study participants, study protocols, and concentration-time profiles measured in e.g. plasma [98].

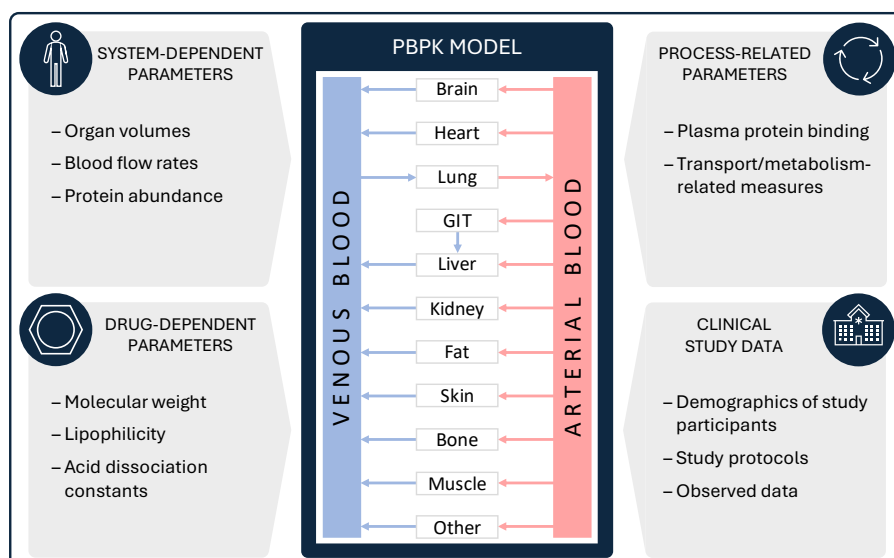


Figure 1.8: Schematic overview of a whole-body PBPK model including examples of system-dependent, drug-dependent, and process-related parameters as well as clinical study data needed for model building. PBPK: physiologically based pharmacokinetic, GIT: gastrointestinal tract.

Although the principle of PBPK modeling was first described in 1937, its practical application has only become increasingly established in recent decades, due in part to technological advances and easier access to *in vitro* data [97, 99]. In contrast to empirical models, the mechanistic nature of PBPK modeling allows extrapolation outside the investigated population and experimental conditions [26, 96]. The resulting possibilities for scaling, e.g. to children [100] or pregnant women [101], as well as mechanistic study of a drug's properties enable a wide range of use cases in the context of both MID₃ and clinical practice [96, 102].

In general, a significant and steady increase in PBPK-related publications can be observed [103]. A review article lists the modeling of DDIs as the largest area of application (28%), followed by general clinical PK (23%), absorption (12%), age (10%), allometry (6%), transport (4%), biologics (4%), pharmacogenetics (4%), pregnancy (2%), and hepatic/renal impairment (2%) [104]. This thesis primarily focuses on the usage of PBPK modeling for the prediction of complex drug interactions.

OBJECTIVES

The overarching objective of this thesis was to illustrate and advance PBPK modeling as a framework for individualized therapy by (i) developing whole-body PBPK models for the CYP₃A substrates tacrolimus, imatinib, and dasatinib, (ii) conducting model-based analyses of diverse interaction effects specifically regarding CYP₃A and CYP₂D6 DD(G)Is, and by (iii) demonstrating the broad applicability of PBPK modeling to address the complexity of real-world drug interactions in therapy decisions.

In line with these objectives, the present work was conducted as part of the ERACoSysMed INSPIRATION project funded by the European Union's Horizon 2020 research and innovation programme, which aimed to establish clinically applicable DDGI models with the purpose of guiding drug treatment [105].

To achieve this, the project consortium held interdisciplinary discussions to identify substances suitable for DDGI modeling based on data availability and therapeutic importance. Among other drugs, tacrolimus, imatinib, and dasatinib were selected as clinically relevant drug candidates for precision dosing. In addition, the CYP₂D6 enzyme was chosen as a key target when addressing DDGIs in clinical practice.

2.1 PROJECT I: PBPK MODELING OF TACROLIMUS

Objectives of project I were (i) to develop a whole-body PBPK model for the immunosuppressant and CYP₃A substrate tacrolimus and (ii) to investigate and model the impact of different CYP₃A5 activity levels, food intake, and DD(G)I scenarios involving several CYP₃A perpetrators on the PK of tacrolimus.

2.2 PROJECT II: PBPK MODELING OF IMATINIB

Objectives of project II were (i) to develop a whole-body PBPK model for the anticancer agent and CYP₂C8/CYP₃A₄/P-gp substrate imatinib and its main metabolite N-desmethyl imatinib (NDMI), including studying and implementing the effects of CYP₃A₄ autoinhibition on imatinib PK, and (ii) to investigate and model imatinib and NDMI as both victim and perpetrator drugs in various DDI scenarios.

2.3 PROJECT III: PBPK MODELING OF DASATINIB

Objectives of project III were (i) to develop a whole-body PBPK model for the anticancer agent and CYP3A4 substrate dasatinib, (ii) to investigate and model the effect of co-administered perpetrator drugs on dasatinib PK, and (iii) to simulate clinically untested DDI scenarios focusing on dasatinib as victim drug, with subsequent model-informed dose adaptations. In addition, the influence of food intake on dasatinib exposure was modeled.

2.4 PROJECT IV: CYP2D6 DDGI NETWORK MODELING

Objectives of project IV were (i) to develop a comprehensive CYP2D6 DDGI network expanding and integrating existing networks with CYP2D6 victim and perpetrator PBPK models, (ii) to validate the network for the prediction of CYP2D6 DGIs, DDIs, and DDGIs, as well as (iii) to simulate clinically untested DDGI scenarios for selected CYP2D6 substrates and generate corresponding model-informed dose adaptations.

METHODS

3.1 COMPOUNDS SELECTED FOR PBPK BASE MODELING

In projects I–III, PBPK base models were developed for the clinically relevant drugs tacrolimus, imatinib, and dasatinib, which are widely applied in immunology/transplantation and oncology and display considerable PK variability [82, 106–110]. The following sections provide a more detailed overview of the challenges associated with their use and current dosing tactics.

3.1.1 *Tacrolimus*

For over 30 years, the calcineurin inhibitor tacrolimus has been the mainstay of immunosuppressive therapy to prevent graft rejection following solid organ transplantation, despite the many challenging aspects of its clinical use [106]. A high degree of inter- and intra-individual PK variability in combination with tacrolimus being an NTI drug not only increases the likelihood of under- and overdosing, but also the risk of subsequent transplant rejection and toxic effects such as nephro- and neurotoxicity, opportunistic infections, and malignancies [89, 107].

Numerous endogenous and exogenous factors have been identified as contributing to the high PK heterogeneity observed. Since tacrolimus is metabolized mainly via CYP3A4 and CYP3A5, its PK is greatly influenced not only by genetic polymorphisms, especially in the CYP3A5 gene [56, 57], but also co-administration of CYP3A perpetrators [85, 94, 111, 112]. In clinical practice, CYP3A-inhibiting azole antimycotics are particularly relevant, as they are often co-prescribed with tacrolimus for the treatment of post-transplant invasive fungal infections [43, 113]. For instance, pretreatment with ketoconazole increases the AUC_{wb} of tacrolimus by 2.9-fold [112]. Furthermore, tacrolimus exhibits a marked food effect, with its maximum whole blood concentration ($C_{\max,wb}$) reduced by up to 77% when taken with meals [114, 115].

To account for individual differences in CYP3A5 activity levels in tacrolimus therapy, the CPIC has provided CYP3A5 phenotype-guided dose recommendations [43]. Moreover, therapeutic drug monitoring (TDM) of tacrolimus whole blood levels and subsequent dose adjustments are routinely performed in clinical practice to indirectly compensate for multiple factors concurrently affecting the PK of tacrolimus [89].

3.1.2 *Imatinib*

More than 20 years ago, approval of the tyrosine kinase inhibitor (TKI) imatinib not only paved the way for a new era in the treatment of chronic myeloid leukemia (CML) but also laid the foundation for the broader field of targeted cancer therapy [109]. Since then, second- and third-generation TKIs such as dasatinib have been developed to overcome resistance to imatinib, primarily caused by mutations in the target oncogene *BCR-ABL* [116]. Nevertheless, imatinib continues to be a primary treatment option for CML and has since been approved for the therapy of further diseases, including acute lymphoblastic leukemia (ALL) and gastrointestinal stromal tumors [82].

Imatinib is largely metabolized via CYP2C8 and CYP3A4 and transported by several proteins, such as P-gp [92, 117]. Its main metabolite, NDMI, represents 10%–15% of the total drug level [118] and displays about one-third of the pharmacological potency exhibited by imatinib [119].

The clinical application of imatinib is complicated by a high inter- and intra-individual variability in PK and marked susceptibility to complex DDI scenarios [108]. While co-administered perpetrator drugs affect the PK of imatinib and NDMI [81, 92, 120], both compounds influence their own degradation as well as the metabolism of co-medications via considerable (auto)inhibition of CYP3A4 and to a lesser extent of CYP2C8 [91, 121]. The exposure of imatinib is, for example, increased by 40% and decreased by 74% when taken with ketoconazole, a CYP3A4 inhibitor, and rifampicin, a CYP3A4 inducer, respectively [81, 120]. Acting as a perpetrator, on the other hand, imatinib causes a 2.6-fold rise in the AUC_{pl} of simvastatin's active metabolite through mechanism-based inactivation of CYP3A4 [121].

Given the potentially intricate interplay between these interactions, standardized imatinib dosing regimens entail an increased risk of sub- or supratherapeutic imatinib plasma levels, leading to treatment failure or toxic effects such as neutropenia, edema, and fluid retention [109, 122]. Although the consensus guidelines of the International Association of TDM and Clinical Toxicology (IATDMCT) conclude that TDM of imatinib can compensate PK variability and toxicity as well as improve efficacy [108], imatinib is still typically dosed according to the “one-size-fits-all” principle [28].

3.1.3 *Dasatinib*

As a dual inhibitor of *BCR-ABL* and *SRC* kinases, the second-generation TKI dasatinib mitigates the impact of mutations in the *BCR-ABL* oncogene on therapeutic response [123, 124]. More than 15 years ago, it was specifically designed and approved for the treatment of CML and ALL in cases of resistance or intolerance towards other TKIs, including imatinib [125]. Today, dasatinib, like imatinib, is one of the frontline treatments for CML [109].

Despite the lower risk of resistance, dasatinib therapy is still associated with numerous challenges: Its highly CYP3A4-dependent metabolism [126]

results in considerable changes in exposure when co-administered with CYP3A4 inhibitors or inducers. While ketoconazole causes a 4.8-fold increase in dasatinib AUC_{pl} , rifampicin reduces its exposure by 84% [127, 128]. Since dasatinib itself exhibits weak inhibition of CYP2C8, CYP3A4, and several transporters, it can also affect the PK of concurrent medications [129–131]. Furthermore, dasatinib’s absorption shows marked sensitivity to shifts in gastric pH, with its AUC_{pl} reduced by up to 78% in the presence of pH-elevating agents [132]. Additionally, studies have demonstrated a certain impact of high-fat meals on dasatinib PK, moderately increasing the time to peak plasma concentration ($T_{max,pl}$) and AUC_{pl} while decreasing the maximum plasma concentration ($C_{max,pl}$) by about one-fourth compared to fasted conditions [128].

Not considering these interaction effects when determining dasatinib dosage regimens increases the risk of clinically relevant consequences: While subtherapeutic concentrations can lead to a potentially serious loss of efficacy, supratherapeutic exposure carries the risk of side effects such as myelosuppression or pleural effusions [109]. Studies have shown that TDM of dasatinib and subsequent dose adjustments can reduce the frequency of pleural effusions [110, 133]. However, since there is presently no consensus on the use of TDM for dasatinib, it is still dosed following the “one-size-fits-all” principle, like imatinib [28, 110].

3.2 SOFTWARE

PBPK base model development, including parameter identification processes and local sensitivity analyses, as well as interaction network creation were performed using the open-source modeling software PK-Sim® and its partner program MoBi® versions 10.0 (project I) and 11.0 (projects II–IV) (Open Systems Pharmacology (OSP) Suite, www.open-systems-pharmacology.org, 2021 and 2022). Applying best practices [134], collected clinical study data was digitized via Engauge Digitizer version 12.1 (projects I, II, and IV; M. Mitchell, <https://markummittchell.github.io/engauge-digitizer/>, 2019) and GetData Graph Digitizer version 2.26.0.20 (project III; © S. Fedorov, 2017). For evaluating the developed PBPK base models and simulated interaction scenarios, the R programming language versions 4.2.1 (projects I and III), 4.2.3 (project II), and 4.3.0 (project IV) were utilized to create plots as well as calculate PK parameters and prediction performance metrics (R Foundation for Statistical Computing, Vienna, Austria, 2022 and 2023) [1–4].

3.3 PBPK BASE MODEL DEVELOPMENT

The PBPK base models for tacrolimus, imatinib, and dasatinib (projects I–III) were built and evaluated according to the same general concept, summarized in the following sections. Substance-specific details can be found in the respective publications [1–3].

3.3.1 Base Model Building

For each selected compound and corresponding metabolite, where applicable, a thorough literature search for clinical study data, physicochemical characteristics, and ADME-related information was conducted prior to model building [1–3].

The gathered plasma or whole blood concentration-time profiles were allocated to a training dataset for model development and a test dataset for model evaluation. Profiles were assigned in a non-randomized manner to form an information-rich training dataset covering a wide range of dosing regimens, different routes of administration, and profiles consisting of many sampling points over a long period of time, while keeping the test dataset as large as possible [1–3].

A virtual individual was designed for each study population based on the published average and mode for age, sex, weight, height, body mass index, and ethnicity to generate model simulations. In the case of missing or partially reported demographic characteristics, a standard individual was created using the population database embedded in PK-Sim®. Relative enzyme and transporter abundances in the individual organs were implemented according to the expression database in PK-Sim®, with the corresponding reference concentration in the organ of highest expression either obtained from the expression database or calculated from literature data [1–4, 135].

To explore the impact of variability in demographics and enzyme/transporter expression levels on the PK of the modeled compounds, virtual populations of 1000 individuals (projects I, II, and IV) or 100 individuals (project III) were established for each study cohort based on provided demographic ranges or an assumed age range of 20–50 years if no information was reported. Moreover, geometric standard deviations of relevant enzyme/transporter concentrations, were provided by the PK-Sim® ontogeny database or derived from *in vitro* data [1–4, 136].

Drug release from oral dosage forms was modeled as a Weibull function (Equation 3.1 [137]). Metabolism and transport processes were implemented either as first-order (Equation 3.2) or Michaelis–Menten kinetics (Equation 3.3), depending on the literature data [1–3].

$$f_d(t) = 1 - \exp\left(\frac{-(t - t_{lag})^b}{a}\right) \quad (3.1)$$

where $f_d(t)$ = fraction of administered dose dissolved at time t , t_{lag} = lag time between drug intake and start of the dissolution process, b = shape parameter, and a = scale parameter.

$$v = CL_{spec} \cdot [E] \cdot [S] \quad (3.2)$$

where v = reaction velocity, CL_{spec} = specific enzymatic clearance, $[E]$ = enzyme concentration, and $[S]$ = free substrate concentration.

$$v = \frac{v_{max} \cdot [S]}{K_M + [S]} = \frac{k_{cat} \cdot [E] \cdot [S]}{K_M + [S]} \quad (3.3)$$

where v = reaction velocity, v_{max} = maximum reaction velocity, $[S]$ = free substrate concentration, K_M = Michaelis–Menten constant, k_{cat} = catalytic rate constant, and $[E]$ = enzyme concentration.

Model input parameters not available in the literature or essential for the quantitative structure-activity relationship (QSAR) calculation methods for permeability and partition in PK-Sim® were optimized during the parameter identification phase using the training dataset. Different metabolic pathways were informed by integrating either concentration-time profiles obtained in PMs of an involved enzyme, *in vitro* fractional contributions of relevant enzymes to the overall metabolism, or clinical DDI study data into the training dataset [1–3].

3.3.2 Base Model Evaluation

The predictive performance of the PBPK base models was assessed visually and quantitatively. First, observed plasma or whole blood concentration-time profiles and corresponding model predictions were plotted and compared. For each observed profile, the deviation of predicted versus *in vivo* AUC_{pl}/AUC_{wb} determined between first and last concentration measurements ($AUC_{last,pl}/AUC_{last,wb}$) and $C_{max,pl}/C_{max,wb}$ values as well as concentration measurements were calculated and displayed in goodness-of-fit plots. A twofold deviation between observed and predicted values was defined as prediction success threshold. In addition, mean relative deviations (MRDs) for predicted concentration-time measurements as well as geometric mean fold errors (GMFEs) for predicted $AUC_{last,pl}/AUC_{last,wb}$ and $C_{max,pl}/C_{max,wb}$ values were calculated according to Equation 3.4 and Equation 3.5, respectively [1–3].

$$MRD = 10^x; \quad x = \sqrt{\frac{\sum_{i=1}^k (\log_{10} \hat{c}_i - \log_{10} c_i)^2}{k}} \quad (3.4)$$

where c_i = i -th observed concentration, \hat{c}_i = predicted concentration corresponding to the i -th observed concentration, and k = number of observed values.

$$GMFE = 10^x; \quad x = \frac{\sum_{i=1}^m \left| \log_{10} \left(\frac{\hat{\rho}_i}{\rho_i} \right) \right|}{m} \quad (3.5)$$

where ρ_i = observed $AUC_{last,pl}/AUC_{last,wb}$ or $C_{max,pl}/C_{max,wb}$ value of study i , $\hat{\rho}_i$ = corresponding predicted $AUC_{last,pl}/AUC_{last,wb}$ or $C_{max,pl}/C_{max,wb}$ value of study i , and m = number of studies.

Finally, a local sensitivity analysis was performed for each modeled compound, determining the sensitivity of the respective $AUC_{last,pl}/AUC_{last,wb}$ to single parameter value changes according to Equation 3.6. Depending on the project, a relative perturbation of either 1000% (variation range 10.0, maximum number of 9 steps; projects I and III) or 10% (variation range 0.1, maximum number of 2 steps; project II) was applied, with the threshold for sensitivity specified as $|0.5|$. Parameters were included if they were optimized and/or assumed to influence $AUC_{last,pl}/AUC_{last,wb}$, e.g. due to their involvement in the QSAR calculation methods of PK-Sim® [1–3].

$$S = \frac{\Delta AUC_{last}}{\Delta p} \cdot \frac{p}{AUC_{last}} \quad (3.6)$$

where S = sensitivity, ΔAUC_{last} = change of $AUC_{last,pl}/AUC_{last,wb}$, Δp = change of the analyzed parameter value, p = original parameter value, and AUC_{last} = simulated $AUC_{last,pl}/AUC_{last,wb}$ at the original parameter value.

3.4 PBPK INTERACTION MODEL DEVELOPMENT

Within the projects of this work, new and existing PBPK base models were used to build and evaluate different types of interaction models, further described in the following sections.

3.4.1 DGI Model Building

In project I, the influence of different CYP3A5 activity levels on the PK of tacrolimus was investigated, while in project IV, CYP2D6 DGI scenarios with several CYP2D6 substrates were simulated. For both projects, the literature was searched for clinical DGI studies which stratified participants by phenotype, genotype, or AS value of CYP3A5 or CYP2D6 and reported corresponding concentration-time profiles. Analogous to the model building procedure for PBPK base models, a virtual mean individual and virtual population were created for each study cohort [1, 4].

In the respective models, different enzymatic activity levels were implemented by applying activity-specific catalytic rate constant (k_{cat}) values, while keeping the Michaelis–Menten constant (K_M) unchanged [1, 4]. CYP3A5 activity was adjusted relative to NMs (100% activity) based on the reported frequency of functional CYP3A5 *1 alleles in each study population. Accordingly, for CYP3A5 PMs, 0% activity was assumed. If no genotyping/phenotyping data were available, ethnicity-based activity levels were incorporated, derived from published prevalence information for CYP3A5 *1 by Birdwell et al. [1, 43]. In the case of CYP2D6, NMs with an AS value of 2 and PMs were assigned activities of 100% and 0%, respectively, with k_{cat} values adjusted according to each study cohort's phenotype or AS value, as described in the original publications of the utilized CYP2D6 substrate models. In the absence of genetic information, the NM phenotype was assumed [4].

3.4.2 DDI Model Building

Metabolic and transport DDI networks were established across all projects. Networks developed for projects I–III centered around the respective model compounds tacrolimus, imatinib, and dasatinib, whereas project IV examined CYP2D6 substrates. For each project, a literature search was conducted for applicable clinical DDI study data. Studies were included if PBPK models were available for the respective victim and perpetrator drugs and concentration-time profiles of the victim with and without perpetrator co-administration were reported. For each study population, a virtual mean individual and virtual population were generated [1–4].

Victim and perpetrator models not developed in the context of this work were taken from the literature (<https://github.com/Clinical-Pharmacy-Saarland-University>, <https://github.com/Open-Systems-Pharmacology>) and adapted as needed. To simulate DDI scenarios, corresponding victim and perpetrator models were linked with relevant interaction mechanisms, i.e. competitive and non-competitive inhibition, mechanism-based inactivation, induction, and down-regulation, implemented according to Equations 3.7–3.12 [1–4, 137].

$$K_{M,app} = K_M \cdot \left(1 + \frac{[CI]}{K_i}\right) \quad (3.7)$$

$$v = \frac{v_{max} \cdot [S]}{K_{M,app} + [S]} = \frac{k_{cat} \cdot [E] \cdot [S]}{K_{M,app} + [S]} \quad (3.8)$$

where $K_{M,app}$ = apparent Michaelis–Menten constant in the presence of the inhibitor, K_M = Michaelis–Menten constant, $[CI]$ = free competitive inhibitor concentration, K_i = dissociation constant of the inhibitor-enzyme/transporter complex, v = reaction velocity, v_{max} = maximum reaction velocity, $[S]$ = free substrate concentration, k_{cat} = catalytic or transport rate constant, and $[E]$ = enzyme concentration.

$$v_{max,app} = \frac{v_{max}}{1 + \frac{[NCI]}{K_i}} \quad (3.9)$$

$$v = \frac{v_{max,app} \cdot [S]}{K_M + [S]} \quad (3.10)$$

where $v_{max,app}$ = apparent maximum reaction velocity in the presence of the inhibitor, v_{max} = maximum reaction velocity, $[NCI]$ = free non-competitive inhibitor concentration, K_i = dissociation constant of the inhibitor-enzyme/transporter complex, v = reaction velocity, $[S]$ = free substrate concentration, and K_M = Michaelis–Menten constant.

$$\frac{d[E]}{dt} = k_{deg} \cdot E_0 - \frac{k_{deg} + k_{inact} \cdot [MBI]}{K_I + [MBI]} \cdot [E] \quad (3.11)$$

where $\frac{d[E]}{dt}$ = enzyme turnover, k_{deg} = degradation rate constant, E_0 = enzyme concentration at time 0, k_{inact} = maximum inactivation rate constant, $[MBI]$ = free mechanism-based inactivator concentration, K_I = concentration for half-maximal inactivation, and $[E]$ = enzyme concentration.

$$\frac{d[E]}{dt} = k_{deg} \cdot E_0 \cdot \frac{1 + (E_{max} \cdot [Ind])}{EC50 + [Ind]} \quad (3.12)$$

where $\frac{d[E]}{dt}$ = enzyme turnover, k_{deg} = degradation rate constant, E_0 = enzyme concentration at time 0, E_{max} = maximal induction effect *in vivo* (negative in the case of down-regulation), $[Ind]$ = free inducer concentration, and $EC50$ = concentration for half maximal induction *in vivo*.

Moreover, in project III, the effect of pH-increasing agents on the PK of dasatinib was investigated and modeled by elevating the simulated gastric pH and additionally extending the gastric emptying time for certain perpetrators [3].

3.4.3 DDGI Model Building

Beyond DGIs and DDIs, projects I and IV also analyzed DDGI scenarios by combining the approaches outlined in the previous sections on DGI and DDI modeling to account for both enzymatic activity variations and perpetrator effects [1, 4].

3.4.4 Food-Effect Model Building

In projects I and III, the effect of food intake on the exposure of tacrolimus and dasatinib was modeled in drug-specific approaches. In the case of tacrolimus, the altered absorption under fed conditions was described by optimizing the release parameters and intestinal permeability, while for dasatinib, the observed delay in $T_{max,pl}$ was predicted by extending the modeled gastric emptying time [1, 3].

3.4.5 Interaction Model Evaluation

Graphical and statistical methods were used to evaluate the modeled interactions. First, predicted and observed plasma or whole blood concentration-time profiles of each victim were visually compared in the presence and absence of the respective interaction effect, i.e. genetic polymorphism (DGI), perpetrator co-administration (DDI), perpetrator co-administration plus genetic polymorphism (DDGI), or food intake. For each interaction scenario,

predicted and observed effect ratios were calculated using Equation 3.13 and compared in goodness-of-fit plots, applying the prediction success limits defined by Guest et al. (including 20% variability) [1–4, 138]. Lastly, GMFE values were calculated for all predicted effect ratios according to Equation 3.5 [1–4].

$$\text{Effect ratio} = \frac{PK \text{ parameter}_{\text{Effect}}}{PK \text{ parameter}_{\text{Reference}}} \quad (3.13)$$

where $PK \text{ parameter} = AUC_{\text{last,pl}}/AUC_{\text{last,wb}}$ or $C_{\text{max,pl}}/C_{\text{max,wb}}$, $PK \text{ parameter}_{\text{Effect}}$ = value of the PK parameter in the presence of the respective interaction effect (genetic polymorphism (DGI), perpetrator co-administration (DDI), perpetrator co-administration plus genetic polymorphism (DDGI), food intake), and $PK \text{ parameter}_{\text{Reference}}$ = value of the PK parameter in the absence of the respective interaction effect (normal enzymatic activity, victim monotherapy, fasted conditions).

3.5 PBPK MODEL-INFORMED DOSE ADAPTATION

The interaction models developed in projects III and IV were further applied to simulate clinically untested DD(G)I scenarios. Here, the impact of one or two co-administered perpetrator drugs on the exposure of dasatinib (project III) or atomoxetine and metoprolol as selected CYP2D6 substrates (project IV) was investigated by linking the respective victim and perpetrator models. Project IV additionally examined the effect of different CYP2D6 AS values. Victim and perpetrator dosing regimens were modeled according to the standard protocols listed in the respective prescribing information. Subsequently, model-informed dose adaptations were performed following the “matching exposure” principle, i.e. increasing or decreasing the victim’s dose until its steady-state exposure aligned with monotherapy levels (80%–125%), in the case of project IV with the exposure of a CYP2D6 NM with an AS value of 2 [3, 4].

RESULTS

4.1 PROJECT I: PBPK MODELING OF TACROLIMUS

Publication

Loer, H. L. H.; Feick, D.; Rüdesheim, S.; Selzer, D.; Schwab, M.; Teutonico, D.; Frechen, S.; van der Lee, M.; Moes, D. J. A. R.; Swen, J. J.; Lehr, T. Physiologically based pharmacokinetic modeling of tacrolimus for food–drug and CYP3A drug–drug–gene interaction predictions. *CPT: Pharmacometrics and Systems Pharmacology* **2023**, *12*, 724–738, DOI: [10.1002/psp4.12946](https://doi.org/10.1002/psp4.12946).

Supplementary Materials

Related Supplementary Materials are available on the accompanying USB storage device and via the following link: <https://pmc.ncbi.nlm.nih.gov/articles/instance/10196430/bin/PSP4-12-724-s002.pdf>.

Copyright

This is an open access article under the terms of CC BY-NC 4.0 (<https://creativecommons.org/licenses/by-nc/4.0/>), which permits use, distribution and reproduction in any medium, provided the original work is properly cited and is not used for commercial purposes. © 2023 The Authors. *CPT: Pharmacometrics & Systems Pharmacology* published by Wiley Periodicals LLC on behalf of American Society for Clinical Pharmacology and Therapeutics.

Author Contributions According to CRediT [5]

Helena Leonie Hanae Loer	Conceptualization, Investigation, Visualization, Writing – Original Draft, Writing – Review & Editing
Denise Feick	Conceptualization, Investigation, Writing – Review & Editing
Simeon Rüdesheim	Conceptualization, Investigation, Writing – Review & Editing
Dominik Selzer	Conceptualization, Investigation, Writing – Review & Editing
Matthias Schwab	Writing – Review & Editing, Funding Acquisition
Donato Teutonico	Writing – Review & Editing
Sebastian Frechen	Writing – Review & Editing
Maaïke van der Lee	Writing – Review & Editing
Dirk Jan A. R. Moes	Writing – Review & Editing
Jesse J. Swen	Writing – Review & Editing
Thorsten Lehr	Conceptualization, Investigation, Writing – Review & Editing, Funding Acquisition

Received: 31 October 2022 | Revised: 20 January 2023 | Accepted: 5 February 2023

DOI: [10.1002/psp4.12946](https://doi.org/10.1002/psp4.12946)

ARTICLE

Physiologically based pharmacokinetic modeling of tacrolimus for food–drug and CYP3A drug–drug–gene interaction predictions

Helena Leonie Hanae Loer¹ | Denise Feick¹ | Simeon Rüdesheim^{1,2} | Dominik Selzer¹ | Matthias Schwab^{2,3,4} | Donato Teutonico⁵ | Sebastian Frechen⁶ | Maaïke van der Lee⁷ | Dirk Jan A. R. Moes⁷ | Jesse J. Swen⁷ | Thorsten Lehr¹

¹Clinical Pharmacy, Saarland University, Saarbrücken, Germany

²Dr. Margarete Fischer-Bosch-Institute of Clinical Pharmacology, Stuttgart, Germany

³Departments of Clinical Pharmacology, Pharmacy and Biochemistry, University of Tübingen, Tübingen, Germany

⁴Cluster of Excellence iFIT (EXC2180) “Image-guided and Functionally Instructed Tumor Therapies”, University of Tübingen, Tübingen, Germany

⁵Translational Medicine & Early Development, Sanofi-Aventis Research & Development, Chilly-Mazarin, France

⁶Bayer AG, Pharmaceuticals, Research & Development, Systems Pharmacology & Medicine, Leverkusen, Germany

⁷Department of Clinical Pharmacy & Toxicology, Leiden University Medical Center, Leiden, The Netherlands

Correspondence

Thorsten Lehr, Clinical Pharmacy, Saarland University, Campus C5 3, 66123 Saarbrücken, Germany.
Email: thorsten.lehr@mx.uni-saarland.de

Abstract

The immunosuppressant and narrow therapeutic index drug tacrolimus is metabolized mainly via cytochrome P450 (CYP) 3A4 and CYP3A5. For its pharmacokinetics (PK), high inter- and intra-individual variability can be observed. Underlying causes include the effect of food intake on tacrolimus absorption as well as genetic polymorphism in the *CYP3A5* gene. Furthermore, tacrolimus is highly susceptible to drug–drug interactions, acting as a victim drug when coadministered with CYP3A perpetrators. This work describes the development of a whole-body physiologically based pharmacokinetic model for tacrolimus as well as its application for investigation and prediction of (i) the impact of food intake on tacrolimus PK (food–drug interactions [FDIs]) and (ii) drug–drug(–gene) interactions (DD[G]Is) involving the CYP3A perpetrator drugs voriconazole, itraconazole, and rifampicin. The model was built in PK-Sim® Version 10 using a total of 37 whole blood concentration–time profiles of tacrolimus (training and test) compiled from 911 healthy individuals covering the administration of tacrolimus as intravenous infusions as well as immediate-release and extended-release capsules. Metabolism was incorporated via CYP3A4 and CYP3A5, with varying activities implemented for different *CYP3A5* genotypes and study populations. The good predictive model performance is demonstrated for the examined food effect studies with 6/6 predicted FDI area under the curve determined between first and last concentration measurements (AUC_{last}) and 6/6 predicted FDI maximum whole blood concentration (C_{max}) ratios within twofold of the respective observed ratios. In addition, 7/7 predicted DD(G)I AUC_{last} and 6/7 predicted DD(G)I C_{max} ratios were within twofold of their observed values. Potential applications of the final model include model-informed drug discovery and development or the support of model-informed precision dosing.

This is an open access article under the terms of the [Creative Commons Attribution-NonCommercial](https://creativecommons.org/licenses/by-nc/4.0/) License, which permits use, distribution and reproduction in any medium, provided the original work is properly cited and is not used for commercial purposes.

© 2023 The Authors. *CPT: Pharmacometrics & Systems Pharmacology* published by Wiley Periodicals LLC on behalf of American Society for Clinical Pharmacology and Therapeutics.

Study Highlights

WHAT IS THE CURRENT KNOWLEDGE ON THE TOPIC?

The pharmacokinetics (PK) of tacrolimus exhibit high inter- and intra-individual variability. Tacrolimus is a substrate of cytochrome P450 (CYP) 3A4 and the polymorphically expressed CYP3A5 enzyme, thus highly susceptible to drug–drug(–gene) interactions. In addition, food intake shows a pronounced effect on tacrolimus PK.

WHAT QUESTION DID THIS STUDY ADDRESS?

This study presents the development of a new whole-body physiologically based pharmacokinetic (PBPK) model for tacrolimus that describes and predicts the influence of food intake and CYP3A perpetrator drugs voriconazole, itraconazole, and rifampicin on tacrolimus PK while incorporating different CYP3A5 activity levels.

WHAT DOES THIS STUDY ADD TO OUR KNOWLEDGE?

The tacrolimus PBPK model helps investigate the underlying mechanisms for the pronounced impact of food intake, CYP3A5 polymorphism, and coadministration of CYP3A perpetrators on tacrolimus exposure and highlights the importance of these individual factors in dosing decisions.

HOW MIGHT THIS CHANGE DRUG DISCOVERY, DEVELOPMENT, AND/OR THERAPEUTICS?

The model can be applied to support model-informed drug development and a holistic precision dosing approach incorporating a comprehensive set of factors affecting the PK of tacrolimus.

INTRODUCTION

Tacrolimus is the cornerstone of current immunosuppression for the prophylaxis of graft rejection following solid organ transplantation.¹ Data from 2020 show that the calcineurin inhibitor was included in approximately 90% of immunosuppressive regimens for adult and pediatric kidney transplant recipients in the United States.²

Tacrolimus is classified as a Biopharmaceutics Classification System Class II drug.³ It demonstrates incomplete absorption across the entire intestine as well as a pronounced intestinal and hepatic first-pass metabolism after oral intake,^{4,5} resulting in a low relative bioavailability of 17%–23%.¹ Moreover, in vitro studies have indicated tacrolimus to be a substrate of P-glycoprotein (P-gp).⁶ Due to extensive binding to erythrocytes, considerably higher tacrolimus whole blood concentrations compared with plasma levels can be observed, with a reported mean blood-to-plasma concentration ratio of 15.⁷ Tacrolimus is predominately metabolized via cytochrome P450 (CYP) enzymes 3A4 and 3A5, without contribution of its metabolites to the pharmacological effect.^{8,9}

As a narrow therapeutic index drug with high inter- and intra-individual pharmacokinetics (PK) variability, the clinical application of tacrolimus can be challenging.¹⁰

Thus, patients taking tacrolimus are subject to therapeutic drug monitoring to reduce the risk of graft rejection in the event of underdosing as well as to prevent overexposure that might result in nephro- and neurotoxicity, infections, and malignancies.⁹ Factors potentially influencing the PK of tacrolimus include a pronounced food effect. Comparing the application under fed versus fasted conditions, the rate of tacrolimus absorption is reduced, resulting in a 33% decreased tacrolimus exposure when administered after a standardized breakfast.^{11,12} Moreover, the PK of tacrolimus is affected by genetic polymorphisms, with the CYP3A5 gene being of particular interest. Following, for example, an oral single dose (SD) administration of tacrolimus, CYP3A5 normal metabolizers (NMs) demonstrate a 35% decreased tacrolimus area under the curve (AUC) compared with a mixed group of intermediate metabolizers (IMs) and poor metabolizers (PMs).¹³ Clinical guidelines allow CYP3A5 genotype-informed dosing.¹⁴

Furthermore, tacrolimus is highly susceptible to drug–drug interactions (DDIs), acting as a victim drug when coadministered with CYP3A perpetrators. Hence, tacrolimus is recommended as a sensitive substrate of CYP3A by the US Food and Drug Administration for use in clinical DDI studies.¹⁵ CYP3A inhibitors cause a significant increase in tacrolimus exposure. Here, azole antifungal agents (e.g.,



itraconazole, voriconazole) are of specific clinical relevance, as invasive fungal infections are among the most important posttransplant infections requiring frequent concomitant use of tacrolimus and azoles.^{16–19} For instance, pretreatment with voriconazole increases the AUC of tacrolimus by more than fourfold, even reaching sixfold in CYP2C19 PMs that express a reduced voriconazole metabolism.¹⁷ In contrast, pretreatment with the antibiotic agent and CYP3A inducer rifampicin reduces the AUC of tacrolimus by 68%.⁵

To improve the safety and efficacy of tacrolimus therapy, factors modulating the PK of tacrolimus, such as food–drug interactions (FDIs) and drug–drug(–gene) interactions (DD[G]Is), should be thoroughly investigated. For this, physiologically based pharmacokinetic (PBPK) modeling allows the study of a drug's PK in different genotypes and interactions with food components or co-administered drugs while covering various (patho-)physiological characteristics.^{20,21} By incorporating factors contributing to a drug's interindividual variability, PBPK modeling can be applied to support model-informed precision dosing.²² Moreover, PBPK modeling is widely acknowledged for the use in model-informed drug discovery and development (MID3), demonstrated by a growing number of PBPK applications submitted to regulatory agencies to address specific research questions, mainly related to DDIs.²³

Objectives of the presented study were therefore (a) the development of a whole-body PBPK model of tacrolimus covering different CYP3A5 activities and clinically relevant formulations as well as the prediction of (b) the influence of food intake on tacrolimus PK and (c) DD(G)Is involving different CYP3A perpetrators, especially azole antifungal agents. The final model will be made publicly accessible (<https://github.com/Open-Systems-Pharmacology>).

METHODS

Software

PK-Sim® and MoBi® Version 10 (Open Systems Pharmacology Suite, www.open-systems-pharmacology.org, 2021) were used for the development of the tacrolimus PBPK model, parameter identification (Levenberg–Marquardt algorithm), and model sensitivity analyses. Published clinical study data were digitized with the help of Engauge Digitizer Version 12.1 (Mitchell et al.²⁴) according to best practices.²⁵ The compilation of plots as well as calculations of PK parameters and quantitative model performance measures were performed using the R programming language Version 4.2.1 (R Foundation for Statistical Computing).

Clinical study data

Whole blood concentration–time profiles of tacrolimus in healthy volunteers were gathered from the literature, covering a broad dosing range of tacrolimus administered intravenously and orally in different formulations. Digitized profiles were divided into a training dataset for model development and a test dataset for model evaluation (ratio 1:3). Here, profile assignment to the test and training datasets was accomplished in a nonrandomized fashion to maximize the set of profiles for model evaluation (test dataset) while preferring information-dense (frequent measurements within a long sampling period) and heterogenous profile data to capture the range of different routes of administration, formulations, and dosage regimens for the training dataset.

PBPK model building

Model development was initiated with an extensive literature search for physicochemical parameters as well as information on the absorption, distribution, metabolism, and excretion of tacrolimus.

For each included study, a representative virtual individual was established based on the mean and mode for age, sex, weight, height, body mass index, and ethnicity of the respective study publication. If demographic information was incomplete, default settings were adopted from the population database accessible in PK-Sim®. Relative expression of relevant transporters and enzymes in different organs was implemented according to the PK-Sim® expression database as described in Table S1. A virtual population of 1000 individuals was created for each study population using the respective reported demographic information to visually assess variability based on these characteristics and metabolizing enzymes. If no data were available, an age range of 20–50 years was assumed. Table S1 provides the geometric standard deviations used for the modeled variation of the relevant transporter and enzyme concentrations.

Unknown model parameters and parameters with a high impact on the results of permeability and partition quantitative structure–activity relationship (QSAR) models of PK-Sim® were fitted using the training dataset. Oral formulations differing in release kinetics were incorporated via separate Weibull functions (Equation 1), with the time to 50% dissolution and shape as model input parameters. In a stepwise approach, tacrolimus model parameters were first optimized based on intravenous and oral administration of immediate-release (IR) capsules (Prograf®). Next, the model was adjusted to extended-release (ER) capsules (Advagraf®) by estimating the respective release

model parameters as well as the intestinal permeability, the latter required to account for different permeability behaviors of IR and ER tacrolimus.

$$f_d(t) = 1 - \exp\left(\frac{-(t - t_{lag})^b}{a}\right) \quad (1)$$

where $f_d(t)$ = fraction of administered dose dissolved at time t , \exp = exponential function, t_{lag} = lag time between drug intake and the start of the dissolution process, b = shape parameter, and a = scale parameter.

Enzyme metabolism was implemented using Michaelis–Menten kinetics (Equation S1). For CYP3A5, different levels of activity were implemented by activity-specific CYP3A5 catalytic rate constants (k_{cat}). Here, the Michaelis–Menten constant (K_M) was fixed for all activity levels to decrease the explorative space of the fitting process. For each study population, the reported fraction of functional *1 allele was used for activity assignment. In the absence of genotype/phenotype information of a study group, CYP3A5 activity was assumed according to the frequency of the *1 allele observed in the respective ethnic group published by Birdwell et al.¹⁴ Assumed relative activities for ethnicities and phenotypes relevant to this work are listed in Table 1. A study investigating CYP3A5 PMs (i.e., lack of CYP3A5 activity) was used to determine CYP3A5 independent metabolism.¹³ Genetic variants in CYP3A4 (e.g., CYP3A4*22) were not considered due to missing information in the study cohorts.

PBPK model evaluation

The final tacrolimus model was evaluated both graphically and statistically. For visual comparison, predicted whole blood

TABLE 1 Frequency of the CYP3A5 *1 allele in different populations,¹⁴ including assumed activity relative to homozygous carriers of the *1 allele.

Population	Frequency of the CYP3A5 *1 allele, %	Assumed activity, %
Phenotype		
Normal metabolizer	100.0	100.0
Poor metabolizer	0.0	0.0
Race and Ethnicity		
African American	60.5	60.5
Asian	25.8	25.8
Latin American	20.2	20.2
Caucasian	7.8	7.8

Abbreviation: CYP, cytochrome P450.

concentration–time profiles were plotted alongside their corresponding observed data points. Goodness-of-fit (GOF) plots were generated to examine the deviation of predicted to observed concentration measurements. Moreover, GOF plots were used for comparison of the calculated AUC determined between first and last concentration measurements (AUC_{last}) and maximum whole blood concentration (C_{max}) values for all predicted versus observed profiles. Predictions within the twofold range of observed values were considered successful. Statistical evaluation was conducted via calculation of mean relative deviations (MRDs) for all predicted concentration–time points (Equation 2) as well as geometric mean fold errors (GMFEs) for predicted AUC_{last} and C_{max} values (Equation 3).

$$MRD = 10^x; \quad x = \sqrt{\frac{\sum_{i=1}^k (\log_{10} \hat{c}_i - \log_{10} c_i)^2}{k}} \quad (2)$$

where c_i = i -th observed concentration, \hat{c}_i = predicted concentration corresponding to the i -th observed concentration, and k = number of observed values.

$$GMFE = 10^x; \quad x = \frac{\sum_{i=1}^m \left| \log_{10} \left(\frac{\hat{p}_i}{p_i} \right) \right|}{m} \quad (3)$$

where p_i = observed AUC_{last} or C_{max} value of study i , \hat{p}_i = corresponding predicted AUC_{last} or C_{max} value of study i , and m = number of studies.

Finally, a local sensitivity analysis was performed for each investigated formulation (for details, see Section S2.8.1).

FDI modeling

The effect of food intake on tacrolimus exposure was estimated based on studies providing whole blood concentration–time profiles under both fed and fasted conditions. Altered absorption of tacrolimus due to food intake was implemented by adjusting not only the Weibull parameters (time to 50% dissolution and shape) but also the intestinal permeability to account for presumed binding of tacrolimus to lipoproteins and food components.

FDI modeling was evaluated by comparing predicted to observed whole blood concentration–time profiles under fed and fasted conditions. Furthermore, for each modeled FDI, observed and predicted FDI AUC_{last} and C_{max} ratios were calculated (Equation 4) with subsequent comparisons applying the limits proposed by Guest et al.²⁶ to determine prediction accuracy (including 20% variability).

$$FDI \text{ PK parameter ratio} = \frac{PK \text{ parameter}_{fed}}{PK \text{ parameter}_{fasted}} \quad (4)$$



where PK parameter = AUC_{last} or C_{max} , PK parameter_{fed} = AUC_{last} or C_{max} of tacrolimus under fed conditions, and PK parameter_{fasted} = AUC_{last} or C_{max} of tacrolimus under fasted conditions.

Finally, GMFE values were determined for all predicted and observed FDI AUC_{last} and C_{max} ratios according to Equation (3).

DD(G)I modeling

The influence of CYP3A perpetrators on tacrolimus PK was investigated by coupling the tacrolimus model with previously published models of voriconazole, itraconazole, and rifampicin.^{27,28} The respective model files were downloaded from <https://github.com/Open-Systems-Pharmacology>. PK-Sim® Version 10 model files for itraconazole and rifampicin were obtained from <https://github.com/Open-Systems-Pharmacology/Itraconazole-Model/releases/tag/v1.3> and <https://github.com/Open-Systems-Pharmacology/Rifampicin-Model/releases/tag/v1.2>. Relevant interaction parameters were incorporated from the literature according to the respective types of interaction reported, that is, induction, competitive inhibition, and mechanism-based inactivation, as described in Section S4.1. One of the voriconazole–tacrolimus–DDIs was included in the training dataset to inform the contribution of intestinal and intrahepatic tacrolimus metabolism.¹⁶

Evaluation of the modeled DD(G)Is was performed analogously to the investigated FDIs as described in the Methods section (“FDI modeling”).

RESULTS

PBPK model building and evaluation

The tacrolimus PBPK model was built and evaluated using a total of 37 whole blood concentration–time profiles (summarized mean values with variance information if available) obtained from 25 clinical studies for the training and test datasets. Included were five intravenous SD applications of 0.015–0.025 mg/kg body weight (BW) tacrolimus as well as 32 oral administrations of therapeutic doses ranging from 0.5 to 10 mg. IR and ER formulations of tacrolimus accounted for 27 (SD) and five (SD and multiple dose [MD]) of the profiles used, respectively. Information on all profiles, including the frequency of the CYP3A5 *1 allele for each study population, is provided in Table S2.

The metabolism of tacrolimus was implemented via CYP3A4 and CYP3A5, with K_M values adopted from the literature and k_{cat} values optimized during the model-building process. For a CYP3A5 NM, the contribution of

CYP3A4 and CYP3A5 to the overall metabolism accounted for 67% and 33%, respectively. A total of 71% of CYP3A metabolism occurred intestinally in a CYP3A5 NM compared with 59% in a CYP3A5 PM. Moreover, weak mechanism-based inactivation of CYP3A4 and CYP3A5 by tacrolimus was incorporated using published inhibition data. Initial Weibull starting parameters for IR and ER formulations were derived from literature dissolution profiles according to Langenbucher et al.^{29–31} During parameter optimization steps, the respective shape values for both formulations and the time to 50% dissolution for ER tacrolimus were adjusted. Furthermore, separate intestinal permeabilities were optimized for IR and ER tacrolimus. A detailed overview of all tacrolimus model parameters is provided in Table S3. A summary of the key modeling assumptions, including the resulting modeling decisions, is available in Table S4. The tacrolimus PBPK model file can be found in Appendix S2.

Overall, the final tacrolimus model showed good descriptive (training dataset) and predictive (test dataset) performance. A representative sample of whole blood concentration–time profiles from both the training and test datasets is provided in Figure 1. Semilogarithmic and linear plots of all predicted and observed profiles are listed in Sections S2.1–S2.2.

Figure 2 displays GOF plots of predicted versus observed concentration measurements as well as AUC_{last} and C_{max} values stratified by the training and test datasets. A total of 96% of all predicted concentration measurements as well as 37/37 of predicted AUC_{last} and 37/37 of predicted C_{max} values were simulated within twofold of their corresponding observed data. The good descriptive and predictive performance of the model could be further demonstrated by the calculated mean MRD of 1.43 as well as mean GMFE _{AUC_{last}} and GMFE _{C_{max}} values of 1.21 and 1.18, respectively. All individual MRD and GMFE values are listed in Tables S5 and S6.

Local sensitivity analyses were performed for SD administrations of intravenous (0.025 mg/kg BW), oral IR (10 mg), and oral ER tacrolimus (10 mg), respectively. The AUC_{last} of intravenous tacrolimus was demonstrated to be most sensitive to perturbations of the acid dissociation constant (literature value), whereas for oral IR and ER tacrolimus, the lipophilicity (optimized) showed the greatest impact on AUC_{last} . A detailed assessment of all sensitivity analyses can be found in Section S2.8.2.

FDI modeling

The effect of food intake on the PK of tacrolimus was modeled and evaluated using four FDI studies, with kilocalories ingested ranging from 600 to 1000 and IR tacrolimus administered 0.33 to 1.5 h after the start of

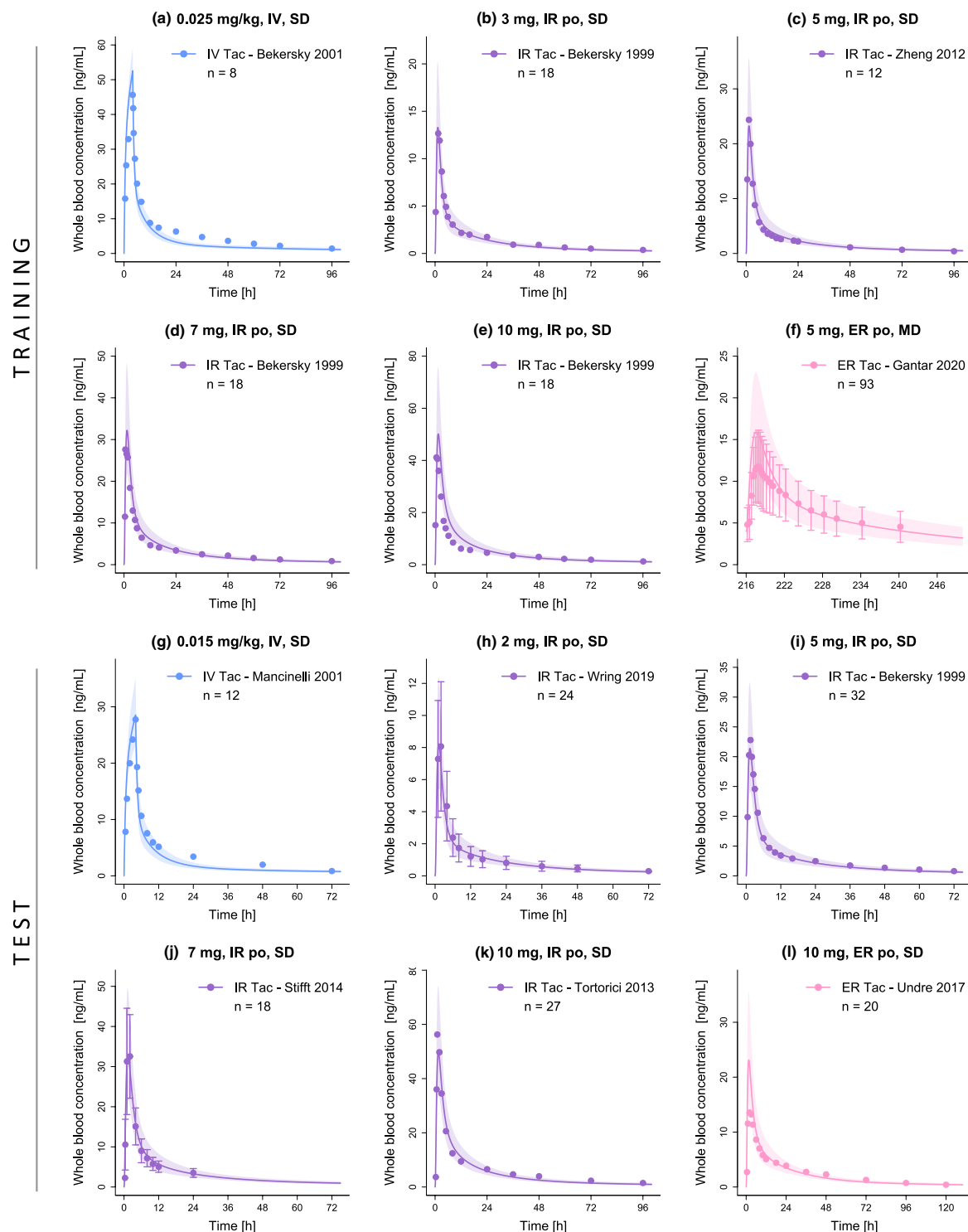


FIGURE 1 Representative plots of whole blood concentration–time profiles of tacrolimus. Stratified by training (a–f) and test (g–l) dataset, solid lines and ribbons represent population predictions ($n = 1000$; geometric mean and geometric standard deviation), whereas corresponding observed data are shown as dots (\pm standard deviation, if available).^{13,44–52} Detailed information on all investigated profiles is provided in Table S2. ER, extended-release; IR, immediate-release; IV, intravenous; MD, multiple dose; n, number of participants; po, oral; SD, single dose; Tac, tacrolimus.

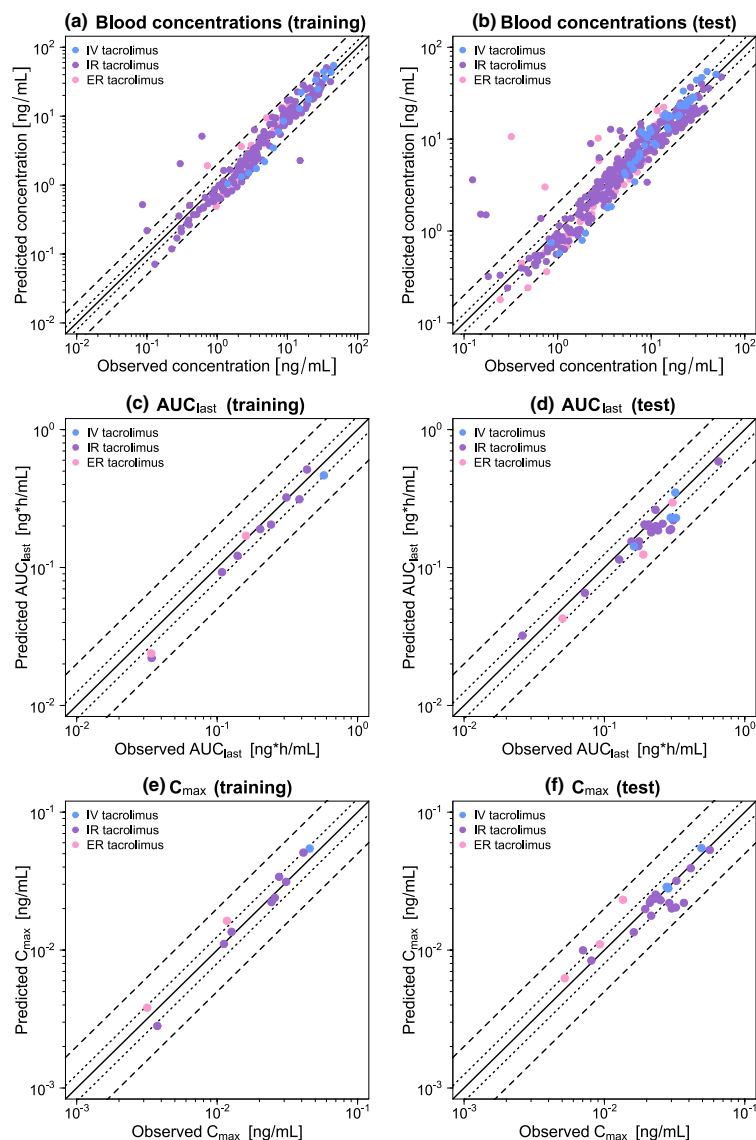


FIGURE 2 Goodness-of-fit plots of the final tacrolimus model. Stratified by training (left column) and test dataset (right column), predicted whole blood concentration measurements (a–b) as well as AUC_{last} (c–d) and C_{max} (e–f) values are plotted against corresponding observed data. The solid line represents the line of identity, whereas dotted lines indicate 1.25-fold and dashed lines twofold deviation from the respective observed value. Detailed information on all investigated profiles is provided in [Table S2](#). AUC_{last} , area under the curve determined between first and last concentration measurements; C_{max} , maximum whole blood concentration; ER, extended-release; IR, immediate-release; IV, intravenous.

each meal.^{11,12,32,33} Two whole blood concentration–time profiles of tacrolimus under fed conditions (668 and 849 kilocalories, 0.33 h after food intake) were used to adjust the Weibull parameters (time to 50% dissolution and shape) as well as the intestinal permeability.¹¹ Compared with parameters for fasted administrations, a 3.3-fold increased time to 50% dissolution (63.0 vs. 18.9 min), a higher shape parameter (0.94 vs. 0.08, both parabolic curves), and a 90% decreased intestinal permeability (3.79×10^{-7} vs. 3.42×10^{-6} cm/s) were estimated for tacrolimus applications under fed conditions. Information on all included studies is provided in [Table S8](#). The FDI model file is included in Appendix S2.

[Figure 3a–f](#) displays the predicted versus observed whole blood concentration–time profiles of IR tacrolimus under fed and fasted conditions, with [Figure 3g,h](#) showing the corresponding predicted versus observed FDI AUC_{last} and FDI C_{max} ratios. Overall, the FDI model demonstrated good predictive performance regarding the effect of food intake on tacrolimus exposure, as 6/6 of predicted FDI AUC_{last} and 6/6 of predicted FDI C_{max} ratios were within the limits proposed by Guest et al.,²⁶ with respective GMFE values averaging 1.21 and 1.19. A list of all individual GMFE values as well as semilogarithmic and linear plots of all predicted and observed whole blood concentration–time profiles are available in Sections [S3.2–S3.5](#).

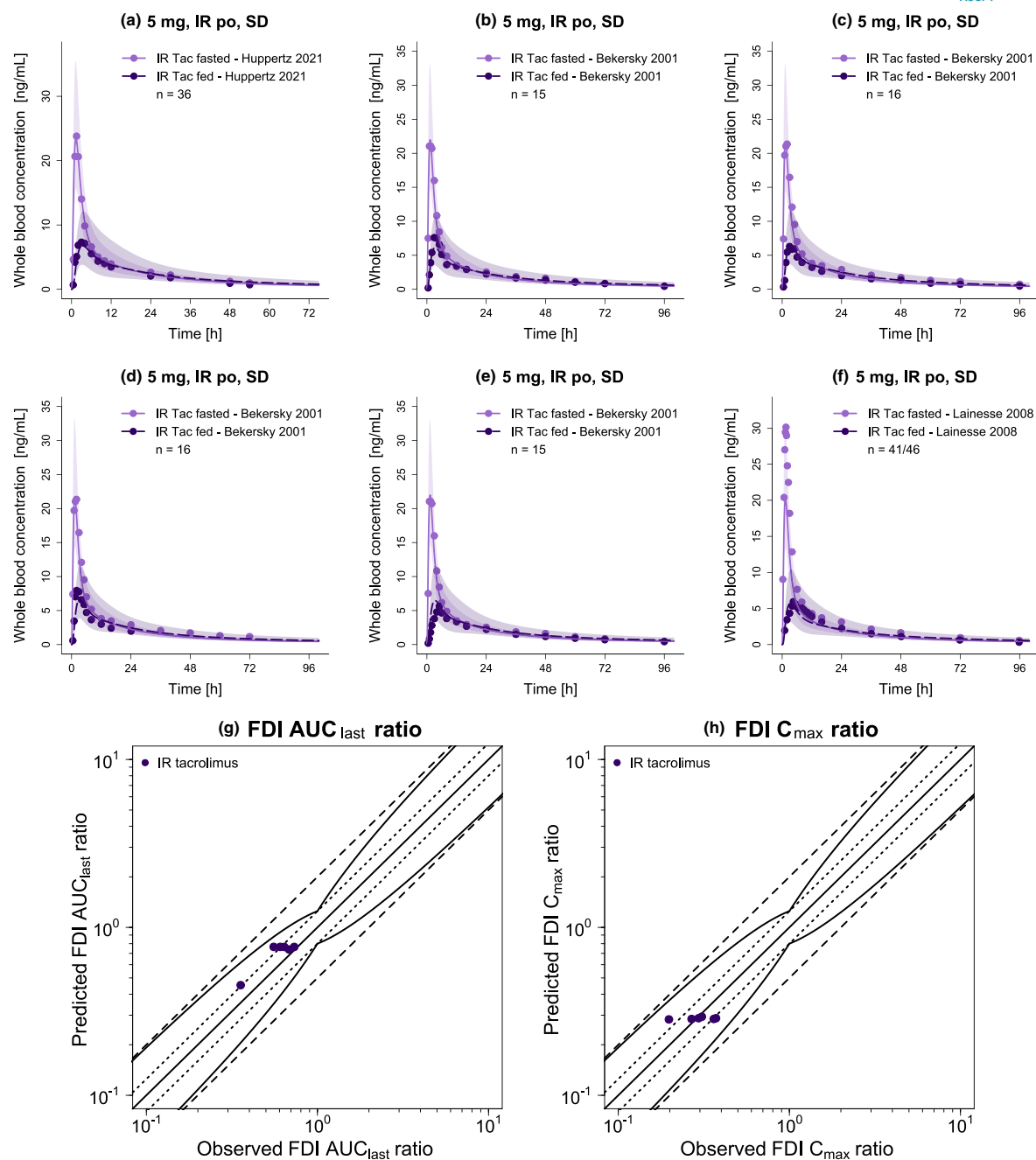


FIGURE 3 Evaluation of the modeled FDI. Presented are predicted whole blood concentration–time profiles (a–f) of IR tacrolimus under fed and fasted conditions alongside corresponding observed data.^{11,12,32,33} Dashed (fed) and solid (fasted) lines and ribbons represent population predictions ($n = 1000$; geometric mean and geometric standard deviation), whereas corresponding observed data are shown as dots. Predicted versus observed FDI AUC_{last} (g) and FDI C_{max} (h) ratios are shown with the solid line representing the line of identity and dotted lines indicating 1.25-fold and dashed lines twofold deviation from the respective observed value, along with the curved lines marking the prediction success limits proposed by Guest et al.,²⁶ including 20% variability. Detailed information on all investigated FDI studies is provided in Table S8. AUC_{last}, area under the curve determined between first and last concentration measurements; C_{max}, maximum whole blood concentration; FDI, food–drug interaction; IR, immediate-release; n, number of participants; po, oral; SD, single dose; Tac, tacrolimus.

DD(G)I modeling

The DD(G)I model, centered around tacrolimus as a CYP3A victim drug, was developed using four DD(G)I studies. For the CYP3A4 mechanism-based inactivator and CYP3A5 competitive inhibitor voriconazole, two studies investigated its pretreatment effect on the PK of IR tacrolimus,^{16,17} with one of the studies specifically examining the extent of inhibition in different CYP2C19 phenotypes, that is, NMs, IMs, and PMs.¹⁷ Furthermore, one study assessed the impact of pretreatment with the CYP3A4 and CYP3A5 competitive inhibitor itraconazole on ER tacrolimus,¹⁸ whereas the last study addressed the pretreatment influence of the CYP3A4 competitive inhibitor and inducer rifampicin on the PK of intravenously and orally (IR) administered tacrolimus.⁵ In two of the aforementioned studies, the CYP3A4 victim drug midazolam was additionally administered. However, as no effect on the PK of tacrolimus was assumed, midazolam administration was not included in the DD(G)I model.^{16,18} Figure 4 presents a schematic overview of the modeled DD(G)I network. Further details on all included DD(G)I studies, as well as model parameters of the DD(G)I partners, are provided in Sections S4.2–S4.3. The DD(G)I model file is included in Appendix S2.

Figure 5 shows predicted versus observed whole blood concentration–time profiles of tacrolimus administered alone or concomitantly with the respective perpetrator drug. For each DD(G)I, predicted versus observed DD(G)I AUC_{last} and C_{max} ratios are displayed in Figure 6, with 7/7 and 6/7 within the limits proposed by Guest et al.,²⁶ respectively. The favorable DD(G)I prediction performance of the model is further demonstrated by low mean GMFE values for the predicted DD(G)I AUC_{last} (1.10) and C_{max} ratios (1.41). A list of all individual GMFE values as well as semilogarithmic and linear plots of all predicted and observed whole blood concentration–time profiles are available in Sections S4.4–S4.7.

DISCUSSION

In the present work, a whole-body PBPK model for tacrolimus was built and evaluated allowing the successful description and prediction of whole blood concentration–time profiles over a broad dosing range of intravenously (0.015–0.025 mg/kg BW, SD) and orally (0.5–10 mg, SD and MD, IR and ER) administered tacrolimus. Subsequently, the final model was applied to predict the effect of food intake on tacrolimus PK as well as DD(G)Is involving tacrolimus as a CYP3A victim drug in subjects with varying CYP3A5 and CYP2C19 activity levels.

The simulated total bioavailability for IR tacrolimus ranges from 12% to 18% depending on the administered dose, coinciding with reported total bioavailability values of $(18 \pm 5)\%$ in healthy individuals.¹ The three determining factors for fraction absorbed, fraction escaping gut wall metabolism (Fg), and fraction escaping first-pass liver metabolism (Fh) are also well reflected in the model: (1) consistent with literature data, the developed model simulates incomplete intestinal absorption of tacrolimus, with 48% of the applied dose absorbed¹; (2) as intravenous profiles are reasonably predicted, we conclude that the hepatic clearance is adequately described, and consequently Fh should be well depicted in the model; (3) the successful prediction of metabolic DDIs suggests a well-described relationship between the fraction absorbed and Fg by the model.

Numerous studies have demonstrated the predominant involvement of CYP3A enzymes in the metabolism of tacrolimus, with CYP3A4 and CYP3A5 being of particular importance, resulting in their inclusion in the model.⁸ To account for interindividual variability caused by the genetic polymorphism of the *CYP3A5* gene, CYP3A5 activity was incorporated for each study population based on the frequency of the functional *1 allele, either determined by genotyping or assumed

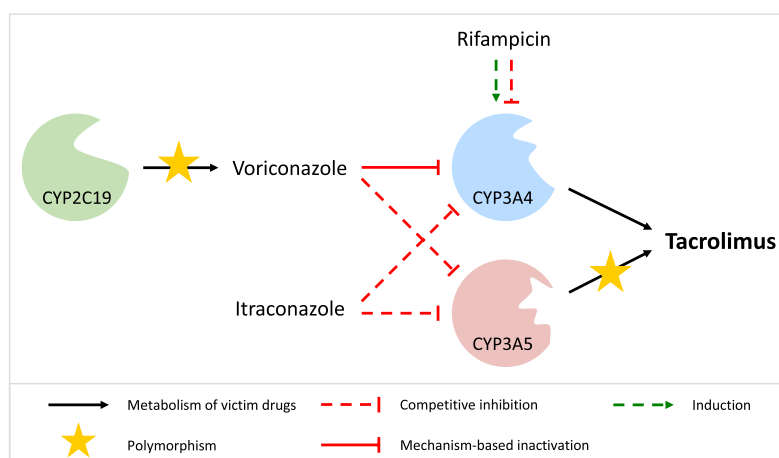


FIGURE 4 Schematic overview of the modeled drug–drug(–gene) interaction network. While tacrolimus acts as a CYP3A4 and CYP3A5 victim drug, voriconazole, itraconazole, and rifampicin represent CYP3A4 perpetrator drugs. Voriconazole and itraconazole additionally inhibit CYP3A5. For simplicity, the mechanism-based inactivation of CYP3A4 and CYP3A5 by tacrolimus is not shown. CYP, cytochrome P450.

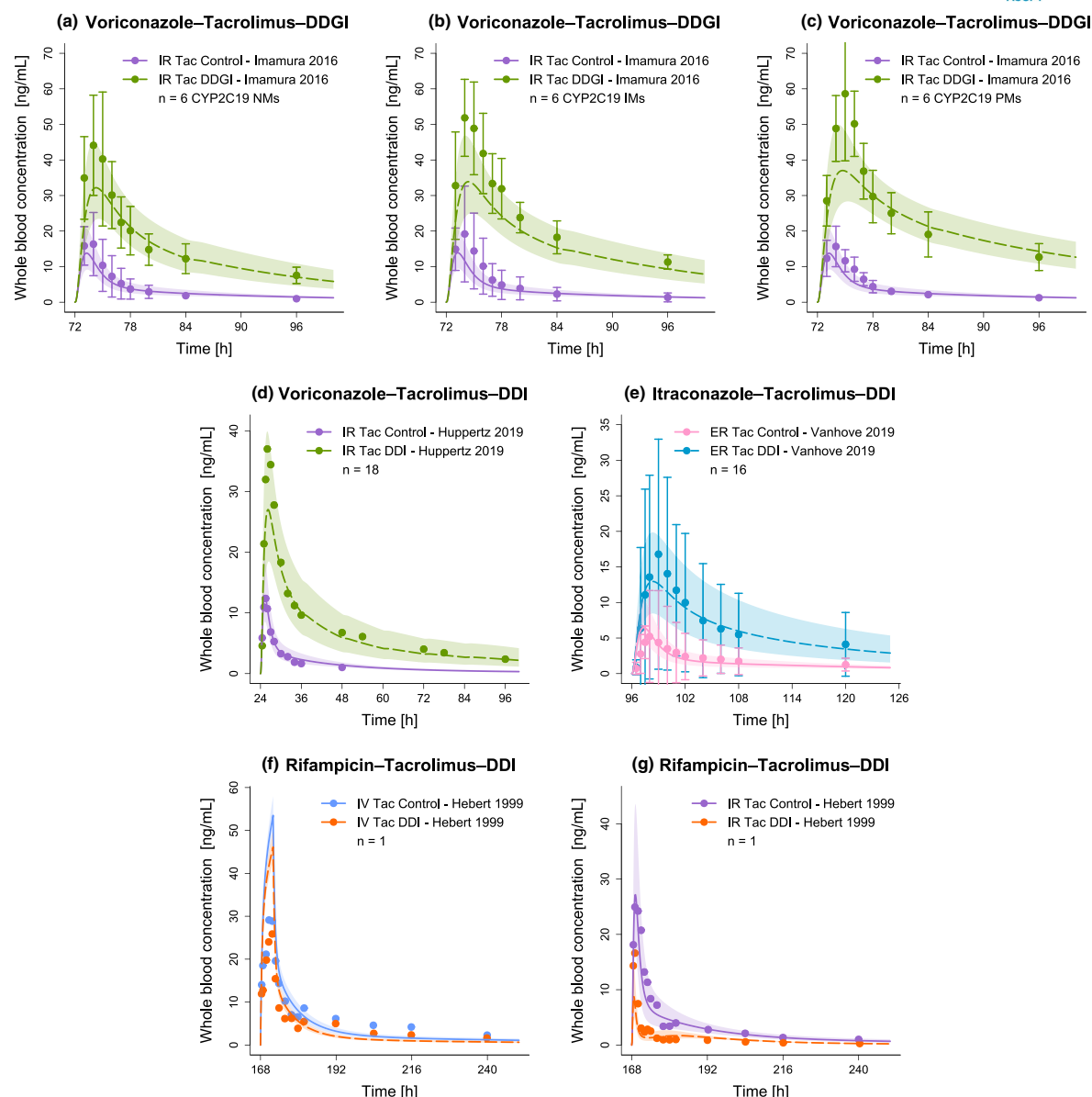


FIGURE 5 Evaluation of the modeled DD(G)Is (Part I). Presented are predicted whole blood concentration–time profiles of tacrolimus without (Control) and with (DD[G]I) intake of the respective perpetrator drug (voriconazole [a–d], itraconazole [e], rifampicin [f–g]) alongside their corresponding observed data.^{5,16–18} Solid (Control) and dashed (DD[G]I) lines and ribbons represent population predictions ($n = 1000$; geometric mean and geometric standard deviation), whereas corresponding observed data are shown as dots (\pm standard deviation, if available). Detailed information on all investigated DD(G)I studies is provided in [Table S10](#). CYP, cytochrome P450; DDGI, drug–drug–gene interaction; DDI, drug–drug interaction; ER, extended-release; IM, intermediate metabolizer; IR, immediate-release; IV, intravenous; n, number of participants; NM, normal metabolizer; PM, poor metabolizer; Tac, tacrolimus.

based on the mode of the respective study participants' race and ethnicity.¹⁴ However, as CYP3A5 genotyping had not been performed in the majority of included studies, this lack of information might have led to biases in the modeling and estimation processes. Here, a larger

and complete PK dataset on specified CYP3A5 genotypes might be required to further improve and refine the genotype-specific modeling of tacrolimus exposure. The same applies to CYP3A4 variants, which have not been considered so far.

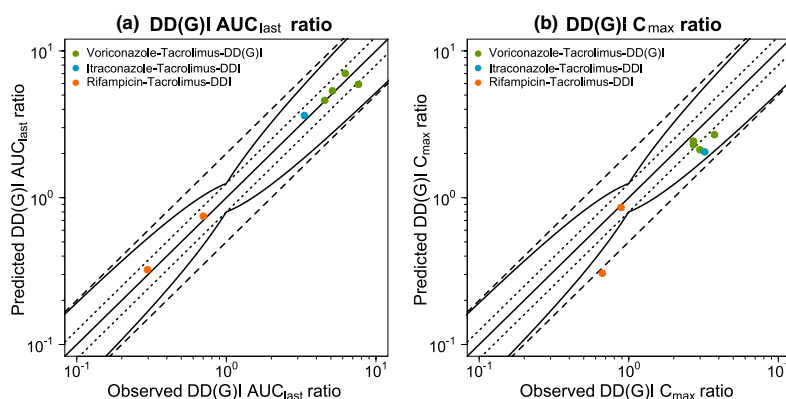


FIGURE 6 Evaluation of the modeled DD(G)Is (Part II). Predicted versus observed DD(G)I AUC_{last} (a) and DD(G)I C_{max} (b) ratios are shown with the solid line representing the line of identity, dotted lines indicating 1.25-fold and dashed lines twofold deviation from the respective observed value, along with the curved lines marking the prediction success limits proposed by Guest et al.²⁶ including 20% variability. Detailed information on all investigated DD(G)I studies is provided in Table S10. AUC_{last} , area under the curve determined between first and last concentration measurements; C_{max} , maximum whole blood concentration; DD(G)I, drug–drug(–gene) interaction; DDI, drug–drug interaction.

To predict the release kinetics of IR and ER tacrolimus, separate Weibull parameter values were used in the absorption model. In addition, it became apparent that different intestinal permeability values had to be optimized for IR and ER tacrolimus to adequately describe the observed data, with a slightly higher permeability value estimated for IR compared with ER tacrolimus (3.42×10^{-6} vs. 1.91×10^{-6} cm/s). For ER tacrolimus, the adjusted permeability was within one order of magnitude of the published in vitro value (6.58×10^{-6} cm/s).³⁰ No reference permeability could be found in the literature for IR tacrolimus. The underlying cause for the observed differences in intestinal permeability for IR and ER formulations is not clear yet, but it is reasonable to assume that different pharmaceutical excipients contained in IR and ER tacrolimus formulations might be the driving factor. For example, only IR tacrolimus capsules include the disintegrant croscarmellose sodium, which has been reported to significantly increase the membrane permeability in the rat small intestine in vitro.^{1,34} Here, dedicated studies addressing oral tacrolimus formulations would be of interest to investigate possible permeability-modulating effects. During model development, besides implementing different intestinal permeabilities for IR and ER tacrolimus, alternative approaches covering different solubilities, supersaturation, or release modeling via particle dissolution were tested. However, these approaches were not adopted because no support for their application could be found in the literature and the prediction of the observed data did not improve.

The final tacrolimus model was successfully applied to predict the influence of food intake on IR tacrolimus whole blood levels. Food effects may result from a variety of mechanisms arising from the interaction of postprandial physiology and compounds. For tacrolimus, the influence of different meal compositions on the exposure has been examined by Bekersky et al., however, the underlying mechanisms are still unknown.^{11,12,35} Therefore, the food effect was empirically modeled. The Weibull parameters were adjusted to represent food-induced changes in release kinetics, for example, due to altered gastric pH. In addition, the intestinal permeability was estimated to account for altered absorption, presumably due to the binding of tacrolimus to lipoproteins and food components, given its pronounced lipophilicity.³⁶ During model development, other approaches to model the effect were pursued, such as a change in solubility, gastric pH, gastric emptying time, or intestinal/hepatic blood flow. However, these approaches were eventually not retained due to an inadequate description of the observed food effect. In the case of a prolonged gastric emptying time, this observation is consistent with the findings of Kuypers et al. showing no significant difference in the extent of absorption in patients with and without delayed gastric emptying.³⁷ According to Deng et al., as tacrolimus is a low extraction drug, a change in splanchnic blood flow would not be expected to affect tacrolimus kinetics; hence, the lack of effect of an increase in intestinal/hepatic blood flow is in line with the literature.^{35,38} The final model describes a more pronounced release and slower absorption under

fed conditions. Overall, a higher fraction of the tacrolimus dose is absorbed than under fasting conditions, with ultimately lower exposure due to increased intestinal metabolism, a finding consistent with a hypothesis proposed by Huppertz et al.¹² Unfortunately, due to the administration of 5 mg IR tacrolimus in all food effect studies, the investigation of the FDI lacked diversity in applied doses and formulations. Hence, additional studies examining different doses and oral formulations of tacrolimus would be necessary to increase the prediction confidence and domain extrapolation of the presented FDI model. In general, to pursue a modeling approach that captures the underlying mechanisms of the food effect, a more diverse set of training data and further studies on mechanisms are needed.

Furthermore, DD(G)I modeling involving tacrolimus as a CYP3A victim drug was successfully performed by coupling the developed tacrolimus model with models of the CYP3A perpetrator drugs voriconazole, itraconazole, and rifampicin while considering different CYP3A5 activity levels.^{27,28} However, a slight underprediction of tacrolimus C_{\max} values can be observed for each modeled DD(G)I. Here, various approaches were explored to refine DD(G)I predictions. Among others, the inclusion of P-gp in the model was tested, as tacrolimus has been identified as a P-gp substrate in vitro and inhibition of P-gp by itraconazole and rifampicin is described in the literature.^{6,39,40} For the final model, the implementation of P-gp was eventually discarded due to its insignificant improvements for DD(G)I predictions. Potential reasons for the remaining slight underprediction of tacrolimus C_{\max} values could be, for example, the involvement of additional, still unknown transporters in the distribution of tacrolimus or a discrepancy between the incorporated expression profiles of CYP3A4 and CYP3A5 and the respective actual in vivo expression in different organs. Overall, depending on the CYP2C19 phenotype, modeled pretreatment with voriconazole increased the total bioavailability of tacrolimus by 2.5-fold (NMs), 2.7-fold (IMs), and 3.1-fold (PMs). In the case of pretreatment with itraconazole and rifampicin, the total bioavailability of tacrolimus increased by 2.4-fold and decreased by 58%, respectively. All three perpetrators showed no effect on the fraction absorbed of tacrolimus.

Other whole-body PBPK models of tacrolimus are available in the literature, focusing, for instance, on pregnant populations or DDIs between tacrolimus and Wuzhi capsule ingredients.^{41,42}

Other investigators used a minimal PBPK model of tacrolimus to also investigate the impact of CYP3A5 genotype on tacrolimus PK in addition to other factors such as hematocrit.⁴³ Due to considerable structural differences between whole-body and minimal PBPK models, significant differences in the observed study populations, and

differing implementation of CYP3A5, a comparison of the two models is difficult. Moreover, due to the minimal overlap of estimated and used model input parameters as well as vast differences in cardinality of training and test datasets, comparing the predictive model performances might not be reasonable.

The presented tacrolimus model provides new important insights by investigating the food effect of tacrolimus as well as clinically relevant DD(G)Is involving CYP3A perpetrators, particularly azole antifungal agents, while considering different CYP3A5 activities. In addition, the model was built and evaluated using a comprehensive set of clinical data, including multiple clinically relevant formulations over wide dosing ranges and a large number of 37 mean whole blood concentration–time profiles obtained from a total of 911 study participants of different ethnicities. However, further studies investigating MD applications of tacrolimus would be beneficial to assess possible tacrolimus accumulation.

To conclude, the developed tacrolimus whole-body PBPK model demonstrates good descriptive and predictive performance in healthy individuals. Moreover, the model was successfully used to investigate and predict the interaction between tacrolimus PK and food intake as well as the influence of the CYP3A perpetrator drugs voriconazole, itraconazole, and rifampicin on tacrolimus exposure in DD(G)I scenarios. Potential applications of the model include MID3 or the support of precision dosing. Once clinical study data and corresponding PBPK models on additional CYP3A perpetrators become available, the model can be extended to further investigate the role of tacrolimus as a CYP3A victim drug. Here, DD(G)I studies analyzing different CYP3A5 genotypes would be of particular interest providing a more detailed understanding of the CYP3A5 polymorphism and its effects on tacrolimus PK. Finally, the model could be expanded to investigate tacrolimus PK in patients, especially recipients of different types of solid organ transplants.

AUTHOR CONTRIBUTIONS

H.L.H.L., D.F., S.R., D.S., M.S., D.T., S.F., M.v.d.L., D.J.A.R.M., J.J.S., and T.L. wrote the manuscript. H.L.H.L., D.F., S.R., D.S., and T.L. designed the research. H.L.H.L. performed the research. H.L.H.L., D.F., S.R., D.S., and T.L. analyzed the data.

ACKNOWLEDGMENT

Open Access funding enabled and organized by Projekt DEAL.

FUNDING INFORMATION

This work is part of the Horizon 2020 INSPIRATION (Qualified Open Systems Pharmacology Modeling



Network of Drug-Drug-Gene Interactions) project. The INSPIRATION project (FKZ 031 L0241) is supported by the German Federal Ministry of Education and Research under the framework of ERACoSysMed (Collaboration on systems medicine funding to promote the implementation of systems biology approaches in clinical research and medical practice). Matthias Schwab was supported in parts by the Robert Bosch Stiftung Stuttgart, Germany, and the Deutsche Forschungsgemeinschaft under Germany's Excellence Strategy-EXC 2180-390900677.

CONFLICT OF INTEREST STATEMENT

Donato Teutonico is an employee of Sanofi and uses Open Systems Pharmacology software, tools, or models in his professional role. Donato Teutonico and Thorsten Lehr are members of the Open Systems Pharmacology Management Team. Sebastian Frechen uses Open Systems Pharmacology software, tools, or models in his professional role and is a member of the Open Systems Pharmacology Sounding Board. All other authors declared no competing interests for this work.

ORCID

Simeon Rüdesheim <https://orcid.org/0000-0002-5741-2511>

Thorsten Lehr <https://orcid.org/0000-0002-8372-1465>

REFERENCES

1. Astellas Pharma, Inc. Highlights of prescribing information PROGRAF® (tacrolimus). 2021.
2. Lentine KL, Smith JM, Hart A, et al. OPTN/SRTR 2020 annual data report: kidney. *Am J Transplant*. 2022;22:21-136. doi:10.1111/ajt.16982
3. Takagi T, Ramachandran C, Bermejo M, Yamashita S, Yu LX, Amidon GL. A provisional biopharmaceutical classification of the top 200 oral drug products in the United States, Great Britain, Spain, and Japan. *Mol Pharm*. 2006;3:631-643. doi:10.1021/mp0600182
4. Tsunashima D, Kawamura A, Murakami M, et al. Assessment of tacrolimus absorption from the human intestinal tract: open-label, randomized, 4-way crossover study. *Clin Ther*. 2014;36:748-759. doi:10.1016/j.clinthera.2014.02.021
5. Hebert MF, Fisher RM, Marsh CL, Dressler D, Bekersky I. Effects of rifampin on tacrolimus pharmacokinetics in healthy volunteers. *J Clin Pharmacol*. 1999;39:91-96. doi:10.1177/00912709922007499
6. Saeki T, Ueda K, Tanigawara Y, Hori R, Komano T. Human P-glycoprotein transports cyclosporin a and FK506. *J Biol Chem*. 1993;268:6077-6080.
7. Venkataramanan R, Swaminathan A, Prasad T, et al. Clinical pharmacokinetics of tacrolimus. *Clin Pharmacokinet*. 1995;29:404-430. doi:10.2165/00003088-199529060-00003
8. Dai Y, Hebert MF, Isoherranen N, et al. Effect of CYP3A5 polymorphism on tacrolimus metabolic clearance in vitro. *Drug Metab Dispos*. 2006;34:836-847. doi:10.1124/dmd.105.008680
9. Brunet M, van Gelder T, Åsberg A, et al. Therapeutic drug monitoring of tacrolimus-personalized therapy: second consensus report. *Ther Drug Monit*. 2019;41:261-307. doi:10.1097/FTD.0000000000000640
10. Kim EJ, Kim SJ, Huh KH, et al. Clinical significance of tacrolimus intra-patient variability on kidney transplant outcomes according to pre-transplant immunological risk. *Sci Rep*. 2021;11:12114. doi:10.1038/s41598-021-91630-4
11. Bekersky I, Dressler D, Mekki QA. Effect of low- and high-fat meals on tacrolimus absorption following 5 mg single oral doses to healthy human subjects. *J Clin Pharmacol*. 2001;41:176-182. doi:10.1177/00912700122009999
12. Huppertz A, Bollmann J, Behnisch R, et al. Differential effect of a continental breakfast on tacrolimus formulations with different release characteristics. *Clin. Pharmacol. Drug Dev*. 2021;10:899-907. doi:10.1002/cpdd.924
13. Zheng S, Tasnif Y, Hebert MF, et al. Measurement and compartmental modeling of the effect of CYP3A5 gene variation on systemic and intrarenal tacrolimus disposition. *Clin Pharmacol Ther*. 2012;92:737-745. doi:10.1038/clpt.2012.175
14. Birdwell KA, Decker B, Barbarino JM, et al. Clinical pharmacogenetics implementation consortium (CPIC) guidelines for CYP3A5 genotype and tacrolimus dosing. *Clin Pharmacol Ther*. 2015;98:19-24. doi:10.1002/cpt.113
15. Drug development and drug interactions: FDA table of substrates, inhibitors and inducers. Accessed April 23, 2022. <https://www.fda.gov/drugs/drug-interactions-labeling/drug-development-and-drug-interactions-table-substrates-inhibitors-and-inducers>
16. Huppertz A, Ott C, Bruckner T, et al. Prolonged-release tacrolimus is less susceptible to interaction with the strong CYP3A inhibitor voriconazole in healthy volunteers. *Clin Pharmacol Ther*. 2019;106:1290-1298. doi:10.1002/cpt.1529
17. Imamura CK, Furihata K, Okamoto S, Tanigawara Y. Impact of cytochrome P450 2C19 polymorphisms on the pharmacokinetics of tacrolimus when coadministered with voriconazole. *J Clin Pharmacol*. 2016;56:408-413. doi:10.1002/jcph.605
18. Vanhove T, Annaert P, Knops N, de Loo H, de Hoon J, Kuypers DRJ. In vivo CYP3A4 activity does not predict the magnitude of interaction between itraconazole and tacrolimus from an extended release formulation. *Basic Clin Pharmacol Toxicol*. 2019;124:50-55. doi:10.1111/bcpt.13092
19. Pappas PG, Alexander BD, Andes DR, et al. Invasive fungal infections among organ transplant recipients: results of the transplant-associated infection surveillance network (TRANSNET). *Clin Infect Dis*. 2010;50:1101-1111. doi:10.1086/651262
20. Zhuang X, Lu C. PBPK modeling and simulation in drug research and development. *Acta Pharm Sin B*. 2016;6:430-440. doi:10.1016/j.apsb.2016.04.004
21. Türk D, Fuhr LM, Marok FZ, et al. Novel models for the prediction of drug-gene interactions. *Expert Opin Drug Metab Toxicol*. 2021;17:1293-1310. doi:10.1080/17425255.2021.1998455
22. Gonzalez D, Rao GG, Bailey SC, et al. Precision dosing: public health need, proposed framework, and anticipated impact. *Clin Transl Sci*. 2017;10:443-454. doi:10.1111/cts.12490
23. Grimstein M, Yang Y, Zhang X, et al. Physiologically based pharmacokinetic modeling in regulatory science: an update from the U.S. Food and Drug Administration's Office of Clinical Pharmacology. *J Pharm Sci*. 2019;108:21-25. doi:10.1016/j.xphs.2018.10.033
24. Mitchell BM, Muftakhidinov TW, Jędrzejewski-Szmek Z. Engauge digitizer software. Accessed September 21, 2021. <https://merkumtmitchell.github.io/engauge-digitizer>

25. Wojtyniak J-G, Britz H, Selzer D, Schwab M, Lehr T. Data digitizing: accurate and precise data extraction for quantitative systems pharmacology and physiologically-based pharmacokinetic modeling. *CPT Pharmacometrics Syst Pharmacol*. 2020;9:322-331. doi:10.1002/psp4.12511
26. Guest EJ, Aarons L, Houston JB, Rostami-Hodjegan A, Galetin A. Critique of the two-fold measure of prediction success for ratios: application for the assessment of drug-drug interactions. *Drug Metab Dispos*. 2011;39:170-173. doi:10.1124/dmd.110.036103
27. Hanke N, Frechen S, Moj D, et al. PBPK models for CYP3A4 and P-gp DDI prediction: a modeling network of rifampicin, itraconazole, clarithromycin, midazolam, alfentanil, and digoxin. *CPT Pharmacometrics Syst Pharmacol*. 2018;7:647-659. doi:10.1002/psp4.12343
28. Li X, Frechen S, Moj D, et al. A physiologically based pharmacokinetic model of voriconazole integrating time-dependent inhibition of CYP3A4, genetic polymorphisms of CYP2C19 and predictions of drug-drug interactions. *Clin Pharmacokinet*. 2020;59:781-808. doi:10.1007/s40262-019-00856-z
29. Petan JA, Undre N, First MR, et al. Physiochemical properties of generic formulations of tacrolimus in Mexico. *Transplant Proc*. 2008;40:1439-1442. doi:10.1016/j.transproceed.2008.03.091
30. Mercuri A, Wu S, Stranzinger S, et al. In vitro and in silico characterisation of tacrolimus released under biorelevant conditions. *Int J Pharm*. 2016;515:271-280. doi:10.1016/j.ijpharm.2016.10.020
31. Langenbucher F. Linearization of dissolution rate by the Weibull distribution. *J Pharm Pharmacol*. 1972;24:979-981. doi:10.1111/j.2042-7158.1972.tb08930.x
32. Bekersky I, Dressler D, Mekki Q. Effect of time of meal consumption on bioavailability of a single oral 5 mg tacrolimus dose. *J Clin Pharmacol*. 2001;41:289-297. doi:10.1177/00912700122010104
33. Lainesse A, Hussain S, Monif T, et al. Bioequivalence studies of tacrolimus capsule under fasting and fed conditions in healthy male and female subjects. *Arzneimittel-Forschung*. 2008;58:242-247. doi:10.1055/s-0031-1296500
34. Takizawa Y, Kishimoto H, Nakagawa M, et al. Effects of pharmaceutical excipients on membrane permeability in rat small intestine. *Int J Pharm*. 2013;453:363-370. doi:10.1016/j.ijpharm.2013.05.055
35. Deng J, Zhu X, Chen Z, et al. A review of food-drug interactions on oral drug absorption. *Drugs*. 2017;77:1833-1855. doi:10.1007/s40265-017-0832-z
36. Koziolk M, Alcaro S, Augustijns P, et al. The mechanisms of pharmacokinetic food-drug interactions – a perspective from the UNGAP group. *Eur J Pharm Sci*. 2019;134:31-59. doi:10.1016/j.ejps.2019.04.003
37. Kuypers DRJ, Claes K, Evenepoel P, Maes B, Vanrenterghem Y. The rate of gastric emptying determines the timing but not the extent of oral tacrolimus absorption: simultaneous measurement of drug exposure and gastric emptying by carbon-14-octanoic acid breath test in stable renal allograft recipients. *Drug Metab Dispos*. 2004;32:1421-1425. doi:10.1124/dmd.104.001503
38. Undre NA, Stevenson P, Schäfer A. Pharmacokinetics of tacrolimus: clinically relevant aspects. *Transplant Proc*. 1999;31:21 S-24 S. doi:10.1016/S0041-1345(99)00788-5
39. Shityakov S, Förster C. In silico structure-based screening of versatile P-glycoprotein inhibitors using polynomial empirical scoring functions. *Adv Appl Bioinform Chem*. 2014;7:1-9. doi:10.2147/AABC.S56046
40. Reitman ML, Chu X, Cai X, et al. Rifampin's acute inhibitory and chronic inductive drug interactions: experimental and model-based approaches to drug-drug interaction trial design. *Clin Pharmacol Ther*. 2011;89:234-242. doi:10.1038/clpt.2010.271
41. Jogiraju VK, Avvari S, Gollen R, Taft DR. Application of physiologically based pharmacokinetic modeling to predict drug disposition in pregnant populations. *Biopharm Drug Dispos*. 2017;38:426-438. doi:10.1002/bdd.2081
42. Zhang H, Bu F, Li L, et al. Prediction of drug-drug interaction between tacrolimus and principal ingredients of Wuzhi capsule in chinese healthy volunteers using physiologically-based pharmacokinetic modelling. *Basic Clin Pharmacol Toxicol*. 2018;122:331-340. doi:10.1111/bcpt.12914
43. Emoto C, Johnson TN, Hahn D, et al. A theoretical physiologically-based pharmacokinetic approach to ascertain covariates explaining the large interpatient variability in tacrolimus disposition. *CPT Pharmacometrics Syst Pharmacol*. 2019;8:273-284. doi:10.1002/psp4.12392
44. Bekersky I, Dressler D, Alak A, Boswell GW, Mekki QA. Comparative tacrolimus pharmacokinetics: normal versus mildly hepatically impaired subjects. *J Clin Pharmacol*. 2001;41:628-635. doi:10.1177/00912700122010519
45. Bekersky I, Dressler D, Mekki QA. Dose linearity after oral administration of tacrolimus 1-mg capsules at doses of 3, 7, and 10 mg. *Clin Ther*. 1999;21:2058-2064. doi:10.1016/S0149-2918(00)87237-9
46. Gantar K, Škerget K, Mochkin I, Bajc A. Meeting regulatory requirements for drugs with a narrow therapeutic index: bioequivalence studies of generic once-daily tacrolimus. *Drug Healthc Patient Saf*. 2020;12:151-160. doi:10.2147/DHPS.S256455
47. Mancinelli LM, Frassetto L, Floren LC, et al. The pharmacokinetics and metabolic disposition of tacrolimus: a comparison across ethnic groups. *Clin Pharmacol Ther*. 2001;69:24-31. doi:10.1067/mcp.2001.113183
48. Wring S, Murphy G, Atiee G, et al. Clinical pharmacokinetics and drug-drug interaction potential for coadministered SCY-078, an oral fungicidal glucan synthase inhibitor, and tacrolimus. *Clin Pharmacol Drug Dev*. 2019;8:60-69. doi:10.1002/cpdd.588
49. Bekersky I, Dressler D, Colburn W, Mekki Q. Bioequivalence of 1 and 5 mg tacrolimus capsules using a replicate study design. *J Clin Pharmacol*. 1999;39:1032-1037. doi:10.1177/00912709922011791
50. Stiff F, Vanmolkot F, Scheffers I, van Bortel L, Neef C, Christiaans M. Rectal and sublingual administration of tacrolimus: a single-dose pharmacokinetic study in healthy volunteers. *Br J Clin Pharmacol*. 2014;78:996-1004. doi:10.1111/bcp.12420
51. Tortorici MA, Parks V, Matschke K, Korth-Bradley J, Patat A. The evaluation of potential pharmacokinetic interaction between sirolimus and tacrolimus in healthy volunteers. *Eur J Clin Pharmacol*. 2013;69:835-842. doi:10.1007/s00228-012-1407-2
52. Undre N, Dickinson J. Relative bioavailability of single doses of prolonged-release tacrolimus administered as a suspension,



orally or via a nasogastric tube, compared with intact capsules: a phase 1 study in healthy participants. *BMJ Open*. 2017;7:1-7. doi:[10.1136/bmjopen-2016-012252](https://doi.org/10.1136/bmjopen-2016-012252)

SUPPORTING INFORMATION

Additional supporting information can be found online in the Supporting Information section at the end of this article.

How to cite this article: Loer HLH, Feick D, Rüdeshiem S, et al. Physiologically based pharmacokinetic modeling of tacrolimus for food–drug and CYP3A drug–drug–gene interaction predictions. *CPT Pharmacometrics Syst Pharmacol*. 2023;12:724-738. doi:[10.1002/psp4.12946](https://doi.org/10.1002/psp4.12946)

4.2 PROJECT II: PBPK MODELING OF IMATINIB

Publication

Loer, H. L. H.; Kovar, C.; Rüdesheim, S.; Marok, F. Z.; Fuhr, L. M.; Selzer, D.; Schwab, M.; Lehr, T. Physiologically based pharmacokinetic modeling of imatinib and N-desmethyl imatinib for drug–drug interaction predictions. *CPT: Pharmacometrics and Systems Pharmacology* **2024**, *13*, 926–940, DOI: [10.1002/psp4.13127](https://doi.org/10.1002/psp4.13127).

Supplementary Materials

Related Supplementary Materials are available on the accompanying USB storage device and via the following link: <https://pmc.ncbi.nlm.nih.gov/articles/PMC11179706/>.

Copyright

This is an open access article under the terms of CC BY-NC 4.0 (<https://creativecommons.org/licenses/by-nc/4.0/>), which permits use, distribution and reproduction in any medium, provided the original work is properly cited and is not used for commercial purposes. © 2024 The Authors. *CPT: Pharmacometrics & Systems Pharmacology* published by Wiley Periodicals LLC on behalf of American Society for Clinical Pharmacology and Therapeutics.

Author Contributions According to CRediT [5]

Helena Leonie Hanae Loer	Conceptualization, Investigation, Visualization, Writing – Original Draft, Writing – Review & Editing
Christina Kovar	Conceptualization, Investigation, Writing – Review & Editing
Simeon Rüdesheim	Conceptualization, Writing – Review & Editing
Fatima Zahra Marok	Conceptualization
Laura Maria Fuhr	Conceptualization
Dominik Selzer	Writing – Review & Editing
Matthias Schwab	Writing – Review & Editing, Funding Acquisition
Thorsten Lehr	Conceptualization, Writing – Review & Editing, Funding Acquisition



ARTICLE

Physiologically based pharmacokinetic modeling of imatinib and *N*-desmethyl imatinib for drug–drug interaction predictions

Helena Leonie Hanae Loer¹ | Christina Kovar^{1,2} | Simeon Rüdesheim^{1,2} |
Fatima Zahra Marok¹ | Laura Maria Fuhr¹ | Dominik Selzer¹ |
Matthias Schwab^{2,3,4} | Thorsten Lehr¹

¹Clinical Pharmacy, Saarland University, Saarbrücken, Germany

²Dr. Margarete Fischer-Bosch-Institute of Clinical Pharmacology, Stuttgart, Germany

³Departments of Clinical Pharmacology, and Pharmacy and Biochemistry, University of Tübingen, Tübingen, Germany

⁴Cluster of Excellence iFIT (EXC2180), Image-Guided and Functionally Instructed Tumor Therapies, University of Tübingen, Tübingen, Germany

Correspondence

Thorsten Lehr, Clinical Pharmacy, Saarland University, Campus C4 3, 66123 Saarbrücken, Germany.
Email: thorsten.lehr@mx.uni-saarland.de

Abstract

The first-generation tyrosine kinase inhibitor imatinib has revolutionized the development of targeted cancer therapy and remains among the frontline treatments, for example, against chronic myeloid leukemia. As a substrate of cytochrome P450 (CYP) 2C8, CYP3A4, and various transporters, imatinib is highly susceptible to drug–drug interactions (DDIs) when co-administered with corresponding perpetrator drugs. Additionally, imatinib and its main metabolite *N*-desmethyl imatinib (NDMI) act as inhibitors of CYP2C8, CYP2D6, and CYP3A4 affecting their own metabolism as well as the exposure of co-medications. This work presents the development of a parent–metabolite whole-body physiologically based pharmacokinetic (PBPK) model for imatinib and NDMI used for the investigation and prediction of different DDI scenarios centered around imatinib as both a victim and perpetrator drug. Model development was performed in PK-Sim® using a total of 60 plasma concentration–time profiles of imatinib and NDMI in healthy subjects and cancer patients. Metabolism of both compounds was integrated via CYP2C8 and CYP3A4, with imatinib additionally transported via P-glycoprotein. The subsequently developed DDI network demonstrated good predictive performance. DDIs involving imatinib and NDMI were simulated with perpetrator drugs rifampicin, ketoconazole, and gemfibrozil as well as victim drugs simvastatin and metoprolol. Overall, 12/12 predicted DDI area under the curve determined between first and last plasma concentration measurements (AUC_{last}) ratios and 12/12 predicted DDI maximum plasma concentration (C_{max}) ratios were within twofold of the respective observed ratios. Potential applications of the final model include model-informed drug development or the support of model-informed precision dosing.

This is an open access article under the terms of the [Creative Commons Attribution-NonCommercial](https://creativecommons.org/licenses/by-nc/4.0/) License, which permits use, distribution and reproduction in any medium, provided the original work is properly cited and is not used for commercial purposes.

© 2024 The Authors. *CPT: Pharmacometrics & Systems Pharmacology* published by Wiley Periodicals LLC on behalf of American Society for Clinical Pharmacology and Therapeutics.

Study Highlights

WHAT IS THE CURRENT KNOWLEDGE ON THE TOPIC?

As a victim drug of cytochrome P450 (CYP) 2C8, CYP3A4, and P-glycoprotein, imatinib is highly susceptible to drug–drug interactions (DDIs). Additionally, acting as a perpetrator, imatinib affects its own metabolism and the exposure of co-medications via inhibition of CYP2C8, CYP2D6, and CYP3A4.

WHAT QUESTION DID THIS STUDY ADDRESS?

This study presents the development of a new whole-body physiologically based pharmacokinetic model of imatinib and its main metabolite *N*-desmethyl imatinib (NDMI). The model was applied to describe and predict the role of imatinib and NDMI as victims and perpetrators within a newly established CYP2C8/CYP2D6/CYP3A4/P-glycoprotein-DDI network.

WHAT DOES THIS STUDY ADD TO OUR KNOWLEDGE?

The DDI network helps to evaluate the effects of co-medication on the pharmacokinetics of imatinib/NDMI and the inhibitory potential of imatinib/NDMI, highlighting the importance of considering imatinib as both victim and perpetrator in clinical practice.

HOW MIGHT THIS CHANGE DRUG DISCOVERY, DEVELOPMENT, AND/OR THERAPEUTICS?

The model can be used to support model-informed drug development and to improve clinical safety and efficacy of imatinib and co-medications through model-based precision dosing.

INTRODUCTION

In 2001, approval of the tyrosine kinase inhibitor (TKI) imatinib for the treatment of Philadelphia chromosome-positive chronic myeloid leukemia (CML) revolutionized not only the therapy of CML, but also the development of targeted cancer therapy in general.¹ Imatinib selectively inhibits the *BCR-ABL* oncoprotein encoded by the Philadelphia chromosome, suppressing its constitutive tyrosine kinase activity and associated uncontrolled proliferation.² However, resistance to imatinib, primarily due to mutations in the *BCR-ABL* oncogene and other factors, necessitated the development of subsequent generations of TKIs.³ Despite this, imatinib remains one of the front-line therapies for CML and has been approved for additional indications, such as acute lymphoblastic leukemia and gastrointestinal stromal tumors (GISTs).⁴

As a Biopharmaceutics Classification System class I drug, imatinib demonstrates high intestinal permeability and solubility.⁵ When administered orally, it is completely absorbed, achieving an absolute bioavailability exceeding 97%.⁶ Imatinib is primarily metabolized via cytochrome P450 (CYP) enzymes 2C8 and 3A4,⁷ with its main metabolite, *N*-desmethyl imatinib (NDMI), accounting for 10%–15% of the overall drug level. NDMI's potency against *BCR-ABL* is approximately three times lower than that of imatinib itself.^{8,9} Furthermore, imatinib has been

identified as a substrate of numerous influx and efflux transporters in vitro, such as organic cation transporter (OCT) 1, OCTN2, organic-anion-transporting polypeptide (OATP) 1A2, OATP1B3, breast cancer resistance protein (BCRP), and P-glycoprotein (P-gp).^{10–12} Following oral administration, 67% and 13% of a single dose (SD) of imatinib are excreted as imatinib-related products in feces and urine, respectively, over a period of 7 days.¹³

Imatinib and its metabolite NDMI are highly susceptible to drug–drug interactions (DDIs), impacting their own metabolism and altering the exposure of co-administered drugs via inhibition of CYP2C8, CYP2D6, and CYP3A4.^{14,15} For instance, pretreatment with imatinib resulted in a 2.6-fold increase in the area under the curve (AUC) of the active metabolite of simvastatin, which is formed by CYP3A4.¹⁶ Consequently, the United States Food and Drug Administration (FDA) lists imatinib as a moderate inhibitor of CYP3A4.¹⁷ However, imatinib does not only act as a perpetrator but also as a victim drug in DDI scenarios. Here, perpetrator drugs affecting imatinib's and NDMI's metabolism via CYP2C8 and CYP3A4 are of particular clinical importance. For example, concomitant administration with the antifungal agent ketoconazole, an inhibitor, increases imatinib exposure by 40%. In contrast, pretreatment with the antibiotic agent rifampicin, an inducer, leads to a 74% reduction in AUC of imatinib.^{18,19} Given the typical



prescription of five to eight drugs per patient in oncology, these interactions present a substantial challenge in terms of therapeutic management during imatinib treatment. A co-medication review of over 4500 patients receiving imatinib identified potential DDIs associated with a decrease in imatinib effectiveness in 43% and an increase in toxicity in 68% of cases.²⁰

Given these complexities, there is a critical need to understand the pharmacokinetics (PK) of imatinib and NDMI, especially regarding their interaction potential. This understanding is vital to enhance the safety and efficacy of imatinib therapy. Therefore, this study aimed to develop a whole-body physiologically based pharmacokinetic (PBPK) model for imatinib and its main metabolite NDMI. Such models are exceptionally useful in investigating the PK of drugs, both independently and within DDI frameworks, as emphasized by the substantial number of PBPK studies submitted to regulatory agencies concentrating on DDI research questions.²¹ Furthermore, the versatility of PBPK modeling, especially in integrating patient-specific demographic, physiological, pathophysiological, and pharmacogenetic data, makes it instrumental in facilitating model-based precision dosing strategies.²² Utilizing the developed imatinib model, this study further conducted predictions and analyses of various complex DDI scenarios, showcasing imatinib as both a victim and perpetrator of such interactions. Numerous PBPK models of imatinib have been developed to explore various research inquiries.^{23–25} However, our approach uniquely extends this body of work by providing a comprehensive whole-body PBPK model that incorporates imatinib's main metabolite NDMI, and examines imatinib as both a victim and a perpetrator drug in DDI scenarios. To promote widespread access and encourage further research, the finalized model files will be made available to the public at <http://models.clinicalpharmacy.me/>.

METHODS

Software

Development of the imatinib PBPK model, including parameter identification and local sensitivity analyses, was performed using PK-Sim® and MoBi® version 11.0 (Open Systems Pharmacology Suite, www.open-systems-pharmacology.org, 2022). Engauge Digitizer version 12.1 (M. Mitchell, <https://markumitchell.github.io/engauge-digitizer/>, 2019) was utilized for the digitization of published clinical study data according to Wojtyniak et al.²⁶ The R programming language version 4.2.3 (R Foundation for Statistical Computing, Vienna,

Austria, 2023) was used to generate plots and calculate PK parameters as well as quantitative model performance measures.

Clinical study data

Plasma concentration–time profiles of imatinib and its main metabolite NDMI were gathered from published literature covering a wide dosing range of imatinib administered either intravenously or orally in SD and multiple dose (MD) studies. Once digitized, the profiles were systematically divided into a training and a test dataset for model development and model evaluation, respectively. The allocation of profiles was conducted in a deliberate, non-randomized fashion. The goal was to construct a training dataset that encompassed a diverse range of dosages and administration forms, ensuring each profile included a wide array of sampling time points over an extended duration. Concurrently, the approach aimed to optimize the size of the test dataset, thereby enhancing its robustness for thorough model evaluation. Only profiles obtained from healthy individuals were selected for the training dataset, whereas CML and GIST patients were included in the test dataset.

Physiologically based pharmacokinetic model building

Prior to building the imatinib parent–metabolite model, an extensive literature search was conducted regarding clinical study data and physicochemical parameters as well as information on the absorption, distribution, metabolism, and excretion (ADME) of imatinib and NDMI.

For model simulations, a representative virtual individual was created for each included study population based on the corresponding reported mean and mode data for age, sex, weight, height, body mass index, and ethnicity. If demographic information was missing or incomplete, a default individual was generated according to the population database provided in PK-Sim®. Relative expressions of relevant transporters and enzymes in the different organs were adopted from the expression database included in PK-Sim®. Tables S1 and S2 list the reference concentration in the respective organ of highest concentration as well as the relative expression profile for each implemented transporter/enzyme. To visually examine the influence of variation in demographic factors, plasma protein binding to α 1-acid glycoprotein (AGP), as well as transporter and metabolizing enzyme abundances on the exposure of imatinib and NDMI, a virtual population of 1000 individuals was established for each study population. If no minimum

and maximum demographic values were provided, an age range of 20–50 years was assumed. Geometric standard deviations applied to the incorporated transporter/enzyme concentrations for the population sampling process are presented in Table S1.

During the parameter identification process, unknown parameter values not reported in the literature or parameters involved in PK-Sim®'s permeability and partition quantitative structure–activity relationship (QSAR) models were fitted using the training dataset. Following oral administration, the release of imatinib was incorporated via a Weibull function (Equation S1). Depending on the information available in the literature, transport and metabolic processes were implemented as either Michaelis–Menten (MM) (Equation S2) or first-order kinetics. The role of relevant enzymes in imatinib metabolism was informed by including published *in vitro* data, detailing the proportional contribution of each relevant enzyme to the total clearance of imatinib, thereby informing the PBPK model with more precise metabolic pathway information.

Physiologically based pharmacokinetic model evaluation

The imatinib parent–metabolite model was evaluated both graphically and statistically. First, predicted plasma concentration–time profiles of imatinib and NDMI were plotted alongside corresponding observed data. Goodness-of-fit plots were generated to assess the deviation of predicted versus observed plasma concentrations, AUC determined between first and last plasma concentration measurements (AUC_{last}), and maximum plasma concentration (C_{max}) values for each profile. A twofold difference from observed values was set as the prediction success threshold. The statistical analysis covered the calculation of mean relative deviations (MRDs) for predicted concentration–time points (Equation 1) and geometric mean fold errors for predicted AUC_{last} and C_{max} values (Equation 2).

$$MRD = 10^x; x = \sqrt{\frac{\sum_{i=1}^k (\log_{10} \hat{c}_i - \log_{10} c_i)^2}{k}} \quad (1)$$

where c_i = i -th observed concentration, \hat{c}_i = predicted concentration corresponding to the i -th observed concentration, and k = number of observed values.

$$GMFE = 10^x; x = \frac{\sum_{i=1}^m \left| \log_{10} \left(\frac{\hat{p}_i}{p_i} \right) \right|}{m} \quad (2)$$

where p_i = observed AUC_{last} or C_{max} value of study i , \hat{p}_i = corresponding predicted AUC_{last} or C_{max} value of study i , and m = number of studies.

Finally, local sensitivity analyses were conducted for imatinib and NDMI, which are described in Section S2.7.1.

Drug–drug interaction network modeling

To investigate the role of imatinib and NDMI acting as either victims or perpetrators in DDI scenarios, the developed model was coupled with previously published PBPK models of rifampicin, ketoconazole, gemfibrozil, simvastatin, and metoprolol.^{27–31} Relevant interaction types, including induction, competitive inhibition, non-competitive inhibition, and mechanism-based inactivation, were incorporated as described in the Open Systems Pharmacology Suite manual,³² with the corresponding interaction parameters adopted from the literature.

The developed DDI network was graphically evaluated by comparing predicted with observed plasma concentration–time profiles of each victim drug with and without co-administration of the respective perpetrator drug. Predicted and observed AUC_{last} and C_{max} ratios were calculated for each DDI scenario according to Equation 3 and compared by applying the limits proposed by Guest et al.³³ to determine prediction accuracy (including 20% variability).

$$DDI \text{ PK parameter ratio} = \frac{PK \text{ parameter}_{DDI}}{PK \text{ parameter}_{Control}} \quad (3)$$

where $PK \text{ parameter} = AUC_{last}$ or C_{max} , $PK \text{ parameter}_{DDI} = AUC_{last}$ or C_{max} of victim drug with perpetrator co-administration, and $PK \text{ parameter}_{Control} = AUC_{last}$ or C_{max} of victim drug control.

Quantitative evaluation was performed by calculating GMFE values (Equation 2) for all predicted DDI AUC_{last} and C_{max} ratios.

RESULTS

Physiologically based pharmacokinetic model building and evaluation

The imatinib parent–metabolite model was developed using 24 clinical studies providing a total of 42 and 18 plasma concentration–time profiles of imatinib and NDMI, respectively. The profiles were allocated to either the training ($n=8$) or the test ($n=52$) dataset. Of these 60 profiles, 40 were collected in healthy subjects, while 20 were derived from CML and GIST patients. Given no apparent difference between plasma profiles of healthy subjects and patients, the developed PBPK model was applied to CML and GIST patients without modifications

to the drug-dependent parameters of imatinib and NDMI or the physiological parameters of the simulated virtual individuals. Routes of administration included intravenous dosing of imatinib via infusion (100 mg, SD) and oral intake as tablet or capsule (25–750 mg, SD and MD). Information on all profiles and study populations used is listed in Table S3.

Figure 1 provides a schematic representation of the transport and metabolic processes implemented in the model. Imatinib metabolism via CYP2C8 and CYP3A4 was incorporated in the model via MM kinetics, accounting for 67% and 33% of NDMI formation, respectively. The model further integrated the transformation of imatinib into unspecified metabolites through CYP3A4, following first-order kinetics. Additionally, P-gp was incorporated as a transport protein for imatinib, with its function modeled using MM kinetics. NDMI metabolism was implemented via CYP2C8, CYP3A4, and a nonspecific first-order hepatic clearance process. The effect of genetic polymorphisms on the incorporated transporters and enzymes was not accounted for in the model due to a lack of studies stratifying their cohorts by genotype or phenotype.

During model building, lipophilicities of imatinib and NDMI which are crucial parameters in several key QSAR equations were optimized. This fitting resulted in values within the reference range for imatinib and approximately one logarithmic unit lower than the reference for NDMI.

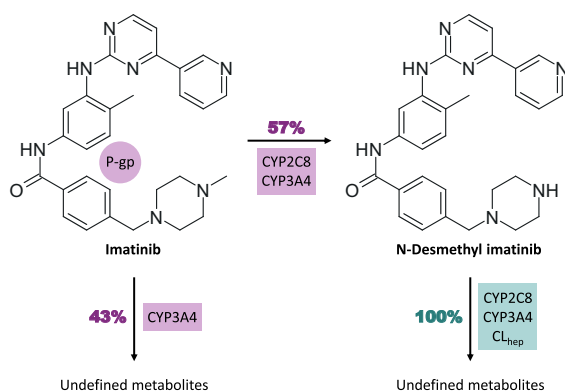


FIGURE 1 Schematic overview of the processes incorporated in the developed imatinib parent-metabolite model. Following administration of a single dose of imatinib, 57% of modeled imatinib metabolism leads to the formation of *N*-desmethyl imatinib via CYP2C8 and CYP3A4, while the remaining pathway involves the conversion of imatinib to undefined metabolites via CYP3A4. In addition, transport via P-gp was included for imatinib. For the metabolism of *N*-desmethyl imatinib, the model incorporates CYP2C8, CYP3A4, and a nonspecific hepatic clearance process. CL_{hep}: hepatic clearance, CYP: cytochrome P450, P-gp: P-glycoprotein.

Parameters for first-order clearance processes were also included in the parameter optimization procedure. For biotransformation steps modeled as MM kinetics, MM constants (K_M) were adopted from the literature, while catalytic rate constants (k_{cat}) were fitted within one magnitude of reported values. Conversely, both K_M and k_{cat} were optimized for the transport of imatinib via P-gp, as the K_M value could not be informed from the literature. In addition, (auto)inhibition was integrated using published data.^{14,34,35} Here, for imatinib, mechanism-based inactivation of CYP3A4 was implemented. Moreover, competitive inhibition of CYP2C8, CYP2D6, P-gp, and BCRP was integrated. With respect to NDMI, competitive inhibition parameters of CYP2C8, CYP2D6, and CYP3A4 were informed via literature.¹⁴ A Weibull function was applied to simulate the release of imatinib from both tablets and capsules, with parameters time to 50% dissolution and shape derived from a tablet dissolution profile of previous work according to Langenbucher et al.^{36,37} The final model parameters for imatinib and NDMI are provided in Table S4.

The developed imatinib PBPK model demonstrated good performance in describing (training dataset) and predicting (test dataset) plasma concentration–time profiles of imatinib and NDMI following intravenous and oral administration of imatinib to healthy subjects and patients. Figure 2 presents a representative selection of imatinib/NDMI population predictions compared to corresponding observed data. Linear and semilogarithmic plots of all model predictions including observed data are provided in Sections S2.1–S2.3.

Goodness-of-fit plots of predicted versus observed plasma concentrations as well as AUC_{last} and C_{max} values separated by dataset are shown in Figure 3. Overall, 92% of predicted imatinib and NDMI concentration measurements as well as 98% of predicted AUC_{last} and 98% of predicted C_{max} values were within twofold of corresponding observed data. Moreover, statistical model evaluation resulted in a mean (range) MRD of predicted plasma concentrations of 1.46 (1.07–2.81) along with mean (range) GMFE_{AUClast} and GMFEC_{max} values of 1.28 (1.00–2.40) and 1.26 (1.00–2.08), respectively. Values for MRD, AUC_{last}, and C_{max} of all profiles are listed in Tables S5 and S6.

Local sensitivity analyses were performed based on simulated steady-state conditions following oral administration of 400 mg imatinib once daily for 28 days. The steady-state AUC of imatinib and NDMI exhibited the greatest sensitivity to changes in the acid dissociation constant of the amino group within the piperazine ring and the unbound fraction (f_u), respectively. Both parameters were adopted from the literature. Of note, given the proximity of the model parameter for the acid dissociation constant (7.84) to the physiological pH of 7.4, an increase of 10% causes only a small change in imatinib and NDMI

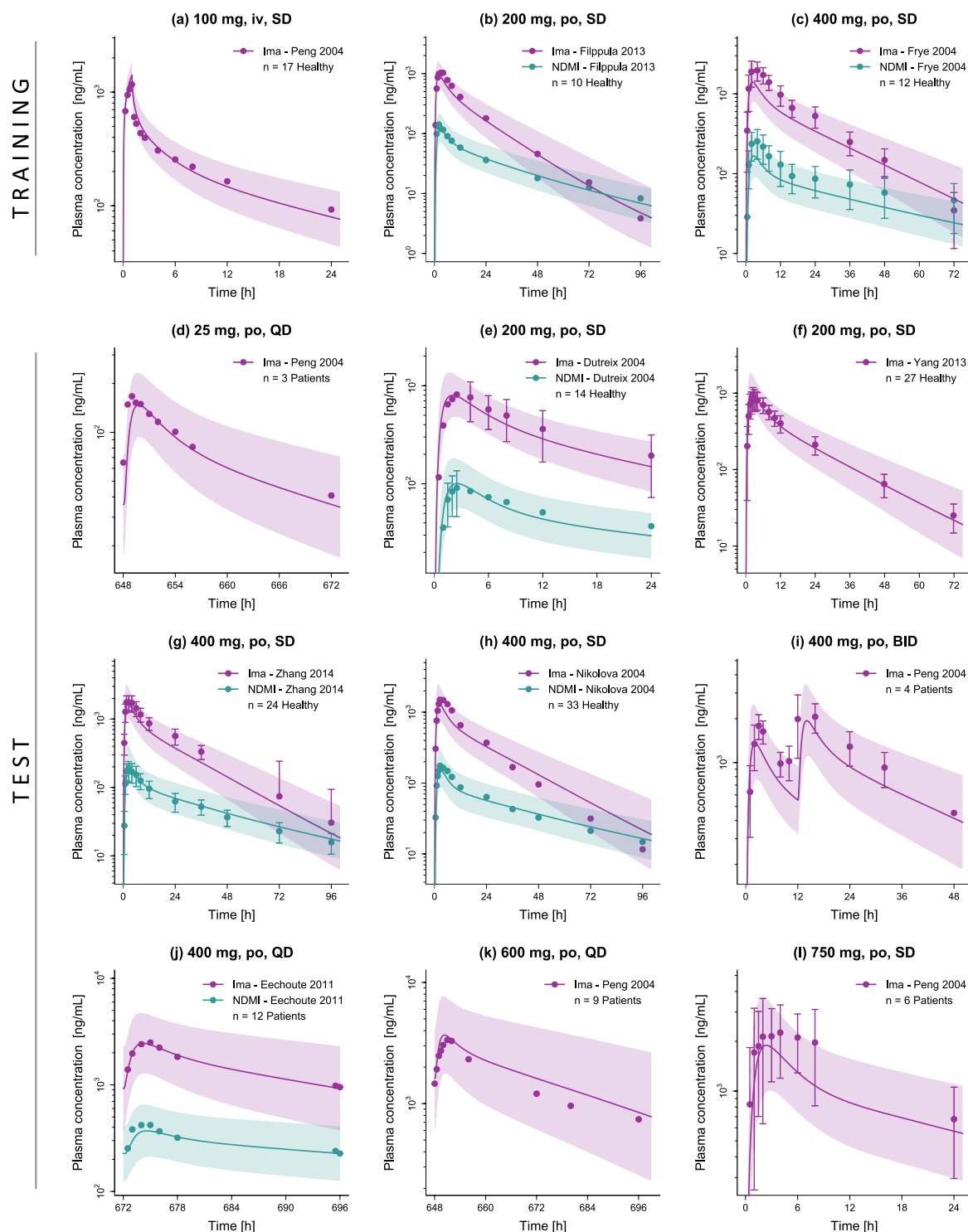


FIGURE 2 Predicted compared to observed plasma concentration–time profiles of imatinib and NDMI of the training (a–c) and test (d–l) dataset. Solid lines and ribbons represent population predictions ($n = 1000$; geometric mean and geometric standard deviation), while corresponding observed data are shown as dots (\pm standard deviation, if available).^{6,18,38,43,47–51} Detailed information on all investigated profiles is provided in [Table S3](#). BID: twice daily, Healthy: healthy subjects, Ima: imatinib, iv: intravenous, n : number of study participants, NDMI: *N*-desmethyl imatinib, Patients: cancer patients, po: oral, QD: once daily, SD: single dose.



AUC values, while a reduction of 10% is associated with a large decrease in exposure. Section S2.7.2 provides a detailed evaluation of the sensitivity analyses.

Drug–drug interaction modeling

The DDI network centered around imatinib as a victim and perpetrator drug was developed using five DDI studies. In total, three studies investigated the influence of perpetrator co-administration on the exposure of imatinib and NDMI. Here, one study examined pretreatment with the competitive CYP2C8/CYP3A4/P-gp inhibitor and inducer rifampicin, while a second study addressed co-treatment with the competitive CYP3A4/P-gp inhibitor and non-competitive CYP2C8 inhibitor ketoconazole.^{18,19} Finally, one study analyzed the effect of pretreatment with the CYP2C8 mechanism-based inactivator gemfibrozil.³⁸

Moreover, DDI studies assessing the influence of imatinib pretreatment on the PK of simvastatin and metoprolol as well as their active metabolites were available, with interactions predominantly caused by CYP3A4 mechanism-based inactivation and CYP2D6 competitive inhibition, respectively.^{15,16} In the case of metoprolol, a drug–drug–gene interaction (DDGI) study was included in which the study population was additionally stratified into CYP2D6 normal metabolizers (NMs) and intermediate metabolizers (IMs). Here, the same K_M value was used for both study cohorts, while phenotype-specific k_{cat} values were applied.²⁸ Because most NMs and IMs were $*1/*10$ and $*10/*10$ genotypes, respectively, k_{cat} values equivalent to 64% and 19% of the wildtype k_{cat} were included in the DDI model. Figure 4 shows a schematic overview of the modeled DDI network, depicting the respective main interaction mechanisms. Detailed information on the DDI studies used and model parameters of each DDI partner are available in Sections S3.1–S3.2.

Predicted versus observed plasma concentration–time profiles of each victim drug with and without co-administration of the respective perpetrator drug are displayed in Figure 5. Table 1 presents the predicted versus observed impact of each perpetrator on the respective victim, stating the exposure (AUC) during perpetrator co-administration relative to the control exposure. Furthermore, predicted versus observed DDI AUC_{last} and C_{max} ratios are shown in Figure 6. In total, 11/12 of predicted DDI AUC_{last} and 10/12 of C_{max} ratios were within the limits proposed by Guest et al.³³ with mean (range) GMFE values of 1.21 (1.02–1.65) and 1.23 (1.01–1.87), respectively. Predicted and observed DDI profiles (linear and semilogarithmic) and corresponding DDI ratios are provided in Sections S3.3–S3.6.

DISCUSSION

In the present work, a parent–metabolite whole-body PBPK model for imatinib was developed demonstrating its capability to accurately describe and predict plasma concentration–time profiles for both imatinib and its main metabolite NDMI. The model is robust across a wide dosing range of intravenously and orally administered imatinib (25–750 mg, SD and MD studies) in both healthy subjects and cancer patients. PK differences between these populations are documented in the literature and were investigated during model building. For instance, a 2–5-fold increase in AGP plasma levels is reported for CML patients compared to healthy subjects, potentially influencing imatinib f_u .³⁹ However, since elevated AGP levels were also observed to normalize during imatinib treatment, no CML-specific f_u value was incorporated in the model.⁴⁰ Overall, imatinib clearance in CML patients appears to depend on both the disease stage and the duration of imatinib use, while in GIST patients, for example, changes in liver function due to hepatic metastases or surgery have been reported.⁴⁰ Given the frequent unavailability of detailed physiological data for cancer patients, mechanistic modeling to account for these differences was constrained. Therefore, our approach remained focused on leveraging broadly applicable physiological parameters. Moreover, given the performance of the unmodified model in both populations (mean MRD: healthy subjects 1.39 vs. patients 1.59), no population-specific adjustments were made to minimize the model's complexity. The final PBPK model was further applied to predict different DDI scenarios involving imatinib and NDMI acting as both victims and perpetrators.

A key constraint of the model lies in the limitations of current knowledge as well as published clinical and in vitro data. For instance, consistent with literature data, when simulating an oral administration of 400 mg imatinib, the entire dose is absorbed.⁶ However, at 83%, the predicted total bioavailability was moderately lower than the reported literature value of more than 97%.⁶ One potential explanation for this discrepancy may lie in the in vivo deconjugation of imatinib glucuronides by gut microbes,⁴¹ a process integral to the enterohepatic circulation (EHC). This phenomenon could lead to the reabsorption of imatinib, influencing its overall bioavailability. Although the model accounts for the EHC of imatinib with a modeled EHC fraction of 1, it does not incorporate the sequential formation and breakdown of imatinib glucuronides. This omission is primarily due to the complexity of these processes and the lack of comprehensive data regarding the conjugation and deconjugation of imatinib, as well as the PK of its various glucuronide forms.

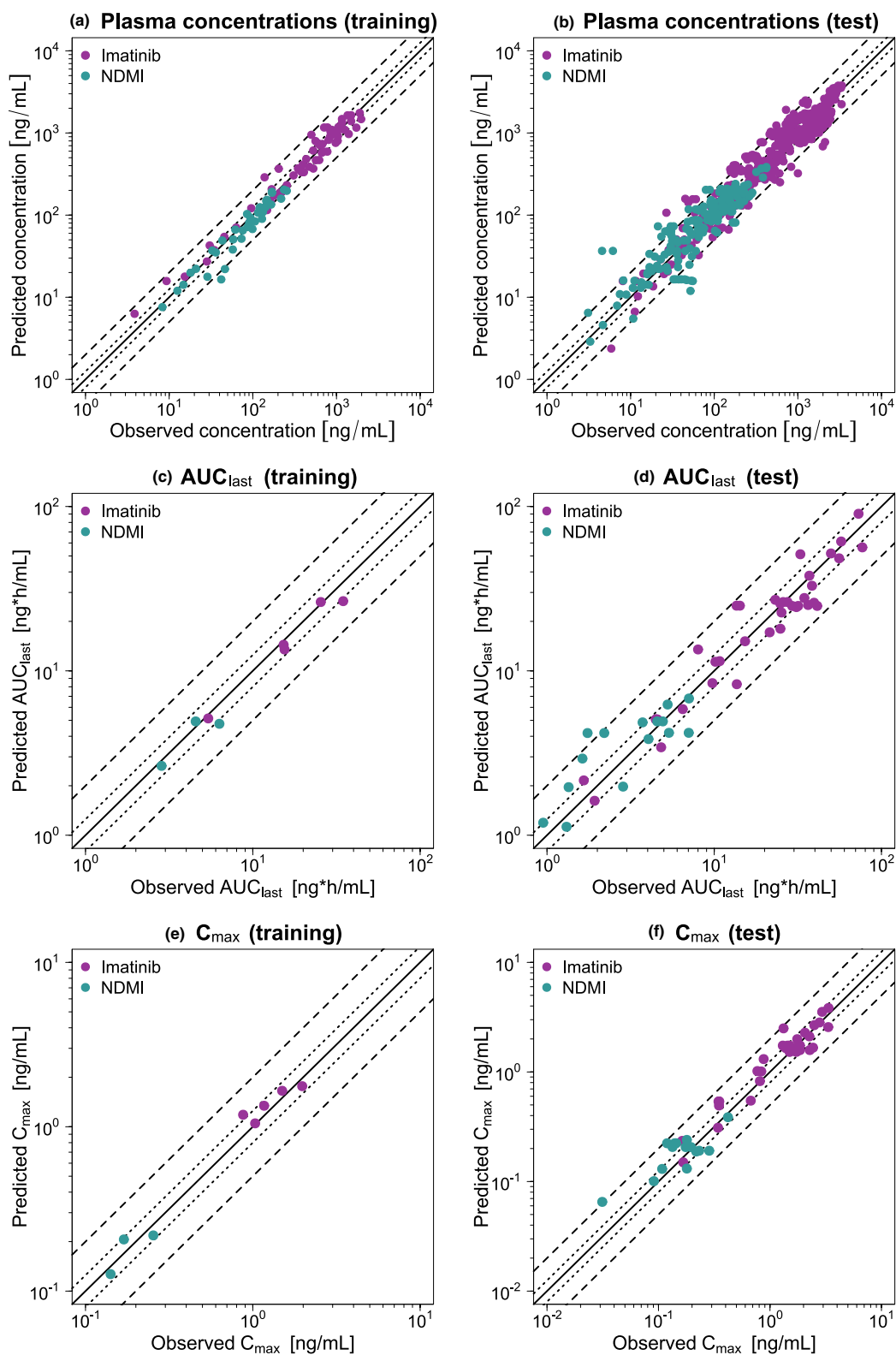


FIGURE 3 Goodness-of-fit plots of the final imatinib parent–metabolite model. Stratified by training (left column) and test dataset (right column), predicted plasma concentration measurements (a, b) as well as AUC_{last} (c, d) and C_{max} (e, f) values are plotted against corresponding observed data. The solid line represents the line of identity, while dotted lines indicate 1.25-fold, and dashed lines twofold deviation from the respective observed value. Detailed information on all investigated profiles is provided in Table S3. AUC_{last} : area under the curve determined between first and last plasma concentration measurements, C_{max} : maximum plasma concentration, NDMI: *N*-desmethyl imatinib.

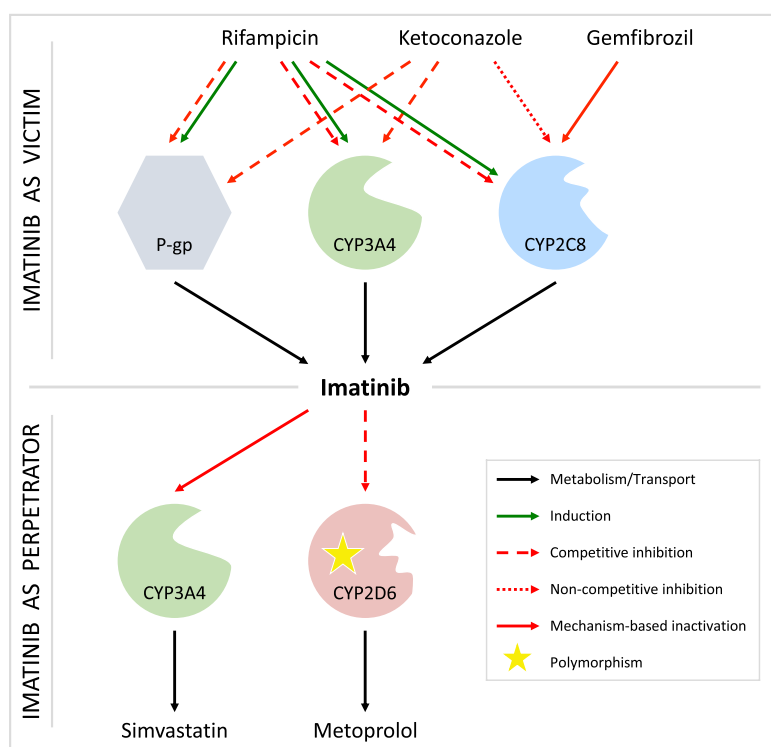


FIGURE 4 Schematic overview of the modeled drug–drug interaction network. The network covers the effects of rifampicin, ketoconazole, and gemfibrozil on the pharmacokinetics of imatinib as a victim, as well as the impact of imatinib as a perpetrator on the plasma levels of simvastatin and metoprolol. The respective main mechanisms of interactions are presented. For simplicity, the interaction effects of and on the corresponding metabolites, such as *N*-desmethyl imatinib, are summarized under the name of the parent drug. CYP: cytochrome P450, P-gp: P-glycoprotein.

Furthermore, imatinib has been identified as a substrate of several influx and efflux transporters in vitro, such as OCT1, OCTN2, OATP1A2, OATP1B3, BCRP, and P-gp,^{10–12} potentially influencing ADME processes. However, the relevance of these transporters in vivo remains uncertain due to conflicting study results. In our model, P-gp was selected as the efflux transporter over BCRP, primarily because the data for P-gp were more consistent and reliable compared to that for BCRP. Incorporating P-gp into the model led to an increase in the predicted urinary excretion of unchanged imatinib, rising from under 2% to about 5% following SD oral administration. This adjustment brings the model's predictions more in line with the urinary excretion rates observed in vivo.^{37,42} During model building, the incorporation of various influx transporters such as OCT1, OCTN2, OATP1A2, and OATP1B3 was tested. Despite considering the integration of these transporters into the model, we ultimately did not include them in the final model. This decision was based on the observation

that their inclusion did not markedly alter the base model's predictive performance or the simulated DDIs, with the total bioavailability consistently estimated around 83%. Furthermore, the data on transport parameters necessary to inform the model were limited and often conflicting. For example, while some studies identified OATP1A2 as a key transporter in imatinib uptake, evidence from pre-treatment with the OATP1A2 inhibitor rosuvastatin indicated no significant impact on imatinib's PK, adding to the ambiguity in these transporters' roles.^{43,44}

Overall, as only one mean intravenous imatinib profile was available from the literature, additional intravenous studies would be of particular interest to further investigate the discrepancy between modeled and reported total bioavailability. Moreover, dedicated studies on the parameterization and quantification of transport processes would be of great value to allow for an even more precise simulation of imatinib's PK. However, as both oral and intravenous administration of imatinib and metabolism to

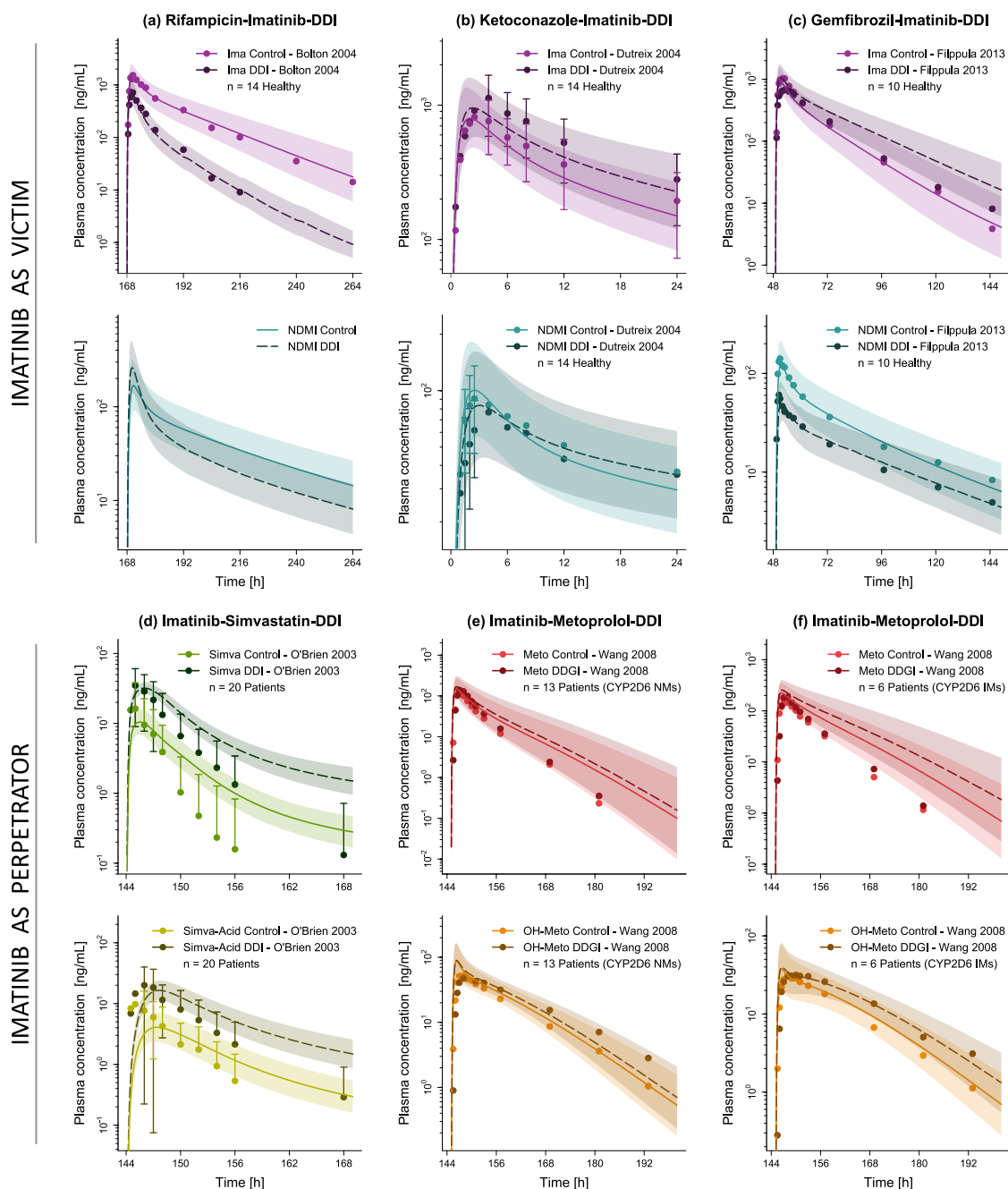
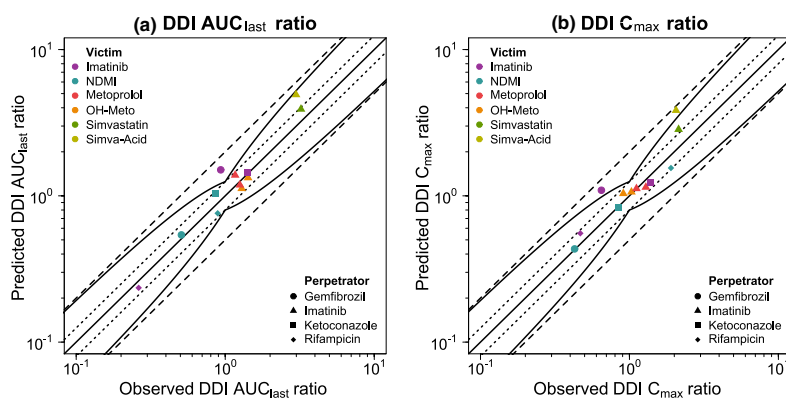


FIGURE 5 Evaluation of the modeled drug-drug interaction network. Presented are predicted plasma concentration-time profiles of victim drugs imatinib (a-c), simvastatin (d), and metoprolol (e, f) without (Control) and with (DDI) co-administration of the respective perpetrator drug rifampicin (a), ketoconazole (b), gemfibrozil (c), or imatinib (d-f), alongside corresponding observed data.^{15,16,18,19,38} Solid (Control) and dashed (DDI) lines and ribbons represent model population predictions ($n = 1000$; geometric mean and geometric standard deviation), while corresponding observed data are shown as dots (\pm standard deviation, if available). For the effect of rifampicin on NDMI, only DDI ratios were reported in the respective study (see Figure 6). Detailed information on all investigated DDI studies is provided in Table S8. CYP: cytochrome P450, DDI: drug-drug interaction, Healthy: healthy subjects, IM: intermediate metabolizer, Ima: imatinib, Meto: metoprolol, n : number of study participants, NDMI: *N*-desmethyl imatinib, NM: normal metabolizer, OH-Meto: hydroxymetoprolol, Patients: cancer patients, Simva: simvastatin, Simva-Acid: simvastatin hydroxy acid.

**TABLE 1** Predicted versus observed impact on the exposure of each victim drug upon perpetrator co-administration.

Victim	Perpetrator	Compound measured	DDI exposure ^a [%]		References
			Predicted	Observed	
Imatinib	Rifampicin	Imatinib	24	26	Bolton 2004 ¹⁹
		NDMI	76	89	
Imatinib	Ketoconazole	Imatinib	144	140	Duttreix 2004 ¹⁸
		NDMI	104	86	
Imatinib	Gemfibrozil	Imatinib	151	93	Filppula 2013 ³⁸
		NDMI	54	51	
Simvastatin	Imatinib	Simvastatin	391	322	O'Brien 2003 ¹⁶
		Simva-Acid	491	299	
Metoprolol ^b	Imatinib	Metoprolol	119	126	Wang 2008 ¹⁵
		OH-Meto	112	129	
Metoprolol ^c	Imatinib	Metoprolol	138	117	Wang 2008 ¹⁵
		OH-Meto	133	142	

^aRelative to the corresponding exposure without perpetrator co-administration.^bCYP2D6 normal metabolizers.^cCYP2D6 intermediate metabolizers, CYP: cytochrome P450, DDI: drug–drug interaction, NDMI: *N*-desmethyl imatinib, OH-Meto: hydroxymetoprolol, Simva-Acid: simvastatin hydroxy acid.**FIGURE 6** Evaluation of the modeled drug–drug interaction network. Predicted versus observed DDI AUC_{last} (a) and DDI C_{max} (b) ratios are shown with the solid line representing the line of identity, dotted lines indicating 1.25-fold, and dashed lines twofold deviation from the respective observed value. Curved lines mark the prediction success limits proposed by Guest et al.³³ including 20% variability. Detailed information on all investigated DDI studies is provided in Table S8. AUC_{last} : area under the curve determined between first and last plasma concentration measurements, C_{max} : maximum plasma concentration, DDI: drug–drug interaction, NDMI: *N*-desmethyl imatinib, OH-Meto: hydroxymetoprolol, Simva-Acid: simvastatin hydroxy acid.

NDMI were well described by the model, we consider hepatic clearance processes, and thus the fraction escaping first-pass liver metabolism, to be adequately represented in the model. Furthermore, the good prediction of mainly metabolic DDIs indicates a well-described relationship between fraction absorbed and fraction escaping gut wall metabolism.

In line with literature reports, CYP2C8 and CYP3A4 were implemented for the metabolism of imatinib and NDMI, while biotransformation via CYP3A5 was excluded

due to its relatively minor role in the biotransformation process.⁷ Here, model predictions for the relative influence on NDMI formation of CYP2C8 (67%) and CYP3A4 (33%) are in close agreement with the approximate *in vitro* literature values of 69% and 31%, respectively.⁷ Overall, 57% of the modeled total metabolism of imatinib is accounted for by the formation of NDMI, closely aligning with *in vitro* findings which reported a similar contribution of 51%.⁷ Listed fractional contributions of CYP2C8 and CYP3A4 to the metabolism of imatinib refer to a simulated SD

administration of imatinib. However, a shift in the enzymatic contributions toward a greater influence of CYP2C8 was observed upon simulated MD administrations of imatinib, most likely due to the pronounced autoinhibition of CYP3A4. Under simulated steady-state conditions, 75% of imatinib metabolism leads to the formation of NDMI (SD: 57%), with an increasing role of CYP2C8 within the NDMI pathway (SD: 67% vs. MD: 84%). This modeled decrease in CYP3A4 contribution to the overall metabolism of imatinib at steady-state reflects the results from DDI studies involving CYP3A perpetrators. Here an effect of ketoconazole on SD administration of imatinib was observed, while ritonavir showed almost no influence on the steady-state AUC of imatinib.^{18,45} This finding could be confirmed via modeling (see Section S3.7). The influence of different polymorphically expressed transporters and enzymes on imatinib exposure has been investigated in previous works. For example, one study showed that the *CYP3A4 rs2242480* polymorphism resulted in significantly lower steady-state imatinib trough concentrations, relative to the wild type.⁴⁶ However, the model does not account for genotype-specific activities of the incorporated transporters and enzymes, primarily due to the scarcity of comprehensive data. Future studies focusing on the impact of various genetic polymorphisms on the plasma levels of imatinib and NDMI, especially over extended periods and not just at trough concentrations, would be valuable. Such research could facilitate the integration of, for example, different CYP3A4 activities into the model, allowing more personalized predictions.

Following the model development process, a DDI network centered around imatinib acting as both a victim and perpetrator drug was successfully established by coupling the final imatinib model with previously published models of the perpetrator drugs rifampicin, ketoconazole, and gemfibrozil, as well as of the victim drugs simvastatin and metoprolol.^{27–31} Good overall predictive performance was attained for the modeled DDI scenarios, reflected by 24/24 predicted AUC_{last} and C_{max} ratios being within twofold of observed ratios. However, the modeled DDI network has limitations due to incomplete or biased published data. For instance, the effect of co-treatment with ketoconazole on imatinib exposure was examined solely in the context of SD administration of ketoconazole. As the metabolites of ketoconazole also exhibit potent inhibition of CYP2C8, CYP3A4, and P-gp, DDI studies involving pretreatment with ketoconazole would be of great interest to analyze the maximum inhibitory effect of ketoconazole and its metabolites on the AUC of imatinib and NDMI.

Various other PBPK models for imatinib are documented in the literature. These models address aspects such as interethnic differences in imatinib PK as well as

dose optimizations for children and adults in DDI scenarios with imatinib as the victim drug.^{23–25} Contrasting with these, our whole-body PBPK model of imatinib encompasses the formation and biotransformation of both imatinib and its main metabolite NDMI. This approach is crucial as NDMI not only contributes to imatinib's pharmacodynamic effects but also plays an important role in inhibiting enzymes such as CYP2C8, CYP2D6, and CYP3A4. Hence, the inclusion of NDMI in the model enhances the model's clinical relevance for imatinib application and provides a more robust framework for the prediction of DDIs. While the activity and the inhibitory effect of NDMI are not overly prominent when imatinib is administered alone given its rather low contribution to the overall exposure, the importance of NDMI can increase greatly depending on the concomitant medication. For example, pretreatment with the inducer rifampicin causes the contribution of NDMI to total exposure to increase from 15% to 38%.¹⁹ In a clinical oncology environment with five to eight drugs prescribed per patient, the importance of NDMI might therefore increase considerably and should not be neglected.²⁰ Furthermore, to the best of our knowledge, the developed DDI network is the first to cover imatinib not only as a victim, but also as a perpetrator drug. In particular, the good model prediction regarding the effect of imatinib on simvastatin exposure, mainly via CYP3A4 inhibition, is of great value as it allows the verification of the appropriate implementation of imatinib autoinhibition.

In summary, the developed imatinib parent-metabolite whole-body PBPK model shows good descriptive and predictive performance for both imatinib and its active metabolite NDMI in healthy subjects and CML/GIST patients. In addition, the role of imatinib and NDMI as CYP2C8, CYP3A4, and P-gp (imatinib) substrates, as well as inhibitors of CYP3A4 and CYP2D6, was successfully investigated and predicted within a newly established DDI network. Potential application areas of the developed model and corresponding imatinib DDI network include model-informed drug development as well as model-based precision dosing for patients. After being evaluated across various DDI scenarios, the imatinib model is capable of integration with any existing and validated PK-Sim® victim or perpetrator model to predict clinically untested DDIs and even multiple DDIs involving more than two DDI partners (e.g., two perpetrators). Hence, the developed imatinib model enables the prediction of effects both by and on imatinib and NDMI across a wide array of clinically relevant polypharmacy scenarios. This capability facilitates the identification and quantification of potential drug interactions. Subsequently, the presented model may be used to generate dose recommendations for imatinib or



relevant victim drugs to improve both therapy safety and efficacy.

AUTHOR CONTRIBUTIONS

H.L.H.L., C.K., D.S., M.S., and T.L. wrote the manuscript. H.L.H.L., C.K., S.R., F.Z.M., L.M.F, and T.L. designed the research. H.L.H.L. performed the research. H.L.H.L. and C.K. analyzed the data.

ACKNOWLEDGMENTS

Open Access funding enabled and organized by Projekt DEAL.

FUNDING INFORMATION

Matthias Schwab was supported by the Robert Bosch Stiftung (Stuttgart, Germany), a grant from the German Federal Ministry of Education and Research (BMBF, 031L0188D, "GUIDE-IBD") and the DFG im Rahmen der Exzellenzstrategie des Bundes und der Länder-EXC 2180-390900677. Thorsten Lehr was supported by the German Federal Ministry of Education and Research (BMBF, Horizon 2020 INSPIRATION grant 643271), under the frame of ERACoSysMed and the European Union Horizon 2021 SafePolyMed (grant 101057639).

CONFLICT OF INTEREST STATEMENT

The authors declared no competing interests for this work.

ORCID

Simeon Rüdesheim <https://orcid.org/0000-0002-5741-2511>

Matthias Schwab <https://orcid.org/0000-0002-9984-075X>

Thorsten Lehr <https://orcid.org/0000-0002-8372-1465>

REFERENCES

- Kantarjian HM, Jain N, Garcia-Manero G, et al. The cure of leukemia through the optimist's prism. *Cancer*. 2022;128:240-259. doi:10.1002/cncr.33933
- Kantarjian HM, Talpaz M, Giles F, Brien SO, Cortes J. New insights into the pathophysiology of chronic myeloid leukemia and imatinib resistance. *Ann Intern Med*. 2006;145:913-923. doi:10.7326/0003-4819-145-12-200612190-00008
- Bixby D, Talpaz M. Seeking the causes and solutions to imatinib-resistance in chronic myeloid leukemia. *Leukemia*. 2011;25:7-22. doi:10.1038/leu.2010.238
- Roskoski RJ. Properties of FDA-approved small molecule protein kinase inhibitors: a 2023 update. *Pharmacol Res*. 2023;187:106552. doi:10.1016/j.phrs.2022.106552
- O'Brien Z, Moghaddam MF. A systematic analysis of physicochemical and ADME properties of all small molecule kinase inhibitors approved by US FDA from January 2001 to October 2015. *Curr Med Chem*. 2017;24:3159-3184. doi:10.2174/0929867324666170523124441
- Peng B, Dutreix C, Mehrling G, et al. Absolute bioavailability of imatinib (Gleevec®) orally versus intravenous infusion. *J Clin Pharmacol*. 2004;44:158-162. doi:10.1177/0091270003262101
- Filppula AM, Neuvonen M, Laitila J, Neuvonen PJ, Backman JT. Autoinhibition of CYP3A4 leads to important role of CYP2C8 in imatinib metabolism: variability in CYP2C8 activity may alter plasma concentrations and response. *Drug Metab Dispos*. 2013;41:50-59. doi:10.1124/dmd.112.048017
- Duckett DR, Cameron MD. Metabolism considerations for kinase inhibitors in cancer treatment. *Expert Opin Drug Metab Toxicol*. 2010;6:1175-1193. doi:10.1517/17425255.2010.506873. [Metabolism](#)
- Manley PW. Investigations into the potential role of metabolites on the anti-leukemic activity of imatinib, nilotinib and midostaurin. *Chimia*. 2019;73:561-570. doi:10.2533/chimia.2019.561
- Hu S, Franke RM, Filipinski KK, et al. Interaction of imatinib with human organic ion carriers. *Clin Cancer Res*. 2008;14:3141-3148. doi:10.1158/1078-0432.CCR-07-4913
- Hamada A, Miyano H, Watanabe H, Saito H. Interaction of imatinib mesilate with human P-glycoprotein. *J Pharmacol Exp Ther*. 2003;307:824-828. doi:10.1124/jpet.103.055574
- Burger H, van Tol H, Boersma AWM, et al. Imatinib mesylate (STI571) is a substrate for the breast cancer resistance protein (BCRP)/ABCG2 drug pump. *Blood*. 2004;104:2940-2942. doi:10.1182/blood-2004-04-1398
- Gschwind HP, Pfaar U, Waldmeier F, et al. Metabolism and disposition of imatinib mesylate in healthy volunteers. *Drug Metab Dispos*. 2005;33:1503-1512. doi:10.1124/dmd.105.004283
- Filppula AM, Laitila J, Neuvonen PJ, Backman JT. Potent mechanism-based inhibition of CYP3A4 by imatinib explains its liability to interact with CYP3A4 substrates. *Br J Pharmacol*. 2012;165:2787-2798. doi:10.1111/j.1476-5381.2011.01732.x
- Wang Y, Zhou L, Dutreix C, et al. Effects of imatinib (Gleevec) on the pharmacokinetics of metoprolol, a CYP2D6 substrate, in Chinese patients with chronic myelogenous leukaemia. *Br J Clin Pharmacol*. 2008;65:885-892. doi:10.1111/j.1365-2125.2008.03150.x
- O'Brien SG, Meinhardt P, Bond E, et al. Effects of imatinib mesylate (STI571, Gleevec) on the pharmacokinetics of simvastatin, a cytochrome P450 3A4 substrate, in patients with chronic myeloid leukaemia. *Br J Cancer*. 2003;89:1855-1859. doi:10.1038/sj.bjc.6601152
- Drug development and drug interactions: FDA table of substrates, inhibitors and inducers. Accessed September 28, 2023. <https://www.fda.gov/drugs/drug-interactions-labeling/health-care-professionals-fdas-examples-drugs-interact-cyp-enzymes-and-transporter-systems>
- Dutreix C, Peng B, Mehrling G, et al. Pharmacokinetic interaction between ketoconazole and imatinib mesylate (Gleevec) in healthy subjects. *Cancer Chemother Pharmacol*. 2004;54:290-294. doi:10.1007/s00280-004-0832-z
- Bolton AE, Peng B, Hubert M, et al. Effect of rifampicin on the pharmacokinetics of imatinib mesylate (Gleevec, STI571) in healthy subjects. *Cancer Chemother Pharmacol*. 2004;53:102-106. doi:10.1007/s00280-003-0722-9
- Bowlin SJ, Xia F, Wang W, Robinson KD, Stanek EJ. Twelve-month frequency of drug-metabolizing enzyme and transporter-based drug-drug interaction potential in patients receiving oral

- enzyme-targeted kinase inhibitor antineoplastic agents. *Mayo Clin Proc.* 2013;88:139-148. doi:[10.1016/j.mayocp.2012.10.020](https://doi.org/10.1016/j.mayocp.2012.10.020)
21. Grimstein M, Yang Y, Zhang X, et al. Physiologically based pharmacokinetic modeling in regulatory science: an update from the U.S. Food and Drug Administration's Office of Clinical Pharmacology. *J Pharm Sci.* 2019;108:21-25. doi:[10.1016/j.xphs.2018.10.033](https://doi.org/10.1016/j.xphs.2018.10.033)
 22. Gonzalez D, Rao GG, Bailey SC, et al. Precision dosing: public health need, proposed framework, and anticipated impact. *Clin Transl Sci.* 2017;10:443-454. doi:[10.1111/cts.12490](https://doi.org/10.1111/cts.12490)
 23. Adiwidjaja J, Gross AS, Boddy AV, McLachlan AJ. Physiologically-based pharmacokinetic model predictions of inter-ethnic differences in imatinib pharmacokinetics and dosing regimens. *Br J Clin Pharmacol.* 2022;88:1735-1750. doi:[10.1111/bcp.15084](https://doi.org/10.1111/bcp.15084)
 24. Adiwidjaja J, Boddy AV, McLachlan AJ. Implementation of a physiologically based pharmacokinetic modeling approach to guide optimal dosing regimens for imatinib and potential drug interactions in paediatrics. *Front Pharmacol.* 2020;10:1672. doi:[10.3389/fphar.2019.01672](https://doi.org/10.3389/fphar.2019.01672)
 25. Gao D, Wang G, Wu H, Wu JH, Zhao X. Prediction for plasma trough concentration and optimal dosing of imatinib under multiple clinical situations using physiologically based pharmacokinetic modeling. *ACS Omega.* 2023;8:13741-13753. doi:[10.1021/acsomega.2c07967](https://doi.org/10.1021/acsomega.2c07967)
 26. Wojtyniak J-G, Britz H, Selzer D, Schwab M, Lehr T. Data digitizing: accurate and precise data extraction for quantitative systems pharmacology and physiologically-based pharmacokinetic modeling. *CPT Pharmacometrics Syst Pharmacol.* 2020;9:322-331. doi:[10.1002/psp4.12511](https://doi.org/10.1002/psp4.12511)
 27. Wojtyniak J-G, Selzer D, Schwab M, Lehr T. Physiologically based precision dosing approach for drug-drug-gene interactions: a simvastatin network analysis. *Clin Pharmacol Ther.* 2021;109:201-211. doi:[10.1002/cpt.2111](https://doi.org/10.1002/cpt.2111)
 28. Rüdesheim S, Wojtyniak JG, Selzer D, et al. Physiologically based pharmacokinetic modeling of metoprolol enantiomers and α -hydroxymetoprolol to describe CYP2D6 drug-gene interactions. *Pharmaceutics.* 2020;12:1200. doi:[10.3390/pharmaceutics12121200](https://doi.org/10.3390/pharmaceutics12121200)
 29. Marok FZ, Wojtyniak JG, Fuhr LM, et al. A physiologically based pharmacokinetic model of ketoconazole and its metabolites as drug-drug interaction perpetrators. *Pharmaceutics.* 2023;12:679. doi:[10.3390/pharmaceutics15020679](https://doi.org/10.3390/pharmaceutics15020679)
 30. Hanke N, Frechen S, Moj D, et al. PBPK models for CYP3A4 and P-gp DDI prediction: a modeling network of rifampicin, itraconazole, clarithromycin, midazolam, alfentanil, and digoxin. *CPT Pharmacometrics Syst Pharmacol.* 2018;7:647-659. doi:[10.1002/psp4.12343](https://doi.org/10.1002/psp4.12343)
 31. Türk D, Hanke N, Wolf S, et al. Physiologically based pharmacokinetic models for prediction of complex CYP2C8 and OATP1B1 (SLCO1B1) drug-drug-gene interactions: a modeling network of gemfibrozil, repaglinide, pioglitazone, rifampicin, clarithromycin and itraconazole. *Clin Pharmacokinet.* 2019;58:1595-1607. doi:[10.1007/s40262-019-00777-x](https://doi.org/10.1007/s40262-019-00777-x)
 32. Open Systems Pharmacology Suite Community. Open Systems Pharmacology Suite Manual, Version 11 2023. Accessed September 30, 2023. <https://docs.open-systems-pharmacology.org/copyright>
 33. Guest EJ, Aarons L, Houston JB, Rostami-Hodjegan A, Galetin A. Critique of the two-fold measure of prediction success for ratios: application for the assessment of drug-drug interactions. *Drug Metab Dispos.* 2011;39:170-173. doi:[10.1124/dmd.110.036103](https://doi.org/10.1124/dmd.110.036103)
 34. Hegedus T, Orfi L, Seprodi A, Váradi A, Sarkadi B, Kéri G. Interaction of tyrosine kinase inhibitors with the human multidrug transporter proteins, MDR1 and MRP1. *Biochim Biophys Acta.* 2002;1587:318-325. doi:[10.1016/S0925-4439\(02\)00095-9](https://doi.org/10.1016/S0925-4439(02)00095-9)
 35. D'Cunha R, Bae S, Murry DJ, An G. TKI combination therapy: strategy to enhance dasatinib uptake by inhibiting Pgp- and BCRP-mediated efflux. *Biopharm Drug Dispos.* 2016;37:397-408. doi:[10.1002/bdd.2022](https://doi.org/10.1002/bdd.2022)
 36. Langenbucher F. Linearization of dissolution rate by the Weibull distribution. *J Pharm Pharmacol.* 1972;24:979-981. doi:[10.1111/j.2042-7158.1972.tb08930.x](https://doi.org/10.1111/j.2042-7158.1972.tb08930.x)
 37. Zidan DW, Hassan WS, Elmasry MS, Shalaby AA. A novel spectrofluorimetric method for determination of imatinib in pure, pharmaceutical preparation, human plasma, and human urine. *Luminescence.* 2018;33:232-242. doi:[10.1002/bio.3406](https://doi.org/10.1002/bio.3406)
 38. Filppula AM, Tornio A, Niemi M, Neuvonen PJ, Backman JT. Gemfibrozil impairs imatinib absorption and inhibits the CYP2C8-mediated formation of its main metabolite. *Clin Pharmacol Ther.* 2013;94:383-393. doi:[10.1038/clpt.2013.92](https://doi.org/10.1038/clpt.2013.92)
 39. Jørgensen HG, Elliott MA, Allan EK, Carr CE, Holyoake TL, Smith KD. α 1-acid glycoprotein expressed in the plasma of chronic myeloid leukemia patients does not mediate significant in vitro resistance to STI571. *Blood.* 2002;99:713-715. doi:[10.1182/blood.V99.2.713](https://doi.org/10.1182/blood.V99.2.713)
 40. Peng B, Lloyd P, Schran H. Clinical pharmacokinetics of imatinib. *Clin Pharmacokinet.* 2005;44:879-894. doi:[10.2165/00003088-200544090-00001](https://doi.org/10.2165/00003088-200544090-00001)
 41. Friedecký D, Mičová K, Faber E, Hrdá M, Šíroková J, Adam T. Detailed study of imatinib metabolism using high-resolution mass spectrometry. *J Chromatogr A.* 2015;1409:173-181. doi:[10.1016/j.chroma.2015.07.033](https://doi.org/10.1016/j.chroma.2015.07.033)
 42. Rodríguez Flores J, Berzas JJ, Castañeda G, Rodríguez N. Direct and fast capillary zone electrophoretic method for the determination of Gleevec and its main metabolite in human urine. *J Chromatogr B Anal Technol Biomed Life Sci.* 2003;794:381-388. doi:[10.1016/S1570-0232\(03\)00518-X](https://doi.org/10.1016/S1570-0232(03)00518-X)
 43. Eechoute K, Franke RM, Loos WJ, et al. Environmental and genetic factors affecting transport of imatinib by OATP1A2. *Clin Pharmacol Ther.* 2011;89:816-820. doi:[10.1038/clpt.2011.42](https://doi.org/10.1038/clpt.2011.42)
 44. Silva CG, Honeywell RJ, Dekker H, Peters GJ. Physicochemical properties of novel protein kinase inhibitors in relation to their substrate specificity for drug transporters. *Expert Opin Drug Metab Toxicol.* 2015;11:703-717. doi:[10.1517/17425255.2015.1006626](https://doi.org/10.1517/17425255.2015.1006626)
 45. van Erp NP, Gelderblom H, Karlsson MO, et al. Influence of CYP3A4 inhibition on the steady-state pharmacokinetics of imatinib. *Clin Cancer Res.* 2007;13:7394-7400. doi:[10.1158/1078-0432.CCR-07-0346](https://doi.org/10.1158/1078-0432.CCR-07-0346)
 46. Liu J, Chen Z, Chen H, et al. Genetic polymorphisms contribute to the individual variations of imatinib mesylate plasma levels and adverse reactions in Chinese GIST patients. *Int J Mol Sci.* 2017;18:603. doi:[10.3390/ijms18030603](https://doi.org/10.3390/ijms18030603)
 47. Frye RF, Fitzgerald SM, Lagattuta TF, Hruska MW, Egorin MJ. Effect of St John's wort on imatinib mesylate pharmacokinetics. *Clin Pharmacol Ther.* 2004;76:323-329. doi:[10.1016/j.clpt.2004.06.007](https://doi.org/10.1016/j.clpt.2004.06.007)



48. Peng B, Hayes M, Resta D, et al. Pharmacokinetics and pharmacodynamics of imatinib in a phase I trial with chronic myeloid leukemia patients. *J Clin Oncol*. 2004;22:935-942. doi:[10.1200/JCO.2004.03.050](https://doi.org/10.1200/JCO.2004.03.050)
49. Yang JS, Cho EG, Huh W, Ko JW, Jung JA, Lee SY. Rapid determination of imatinib in human plasma by liquid chromatography-tandem mass spectrometry: application to a pharmacokinetic study. *Bull Korean Chem Soc*. 2013;34:2425-2430. doi:[10.5012/bkcs.2013.34.8.2425](https://doi.org/10.5012/bkcs.2013.34.8.2425)
50. Zhang Y, Qiang S, Yu Z, et al. LC-MS-MS determination of imatinib and N-desmethyl imatinib in human plasma. *J Chromatogr Sci*. 2014;52:344-350. doi:[10.1093/chromsci/bmt037](https://doi.org/10.1093/chromsci/bmt037)
51. Nikolova Z, Peng B, Hubert M, et al. Bioequivalence, safety, and tolerability of imatinib tablets compared with capsules. *Cancer Chemother Pharmacol*. 2004;53:433-438. doi:[10.1007/s00280-003-0756-z](https://doi.org/10.1007/s00280-003-0756-z)

SUPPORTING INFORMATION

Additional supporting information can be found online in the Supporting Information section at the end of this article.

How to cite this article: Loer HLH, Kovar C, Rüdesheim S, et al. Physiologically based pharmacokinetic modeling of imatinib and N-desmethyl imatinib for drug–drug interaction predictions. *CPT Pharmacometrics Syst Pharmacol*. 2024;13:926-940. doi:[10.1002/psp4.13127](https://doi.org/10.1002/psp4.13127)

4.3 PROJECT III: PBPK MODELING OF DASATINIB

Publication

Kovar, C.; Loer, H. L. H.; Rüdesheim, S.; Fuhr, L. M.; Marok, F. Z.; Selzer, D.; Schwab, M.; Lehr, T. A physiologically-based pharmacokinetic precision dosing approach to manage dasatinib drug–drug interactions. *CPT: Pharmacometrics and Systems Pharmacology* **2024**, *13*, 1144–1159, DOI: [10.1002/psp4.13146](https://doi.org/10.1002/psp4.13146).

Supplementary Materials

Related Supplementary Materials are available on the accompanying USB storage device and via the following link: <https://pmc.ncbi.nlm.nih.gov/articles/instance/11247110/bin/PSP4-13-1144-s002.pdf>.

Copyright

This is an open access article under the terms of CC BY-NC 4.0 (<https://creativecommons.org/licenses/by-nc/4.0/>), which permits use, distribution and reproduction in any medium, provided the original work is properly cited and is not used for commercial purposes. © 2024 The Authors. *CPT: Pharmacometrics & Systems Pharmacology* published by Wiley Periodicals LLC on behalf of American Society for Clinical Pharmacology and Therapeutics.

Author Contributions According to CRediT [5]

Christina Kovar	Conceptualization, Investigation, Visualization, Writing – Original Draft, Writing – Review & Editing
Helena Leonie Hanae Loer	Conceptualization, Investigation, Writing – Review & Editing
Simeon Rüdesheim	Conceptualization, Writing – Review & Editing
Laura Maria Fuhr	Conceptualization
Fatima Zahra Marok	Conceptualization
Dominik Selzer	Writing – Review & Editing
Matthias Schwab	Writing – Review & Editing, Funding Acquisition
Thorsten Lehr	Conceptualization, Writing – Review & Editing, Funding Acquisition

Received: 14 December 2023 | Revised: 28 February 2024 | Accepted: 2 April 2024

DOI: [10.1002/psp4.13146](https://doi.org/10.1002/psp4.13146)

ARTICLE

A physiologically-based pharmacokinetic precision dosing approach to manage dasatinib drug–drug interactions

Christina Kovar^{1,2} | Helena Leonie Hanae Loer¹ | Simeon Rüdesheim^{1,2} |
Laura Maria Fuhr¹ | Fatima Zahra Marok¹ | Dominik Selzer¹ |
Matthias Schwab^{2,3,4} | Thorsten Lehr¹

¹Clinical Pharmacy, Saarland University, Saarbrücken, Germany

²Dr. Margarete Fischer-Bosch Institute of Clinical Pharmacology, Stuttgart, Germany

³Departments of Clinical Pharmacology, and Pharmacy and Biochemistry, University of Tübingen, Tübingen, Germany

⁴Cluster of Excellence iFIT (EXC2180), Image-Guided and Functionally Instructed Tumor Therapies, University of Tübingen, Tübingen, Germany

Correspondence

Thorsten Lehr, Clinical Pharmacy, Saarland University, Campus C5 3, Saarbrücken 66123, Germany.
Email: thorsten.lehr@mx.uni-saarland.de

Abstract

Dasatinib, a second-generation tyrosine kinase inhibitor, is approved for treating chronic myeloid and acute lymphoblastic leukemia. As a sensitive cytochrome P450 (CYP) 3A4 substrate and weak base with strong pH-sensitive solubility, dasatinib is susceptible to enzyme-mediated drug–drug interactions (DDIs) with CYP3A4 perpetrators and pH-dependent DDIs with acid-reducing agents. This work aimed to develop a whole-body physiologically-based pharmacokinetic (PBPK) model of dasatinib to describe and predict enzyme-mediated and pH-dependent DDIs, to evaluate the impact of strong and moderate CYP3A4 inhibitors and inducers on dasatinib exposure and to support optimized dasatinib dosing. Overall, 63 plasma profiles from perorally administered dasatinib in healthy volunteers and cancer patients were used for model development. The model accurately described and predicted plasma profiles with geometric mean fold errors (GMFEs) for area under the concentration–time curve from the first to the last timepoint of measurement (AUC_{last}) and maximum plasma concentration (C_{max}) of 1.27 and 1.29, respectively. Regarding the DDI studies used for model development, all (8/8) predicted AUC_{last} and C_{max} ratios were within twofold of observed ratios. Application of the PBPK model for dose adaptations within various DDIs revealed dasatinib dose reductions of 50%–80% for strong and 0%–70% for moderate CYP3A4 inhibitors and a 2.3–3.1-fold increase of the daily dasatinib dose for CYP3A4 inducers to match the exposure of dasatinib administered alone. The developed model can be further employed to personalize dasatinib therapy, thereby help coping with clinical challenges resulting from DDIs and patient-related factors, such as elevated gastric pH.

This is an open access article under the terms of the [Creative Commons Attribution-NonCommercial-NoDerivs](https://creativecommons.org/licenses/by-nc-nd/4.0/) License, which permits use and distribution in any medium, provided the original work is properly cited, the use is non-commercial and no modifications or adaptations are made.

© 2024 The Authors. *CPT: Pharmacometrics & Systems Pharmacology* published by Wiley Periodicals LLC on behalf of American Society for Clinical Pharmacology and Therapeutics.

Study Highlights

WHAT IS THE CURRENT KNOWLEDGE ON THE TOPIC?

As a sensitive cytochrome P450 (CYP) 3A4 substrate and weak base with strong pH-sensitive solubility, dasatinib is susceptible to enzyme-mediated and pH-dependent drug–drug interactions (DDIs) with CYP3A4 perpetrator drugs and acid-reducing agents, respectively.

WHAT QUESTION DID THIS STUDY ADDRESS?

This work aimed to develop a whole-body physiologically-based pharmacokinetic (PBPK) model of dasatinib to describe and predict enzyme-mediated and pH-dependent DDIs as well as to investigate a selection of clinically relevant DDIs, supporting optimized dasatinib precision dosing.

WHAT DOES THIS STUDY ADD TO OUR KNOWLEDGE?

A PBPK model for the CYP3A4 substrate dasatinib was developed and coupled with various strong and moderate CYP3A4 perpetrator models to provide model-based dasatinib dosing recommendations within single as well as complex multiple DDIs.

HOW MIGHT THIS CHANGE DRUG DISCOVERY, DEVELOPMENT, AND/OR THERAPEUTICS?

The presented dasatinib model may serve as a tool to further personalize dasatinib therapy, providing strategies to navigate clinical challenges that result from single and multiple DDIs and/or patient-related factors or to perform DDI simulations with drugs under development involving dasatinib as sensitive CYP3A4 substrate.

INTRODUCTION

The introduction of tyrosine kinase inhibitors (TKIs) transformed the treatment and prognosis of chronic myeloid leukemia (CML), a myeloproliferative disorder accounting for approximately 15% of all newly diagnosed leukemias in adults.¹ Dasatinib (Sprycel®), an oral second-generation and multi-targeted TKI, is utilized in the treatment of Philadelphia chromosome positive (Ph+) CML in all phases and is also approved for Ph+ acute lymphoblastic leukemia (ALL).² Here, a comprehensive understanding of its pharmacokinetics (PK), encompassing absorption, distribution, metabolism and excretion (ADME) is vital for maximizing therapeutic efficacy and managing side effects.

Dasatinib, a weak base and a Biopharmaceutical Classification System (BCS) class II compound, demonstrates low solubility and high permeability, making it prone to drug–drug interactions (DDIs) with acid-reducing agents (ARAs) because of its pH-dependent solubility.³ Given its strong pH-dependent solubility with improved solubility in acidic conditions, co-administration with proton pump inhibitors (PPIs), H₂-antagonists, and antacids can modify its absorption and consequently, therapeutic efficacy.^{4,5}

Dasatinib is primarily metabolized by cytochrome P450 (CYP) 3A4 via hydroxylation and N-dealkylation to three major metabolites.^{6,7} Hence, systemic exposure of dasatinib can be significantly impacted by DDIs with both CYP3A4 inhibitors and inducers. The United States Food and Drug Administration has listed dasatinib as a sensitive CYP3A4 substrate for use in clinical DDI studies.⁸ For instance, the strong CYP3A4 inhibitor ketoconazole increased dasatinib's area under the concentration–time curve (AUC) over one dosing interval nearly five-fold.⁹ Conversely, pretreatment with rifampicin, a strong CYP3A4 inducer, can decrease the AUC by approximately 80%.³ Moreover, dasatinib can affect the PK of other drugs, acting as a weak mechanism-based inhibitor of CYP3A4 and a competitive inhibitor of CYP2C8 and several transporters, such as organic anion transporting polypeptide (OATP) 1B1 and OATP1B3.^{10–12}

Given dasatinib's susceptibility to both enzyme-mediated and pH-dependent DDIs, managing its therapeutic application presents clinical challenges. Here, physiologically-based pharmacokinetic (PBPK) modeling emerges as a valuable tool for exploring DDI scenarios and supporting precision dosing of dasatinib.¹³ Specifically, the PBPK approach can provide insights into how various drugs might influence dasatinib PK



by modeling their complex biological ADME and interaction processes. Furthermore, these models can be utilized to simulate and predict the PK, guiding optimization of treatment regimens under complex conditions, such as multiple DDIs, thereby facilitating personalized and safer treatment strategies.¹⁴

Considering dasatinib's complex PK profile and its susceptibility to DDIs, this study aimed to develop a whole-body PBPK model with the objective to describe and predict the impact of various clinically studied DDIs including enzyme-mediated and pH-dependent DDIs on the exposure of dasatinib. As the package insert does not provide explicit dose adaptations for dasatinib when a specific perpetrator drug is co-administered,¹⁵ our PBPK model was applied to simulate a selection of clinically relevant DDI scenarios involving various CYP3A4 perpetrator drugs, not previously explored in clinical DDI trials. Among others, simulations with the potent antifungal agents fluconazole, itraconazole, ketoconazole, and voriconazole as well as macrolide antibiotics such as clarithromycin were performed as patients with blood malignancies are more susceptible to opportunistic infections.^{16,17} Notably, since around a third of CML patients suffer on anxiety and depression particularly during TKI therapy,¹⁸ co-administration of selective serotonin reuptake inhibitors as effective antidepressants (e.g., fluvoxamine) frequently occurs. As a result, model-based dose adaptations for dasatinib, under co-treatment with these CYP3A4 inhibitors and additionally, with different CYP3A4 inducers, were performed to enhance support for precision dosing in patients. The model files will be made publicly available in the Clinical Pharmacy Saarland University GitHub repository (<http://models.clinicalpharmacy.me/>).

METHODS

Software

The dasatinib PBPK model was developed using PK-Sim® and MoBi® (Open Systems Pharmacology Suite version 11.0, <http://www.open-systems-pharmacology.org>).¹⁹ Digitization of published concentration–time profiles was performed with GetData Graph Digitizer version 2.26.0.20 (© S. Fedorov) according to Wojtyniak and coworkers.²⁰ Model parameter estimation via the Levenberg–Marquardt algorithm and local sensitivity analysis were conducted within PK-Sim®. Calculation of PK parameters, model performance metrics as well as generation of graphics and dose adaptations were employed using R 4.2.1 (R Foundation for Statistical Computing, Vienna, Austria).²¹

PBPK model building

PBPK model development was initiated with a comprehensive literature search to gather information about the physicochemical properties and ADME processes of dasatinib. Plasma concentration–time profiles following oral administration of dasatinib (as tablet, solution, or suspension) at fasted and fed state were extracted from 19 clinical trials including single- and multiple-dose studies with healthy volunteers and cancer patients. An overview of all clinical studies, including administration protocols and demographics of participants, is presented in [Tables S1, S7 and S9](#).

For the development of the dasatinib PBPK model, a middle-out approach was employed. The concentration–time profiles were digitized and divided into a training and test dataset for model building (5 profiles) and evaluation (58 profiles), respectively. The middle-out strategy merges prior information on drug- and system-specific parameters with a parameter estimation step based on clinical trial data.²² Initial model input parameters were informed through a combination of *in vitro*, *in silico*, and clinical data. If model parameter values could not be reliably sourced via literature or were pivotal for critical quantitative structure–activity relationship estimations, parameter estimation was performed by fitting model simulations to the plasma profiles of the training dataset.

Dissolution kinetics of dasatinib tablets, suspensions and solutions were described using a mechanistic Noyes–Whitney type model, selected for its applicability to particle dissolution processes. Model parameterization utilized either particle size distributions derived from the literature (for suspensions and tablets)²³ or immediately dissolved particle radii of <0.01 μm (for solutions).²⁴ Dasatinib supersaturation in the intestine was considered, as indicated by prior research,²⁵ but redissolution processes of precipitated drug were discarded because of dasatinib's low intestinal solubility.²³

Virtual “mean individuals” were created for each study as outlined in [Section S1.2](#). In addition, population simulations were employed to predict the drug's PK across a virtual population, accounting for variability in physiological factors (see [Section S1.3](#)). Here, we created virtual populations of 100 individuals for each study, mirroring the demographics of the actual study populations. The ethnicity and demographic characteristics for these simulations were selected based on the specific study participant profiles, utilizing distributions from relevant databases. These included the third National Health and Nutrition Examination Survey (NHANES) for White Americans,²⁶ the International Commission on Radiological Protection (ICRP) database for Europeans²⁷ and the integrated

database for the Japanese population.²⁸ Population variability in CYP3A4 expression was considered by varying the corresponding reference concentration within the virtual population according to Table S2.

PBPK model evaluation

PBPK model performance was evaluated using graphical and quantitative approaches. The predicted plasma concentration–time profiles were compared with corresponding observed profiles. Goodness of fit plots were generated to compare predicted and observed AUC from the first to the last timepoint of measurement (AUC_{last}), maximum plasma concentration (C_{max}) values and plasma concentrations, respectively. As quantitative measures, the mean relative deviation (MRD) of predicted plasma concentrations and the geometric mean fold error (GMFE) of predicted AUC_{last} and C_{max} values were calculated as previously described.²⁹ Additionally, a local sensitivity analysis was performed as described in Section S2.4.1.

PBPK drug–drug interaction modeling

Modeling of clinically studied DDI scenarios was performed with five perpetrator drugs (ketoconazole, rifampicin, rabeprazole, famotidine and Maalox®, an over-the-counter antacid containing aluminum hydroxide and magnesium hydroxide as active ingredients) and one victim drug (simvastatin).^{3–5,9} The investigated DDI scenarios were categorized into two primary types: enzyme-mediated DDIs and pH-dependent DDIs. For the enzyme-mediated DDIs, the dasatinib PBPK model was coupled with previously published PBPK models of ketoconazole,²⁹ rifampicin³⁰ and simvastatin.³¹ Here, inhibition and induction processes were implemented as described in the Open Systems Pharmacology Suite manual,³² using interaction parameters sourced from published PBPK models for each perpetrator drug.^{29,30} For the pH-dependent DDIs, the reduced gastric solubility due to intake of the ARAs rabeprazole,⁴ famotidine⁵ and Maalox®⁵ was captured by increasing the gastric pH as previously performed³³ and adjusting the gastric emptying time for rabeprazole and Maalox®. Gastric pH values were only measured in the DDI study with rabeprazole.⁴ Here, the mean gastric pH was measured to be 4.1 (2.8–5.2) following the administration of 20 mg rabeprazole and 0.7 (0.5–3.6) after intake of 20 mg rabeprazole plus 1500 mg betaine hydrochloride (BHCl), respectively, while the median gastric pH in the control group was 0.6 (0.5–1.8).⁴ For administration of 40 mg famotidine (10 h prior to a 50 mg

dasatinib intake), the gastric pH was adjusted to 2.8, as reported in the literature.³⁴ In a separate instance involving the concomitant administration of 30 mL Maalox®, the gastric pH was adjusted to 3.0, as documented in a different study.³⁵ For the control setting, the PK-Sim® default gastric pH of 2.0 in the fasted state was utilized.

PBPK drug–drug interaction model evaluation

Performance of the DDI model was evaluated by graphical comparison of predicted and observed plasma concentration–time profiles with and without concomitant use of the perpetrator drugs. DDI effects were evaluated by calculating predicted AUC_{last} and C_{max} effect ratios according to Equations 1 and 2 comparing predicted ratios to the respective observed values. Here, the prediction success limits proposed by Guest et al. were applied to assess predictive accuracy for DDI ratios, representing a stricter criterium for DDI predictions than the traditional twofold range, especially when the relative AUC and C_{max} change is small.

$$AUC_{last} \text{ ratio} = \frac{AUC_{last, \text{ effect}}}{AUC_{last, \text{ control}}} \quad (1)$$

$$C_{max} \text{ ratio} = \frac{C_{max, \text{ effect}}}{C_{max, \text{ control}}} \quad (2)$$

For DDI model performance evaluation, $AUC_{last, \text{ effect}}$ and $C_{max, \text{ effect}}$ represent the AUC_{last} and C_{max} values of the victim drug when administered with the perpetrator drug. Conversely, $AUC_{last, \text{ control}}$ and $C_{max, \text{ control}}$ represent the AUC_{last} and C_{max} values of the victim drug when administered alone.

Exposure simulations for model-informed precision dosing

The developed PBPK model was applied to simulate dasatinib exposure in untested DDI scenarios with moderate and strong inhibitors as well as inducers of CYP3A4: The model was coupled with previously published PBPK perpetrator models of the inhibitors clarithromycin,³⁰ erythromycin,³⁶ fluconazole,³⁷ fluvoxamine,³⁸ grapefruit juice,³⁹ itraconazole,³⁰ and voriconazole⁴⁰ as well as the inducers carbamazepine⁴¹ and efavirenz^{41,42} to evaluate their impact on the exposure of dasatinib. Additionally, co-administration of dasatinib with two perpetrator drugs simultaneously was investigated. Inhibition and induction processes were implemented using interaction



parameters from the respective published PBPK models. The selected dosing regimens for each perpetrator drug and further information on the exposure simulations are given in Section S5.1. The magnitude of dose adjustments in the simulated DDI scenarios matching the exposure of dasatinib monotherapy was investigated for the two recommended daily dasatinib dosing regimens of 100 mg and 140 mg. Here, the simulated dasatinib doses were adapted in increments of 10 mg (in a range of 20–420 mg) until the steady-state AUC (AUC_{ss}) matched the AUC_{ss} (80%–125%) of the monotherapy setting.

RESULTS

PBPK model building and evaluation

The training dataset for model building included five mean plasma concentration–time profiles from three single-dose and one multiple-dose study in healthy volunteers as well as a DDI study with ketoconazole in cancer patients, covering a dasatinib dose range from 20 to 140 mg. The test dataset consisted of 58 mean plasma profiles from healthy volunteers and cancer patients, who received single and multiple doses of dasatinib ranging from 15 to 200 mg.

Modeled elimination processes included metabolism via CYP3A4, implemented as Michaelis–Menten kinetics, an unspecific hepatic clearance to cover CYP3A4-independent metabolism and renal excretion through passive glomerular filtration. The Michaelis–Menten constant (K_m) for metabolism via CYP3A4, inhibition constants for CYP2C8, OATP1B1, and OATP1B3 as well as the CYP3A4 mechanism-based inhibition parameters of dasatinib were derived from the literature.^{7,11,12} Catalytic rate constant for CYP3A4-mediated metabolism ($k_{cat,CYP3A4}$) and the unspecific hepatic clearance were fitted. Here, $k_{cat,CYP3A4}$ was informed by including the ketoconazole DDI study for model training. Based on the estimated $k_{cat,CYP3A4}$ and the corresponding K_m obtained from in vitro studies, an overall fraction metabolized via CYP3A4 resulting from metabolism in all tissues expressing this enzyme (see Table S3) was predicted to be ~92% of the absorbed drug. An overview of all integrated metabolic pathways and investigated DDIs is illustrated in Figure 1a–c, respectively. Drug-dependent model input parameters of dasatinib are listed in Table S4. The PBPK model file of dasatinib can be found in Appendix S2.

Plasma concentration–time profiles of the training dataset, a selection of plasma profiles of the test dataset and the corresponding goodness of fit plots showing predicted compared with observed AUC_{last} , C_{max} , and plasma concentrations are depicted in Figure 2.

Overall, the developed whole-body PBPK model of dasatinib successfully described and predicted plasma concentration–time profiles of the training and test dataset including their shapes in both healthy volunteers and cancer patients. In addition, the model was able to capture minor effects of meal intake on dasatinib PK as demonstrated in Section S4. For the entire dasatinib dataset, 96% of predicted AUC_{last} , 98% of predicted C_{max} values, and 90% of predicted plasma concentrations were within the two-fold acceptance criterion of their observed values. GMFEs for predicted AUC_{last} and C_{max} values were 1.27 (training dataset: 1.12 and test dataset: 1.28) and 1.29 (training dataset: 1.18 and test dataset: 1.30), respectively, while the overall MRD value for predicted plasma concentrations was 1.54. Detailed values are presented in Tables S5 and S6. Considering the training and test dataset separately, MRD values were calculated to be 1.35 and 1.56, respectively. Moreover, 49 out of 53 plasma concentration–times profiles show MRD values ≤ 2 , supporting the adequate model predictions of longitudinal plasma concentration–time profile trajectories. As shown in Figure S6, residuals are randomly dispersed over time with no apparent trend, suggesting that the model does not exhibit systematic bias across the range of fits and predictions.

Of note, about half of the observed plasma profiles of cancer patients showed consistently lower plasma concentrations compared with the concentrations in healthy volunteers receiving similar dasatinib doses. As mentioned before, gastric pH plays a pivotal role in modulating dasatinib absorption. Moreover, co-morbidities and administration of ARAs could negatively affect the absorption of dasatinib. To mitigate these factors and refine model predictions, we adjusted the gastric pH for a subset of cancer patients showing consistently lower dasatinib exposure compared with healthy volunteers to the upper end of the physiological range in the fasted state (1.5–2.5).⁴³ As a result, the model performance could be improved, reducing the MRD for the corresponding plasma profiles from 1.92 to 1.60. Local sensitivity analysis, conducted for a 100 mg once daily dosing regimen, identified the two pK_a values, gastric pH and lipophilicity as the parameters most sensitive to dasatinib exposure at steady-state (details are presented in Section S2.4.2).

PBPK drug–drug interaction modeling and evaluation

Eight dasatinib plasma profiles from five clinical DDI studies^{3–5,9} were employed to prepare and evaluate the model predicting DDI scenarios. In enzyme-mediated DDI studies, dasatinib (acting as victim drug) was

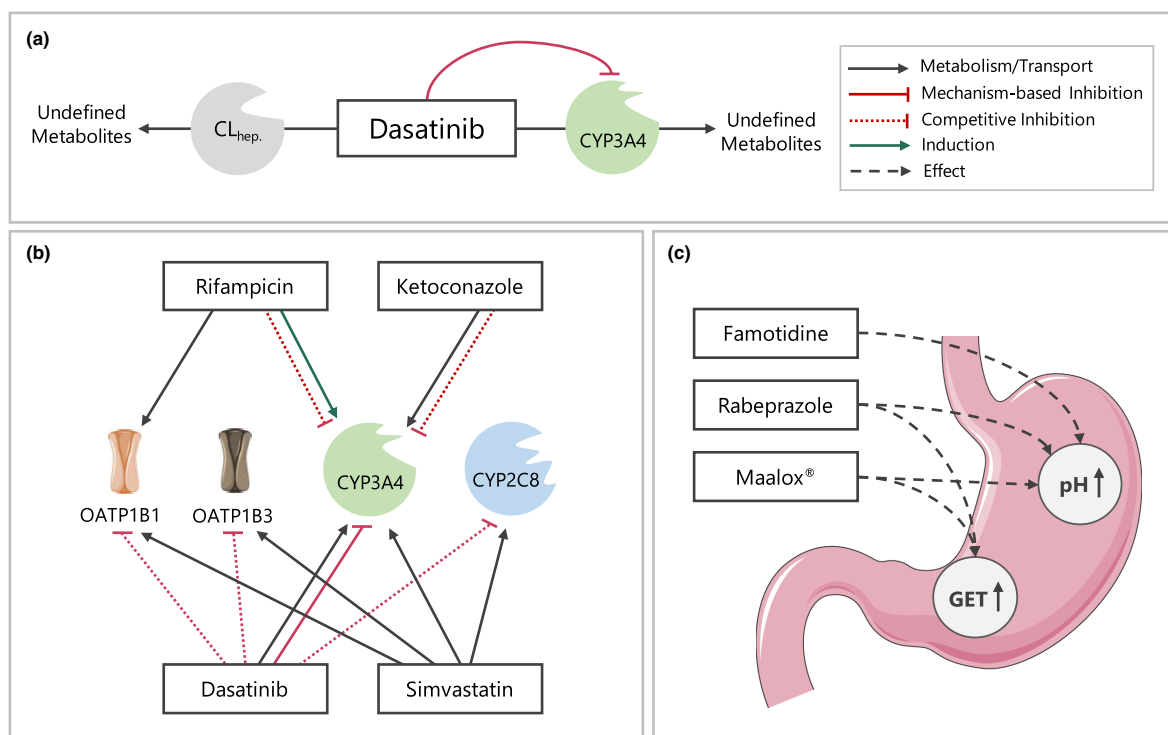


FIGURE 1 Schematic overview of implemented metabolic processes in the dasatinib PBPK model (a) as well as investigated DDIs including enzyme-mediated (b) and pH-dependent DDIs (c). Drawings by Servier, licensed under CC BY 3.0.⁵⁵ CL_{hep}, unspecific hepatic clearance; CYP, cytochrome P450; DDIs, drug–drug interactions; GET, gastric emptying time; OATP, organic anion transporting polypeptide.

administered with and without the perpetrator drugs ketoconazole (CYP3A4 competitive inhibition²⁹) and rifampicin (CYP3A4 induction and CYP3A4 competitive inhibition³⁰), respectively. Furthermore, plasma profiles of the victim drug simvastatin lactone and its metabolite simvastatin acid administered with and without dasatinib were included for model evaluation. Here, dasatinib acts as a CYP3A4 mechanism-based inhibitor and CYP2C8, OATP1B1 and OATP1B3 competitive inhibitor. Simulated and observed plasma concentration–time profiles of all modeled enzyme-mediated DDIs are depicted in Figure 3. The DDI model files are included in Appendix S2.

For the investigation of pH-dependent DDIs, plasma profiles of dasatinib with and without administration of the ARAs rabeprazole,⁴ rabeprazole plus HCl,⁴ famotidine and Maalox[®]⁵ were available for model evaluation. The corresponding plasma profiles of the different pH-dependent DDI scenarios are depicted in Figure 4. Additional information on the DDI studies is provided in Table S7.

Figure 5 depicts the goodness of fit plots, comparing predicted to observed AUC_{last} and C_{max} ratios for dasatinib — modulated by intake of perpetrators ketoconazole, rifampicin, the antacid Maalox[®], PPI rabeprazole, and

FIGURE 2 Selection of predicted and observed dasatinib plasma concentration–time profiles of the training (a–d) and the test dataset (e–i) on a linear scale as well as goodness of fit plots of predicted versus observed AUC_{last} (j), C_{max} (k) and plasma concentrations (l). Blue and light blue solid lines show predicted geometric mean concentration–time profiles in healthy volunteers and cancer patients, respectively, with colored ribbons illustrating the corresponding geometric standard deviation of the population simulations ($n = 100$). Points demonstrate the mean observed data of dasatinib with the corresponding standard deviation (if depicted in the respective publication). Linear and semilogarithmic predicted and observed plasma concentration–time profiles of all studies are shown in Sections S2.1 and S2.2. In the goodness of fit plots, solid lines mark the lines of identity, dotted lines indicate 1.25-fold and dashed lines twofold deviation. /, no information available; AUC_{last}, areas under the plasma concentration–time curves from the first to the last timepoint of measurement; bid, twice a day; C_{max}, maximum plasma concentration; md, multiple dose; n , number of participants; PFOS, powder for oral suspension; po, peroral; Q5D, five consecutive days once daily dosing followed by two nontreatment days; qd, once a day; sd, single dose; tab, tablet.

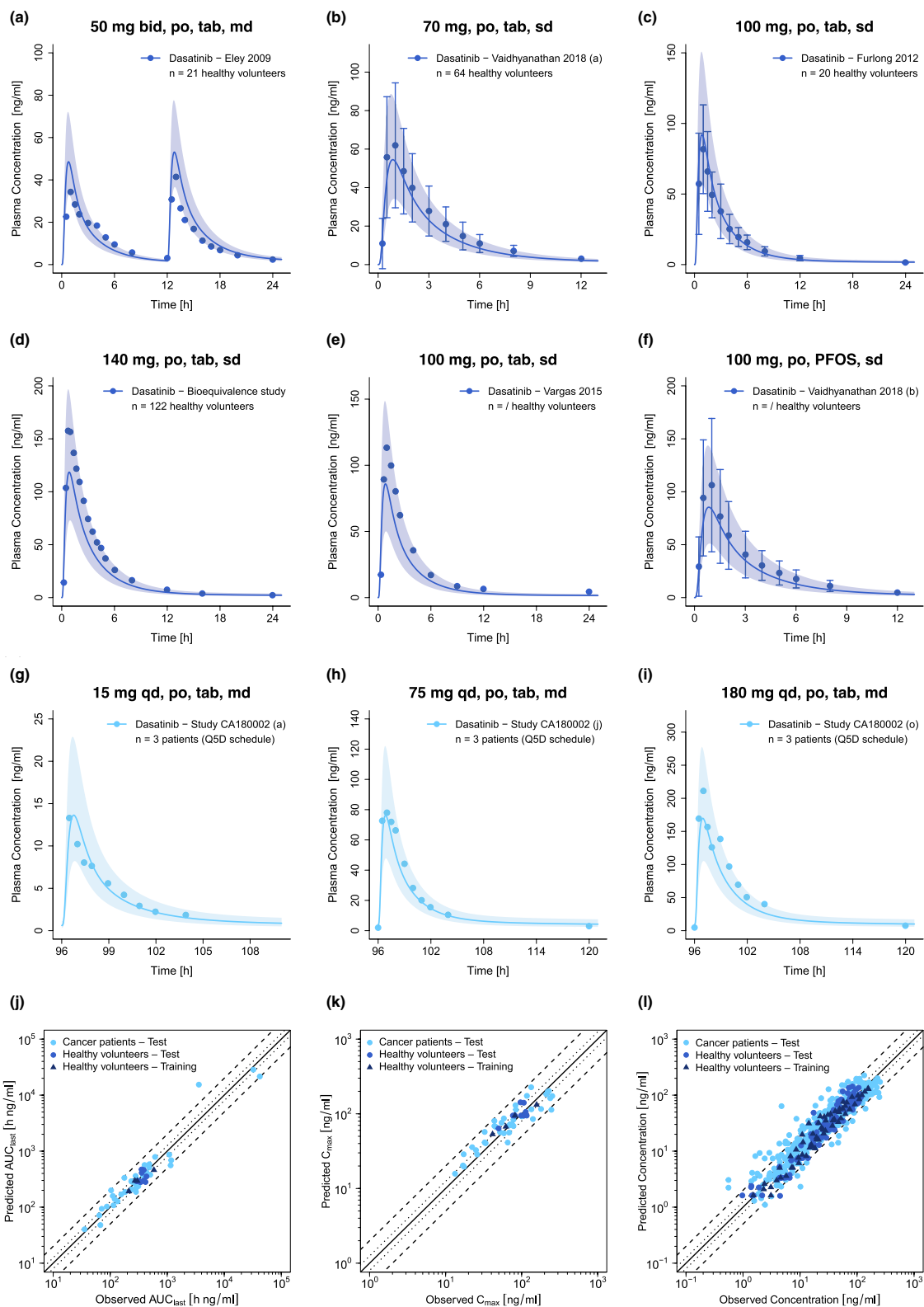


FIGURE 3 Predicted and observed plasma concentration–time profiles for enzyme-mediated DDIs with dasatinib acting as victim (a, b) and perpetrator drug (c, d). The solid lines show predicted geometric mean concentration–time profiles with (colored) and without (gray) intake of the perpetrator drug and ribbons show the corresponding geometric standard deviation of the population simulations ($n=100$). Points depict mean observed data with corresponding standard deviation of dasatinib, while squares and triangles depict the observed data with corresponding standard deviation of simvastatin lactone and simvastatin acid, respectively. Predicted and observed plasma concentration–time profiles of all studies on a semilogarithmic scale are shown in Section S3.2.1. DDIs, drug–drug interactions; n , number of participants.

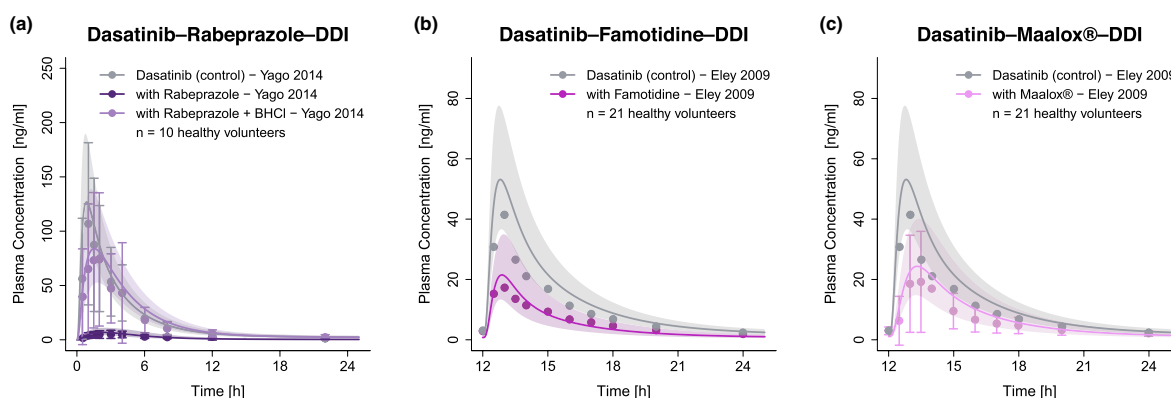
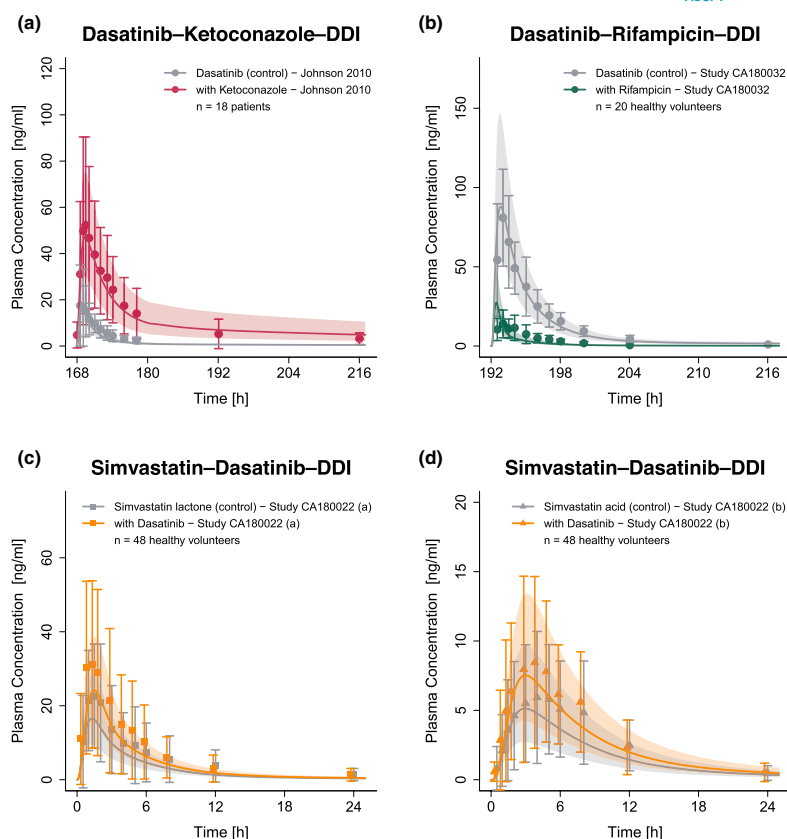


FIGURE 4 Predicted and observed plasma concentration–time profiles of dasatinib for the pH-dependent DDIs. The solid lines show predicted geometric mean concentration–time profiles with (colored) and without (gray) the intake of the perpetrator drug and ribbons show the corresponding geometric standard deviation of the population simulations ($n=100$). Points depict mean observed data with corresponding standard deviation of dasatinib (if depicted in the respective publication). Predicted and observed plasma concentration–time profiles of all studies on a semilogarithmic scale are shown in Section S3.2.2. BHCl, betaine hydrochloride; DDIs, drug–drug interactions; n , number of participants.

H₂-blocker famotidine — as well as simvastatin lactone and its metabolite simvastatin acid, impacted by dasatinib administration. GMFEs for the predicted AUC_{last} and

C_{max} ratios were 1.19 and 1.08 for pH-dependent DDIs, 1.37 and 1.57 for enzyme-mediated DDIs with dasatinib acting as victim drug as well as 1.21 and 1.07 for DDIs with

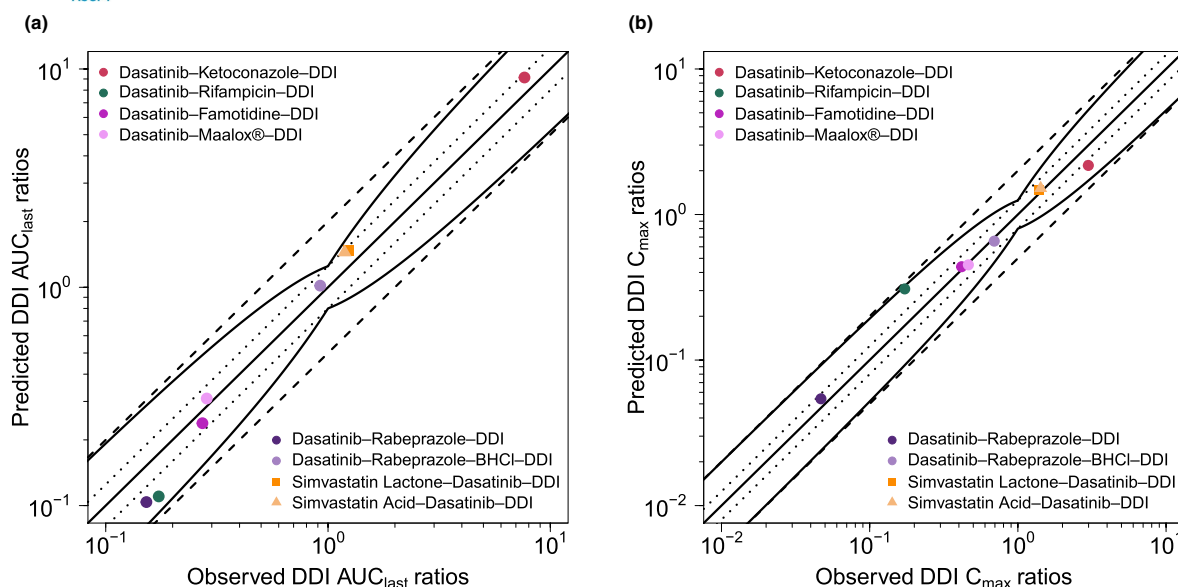


FIGURE 5 Predicted versus observed DDI AUC_{last} ratios (a) and DDI C_{max} ratios (b) of dasatinib (circles), simvastatin lactone (squares) and simvastatin acid (triangles). The straight solid lines mark the lines of identity, the curved lines show the limits of the predictive measure proposed by Guest et al. with 1.25-fold variability.⁵⁶ Dotted lines indicate 1.25-fold and dashed lines twofold deviation. AUC_{last} , area under the plasma concentration–time curve from the first to the last timepoint of measurement; BHCl, betaine hydrochloride; C_{max} , maximum plasma concentration; DDI, drug–drug interaction.

dasatinib acting as perpetrator drug. Moreover, all AUC_{last} and C_{max} ratios lie within the limits proposed by Guest et al. (see Figure 5). Additionally, 7 out of 8 AUC_{last} and C_{max} ratios were within 1.5-fold of observed ratios. Only the DDI with rifampicin, a strong CYP3A4 inducer and weak CYP3A4 inhibitor, was outside the stricter 1.5-fold range with AUC_{last} and C_{max} ratios of 0.64 and 1.79, respectively. All predicted and observed values for AUC_{last} and C_{max} ratios are listed in Table S8.

Exposure simulations for model-informed precision dosing

The developed PBPK model was applied to simulate DDI scenarios of dasatinib with various strong and moderate CYP3A4 inhibitors and inducers. Subsequently, model-based dasatinib dose adaptations were simulated based on the exposure matching principle. A selection of the corresponding plasma concentration–time profiles with and without adapted dasatinib doses is provided in Figure 6 and profiles for all investigated DDI settings in Figures S13 and S14.

Model exposure simulations revealed that co-administration of the perpetrator drugs may result in mean dasatinib AUC_{ss} increases of up to 4.6-fold and reductions of up to 70% (see Table S12). Based on exposure matching

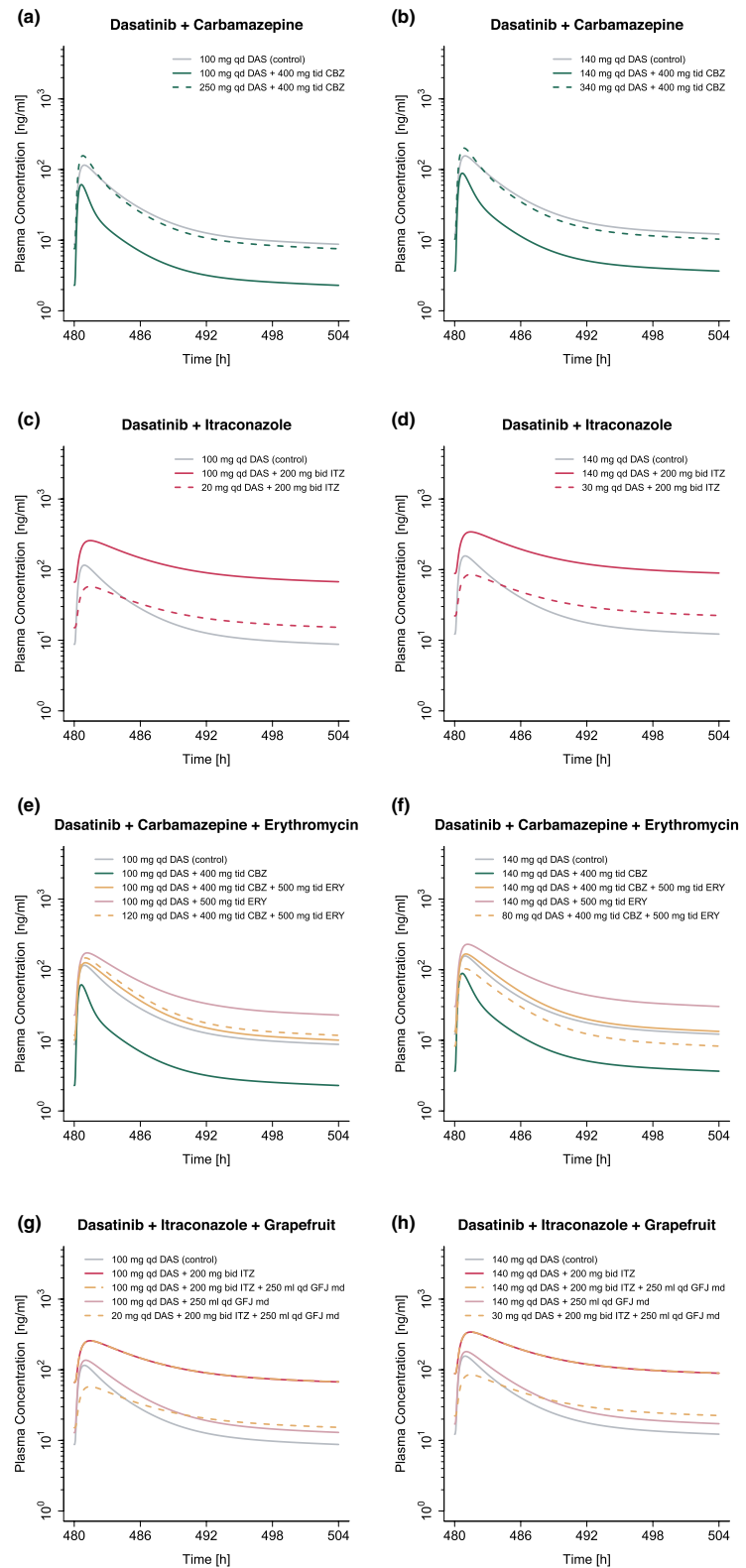
simulations, this translated into a dasatinib dose range of 20–310 (30–360) mg to match the PBPK simulated monotherapy AUC_{ss} from 100 (140) mg dasatinib (see Figure 7). Model simulations revealed dose reductions of 50%–80% for strong and 0%–70% for moderate inhibitors. In contrast, during co-administration of inducers, a 2.3–3.1-fold increase of dasatinib dose was required to match the exposure of dasatinib monotherapy.

Additionally, co-administration with drugs like carbamazepine and erythromycin or itraconazole and grapefruit juice resulted in dose reductions of up to 20% and 80%, respectively. Table S12 provides an overview of all DDI scenarios, including AUC_{ss} effect ratios and dose adjustments to match monotherapy exposure for 100 mg and 140 mg daily dasatinib.

DISCUSSION

In this study, a whole-body PBPK model of dasatinib was successfully developed integrating data from a total of 19 clinical trials. The model was able to describe and predict dasatinib plasma concentration–time profiles in healthy volunteers and cancer patients, covering a dasatinib dose range of 15–200 mg. Several dasatinib PBPK models have been published in the literature, including three models that investigated either the DDI potential of

FIGURE 6 Model-based dose adaptations for dasatinib within single (a–d) and multiple DDI scenarios (e–h) including moderate and strong CYP3A4 inhibitors and inducers. The first and second column represent the simulation results after administration of 100 mg and 140 mg dasatinib daily, respectively. Solid lines show the model predictions with (colored) and without (gray) intake of perpetrator drug. Colored dashed lines represent model predictions in the presence of perpetrator drug(s), using an adapted dasatinib dose. For the dosing simulations a virtual European male individual, 64 years of age and default values for body weight and height according to the International Commission on Radiological Protection (ICRP) database, was used. Bid, twice a day; CBZ, carbamazepine; DAS, dasatinib; DDI, drug–drug interaction; ERY, erythromycin; GFJ, grapefruit juice; ITZ, itraconazole; md, multiple dose; qd, once a day; tid, three times a day.



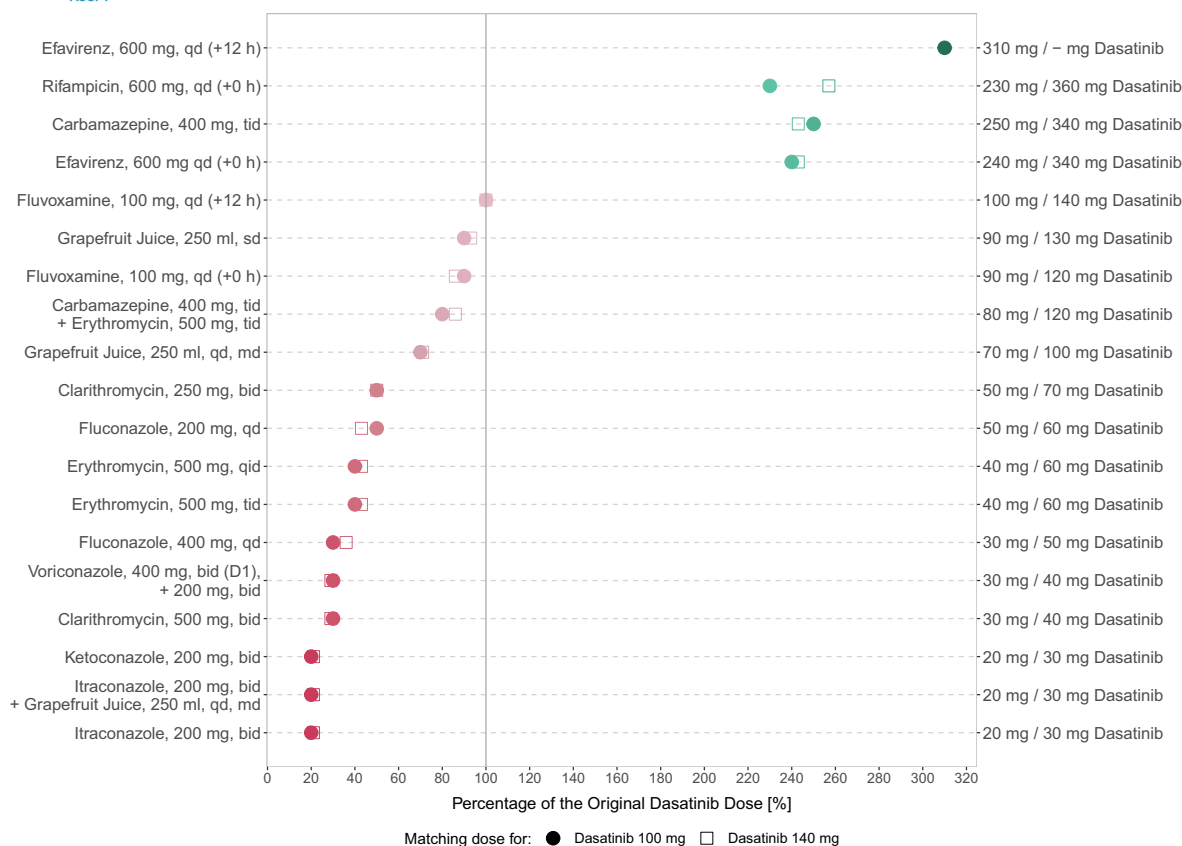


FIGURE 7 Overview of model-based dose adaptations for dasatinib within single and multiple DDI scenarios based on the exposure matching principle, where points and squares show the percentage of the original dasatinib dose that match the PBPK simulated monotherapy AUC_{ss} at 100 mg and 140 mg, respectively. A virtual European male individual, 64 years of age and default values for body weight and height according to the International Commission on Radiological Protection (ICRP) database, was used for the dosing simulations. Red symbols depict dasatinib dose reductions and green symbols depict dasatinib dose elevations. The darker the color, the higher the magnitude of dasatinib dose adaptation. –, dose adaptations outside the simulated dose range; AUC_{ss} , steady-state area under the concentration–time curve; bid, twice a day; D, day; md, multiple dose; qd, once daily; qid, four times a day; sd, single dose; tab, tablet; tid, three times a day.

dasatinib mediated by enzymes and/or transporters^{11,12} or the effects of varying formulations on dasatinib PK.²³ In contrast to previous work, the presented model was used to investigate a comprehensive range of clinically relevant enzyme-mediated and pH-dependent DDI scenarios in healthy volunteers and cancer patients within a single framework. For model development, a larger number of clinical studies involving a broader dose range (15–200 mg) of dasatinib was used compared with published PBPK models. Moreover, the model was utilized to simulate various DDI scenarios that have not yet been investigated in clinical trials and to provide model-based dose adaptations, supporting precision dosing approaches for dasatinib. Furthermore, our established PBPK model extends the openly accessible PBPK model library with an additional sensitive CYP3A4 substrate and can be applied

by the research community for various applications such as additional population-specific DDI simulations and dose adaptations, DDI simulations with drugs under development involving dasatinib as a sensitive CYP3A4 substrate, or to develop and evaluate new PBPK models.

In our PBPK model, fraction absorbed after administration of dasatinib tablets across the dose range of 20–420 mg varied between 80% and 41% (Table S14). Additionally, the respective modeled absolute bioavailability ranged from 20% to 28% for the dose range of 20–420 mg (Table S14). Due to lack of intravenous data the modeled bioavailability values could not be compared with clinically observed data.⁴⁴ Dasatinib is primarily metabolized via CYP3A4, accounting for ~92% of the absorbed drug, consistent with literature reports.⁷ Moreover, only 0.1% of absorbed dasatinib was excreted unchanged in urine, which is in line

with results from a human ADME study.⁶ In vitro studies suggested that dasatinib may be a substrate of the efflux transporters breast cancer resistance protein (BCRP) and P-glycoprotein (P-gp).⁴⁵ However, recent in vivo studies by Kamath et al. found no significant involvement of P-gp in modulating the rate and extent of intestinal absorption.⁴⁶ Consequently, and due to the absence of in vitro K_m values, P-gp and BCRP were not incorporated into the PBPK model.

A good descriptive and predictive performance for DDIs was demonstrated by GMFEs of 1.24 and 1.18 for predicted AUC_{last} and C_{max} effect ratios, respectively. The DDIs emphasize the significant role of CYP3A4 in dasatinib metabolism and the importance to adapt dasatinib therapy in DDI settings to increase both patient safety and treatment efficacy. Due to the potential risk of adverse events resulting from increased dasatinib exposure during CYP3A4 inhibition, the package insert advises against the concomitant use of dasatinib and strong CYP3A4 inhibitors.^{15,47} However, if such combination is unavoidable, the package insert recommends considering dose adaptations to 20 (40) mg dasatinib daily instead of 100 (140) mg for all strong inhibitors, while dosing recommendations for moderate CYP3A4 inhibitors are not provided.¹⁵ Consequently, our developed PBPK model was applied in tandem with models of various strong and moderate CYP3A4 perpetrators to conduct DDI simulations to support dasatinib precision dosing.

The performed model simulations suggest that a “one-dose-fits-all” approach during co-treatment with strong or moderate inhibitors may lead to suboptimal dasatinib exposures: If combination of dasatinib with strong CYP3A4 inhibitors is unavoidable, dasatinib dose reductions of 50%–80% should be considered, depending on the inhibitor and selected dosing regimen, to match dasatinib AUC_{ss} during monotherapy. This translates into a dasatinib dose range of 20–50 mg for the 100 mg dosing regimen and 30–70 mg for the 140 mg dosing regimen. Moreover, simulations suggest dose reductions of 0%–70% for co-treatment with moderate CYP3A4 inhibitors, depending on individual factors such as perpetrator drug and timing of drug administration (detailed numeric dasatinib dose adaptations are listed in Table S12). Furthermore, while simulations with a single dose of 250 mL grapefruit juice showed only a marginal increase in dasatinib exposure (~15%), a daily intake led to an AUC_{ss} increase of up to 40%, supporting the package insert guidance to avoid concomitant intake of dasatinib with grapefruit juice.

The PBPK model was additionally used to simulate the impact of CYP3A4 induction on dasatinib exposure, a situation for which only qualitative recommendations are available in the package insert: Concomitant strong inducers should be avoided, and if co-administration is

inevitable, a dose increase considered.¹⁵ Our model simulations suggest that a 2.3–3.1-fold increase in dasatinib dose would match the exposure of dasatinib monotherapy. However, if adapting the dasatinib dose to higher values that were neither part of the model training/test dataset nor clinically studied, it is crucial to carefully monitor patients for potential toxicities (e.g., pleural effusion or hematological toxicities).^{15,47}

Moreover, the effect of dose staggering was exemplarily investigated for fluvoxamine (moderate competitive CYP3A4 inhibitor) and efavirenz (moderate CYP3A4 inducer) as both drugs should be preferably taken in the evening according to the package insert. While no dose adaptations were needed for fluvoxamine with a 12 h staggered intake, the effect on dasatinib's AUC_{ss} increased when efavirenz was given 12 h staggered to dasatinib (see Figure 7 and Table S12).

Dasatinib's pH-dependent DDIs represent another type of clinical interaction. In the investigated pH-dependent DDIs, rabeprazole, famotidine and Maalox® co-treatment showed strong impact on dasatinib PK with simulated AUC_{last} effect ratios of 0.10, 0.24 and 0.31, respectively. Successful predictions of the DDI scenarios were attained by elevating the gastric pH constantly over time to the literature values of 4.1, 2.8, and 3.0, respectively, and estimating the elevated gastric emptying times to be 60.1 min for rabeprazole and 31.3 min for Maalox®. The impact of Maalox® on gastric emptying time has been reported in the literature,⁴⁸ while the effect of PPIs is volunteers of ongoing debate and necessitates further investigation.^{49,50} Given the dynamic changes in gastric pH following the administration of ARAs, offering precise dosing recommendations for such DDI scenarios becomes challenging. However, the effect of antacids, which directly neutralize gastric acid, diminishes approximately 2 h post-dose.⁵¹ Consequently, antacids taken 2 h before dasatinib do not significantly alter dasatinib exposure.⁵ In contrast, the reduction in gastric acid production through H_2 -antagonists can persist for up to 12 h and the suppression induced by PPIs can continue for several days after stopping the PPI treatment.⁵¹ Therefore, ARAs that have a shorter duration of pH elevation, such as antacids, should be preferred.

Besides single DDIs, two exemplary multiple DDIs were investigated. While the single DDI with carbamazepine (strong CYP3A4 inducer) required a 2.4-fold increase in dasatinib dose to match the exposure of dasatinib monotherapy, the additional administration of erythromycin (moderate, irreversible CYP3A4 inhibitor) compensated this effect, overall resulting in a 20% dose reduction. In contrast, the additional intake of grapefruit juice to the strong CYP3A4 inhibitor itraconazole did not impact the simulated dose adaptation for the single dasatinib–itraconazole–DDI (80% dose reduction).



The dasatinib model was evaluated in a comprehensive PBPK DDI network, offering predictions for various clinical situations. It can explore single and multiple DDIs with dasatinib as the victim drug. The dasatinib perpetrator model, tested with the dasatinib–simvastatin DDI, holds potential for future research, especially concerning CYP3A4, CYP2C8, OATP1B1, and OATP1B3 substrates with a narrow therapeutic index. This underscores the importance of DDIs in long-term dasatinib treatment.

There are limitations to this study, which merit consideration and will be explored in the forthcoming paragraphs. Metabolites of dasatinib were not incorporated into the PBPK model, as they are not considered clinically relevant.⁶ However, during strong CYP3A4 induction, plasma concentrations of active metabolites could potentially increase to clinically relevant exposures, which was not addressed in our dosing recommendations. Contrary to CYP3A4 genetic variants, CYP3A5 polymorphisms are known to significantly affect the PK of many CYP3A substrates.⁵² Consequently, due to the minor contribution of CYP3A5 to the metabolism of dasatinib,⁷ CYP3A genetic variants were not considered in this work. While our PBPK model accounts for differences in patient demographics, such as age, which affects various physiological parameters including glomerular filtration rate (GFR), blood flow rates and tissue volumes, pathophysiologic changes for cancer patients (e.g., enzyme expression or α 1-acid glycoprotein levels [AGP]) were not integrated because of lack of specific information from clinical study reports. However, population variability in CYP3A4 enzyme expression or AGP levels was considered in the population simulations.

A less precise prediction performance compared with other explored DDIs could be observed for the DDI with rifampicin applying a stricter criterium of 1.5-fold range. Here, predicted AUC_{last} and C_{max} ratios deviated more than 1.5-fold from the observed ratios. Of note, rifampicin is not only an inhibitor and inducer of several enzymes, but also of several transporters like the efflux transporter P-gp. Incorporation of P-gp in the dasatinib PBPK model was investigated during model building; however, no significant improvement of DDI predictions involving rifampicin could be observed that has further encouraged to not include P-gp in the final model. Similar limitations regarding DDI predictions with rifampicin have also been reported in previous work because of the complex inhibition and induction mechanisms for several enzymes and transporters.^{53,54}

The dosing simulations and subsequent dose adaptations were based on the exposure matching principle, utilizing dasatinib AUC_{ss} as exposure metric as described in the package insert.¹⁵ However, it should be noted that despite achieving similar AUC_{ss} values for the control and

DDI scenarios through dose adaptations, differences in plasma profile trajectories and thus C_{max} and trough concentrations (C_{min}) can lead to differences in drug efficacy and safety. Dose-adapted plasma profiles during CYP3A4 inducer co-treatment showed higher C_{max} values while plasma profiles during inhibitor co-treatment showed higher C_{min} values compared with the simulated plasma profiles during monotherapy. An exposure–response analysis identified elevation in C_{min} as the most significant predictor for pleural effusion, a key adverse event during dasatinib therapy.⁴⁷ Hence, close monitoring of patients for toxicities is inevitable particularly during CYP3A4 inhibitor co-treatment and concomitant use with strong inhibitors should be avoided in clinical practice.

Finally, the recommended dasatinib dose for each DDI scenario represents an estimated average dose that can be affected by different sources of variability and uncertainties (e.g., enzyme abundance). For dosing simulations, a virtual European male individual, 64 years of age and default values for body weight and height according to the ICRP database was used. While also complex scenarios like multiple DDIs were simulated, the applicability of the provided dosing recommendations to patients with diverse clinical characteristics (e.g., hepatic impairment) is not warranted and was beyond the scope of this study. However, our PBPK model offers a foundation for future applications to personalize dasatinib therapy by using individual demographics, physiology, and enzyme activity, creating a “virtual twin” of the patient. Clinical studies are yet required to confirm the advantage of such a precision dosing approach for dasatinib therapy including efficacy and safety over the broad dose range that was required in the various DDI simulations to match the dasatinib exposure during monotherapy.

To conclude, a comprehensive whole-body PBPK model was successfully developed for dasatinib, a sensitive CYP3A4 substrate. The established model was leveraged to simulate several previously unexplored DDI scenarios, resulting in model-based dosing recommendations for dasatinib. Moreover, the model could serve as a tool to further optimize and personalize dasatinib therapy, providing strategies to navigate clinical challenges that result from single and multiple DDIs and/or patient-related factors, such as elevated gastric pH. Finally, it extends the openly accessible PBPK model library with an additional sensitive CYP3A4 substrate and can be applied by the research community to investigate future single and multiple DDI scenarios involving dasatinib.

AUTHOR CONTRIBUTIONS

C.K., H.L.H.L., S.R., D.S., M.S. and T.L. wrote the manuscript; C.K., H.L.H.L., L.M.F., F.Z.M., S.R. and T.L. designed the research; C.K. performed the research; C.K. and H.L.H.L. analyzed the data.

ACKNOWLEDGMENTS

We thank Elisabeth Emmerich for supporting this work during her internship at Saarland University. Open Access funding enabled and organized by Projekt DEAL.

FUNDING INFORMATION

Matthias Schwab was supported by the Robert Bosch Stiftung (Stuttgart, Germany), a grant from the German Federal Ministry of Education and Research (BMBF, 031L0188D, "GUIDE-IBD") and the DFG im Rahmen der Exzellenzstrategie des Bundes und der Länder-EXC 2180-390900677. Thorsten Lehr was supported by the German Federal Ministry of Education and Research (BMBF, Horizon 2020 INSPIRATION grant 643271), under the frame of ERACoSysMed and the European Union Horizon 2021 SafePolyMed (grant 101057639).

CONFLICT OF INTEREST STATEMENT

The authors declared no competing interests for this work.

ORCID

Christina Kovar  <https://orcid.org/0000-0003-0155-9861>

Simeon Rüdesheim  <https://orcid.org/0000-0002-5741-2511>

Dominik Selzer  <https://orcid.org/0000-0002-4126-0816>

Matthias Schwab  <https://orcid.org/0000-0002-9984-075X>

Thorsten Lehr  <https://orcid.org/0000-0002-8372-1465>

REFERENCES

1. American Cancer Society. Cancer facts and figures. American Cancer Society website. <https://www.cancer.org/cancer/chronic-myeloid-leukemia/about/statistics.html>. Accessed February 1, 2023.
2. European Medicines Agency (EMA). Annex I: summary of product characteristics (Sprycel). European Medicines Agency website. https://www.ema.europa.eu/en/documents/product-information/sprycel-epar-product-information_en.pdf. Accessed January 18, 2023.
3. Center for Drug Evaluation. Clinical pharmacology and biopharmaceutics review(s): NDA Review – Dasatinib. U.S. Food and Drug Administration website. https://www.accessdata.fda.gov/drugsatfda_docs/nda/2006/021986s000_Sprycel_ClinPharmR.pdf. Accessed August 04, 2022.
4. Yago MR, Frymoyer A, Benet LZ, et al. The use of beta-tine HCl to enhance dasatinib absorption in healthy volunteers with rabeprazole-induced hypochlorhydria. *AAPS J*. 2014;16:1358-1365.
5. Eley T, Luo FR, Agrawal S, et al. Phase I study of the effect of gastric acid pH modulators on the bioavailability of oral dasatinib in healthy subjects. *J Clin Pharmacol*. 2009;49:700-709.
6. Christopher LJ, Cui D, Wu C, et al. Metabolism and disposition of dasatinib after oral administration to humans. *Drug Metab Dispos*. 2008;36:1357-1364.
7. Wang L, Christopher LJ, Cui D, et al. Identification of the human enzymes involved in the oxidative metabolism of dasatinib: an effective approach for determining metabolite formation kinetics. *Drug Metab Dispos*. 2008;36:1828-1839.
8. U.S. Food and Drug Administration (FDA). Drug development and drug interactions | table of substrates, inhibitors and inducers. <https://www.fda.gov/drugs/drug-interactions-labeling/drug-development-and-drug-interactions-table-substrates-inhibitors-and-inducers>. Accessed February 01, 2023.
9. Johnson FM, Agrawal S, Burris H, et al. Phase 1 pharmacokinetic and drug-interaction study of dasatinib in patients with advanced solid tumors. *Cancer*. 2010;116:1582-1591.
10. Li X, He Y, Ruiz CH, Koenig M, Cameron MD, Vojtkovsky T. Characterization of dasatinib and its structural analogs as CYP3A4 mechanism-based inactivators and the proposed bioactivation pathways. *Drug Metab Dispos*. 2009;37:1242-1250.
11. Pahwa S, Alam K, Crowe A, et al. Pretreatment with rifampicin and tyrosine kinase inhibitor Dasatinib potentiates the inhibitory effects toward OATP1B1- and OATP1B3-mediated transport. *J Pharm Sci*. 2017;106:2123-2135.
12. Chang M, Bathena S, Christopher LJ, Shen H, Roy A. Prediction of drug-drug interaction potential mediated by transporters between dasatinib and metformin, pravastatin, and rosuvastatin using physiologically based pharmacokinetic modeling. *Cancer Chemother Pharmacol*. 2022;89:383-392.
13. Gonzalez D, Rao GG, Bailey SC, et al. Precision dosing: public health need, proposed framework, and anticipated impact. *Clin Transl Sci*. 2017;10:443-454.
14. Grimstein M, Yang Y, Zhang X, et al. Physiologically based pharmacokinetic modeling in regulatory science: an update from the U.S. Food and Drug Administration's Office of Clinical Pharmacology. *J Pharm Sci*. 2019;108:21-25.
15. Bristol-Myers Squibb Company. Sprycel U.S. prescribing information website. https://packageinserts.bms.com/pi/pi_sprycel.pdf. Accessed 01 March 2023.
16. Rodriguez GH, Ahmed SI, Al-Akhrass F, Rallapalli V, Safdar A. Characteristics of, and risk factors for, infections in patients with cancer treated with dasatinib and a brief review of other complications. *Leuk Lymphoma*. 2012;53:1530-1535.
17. Shariati A, Moradabadi A, Chegini Z, Khosbayan A, Didehdar M. An overview of the Management of the Most Important Invasive Fungal Infections in patients with blood malignancies. *Infect Drug Resist*. 2020;13:2329-2354.
18. Shi D, Li Z, Li Y, Jiang Q. Variables associated with self-reported anxiety and depression symptoms in patients with chronic myeloid leukemia receiving tyrosine kinase inhibitor therapy. *Leuk Lymphoma*. 2021;62:640-648.
19. Lippert J, Burghaus R, Edginton A, et al. Open systems pharmacology community-an open access, open source, Open Science approach to modeling and simulation in pharmaceutical sciences. *CPT Pharmacometrics Syst Pharmacol*. 2019;8:878-882.
20. Wojtyniak J-G, Britz H, Selzer D, Schwab M, Lehr T. Data digitizing: accurate and precise data extraction for quantitative systems pharmacology and physiologically-based pharmacokinetic modeling. *CPT Pharmacometrics Syst Pharmacol*. 2020;9:322-331.
21. R Core Team. *R: A Language and Environment for Statistical Computing*. R Foundation for Statistical Computing; 2021.



22. Tsamandouras N, Rostami-Hodjegan A, Aarons L. Combining the “bottom up” and “top down” approaches in pharmacokinetic modelling: fitting PBPK models to observed clinical data. *Br J Clin Pharmacol*. 2015;79:48-55.
23. Vaidhyanathan S, Wang X, Crison J, et al. Bioequivalence comparison of pediatric Dasatinib formulations and elucidation of absorption mechanisms through integrated PBPK modeling. *J Pharm Sci*. 2019;108:741-749.
24. Willmann S, Thelen K, Becker C, Dressman JB, Lippert J. Mechanism-based prediction of particle size-dependent dissolution and absorption: cilostazol pharmacokinetics in dogs. *Eur J Pharm Biopharm*. 2010;76:83-94.
25. Tsume Y, Takeuchi S, Matsui K, Amidon GE, Amidon GL. In vitro dissolution methodology, mini-gastrointestinal simulator (mGIS), predicts better in vivo dissolution of a weak base drug, dasatinib. *Eur J Pharm Sci*. 2015;76:203-212.
26. National Center for Health Statistics. Third National Health and Nutrition Examination Survey (NHANES III). Tech. rep., Hyattsville, MD, 20782. 1997.
27. Valentin J. Basic anatomical and physiological data for use in radiological protection: reference values. *Ann ICRP*. 2002;32:1-277.
28. Schlender J. A report including the description of the physiology base of the Japanese population implemented in PK-Sim. Github website. https://github.com/Open-Systems-Pharmacology/OSPSuite.Documentation/blob/master/Japanese_Population/Report.md. Accessed August 4, 2022.
29. Marok FZ, Wojtyniak JG, Fuhr LM, et al. A physiologically based pharmacokinetic model of ketoconazole and its metabolites as drug–drug interaction perpetrators. *Pharmaceutics*. 2023;15:15.
30. Hanke N, Frechen S, Moj D, et al. PBPK models for CYP3A4 and P-gp DDI prediction: a modeling network of rifampicin, Itraconazole, clarithromycin, midazolam, Alfentanil, and digoxin. *CPT Pharmacometrics Syst Pharmacol*. 2018;7:647-659.
31. Wojtyniak J-G, Selzer D, Schwab M, Lehr T. Physiologically based precision dosing approach for drug-drug-gene interactions: a simvastatin network analysis. *Clin Pharmacol Ther*. 2021;109:201-211.
32. Open Systems Pharmacology Suite Community. Open systems pharmacology suite manual. Github website. <https://raw.githubusercontent.com/Open-Systems-Pharmacology/OSPSuite.Documentation/master/Open-Systems-Pharmacology-Suite.pdf>. Accessed November 23, 2021.
33. Dong Z, Li J, Wu F, et al. Application of physiologically-based pharmacokinetic modeling to predict gastric pH-dependent drug-drug interactions for Weak Base drugs. *CPT Pharmacometrics Syst Pharmacol*. 2020;9:456-465.
34. Okada M, Yao T, Sakurai T, et al. A comparative study of once-a-day morning and once-a-day bedtime administration of 40 mg famotidine in treating gastric ulcers. *Am J Gastroenterol*. 1992;87:1009-1013.
35. Decktor DL, Malcolm Robinson SG. Comparative effects of liquid antacids on esophageal and gastric pH in patients with heartburn. *Am J Ther*. 1995;2:481-486.
36. Dallmann A, Solodenko J, Wendl T, Frechen S. Building and evaluation of a PBPK model for erythromycin in healthy adults. Github website. https://github.com/Open-Systems-Pharmacology/OSP-PBPK-Model-Library/blob/master/Erythromycin/Erythromycin_evaluation_report.pdf. Accessed October 18, 2022.
37. Eriksson J, Solodenko J. Building and evaluation of a PBPK model for fluconazole in healthy adults. Github website. https://github.com/Open-Systems-Pharmacology/OSP-PBPK-Model-Library/blob/master/Fluconazole/fluconazole_evaluation_report.pdf. Accessed August 17, 2023.
38. Britz H, Hanke N, Volz AK, et al. Physiologically-based pharmacokinetic models for CYP1A2 drug–drug interaction prediction: a modeling network of fluvoxamine, theophylline, caffeine, rifampicin, and midazolam. *CPT Pharmacometrics Syst Pharmacol*. 2019;8:296-307.
39. Fuhr LM, Marok FZ, Fuhr U, Selzer D, Lehr T. Physiologically based pharmacokinetic modeling of bergamottin and 6,7-dihydroxybergamottin to describe CYP3A4 mediated grapefruit-drug interactions. *Clin Pharmacol Ther*. 2023;114:470-482.
40. Li X, Frechen S, Moj D, et al. A physiologically based pharmacokinetic model of Voriconazole integrating time-dependent inhibition of CYP3A4, genetic polymorphisms of CYP2C19 and predictions of drug–drug interactions. *Clin Pharmacokinet*. 2020;59:781-808.
41. Fuhr LM, Marok FZ, Hanke N, Selzer D, Lehr T. Pharmacokinetics of the CYP3A4 and CYP2B6 inducer carbamazepine and its drug-drug interaction potential: a physiologically based pharmacokinetic modeling approach. *Pharmaceutics*. 2021;13:1-21.
42. Wendl T, Frechen S, Solodenko J, Dallmann A. Building and evaluation of a PBPK model for Efavirenz in healthy adults. Github website. https://github.com/Open-Systems-Pharmacology/OSP-PBPK-Model-Library/blob/master/Efavirenz/efavirenz_evaluation_report.pdf. Accessed 18 October 2022.
43. Willmann S, Schmitt W, Keldenich J, Lippert J, Dressman JB. A physiological model for the estimation of the fraction dose absorbed in humans. *J Med Chem*. 2004;47:4022-4031.
44. Levêque D, Becker G, Bilger K, Natarajan-Amé S. Clinical pharmacokinetics and pharmacodynamics of Dasatinib. *Clin Pharmacokinet*. 2020;59:849-856.
45. Hiwase DK, Saunders V, Hewett D, et al. Dasatinib cellular uptake and efflux in chronic myeloid leukemia cells: therapeutic implications. *Clin Cancer Res*. 2008;14:3881-3888.
46. Kamath AV, Wang J, Lee FY, Marathe PH. Preclinical pharmacokinetics and in vitro metabolism of dasatinib (BMS-354825): a potent oral multi-targeted kinase inhibitor against SRC and BCR-ABL. *Cancer Chemother Pharmacol*. 2008;61:365-376.
47. Wang X, Roy A, Hochhaus A, Kantarjian HM, Chen T-T, Shah NP. Differential effects of dosing regimen on the safety and efficacy of dasatinib: retrospective exposure-response analysis of a phase III study. *Clin Pharm*. 2013;5:85-97.
48. Monés J, Carrio I, Sainz S, et al. Gastric emptying of two radio-labelled antacids with simultaneous monitoring of gastric pH. *Eur J Nucl Med*. 1995;22:1123-1128.
49. Jones MP, Shah D, Ebert CC. Effects of rabeprazole sodium on gastric emptying, electrogastronomy, and fullness. *Dig Dis Sci*. 2003;48:69-73.
50. Anjiki H, Sanaka M, Kuyama Y. Dual effects of rabeprazole on solid-phase gastric emptying assessed by the ¹³C-octanoate breath test. *Digestion*. 2005;72:189-194.
51. Patel D, Bertz R, Ren S, Boulton DW, Någård M. A systematic review of gastric acid-reducing agent-mediated drug–drug interactions with orally administered medications. *Clin Pharmacokinet*. 2020;59:447-462.

52. Wojnowski L, Kamdem LK. Clinical implications of CYP3A polymorphisms. *Expert Opin Drug Metab Toxicol*. 2006;2:171-182.
53. Jia G, Ren C, Wang H, Fan C. Prediction of drug–drug interactions between roflumilast and CYP3A4/1A2 perpetrators using a physiologically-based pharmacokinetic (PBPK) approach. *BMC Pharmacol Toxicol*. 2024;25:4.
54. Loer HLH, Feick D, Rüdesheim S, et al. Physiologically based pharmacokinetic modeling of tacrolimus for food-drug and CYP3A drug–drug-gene interaction predictions. *CPT Pharmacometrics Syst Pharmacol*. 2023;12:724-738.
55. Les Laboratoires Servier. Servier Medical Art. <https://smart.servier.com>. Accessed July 10, 2023.
56. Guest EJ, Aarons L, Houston JB, Rostami-Hodjegan A, Galetin A. Critique of the two-fold measure of prediction success for ratios: application for the assessment of drug-drug interactions. *Drug Metab Dispos*. 2011;39:170-173.

SUPPORTING INFORMATION

Additional supporting information can be found online in the Supporting Information section at the end of this article.

How to cite this article: Kovar C, Loer HLH, Rüdesheim S, et al. A physiologically-based pharmacokinetic precision dosing approach to manage dasatinib drug–drug interactions. *CPT Pharmacometrics Syst Pharmacol*. 2024;13:1144-1159. doi:[10.1002/psp4.13146](https://doi.org/10.1002/psp4.13146)

4.4 PROJECT IV: CYP2D6 DDGI NETWORK MODELING

Publication

Rüdesheim, S.*; Loer, H. L. H.*; Feick, D.; Marok, F. Z.; Fuhr, L. M.; Selzer, D.; Teutonico, D.; Schneider, A. R. P.; Solodenko, J.; Frechen, S.; van der Lee, M.; Moes, D. J. A. R.; Swen, J. J.; Schwab, M.; Lehr, T. A comprehensive CYP2D6 drug–drug–gene interaction network for application in precision dosing and drug development. *Clinical Pharmacology & Therapeutics* **2025**, *117*, 1718–1731, DOI: [10.1002/cpt.3604](https://doi.org/10.1002/cpt.3604).

* Authors contributed equally

Supplementary Materials

Related Supplementary Materials are available on the accompanying USB storage device and via the following link: [https://ascpt.onlinelibrary.wiley.com/action/downloadSupplement?doi=10.1002%2Fcpt.3604&file = cpt3604-sup-0001-Supinfo.pdf](https://ascpt.onlinelibrary.wiley.com/action/downloadSupplement?doi=10.1002%2Fcpt.3604&file=cpt3604-sup-0001-Supinfo.pdf).

Copyright









This is an open access article under the terms of CC BY-NC 4.0 (<https://creativecommons.org/licenses/by-nc/4.0/>), which permits use, distribution and reproduction in any medium, provided the original work is properly cited and is not used for commercial purposes. © 2025 The Authors. *Clinical Pharmacology & Therapeutics* published by Wiley Periodicals LLC on behalf of American Society for Clinical Pharmacology and Therapeutics.

Author Contributions According to CRediT [5]

Simeon Rüdesheim	Conceptualization, Investigation, Visualization, Writing – Original Draft, Writing – Review & Editing
Helena Leonie Hanae Loer	Conceptualization, Investigation, Visualization, Writing – Original Draft, Writing – Review & Editing
Denise Feick	Conceptualization, Investigation, Writing – Review & Editing
Fatima Zahra Marok	Writing – Review & Editing
Laura Maria Fuhr	Writing – Review & Editing
Dominik Selzer	Conceptualization, Investigation, Writing – Review & Editing
Donato Teutonico	Writing – Review & Editing
Annika R. P. Schneider	Writing – Review & Editing
Juri Solodenko	Writing – Review & Editing
Sebastian Frechen	Writing – Review & Editing
Maaïke van der Lee	Writing – Review & Editing
Dirk Jan A. R. Moes	Writing – Review & Editing
Jesse J. Swen	Writing – Review & Editing
Matthias Schwab	Writing – Review & Editing, Funding Acquisition
Thorsten Lehr	Conceptualization, Writing – Review & Editing, Funding Acquisition

ARTICLE

A Comprehensive CYP2D6 Drug–Drug–Gene Interaction Network for Application in Precision Dosing and Drug Development

Simeon Rüdesheim^{1,2,†} , Helena Leonie Hanae Loer^{1,†}, Denise Feick^{1,3}, Fatima Zahra Marok¹, Laura Maria Fuhr¹, Dominik Selzer¹ , Donato Teutonico⁴, Annika R. P. Schneider⁵, Juri Solodenko⁵ , Sebastian Frechen⁵, Maaïke van der Lee⁶ , Dirk Jan A. R. Moes⁶ , Jesse J. Swen⁶ , Matthias Schwab^{2,7,8}  and Thorsten Lehr^{1,*} 

Conducting clinical studies on drug–drug–gene interactions (DDGIs) and extrapolating the findings into clinical dose recommendations is challenging due to the high complexity of these interactions. Here, physiologically-based pharmacokinetic (PBPK) modeling networks present a new avenue for exploring such complex scenarios, potentially informing clinical guidelines and handling patient-specific DDGIs at the bedside. Moreover, they provide an established framework for drug–drug interaction (DDI) submissions to regulatory agencies. The cytochrome P450 (CYP) 2D6 enzyme is particularly prone to DDGIs due to the high prevalence of genetic variation and common use of CYP2D6 inhibiting drugs. In this study, we present a comprehensive PBPK network covering CYP2D6 drug–gene interactions (DGIs), DDIs, and DDGIs. The network covers sensitive and moderate sensitive substrates, and strong and weak inhibitors of CYP2D6 according to the United States Food and Drug Administration (FDA) guidance. For the analyzed CYP2D6 substrates and inhibitors, DD(G)Is mediated by CYP3A4 and P-glycoprotein were included. Overall, the network comprises 23 compounds and was developed based on 30 DGI, 45 DDI, and seven DDGI studies, covering 32 unique drug combinations. Good predictive performance was demonstrated for all interaction types, as reflected in mean geometric mean fold errors of 1.40, 1.38, and 1.56 for the DD(G)I area under the curve ratios as well as 1.29, 1.43, and 1.60 for DD(G)I maximum plasma concentration ratios. Finally, the presented network

Study Highlights

WHAT IS THE CURRENT KNOWLEDGE ON THE TOPIC?

☑ The cytochrome P450 (CYP) 2D6 enzyme, responsible for the metabolism of 20%–25% of clinically used drugs, is particularly prone to drug–drug–gene interactions (DDGIs) due to the high prevalence of structural and allelic variants as well as its propensity to be affected by enzyme inhibition during drug–drug interactions (DDIs).

WHAT QUESTION DID THIS STUDY ADDRESS?

☑ This study presents the development of a comprehensive physiologically-based pharmacokinetic (PBPK) CYP2D6 DD(G)I modeling network comprising various important CYP2D6 victim and perpetrator drug models. For selected CYP2D6 victim drugs, clinically untested DDGI scenarios were simulated, and model-based dose adjustments were calculated, following the matching-exposure principle.

WHAT DOES THIS STUDY ADD TO OUR KNOWLEDGE?

☑ The newly established CYP2D6 DDGI network can predict interactions for a wide range of drugs, providing reliable

forecasts for tested DDGIs and predictions of untested scenarios. This enhances our ability to make informed decisions regarding dose adjustments for untested DDGI scenarios in clinical settings, particularly for patients with varying CYP2D6 enzyme activity.

HOW MIGHT THIS CHANGE CLINICAL PHARMACOLOGY OR TRANSLATIONAL SCIENCE?

☑ The approach presented in this study facilitates more precise model-informed dosing strategies considering both individual genetic profiles as well as multiple drug interactions. Additionally, it presents a robust framework for simulating and understanding complex DDGIs, supplementing knowledge gained from clinical DDGI trials and potentially accelerating drug development and regulatory processes.

Received July 26, 2024; accepted February 3, 2025. doi:10.1002/cpt.3604

was utilized to calculate dose adaptations for CYP2D6 substrates atomoxetine (sensitive) and metoprolol (moderate sensitive) for clinically untested DDGI scenarios, showcasing a potential clinical application of DDGI model networks in the field of model-informed precision dosing.

¹Clinical Pharmacy, Saarland University, Saarbrücken, Germany; ²Dr. Margarete Fischer-Bosch-Institute of Clinical Pharmacology, Stuttgart, Germany; ³Drug Metabolism and Pharmacokinetics, Sanofi R&D, Frankfurt am Main, Germany; ⁴Translational Medicine & Early Development, Sanofi R&D, Vitry-sur-Seine, France; ⁵Bayer AG, Pharmaceuticals, Research & Development, Model-Informed Drug Development, Leverkusen, Germany; ⁶Department of Clinical Pharmacy & Toxicology, Leiden University Medical Center, Leiden, The Netherlands; ⁷Departments of Clinical Pharmacology, Pharmacy and Biochemistry, University of Tübingen, Tübingen, Germany; ⁸Cluster of Excellence IFIT (EXC2180) "Image-guided and Functionally Instructed Tumor Therapies", University of Tübingen, Tübingen, Germany. *Correspondence: Thorsten Lehr (thorsten.lehr@uni-saarland.de)

[†]These authors contributed equally to this work.

Drug–drug interactions (DDIs) and drug–gene interactions (DGIs) are key drivers of adverse drug reactions (ADRs), significantly contributing to hospitalizations and in-hospital mortality.^{1,2} DDIs arise when the perpetrator drug alters the pharmacokinetics (PK) or pharmacodynamics of the victim drug. PK interactions frequently involve cytochrome P450 (CYP) isozymes or important drug-transporting proteins, such as P-glycoprotein (P-gp), which are essential in the absorption, distribution, metabolism, and excretion (ADME) processes of many clinically used drugs.^{3,4} In the case of DGIs, genetic variation of specific pharmacogenes can result in varying activities of the affected enzyme or transporter influencing a drug's PK.

In clinical practice, DDIs and DGIs often occur simultaneously in the form of drug–drug–gene interactions (DDGIs).⁵ However, separate alerts arise in electronic prescribing systems for DDIs and DGIs, aggravating clinical decision making. Here, CYP2D6 is one of the most susceptible enzymes to DDGIs.^{4,6} This liability arises from two primary factors: the relatively high prevalence of structural and allelic variants of the *CYP2D6* gene which can have substantial effects on enzymatic activity, and the enzyme's propensity for DDIs due to its role in metabolizing an estimated 20%–25% of clinically used drugs.^{4,7} Genetic variants in the *CYP2D6* gene result in different metabolizer phenotypes, ranging from poor metabolizers, carrying two loss-of-function alleles, to ultrarapid metabolizers, typically possessing more than two active *CYP2D6* alleles.^{3,8} In addition to the *CYP2D6* genotype, administration of strong CYP2D6 inhibitors, such as paroxetine or bupropion, can markedly decrease CYP2D6 activity, often resulting in a change of the apparent phenotype commonly referred to as "phenocconversion".⁹ To improve the safety and efficacy of CYP2D6 substrates, it is essential to consider the influence of CYP2D6 activity and concomitant medications on the PK of substrates not only individually but also in their combined effect.

Assessing DDGIs in clinical settings is inherently challenging due to the complexity of simultaneously occurring interactions given the vast number of potential combinations of genetically determined activity levels and relevant drug combinations. Thus, DDGIs pose a significant obstacle in clinical research and practice as it is impossible to perform formal studies covering all combinations.¹⁰ Additionally, applying the findings of published clinical DDGI trials to the real world is challenging, due to the limited transferability arising from the often narrow scope of these studies. These studies typically focus on a small selection of drugs and genetic variations and tend to include predominantly young, healthy male participants.⁵

Here, physiologically-based pharmacokinetic (PBPK) modeling has become an indispensable tool in model-informed drug discovery and development (MID3),¹¹ providing a suitable approach to investigate and predict DDGIs.⁵ PBPK models offer a mechanistic framework, integrating system-dependent parameters (e.g., age, sex, ethnicity, body weight, organ volumes, and perfusion rates) and drug-dependent parameters (e.g., solubility, permeability, transport, protein binding, and metabolic pathways). Moreover, they allow the detailed implementation of DDI processes. Hence, PBPK modeling can be used to conduct virtual clinical DD(G)I trials, enabling the prediction of DD(G)I scenarios prior to conducting a dedicated clinical trial, potentially reducing time, cost and risks associated with such studies. Regulatory authorities, such as the US Food and Drug Administration (FDA) and the European Medicines Agency (EMA) advocate for the utilization of PBPK modeling to address various research challenges, such as the investigation of DDI or organ impairment, and regularly publish guidelines to support its application.^{12,13} Examining and predicting the DDI potential of investigational drugs requires a well-established library of PBPK models for index perpetrator and victim drugs. These libraries can facilitate the assessment of the DDI potential, and therefore, accelerate the process of MID3.¹⁴ Here, the FDA table of Drug Development and Drug Interactions provides comprehensive guidance on the selection of substrates, inhibitors, and inducers for concomitant use in clinical DDI studies and drug labeling.¹⁵

The objectives of this work were to (i) establish and evaluate a comprehensive CYP2D6 DDGI network by extending and combining previously published PBPK DD(G)I networks and models of CYP2D6 substrates and inhibitors, (ii) to apply the network to predict a selection of not yet clinically studied DD(G)I scenarios, (iii) to derive model-based dose adjustments for these DD(G)I scenarios. All model files will be made publicly available in the Clinical Pharmacy Saarland University PBPK model library (<http://models.clinicalpharmacy.me>).

METHODS

Software

PBPK modeling, DD(G)I simulations and simulations of sensitivity analyses were performed using PK-Sim[®] and MoBi[®] (version 11, OSP Suite, <http://www.open-systems-pharmacology.org>). Plasma concentration–time profiles were digitized from the published literature using Engauge Digitizer 10.12 (© M. Mitchell, <https://markumitchell.github.io/engauge-digitizer>). The R programming language version 4.3.0 was used for model evaluation purposes, including the generation of plots and the calculation of pharmacokinetic parameters and statistics.

ARTICLE

DD(G)I network development

A comprehensive literature review in PubMed was undertaken to gather clinical DD(G)I studies, adhering to the following criteria: (i) availability of corresponding PBPK models developed with the OSP suite for the compounds investigated in the DD(G)I studies; (ii) DD(G)Is involving CYP2D6 victim drugs; (iii) availability of plasma concentration–time profiles of the victim drug, preferably measured during as well as prior to perpetrator co-administration, and (iv) stratification by CYP2D6 phenotype, genotype or activity score. Afterward, the CYP2D6 DD(G)I network was established by linking and combining published PBPK models with pre-existing networks^{16–18} to simulate the DD(G)I scenarios collected from the literature. In addition, a new PBPK model for the CYP2D6 substrate desipramine and its metabolite 2-hydroxydesipramine was developed, as described in **Section S1**.

For each study cohort, a virtual population of 1,000 individuals was created based on the reported study population characteristics. Specifically, age, weight, and height ranges, as well as ethnicity were considered to vary organ and tissue volumes and perfusion rates according to the PK-Sim[®] database. Additional variability was implemented by varying expressions of metabolizing enzymes, transport proteins, and protein binding partners according to the PK-Sim[®] expression database as well as the parameters reported in **Table S8**. Relative expressions of metabolizing enzymes, transport proteins, and protein binding partners used for the creation of virtual populations are given in **Tables S9, S10**. CYP2D6 activity levels were adjusted according to the respective study report. If no information on the CYP2D6 phenotype/genotype of a study population was available, a CYP2D6 normal metabolizer phenotype was assumed, as it is the most commonly reported phenotype in the included clinical studies.

Effect model evaluation

To evaluate the effects of DGIs, DDIs, and DDGIs, population predictions of victim drug concentrations were plotted alongside their respective observed plasma concentrations alone and during perpetrator co-administration. Furthermore, predicted compared with observed DD(G)I ratios were calculated according to **Eq. 1** and visually compared in goodness-of-fit plots.

$$\text{Effect PK ratio} = \frac{\text{PK}_{\text{Effect}}}{\text{PK}_{\text{Reference}}} \quad (1)$$

where effect PK ratio = ratio of the PK parameter (area under the plasma concentration–time curve from the time of the first measurement to the time of the last measurement (AUC_{last}) or maximum plasma concentration (C_{max})) for the investigated effect (variant CYP2D6 activity and/or drug co-administration), $\text{PK}_{\text{Effect}}$ = value of the PK parameter for the investigated effect and $\text{PK}_{\text{Reference}}$ = value of the PK parameter for the respective reference (i.e., normal CYP2D6 activity and/or victim drug alone). Normal CYP2D6 activity was defined as the normal metabolizer phenotype or an activity score of 2 if genotypes or activity scores were reported.

DD(G)I ratios were assessed according to limits proposed by Guest *et al.* including 20% variability.¹⁹ Additionally, geometric mean fold errors (GMFEs) of DD(G)I AUC_{last} and C_{max} ratios were calculated according to **Eq. 2**.

$$\text{GMFE} = 10^x; x = \frac{\sum_{i=1}^n \left| \log_{10} \left(\frac{\hat{p}_i}{p_i} \right) \right|}{n} \quad (2)$$

where \hat{p}_i = predicted AUC_{last} or C_{max} value of study i , p_i = corresponding observed AUC_{last} or C_{max} value of study i , n = number of studies.

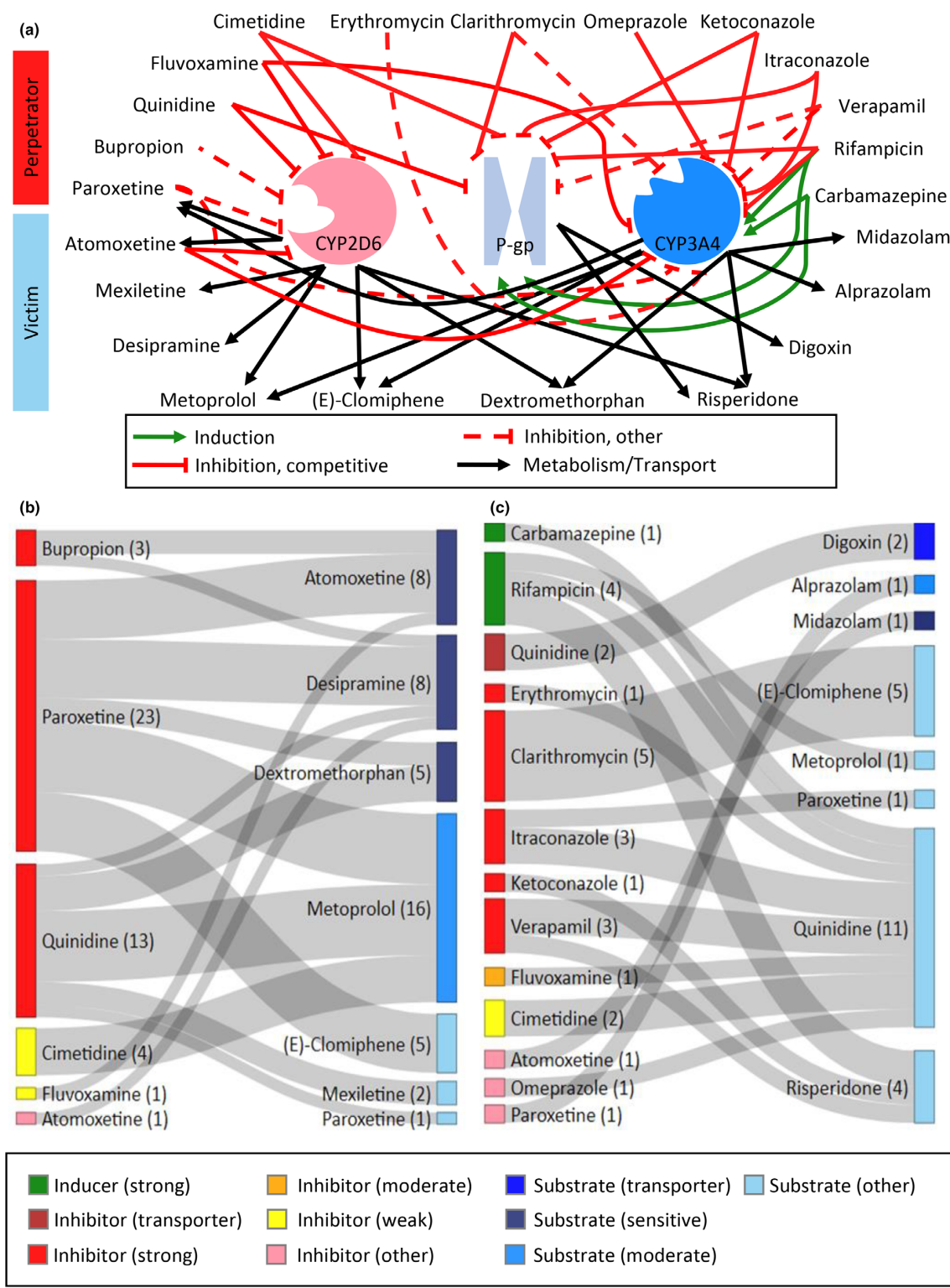
Model-informed dose adaptations

The final DDGI network was used to simulate drug exposure for the sensitive CYP2D6 substrate atomoxetine and the moderately sensitive CYP2D6 substrate metoprolol in untested D(D)GI scenarios. The analysis evaluated the exposures of both victim drugs during the co-administration of one or multiple perpetrator drugs (CYP2D6 and CYP3A4 inhibitors), considering the range of CYP2D6 activity scores evaluated during DD(G)I network development, that is, from 0 (poor metabolizer) to 3 (ultrarapid metabolizer). For each activity score group, a virtual European male, aged 30, weighing 73 kg and measuring 176 cm of height, was created based on the International Commission on Radiological Protection (ICRP) database for use in the simulations. CYP2D6 activity for the different virtual individuals was adjusted based on the respective activity score.²⁰ Administration protocols for the victim and perpetrator drugs were simulated according to the standard doses stated in the respective prescribing information, as listed in **Section S8**. Subsequently, dose adjustments were performed for the simulated D(D)GI scenarios matching the exposure of victim monotherapy for activity score 2 (normal metabolizer, wild-type). Since simulated DD(G)I scenarios were expected to typically result in dose reductions, victim doses were adjusted more finely, using 1% steps for doses <100% of the original. For doses exceeding 100%, adjustments were simulated in 10% steps to optimally align the steady-state AUC (AUC_{ss}) with the reference exposure following the matching-exposure principle.

RESULTS**DD(G)I network development**

The presented network includes a total of 23 drugs, eight of which are CYP2D6 substrates. Of these substrates, atomoxetine, desipramine, and dextromethorphan are categorized by the FDA as sensitive substrates, and metoprolol as a moderately sensitive substrate of CYP2D6. Four drugs ((*E*)-clomiphene, mexiletine, paroxetine, and risperidone) are currently not yet classified as substrates of CYP2D6 by the FDA but show a considerable susceptibility to CYP2D6 DDGIs.^{16,17,20} Additionally, to cover DD(G)Is mediated by CYP3A4 and P-gp involving substrates or inhibitors of CYP2D6, various perpetrators and victims of CYP3A4 and P-gp were included in the network. **Figure 1a** provides an overview of the modeled DD(G)I network. **Figure 1b,c** shows an overview of model compounds and drug combinations included in the network as well as their

Figure 1 (a) Physiologically-based pharmacokinetic drug–drug–gene interaction network. Schematic illustration of the modeled interactions of CYP2D6 perpetrator and victim drugs. Black arrows indicate metabolism or transport, green arrows indicate induction, red solid lines indicate competitive inhibition, red dashed lines down-regulation (bupropion), noncompetitive inhibition (verapamil P-gp inhibition), or mechanism-based inactivation (others). (b, c) Drug–drug–(gene) interaction matrix for modeled interactions mediated by (a) CYP2D6 and (b) CYP3A4 and P-gp. Colors indicate categories according to the FDA's *Examples of Drugs that Interact with CYP Enzymes and Transporter Systems*.⁴¹ Height of the gray ribbons indicates the number of clinical studies for the respective interaction covered by the network, numbers in brackets indicate the number of clinical interaction studies for the corresponding compound. CYP, cytochrome P450; P-gp, P-glycoprotein.



ARTICLE

FDA substrate, inhibitor, or inducer category alongside the corresponding number of modeled clinical studies.

Previously published models of paroxetine,²⁰ quinidine,¹⁸ dextromethorphan,²¹ (*E*)-clomiphene,¹⁶ mexiletine,¹⁷ carbamazepine,^{18,22} rifampicin,¹⁴ clarithromycin,²³ erythromycin,²⁴ itraconazole,¹⁴ ketoconazole,²⁵ verapamil,²⁶ omeprazole,¹⁷ digoxin,²³ midazolam,²³ alprazolam, and risperidone²⁰ were used without modifications to the model structure. The bupropion model²⁵ was modified to include down-regulation and competitive inhibition of CYP2D6 by bupropion and its metabolites as described in the literature.^{27,28} CYP2D6 competitive inhibition was implemented in the fluvoxamine²⁹, cimetidine,²⁶ and atomoxetine²⁰ models using published values.^{30–32} Competitive inhibition of CYP2C19 was additionally implemented in the fluvoxamine model, as well as competitive inhibition of CYP3A4 in the atomoxetine model, both according to literature reports.^{32,33} A CYP3A4-mediated clearance of metoprolol was incorporated as a surrogate pathway in the corresponding model³⁴ to account for the inducible residual metabolism of metoprolol.³⁵ All parameters implemented in the respective models related to the inhibition/induction of as well as metabolism/transport by CYP2D6, CYP3A4, and P-gp are listed in [Tables S11, S12](#). Detailed results for the building and evaluation of the newly developed desipramine model are presented in [Sections S2 and S3](#).

The overall CYP2D6 DGI model performance of CYP2D6 substrates was evaluated using a total of 30 clinical DGI studies in which subjects had been stratified by CYP2D6 activity score or phenotype. The effect of varying CYP2D6 activity was assessed for 85 DGI scenarios involving 17 compounds (parent drug and respective metabolites or enantiomers), comprising atomoxetine, clomiphene (including metabolites (*E*)-4-hydroxy-*N*-desethylclomiphene, (*E*)-*N*-desethylclomiphene and (*E*)-4-hydroxyclophene), desipramine (including metabolite 2-hydroxydesipramine), dextromethorphan (including metabolite dextrophan), metoprolol (including enantiomers (*S*)-metoprolol and (*R*)-metoprolol, as well as their metabolite α -hydroxymetoprolol), mexiletine, paroxetine, and risperidone (including metabolite 9-hydroxyrisperidone).

Furthermore, DD(G)I network modeling was performed using 45 clinical DDI and seven clinical DDGI studies covering 121 DDI and 42 DDGI scenarios as well as 32 unique drug combinations. In total, six CYP2D6 perpetrator drugs were

included with bupropion, paroxetine, and quinidine being categorized as strong CYP2D6 inhibitors and cimetidine and fluvoxamine as weak CYP2D6 inhibitors. Additionally, atomoxetine was included as an inhibitor of CYP2D6 as it has been reported to inhibit CYP2D6 *in vitro*.³² Moreover, DD(G)Is mediated by CYP3A4 and P-gp involving substrates or inhibitors of CYP2D6 were added to the presented network due to their relevance for predicting complex DD(G)Is. For instance, the model of the CYP2D6 substrate risperidone also includes metabolism by CYP3A4 and transport via P-gp,³⁶ warranting the inclusion of CYP3A4 and P-gp inhibitor models in the network to cover the respective DDIs. Conversely, the model of the strong CYP2D6 inhibitor paroxetine includes inhibition of CYP3A4.²⁰ Therefore, the PBPK models of CYP3A4 victims were included in the network to describe the corresponding DDIs reported in the literature. Here, eight victim drugs cover one substrate of P-gp (digoxin), one sensitive substrate of CYP3A4 (midazolam), one moderate sensitive substrate of CYP3A4 (alprazolam) as well as five currently uncategorized substrates of CYP3A4 ((*E*)-clomiphene, metoprolol, paroxetine, quinidine, and risperidone). Perpetrators include one inhibitor of P-gp (quinidine), five strong inhibitors of CYP3A4 (clarithromycin, erythromycin, itraconazole, ketoconazole, and verapamil), one moderate inhibitor of CYP3A4 (fluvoxamine, also a strong inhibitor of CYP2C19), one weak inhibitor of CYP3A4 (cimetidine), two strong inducers of CYP3A4 (carbamazepine and rifampicin) as well as three uncategorized inhibitors of CYP3A4 (atomoxetine, omeprazole, and paroxetine). Detailed information on all modeled DD(G)I studies is provided in [Section S6](#).

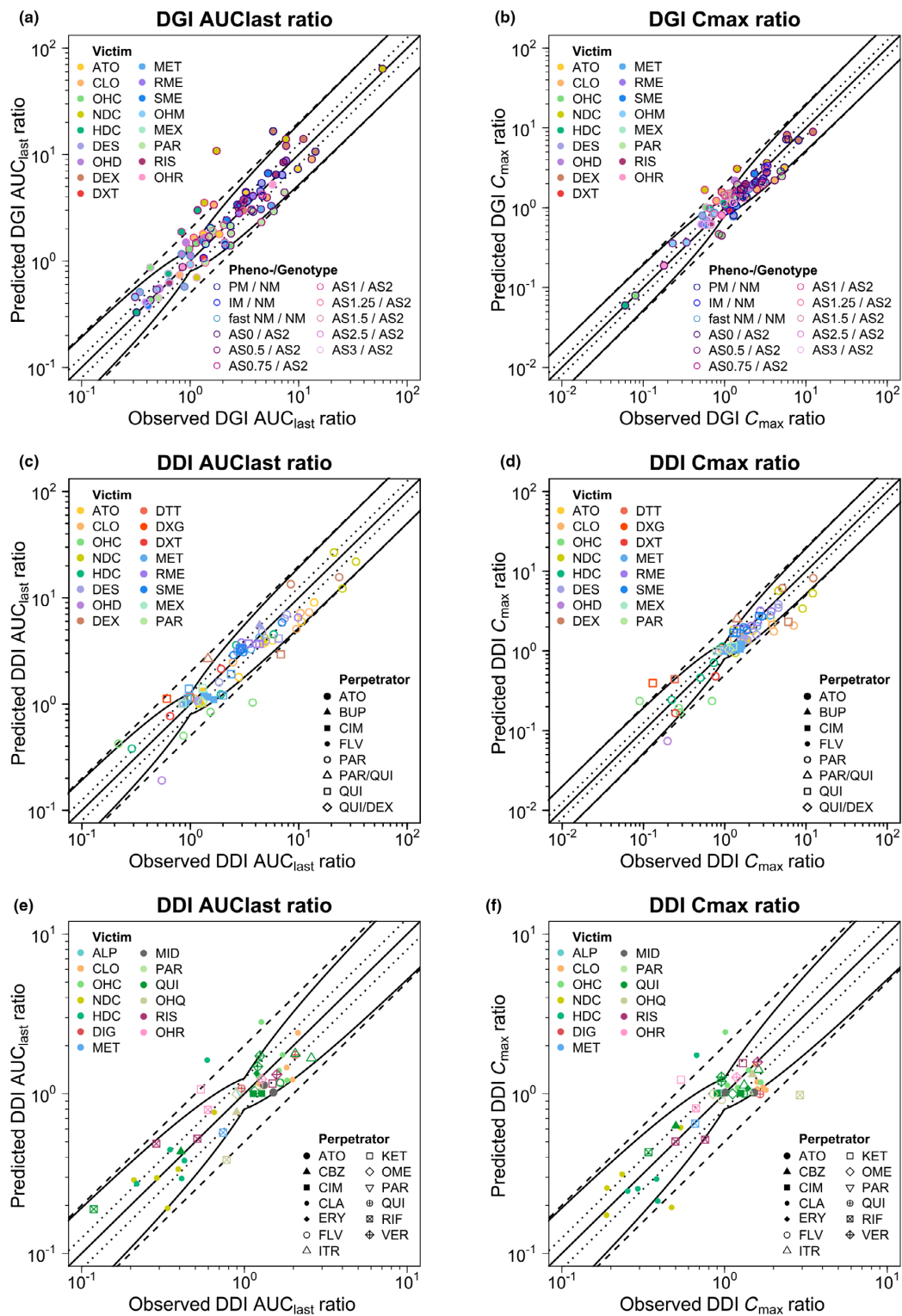
DGI model evaluation

Predicted DGI AUC_{last} and C_{max} ratios were in good agreement with observed DGI ratios as depicted in [Figure 2a,b](#). Mean GMFEs for predicted DGI AUC_{last} and C_{max} ratios for all CYP2D6 substrates were 1.40 and 1.29, respectively, as listed in [Table 1](#). Predicted and observed DGI AUC_{last} and C_{max} ratios for all studies are presented in [Section S5](#).

DDI model evaluation

The developed network showed good predictive performance regarding DDI AUC_{last} and C_{max} ratios, as demonstrated in [Figure 2c–f](#). Mean GMFE values of 1.40 and 1.45 were obtained for the predicted DDI AUC_{last} and C_{max} ratios of the CYP2D6

Figure 2 Predicted vs. observed DGI (a) AUC_{last} and (b) C_{max} ratios as well as DDI (c, e) AUC_{last} and (d, f) C_{max} ratios, stratified by (c, d) CYP2D6-mediated DDIs and (e, f) non-CYP2D6-mediated DDIs, of CYP2D6 substrates included in the network. Colored symbols represent the victim drugs; their shape corresponds to the respective perpetrator and their colored borders correspond to the respective phenotype or genotype as well as the reference genotype or phenotype. The solid straight black line marks the line of identity. Curved black lines show prediction success limits according to Guest *et al.*¹⁹, including 1.25-fold variability. Black dotted lines show the 1.25-fold range, dashed black lines indicate the twofold range. ALP, alprazolam; AS, CYP2D6 activity score; ATO, atomoxetine; AUC_{last} , area under the plasma concentration–time curve from the time of the first measurement to the time of the last measurement; BUP, bupropion; CBZ, carbamazepine; CIM, cimetidine; CLA, clarithromycin; CLO, (*E*)-clomiphene; C_{max} , maximum plasma concentration; DDI, drug–drug interaction; DES, desipramine; DEX, dextromethorphan; DGI, drug–gene interaction; DIG, digoxin; DTT, total dextrophan; DXT, dextrophan; ERY, erythromycin; FLV, fluvoxamine; HDC, (*E*)-4-hydroxy-*N*-desethylclomiphene; IM, intermediate metabolizer; ITR, itraconazole; KET, ketoconazole; MET, metoprolol racemate; MEX, mexiletine; MID, midazolam; NDC, (*E*)-*N*-desethylclomiphene; NM, normal metabolizer; OHC, (*E*)-4-hydroxyclophene; OHD, 2-hydroxydesipramine; OHM, α -hydroxymetoprolol; OHQ, 3-hydroxyquinidine; OHR, 9-hydroxyrisperidone; OME, omeprazole; PAR, paroxetine; PM, poor metabolizer; QUI, quinidine; RIF, rifampicin; RIS, risperidone; RME, (*R*)-metoprolol; SME, (*S*)-metoprolol; VER, verapamil.



ARTICLE

DDIs, respectively, while for the non-CYP2D6 DDIs, GMFE values were 1.33 and 1.38 for DDI AUC_{last} and C_{max} ratios, respectively. **Table 1** shows the mean GMFE values and ranges stratified by mechanisms of interaction. Additionally, **Table 2** shows mean GMFE values and ranges for the different DDIs grouped by CYP2D6 perpetrator and victim drugs, respectively. Plasma concentration–time profiles in semilogarithmic and linear representation as well as predicted vs. observed DDI AUC_{last} and C_{max} ratios of all DDI scenarios are provided in **Section S6**.

DDGI model evaluation

Figure 3a,b shows the predicted vs. observed DDGI AUC_{last} and C_{max} ratios of the included DDGI scenarios, demonstrating overall good predictive performance of the network. Mean GMFE values of 1.61 and 1.64 were obtained for the predicted DDGI AUC_{last} and C_{max} ratios of the CYP2D6 DDGIs, respectively, while for the non-CYP2D6 DDGIs values of 1.49 and 1.54 were calculated. **Table 1** lists the mean GMFE values and range stratified by mechanism of interaction. A selection of simulated DDGIs involving the CYP2D6 victim drugs atomoxetine and desipramine as well as perpetrator drugs bupropion and paroxetine for different CYP2D6 phenotypes is presented as plasma concentration–time profiles in **Figure 3c–f**. Plasma concentration–time profiles in semilogarithmic and linear representation as well as predicted vs. observed DDGI AUC_{last} and C_{max} ratios of all DDGI scenarios can be found in **Sections S6 and S7**.

Model-informed dose adaptations

The final network was applied to simulate D(D)GI scenarios involving the CYP2D6 victim drugs atomoxetine and metoprolol with various combinations of strong and weak inhibitors of CYP2D6 and CYP3A4 across different CYP2D6 activity scores. Paroxetine and quinidine were selected as CYP2D6 perpetrators and itraconazole as CYP3A4 inhibitor. Cimetidine was selected as a weak inhibitor of both CYP2D6 and CYP3A4. Moreover, activity scores of 0, 0.25, 0.5, 1, 1.25, 1.5, 2 (wild-type) and 3 were assumed for simulated D(D)GI scenarios. Model exposure simulations revealed that co-administration of the perpetrator drugs may result in AUC_{ss} increases of up to 14.8-fold and 8.5-fold as well as reductions of up to 0.5-fold and 0.6-fold of the reference AUC_{ss} for atomoxetine and metoprolol, respectively. Fold changes in AUC_{ss} for the different scenarios compared with the reference AUC_{ss} are presented in **Figure 4**. All simulated D(D)GI scenarios including administration protocols of the respective victim and perpetrator drugs are listed in **Figure 5**. Simulations to match the respective model-simulated monotherapy AUC_{ss} for the CYP2D6 activity score 2 yielded a dose range of 2.4–72 mg (6%–180% of the original dose) for atomoxetine and 12–160 mg (12%–160% of the original dose) for metoprolol (**Figure 5**). As shown in **Figures S68 and S69**, dose adjustments resulted in simulated exposures well within the bioequivalence criteria (80%–125%) compared with the reference exposure.

DISCUSSION

In this study, we present a newly established DD(G)I network centered around the highly polymorphic CYP2D6 enzyme, prone to

DDIs, DGIs, and DDGIs. The presented network was built based on various previously published models and compound-specific DD(G)I networks, combining and expanding them for a total of 32 distinct drug combinations involving 23 different compound models, also including 18 metabolites. The research presented in this study introduces a comprehensive CYP2D6 DDGI network that significantly advances beyond prior efforts. Specifically compared with the previously published quinidine DDGI modeling study by Feick *et al.*,¹⁸ the CYP2D6 network expands the scope to include eight additional CYP2D6 drugs—three victims and five perpetrators—encompassing a broader spectrum of interaction mechanisms, such as CYP2D6 down-regulation by bupropion and mechanism-based inactivation by paroxetine. The comprehensive coverage of CYP2D6 victim and perpetrator drugs, interaction scenarios, and interaction mechanisms within the developed network allows for a more nuanced understanding of CYP2D6 interactions. The good predictive performance of the network was evaluated using established graphical and quantitative measures. Subsequently, model-based dose adjustments for simulated clinically untested D(D)GI scenarios were performed for the CYP2D6 substrates atomoxetine and metoprolol.

Previous studies have outlined the potential of PBPK DDGI networks in clinical applications and how these models may be used to generate model-guided dose adaptations even in highly complex situations. For instance, Türk *et al.* provided dose adaptations covering the combined effect of genetic variants in two pharmacogenes (*CYP2C8* and *SLCO1B1*) and co-administration of perpetrator drugs, such as gemfibrozil and itraconazole.³⁷ Similarly, Wojtyniak and colleagues presented a DD(G)I network centered around simvastatin highlighting the combinatorial complexities occurring from DDGIs.¹⁰ The presented network was established based on a large number of CYP2D6 victim and perpetrator drugs as well as observed clinical data to provide a comprehensive foundation for the prediction of clinically untested CYP2D6 DD(G)I and even multiple DD(G)I scenarios with more than one perpetrator. To demonstrate the multitude of combinatorial possibilities of interactions, the effect of several CYP2D6 and CYP3A4 perpetrators on the exposure of the sensitive CYP2D6 substrate atomoxetine and the moderately sensitive CYP2D6 substrate metoprolol was predicted for different CYP2D6 activity scores. In a next step, model-based dose adjustments were performed to demonstrate the translation of the model predictions into patient-relevant information for clinical application. However, the applicability of this approach for patient-individual dose adaptations is constrained by the extensive interindividual variability in the CYP2D6 enzyme activity, even when accounting for CYP2D6 activity scores.²¹ Like the population approach, individual predictions using PBPK models could be substantially improved with the integration of patient-specific PK measurements and individual PK data.³⁸ Here, hybrid population PBPK approaches may increase the confidence in individual PBPK model predictions, especially when used for clinical decision making.³⁸ Our presented network can serve as a basis for such hybrid approaches.

The dose adjustments performed for atomoxetine and metoprolol resulted in substantial increases or decreases in the respective dose, highlighting the need for individual dose adaptations. Model

Table 1 Summary of geometric mean fold errors (GMFEs) for DGI, DDI, and DDGI predictions

Scenario	n	Mean GMFE (range)	
		AUC _{last}	C _{max}
CYP2D6 DGIs	85	1.40 (1.00–6.19)	1.29 (1.00–2.95)
CYP2D6 DDIs	72	1.40 (1.00–3.64)	1.45 (1.01–3.41)
Competitive inhibitors	21	1.32 (1.04–2.33)	1.39 (1.01–3.03)
MBI/other inhibitors	51	1.43 (1.00–3.64)	1.48 (1.02–3.41)
Other DDIs	49	1.33 (1.02–2.75)	1.38 (1.00–2.96)
Competitive inhibitors	15	1.28 (1.09–1.97)	1.31 (1.00–2.27)
MBI	26	1.34 (1.02–2.75)	1.40 (1.00–2.59)
Inducers	8	1.40 (1.02–2.02)	1.41 (1.01–2.96)
All DDIs	121	1.38 (1.00–3.64)	1.43 (1.01–3.41)
CYP2D6 DDGIs	26	1.61 (1.01–3.55)	1.64 (1.05–3.71)
Competitive inhibitions	3	1.61 (1.09–1.96)	1.30 (1.17–1.40)
MBI/other inhibitors	23	1.61 (1.01–3.55)	1.68 (1.05–3.71)
Other DDGIs – MBI	16	1.49 (1.02–2.42)	1.54 (1.02–3.31)
All DDGIs	42	1.56 (1.01–3.55)	1.60 (1.02–3.71)

AUC_{last}, Area under the plasma concentration–time profile from the time of the first measurement to the time of the last measurement; C_{max}, maximum plasma concentration; DDGIs, Drug–drug–gene interactions; DDIs, drug–drug interactions; DGIs, drug–gene interactions; GMFE, geometric mean fold error; MBI, mechanism-based inhibition; n = number of investigated interaction scenarios.

simulations indicate that to match the exposure of atomoxetine in poor metabolizers (activity score 0) with the reference exposure (activity score 2, no co-medication), a dose reduction to 6% of the original atomoxetine dose is required. Additionally, simulations reveal that co-administrations of strong CYP2D6 inhibitors quinidine and paroxetine either alone or in combination with other CYP2D6 or CYP3A4 inhibitors resulted in a significant reduction in CYP2D6 activity across all activity scores above 0. This results in atomoxetine exposures similar to those simulated in poor metabolizers (activity score 0). Consequently, similarly extensive dose reductions are necessary to match their exposure levels to the reference group. The observed phenoconversion is consistent with the FDA-approved label for STRATTERA[®], stating that atomoxetine blood levels are increased ~10-fold in poor metabolizers or those taking strong CYP2D6 inhibitors.³⁹ Accordingly, the label recommends a dose reduction to 40% of the target dose for these individuals, with an optional subsequent dose escalation to 100% if symptoms fail to improve after four weeks and the initial dose is well-tolerated. This recommendation is likely based on the observation of only modest differences in the frequency of ADRs between normal and poor metabolizers of CYP2D6 alongside the generally well-tolerated atomoxetine doses. Additionally, while the label recommendations use traditional CYP2D6 phenotype categories, dose adjustments derived from our model simulations

Table 2 Summary of geometric mean fold errors (GMFEs) for CYP2D6 DDI predictions by perpetrator and victim

Compound	n	Mean GMFE (range)	
		AUC _{last}	C _{max}
CYP2D6 perpetrators			
Atomoxetine	1	1.09	1.06
Bupropion	3	1.30 (1.27–1.36)	1.18 (1.02–1.36)
Cimetidine	4	1.24 (1.10–1.49)	1.31 (1.10–1.48)
Fluvoxamine	1	1.04	1.17
Paroxetine	48	1.44 (1.00–3.64)	1.50 (1.02–3.41)
Quinidine	15	1.37 (1.08–2.33)	1.44 (1.01–3.03)
CYP2D6 victims			
Atomoxetine	8	1.41 (1.04–1.77)	1.22 (1.02–1.43)
(E)-Clomiphene	20	1.56 (1.00–3.64)	1.72 (1.04–3.41)
Desipramine	11	1.35 (1.04–2.86)	1.38 (1.06–2.68)
Dextromethorphan	8	1.62 (1.11–2.33)	1.94 (1.20–3.03)
Metoprolol	22	1.21 (1.00–1.66)	1.19 (1.01–1.48)
Mexiletine	2	1.13 (1.08–1.18)	1.19 (1.11–1.26)
Paroxetine	1	1.23	1.10

AUC_{last}, Area under the plasma concentration–time profile from the time of the first measurement to the time of the last measurement; C_{max}, maximum plasma concentration; DDIs, drug–drug interactions; GMFE, geometric mean fold error; n = number of investigated interaction scenarios.

utilize the more detailed activity score categories.⁸ The broad normal metabolizer category used as the reference in label dosing contrasts with the specific activity score of 2 used in model-based adjustments, explaining the variance in recommended dose reductions for poor metabolizers and patients on strong CYP2D6 inhibitors. For metoprolol, the Dutch Pharmacogenetics Working Group (DPWG) provides dose adjustments based on CYP2D6 phenotypes.⁴⁰ Model-derived dose recommendations for metoprolol in DGI scenarios have been found to be largely consistent with DPWG recommendations.³⁴ The current study extends these recommendations to DDGI scenarios, incorporating the isolated and combined effects of strong CYP2D6 inhibitors paroxetine and quinidine, the effect of strong CYP3A4 inhibitor itraconazole, as well as the effect of weak CYP2D6 and CYP3A4 inhibitor cimetidine on the PK of metoprolol. Here, the most significant effect was observed with the co-administration of quinidine and itraconazole, necessitating a reduction of the metoprolol dose to 12% of the original dose. While the presented dose adjustments were performed based on AUC_{ss}, dose adjustments using PBPK models can also be performed for other PK parameters, such as trough concentration (C_{trough}) or C_{max}, when appropriate for the drug of interest.

In the future, the network can be expanded by developing novel PBPK models of victims or perpetrators within the OSP framework enabling the prediction of an even broader range of clinically relevant DD(G)I scenarios. The PBPK approach facilitates the prediction of concomitant medications and generation of individual optimizations, as highlighted in this work. While PBPK models are versatile and beneficial for clinical applications, such as dose optimizations, their adoption in clinical practice remains limited.

ARTICLE

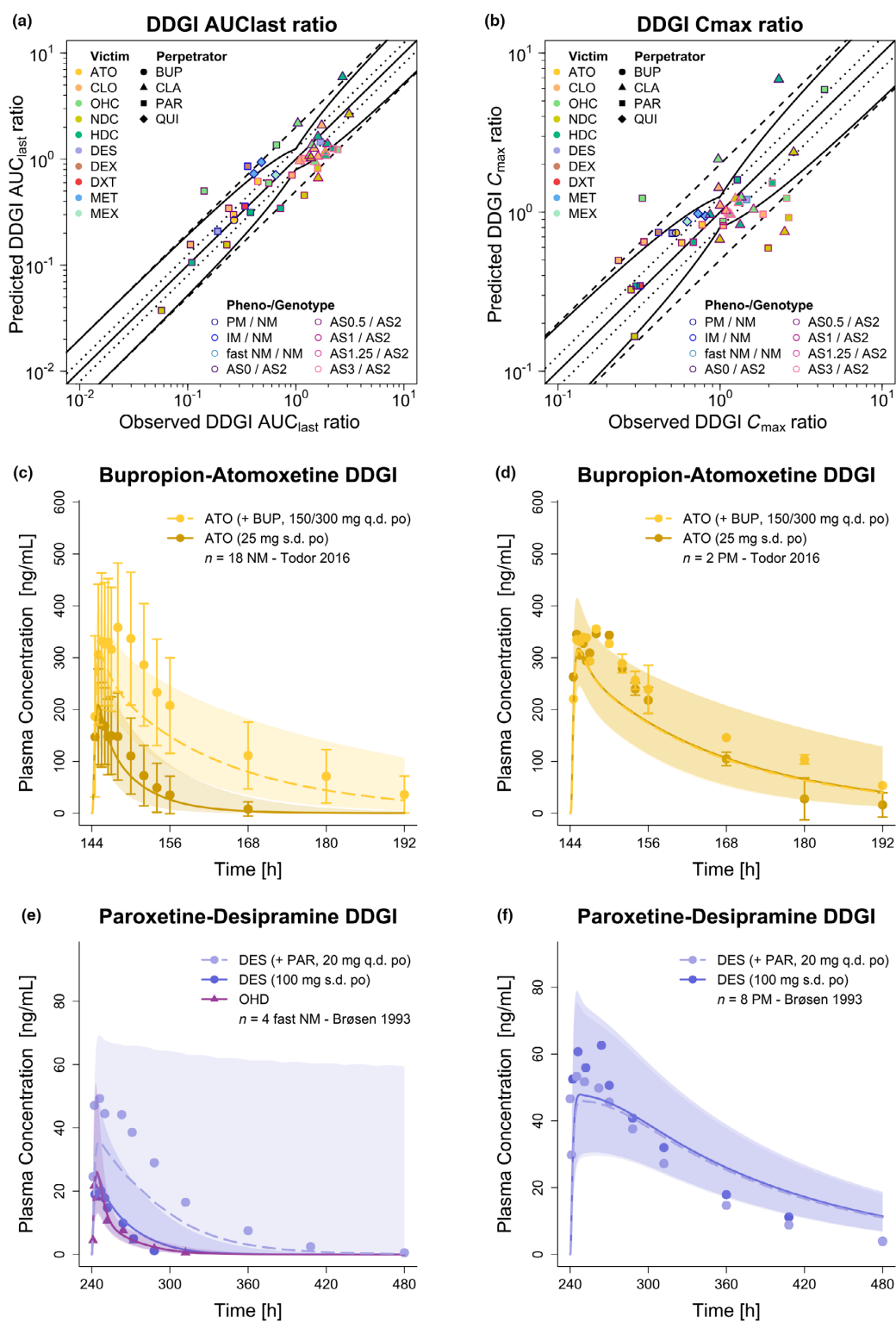


Figure 3 Predicted vs. observed DDGI (a) AUC_{last} and (b) C_{max} ratios of CYP2D6 substrates included in the network. Colored symbols represent the victim drugs; their shape corresponds to the respective perpetrator; their colored borders correspond to the respective phenotype or genotype as well as the reference genotype or phenotype. The solid straight black line marks the line of identity. Curved black lines show prediction success limits according to Guest *et al.*,¹⁹ including 1.25-fold variability. Black dotted lines show the 1.25-fold range, dashed black lines indicate the twofold range. (c–f) Selection of modeled DDGIs. Predicted compared with observed plasma concentration–time profiles of the respective victim drug alone and after pretreatment with and/or concomitant administration of a perpetrator drug: (c, d) atomoxetine with and without bupropion pretreatment in (c) CYP2D6 normal metabolizers and (d) poor metabolizers and (e, f) desipramine with and without paroxetine pretreatment in (e) fast CYP2D6 normal metabolizers⁴⁹ and (f) poor metabolizers. Predicted population geometric means are shown as lines (solid: victim drug alone, dashed: victim drug during DDGI), predicted geometric standard deviations are shown as shaded areas and observed data are shown as dots (parent compound) and triangles (metabolite, if available) (\pm standard deviation, if reported).^{43,49} AS, CYP2D6 activity score; ATO, atomoxetine; AUC_{last} , area under the plasma concentration–time curve from the time of the first measurement to the time of the last measurement; b.i.d., twice daily; BUP, bupropion; CLA, clarithromycin; CLO, (E)-clomiphene; C_{max} , maximum plasma concentration; DDGI, drug–drug–gene interaction; DES, desipramine; DEX, dextromethorphan; DXT, dextropropanolol; HDC, (E)-4-hydroxy-N-desethylclomiphene; IM, intermediate metabolizer; MET, metoprolol racemate; MEX, mexiletine; MID, midazolam; n, number of study participants; NDC, (E)-N-desethylclomiphene; NM, normal metabolizer; OHC, (E)-4-hydroxyclophosphamide; OHD, 2-hydroxydesipramine; OHQ, 3-hydroxyquinidine; PAR, paroxetine; PM, poor metabolizer; po, oral; q.d., once daily; QUI, quinidine; s.d., single dose.

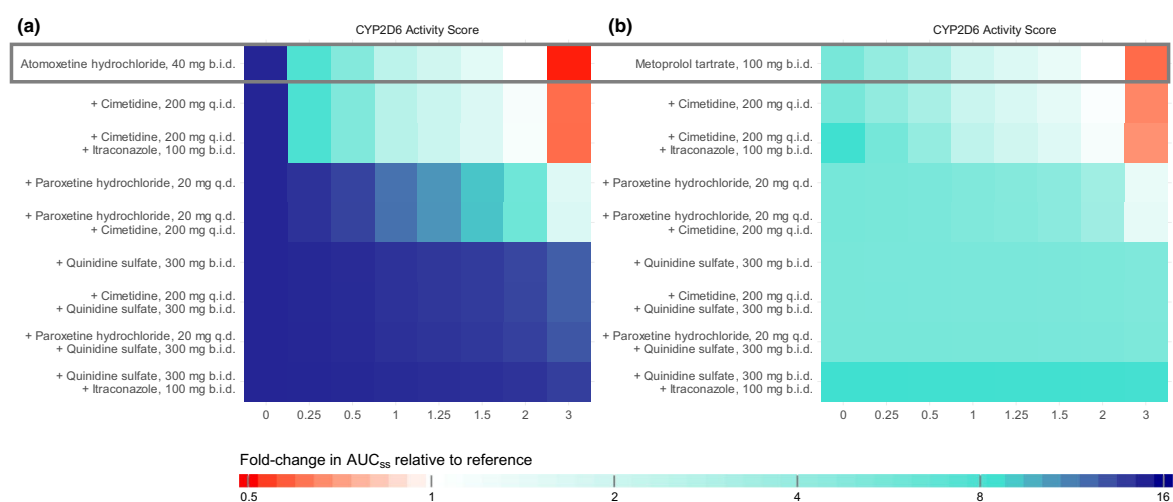


Figure 4 Fold-change in AUC_{ss} relative to the reference AUC_{ss} (activity score 2, no DDI) across different D(D)GI scenarios before dose adaptations for (a) atomoxetine and (b) metoprolol. Colors indicate the extent and direction of the deviation from the reference AUC_{ss} . AUC_{ss} , area under the concentration–time curve during steady state; b.i.d., twice a day; D(D)GI, drug(–drug)–gene interaction; q.d., once daily; q.i.d., four times a day.

This is chiefly due to a lack of clinical acceptance caused by an apparent lack of usability by the target user group or accountability issues.⁵ Here, our network can serve as the foundation for PBPK-driven clinical decision support systems (CDSS) for clinicians and patients. These CDSS aim to generate optimal model-based doses for an individual patient based on the underlying victim and perpetrator models of the relevant medication as well as patient-specific genetic and demographic input data. Additionally, CDSS can provide a more accessible way to leverage the potential of PBPK networks outside of dedicated modeling software, consequently lowering the barriers of access and improving clinical utility.⁵

In total, the presented CYP2D6 network was built and evaluated based on 85 DGI, 121 DDI, and 42 DDGI scenarios demonstrating good predictive performance for all interaction types. Moreover, the developed network shows good coverage of the *FDA Table of Substrates, Inhibitors and Inducers* for the CYP2D6 enzyme with three strong inhibitors, two weak inhibitors, three

sensitive substrates and one moderately sensitive substrate included.⁴¹ Paroxetine, a strong clinical index inhibitor of CYP2D6 is featured while desipramine and dextromethorphan provide two sensitive clinical index substrates of CYP2D6.¹⁵ However, due to the absence of compatible PBPK models in the published literature, no moderate CYP2D6 inhibitors listed by the FDA are currently represented in the network. Once such models become available, our network can be expanded accordingly. This modularity is essential for incorporating new data and models, enhancing the network's utility and accuracy over time. Additionally, good coverage of the *FDA Table of Substrates, Inhibitors and Inducers* ensures regulatory compliance and applicability to a broad range of clinical scenarios. Hence, our network may aid clinical decision-making, especially in the context of MID3, where previously published PBPK DD(G)I networks have shown to be of considerable interest complementing clinical studies. For instance, extrapolations from moderate inhibitors to weak or strong

ARTICLE

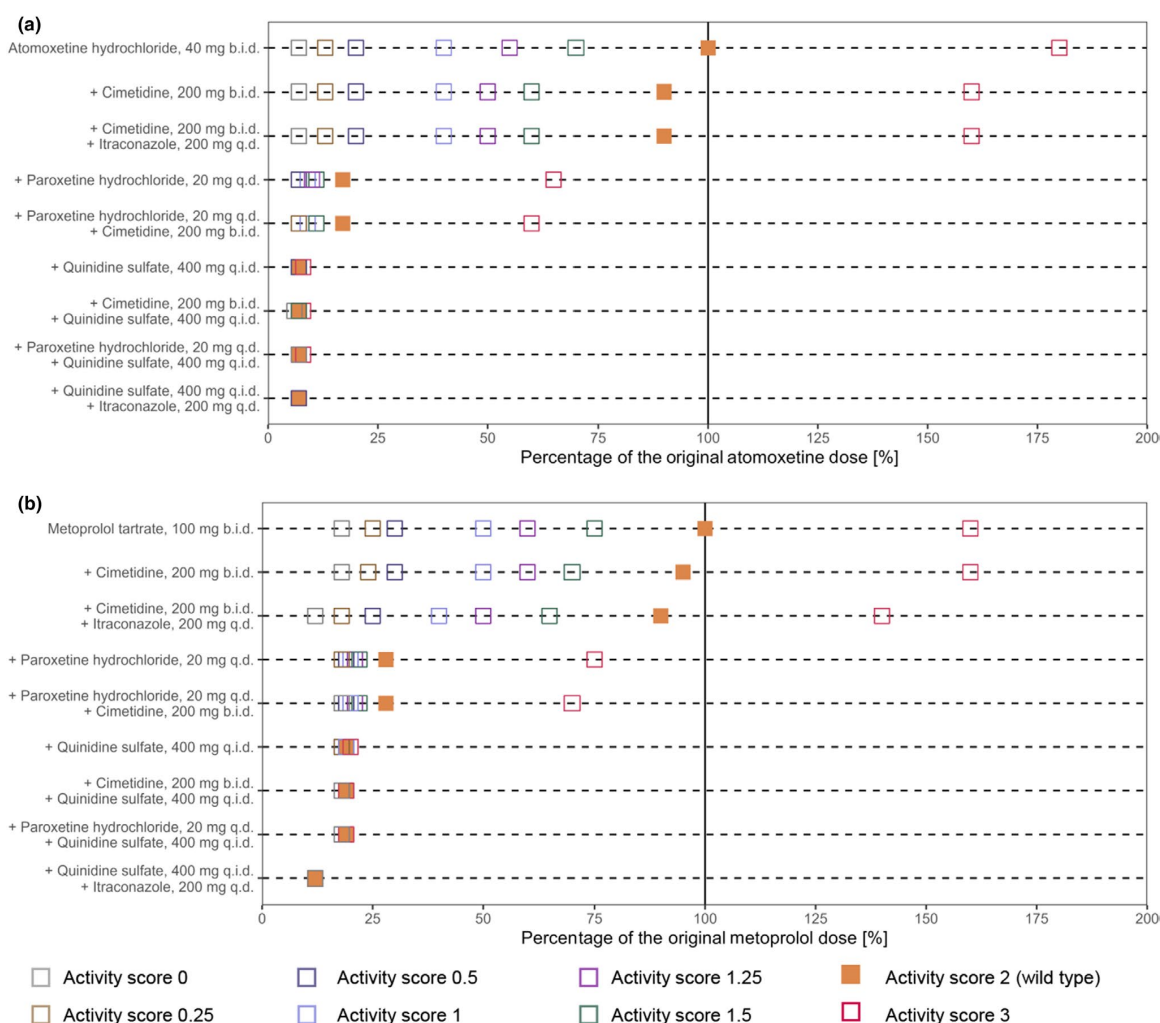


Figure 5 Overview of model-based dose adaptations for (a) atomoxetine and (b) metoprolol within single and multiple D(D)GI scenarios based on the exposure matching principle, where points and squares show the percentage of the original dose that match the PBPK simulated monotherapy AUC_{ss} for activity score 2. Colored symbols depict dose reductions for the different activity scores. AUC_{ss} , area under the concentration–time curve during steady state; b.i.d., twice a day; D(D)GI, drug(–drug)–gene interaction; PBPK, physiologically-based pharmacokinetic; q.d., once daily; q.i.d., four times a day.

inhibitors using a CYP3A4 DDI network have been successfully applied to support and accelerate clinical development.⁴² Here, PBPK interaction networks offer a robust framework for simulating and predicting drug interactions *in silico*, potentially reducing the need for early-phase clinical trials.⁵

Most models within the network were utilized without modifications to their original configurations. However, PBPK models for atomoxetine, bupropion, cimetidine, and fluvoxamine were extended to include additional interaction parameters that mechanistically describe DDIs mediated by these drugs. All interaction parameters implemented in the respective models were sourced from the published literature. For instance, the bupropion model was modified to reflect its unique interaction mechanism, a mix of

competitive inhibition and down-regulation of CYP2D6 caused by bupropion and its metabolites hydroxybupropion, erythrohydrobupropion, and threohydrobupropion as described by Sager *et al.*²⁷ These model extensions were necessary to accurately capture the interactions between bupropion and the CYP2D6 victim drugs atomoxetine and desipramine.^{28,43} In the case of metoprolol, the model was refined to include a CYP3A4-mediated clearance pathway, replacing a previously implemented non-specific pathway. This adjustment aligns with *in vitro* evidence suggesting that metoprolol's metabolism is partially mediated by CYP3A4.³⁵ Although CYP2D6 is generally considered non-inducible by prototypical CYP inducers, such as carbamazepine and rifampicin, Bennett *et al.* have reported an increase of metoprolol AUC after

rifampicin co-administration by ~30% indicating additional non-CYP2D6-mediated metabolism.⁴⁴

Further adaptations of the network models may increase their predictive performance to cover various additional DDGI scenarios. This includes incorporating *in vitro* interaction parameters for metabolites currently not included in the respective models, as metabolites often contribute to the apparent interactions caused by their parent drug. For instance, Sauer and colleagues reported an additive effect of CYP3A4 inhibition caused by atomoxetine and its metabolites N-desmethyatomoxetine and 4-hydroxyatomoxetine, which are not included in the current atomoxetine model.³² In addition, models can be refined once new insights into the PK of a drug emerge. For instance, predicted desipramine profiles show a trend toward underprediction in DDI scenarios, although all interaction PK ratios were within the limits proposed by Guest *et al.*¹⁹ This discrepancy may have been caused by possible transport processes that were not included in the desipramine model but may be targeted by perpetrators. For example, experiments with rats indicate that P-gp inhibitors can increase desipramine brain concentrations.⁴⁵ However, since no broad knowledge and especially quantifying parameters on the potential transport of desipramine by P-gp were available in the literature, P-gp-mediated transport was not included in the model. Should further data indicating relevant transport by P-gp or other transporters *in vivo* become available, the desipramine model can be refined accordingly. Overall, these adaptations showcase the mechanistic flexibility of PBPK models and their adaptability to describe complex DDGI scenarios.

Although a large amount of data was used for network development and evaluation, the generalizability of the network predictions may be limited to some extent caused by the design of the clinical studies used. For instance, most studies were conducted with European or American subjects, while data on Asian subjects were only available for the victim drugs atomoxetine, paroxetine, and risperidone. Hence, the predictive performance may vary for ethnicities not represented in the respective study cohorts. Moreover, as study participants typically were healthy men aged around 30, the predictive performance may differ for women and older patients. Finally, the predictive performance of the presented network in various other vulnerable patient populations, such as pediatric patients or patients with renal or hepatic impairment, remains unknown. Here, previous examples highlight how PBPK DD(G)I models can be adapted to cover these scenarios.^{46–48} Additional studies covering a wider range of demographic characteristics of study participants would be of interest to extend and evaluate the developed network, increasing its clinical utility in predicting real-world scenarios.

In conclusion, this work presents a comprehensive whole-body PBPK DDGI network that can describe and predict the simultaneous effects of CYP2D6 activities and concomitant administrations of various perpetrator drugs on the PK of victim drugs. Overall, the developed network not only provides a valuable basis for the realization of PBPK MIPD for CYP2D6 victim drugs, but also represents a well-suited foundation for applications within MID3 due to the broad coverage of CYP2D6 victim and perpetrator drugs. The modular nature of PBPK models supports this

broad applicability of the network by facilitating future extensions through the inclusion of additional perpetrator or victim drugs. Therefore, all model files will be made publicly available (<http://models.clinicalpharmacy.me>).

SUPPORTING INFORMATION

Supplementary information accompanies this paper on the *Clinical Pharmacology & Therapeutics* website (www.cpt-journal.com).

ACKNOWLEDGMENTS

Open Access funding enabled and organized by Projekt DEAL.

FUNDING

This work is part of the Horizon 2020 INSPIRATION (Qualified Open Systems Pharmacology Modeling Network of Drug–Drug–Gene–Interactions) project. The INSPIRATION project (grant 643272, FKZ 031L0241) is supported by the German Federal Ministry of Education and Research and ZonMW (9003035202) under the framework of ERACoSysMed. Matthias Schwab was supported in parts by the Robert Bosch Stiftung Stuttgart, Germany, and the Deutsche Forschungsgemeinschaft (DFG) under Germany's Excellence Strategy-EXC 2180–390900677. Thorsten Lehr, Jesse J. Swen and Maaik van der Lee were supported by the European Union Horizon 2021 SafePolyMed (grant 101057639).

CONFLICT OF INTEREST

Denise Feick and Donato Teutonico are employees of Sanofi and may hold shares and/or stock options in the company. Annika Schneider and Juri Solodenko are employees of Bayer AG. Sebastian Frechen was an employee of Bayer AG. Juri Solodenko and Annika Schneider use Open Systems Pharmacology software, tools, or models in their professional roles. Donato Teutonico, Juri Solodenko and Thorsten Lehr are members of the Open Systems Pharmacology Management Team. Sebastian Frechen was a member of the Open Systems Pharmacology Sounding Board. All other authors declared no competing interest for this work.

AUTHOR CONTRIBUTIONS

All authors wrote the manuscript. S.R., H.L.H.L., D.F., D.S., and T.L. designed the research. S.R., H.L.H.L., and D.F. performed the research. S.R., H.L.H.L., D.F., and D.S. analyzed the data.

© 2025 The Author(s). *Clinical Pharmacology & Therapeutics* published by Wiley Periodicals LLC on behalf of American Society for Clinical Pharmacology and Therapeutics.

This is an open access article under the terms of the [Creative Commons Attribution](https://creativecommons.org/licenses/by/4.0/) License, which permits use, distribution and reproduction in any medium, provided the original work is properly cited.

1. Pirmohamed, M. *et al.* Adverse drug reactions as cause of admission to hospital: prospective analysis of 18 820 patients. *BMJ* **329**, 15–19 (2004).
2. Lazarou, J., Pomeranz, B.H. & Corey, P.N. Incidence of adverse drug reactions in hospitalized patients. *JAMA* **279**, 1200–1205 (1998).
3. Zanger, U.M. & Schwab, M. Cytochrome P450 enzymes in drug metabolism: regulation of gene expression, enzyme activities, and impact of genetic variation. *Pharmacol Ther* **138**, 103–141 (2013).
4. Bahar, M.A., Setiawan, D., Hak, E. & Wilffert, B. Pharmacogenetics of drug–drug interaction and drug–gene interaction: a systematic review on CYP2C9, CYP2C19 and CYP2D6. *Pharmacogenomics* **18**, 701–739 (2017).
5. Türk, D. *et al.* Novel models for the prediction of drug–gene interactions. *Expert Opin Drug Metab Toxicol* **17**, 1293–1310 (2021).
6. Bahar, M.A., Kamp, J., Borgsteede, S.D., Hak, E. & Wilffert, B. The impact of CYP2D6 mediated drug–drug interaction: a systematic

ARTICLE

- review on a combination of metoprolol and paroxetine/fluoxetine. *Br J Clin Pharmacol* **84**, 2704–2715 (2018).
7. Zanger, U.M., Turpeinen, M., Klein, K. & Schwab, M. Functional pharmacogenetics/genomics of human cytochromes P450 involved in drug biotransformation. *Anal Bioanal Chem* **392**, 1093–1108 (2008).
 8. Gaedigk, A. *et al.* The CYP2D6 activity score: translating genotype information into a qualitative measure of phenotype. *Clin Pharmacol Ther* **83**, 234–242 (2008).
 9. Storelli, F. *et al.* Impact of CYP2D6 functional allelic variations on Phenoconversion and drug-drug interactions. *Clin Pharmacol Ther* **104**, 148–157 (2018).
 10. Wojtyniak, J., Selzer, D., Schwab, M. & Lehr, T. Physiologically based precision dosing approach for drug-drug-gene interactions: a simvastatin network analysis. *Clin Pharmacol Ther* **109**, 201–211 (2021).
 11. Polak, S., Tylutki, Z., Holbrook, M. & Wiśniewska, B. Better prediction of the local concentration–effect relationship: the role of physiologically based pharmacokinetics and quantitative systems pharmacology and toxicology in the evolution of model-informed drug discovery and development. *Drug Discov Today* **24**, 1344–1354 (2019).
 12. EMA Guideline on the reporting of physiologically based pharmacokinetic (PBPK) modelling and simulation. EMA/CHMP/4, 3–15 (2018).
 13. U.S. Food and Drug Administration. The Use of Physiologically Based Pharmacokinetic Analyses — Biopharmaceutics Applications for Oral Drug Product Development, Manufacturing Changes, and Controls. Draft (2020).
 14. Hanke, N. *et al.* PBPK models for CYP3A4 and P-gp DDI prediction: a modeling network of rifampicin, itraconazole, clarithromycin, midazolam, alfentanil, and digoxin. *CPT Pharmacometrics Syst Pharmacol* **7**, 647–659 (2018).
 15. U.S. Food and Drug Administration. Drug Development and Drug Interactions | Table of Substrates, Inhibitors and Inducers | FDA <<https://www.fda.gov/drugs/drug-interactions-labeling/drug-development-and-drug-interactions-table-substrates-inhibitors-and-inducers#table3-1>> (2023). Accessed May 23, 2023.
 16. Kovar, C. *et al.* Prediction of drug-drug-gene interaction scenarios of (E)-clomiphene and its metabolites using physiologically based pharmacokinetic modeling. *Pharmaceutics* **14**, 2604 (2022).
 17. Kanacher, T. *et al.* A physiologically-based pharmacokinetic (PBPK) model network for the prediction of CYP1A2 and CYP2C19 drug-drug-gene interactions with fluvoxamine, omeprazole, S-mephenytoin, moclobemide, tizanidine, mexiletine, Ethinylestradiol, and caffeine. *Pharmaceutics* **12**, 1–15 (2020).
 18. Feick, D. *et al.* Physiologically-based pharmacokinetic modeling of quinidine to establish a CYP3A4, P-gp, and CYP2D6 drug-drug-gene interaction network. *CPT Pharmacometrics Syst Pharmacol* **12**, 1143–1156 (2023).
 19. Guest, E.J., Aarons, L., Houston, J.B., Rostami-Hodjegan, A. & Galetin, A. Critique of the two-fold measure of prediction success for ratios: application for the assessment of drug-drug interactions. *Drug Metab Dispos* **39**, 170–173 (2011).
 20. Rüdeshheim, S. *et al.* Physiologically based pharmacokinetic modeling to describe the CYP2D6 activity score-dependent metabolism of paroxetine, atomoxetine and risperidone. *Pharmaceutics* **14**, 1734 (2022).
 21. Rüdeshheim, S., Selzer, D., Fuhr, U., Schwab, M. & Lehr, T. Physiologically-based pharmacokinetic modeling of dextromethorphan to investigate interindividual variability within CYP2D6 activity score groups. *CPT Pharmacometrics Syst Pharmacol* **11**, 494–511 (2022).
 22. Fuhr, L.M., Marok, F.Z., Hanke, N., Selzer, D. & Lehr, T. Pharmacokinetics of the CYP3A4 and CYP2B6 inducer carbamazepine and its drug–drug interaction potential: a physiologically based pharmacokinetic modeling approach. *Pharmaceutics* **13**, 270 (2021).
 23. Moj, D. *et al.* Clarithromycin, midazolam, and digoxin: application of PBPK modeling to gain new insights into drug-drug interactions and Co-medication regimens. *AAPS J* **19**, 298–312 (2017).
 24. Frechen, S. & Dallmann, A. Building and Evaluation of a PBPK Model for Erythromycin in Healthy Adults <https://github.com/Open-Systems-Pharmacology/OSP-PBPK-Model-Library/blob/v9.1/Erythromycin/Erythromycin_evaluation_report.pdf>. Accessed November 28, 2023.
 25. Marok, F.Z. *et al.* A physiologically based pharmacokinetic model of ketoconazole and its metabolites as drug-drug interaction perpetrators. *Pharmaceutics* **15**, 679 (2023).
 26. Hanke, N. *et al.* A mechanistic, enantioselective, physiologically based pharmacokinetic model of verapamil and Norverapamil, built and evaluated for drug–drug interaction studies. *Pharmaceutics* **12**, 556 (2020).
 27. Sager, J.E. *et al.* In vitro to in vivo extrapolation of the complex drug-drug interaction of bupropion and its metabolites with CYP2D6; simultaneous reversible inhibition and CYP2D6 downregulation. *Biochem Pharmacol* **123**, 85–96 (2017).
 28. Reese, M.J. *et al.* An in vitro mechanistic study to elucidate the desipramine/bupropion clinical drug-drug interaction. *Drug Metab Dispos* **36**, 1198–1201 (2008).
 29. Britz, H. *et al.* Physiologically-based pharmacokinetic models for CYP1A2 drug-drug interaction prediction: a modeling network of fluvoxamine, theophylline, caffeine, rifampicin, and midazolam. *CPT Pharmacometrics Syst Pharmacol* **8**, 296–307 (2019).
 30. Crewe, H.K., Lennard, M.S., Tucker, G.T., Woods, F.R. & Haddock, R.E. The effect of selective serotonin re-uptake inhibitors on cytochrome P4502D6 (CYP2D6) activity in human liver microsomes. *Br J Clin Pharmacol* **34**, 262–265 (1992).
 31. Madeira, M., Levine, M., Chang, T.K.H., Mirfazaelian, A. & Bellward, G.D. The effect of cimetidine on dextromethorphan O-demethylase activity of human liver microsomes and recombinant CYP2D6. *Drug Metab Dispos* **32**, 460–467 (2004).
 32. Sauer, J.-M. *et al.* Atomoxetine hydrochloride: clinical drug-drug interaction prediction and outcome. *J Pharmacol Exp Ther* **308**, 410–418 (2004).
 33. Iga, K. Dynamic and static simulations of fluvoxamine-perpetrated drug-drug interactions using multiple cytochrome P450 inhibition modeling, and determination of perpetrator-specific CYP isoform inhibition constants and fractional CYP isoform contributions to Vic. *J Pharm Sci* **105**, 1307–1317 (2016).
 34. Rüdeshheim, S. *et al.* Physiologically based pharmacokinetic modeling of metoprolol enantiomers and α -Hydroxymetoprolol to describe CYP2D6 drug-gene interactions. *Pharmaceutics* **12**, 1200 (2020).
 35. Berger, B., Bachmann, F., Duthaler, U., Krähenbühl, S. & Haschke, M. Cytochrome P450 enzymes involved in metoprolol metabolism and use of metoprolol as a CYP2D6 phenotyping probe drug. *Front Pharmacol* **9**, 1–11 (2018).
 36. Kneller, L.A., Abad-Santos, F. & Hempel, G. Physiologically based pharmacokinetic modelling to describe the pharmacokinetics of risperidone and 9-Hydroxyrisperidone according to cytochrome P450 2D6 phenotypes. *Clin Pharmacokinet* **59**, 51–65 (2020).
 37. Türk, D. *et al.* Physiologically based pharmacokinetic models for prediction of complex CYP2C8 and OATP1B1 (SLC01B1) drug–drug–gene interactions: a modeling network of gemfibrozil, repaglinide, pioglitazone, rifampicin, clarithromycin and itraconazole. *Clin Pharmacokinet* **58**, 1595–1607 (2019).
 38. Wedagedera, J.R. *et al.* Population PBPK modeling using parametric and nonparametric methods of the Simcyp simulator, and Bayesian samplers. *CPT Pharmacometrics Syst Pharmacol* **11**, 755–765 (2022).
 39. Eli Lilly and Company STRATTERA Labeling-Package Insert – Drugs@FDA <https://www.accessdata.fda.gov/drugsatfda_docs/label/2002/21411_strattera_lbl.pdf>. Accessed June 8, 2023.
 40. The Royal Dutch Pharmacists Association – Pharmacogenetics Working Group (DPWG) Annotation of DPWG Guideline for metoprolol and CYP2D6 <<https://www.pharmgkb.org/guidelineAnnotation/PA166104995>>. Accessed September 22, 2020.
 41. U.S. Food and Drug Administration. For Healthcare Professionals | FDA's Examples of Drugs that Interact with CYP Enzymes and Transporter Systems | FDA <<https://www.fda.gov/drugs/drug-interactions-labeling/healthcare-professionals-fdas-examples-drugs-interact-cyp-enzymes-and-transporter-systems>>. Accessed June 8, 2023.

42. Wendl, T., Frechen, S., Gerisch, M., Heinig, R. & Eissing, T. Physiologically-based pharmacokinetic modeling to predict CYP3A4-mediated drug-drug interactions of finerenone. *CPT Pharmacometrics Syst Pharmacol* **11**, 199–211 (2022).
43. Todor, I. *et al.* Evaluation of a potential metabolism-mediated drug-drug interaction between atomoxetine and bupropion in healthy volunteers. *J Pharm Pharm Sci* **19**, 198 (2016).
44. Bennett, P.N., John, V.A. & Whitmarsh, V.B. Effect of rifampicin on metoprolol and antipyrine kinetics. *Br J Clin Pharmacol* **13**, 387–391 (1982).
45. O'Brien, F.E., Dinan, T.G., Griffin, B.T. & Cryan, J.F. Interactions between antidepressants and P-glycoprotein at the blood-brain barrier: clinical significance of in vitro and in vivo findings. *Br J Pharmacol* **165**, 289–312 (2012).
46. Hanke, N. *et al.* A comprehensive whole-body physiologically based pharmacokinetic drug–drug–gene interaction model of metformin and cimetidine in healthy adults and renally impaired individuals. *Clin Pharmacokinet* **59**, 1419–1431 (2020).
47. Gerner, B. & Scherf-Clavel, O. Physiologically based pharmacokinetic modelling of Cabozantinib to simulate enterohepatic recirculation, drug–drug interaction with rifampin and liver impairment. *Pharmaceutics* **13**, 778 (2021).
48. Kovar, L. *et al.* Physiologically-based pharmacokinetic (PBPK) modeling providing insights into fentanyl pharmacokinetics in adults and pediatric patients. *Pharmaceutics* **12**, 908 (2020).
49. Brøsen, K., Hansen, J.G., Nielsen, K.K., Sindrup, S.H. & Gram, L.F. Inhibition by paroxetine of desipramine metabolism in extensive but not in poor metabolizers of sparteine. *Eur J Clin Pharmacol* **44**, 349–355 (1993).

DISCUSSION AND FUTURE DIRECTIONS

The present thesis explores the potential of PBPK modeling as a framework for individualized therapy, specifically focusing on its applicability for mechanistically describing and predicting complex drug interactions and translating findings into dosage decisions.

Within this work, new whole-body PBPK models for the clinically relevant CYP₃A victim drugs tacrolimus, imatinib, and dasatinib, used in the fields of immunology and transplantation as well as oncology, were developed. Moreover, a comprehensive interaction network centered around the CYP₂D6 isozyme was built, incorporating 23 different victim and perpetrator drugs. The established models and CYP₂D6 network were applied to study the underlying mechanisms as well as impact on victim exposure of a wide range of metabolic DD(G)Is and other PK-related interaction types. Lastly, clinically untested interaction scenarios for selected victim drugs were simulated and model-based dose adjustments were performed to demonstrate the broad applicability and enormous potential of PBPK modeling to bridge the critical knowledge gap between clinical interaction study results and complex real-world drug interactions.

The following sections provide a detailed examination of PBPK modeling in relation to the prediction of complex drug interactions, its application in MIPD, and its role in MID₃. Each section discusses the current landscape, strengths, and limitations of PBPK modeling in the respective context, integrating key findings from this thesis. For each area, an outlook is presented on the potential of PBPK modeling to advance individualized therapy, emphasizing the specific contributions of this research.

5.1 PBPK MODELING OF COMPLEX DRUG INTERACTIONS

PBPK modeling is generally suited for studying and predicting drug interactions due to its mechanistic nature, enabling detailed integration of interaction processes [26, 96]. While DDIs represent one of the main application areas of PBPK modeling [103], published work also demonstrates its use in the investigation of DGI effects [139–141]. In addition, PBPK modeling was shown to allow the description of pathological factors on a drug's PK, such as renal impairment due to chronic kidney disease [142] or inflammation-induced enzyme inhibition [143].

Importantly, a key strength of PBPK modeling lies in its ability to mechanistically investigate and quantify not only isolated interaction effects on the PK of a drug but also multiple factors simultaneously, enabling the prediction of complex drug interactions [21, 96, 144], such as DDGIs. In general, PBPK modeling, especially whole-body modeling, allows the complicated interplay between parameters and processes influencing PK to

be modeled holistically, thereby distinguishing itself from other modeling methods [145].

In the course of this work, a large variety of interaction scenarios were investigated, providing insights into the broad spectrum of drug interactions addressable by PBPK modeling. The CYP3A substrates tacrolimus, imatinib, and dasatinib were selected for model development in projects I–III due to their considerable PK variability, susceptibility to a wide range of drug interactions, as well as status as frontline therapies in areas of high unmet medical need [82, 106–110]. Overall, they were considered clinically relevant drug candidates for precision dosing whose PK properties should be thoroughly investigated in interaction scenarios [1–3]. Project IV focused on CYP2D6, selected as the key enzyme of the established DDGI network due to its clinical importance, high prevalence of allelic variants resulting in a large variation in enzymatic activity, and marked susceptibility to perpetrator effects [4].

Projects I and III illustrate how PBPK modeling can predict not only classical isolated metabolic DDIs, but also DDGIs and DDIs related to different ADME processes. In project I, PBPK modeling was successfully applied to describe and predict the effects of phenotype/ethnicity-dependent CYP3A5 activity and co-administered CYP3A perpetrator drugs on the PK of tacrolimus [1]. Project III illustrates the ability of PBPK modeling to capture the effect of pH-increasing agents on the absorption of dasatinib [3]. Furthermore, both projects demonstrate the capability of PBPK modeling to quantify the effects of factors beyond perpetrator drugs, such as food components, on victim PK [1, 3].

The modeling of imatinib in project II provides a good showcase for the strength of PBPK modeling to predict complex PK-related drug interactions, given its ability to capture mutually influencing interaction processes [2]. Not only does the model effectively describe the shift towards an enhanced role of CYP2C8 in the steady-state metabolism of imatinib due to CYP3A4 autoinhibition [92], but also the resulting altered impact of CYP3A4 perpetrators on the PK of imatinib after multiple versus single dose imatinib application [2, 120, 146]. Moreover, when simulating DDIs, the model can account for the inhibitory effect of imatinib on the metabolism/transport of co-administered perpetrator drugs and the associated changes in their influence on imatinib PK, as well as perpetrator-dependent intrahepatic increases in NDMI concentrations, potentially triggering its inhibitory potential [2].

Lastly, the comprehensive CYP2D6 network established in project IV takes advantage of the modular nature of PBPK modeling, allowing flexible linkage of existing models and smaller interaction networks into a large network, thus facilitating the prediction of complex DD(G)I scenarios. In addition to 85 DGI and 121 DDI scenarios, PBPK modeling of 42 DDGIs is shown, demonstrating in particular the level of detail PBPK modeling offers for modeling pharmacogenetic influences by successfully predicting the varying impact of nine different CYP2D6 activity levels on victim exposure in D(D)GI scenarios [4].

As promising as the PBPK modeling approach is, there are also limiting factors. One of the main challenges is the enormous amount of system-dependent, drug-dependent, and process-related data needed for model development, which is not always readily available [103]. Successful modeling of DD(G)Is, as an example, depends on sufficient information about the various metabolic pathways and transport processes of a drug [147]. However, in recent years, machine learning and artificial intelligence have been increasingly pursued as a promising approach to predict missing PK input parameters [148, 149]. Moreover, the mechanistic description of an interaction is only possible if the respective mechanism is properly understood and reported. To illustrate, the reason behind the observed effect of food intake on tacrolimus PK is still not fully known [115], necessitating the use of assumptions in its modeling [1]. Finally, the development of robust DD(G)I models may be limited by the type and amount of clinical DD(G)I data available, as, for example, DD(G)I studies usually involve healthy young men rather than patients [16, 17], and the interaction effect is often only examined in relation to a single administration of the respective victim and not multiple dosing [17].

Overall, the projects in the present thesis underline the ability of PBPK modeling to describe and predict a broad spectrum of complex drug interactions. PBPK modeling thus proves to be a suitable approach not only to study a drug's PK in detail, but also to provide a basis for the inclusion of pharmacogenetic and co-medication effects in the context of individualized therapy and precision dosing.

5.2 PBPK MODELING IN MIPD

5.2.1 *Current Status of MIPD*

Although MIPD is considered clinically relevant and promising for the realization of personalized medicine, its implementation has so far mostly been limited to small-scale local initiatives between universities and individual hospitals [26, 150]. This is partly due to MIPD relying on extensive data, such as patient demographic and physiological characteristics, drug properties, and clinical observations, which are often scarce [26]. Moreover, among healthcare professionals there appears to be a frequent lack of the necessary expertise in the fields of pharmacology, pharmacometrics, and pharmacogenetics needed to effectively implement personalized medicine and MIPD in clinical practice [26, 151].

Another major obstacle is the outstanding clinical demonstration of MIPD's benefits over conventional methods, which is hampered by the availability of only retrospective data rather than prospective studies. Performing dedicated trials proves difficult as, among other factors, the sample size is often insufficient, a suitable PK model needs to be selected, and capped dosing ranges further complicate study designs [150].

However, efforts to broaden the clinical implementation of MIPD have increased over the last few years, with studies being conducted, for example, to demonstrate the potential of MIPD using virtual patients [152] or to develop standardized workflows for the integration of MIPD in hospitals [153]. In addition, several dedicated national and transnational symposia and workshops on the status and advancement of MIPD have been held [26, 154, 155].

The principle of MIPD encompasses various modeling concepts, such as real-time MIPD using population PK (PopPK) models coupled with Bayesian methodology and TDM data [26, 154]. Here, PopPK modeling combines the analysis of PK and covariates to explain and predict the variability in drug concentrations within a population [156]. The Bayesian approach is additionally applied to update prior information as feedback control and to dynamically refine model predictions using real-time TDM data [26]. In recent years, however, PBPK modeling has received increasing attention in the context of MIPD [154].

5.2.2 *Potential and Limitations of PBPK-MIPD*

PBPK modeling is seen as a promising framework for MIPD as it differs from other MIPD strategies in its mechanistic nature, supporting extrapolation beyond studied populations and experimental conditions [26, 96]. Moreover, the possibility of mechanistically including a patient's individual (patho-)physiological characteristics in PBPK modeling enables the creation of so-called virtual twins mirroring real-world patients, as previously demonstrated for the neuroleptic agent olanzapine [24, 157]. Finally, PBPK modeling is less dependent on TDM data. This allows the prospective determination of dose recommendations based on the respective patient and medication characteristics before the initiation of therapy [21, 154]. It is additionally less constrained by TDM and TDM data-related limitations, such as high costs [158] and logistical challenges in sample collection and processing [108].

Particularly relevant indication areas for the integration of precision dosing into drug therapy include immunology and transplantation as well as oncology, given the substantial morbidity and mortality [113, 159, 160] and overall high unmet medical need [25, 29]. Not surprisingly, numerous MIPD-related research articles can be found in the literature, focusing however predominantly on the development of PopPK models both in the case of the immunosuppressant tacrolimus [161] and in the field of oncology [162].

The PBPK models developed in projects I–III of this thesis for the front-line therapies tacrolimus, imatinib, and dasatinib can thus contribute to advancing the currently underrepresented PBPK-MIPD approach in immunology/transplantation and oncology as well as creating a basis for its clinical application. The models show good predictive performance of the respective PK and were each validated for a wide range of drug interactions, providing an important platform for extrapolation to other clinically rele-

vant interaction scenarios [1–3]. Here, these models differ from previously published whole-body PBPK interaction models [131, 163–165], by encompassing a broad spectrum of different interaction types and mechanisms in single frameworks [1–3].

Furthermore, the CYP2D6 DDGI network established in project IV provides a comprehensive basis for the clinical implementation of PBPK-MIPD in general. Given the great number of included victim and perpetrator drugs as well as modeled DD(G)I scenarios, the network presents a robust framework for simulating and investigating complex CYP2D6 DDGIs in the context of MIPD [4].

Based on the developed dasatinib model (project III) and CYP2D6 network (project IV), the ability of PBPK modeling to predict clinically untested CYP3A4 DDI and CYP2D6 DDGI scenarios was exemplified for dasatinib and the CYP2D6 substrates atomoxetine and metoprolol [3, 4]. The projects illustrate the vast potential of PBPK modeling, not only in providing dose recommendations for complex and diverse interaction scenarios beyond the capabilities of clinical trials, but also in refining dosing guidance for more straightforward interactions covered in prescribing information or guidelines [3, 4].

For instance, in the case of 140 mg dasatinib, model-informed dose reductions range from 50% to 80%, depending on the strong CYP3A4 inhibitor co-administered [3]. In contrast, the prescribing information recommends a fixed reduction by 71%, irrespective of the type or quantity of strong CYP3A4 inhibitor [166]. This difference illustrates the potential of considering a patient's specific co-medication in clinical practice, compared to mere categorization, i.e. weak, moderate, or strong perpetrator, for more detailed management of drug levels [3].

In the case of atomoxetine and metoprolol, CYP2D6 phenotype-dependent dosages are provided in the prescribing information and DPWG guideline, respectively [167, 168]. However, since several AS values are translated into one phenotype [63], CYP2D6 AS-dependent dose finding via PBPK-MIPD, as demonstrated in project IV, represents an even more detailed and individualized approach [4]. It should be noted, that while AS-based dosing allows a finer subdivision than the phenotypic equivalent, high inter-individual CYP2D6 activity can still be observed within AS groups [140]. In this context, applying a hybrid population PBPK approach, for which the developed CYP2D6 network can serve as a basis, could facilitate further refinement of individual predictions by incorporating corresponding PK data [4, 169].

Despite the great potential of PBPK modeling in MIPD, it is also subject to limitations and obstacles. For example, the reliability of model-based dose recommendations for clinically untested interaction scenarios is highly dependent on the data available for model development. Although simulation outside the investigated dose range is possible, the behavior of a drug in terms of PK nonlinearity or linearity, for instance, may be incorrectly captured. Similarly, when multiple victim and perpetrator drugs are linked, the models may not be sufficiently validated for all interaction

processes occurring *in vivo*. Another challenge lies in the comprehensive patient information required for the creation of virtual twins, which is not always readily available. This specifically includes genotyping data for relevant enzymes and transporters, necessary for individual consideration of corresponding activity levels in dosing decisions [26]. The more recent concept of preemptively testing several genes in parallel on a panel basis and documenting the resulting genotypes/phenotypes in patient records [50] represents a promising method for widespread genotyping [170].

In the present work, the virtual twin approach could only be implemented to a limited extent, as most available studies provided mean rather than individual data. Nonetheless, virtual twins representing a typical individual for each study population were created based on the reported mean and modal demographics of study participants [1–4].

Overall, the projects in this thesis demonstrate the ability of PBPK modeling to predict complex, clinically untested DD(G)I scenarios. Combined with the possibility of creating patient-specific virtual twins, PBPK modeling thus offers the potential to simulate a patient's entire medication and adjust doses via MIPD in the scope of individualized therapy. New whole-body PBPK models for tacrolimus, imatinib, and dasatinib were successfully developed and validated for the prediction of the respective PK with and without the influence of complex interaction effects [1–3]. Moreover, the established CYP2D6 network provides a broad framework for the investigation and prediction of CYP2D6-mediated DD(G)Is in the context of PBPK-MIPD for CYP2D6 substrates [4]. To advance the integration of PBPK-MIPD into clinical practice, the prospective clinical evaluation of model predictions and model-based dose recommendations now represents the critical and exciting next step [162].

5.2.3 Clinical Implementation of PBPK-MIPD

To facilitate the clinical application of precision medicine, clinical decision support systems (CDSSs) are increasingly being developed to aid healthcare professionals, for example, in assessing individual health risks [6]. Likewise, such systems hold great potential for expanding the routine use of PBPK-MIPD and MIPD in general. When integrated with electronic prescribing systems and linked to electronic health records (EHRs), they can streamline the use of complex underlying models while consolidating and expanding results and alerts from separate CDSSs by considering multiple influential factors simultaneously [26, 171].

Examples illustrating the MIPD-CDSS concept can be found in the literature, including a TDM tool utilizing PopPK modeling for vancomycin dosing (<https://pipet.shinyapps.io/vancomycin/>), presented during the 1st Asian Symposium on Precision Dosing [154]. However, although a lot of work is ongoing in the field of dose individualization, the development of corresponding CDSSs is lagging behind [26].

To advance PBPK-MIPD towards clinical implementation, a CDSS prototype was created as part of the INSPIRATION European Union project in interdisciplinary collaboration with hospital pharmacists and physicians as well as modeling experts. Alongside various perpetrator drugs, tacrolimus, imatinib, and dasatinib were included as victim drugs using the PBPK models developed in projects I–III.

The established CDSS supports the entry of individual patient characteristics such as age, weight, ethnicity as well as administration regimens of the respective victim and perpetrator drug(s). In the case of tacrolimus, the *CYP3A5* genotype can additionally be specified. Beyond the simulation of victim monotherapy using default model settings, predictions can be individually refined by informing the CDSS with clinical data of the respective patient and subsequent patient-specific optimization of a parameter characterized by high inter-individual variability, such as the *CYP3A5* k_{cat} for tacrolimus (Figure 5.1). Predefined population variabilities of the specified parameters serve as reference. Moreover, the CDSS allows simulation of DD(G)Is and model-informed dose adjustments depending on a selected PK target variable and range (Figure 5.2).

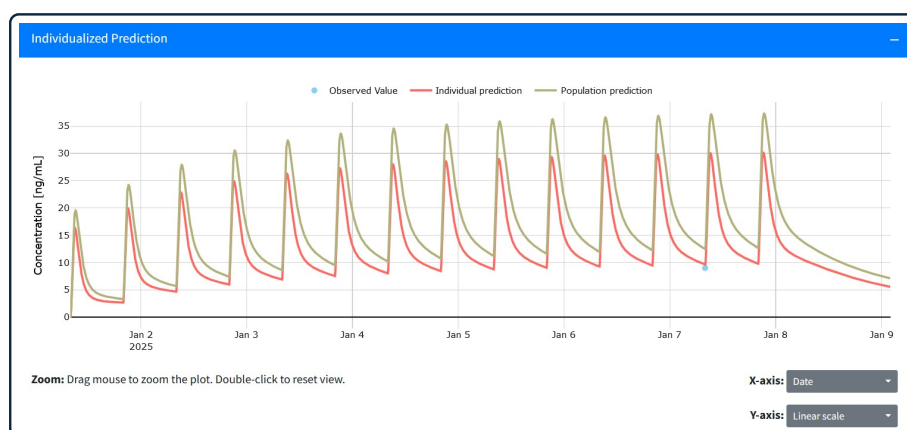


Figure 5.1: Screenshot of the “Individualized Prediction” function integrated in the decision support system developed as part of the INSPIRATION European Union project. Simulation of oral monotherapy with 5 mg of the *CYP3A* substrate tacrolimus twice daily without model adjustments (population prediction) and with patient-specific adaptation of the *CYP3A5* catalytic rate constant k_{cat} based on observed individual data and predefined population variability (individual prediction). The output is shown for a male European, 30 years old, 70 kg in weight, 175 cm tall, and *CYP3A5* normal metabolizer. CYP: cytochrome P450.

However, before an MIPD-CDSS can be implemented in routine practice, several prerequisites must be fulfilled, with one of the most relevant being the validation of not only the integrated models but also the CDSS itself for clinical use. A key difficulty in this regard and in general is the classification of CDSSs as medical devices by regulatory agencies, placing them under stricter regulations [171]. Moreover, healthcare professionals must complete comprehensive training on the pharmacological and PK background as well as practical application of the respective CDSS [26]. Lastly, sufficiently documented patient information would be required to automatically create virtual twins by linking the CDSS with EHRs [171].

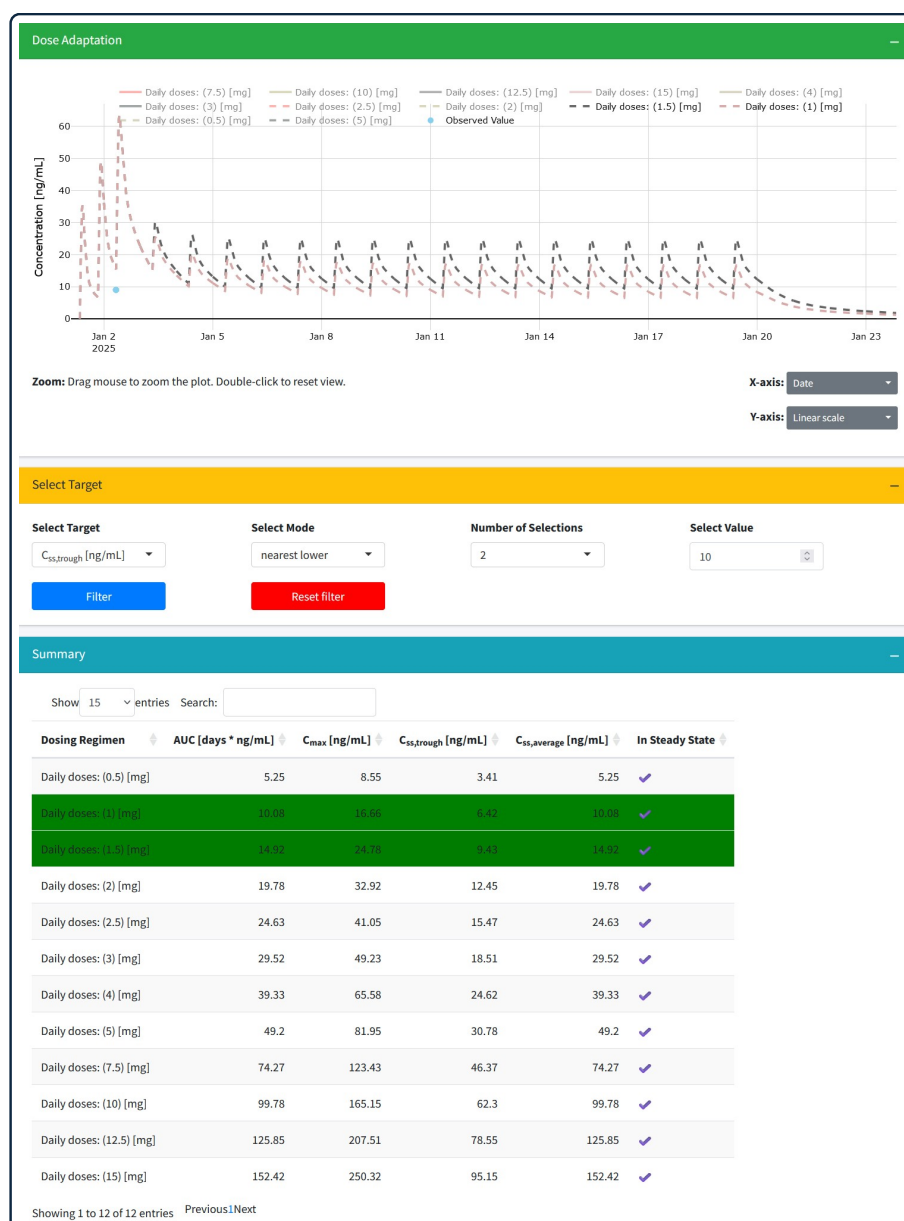


Figure 5.2: Screenshot of the “Dose Adaptation” function integrated in the decision support system developed as part of the INSPIRATION European Union project. Simulation of oral therapy with 5 mg of the CYP_{3A} substrate tacrolimus twice daily and 200 mg of the CYP_{3A} inhibitor voriconazole twice daily. Starting with the fourth administration, various doses of tacrolimus were simulated, setting the trough concentration under “Select Target” as target variable with a maximum value of 10 ng/mL [89] and limiting the selection of suitable doses to two. In the “Summary” tab, doses that meet the selected requirements are highlighted in green (in this case daily doses of 1 mg and 1.5 mg tacrolimus), all other simulations are subsequently hidden in the concentration-time plot. The output is shown for a male European, 30 years old, 70 kg in weight, 175 cm tall, and CYP_{3A5} normal metabolizer. AUC: area under the concentration-time curve, C_{max} : maximum concentration, $C_{ss, average}$: average steady-state concentration, $C_{ss, trough}$: through steady-state concentration, CYP: cytochrome P₄₅₀.

Overall, PBPK-MIPD-CDSSs represent a promising approach for the integration of corresponding models into clinical practice, thus advancing the field of PBPK-MIPD. They not only offer the potential to facilitate individual dose determination and adjustment but also enable the identification of alternative medications to avoid DD(G)Is in advance [26].

5.3 PBPK MODELING IN MID3

In contrast to MIPD, MID3 has already been practiced for about three decades to support decision-making while reducing cost and time factors in the discovery and development of new therapies [172, 173]. An important step towards routine implementation represented the codification of MID3 in the FDA's 2017 Prescription Drug User Fee Act Reauthorization (PDUFA VI, 2018–2022) [174]. In a survey conducted in 2017, industry, FDA, and the European Medicines Agency (EMA) all reported an increasing influence of MID3 on decision-making and predicted a further upward trend in the future [173].

Alongside PopPK and exposure-response modeling, PBPK modeling has become one of the main MID3 approaches [172] and is applied throughout from the early discovery phase to late-stage drug development [102]. Dedicated guidelines published by regulatory authorities such as the FDA and EMA [175, 176] as well as a steadily increasing number of submissions involving PBPK modeling highlight its growing relevance in MID3 [177, 178]. In addition, the PBPK modeling approach is constantly being expanded. For example, combined PBPK and quantitative systems pharmacology (QSP) models were introduced in MID3 in recent years, enabling analysis of both drug exposure and drug response in respective patient populations [174, 179].

A particular benefit of PBPK modeling, in addition to its mechanistic character, is the previously mentioned ability to extrapolate outside analyzed populations and study settings [26, 96]. This allows “what-if” scenarios to be simulated early on in drug development to explore various effects, including co-medications, pharmacogenetic polymorphisms, age, ethnicity, or disease state, on the respective drug exposure [179, 180]. Especially when investigating the DDI potential of new compounds, an integral part of drug development [181], PBPK modeling is now routinely used [172] and is even highlighted in the FDA guidance for clinical drug interaction studies as an approach for conducting *in silico* DDI studies [23]. The ability to perform such virtual trials allows the analysis of a vast number of clinically relevant scenarios beyond the possibilities of conventional clinical studies, not only in the field of DDIs, but in general. Further advantages include a reduced risk for patients and an accelerated path to approval by carrying out virtual studies earlier in the drug development process than *in vivo* trials [7].

One of the prerequisites for conducting virtual DD(G)I studies is a large model library containing models validated for the prediction of various DD(G)I scenarios [23, 182]. Here, the FDA-listed index substrates and perpetrators for use in index DDI studies, as well as generally classified substrates

and perpetrators of certain CYP enzymes and transporters, provide a useful reference [75, 76].

The PBPK models developed in projects I–III extend the OSP model library by two drugs classified by the FDA as sensitive CYP3A4 substrates (tacrolimus and dasatinib) and one listed CYP3A4 moderate inhibitor (imatinib) [1–3, 76]. All three models were evaluated with various drug interaction scenarios and can thus be used to perform *in silico* DDI studies within the framework of MID3 [1–3]. Furthermore, due to its comprehensive nature, the CYP2D6 network created in project IV provides a broad basis for CYP2D6-related virtual DD(G)I trials [4]. Besides a generally good coverage of substrates and perpetrators listed by the FDA [4, 76], the network also contains two of three classified index substrates and one of two strong index inhibitors [4, 75]. By encompassing diverse interaction mechanisms, i.e. down-regulation, competitive inhibition, and mechanism-based inactivation, the network further allows detailed investigation of metabolism by and effects on CYP2D6 [4].

As described in more detail in Section 5.2.2, PBPK modeling was demonstrated as a suitable approach for the simulation of clinically untested interaction scenarios and corresponding model-based dose adjustments using dasatinib (project III) and the CYP2D6 substrates atomoxetine and metoprolol (project IV) as case examples [3, 4]. While at the individual patient level, PBPK modeling thus enables patient-specific dose finding in the context of MIPD, within MID3 it allows virtual DD(G)I studies to be conducted and dose recommendations to be generated for various “what-if” scenarios [179]. Specifically, project IV illustrates the potential of PBPK modeling to cumulatively capture multiple factors influencing a drug’s PK in dose recommendations, such as the effects of CYP2D6 phenotype and co-administered CYP2D6 perpetrator(s) – a level of complexity rarely assessed in clinical trials but relevant in clinical practice [10]. Resulting dosage suggestions can directly support a more individualized therapy upon integration into the respective prescription information. In this context, the growing importance and regulatory acceptance of PBPK modeling in MID3 is reflected by a tenfold increase in the number of PBPK models used as input for FDA drug labeling in the last 10 years [179]. However, it should be noted that recommendations based on multiple factors, as presented in project IV, are still rarely included in prescribing information, but offer a promising outlook for the future [10].

Although PBPK modeling is becoming more and more relevant in MID3, MID3 in general has not yet reached its full potential despite its routine use [174]. Lack of acceptance by statisticians, clinicians, and clinical pharmacologists has been cited by industry, FDA, and EMA as one of the main limiting factors. Proposed solutions include more targeted education of decision-makers through workshops and guidelines and the involvement of modeling scientists early in the decision-making process [173]. In this context, the FDA published a draft guidance for industry on general principles of MID3 in late 2024 [183].

Overall, this thesis underlines the ability of PBPK modeling to perform virtual DD(G)I trials and generate model-based dose recommendations within the MID3 framework. Here, the PBPK models developed for the CYP3A substrates tacrolimus, imatinib, and dasatinib, as well as the comprehensive CYP2D6 DDGI network, provide a broad basis for the prediction of different complex interaction scenarios. Moreover, given the central role of CYP3A4 and CYP2D6 in the metabolism of many drugs and their increased susceptibility to PK-related interactions, the results of this thesis can be transferred to a broad variety of drugs studied in MID3 and provide useful information for future PK analyses and modeling endeavors.

CONCLUSION

The management of DGIs, DDIs, and particularly DDGIs plays a central role in improving treatment efficacy and safety in the context of personalized medicine and precision dosing. However, given the virtually infinite number of potential interaction scenarios, it is impossible to investigate all interactions in dedicated clinical trials. The projects of this thesis highlight PBPK modeling as a powerful tool to bridge the critical knowledge gap between clinical interaction study results and complex real-world interaction scenarios.

The newly developed CYP2D6 network and PBPK models for the CYP3A substrates tacrolimus, imatinib, and dasatinib effectively demonstrate the applicability of PBPK modeling to mechanistically describe and predict clinically tested drug interactions across a broad range of complex DD(G)I scenarios and other PK-related interactions. Beyond this, the ability of PBPK modeling to simulate clinically untested DD(G)I scenarios including model-based dose adjustments was showcased for a wide spectrum of interactions. As such, PBPK modeling was shown to offer a strong framework for advancing individualized therapy, both in the context of MIPD through patient-specific dose adjustments and within MID₃ via the inclusion of multifactor-dependent dose recommendations derived from virtual DD(G)I studies in prescribing information.

Overall, the PBPK models and comprehensive CYP2D6 network developed in this thesis provide a solid foundation for exploring untested CYP3A and CYP2D6 DD(G)I scenarios in MIPD and MID₃, thereby advancing both the use of PBPK modeling and the disciplines themselves. The tacrolimus, imatinib, and dasatinib models can specifically serve as a basis to facilitate the clinical implementation of PBPK-MIPD in the critical areas of immunology and transplantation as well as oncology.

In summary, this work demonstrates the value of PBPK modeling in helping to realize the full potential of precision dosing. By mechanistically translating complex drug interactions into actionable treatment guidance, PBPK modeling can ultimately pave the way toward more individualized therapy.

BIBLIOGRAPHY

1. Loer, H. L. H.; Feick, D.; Rüdesheim, S.; Selzer, D.; Schwab, M.; Teutonico, D.; Frechen, S.; van der Lee, M.; Moes, D. J. A. R.; Swen, J. J.; Lehr, T. Physiologically based pharmacokinetic modeling of tacrolimus for food–drug and CYP₃A drug–drug–gene interaction predictions. *CPT: Pharmacometrics and Systems Pharmacology* **2023**, *12*, 724–738, DOI: [10.1002/psp4.12946](https://doi.org/10.1002/psp4.12946).
2. Loer, H. L. H.; Kovar, C.; Rüdesheim, S.; Marok, F. Z.; Fuhr, L. M.; Selzer, D.; Schwab, M.; Lehr, T. Physiologically based pharmacokinetic modeling of imatinib and N-desmethyl imatinib for drug–drug interaction predictions. *CPT: Pharmacometrics and Systems Pharmacology* **2024**, *13*, 926–940, DOI: [10.1002/psp4.13127](https://doi.org/10.1002/psp4.13127).
3. Kovar, C.; Loer, H. L. H.; Rüdesheim, S.; Fuhr, L. M.; Marok, F. Z.; Selzer, D.; Schwab, M.; Lehr, T. A physiologically-based pharmacokinetic precision dosing approach to manage dasatinib drug–drug interactions. *CPT: Pharmacometrics and Systems Pharmacology* **2024**, *13*, 1144–1159, DOI: [10.1002/psp4.13146](https://doi.org/10.1002/psp4.13146).
4. Rüdesheim, S.; Loer, H. L. H.; Feick, D.; Marok, F. Z.; Fuhr, L. M.; Selzer, D.; Teutonico, D.; Schneider, A. R. P.; Solodenko, J.; Frechen, S.; van der Lee, M.; Moes, D. J. A. R.; Swen, J. J.; Schwab, M.; Lehr, T. A comprehensive CYP₂D₆ drug–drug–gene interaction network for application in precision dosing and drug development. *Clinical Pharmacology & Therapeutics* **2025**, *117*, 1718–1731, DOI: [10.1002/cpt.3604](https://doi.org/10.1002/cpt.3604).
5. Brand, A.; Allen, L.; Altman, M.; Hlava, M.; Scott, J. Beyond authorship: Attribution, contribution, collaboration, and credit. *Learned Publishing* **2015**, *28*, 151–155, DOI: [10.1087/20150211](https://doi.org/10.1087/20150211).
6. Chan, I. S.; Ginsburg, G. S. Personalized medicine: Progress and promise. *Annual Review of Genomics and Human Genetics* **2011**, *12*, 217–244, DOI: [10.1146/annurev-genom-082410-101446](https://doi.org/10.1146/annurev-genom-082410-101446).
7. Lehrach, H. Virtual clinical trials, an essential step in increasing the effectiveness of the drug development process. *Public Health Genomics* **2015**, *18*, 366–371, DOI: [10.1159/000441553](https://doi.org/10.1159/000441553).
8. Spear, B. B.; Heath-Chiozzi, M.; Huff, J. Clinical application of pharmacogenetics. *Trends in Molecular Medicine* **2001**, *7*, 201–204, DOI: [10.1016/S1471-4914\(01\)01986-4](https://doi.org/10.1016/S1471-4914(01)01986-4).
9. Mo, H.; Denny, J. C. The U.S. National Library of Medicine’s impact on precision and genomic medicine. *Information Services and Use* **2022**, *42*, 71–80, DOI: [10.3233/ISU-210144](https://doi.org/10.3233/ISU-210144).

10. Gonzalez, D.; Rao, G. G.; Bailey, S. C.; Brouwer, K. L.; Cao, Y.; Crona, D. J.; Kashuba, A. D.; Lee, C. R.; Morbitzer, K.; Patterson, J. H.; Wiltshire, T.; Easter, J.; Savage, S. W.; Powell, J. R. Precision dosing: Public health need, proposed framework, and anticipated impact. *Clinical and Translational Science* **2017**, *10*, 443–454, DOI: [10.1111/cts.12490](https://doi.org/10.1111/cts.12490).
11. Peck, R. W. Precision medicine is not just genomics: The right dose for every patient. *Annual Review of Pharmacology and Toxicology* **2018**, *58*, 105–122, DOI: [10.1146/annurev-pharmtox-010617-052446](https://doi.org/10.1146/annurev-pharmtox-010617-052446).
12. Verbeurgt, P.; Mamiya, T.; Oesterheld, J. How common are drug and gene interactions? Prevalence in a sample of 1143 patients with CYP2C9, CYP2C19 and CYP2D6 genotyping. *Pharmacogenomics* **2014**, *15*, 655–665, DOI: [10.2217/pgs.14.6](https://doi.org/10.2217/pgs.14.6).
13. Cacabelos, R.; Cacabelos, N.; Carril, J. C. The role of pharmacogenomics in adverse drug reactions. *Expert Review of Clinical Pharmacology* **2019**, *12*, 407–442, DOI: [10.1080/17512433.2019.1597706](https://doi.org/10.1080/17512433.2019.1597706).
14. Cruciol-Souza, J. M.; Thomson, J. C. Prevalence of potential drug-drug interactions and its associated factors in a Brazilian teaching hospital. *Journal of Pharmacy and Pharmaceutical Sciences* **2006**, *9*, 427–433.
15. Sánchez Muñoz-Torrero, J. F.; Barquilla, P.; Velasco, R.; Fernández Capitan, M. D. C.; Pacheco, N.; Vicente, L.; Chicón, J. L.; Trejo, S.; Zamorano, J.; Lorenzo Hernandez, A. Adverse drug reactions in internal medicine units and associated risk factors. *European Journal of Clinical Pharmacology* **2010**, *66*, 1257–1264, DOI: [10.1007/s00228-010-0866-6](https://doi.org/10.1007/s00228-010-0866-6).
16. Clark, L. T.; Watkins, L.; Piña, I. L.; Elmer, M.; Akinboboye, O.; Gorham, M.; Jamerson, B.; McCullough, C.; Pierre, C.; Polis, A. B.; Puckrein, G.; Regnante, J. M. Increasing diversity in clinical trials: Overcoming critical barriers. *Current Problems in Cardiology* **2019**, *44*, 148–172, DOI: [10.1016/j.cpcardiol.2018.11.002](https://doi.org/10.1016/j.cpcardiol.2018.11.002).
17. Tornio, A.; Filppula, A. M.; Niemi, M.; Backman, J. T. Clinical studies on drug–drug interactions involving metabolism and transport: methodology, pitfalls, and interpretation. *Clinical Pharmacology and Therapeutics* **2019**, *105*, 1345–1361, DOI: [10.1002/cpt.1435](https://doi.org/10.1002/cpt.1435).
18. Wojtyniak, J.-G.; Selzer, D.; Schwab, M.; Lehr, T. Physiologically based precision dosing approach for drug-drug-gene interactions: A simvastatin network analysis. *Clinical Pharmacology and Therapeutics* **2021**, *109*, 201–211, DOI: [10.1002/cpt.2111](https://doi.org/10.1002/cpt.2111).
19. Bowlin, S. J.; Xia, F.; Wang, W.; Robinson, K. D.; Stanek, E. J. Twelve-month frequency of drug-metabolizing enzyme and transporter-based drug-drug interaction potential in patients receiving oral enzyme-targeted kinase inhibitor antineoplastic agents. *Mayo Clinic Proceedings* **2013**, *88*, 139–148, DOI: [10.1016/j.mayocp.2012.10.020](https://doi.org/10.1016/j.mayocp.2012.10.020).

20. Türk, D.; Fuhr, L. M.; Marok, F. Z.; Rüdesheim, S.; Kühn, A.; Selzer, D.; Schwab, M.; Lehr, T. Novel models for the prediction of drug–gene interactions. *Expert Opinion on Drug Metabolism & Toxicology* **2021**, *17*, 1293–1310, DOI: [10.1080/17425255.2021.1998455](https://doi.org/10.1080/17425255.2021.1998455).
21. Emoto, C.; McPhail, B. T.; Fukuda, T. Clinical applications of physiologically based pharmacokinetic modeling: Perspectives on the advantages and challenges. *Therapeutic Drug Monitoring* **2020**, *42*, 157–158, DOI: [10.1097/FTD.0000000000000714](https://doi.org/10.1097/FTD.0000000000000714).
22. Türk, D.; Hanke, N.; Wolf, S.; Frechen, S.; Eissing, T.; Wendl, T.; Schwab, M.; Lehr, T. Physiologically based pharmacokinetic models for prediction of complex CYP2C8 and OATP1B1 (SLCO1B1) drug–drug–gene interactions: A modeling network of gemfibrozil, repaglinide, pioglitazone, rifampicin, clarithromycin and itraconazole. *Clinical Pharmacokinetics* **2019**, *58*, 1595–1607, DOI: [10.1007/s40262-019-00777-x](https://doi.org/10.1007/s40262-019-00777-x).
23. US Food and Drug Administration. Clinical drug interaction studies – Cytochrome P450 enzyme- and transporter-mediated drug interactions – Guidance for industry. https://www.google.com/url?sa=t&source=web&rct=j&opi=89978449&url=https://downloads.regulations.gov/FDA-2017-D-5961-0023/attachment_1.pdf&ved=2ahUKEwjbtTBwMwMxWs9AIHHVjZJUEQFnoECCAQAQ&usq=A0vVaw0tP2nvTXZo2irr0ippH80k (accessed 08/15/2024).
24. Polasek, T. M.; Tucker, G. T.; Sorich, M. J.; Wiese, M. D.; Mohan, T.; Rostami-Hodjegan, A.; Korprasertthaworn, P.; Perera, V.; Rowland, A. Prediction of olanzapine exposure in individual patients using physiologically based pharmacokinetic modelling and simulation. *British Journal of Clinical Pharmacology* **2018**, *84*, 462–476, DOI: [10.1111/bcp.13480](https://doi.org/10.1111/bcp.13480).
25. Tyson, R. J.; Park, C. C.; Powell, J. R.; Patterson, J. H.; Weiner, D.; Watkins, P. B.; Gonzalez, D. Precision dosing priority criteria: Drug, disease, and patient population variables. *Frontiers in Pharmacology* **2020**, *11*, 420, DOI: [10.3389/fphar.2020.00420](https://doi.org/10.3389/fphar.2020.00420).
26. Darwich, A. S.; Ogungbenro, K.; Vinks, A. A.; Powell, J. R.; Reny, J. L.; Marsousi, N.; Daali, Y.; Fairman, D.; Cook, J.; Lesko, L. J.; McCune, J. S.; Knibbe, C. A.; de Wildt, S. N.; Leeder, J. S.; Neely, M.; Zuppa, A. F.; Vicini, P.; Aarons, L.; Johnson, T. N.; Boiani, J.; Rostami-Hodjegan, A. Why has model-informed precision dosing not yet become common clinical reality? Lessons from the past and a roadmap for the future. *Clinical Pharmacology and Therapeutics* **2017**, *101*, 646–656, DOI: [10.1002/cpt.659](https://doi.org/10.1002/cpt.659).
27. Burns, M. Management of narrow therapeutic index drugs. *Journal of Thrombosis and Thrombolysis* **1999**, *7*, 137–143, DOI: [10.1023/A:1008829403320](https://doi.org/10.1023/A:1008829403320).

28. Groenland, S. L.; Mathijssen, R. H.; Beijnen, J. H.; Huitema, A. D.; Steeghs, N. Individualized dosing of oral targeted therapies in oncology is crucial in the era of precision medicine. *European Journal of Clinical Pharmacology* **2019**, *75*, 1309–1318, DOI: [10.1007/s00228-019-02704-2](https://doi.org/10.1007/s00228-019-02704-2).
29. Scavone, C.; Di Mauro, G.; Mascolo, A.; Berrino, L.; Rossi, F.; Capuano, A. The new paradigms in clinical research: From early access programs to the novel therapeutic approaches for unmet medical needs. *Frontiers in Pharmacology* **2019**, *10*, 111, DOI: [10.3389/fphar.2019.00111](https://doi.org/10.3389/fphar.2019.00111).
30. Punt, C. J. A.; Koopman, M.; Vermeulen, L. From tumour heterogeneity to advances in precision treatment of colorectal cancer. *Nature Reviews Clinical Oncology* **2017**, *14*, 235–246, DOI: [10.1038/nrclinonc.2016.171](https://doi.org/10.1038/nrclinonc.2016.171).
31. Schwartz, J. B. The current state of knowledge on age, sex, and their interactions on clinical pharmacology. *Clinical Pharmacology and Therapeutics* **2007**, *82*, 87–96, DOI: [10.1038/sj.clpt.6100226](https://doi.org/10.1038/sj.clpt.6100226).
32. Spong, C. Y.; Bianchi, D. W. Improving public health requires inclusion of underrepresented populations in research. *JAMA - Journal of the American Medical Association* **2018**, *319*, 337–338, DOI: [10.1001/jama.2017.19138](https://doi.org/10.1001/jama.2017.19138).
33. Daly, A. K. Pharmacogenetics and human genetic polymorphisms. *Biochemical Journal* **2010**, *429*, 435–449, DOI: [10.1042/BJ20100522](https://doi.org/10.1042/BJ20100522).
34. Ingelman-Sundberg, M.; Sim, S. C.; Gomez, A.; Rodriguez-Antona, C. Influence of cytochrome P450 polymorphisms on drug therapies: Pharmacogenetic, pharmacoepigenetic and clinical aspects. *Pharmacology and Therapeutics* **2007**, *116*, 496–526, DOI: [10.1016/j.pharmthera.2007.09.004](https://doi.org/10.1016/j.pharmthera.2007.09.004).
35. Rendic, S.; Guengerich, F. P. Survey of human oxidoreductases and cytochrome P450 enzymes involved in the metabolism of xenobiotic and natural chemicals. *Chemical Research in Toxicology* **2015**, *28*, 38–42, DOI: [10.1021/tx500444e](https://doi.org/10.1021/tx500444e).
36. Zanger, U. M.; Schwab, M. Cytochrome P450 enzymes in drug metabolism: Regulation of gene expression, enzyme activities, and impact of genetic variation. *Pharmacology and Therapeutics* **2013**, *138*, 103–141, DOI: [10.1016/j.pharmthera.2012.12.007](https://doi.org/10.1016/j.pharmthera.2012.12.007).
37. Pharmacogene Variation Consortium (PharmVar). Gaedigk et al. 2021, CPT 110:542-545 (PMID 34091888), Gaedigk et al. 2020, CPT 107:43-46 (PMID 31758698), Gaedigk et al 2019, CPT 105:29-32, and Gaedigk et al. 2018, CPT 103(3):399-401 (PMID 29134625), www.PharmVar.org (accessed 08/21/2024).

38. Santos, M.; Niemi, M.; Hiratsuka, M.; Kumondai, M.; Ingelman-Sundberg, M.; Lauschke, V. M.; Rodríguez-Antona, C. Novel copy-number variations in pharmacogenes contribute to interindividual differences in drug pharmacokinetics. *Genetics in Medicine* **2018**, *20*, 622–629, DOI: [10.1038/gim.2017.156](https://doi.org/10.1038/gim.2017.156).
39. Sehn, J. K. In *Clinical Genomics*, 2015; Chapter "Insertions and deletions (indels)", pp 129–150, DOI: [10.1016/B978-0-12-404748-8.00009-5](https://doi.org/10.1016/B978-0-12-404748-8.00009-5).
40. Stranger, B. E.; Forrest, M. S.; Dunning, M.; Ingle, C. E.; Beazlsy, C.; Thorne, N.; Redon, R.; Bird, C. P.; De Grassi, A.; Lee, C.; Tyler-Smith, C.; Carter, N.; Scherer, S. W.; Tavaré, S.; Deloukas, P.; Hurles, M. E.; Dermitzakis, E. T. Relative impact of nucleotide and copy number variation on gene expression phenotypes. *Science* **2007**, *315*, 848–853, DOI: [10.1126/science.1136678](https://doi.org/10.1126/science.1136678).
41. Redon, R.; Ishikawa, S.; Fitch, K. R.; Feuk, L.; Perry, G. H.; Andrews, T. D.; Fiegler, H.; Shapero, M. H.; Carson, A. R.; Chen, W.; Cho, E. K.; Dallaire, S.; Freeman, J. L.; Juan, R.; Gratacos, M.; Huang, J.; Kalaitzopoulos, D.; Komura, D.; Okamura, K.; Shen, F.; Somerville, M. J.; Tchinda, J. Global variation in copy number in the human genome. *Nature* **2009**, *444*, 444–454, DOI: [10.1038/nature05329](https://doi.org/10.1038/nature05329).
42. Hicks, J. K.; Bishop, J. R.; Sangkuhl, K.; Müller, D. J.; Ji, Y.; Leckband, S. G.; Leeder, J. S.; Graham, R. L.; Chiulli, D. L.; Llerena, A.; Skaar, T. C.; Scott, S. A.; Stingl, J. C.; Klein, T. E.; Caudle, K. E.; Gaedigk, A. Clinical Pharmacogenetics Implementation Consortium (CPIC) guideline for CYP2D6 and CYP2C19 genotypes and dosing of selective serotonin reuptake inhibitors. *Clinical Pharmacology and Therapeutics* **2015**, *98*, 127–134, DOI: [10.1002/cpt.147](https://doi.org/10.1002/cpt.147).
43. Birdwell, K. A.; Decker, B.; Barbarino, J. M.; Peterson, J. F.; Stein, C. M.; Sadee, W.; Wang, D.; Vinks, A. A.; He, Y.; Swen, J. J.; Leeder, J. S.; Van Schaik, R. H.; Thummel, K. E.; Klein, T. E.; Caudle, K. E.; MacPhee, I. A. Clinical Pharmacogenetics Implementation Consortium (CPIC) guidelines for CYP3A5 genotype and tacrolimus dosing. *Clinical Pharmacology and Therapeutics* **2015**, *98*, 19–24, DOI: [10.1002/cpt.113](https://doi.org/10.1002/cpt.113).
44. Scott, S. A.; Sangkuhl, K.; Gardner, E. E.; Stein, C. M.; Hulot, J. S.; Johnson, J. A.; Roden, D. M.; Klein, T. E.; Shuldiner, A. R. Clinical Pharmacogenetics Implementation Consortium guidelines for cytochrome P450-2C19 (CYP2C19) genotype and clopidogrel therapy. *Clinical Pharmacology and Therapeutics* **2011**, *90*, 328–332, DOI: [10.1038/clpt.2011.132](https://doi.org/10.1038/clpt.2011.132).
45. Caudle, K. E.; Dunnenberger, H. M.; Freimuth, R. R.; Peterson, J. F.; Burlison, J. D.; Whirl-Carrillo, M.; Scott, S. A.; Rehm, H. L.; Williams, M. S.; Klein, T. E.; Relling, M. V.; Hoffman, J. M. Standardizing terms for clinical pharmacogenetic test results: Consensus terms from the Clinical Pharmacogenetics Implementation Consortium (CPIC). *Genetics in Medicine* **2017**, *19*, 215–223, DOI: [10.1038/gim.2016.87](https://doi.org/10.1038/gim.2016.87).

46. Swen, J. J.; Wilting, I.; de Goede, A. L.; Grandia, L.; Mulder, H.; Touw, D. J.; Boer, A. D.; Conemans, J. M.; Egberts, T. C.; Klungel, O. H.; Koopmans, R.; Weide, J. V. D.; Wilffert, B.; Guchelaar, H. J.; Deneer, V. H. Pharmacogenetics: From bench to byte. *Clinical Pharmacology and Therapeutics* **2008**, *83*, 781–787, DOI: [10.1038/sj.clpt.6100507](https://doi.org/10.1038/sj.clpt.6100507).
47. Swen, J. J.; Nijenhuis, M.; De Boer, A.; Grandia, L.; Maitland-Van Der Zee, A. H.; Mulder, H.; Rongen, G. A.; Van Schaik, R. H.; Schalekamp, T.; Touw, D. J.; Van Der Weide, J.; Wilffert, B.; Deneer, V. H.; Guchelaar, H. J. Pharmacogenetics: From bench to byte - an update of guidelines. *Clinical Pharmacology and Therapeutics* **2011**, *89*, 662–673, DOI: [10.1038/clpt.2011.34](https://doi.org/10.1038/clpt.2011.34).
48. Barbarino, J. M.; Whirl-Carrillo, M.; Altman, R. B.; Klein, T. E. PharmGKB: A worldwide resource for pharmacogenomic information. *Wiley Interdisciplinary Reviews: Systems Biology and Medicine* **2018**, *10*, e1417, DOI: [10.1002/wsbm.1417](https://doi.org/10.1002/wsbm.1417).
49. Whirl-Carrillo, M.; Huddart, R.; Gong, L.; Sangkuhl, K.; Thorn, C. F.; Whaley, R.; Klein, T. E. An evidence-based framework for evaluating pharmacogenomics knowledge for personalized medicine. *Clinical Pharmacology and Therapeutics* **2021**, *110*, 563–572, DOI: [10.1002/cpt.2350](https://doi.org/10.1002/cpt.2350).
50. Dunnenberger, H. M.; Crews, K. R.; Hoffman, J. M.; Caudle, K. E.; Broeckel, U.; Howard, S. C.; Hunkler, R. J.; Klein, T. E.; Evans, W. E.; Relling, M. V. Preemptive clinical pharmacogenetics implementation: Current programs in five US medical centers. *Annual Review of Pharmacology and Toxicology* **2015**, *55*, 89–106, DOI: [10.1146/annurev-pharmtox-010814-124835](https://doi.org/10.1146/annurev-pharmtox-010814-124835).
51. Ohtsuki, S.; Schaefer, O.; Kawakami, H.; Inoue, T.; Liehner, S.; Saito, A.; Ishiguro, N.; Kishimoto, W.; Ludwig-Schwellinger, E.; Ebner, T.; Terasaki, T. Simultaneous absolute protein quantification of transporters, cytochromes P450, and UDP-glucuronosyltransferases as a novel approach for the characterization of individual human liver: Comparison with mRNA levels and activities. *Drug Metabolism and Disposition* **2012**, *40*, 83–92, DOI: [10.1124/dmd.111.042259](https://doi.org/10.1124/dmd.111.042259).
52. Kuehl, P.; Zhang, J.; Lin, Y.; Lamba, J.; Assem, M.; Schuetz, J.; Watkins, P. B.; Daly, A.; Wrighton, S. A.; Hall, S. D.; Maurel, P.; Relling, M.; Brimer, C.; Yasuda, K.; Venkataramanan, R.; Strom, S.; Thummel, K.; Boguski, M. S.; Schuetz, E. Sequence diversity in CYP3A promoters and characterization of the genetic basis of polymorphic CYP3A5 expression. *Nature Genetics* **2001**, *27*, 383–391, DOI: [10.1038/86882](https://doi.org/10.1038/86882).
53. Chen, L.; Prasad, G. V. CYP3A5 polymorphisms in renal transplant recipients: Influence on tacrolimus treatment. *Pharmacogenomics and Personalized Medicine* **2018**, *11*, 23–33, DOI: [10.2147/PGPM.S107710](https://doi.org/10.2147/PGPM.S107710).

54. Bains, R. K.; Kovacevic, M.; Plaster, C. A.; Tarekegn, A.; Bekele, E.; Bradman, N. N.; Thomas, M. G. Molecular diversity and population structure at the cytochrome P450 3A5 gene in Africa. *BMC Genetics* **2013**, *14*, 34, DOI: [10.1186/1471-2156-14-34](https://doi.org/10.1186/1471-2156-14-34).
55. Jin, Y.; Wang, Y. H.; Miao, J.; Li, L.; Kovacs, R. J.; Marunde, R.; Hamman, M. A.; Phillips, S.; Hilligoss, J.; Hall, S. D. Cytochrome P450 3A5 genotype is associated with verapamil response in healthy subjects. *Clinical Pharmacology and Therapeutics* **2007**, *82*, 579–585, DOI: [10.1038/sj.clpt.6100208](https://doi.org/10.1038/sj.clpt.6100208).
56. Mancinelli, L. M.; Frassetto, L.; Floren, L. C.; Dressler, D.; Carrier, S.; Bekersky, I.; Benet, L. Z.; Christians, U. The pharmacokinetics and metabolic disposition of tacrolimus: A comparison across ethnic groups. *Clinical Pharmacology and Therapeutics* **2001**, *69*, 24–31, DOI: [10.1067/mcp.2001.113183](https://doi.org/10.1067/mcp.2001.113183).
57. Zheng, S.; Tasnif, Y.; Hebert, M. F.; Davis, C. L.; Shitara, Y.; Calamia, J. C.; Lin, Y. S.; Shen, D. D.; Thummel, K. E. Measurement and compartmental modeling of the effect of CYP3A5 gene variation on systemic and intrarenal tacrolimus disposition. *Clinical Pharmacology and Therapeutics* **2012**, *92*, 737–745, DOI: [10.1038/clpt.2012.175](https://doi.org/10.1038/clpt.2012.175).
58. Zhou, Y.; Ingelman-Sundberg, M.; Lauschke, V. M. Worldwide distribution of cytochrome P450 alleles: A meta-analysis of population-scale sequencing projects. *Clinical Pharmacology and Therapeutics* **2017**, *102*, 688–700, DOI: [10.1002/cpt.690](https://doi.org/10.1002/cpt.690).
59. Wang, D.; Guo, Y.; Wrighton, S. A.; Cooke, G. E.; Sadee, W. Intronic polymorphism in CYP3A4 affects hepatic expression and response to statin drugs. *Pharmacogenomics J.* **2011**, *11*, 274–286, DOI: [10.1038/tpj.2010.28](https://doi.org/10.1038/tpj.2010.28).
60. Mulder, T. A.; van Eerden, R. A.; de With, M.; Elens, L.; Hesselink, D. A.; Matic, M.; Bins, S.; Mathijssen, R. H.; van Schaik, R. H. CYP3A4*22 genotyping in clinical practice: Ready for implementation? *Frontiers in Genetics* **2021**, *12*, 711943, DOI: [10.3389/fgene.2021.711943](https://doi.org/10.3389/fgene.2021.711943).
61. Wojnowski, L.; Kamdem, L. K. Clinical implications of CYP3A polymorphisms. *Expert Opinion on Drug Metabolism and Toxicology* **2006**, *2*, 171–182, DOI: [10.1517/17425255.2.2.171](https://doi.org/10.1517/17425255.2.2.171).
62. Gaedigk, A.; Simon, S. D.; Pearce, R. E.; Bradford, L. D.; Kennedy, M. J.; Leeder, J. S. The CYP2D6 activity score: Translating genotype information into a qualitative measure of phenotype. *Clinical Pharmacology and Therapeutics* **2008**, *83*, 234–242, DOI: [10.1038/sj.clpt.6100406](https://doi.org/10.1038/sj.clpt.6100406).
63. Caudle, K. E.; Sangkuhl, K.; Whirl-Carrillo, M.; Swen, J. J.; Haidar, C. E.; Klein, T. E.; Gammal, R. S.; Relling, M. V.; Scott, S. A.; Hertz, D. L.; Guchelaar, H. J.; Gaedigk, A. Standardizing CYP2D6 genotype to phenotype translation: Consensus recommendations from the Clinical Pharmacogenetics Implementation Consortium and Dutch

- Pharmacogenetics Working Group. *Clinical and Translational Science* **2020**, *13*, 116–124, DOI: [10.1111/cts.12692](https://doi.org/10.1111/cts.12692).
64. Sistonen, J.; Sajantila, A.; Lao, O.; Corander, J.; Barbujani, G.; Fuselli, S. CYP2D6 worldwide genetic variation shows high frequency of altered activity variants and no continental structure. *Pharmacogenetics and Genomics* **2007**, *17*, 93–101, DOI: [10.1097/01.fpc.0000239974.69464.f2](https://doi.org/10.1097/01.fpc.0000239974.69464.f2).
 65. Novalbos, J.; López-Rodríguez, R.; Román, M.; Gallego-Sandín, S.; Ochoa, D.; Abad-Santos, F. Effects of CYP2D6 genotype on the pharmacokinetics, pharmacodynamics, and safety of risperidone in healthy volunteers. *Journal of Clinical Psychopharmacology* **2010**, *30*, 504–511, DOI: [10.1097/JCP.0b013e3181ee84c7](https://doi.org/10.1097/JCP.0b013e3181ee84c7).
 66. Seeringer, A.; Brockmöller, J.; Bauer, S.; Kirchheiner, J. Enantiospecific pharmacokinetics of metoprolol in CYP2D6 ultra-rapid metabolizers and correlation with exercise-induced heart rate. *European Journal of Clinical Pharmacology* **2008**, *64*, 883–888, DOI: [10.1007/s00228-008-0504-8](https://doi.org/10.1007/s00228-008-0504-8).
 67. Cascorbi, I. Drug interactions-principles, examples and clinical consequences. *Deutsches Arzteblatt International* **2012**, *109*, 546–555, DOI: [10.3238/arztebl.2012.0546](https://doi.org/10.3238/arztebl.2012.0546).
 68. Palleria, C.; Di Paolo, A.; Giofrè, C.; Caglioti, C.; Leuzzi, G.; Siniscalchi, A.; De Sarro, G.; Gallelli, L. Pharmacokinetic drug-drug interaction and their implication in clinical management. *Journal of Research in Medical Sciences* **2013**, *18*, 601–610.
 69. Deodhar, M.; Al Rihani, S. B.; Arwood, M. J.; Darakjian, L.; Dow, P.; Turgeon, J.; Michaud, V. Mechanisms of CYP450 inhibition: Understanding drug-drug interactions due to mechanism-based inhibition in clinical practice. *Pharmaceutics* **2020**, *12*, 846, DOI: [10.3390/pharmaceutics12090846](https://doi.org/10.3390/pharmaceutics12090846).
 70. Peng, Y.; Cheng, Z.; Xie, F. Evaluation of pharmacokinetic drug-drug interactions: A review of the mechanisms, in vitro and in silico approaches. *Metabolites* **2021**, *11*, 75, DOI: [10.3390/metabo11020075](https://doi.org/10.3390/metabo11020075).
 71. Gessner, A.; König, J.; Fromm, M. F. Clinical aspects of transporter-mediated drug–drug interactions. *Clinical Pharmacology and Therapeutics* **2019**, *105*, 1386–1394, DOI: [10.1002/cpt.1360](https://doi.org/10.1002/cpt.1360).
 72. International Transporter Consortium; Giacomini, K.; Huang, S.-M.; Tweedie, D. J.; Benet, L. Z.; Brouwer, K. L. R.; Chu, X.; Dahlin, A.; Evers, R.; Fischer, V.; Hillgren, K. M.; Hoffmaster, K. A.; Ishikawa, T.; Keppler, D.; Kim, R. B.; Lee, C. A.; Niemi, M.; Polli, J. W.; Sugiyama, Y.; Swaan, P. W.; Ware, J. A.; Wright, S. H.; Yee, S. W.; Zamek-Gliszczynski, M. J.; Zhang, L. Membrane transporters in drug development. *Nat Rev Drug Discov* **2010**, *9*, 215–236, DOI: [10.1038/nrd3028](https://doi.org/10.1038/nrd3028).

73. Zhang, L.; Huang, S. M.; Reynolds, K.; Madabushi, R.; Zineh, I. Transporters in drug development: Scientific and regulatory considerations. *Clinical Pharmacology and Therapeutics* **2018**, *104*, 793–796, DOI: [10.1002/cpt.1214](https://doi.org/10.1002/cpt.1214).
74. Deng, J.; Zhu, X.; Chen, Z.; Fan, C. H.; Kwan, H. S.; Wong, C. H.; Shek, K. Y.; Zuo, Z.; Lam, T. N. A review of food–drug interactions on oral drug absorption. *Drugs* **2017**, *77*, 1833–1855, DOI: [10.1007/s40265-017-0832-z](https://doi.org/10.1007/s40265-017-0832-z).
75. US Food and Drug Administration. Table of substrates, inhibitors and inducers. <https://www.fda.gov/drugs/drug-interactions-labeling/drug-development-and-drug-interactions-table-substrates-inhibitors-and-inducers> (accessed 09/08/2024).
76. US Food and Drug Administration. FDA’s examples of drugs that interact with CYP enzymes and transporter systems. <https://www.fda.gov/drugs/drug-interactions-labeling/healthcare-professionals-fdas-examples-drugs-interact-cyp-enzymes-and-transporter-systems> (accessed 09/08/2024).
77. Pelkonen, O.; Turpeinen, M.; Hakkola, J.; Honkakoski, P.; Hukkanen, J.; Raunio, H. Inhibition and induction of human cytochrome P450 enzymes: Current status. *Archives of Toxicology* **2008**, *82*, 667–715, DOI: [10.1007/s00204-008-0332-8](https://doi.org/10.1007/s00204-008-0332-8).
78. Tompkins, L. M.; Wallace, A. D. Mechanisms of cytochrome P450 induction. *Journal of Biochemical and Molecular Toxicology* **2007**, *21*, 176–181, DOI: [10.1002/jbt.20180](https://doi.org/10.1002/jbt.20180).
79. Chang, T. K.; Waxman, D. J. Synthetic drugs and natural products as modulators of constitutive androstane receptor (CAR) and pregnane X receptor (PXR). *Drug Metabolism Reviews* **2006**, *38*, 51–73, DOI: [10.1080/03602530600569828](https://doi.org/10.1080/03602530600569828).
80. Chai, X.; Zeng, S.; Xie, W. Nuclear receptors PXR and CAR: Implications for drug metabolism regulation, pharmacogenomics and beyond. *Expert Opinion on Drug Metabolism and Toxicology* **2013**, *9*, 253–266, DOI: [10.1517/17425255.2013.754010](https://doi.org/10.1517/17425255.2013.754010).
81. Bolton, A. E.; Peng, B.; Hubert, M.; Krebs-Brown, A.; Capdeville, R.; Keller, U.; Seiberling, M. Effect of rifampicin on the pharmacokinetics of imatinib mesylate (Gleevec, STI571) in healthy subjects. *Cancer Chemotherapy and Pharmacology* **2004**, *53*, 102–106, DOI: [10.1007/s00280-003-0722-9](https://doi.org/10.1007/s00280-003-0722-9).
82. Roskoski, R. J. Properties of FDA-approved small molecule protein kinase inhibitors: A 2023 update. *Pharmacological Research* **2023**, *187*, 106552, DOI: [10.1016/j.phrs.2022.106552](https://doi.org/10.1016/j.phrs.2022.106552).

83. Reitman, M. L.; Chu, X.; Cai, X.; Yabut, J.; Venkatasubramanian, R.; Zajic, S.; Stone, J. A.; Ding, Y.; Witter, R.; Gibson, C.; Roupe, K.; Evers, R.; Wagner, J. A.; Stoch, A. Rifampin's acute inhibitory and chronic inductive drug interactions: Experimental and model-based approaches to drug-drug interaction trial design. *Clinical Pharmacology and Therapeutics* **2011**, *89*, 234–242, DOI: [10.1038/clpt.2010.271](https://doi.org/10.1038/clpt.2010.271).
84. Willson, T. M.; Kliewer, S. A. PXR, CAR and drug metabolism. *Nature Reviews Drug Discovery* **2002**, *1*, 259–266, DOI: [10.1038/nrd753](https://doi.org/10.1038/nrd753).
85. Vanhove, T.; Annaert, P.; Knops, N.; de Loor, H.; de Hoon, J.; Kuypers, D. R. In vivo CYP3A4 activity does not predict the magnitude of interaction between itraconazole and tacrolimus from an extended release formulation. *Basic and Clinical Pharmacology and Toxicology* **2019**, *124*, 50–55, DOI: [10.1111/bcpt.13092](https://doi.org/10.1111/bcpt.13092).
86. Nichols, A. I.; Fatato, P.; Shenouda, M.; Paul, J.; Isler, J. A.; Pedersen, R. D.; Jiang, Q.; Ahmed, S.; Patroneva, A. The effects of desvenlafaxine and paroxetine on the pharmacokinetics of the cytochrome P450 2D6 substrate desipramine in healthy adults. *Journal of Clinical Pharmacology* **2009**, *49*, 219–228, DOI: [10.1177/0091270008326716](https://doi.org/10.1177/0091270008326716).
87. Orr, S. T.; Ripp, S. L.; Ballard, T. E.; Henderson, J. L.; Scott, D. O.; Obach, R. S.; Sun, H.; Kalgutkar, A. S. Mechanism-based inactivation (MBI) of cytochrome P450 enzymes: Structure-activity relationships and discovery strategies to mitigate drug-drug interaction risks. *Journal of Medicinal Chemistry* **2012**, *55*, 4896–4933, DOI: [10.1021/jm300065h](https://doi.org/10.1021/jm300065h).
88. Tornio, A.; Niemi, M.; Neuvonen, M.; Laitila, J.; Kalliokoski, A.; Neuvonen, P. J.; Backman, J. T. The effect of gemfibrozil on repaglinide pharmacokinetics persists for at least 12 h after the dose: Evidence for mechanism-based inhibition of CYP2C8 in vivo. *Clinical Pharmacology and Therapeutics* **2008**, *84*, 403–411, DOI: [10.1038/clpt.2008.34](https://doi.org/10.1038/clpt.2008.34).
89. Brunet, M.; Van Gelder, T.; Åsberg, A.; Haufroid, V.; Hesselink, D. A.; Langman, L.; Lemaitre, F.; Marquet, P.; Seger, C.; Shipkova, M.; Vinks, A.; Wallemacq, P.; Wieland, E.; Woillard, J. B.; Barten, M. J.; Budde, K.; Colom, H.; Dieterlen, M. T.; Elens, L.; Johnson-Davis, K. L.; Kunicki, P. K.; Macphee, I.; Masuda, S.; Mathew, B. S.; Millán, O.; Mizuno, T.; Moes, D. J. A.; Monchaud, C.; Noceti, O.; Pawinski, T.; Picard, N.; Van Schaik, R.; Sommerer, C.; Vethe, N. T.; De Winter, B.; Christians, U.; Bergan, S. Therapeutic drug monitoring of tacrolimus-personalized therapy: Second consensus report. *Therapeutic Drug Monitoring* **2019**, *41*, 261–307, DOI: [10.1097/FTD.0000000000000640](https://doi.org/10.1097/FTD.0000000000000640).
90. Taylor, D.; Poulou, S.; Clark, I. The cardiovascular safety of tricyclic antidepressants in overdose and in clinical use. *Therapeutic Advances in Psychopharmacology* **2024**, *14*, 20451253241243297, DOI: [10.1177/20451253241243297](https://doi.org/10.1177/20451253241243297).

91. Filppula, A. M.; Laitila, J.; Neuvonen, P. J.; Backman, J. T. Potent mechanism-based inhibition of CYP_{3A4} by imatinib explains its liability to interact with CYP_{3A4} substrates. *British Journal of Pharmacology* **2012**, *165*, 2787–2798, DOI: [10.1111/j.1476-5381.2011.01732.x](https://doi.org/10.1111/j.1476-5381.2011.01732.x).
92. Filppula, A. M.; Neuvonen, M.; Laitila, J.; Neuvonen, P. J.; Backman, J. T. Autoinhibition of CYP_{3A4} leads to important role of CYP_{2C8} in imatinib metabolism: Variability in CYP_{2C8} activity may alter plasma concentrations and response. *Drug Metabolism and Disposition* **2013**, *41*, 50–59, DOI: [10.1124/dmd.112.048017](https://doi.org/10.1124/dmd.112.048017).
93. Mürdter, T. Impact of CYP_{2D6} genotype and co-medication with paroxetine and clarithromycin on clomiphen metabolism in vivo. *Abstracts of the 82nd Annual Meeting of the German Society for Experimental and Clinical Pharmacology and Toxicology (DGPT) in Naunyn-Schmiedeberg's Archives of Pharmacology* **2016**.
94. Imamura, C. K.; Furihata, K.; Okamoto, S.; Tanigawara, Y. Impact of cytochrome P₄₅₀ 2C₁₉ polymorphisms on the pharmacokinetics of tacrolimus when coadministered with voriconazole. *Journal of Clinical Pharmacology* **2016**, *56*, 408–413, DOI: [10.1002/jcph.605](https://doi.org/10.1002/jcph.605).
95. Malki, M. A.; Pearson, E. R. Drug–drug–gene interactions and adverse drug reactions. *Pharmacogenomics Journal* **2020**, *20*, 355–366, DOI: [10.1038/s41397-019-0122-0](https://doi.org/10.1038/s41397-019-0122-0).
96. Tsamandouras, N.; Rostami-Hodjegan, A.; Aarons, L. Combining the 'bottom up' and 'top down' approaches in pharmacokinetic modelling: Fitting PBPK models to observed clinical data. *British Journal of Clinical Pharmacology* **2015**, *79*, 48–55, DOI: [10.1111/bcp.12234](https://doi.org/10.1111/bcp.12234).
97. Zhuang, X.; Lu, C. PBPK modeling and simulation in drug research and development. *Acta Pharmaceutica Sinica B* **2016**, *6*, 430–440, DOI: [10.1016/j.apsb.2016.04.004](https://doi.org/10.1016/j.apsb.2016.04.004).
98. Kuepfer, L.; Niederalt, C.; Wendl, T.; Schlender, J. F.; Willmann, S.; Lippert, J.; Block, M.; Eissing, T.; Teutonico, D. Applied concepts in PBPK modeling: How to build a PBPK/PD model. *CPT: Pharmacometrics and Systems Pharmacology* **2016**, *5*, 516–531, DOI: [10.1002/psp4.12134](https://doi.org/10.1002/psp4.12134).
99. Teorell, T. Kinetics of distribution of substances administered to the body. I. The extravascular modes of administration. *Archives internationales de pharmacodynamie et de thérapie* **1937**, *57*, 205–225.
100. Kovar, L.; Schräpel, C.; Selzer, D.; Kohl, Y.; Bals, R.; Schwab, M.; Lehr, T. Physiologically-based pharmacokinetic (PBPK) modeling of buprenorphine in adults, children and preterm neonates. *Pharmaceutics* **2020**, *12*, 578, DOI: [10.3390/pharmaceutics12060578](https://doi.org/10.3390/pharmaceutics12060578).
101. Dallmann, A.; Ince, I.; Solodenko, J.; Meyer, M.; Willmann, S.; Eissing, T.; Hempel, G. Physiologically based pharmacokinetic modeling of renally cleared drugs in pregnant women. *Clinical Pharmacokinetics* **2017**, *56*, 1525–1541, DOI: [10.1007/s40262-017-0538-0](https://doi.org/10.1007/s40262-017-0538-0).

102. Jones, H. M.; Dickins, M.; Youdim, K.; Gosset, J. R.; Attkins, N. J.; Hay, T. L.; Gurrell, I. K.; Logan, Y. R.; Bungay, P. J.; Jones, B. C.; Gardner, I. B. Application of PBPK modelling in drug discovery and development at Pfizer. *Xenobiotica* **2012**, *42*, 94–106, DOI: [10.3109/00498254.2011.627477](https://doi.org/10.3109/00498254.2011.627477).
103. Huang, H.; Zhao, W.; Qin, N.; Duan, X. Recent progress on physiologically based pharmacokinetic (PBPK) model: A review based on bibliometrics. *Toxics* **2024**, *12*, 433, DOI: [10.3390/toxics12060433](https://doi.org/10.3390/toxics12060433).
104. Sager, J. E.; Yu, J.; Ragueneau-Majlessi, I.; Isoherranen, N. Physiologically based pharmacokinetic (PBPK) modeling and simulation approaches: A systematic review of published models, applications, and model verification. *Drug Metabolism and Disposition* **2015**, *43*, 1823–1837, DOI: [10.1124/dmd.115.065920](https://doi.org/10.1124/dmd.115.065920).
105. Homepage ERACoSysMed INSPIRATION. <https://eracosysmed-inspiration.github.io/> (accessed 10/29/2024).
106. Ong, S. C.; Gaston, R. S. Thirty years of tacrolimus in clinical practice. *Transplantation* **2021**, *105*, 484–495, DOI: [10.1097/TP.0000000000003350](https://doi.org/10.1097/TP.0000000000003350).
107. Kim, E. J.; Kim, S. J.; Huh, K. H.; Kim, B. S.; Kim, M. S.; Kim, S. I.; Kim, Y. S.; Lee, J. Clinical significance of tacrolimus intra-patient variability on kidney transplant outcomes according to pre-transplant immunological risk. *Scientific Reports* **2021**, *11*, 12114, DOI: [10.1038/s41598-021-91630-4](https://doi.org/10.1038/s41598-021-91630-4).
108. Clarke, W. A.; Chatelut, E.; Fotoohi, A. K.; Larson, R. A.; Martin, J. H.; Mathijssen, R. H.; Salamone, S. J. Therapeutic drug monitoring in oncology: International Association of Therapeutic Drug Monitoring and Clinical Toxicology consensus guidelines for imatinib therapy. *European Journal of Cancer* **2021**, *157*, 428–440, DOI: [10.1016/j.ejca.2021.08.033](https://doi.org/10.1016/j.ejca.2021.08.033).
109. Kantarjian, H. M.; Jain, N.; Garcia-Manero, G.; Welch, M. A.; Ravandi, F.; Wierda, W. G.; Jabbour, E. J. The cure of leukemia through the optimist's prism. *Cancer* **2022**, *128*, 240–259, DOI: [10.1002/cnccr.33933](https://doi.org/10.1002/cnccr.33933).
110. He, S.; Bian, J.; Shao, Q.; Zhang, Y.; Hao, X.; Luo, X.; Feng, Y.; Huang, L. Therapeutic drug monitoring and individualized medicine of dasatinib: Focus on clinical pharmacokinetics and pharmacodynamics. *Frontiers in Pharmacology* **2021**, *12*, 797881, DOI: [10.3389/fphar.2021.797881](https://doi.org/10.3389/fphar.2021.797881).
111. Hebert, M. F.; Fisher, R. M.; Marsh, C. L.; Dressler, D.; Bekersky, I. Effects of rifampin on tacrolimus pharmacokinetics in healthy volunteers. *Journal of Clinical Pharmacology* **1999**, *39*, 91–96, DOI: [10.1177/00912709922007499](https://doi.org/10.1177/00912709922007499).

112. Floren, L. C.; Bekersky, I.; Benet, L. Z.; Mekki, Q.; Dressier, D.; Lee, J. W.; Roberts, J. P.; Hebert, M. F. Tacrolimus oral bioavailability doubles with coadministration of ketoconazole. *Clinical Pharmacology and Therapeutics* **1997**, *62*, 41–49, DOI: [10.1016/S0009-9236\(97\)90150-8](https://doi.org/10.1016/S0009-9236(97)90150-8).
113. Pappas, P. G.; Alexander, B. D.; Andes, D. R.; Hadley, S.; Kauffman, C. A.; Freifeld, A.; Anaissie, E. J.; Brumble, L. M.; Herwaldt, L.; Ito, J.; Kontoyiannis, D. P.; Marshall Lyon, G.; Marr, K. A.; Morrison, V. A.; Park, B. J.; Patterson, T. F.; Perl, T. M.; Oster, R. A.; Schuster, M. G.; Walker, R.; Walsh, T. J.; Wannemuehler, K. A.; Chiller, T. M. Invasive fungal infections among organ transplant recipients: Results of the Transplant-Associated Infection Surveillance Network (TRANSNET). *Clinical Infectious Diseases* **2010**, *50*, 1101–1111, DOI: [10.1086/651262](https://doi.org/10.1086/651262).
114. Bekersky, I.; Dressler, D.; Mekki, Q. A. Effect of low- and high-fat meals on tacrolimus absorption following 5 mg single oral doses to healthy human subjects. *Journal of Clinical Pharmacology* **2001**, *41*, 176–182, DOI: [10.1177/00912700122009999](https://doi.org/10.1177/00912700122009999).
115. Huppertz, A.; Bollmann, J.; Behnisch, R.; Bruckner, T.; Zorn, M.; Burhenne, J.; Haefeli, W. E.; Czock, D. Differential effect of a continental breakfast on tacrolimus formulations with different release characteristics. *Clinical Pharmacology in Drug Development* **2021**, *10*, 899–907, DOI: [10.1002/cpdd.924](https://doi.org/10.1002/cpdd.924).
116. Bixby, D.; Talpaz, M. Seeking the causes and solutions to imatinib-resistance in chronic myeloid leukemia. *Leukemia* **2011**, *25*, 7–22, DOI: [10.1038/leu.2010.238](https://doi.org/10.1038/leu.2010.238).
117. Hamada, A.; Miyano, H.; Watanabe, H.; Saito, H. Interaction of imatinib mesilate with human P-glycoprotein. *Journal of Pharmacology and Experimental Therapeutics* **2003**, *307*, 824–828, DOI: [10.1124/jpet.103.055574](https://doi.org/10.1124/jpet.103.055574).
118. Duckett, D. R.; Cameron, M. D. Metabolism considerations for kinase inhibitors in cancer treatment. *Expert Opinion on Drug Metabolism & Toxicology* **2010**, *6*, 1175–1193, DOI: [10.1517/17425255.2010.506873](https://doi.org/10.1517/17425255.2010.506873).
119. Manley, P. W. Investigations into the potential role of metabolites on the anti-leukemic activity of imatinib, nilotinib and midostaurin. *Chimia* **2019**, *73*, 561–570, DOI: [10.2533/chimia.2019.561](https://doi.org/10.2533/chimia.2019.561).
120. Dutreix, C.; Peng, B.; Mehring, G.; Hayes, M.; Capdeville, R.; Pokorný, R.; Seiberling, M. Pharmacokinetic interaction between ketoconazole and imatinib mesylate (Glivec) in healthy subjects. *Cancer Chemotherapy and Pharmacology* **2004**, *54*, 290–294, DOI: [10.1007/s00280-004-0832-z](https://doi.org/10.1007/s00280-004-0832-z).
121. O'Brien, S. G.; Meinhardt, P.; Bond, E.; Beck, J.; Peng, B.; Dutreix, C.; Mehring, G.; Milosavljev, S.; Huber, C.; Capdeville, R.; Fischer, T. Effects of imatinib mesylate (ST1571, Glivec) on the pharmacokinetics of simvastatin, a cytochrome P450 3A4 substrate, in patients with

- chronic myeloid leukaemia. *British Journal of Cancer* **2003**, 89, 1855–1859, DOI: [10.1038/sj.bjc.6601152](https://doi.org/10.1038/sj.bjc.6601152).
122. Park, S. J.; Choi, I. K.; Seo, H. Y.; Sung, H. J.; Park, K. H.; Kim, S. J.; Oh, S. C.; Seo, J. H.; Choi, C. W.; Kim, B. S.; Shin, S. W.; Kim, Y. H.; Kim, J. S. Reduced dose of imatinib for patients with chronic myeloid leukemia and low body surface area. *Acta Haematologica* **2007**, 118, 219–221, DOI: [10.1159/00011777](https://doi.org/10.1159/00011777).
 123. Lombardo, L. J.; Lee, F. Y.; Chen, P.; Norris, D.; Barrish, J. C.; Behnia, K.; Castaneda, S.; Cornelius, L. A.; Das, J.; Doweyko, A. M.; Fairchild, C.; Hunt, J. T.; Inigo, I.; Johnston, K.; Kamath, A.; Kan, D.; Klei, H.; Marathe, P.; Pang, S.; Peterson, R.; Pitt, S.; Schieven, G. L.; Schmidt, R. J.; Tokarski, J.; Wen, M. L.; Wityak, J.; Borzilleri, R. M. Discovery of N-(2-chloro-6-methylphenyl)-2-(6-(4-(2-hydroxyethyl)-piperazin-1-yl)-2-methylpyrimidin-4-ylamino)thiazole-5-carboxamide (BMS-354825), a dual Src/Abl kinase inhibitor with potent antitumor activity in preclinical assays. *Journal of Medicinal Chemistry* **2004**, 47, 6658–6661, DOI: [10.1021/jm049486a](https://doi.org/10.1021/jm049486a).
 124. Kantarjian, H.; Jabbour, E.; Grimley, J.; Kirkpatrick, P. Dasatinib. *Nature Reviews Drug Discovery* **2006**, 5, 717–718, DOI: [10.1038/nrd2135](https://doi.org/10.1038/nrd2135).
 125. Brave, M.; Goodman, V.; Kaminskas, E.; Farrell, A.; Timmer, W.; Pope, S.; Harapanhalli, R.; Saber, H.; Morse, D.; Bullock, J.; Men, A.; Noory, C.; Ramchandani, R.; Kenna, L.; Booth, B.; Gobburu, J.; Jiang, X.; Sridhara, R.; Justice, R.; Pazdur, R. Sprycel for chronic myeloid leukemia and Philadelphia chromosome - Positive acute lymphoblastic leukemia resistant to or intolerant of imatinib mesylate. *Clinical Cancer Research* **2008**, 14, 352–359, DOI: [10.1158/1078-0432.CCR-07-4175](https://doi.org/10.1158/1078-0432.CCR-07-4175).
 126. Wang, L.; Christopher, L. J.; Cui, D.; Li, W.; Iyer, R.; Humphreys, W. G.; Zhang, D. Identification of the human enzymes involved in the oxidative metabolism of dasatinib: An effective approach for determining metabolite formation kinetics. *Drug Metabolism and Disposition* **2008**, 36, 1828–1839, DOI: [10.1124/dmd.107.020255](https://doi.org/10.1124/dmd.107.020255).
 127. Johnson, F. M.; Agrawal, S.; Burris, H.; Rosen, L.; Dhillon, N.; Hong, D.; Blackwood-Chirchir, A.; Luo, F. R.; Sy, O.; Kaul, S.; Chiappori, A. A. Phase 1 pharmacokinetic and drug-interaction study of dasatinib in patients with advanced solid tumors. *Cancer* **2010**, 116, 1582–1591, DOI: [10.1002/cncr.24927](https://doi.org/10.1002/cncr.24927).
 128. Center for Drug Evaluation. Clinical pharmacology and biopharmaceutics review(s): NDA Review – Dasatinib. US Food and Drug Administration website. https://www.accessdata.fda.gov/drugsatfda_docs/nda/2006/021986s000_Sprycel__ClinPharmR.pdf (accessed 08/04/2022).

129. Li, X.; He, Y.; Ruiz, C. H.; Koenig, M.; Cameron, M. D.; Vojkovsky, T. Characterization of dasatinib and its structural analogs as CYP3A4 mechanism-based inactivators and the proposed bioactivation pathways. *Drug Metabolism and Disposition* **2009**, *37*, 1242–1250, DOI: [10.1124/dmd.108.025932](https://doi.org/10.1124/dmd.108.025932).
130. Pahwa, S.; Alam, K.; Crowe, A.; Farasyn, T.; Neuhoﬀ, S.; Hatley, O.; Ding, K.; Yue, W. Pretreatment with rifampicin and tyrosine kinase inhibitor dasatinib potentiates the inhibitory eﬀects toward OATP1B1- and OATP1B3-mediated transport without aﬀecting plasma membrane localization of the transporters. *Journal of pharmaceutical sciences* **2017**, *106*, 2123–2135, DOI: [10.1016/j.xphs.2017.03.022](https://doi.org/10.1016/j.xphs.2017.03.022).
131. Chang, M.; Bathena, S.; Christopher, L. J.; Shen, H.; Roy, A. Prediction of drug–drug interaction potential mediated by transporters between dasatinib and metformin, pravastatin, and rosuvastatin using physiologically based pharmacokinetic modeling. *Cancer Chemotherapy and Pharmacology* **2022**, *89*, 383–392, DOI: [10.1007/s00280-021-04394-z](https://doi.org/10.1007/s00280-021-04394-z).
132. Yago, M. R.; Frymoyer, A.; Benet, L. Z.; Smelick, G. S.; Frassetto, L. A.; Ding, X.; Dean, B.; Salphati, L.; Budha, N.; Jin, J. Y.; Dresser, M. J.; Ware, J. A. The use of betaine HCl to enhance dasatinib absorption in healthy volunteers with rabeprazole-induced hypochlorhydria. *AAPS Journal* **2014**, *16*, 1358–1365, DOI: [10.1208/s12248-014-9673-9](https://doi.org/10.1208/s12248-014-9673-9).
133. Rousselot, P.; Mollica, L.; Guilhot, J.; Guerci, A.; Nicolini, F. E.; Etienne, G.; Legros, L.; Charbonnier, A.; Coiteux, V.; Dartigeas, C.; Escoﬀre-Barbe, M.; Roy, L.; Cony-Makhoul, P.; Dubruille, V.; Gardembas, M.; Huguet, F.; Réa, D.; Cayssials, E.; Guilhot, F.; Bergeron, A.; Molimard, M.; Mahon, F. X.; Cayuela, J. M.; Busque, L.; Bouchet, S. Dasatinib dose optimisation based on therapeutic drug monitoring reduces pleural eﬀusion rates in chronic myeloid leukaemia patients. *British Journal of Haematology* **2021**, *194*, 393–402, DOI: [10.1111/bjh.17654](https://doi.org/10.1111/bjh.17654).
134. Wojtyniak, J. G.; Britz, H.; Selzer, D.; Schwab, M.; Lehr, T. Data digitizing: Accurate and precise data extraction for quantitative systems pharmacology and physiologically-based pharmacokinetic modeling. *CPT: Pharmacometrics and Systems Pharmacology* **2020**, *9*, 322–331, DOI: [10.1002/psp4.12511](https://doi.org/10.1002/psp4.12511).
135. Meyer, M.; Schneckener, S.; Ludewig, B.; Kuepfer, L.; Lippert, J. Using expression data for quantification of active processes in physiologically based pharmacokinetic modeling. *Drug metabolism and disposition: the biological fate of chemicals* **2012**, *40*, 892–901, DOI: [10.1124/dmd.111.043174](https://doi.org/10.1124/dmd.111.043174).
136. Open Systems Pharmacology Suite Community. PK-Sim® Ontogeny Database Documentation, Version 7.3. <https://github.com/Open-Systems-Pharmacology/OSPSuite.Documentation/blob/master/PK-Sim%20Ontogeny%20Database%20Version%207.3.pdf> (accessed 04/30/2022).

137. Open Systems Pharmacology Suite Community. Open Systems Pharmacology Suite Manual, Version 11.1. <https://docs.open-systems-pharmacology.org/copyright> (accessed 02/15/2023).
138. Guest, E. J.; Aarons, L.; Houston, J. B.; Rostami-Hodjegan, A.; Galetin, A. Critique of the two-fold measure of prediction success for ratios: Application for the assessment of drug-drug interactions. *Drug Metabolism and Disposition* **2011**, *39*, 170–173, DOI: [10.1124/dmd.110.036103](https://doi.org/10.1124/dmd.110.036103).
139. Loer, H. L. H.; Türk, D.; Mantilla, J. D. G.; Selzer, D.; Lehr, T. Physiologically based pharmacokinetic (PBPK) modeling of clopidogrel and its four relevant metabolites for CYP2B6, CYP2C8, CYP2C19, and CYP3A4 drug-drug-gene interaction predictions. *Pharmaceutics* **2022**, *14*, 915, DOI: [10.3390/pharmaceutics14050915](https://doi.org/10.3390/pharmaceutics14050915).
140. Rüdesheim, S.; Selzer, D.; Fuhr, U.; Schwab, M.; Lehr, T. Physiologically based pharmacokinetic modeling of dextromethorphan to investigate interindividual variability within CYP2D6 activity score groups. *CPT: Pharmacometrics and Systems Pharmacology* **2022**, *11*, 494–511, DOI: [10.1002/psp4.12776](https://doi.org/10.1002/psp4.12776).
141. Marok, F. Z.; Fuhr, L. M.; Hanke, N.; Selzer, D.; Lehr, T. Physiologically based pharmacokinetic modeling of bupropion and its metabolites in a CYP2B6 drug-drug-gene interaction network. *Pharmaceutics* **2021**, *13*, 331, DOI: [10.3390/pharmaceutics13030331](https://doi.org/10.3390/pharmaceutics13030331).
142. Hsueh, C. H.; Hsu, V.; Zhao, P.; Zhang, L.; Giacomini, K. M.; Huang, S. M. PBPK modeling of the effect of reduced kidney function on the pharmacokinetics of drugs excreted renally by organic anion transporters. *Clinical Pharmacology and Therapeutics* **2018**, *103*, 485–492, DOI: [10.1002/cpt.750](https://doi.org/10.1002/cpt.750).
143. Simon, F.; Gautier-Veyret, E.; Truffot, A.; Chenel, M.; Payen, L.; Stanke-Labesque, F.; Tod, M. Modeling approach to predict the impact of inflammation on the pharmacokinetics of CYP2C19 and CYP3A4 substrates. *Pharmaceutical Research* **2021**, *38*, 415–428, DOI: [10.1007/s11095-021-03019-7](https://doi.org/10.1007/s11095-021-03019-7).
144. El-Khateeb, E.; Burkhill, S.; Murby, S.; Amirat, H.; Rostami-Hodjegan, A.; Ahmad, A. Physiological-based pharmacokinetic modeling trends in pharmaceutical drug development over the last 20-years; in-depth analysis of applications, organizations, and platforms. *Biopharmaceutics and Drug Disposition* **2021**, *42*, 107–117, DOI: [10.1002/bdd.2257](https://doi.org/10.1002/bdd.2257).
145. Naga, D.; Parrott, N.; Ecker, G. F.; Olivares-Morales, A. Evaluation of the success of high-throughput physiologically based pharmacokinetic (HT-PBPK) modeling predictions to inform early drug discovery. *Molecular Pharmaceutics* **2022**, *19*, 2203–2216, DOI: [10.1021/ACS.MOLPHARMACEUT.2C00040](https://doi.org/10.1021/ACS.MOLPHARMACEUT.2C00040).

146. Van Erp, N. P.; Gelderblom, H.; Karlsson, M. O.; Li, J.; Zhao, M.; Ouw-erkerk, J.; Nortier, J. W.; Guchelaar, H. J.; Baker, S. D.; Sparreboom, A. Influence of CYP3A4 inhibition on the steady-state pharmacokinetics of imatinib. *Clinical Cancer Research* **2007**, *13*, 7394–7400, DOI: [10.1158/1078-0432.CCR-07-0346](https://doi.org/10.1158/1078-0432.CCR-07-0346).
147. Rowland Yeo, K.; Venkatakrishnan, K. Physiologically-based pharmacokinetic models as enablers of precision dosing in drug development: Pivotal role of the human mass balance study. *Clinical Pharmacology and Therapeutics* **2021**, *109*, 51–54, DOI: [10.1002/cpt.2092](https://doi.org/10.1002/cpt.2092).
148. Chou, W. C.; Lin, Z. Machine learning and artificial intelligence in physiologically based pharmacokinetic modeling. *Toxicological Sciences* **2023**, *191*, 1–14, DOI: [10.1093/toxsci/kfac101](https://doi.org/10.1093/toxsci/kfac101).
149. Kamiya, Y.; Handa, K.; Miura, T.; Ohori, J.; Kato, A.; Shimizu, M.; Kitajima, M.; Yamazaki, H. Machine learning prediction of the three main input parameters of a simplified physiologically based pharmacokinetic model subsequently used to generate time-dependent plasma concentration data in humans after oral doses of 212 disparate chemicals. *Biological and Pharmaceutical Bulletin* **2022**, *45*, 124–128, DOI: [10.1248/bpb.b21-00769](https://doi.org/10.1248/bpb.b21-00769).
150. Minichmayr, I. K.; Dreesen, E.; Centanni, M.; Wang, Z.; Hoffert, Y.; Friberg, L. E.; Wicha, S. G. Model-informed precision dosing: State of the art and future perspectives. *Advanced Drug Delivery Reviews* **2024**, *215*, 115421, DOI: [10.1016/j.addr.2024.115421](https://doi.org/10.1016/j.addr.2024.115421).
151. Storelli, F.; Samer, C.; Reny, J. L.; Desmeules, J.; Daali, Y. Complex drug–drug–gene–disease interactions involving cytochromes P450: Systematic review of published case reports and clinical perspectives. *Clinical Pharmacokinetics* **2018**, *57*, 1267–1293, DOI: [10.1007/s40262-018-0650-9](https://doi.org/10.1007/s40262-018-0650-9).
152. Faelens, R.; Wang, Z.; Bouillon, T.; Declerck, P.; Ferrante, M.; Vermeire, S.; Dreesen, E. Model-informed precision dosing during infliximab induction therapy reduces variability in exposure and endoscopic improvement between patients with ulcerative colitis. *Pharmaceutics* **2021**, *13*, 1623, DOI: [10.3390/pharmaceutics13101623](https://doi.org/10.3390/pharmaceutics13101623).
153. Swartling, M.; Hamberg, A. K.; Furebring, M.; Tängdén, T.; Nielsen, E. I. Model-informed precision dosing of vancomycin in clinical practice: An intervention development study. *International Journal of Clinical Pharmacy* **2024**, *47*, 178–186, DOI: [10.1007/s11096-024-01822-x](https://doi.org/10.1007/s11096-024-01822-x).
154. Polasek, T. M.; Rostami-Hodjegan, A.; Yim, D. S.; Jamei, M.; Lee, H.; Kimko, H.; Kim, J. K.; Nguyen, P. T. T.; Darwich, A. S.; Shin, J. G. What does it take to make model-informed precision dosing common practice? Report from the 1st Asian Symposium on Precision Dosing. *AAPS Journal* **2019**, *21*, 17, DOI: [10.1208/s12248-018-0286-6](https://doi.org/10.1208/s12248-018-0286-6).

155. US Food and Drug Administration. Precision dosing workshop. <https://www.fda.gov/drugs/precision-dosing-defining-need-and-approaches-deliver-individualized-drug-dosing-real-world-setting> (accessed 01/05/2025).
156. Aarons, L. Population pharmacokinetics: Theory and practice. *British Journal of Clinical Pharmacology* **1991**, 32, 669–670, DOI: [10.1111/j.1365-2125.1991.tb03971.x](https://doi.org/10.1111/j.1365-2125.1991.tb03971.x).
157. Polasek, T. M.; Rostami-Hodjegan, A. Virtual twins: Understanding the data required for model-informed precision dosing. *Clinical Pharmacology and Therapeutics* **2020**, 107, 742–745, DOI: [10.1002/cpt.1778](https://doi.org/10.1002/cpt.1778).
158. Menz, B. D.; Stocker, S. L.; Verougstraete, N.; Kocic, D.; Galettis, P.; Stove, C. P.; Reuter, S. E. Barriers and opportunities for the clinical implementation of therapeutic drug monitoring in oncology. *British Journal of Clinical Pharmacology* **2021**, 87, 227–236, DOI: [10.1111/bcp.14372](https://doi.org/10.1111/bcp.14372).
159. Curtin, S. C.; Tejada-Vera, B.; Bastian, B. A. Deaths: Leading causes for 2021. *National Vital Statistics Reports* **2024**, 73, DOI: [10.15620/cdc/147882](https://doi.org/10.15620/cdc/147882).
160. Fraley, D. S.; Burr, R.; Bernardini, J.; Angus, D.; Kramer, D. J.; Johnson, J. P. Impact of acute renal failure on mortality in end-stage liver disease with or without transplantation. *Kidney International* **1998**, 54, 518–524, DOI: [10.1046/j.1523-1755.1998.00004.x](https://doi.org/10.1046/j.1523-1755.1998.00004.x).
161. Hoffert, Y.; Dia, N.; Vanuytsel, T.; Vos, R.; Kuypers, D.; Van Cleemput, J.; Verbeek, J.; Dreesen, E. Model-informed precision dosing of tacrolimus: A systematic review of population pharmacokinetic models and a benchmark study of software tools. *Clinical Pharmacokinetics* **2024**, 63, 1407–1421, DOI: [10.1007/s40262-024-01414-y](https://doi.org/10.1007/s40262-024-01414-y).
162. Darwich, A. S.; Ogungbenro, K.; Hatley, O. J.; Rostami-Hodjegan, A. Role of pharmacokinetic modeling and simulation in precision dosing of anticancer drugs. *Translational Cancer Research* **2017**, 6, S1512–S1529, DOI: [10.21037/tcr.2017.09.14](https://doi.org/10.21037/tcr.2017.09.14).
163. Zhang, H.; Bu, F.; Li, L.; Jiao, Z.; Ma, G.; Cai, W.; Zhuang, X.; Lin, H. S.; Shin, J. G.; Xiang, X. Prediction of drug–drug interaction between tacrolimus and principal ingredients of wuzhi capsule in Chinese healthy volunteers using physiologically-based pharmacokinetic modelling. *Basic and Clinical Pharmacology and Toxicology* **2018**, 122, 331–340, DOI: [10.1111/bcpt.12914](https://doi.org/10.1111/bcpt.12914).
164. Gao, D.; Wang, G.; Wu, H.; Wu, J. H.; Zhao, X. Prediction for plasma trough concentration and optimal dosing of imatinib under multiple clinical situations using physiologically based pharmacokinetic modeling. *ACS Omega* **2023**, 8, 13741–13753, DOI: [10.1021/acsomega.2c07967](https://doi.org/10.1021/acsomega.2c07967).

165. Adiwidjaja, J.; Boddy, A. V.; McLachlan, A. J. Implementation of a physiologically based pharmacokinetic modeling approach to guide optimal dosing regimens for imatinib and potential drug interactions in paediatrics. *Frontiers in Pharmacology* **2020**, *10*, 1672, DOI: [10.3389/fphar.2019.01672](https://doi.org/10.3389/fphar.2019.01672).
166. Bristol-Myers Squibb Company. Sprycel US prescribing information website. https://packageinserts.bms.com/pi/pi_sprycel.pdf (accessed 03/01/2023).
167. Eli Lilly and Company STRATTERA Labeling-Package Insert - Drugs @FDA. https://www.accessdata.fda.gov/drugsatfda_docs/label/2002/21411_strattera_lbl.pdf (accessed 06/08/2023).
168. The Royal Dutch Pharmacists Association - Pharmacogenetics Working Group (DPWG) annotation of DPWG guideline for metoprolol and CYP2D6. <https://www.pharmgkb.org/guidelineAnnotation/PA166104995> (accessed 09/22/2020).
169. Wedagedera, J. R.; Afuape, A.; Chirumamilla, S. K.; Momiji, H.; Leary, R.; Dunlavey, M.; Matthews, R.; Abduljalil, K.; Jamei, M.; Bois, F. Y. Population PBPK modeling using parametric and nonparametric methods of the Simcyp Simulator, and Bayesian samplers. *CPT: Pharmacometrics and Systems Pharmacology* **2022**, *11*, 755–765, DOI: [10.1002/psp4.12787](https://doi.org/10.1002/psp4.12787).
170. Swen, J. J.; van der Wouden, C. H.; En Manson, L.; Abdullah-Koolmees, H.; Blagec, K.; Blagus, T.; Böhringer, S.; Cambon-Thomsen, A; E, C.; Cheung, K. C.; Deneer, V. H.; Dupui, M; Ingelman-Sundberg, M; Jonsson, S; Joefield-Roka, C; Just, K. S.; Karlsson, M. O.; Konta, L; Koopmann, R; Kriek, M; Lehr, T; Mitropoulou, C; Rial-Sebbag, E; Rollinson, V; Roncato, R; Samwald, M; Schaeffeler, E; Skokou, M; Schwab, M; Steinberger, D; Stingl, J. C.; Tremmel, R; Turner, R. M.; van Rhenen, M. H.; Dávila Fajardo, C. L.; Dolžan, V; Patrinos, G. P.; Pirmohamed, M; Sunder-Plassmann, G; Toffoli, G; Guchelaar, H. J.; Ubiquitous Pharmacogenomics Consortium. A 12-gene pharmacogenetic panel to prevent adverse drug reactions: An open-label, multicentre, controlled, cluster-randomised crossover implementation study. *The Lancet* **2023**, *401*, 347–356, DOI: [10.1016/S0140-6736\(22\)01841-4](https://doi.org/10.1016/S0140-6736(22)01841-4).
171. Darwich, A. S.; Polasek, T. M.; Aronson, J. K.; Ogungbenro, K.; Wright, D. F.; Achour, B.; Reny, J. L.; Daali, Y.; Eiermann, B.; Cook, J.; Lesko, L.; McLachlan, A. J.; Rostami-Hodjegan, A. Model-informed precision dosing: Background, requirements, validation, implementation, and forward trajectory of individualizing drug therapy. *Annual Review of Pharmacology and Toxicology* **2021**, *61*, 225–245, DOI: [10.1146/annurev-pharmtox-033020-113257](https://doi.org/10.1146/annurev-pharmtox-033020-113257).
172. Madabushi, R.; Seo, P.; Zhao, L.; Tegenge, M.; Zhu, H. Review: Role of model-informed drug development approaches in the lifecycle of drug development and regulatory decision-making. *Pharmaceutical Research* **2022**, *39*, 1669–1680, DOI: [10.1007/s11095-022-03288-w](https://doi.org/10.1007/s11095-022-03288-w).

173. Marshall, S.; Madabushi, R.; Manolis, E.; Krudys, K.; Staab, A.; Dykstra, K.; Visser, S. A. Model-informed drug discovery and development: Current industry good practice and regulatory expectations and future perspectives. *CPT: Pharmacometrics and Systems Pharmacology* **2019**, *8*, 87–96, DOI: [10.1002/psp4.12372](https://doi.org/10.1002/psp4.12372).
174. Lesko, L. J. Perspective on model-informed drug development. *CPT: Pharmacometrics and Systems Pharmacology* **2021**, *10*, 1127–1129, DOI: [10.1002/psp4.12699](https://doi.org/10.1002/psp4.12699).
175. US Food and Drug Administration. Physiologically based pharmacokinetic analyses – Format and content – Guidance for industry. <https://www.fda.gov/media/101469/download> (accessed 09/21/2024).
176. European Medicines Agency. Reporting of physiologically based pharmacokinetic (PBPK) modelling and simulation – Scientific guideline. <https://www.ema.europa.eu/en/reporting-physiologically-based-pharmacokinetic-pbpbk-modelling-simulation-scientific-guideline> (accessed 09/21/2024).
177. Sun, Z.; Zhao, N.; Zhao, X.; Wang, Z.; Liu, Z.; Cui, Y. Application of physiologically based pharmacokinetic modeling of novel drugs approved by the U.S. food and drug administration. *European Journal of Pharmaceutical Sciences* **2024**, *200*, 106838, DOI: [10.1016/j.ejps.2024.106838](https://doi.org/10.1016/j.ejps.2024.106838).
178. Grimstein, M.; Yang, Y.; Zhang, X.; Grillo, J.; Huang, S. M.; Zineh, I.; Wang, Y. Physiologically based pharmacokinetic modeling in regulatory science: An update from the U.S. Food and Drug Administration's Office of Clinical Pharmacology. *Journal of Pharmaceutical Sciences* **2019**, *108*, 21–25, DOI: [10.1016/j.xphs.2018.10.033](https://doi.org/10.1016/j.xphs.2018.10.033).
179. Rowland Yeo, K.; Gil Berglund, E.; Chen, Y. Dose optimization informed by PBPK modeling: State-of-the art and future. *Clinical Pharmacology and Therapeutics* **2024**, *116*, 563–576, DOI: [10.1002/cpt.3289](https://doi.org/10.1002/cpt.3289).
180. Polak, S.; Tylutki, Z.; Holbrook, M.; Wiśniowska, B. Better prediction of the local concentration–effect relationship: The role of physiologically based pharmacokinetics and quantitative systems pharmacology and toxicology in the evolution of model-informed drug discovery and development. *Drug Discovery Today* **2019**, *24*, 1344–1354, DOI: [10.1016/j.drudis.2019.05.016](https://doi.org/10.1016/j.drudis.2019.05.016).
181. Zhang, L.; Zhang, Y. D.; Zhao, P.; Huang, S. M. Predicting drug-drug interactions: An FDA perspective. *AAPS Journal* **2009**, *11*, 300–306, DOI: [10.1208/s12248-009-9106-3](https://doi.org/10.1208/s12248-009-9106-3).
182. Hanke, N.; Frechen, S.; Moj, D.; Britz, H.; Eissing, T.; Wendl, T.; Lehr, T. PBPK models for CYP3A4 and P-gp DDI prediction: A modeling network of rifampicin, itraconazole, clarithromycin, midazolam, alfentanil, and digoxin. *CPT: Pharmacometrics and Systems Pharmacology* **2018**, *7*, 647–659, DOI: [10.1002/psp4.12343](https://doi.org/10.1002/psp4.12343).

183. US Food and Drug Administration. M15 general principles for model-informed drug development – Draft guidance document. <https://www.fda.gov/media/184747/download> (accessed 01/10/2025).

PUBLICATIONS

A.1 ORIGINAL RESEARCH ARTICLES

1. Loer, H. L. H.; Türk, D.; Gómez-Mantilla, J. D.; Selzer, D.; Lehr, T. Physiologically based pharmacokinetic (PBPK) modeling of clopidogrel and its four relevant metabolites for CYP2B6, CYP2C8, CYP2C19, and CYP3A4 drug-drug-gene interaction predictions. *Pharmaceutics* **2022**, *14*, 915. DOI: [10.3390/pharmaceutics14050915](https://doi.org/10.3390/pharmaceutics14050915).
2. Loer, H. L. H.; Feick, D.; Rüdesheim, S.; Selzer, D.; Schwab, M.; Teutonico, D.; Frechen, S.; van der Lee, M.; Moes, D. J. A. R.; Swen, J. J.; Lehr, T. Physiologically based pharmacokinetic modeling of tacrolimus for food–drug and CYP3A drug–drug–gene interaction predictions. *CPT: Pharmacometrics and Systems Pharmacology* **2023**, *12*, 724–738, DOI: [10.1002/psp4.12946](https://doi.org/10.1002/psp4.12946).
3. Feick, D.; Rüdesheim, S.; Marok, F. Z.; Selzer, D.; Loer, H. L. H.; Teutonico, D.; Frechen, S.; van der Lee, M.; Moes, D. J. A. R.; Swen, J. J.; Schwab, M.; Lehr, T. Physiologically-based pharmacokinetic modeling of quinidine to establish a CYP3A4, P-gp, and CYP2D6 drug–drug–gene interaction network. *CPT: Pharmacometrics and Systems Pharmacology* **2023**, *12*, 1143–1156. DOI: [10.1002/psp4.12981](https://doi.org/10.1002/psp4.12981).
4. Loer, H. L. H.; Kovar, C.; Rüdesheim, S.; Marok, F. Z.; Fuhr, L. M.; Selzer, D.; Schwab, M.; Lehr, T. Physiologically based pharmacokinetic modeling of imatinib and N-desmethyl imatinib for drug–drug interaction predictions. *CPT: Pharmacometrics and Systems Pharmacology* **2024**, *13*, 926–940, DOI: [10.1002/psp4.13127](https://doi.org/10.1002/psp4.13127).
5. Kovar, C.; Loer, H. L. H.; Rüdesheim, S.; Fuhr, L. M.; Marok, F. Z.; Selzer, D.; Schwab, M.; Lehr, T. A physiologically-based pharmacokinetic precision dosing approach to manage dasatinib drug–drug interactions. *CPT: Pharmacometrics and Systems Pharmacology* **2024**, *13*, 1144–1159, DOI: [10.1002/psp4.13146](https://doi.org/10.1002/psp4.13146).
6. Rüdesheim, S.*; Loer, H. L. H.*; Feick, D.; Marok, F. Z.; Fuhr, L. M.; Selzer, D.; Teutonico, D.; Schneider, A. R. P.; Solodenko, J.; Frechen, S.; van der Lee, M.; Moes, D. J. A. R.; Swen, J. J.; Schwab, M.; Lehr, T. A comprehensive CYP2D6 drug–drug–gene interaction network for application in precision dosing and drug development. *Clinical Pharmacology & Therapeutics* **2025**, *117*, 1718–1731, DOI: [10.1002/cpt.3604](https://doi.org/10.1002/cpt.3604).

* Authors contributed equally

7. Wu, Y.; Loer, H. L. H.; Zhang, Y.; Zhong, D.; Jiang, Y.; Hu, J.; Fuhr, U.; Lehr, T.; Diao, X. Development and verification of a physiologically based pharmacokinetic model of furmonertinib and its main metabolite for drug–drug interaction predictions. *CPT: Pharmacometrics and Systems Pharmacology* **2025**, DOI: [10.1002/psp4.70052](https://doi.org/10.1002/psp4.70052).

A.2 CONFERENCE ABSTRACTS AND POSTERS

1. Loer, H. L. H.; Türk, D.; Selzer, D.; Lehr, T. Dose adaptations for drug-gene and drug-drug interactions involving clopidogrel – A physiologically based pharmacokinetic (PBPK) modeling approach. 30th Population Approach Group Europe (PAGE) meeting, **2022**, Ljubljana, Slovenia.
2. Loer, H. L. H.; Feick, D.; Lehr, T. Physiologically based pharmacokinetic (PBPK) modeling of tacrolimus for CYP3A drug-drug-gene interaction predictions. Annual Meeting of the German Pharmaceutical Society (DPhG), **2022**, Marburg, Germany.
3. Loer, H. L. H.; Kovar, C.; Schwab, M.; Lehr, T. Physiologically based pharmacokinetic modeling of imatinib and its main metabolite for drug-drug interaction predictions. 31st Population Approach Group Europe (PAGE) meeting, **2023**, A Coruña, Spain.
4. Kovar, C.; Loer, H. L. H.; Schwab, M.; Lehr, T. Physiologically based pharmacokinetic modeling of dasatinib to describe enzyme-mediated and pH-dependent drug-drug interaction scenarios. 31st Population Approach Group Europe (PAGE) meeting, **2023**, A Coruña, Spain.
5. Loer, H. L. H.*; Rüdesheim, S.*; Feick, D.; Selzer, D.; Schwab, M.; Lehr, T. Unraveling the CYP2D6 drug-drug-gene interaction network: A comprehensive PBPK analysis of key substrates and inhibitors. 32nd Population Approach Group Europe (PAGE) meeting, **2024**, Rome, Italy.

* Authors contributed equally

SUPPLEMENTARY MATERIALS

The following [Sections B.1–B.4](#) present the Supplementary Materials for the publications [1–4] related to projects I–IV:

- I Loer, H. L. H.; Feick, D.; Rüdesheim, S.; Selzer, D.; Schwab, M.; Teutonico, D.; Frechen, S.; van der Lee, M.; Moes, D. J. A. R.; Swen, J. J.; Lehr, T. Physiologically based pharmacokinetic modeling of tacrolimus for food–drug and CYP3A drug–drug–gene interaction predictions. *CPT: Pharmacometrics and Systems Pharmacology* **2023**, *12*, 724–738, DOI: [10.1002/psp4.12946](#). ([Section B.1](#))
- II Loer, H. L. H.; Kovar, C.; Rüdesheim, S.; Marok, F. Z.; Fuhr, L. M.; Selzer, D.; Schwab, M.; Lehr, T. Physiologically based pharmacokinetic modeling of imatinib and N-desmethyl imatinib for drug–drug interaction predictions. *CPT: Pharmacometrics and Systems Pharmacology* **2024**, *13*, 926–940, DOI: [10.1002/psp4.13127](#). ([Section B.2](#))
- III Kovar, C.; Loer, H. L. H.; Rüdesheim, S.; Fuhr, L. M.; Marok, F. Z.; Selzer, D.; Schwab, M.; Lehr, T. A physiologically-based pharmacokinetic precision dosing approach to manage dasatinib drug–drug interactions. *CPT: Pharmacometrics and Systems Pharmacology* **2024**, *13*, 1144–1159, DOI: [10.1002/psp4.13146](#). ([Section B.3](#))
- IV Rüdesheim, S.*; Loer, H. L. H.*; Feick, D.; Marok, F. Z.; Fuhr, L. M.; Selzer, D.; Teutonico, D.; Schneider, A. R. P.; Solodenko, J.; Frechen, S.; van der Lee, M.; Moes, D. J. A. R.; Swen, J. J.; Schwab, M.; Lehr, T. A comprehensive CYP2D6 drug–drug–gene interaction network for application in precision dosing and drug development. *Clinical Pharmacology & Therapeutics* **2025**, *117*, 1718–1731, DOI: [10.1002/cpt.3604](#). ([Section B.4](#))

* Authors contributed equally

B.1 PROJECT I: PBPK MODELING OF TACROLIMUS

CPT: PHARMACOMETRICS & SYSTEMS PHARMACOLOGY

Physiologically Based Pharmacokinetic Modeling of Tacrolimus for Food-Drug and CYP3A Drug-Drug-Gene Interaction Predictions

Supplement S1 - Model Information and Evaluation

Helena Leonie Hanae Loer¹, Denise Feick¹, Simeon Rüdesheim^{1,2}, Dominik Selzer¹, Matthias Schwab^{2,3,4}, Donato Teutonico⁵, Sebastian Frechen⁶, Maaïke van der Lee⁷, Dirk Jan A. R. Moes⁷, Jesse J. Swen⁷, Thorsten Lehr¹

¹Clinical Pharmacy, Saarland University, Saarbrücken, Germany

²Dr. Margarete Fischer-Bosch-Institute of Clinical Pharmacology, Stuttgart, Germany

³Departments of Clinical Pharmacology, and of Biochemistry and Pharmacy, University of Tübingen, Tübingen, Germany

⁴Cluster of Excellence iFIT (EXC2180) "Image-guided and Functionally Instructed Tumor Therapies", University of Tübingen, Tübingen, Germany

⁵Translational Medicine & Early Development, Sanofi-Aventis R&D, Chilly-Mazarin, France

⁶Bayer AG, Pharmaceuticals, Research & Development, Systems Pharmacology & Medicine, Leverkusen, Germany

⁷Department of Clinical Pharmacy & Toxicology, Leiden University Medical Center, Leiden, The Netherlands

Funding:

This work is part of the Horizon 2020 INSPIRATION (Qualified Open Systems Pharmacology Modeling Network of Drug-Drug-Gene-Interactions) project. The INSPIRATION project (FKZ 031L0241) is supported by the German Federal Ministry of Education and Research under the framework of ERACoSysMed. Matthias Schwab was supported in parts by the Robert Bosch Stiftung Stuttgart, Germany, and the Deutsche Forschungsgemeinschaft (DFG) under Germany's Excellence Strategy-EXC 2180-390900677.

Conflict of Interest:

Donato Teutonico is an employee of Sanofi. Donato Teutonico uses Open Systems Pharmacology software, tools, or models in his professional role. Donato Teutonico and Thorsten Lehr are members of the Open Systems Pharmacology Management Team. Sebastian Frechen uses Open Systems Pharmacology software, tools, or models in his professional role. Sebastian Frechen is a member of the Open Systems Pharmacology Sounding Board. All other authors declared no competing interests for this work.

Corresponding Author:

Thorsten Lehr, PhD
Clinical Pharmacy
Saarland University
Campus C5 3
66123 Saarbrücken
Germany

Contents

S1 Physiologically Based Pharmacokinetic Model Building	3
S1.1 System-dependent Parameters	3
S1.2 Michaelis-Menten Kinetics	3
S1.3 Clinical Study Data	4
S1.4 Drug-dependent Parameters	6
S2 Physiologically Based Pharmacokinetic Model Evaluation	8
S2.1 Whole Blood Concentration-Time Profiles (Semilogarithmic)	8
S2.1.1 Intravenous Tacrolimus	8
S2.1.2 Immediate-Release Oral Tacrolimus	9
S2.1.3 Extended-Release Oral Tacrolimus	12
S2.2 Whole Blood Concentration-Time Profiles (Linear)	13
S2.2.1 Intravenous Tacrolimus	13
S2.2.2 Immediate-Release Oral Tacrolimus	14
S2.2.3 Extended-Release Oral Tacrolimus	17
S2.3 Urinary Excretion Profiles	17
S2.4 Whole Blood Concentration Goodness-of-Fit Plots	18
S2.5 AUC_{last} and C_{max} Goodness-of-Fit Plots	19
S2.6 MRD of Whole Blood Concentration Predictions	20
S2.7 Predicted and Observed AUC_{last} and C_{max} Values	21
S2.8 Local Sensitivity Analysis	23
S2.8.1 Methods	23
S2.8.2 Results	23
S3 Food-Drug Interaction Modeling	26
S3.1 Clinical Study Data	26
S3.2 Whole Blood Concentration-Time Profiles (Semilogarithmic)	28
S3.3 Whole Blood Concentration-Time Profiles (Linear)	29
S3.4 FDI AUC_{last} and FDI C_{max} Ratio Goodness-of-Fit Plots	30
S3.5 Predicted and Observed FDI AUC_{last} and FDI C_{max} Ratios	31
S4 Drug-Drug(-Gene) Interaction Modeling	32
S4.1 Types of Interactions Implemented	32
S4.1.1 Competitive Inhibition	32
S4.1.2 Mechanism-Based Inactivation	32
S4.1.3 Induction	32
S4.2 Clinical Study Data	33
S4.3 Drug-dependent Parameters DD(G)I Partner	34
S4.3.1 Voriconazole	34
S4.3.2 Itraconazole	35
S4.3.3 Rifampicin	38
S4.4 Whole Blood Concentration-Time Profiles (Semilogarithmic)	40
S4.5 Whole Blood Concentration-Time Profiles (Linear)	41
S4.6 DD(G)I AUC_{last} and DD(G)I C_{max} Ratio Goodness-of-Fit Plots	42
S4.7 Predicted and Observed DD(G)I AUC_{last} and DD(G)I C_{max} Ratios	43
Bibliography	44

S1 Physiologically Based Pharmacokinetic Model Building

S1.1 System-dependent Parameters

Table S1: System-dependent parameters

Enzyme/ Transporter	Reference concentration		Relative organ expression ^c	Localization/ Direction	Half-life liver [h]	Half-life intestine [h]
	Mean ^a [μmol/L]	GeoSD ^b				
AADAC	1.0 ^d	1.40 ^e	RT-PCR [1]	intracellular	36	23
CYP2C19	0.76 [2]	1.79 (liver) [3]	RT-PCR [4]	intracellular	26	23
CYP3A4	4.32 [2]	1.18 (liver) [3] 1.45 (duodenum) [3]	RT-PCR [4]	intracellular	36	23
CYP3A5	0.04 [2]	2.25 (liver) [3]	RT-PCR [4]	intracellular	36	23
OATP1B1	0.07 ^f [5]	1.54 [5]	RT-PCR [6]	influx	36	23
P-gp	1.41 [7]	1.60 [5]	RT-PCR ^g [6]	efflux	36	23

AADAC: arylacetamide deacetylase, CYP: cytochrome P450, OATP: organic-anion-transporting polypeptide, P-gp: P-glycoprotein, RT-PCR: reverse transcription polymerase chain reaction.

^a: μmol protein/L in the tissue of highest expression

^b: geometric standard deviation of the reference concentration

^c: according to the PK-Sim[®] expression database

^d: if no information was available, the mean reference concentration was set to 1.0 μmol/L and the catalytic rate constant was optimized according to [8]

^e: if no information was available, a moderate variability of 35% coefficient of variation was assumed (1.40 GeoSD)

^f: calculated from transporter per mg membrane protein x 37.0 mg membrane protein per g liver [5]

^g: relative expression in the intestinal mucosa increased by factor 3.57

S1.2 Michaelis-Menten Kinetics

$$v = \frac{v_{max} \cdot [S]}{K_M + [S]} = \frac{k_{cat} \cdot [E] \cdot [S]}{K_M + [S]} \quad (\text{S1})$$

where v = reaction velocity, v_{max} = maximum reaction velocity, $[S]$ = free substrate concentration, K_M = Michaelis-Menten constant, k_{cat} = catalytic rate constant, and $[E]$ = enzyme concentration.

S1.3 Clinical Study Data

Table S2: Clinical studies of tacrolimus used for PBPK model development

Tacrolimus dosing regimen		n	Females	Ethnicity ^a	Frequency ^a of	Age	Weight	Height	Dataset	Reference
Route	Dose [mg]		[%]		<i>CYP3A5*1</i> [%]	[years]	[kg]	[cm]		
iv (inf, 4 h, SD)	0.015/kg	12	33	Black American	60.5	32.2±10.8	-	-	test	Mancinelli 2001 [9]
iv (inf, 4 h, SD)	0.015/kg	12	42	White American	7.8	44.6±19.1	-	-	test	Mancinelli 2001 [9]
iv (inf, 4 h, SD)	0.015/kg	12	50	Mexican American	20.2	35.7±11.6	-	-	test	Mancinelli 2001 [9]
iv (inf, 4 h, SD)	0.025/kg	8	25	White American	7.8	28±10 (20–50)	78.1±12.9 (67.6–105)	-	training	Bekersky 2001 [10]
iv (inf, 4 h, SD)	0.025/kg	1	0	White American	0	-	-	-	test	Floren 1997 [11]
po (IR cap, SD)	0.5	36	0	Asian	25.8	26.8±5.75 (19–36)	60.77±7.51 (50.0–77.6)	167.24±4.72 (158.5–180.0)	training	Mathew 2011 [12]
po (IR cap, SD)	2	47	0	Asian	25.8	(19–30)	70.0±6.77	-	training	Kim 2017 [13]
po (IR cap, SD)	2	24	0	White American	7.8	37.6	-	-	test	Wring 2019 [14]
po (IR cap, SD)	2	19	11	Japanese	25.8	(22–47)	(50–90)	-	test	Itagaki 2004 [15]
po (IR cap, SD)	3	18	0	White American	7.8	29±7.0 (20–44)	78.6±10.0 (56–90)	178±7.4 (168–188)	training	Bekersky 1999 [16]
po (IR cap, SD)	3	32	34	White American	7.8	38±13.4	76.1±12.0	-	test	Bekersky 1998 [17]
po (IR cap, SD)	3.5	36	50	White American	7.8	25.8 (20–40)	69.8 (47.5–92.4)	173.5 (156.0–195.0)	test	Sansone-Parsons 2007 [18]
po (IR cap, SD)	5	12	58	White American	0	23.5±3.5	66.5±13.5	-	training	Zheng 2012 [19]
po (IR cap, SD)	5	109	0	Asian	25.8	27.8±6.13 (18–44)	61.30±7.44 (46.8–83.0)	167.64±5.51 (153.5–180.0)	training	Mathew 2011 [12]
po (IR cap, SD)	5	8	25	White American	7.8	28±10 (20–50)	78.1±12.9 (67.6–105)	-	training	Bekersky 2001 [10]
po (IR cap, SD)	5	32	34	White American	7.8	31±11 (19–53)	74±11.1 (54.9–94.5)	174.5±8 (159–189)	test	Bekersky 1999 [20]
po (IR cap, SD)	5	12	33	Black American	60.5	32.2±10.8	-	-	test	Mancinelli 2001 [9]
po (IR cap, SD)	5	12	42	White American	7.8	44.6±19.1	-	-	test	Mancinelli 2001 [9]
po (IR cap, SD)	5	12	50	Mexican American	20.2	35.7±11.6	-	-	test	Mancinelli 2001 [9]
po (IR cap, SD)	5	41	81	White American	7.8	47±13 (21–66)	68.0±8.3 (53.1–85.5)	164.8±7.4 (151.5–180.5)	test	Lainesse 2008 [21]

–: not given, ^a: implemented, cap: capsule, CYP: cytochrome P450, d: dosage period in days, ER: extended-release, inf: infusion, IR: immediate-release, iv: intravenous, MD: multiple dose (once daily), n: number of participants, po: oral, SD: single dose; values for age, weight and height are shown as mean ± standard deviation (range).

Table S2: Clinical studies of tacrolimus used for PBPK model development (*continued*)

Tacrolimus dosing regimen		n	Females	Ethnicity ^a	Frequency ^a of	Age	Weight	Height	Dataset	Reference
Route	Dose [mg]		[%]		<i>CYP3A5*1</i> [%]	[years]	[kg]	[cm]		
po (IR cap, SD)	5	32	34	White American	7.8	31±11 (19–53)	74±11.1 (54.9–94.5)	174.5±8 (159–189)	test	Bekersky 1999 [20]
po (IR cap, SD)	5	15	0	White American	7.8	32.6±10.1 (20–45)	85.2±9.42 (70.9–102)	179±5.77 (170–190)	test	Bekersky 2001 [22]
po (IR cap, SD)	5	24	38	White American	7.8	35±11.4	75.2±14.5	-	test	Groll 2017 [23]
po (IR cap, SD)	5	36	50	European	7.8	27±8.3	72±13	175±9	test	Huppertz 2021 [24]
po (IR cap, SD)	5	36	0	White American	7.8	26±6 (20–49)	75.5±10.4 (52.7–100.1)	-	test	Dowell 2007 [25]
po (IR cap, SD)	5	16	0	White American	7.8	34.0±9.23 (22–45)	82.5±10.3 (64.1–100)	183±6.48 (173–193)	test	Bekersky 2001 [26]
po (IR cap, SD)	5	25	44	White American	7.8	-	-	-	test	Alloway 2020 [27]
po (IR cap, SD)	7	18	0	White American	7.8	29±7.0 (20–44)	78.6±10.0 (56–90)	178±7.4 (168–188)	training	Bekersky 1999 [16]
po (IR cap, SD)	7	18	67	European	7.8	39±16	-	-	test	Stift 2014 [28]
po (IR cap, SD)	8	1	0	White American	0	-	-	-	test	Floren 1997 [11]
po (IR cap, SD)	10	18	0	White American	7.8	29±7.0 (20–44)	78.6±10.0 (56–90)	178±7.4 (168–188)	training	Bekersky 1999 [16]
po (IR cap, SD)	10	27	0	European	7.8	31.4±8.6 (18–46)	71.4±8.0 (57–91)	-	test	Tortorici 2013 [29]
po (ER cap, SD)	2	21	0	White American	7.8	-	86.6	-	training	Mercuri 2016 [30]
po (ER cap, SD)	3	16	0	European	15.6	(18–28)	-	-	test	Vanhove 2019 [31]
po (ER cap, MD, 10d)	5	93	0	European	7.8	-	-	-	training	Gantar 2020 [32]
po (ER cap, SD)	5	113	-	European	7.8	-	-	-	test	Gantar 2020 [32]
po (ER cap, SD)	10	20	0	European	7.8	34 (20–54)	75.2 (53.5–96.9)	-	test	Undre 2017 [33]

–: not given, ^a: implemented, cap: capsule, CYP: cytochrome P450, d: dosage period in days, ER: extended-release, inf: infusion, IR: immediate-release, iv: intravenous, MD: multiple dose (once daily), n: number of participants, po: oral, SD: single dose; values for age, weight and height are shown as mean ± standard deviation (range).

S1.4 Drug-dependent Parameters

Table S3: Drug-dependent parameters of the final tacrolimus PBPK model

Parameter	Unit	Value	Source	Literature	Reference	Description
Tacrolimus						
Molecular weight	g/mol	804.03	Lit.	804.03	[36]	Molecular weight
pKa, acid		9.96	Lit.	9.96	[36]	Acid dissociation constant
Solubility (pH)	mg/mL	0.01 (7.4)	Lit.	0.01 (7.4)	[36]	Solubility
Lipophilicity	log units	5.37	Opt.	2.74–5.594	[36–38]	Lipophilicity
f_u	%	1.2	Lit.	1.2	[39]	Fraction unbound
CYP3A4 $K_M \rightarrow$ sink	$\mu\text{mol/L}$	0.21	Lit.	0.21 ^a , 1.5	[40, 41]	Michaelis-Menten constant
CYP3A4 $k_{\text{cat}} \rightarrow$ sink	1/min	4.42	Opt.	0.72, 8.0	[40, 41]	Catalytic rate constant
CYP3A5 $K_M \rightarrow$ sink	$\mu\text{mol/L}$	0.21	Lit.	0.21 ^a , 1.4	[40, 41]	Michaelis-Menten constant
CYP3A5 NM (100%) $k_{\text{cat}} \rightarrow$ sink	1/min	47.30	Opt.	1.1, 17.0	[40, 41]	Catalytic rate constant
CYP3A5 PM (0%) $k_{\text{cat}} \rightarrow$ sink	1/min	0	Calc.	-	-	Catalytic rate constant
GFR fraction		1 ^b	Asm.	-	-	Filtered drug in the urine
EHC continuous fraction		1	Asm.	-	-	Bile fraction continuously released
Intestinal permeability IR Tac fasted	cm/s	$3.42 \cdot 10^{-6}$	Opt.	-	-	Transcellular intestinal permeability
Intestinal permeability IR Tac fed	cm/s	$3.79 \cdot 10^{-7}$	Opt.	-	-	Transcellular intestinal permeability
Intestinal permeability ER Tac fasted	cm/s	$1.91 \cdot 10^{-6}$	Opt.	$6.58 \cdot 10^{-6}$	[30]	Transcellular intestinal permeability
Cellular permeability	cm/min	0.02	Calc.	Charge dependent Schmitt	[42]	Permeability into the cellular space
Partition coefficients			Calc.	Berezhkovskiy	[43]	Organ-plasma partition coefficients
Dissolution time (Weibull) IR Tac fasted	min	18.85	Lit.	18.85 ^c	[44]	Dissolution time (50%)
Dissolution shape (Weibull) IR Tac fasted		0.08	Opt.	0.12 ^c	[44]	Dissolution shape
Dissolution time (Weibull) IR Tac fed	min	63.03	Opt.	-	-	Dissolution time (50%)
Dissolution shape (Weibull) IR Tac fed		0.94	Opt.	-	-	Dissolution shape
Dissolution time (Weibull) ER Tac fasted	h	3.40	Lit.	3.13 ^c	[30]	Dissolution time (50%)
Dissolution shape (Weibull) ER Tac fasted		0.06	Opt.	0.12 ^c	[30]	Dissolution shape
CYP3A4 K_i	$\mu\text{mol/L}$	0.04	Lit.	0.04 ^a	[45]	Diss. const. inhibitor-enzyme complex (CI)
CYP3A4 K_I	$\mu\text{mol/L}$	2.66	Lit.	2.66	[45]	Conc. for half-maximal inactivation (MBI)
CYP3A4 k_{inact}	1/min	0.30	Lit.	0.30	[45]	Maximum inactivation rate constant (MBI)
CYP3A5 K_I	$\mu\text{mol/L}$	2.69	Lit.	2.69	[45]	Conc. for half-maximal inactivation (MBI)
CYP3A5 k_{inact}	1/min	0.21	Lit.	0.21	[45]	Maximum inactivation rate constant (MBI)

-: not available, ^a: *in vitro* values corrected for binding in the assay ($f_{u,\text{mic}}$) calculated according to [34], ^b: a GFR fraction of 1 corresponds to passive glomerular filtration of a compound, ^c: obtained from literature dissolution profile according to [35], asm.: assumed, calc.: calculated, CI: competitive inhibition, conc.: concentration, const.: constant, CYP: cytochrome P450, EHC: enterohepatic circulation, diss.: dissociation, ER: extended-release, GFR: glomerular filtration rate, IR: immediate-release, lit.: literature, MBI: mechanism-based inactivation, NM: normal metabolizer, opt.: optimized, PM: poor metabolizer, Tac: tacrolimus.

Table S4: Key modeling assumptions, including the resulting modeling decisions

Assumption	Modeling Decision
The liberation of IR and ER tacrolimus can be described using Weibull functions.	Different Weibull functions were implemented for IR and ER tacrolimus.
The excipients contained in IR and ER tacrolimus capsules may affect intestinal permeability differently.	A slightly higher intestinal permeability was incorporated for IR tacrolimus than for ER tacrolimus.
CYP3A4 and CYP3A5 are predominantly involved in the metabolism of tacrolimus.	CYP3A4 and CYP3A5 were incorporated as metabolizing enzymes.
The functional <i>CYP3A5</i> *1 allele and the nonfunctional *3 allele exhibit 100% and 0% activity, respectively.	The reported fraction of functional *1 allele in a study population was used for activity assignment relative to homozygous carriers of the *1 allele. Different levels of activity were implemented by activity-specific CYP3A5 k_{cat} values, i.e., 100% relative activity corresponded to a k_{cat} of 100%.
Frequencies of *1 alleles reported for different ethnic groups are representative for frequencies in the study populations.	In the absence of genotype/phenotype information of a study group, CYP3A5 activity was assumed according to the frequency of the *1 allele observed in the respective ethnic group.
Renal excretion of tacrolimus occurs via passive glomerular filtration.	In PK-Sim [®] , a GFR fraction of 1 was implemented for tacrolimus.
Under fed conditions, the release kinetics differ from those under fasted conditions, e.g., due to altered gastric pH.	Different Weibull functions were implemented for fasted and fed conditions.
Under fed conditions, the absorption of tacrolimus is altered, presumably due to the binding of tacrolimus to lipoproteins and food components, given its pronounced lipophilicity.	A lower intestinal permeability was incorporated for fed conditions compared to fasted conditions.
CYP: cytochrome P450, ER: extended-release, GFR: glomerular filtration rate, IR: immediate-release, k_{cat} : catalytic rate constant.	

S2 Physiologically Based Pharmacokinetic Model Evaluation

S2.1 Whole Blood Concentration-Time Profiles (Semilogarithmic)

S2.1.1 Intravenous Tacrolimus

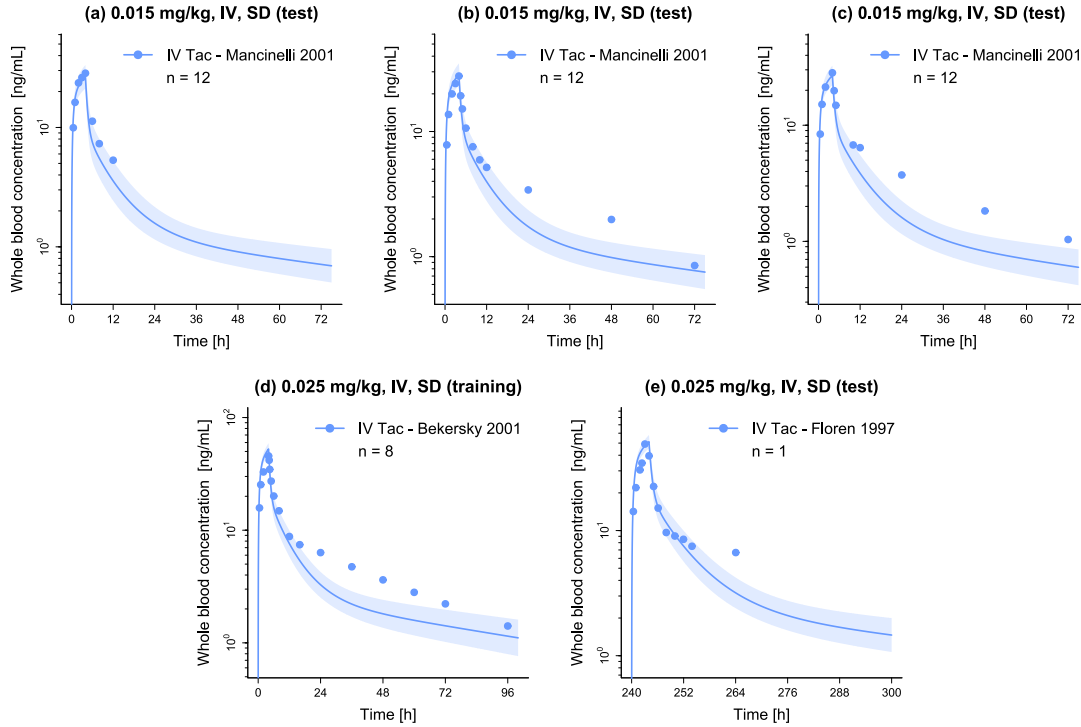


Figure S1: Semilogarithmic plots of predicted whole blood concentration-time profiles of IV tacrolimus (fasted). Solid lines and ribbons represent population predictions ($n = 1000$; geometric mean and geometric standard deviation), while corresponding observed data are shown as dots [9–11]. IV: intravenous, n: number of participants, SD: single dose, Tac: tacrolimus.

S2.1.2 Immediate-Release Oral Tacrolimus

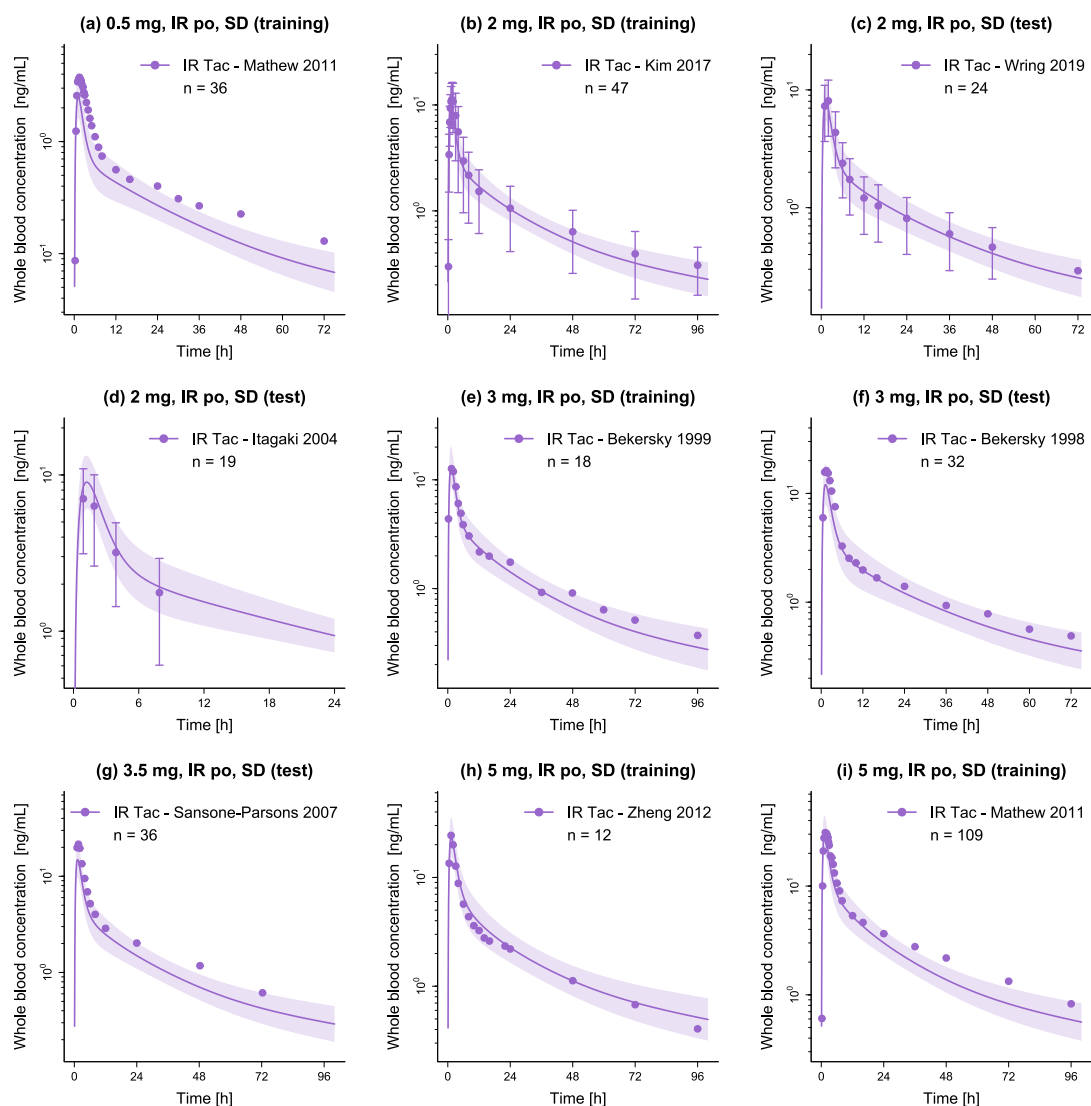


Figure S2: Semilogarithmic plots of predicted whole blood concentration-time profiles of IR tacrolimus (fasted). Solid lines and ribbons represent population predictions ($n = 1000$; geometric mean and geometric standard deviation), while corresponding observed data are shown as dots (\pm standard deviation, if available) [12–19]. IR: immediate-release, n: number of participants, po: oral, SD: single dose, Tac: tacrolimus.

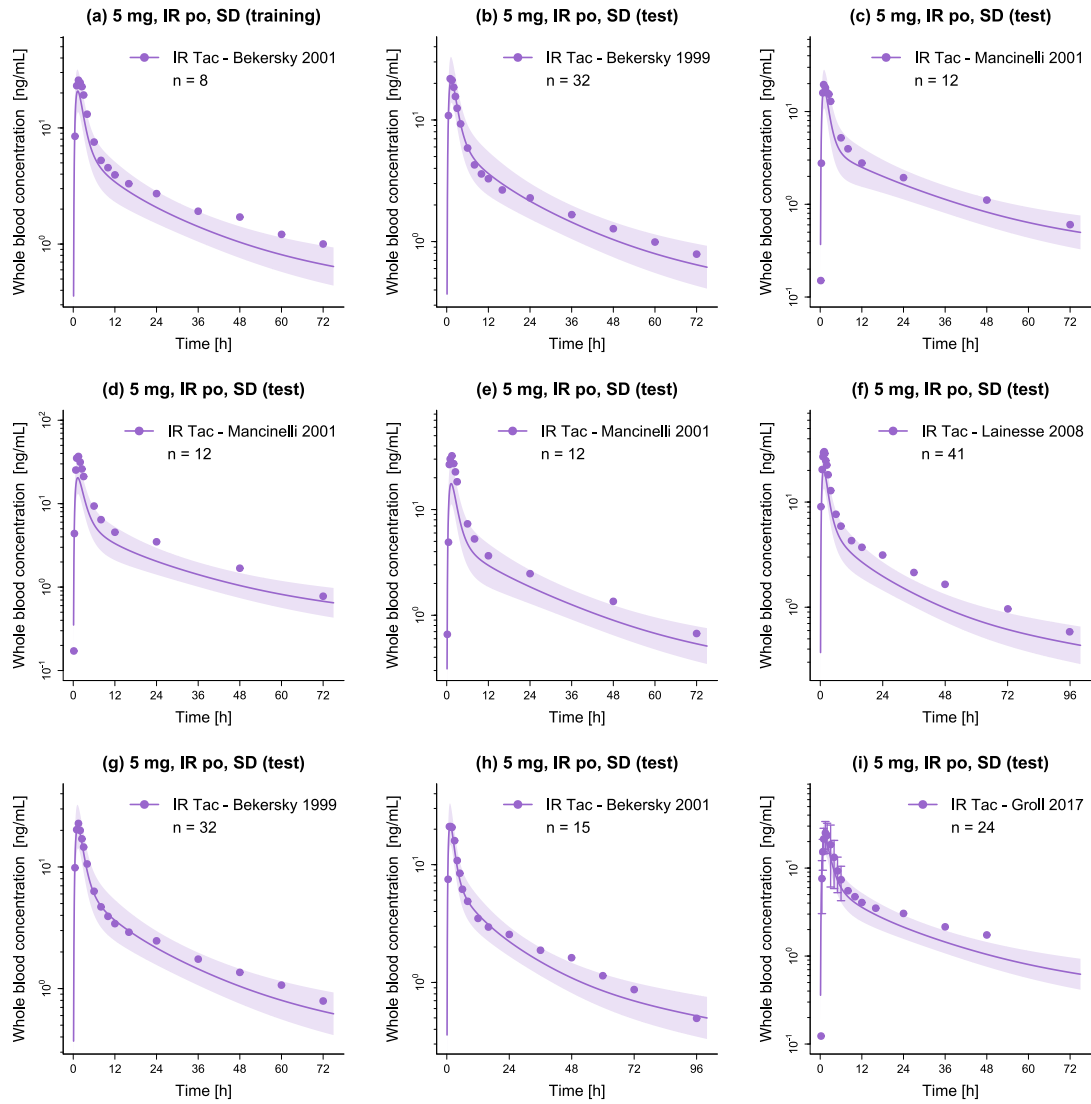


Figure S3: Semilogarithmic plots of predicted whole blood concentration-time profiles of IR tacrolimus (fasted). Solid lines and ribbons represent population predictions ($n = 1000$; geometric mean and geometric standard deviation), while corresponding observed data are shown as dots (\pm standard deviation, if available) [9, 10, 20–23]. IR: immediate-release, n: number of participants, po: oral, SD: single dose, Tac: tacrolimus.

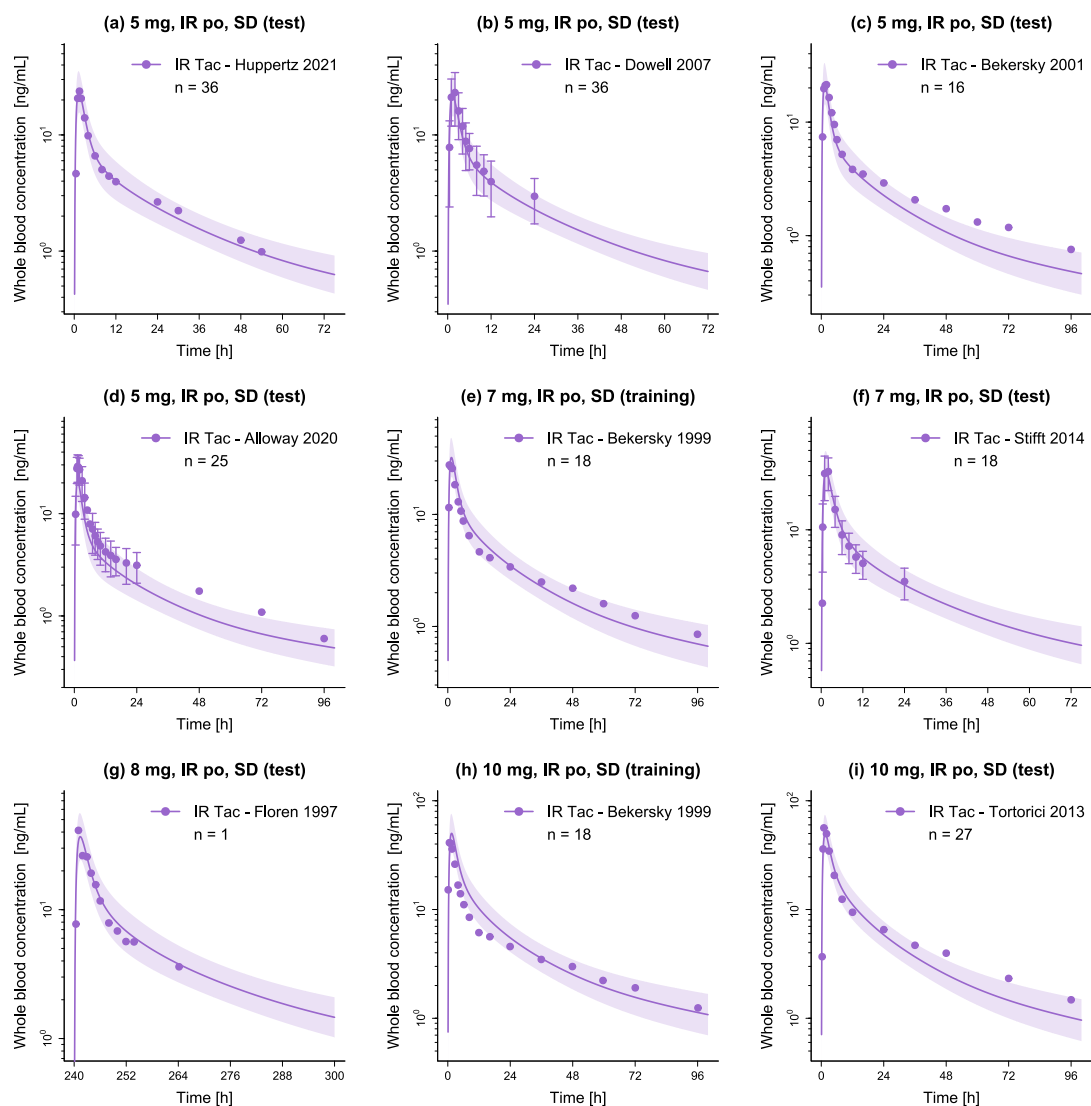


Figure S4: Semilogarithmic plots of predicted whole blood concentration-time profiles of IR tacrolimus (fasted). Solid lines and ribbons represent population predictions ($n = 1000$; geometric mean and geometric standard deviation), while corresponding observed data are shown as dots (\pm standard deviation, if available) [11, 16, 24–29]. IR: immediate-release, n: number of participants, po: oral, SD: single dose, Tac: tacrolimus.

S2.1.3 Extended-Release Oral Tacrolimus

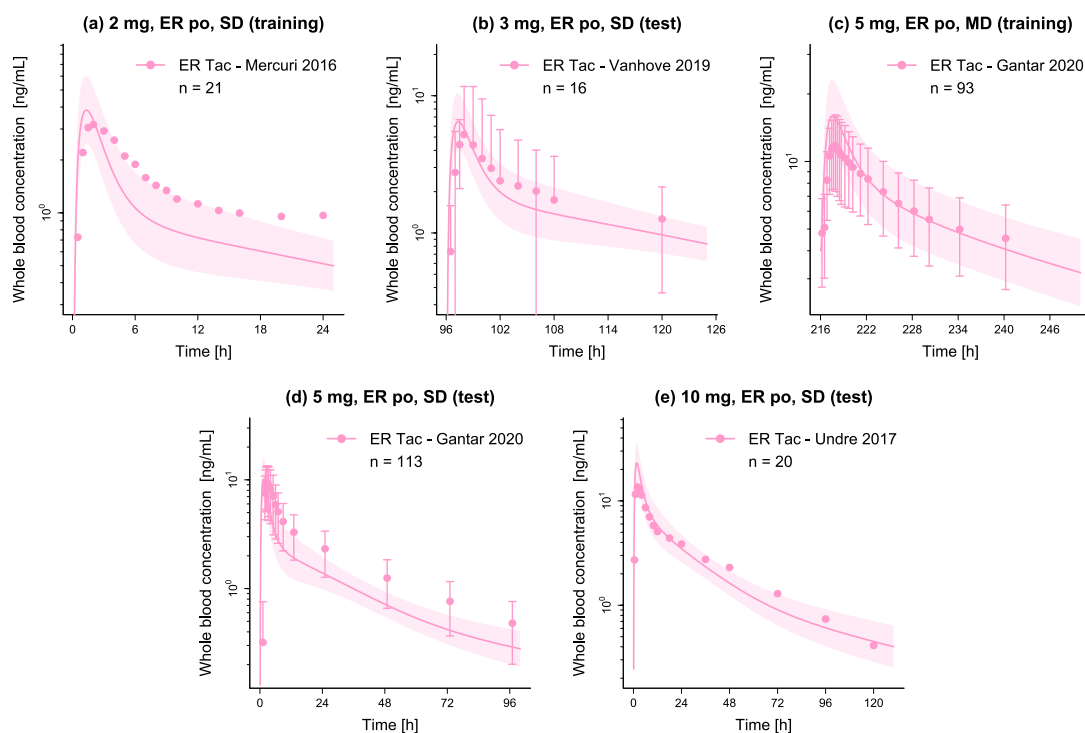


Figure S5: Semilogarithmic plots of predicted whole blood concentration-time profiles of ER tacrolimus (fasted). Solid lines and ribbons represent population predictions (n = 1000; geometric mean and geometric standard deviation), while corresponding observed data are shown as dots (± standard deviation, if available) [30–33]. ER: extended-release, MD: multiple dose, n: number of participants, po: oral, SD: single dose, Tac: tacrolimus.

S2.2 Whole Blood Concentration-Time Profiles (Linear)

S2.2.1 Intravenous Tacrolimus

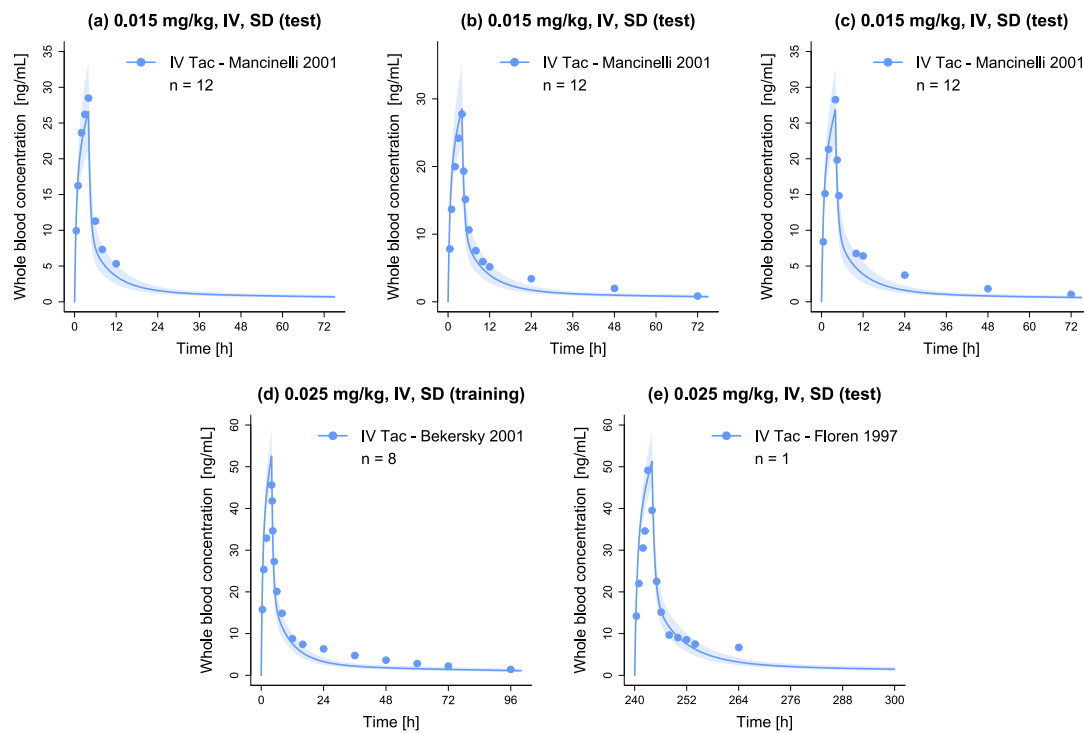


Figure S6: Linear plots of predicted whole blood concentration-time profiles of IV tacrolimus (fasted). Solid lines and ribbons represent population predictions ($n = 1000$; geometric mean and geometric standard deviation), while corresponding observed data are shown as dots [9–11]. IV: intravenous, n: number of participants, SD: single dose, Tac: tacrolimus.

S2.2.2 Immediate-Release Oral Tacrolimus

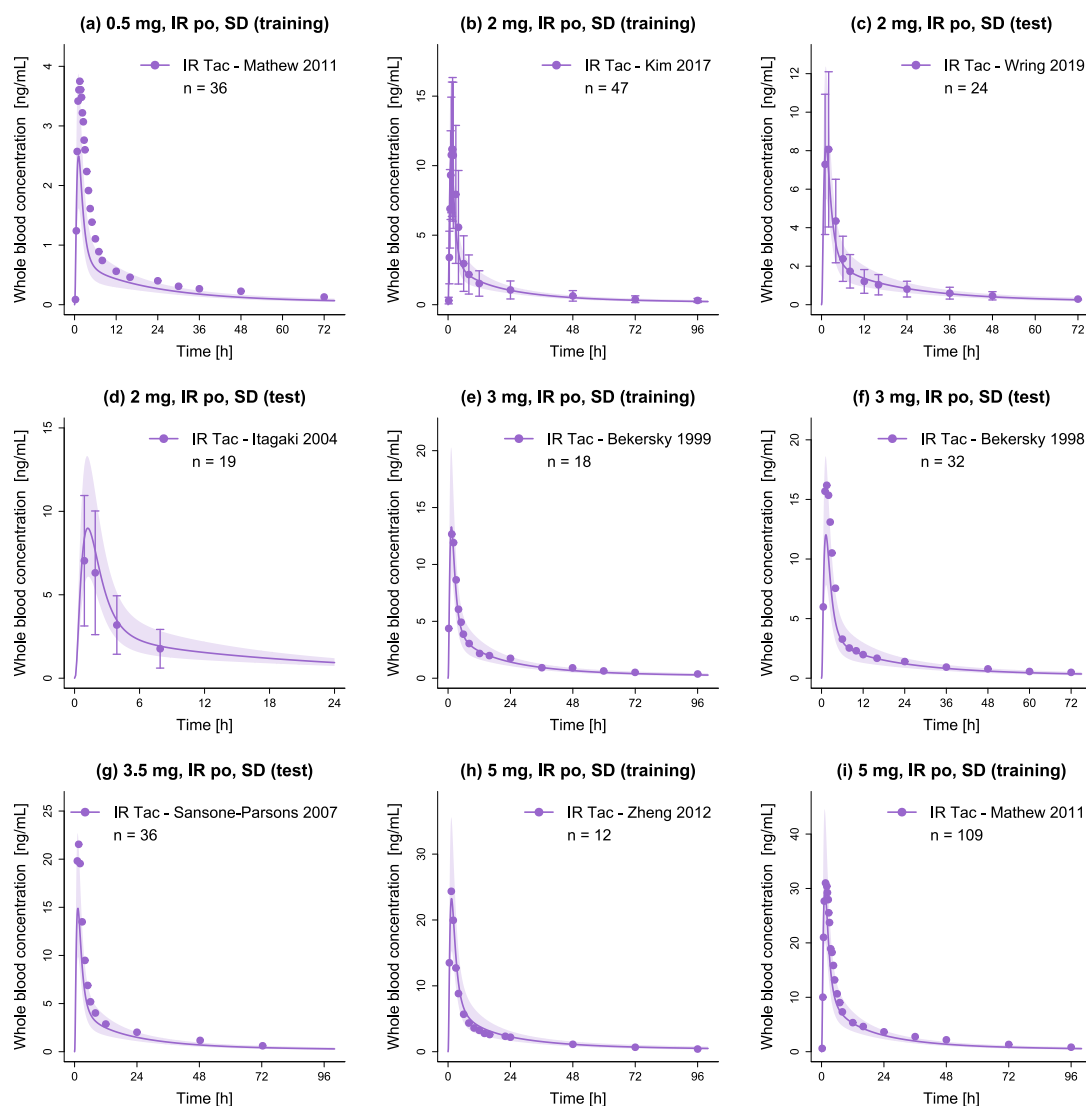


Figure S7: Linear plots of predicted whole blood concentration-time profiles of IR tacrolimus (fasted). Solid lines and ribbons represent population predictions ($n = 1000$; geometric mean and geometric standard deviation), while corresponding observed data are shown as dots (\pm standard deviation, if available) [12–19]. IR: immediate-release, n: number of participants, po: oral, SD: single dose, Tac: tacrolimus.

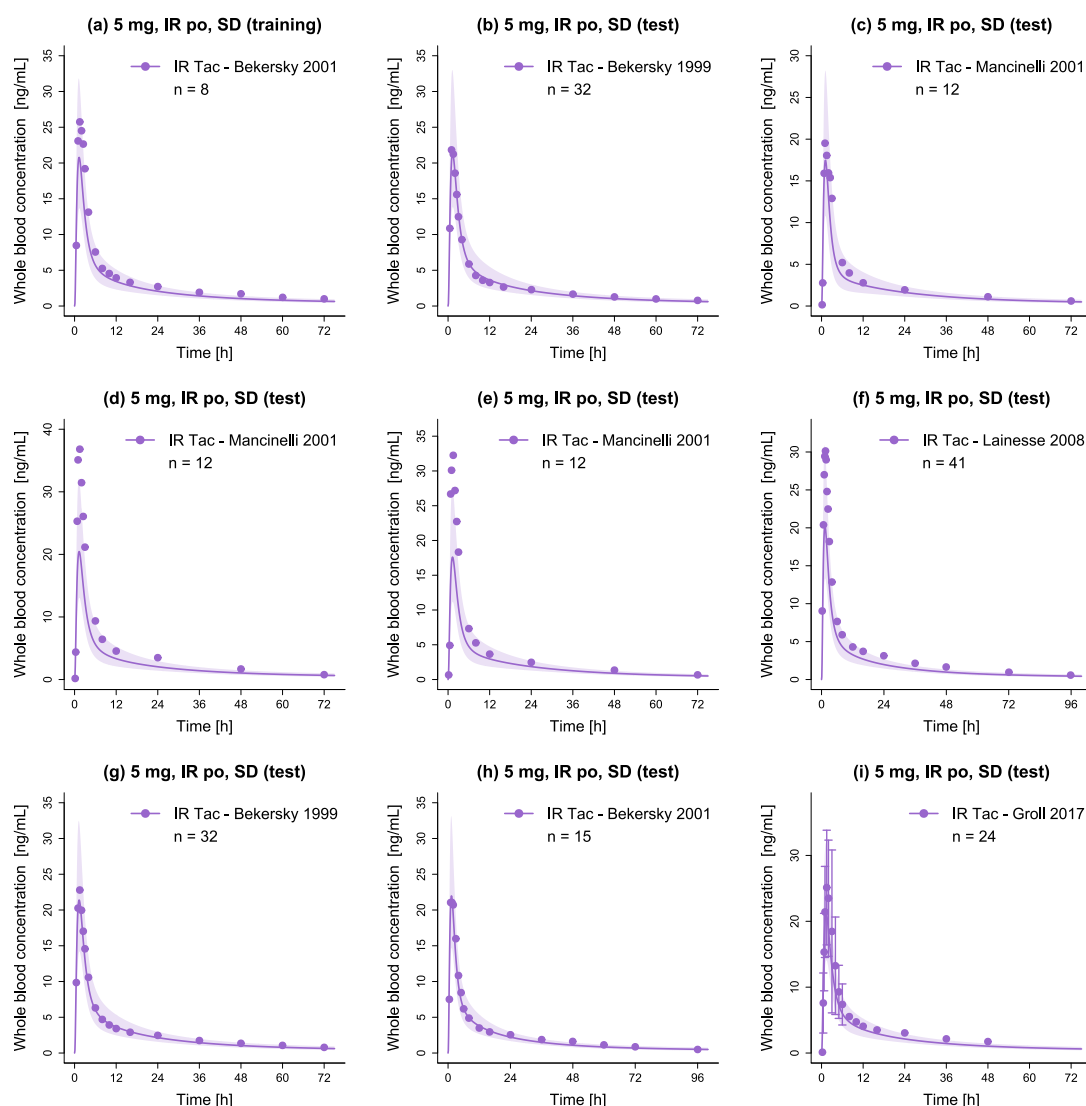


Figure S8: Linear plots of predicted whole blood concentration-time profiles of IR tacrolimus (fasted). Solid lines and ribbons represent population predictions ($n = 1000$; geometric mean and geometric standard deviation), while corresponding observed data are shown as dots (\pm standard deviation, if available) [9, 10, 20–23]. IR: immediate-release, n: number of participants, po: oral, SD: single dose, Tac: tacrolimus.

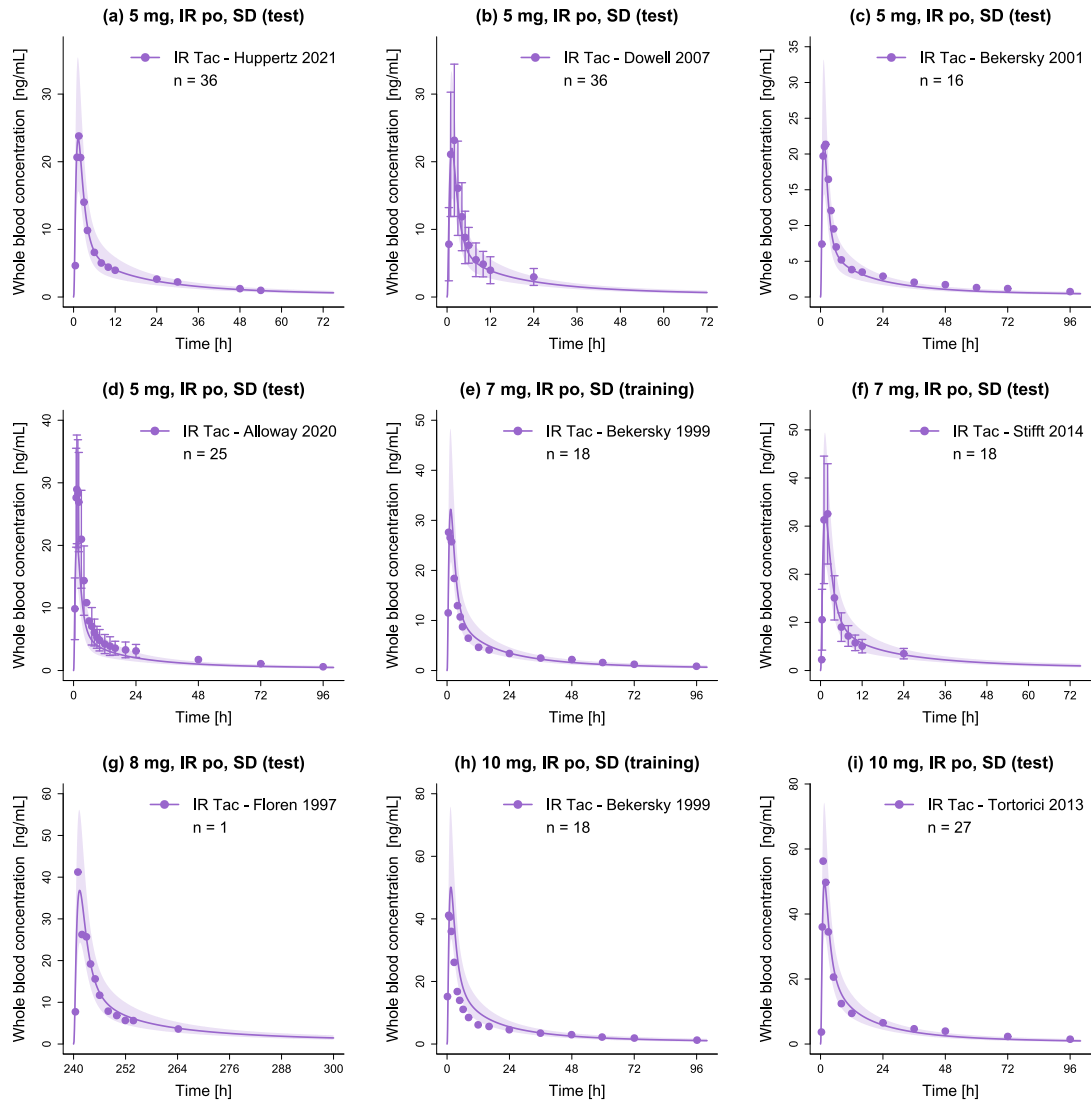


Figure S9: Linear plots of predicted whole blood concentration-time profiles of IR tacrolimus (fasted). Solid lines and ribbons represent population predictions ($n = 1000$; geometric mean and geometric standard deviation), while corresponding observed data are shown as dots (\pm standard deviation, if available) [11, 16, 24–29]. IR: immediate-release, n: number of participants, po: oral, SD: single dose, Tac: tacrolimus.

S2.2.3 Extended-Release Oral Tacrolimus

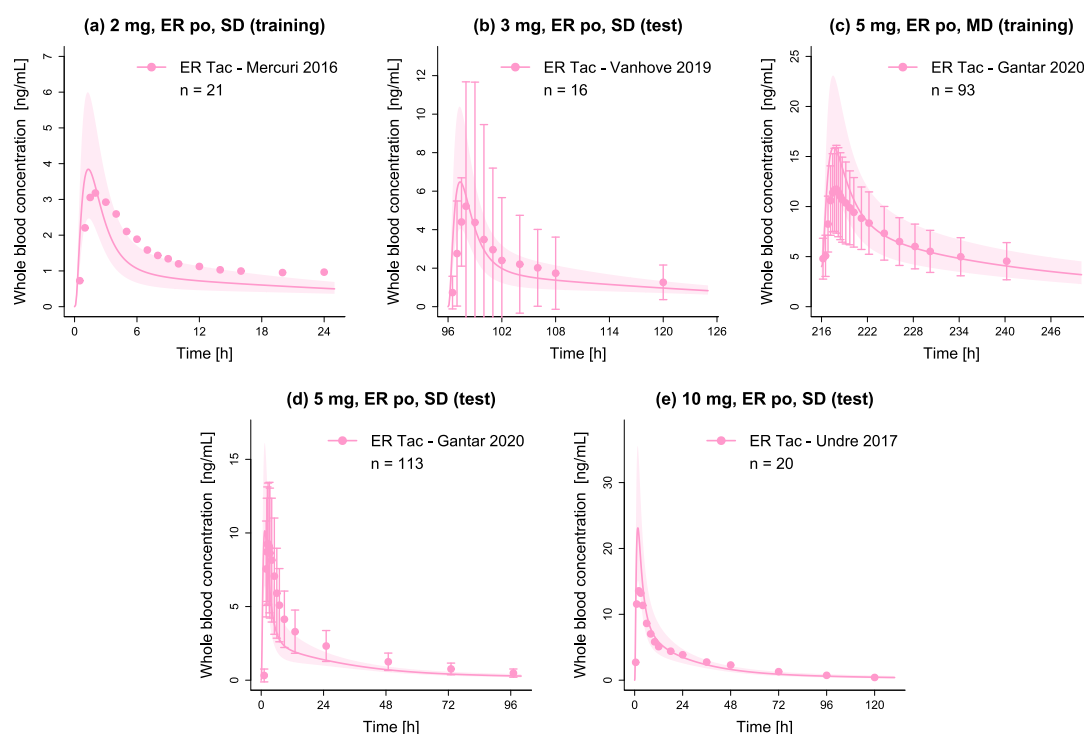


Figure S10: Linear plots of predicted whole blood concentration-time profiles of ER tacrolimus (fasted). Solid lines and ribbons represent population predictions ($n = 1000$; geometric mean and geometric standard deviation), while corresponding observed data are shown as dots (\pm standard deviation, if available) [30–33]. ER: extended-release, MD: multiple dose, n: number of participants, po: oral, SD: single dose, Tac: tacrolimus.

S2.3 Urinary Excretion Profiles

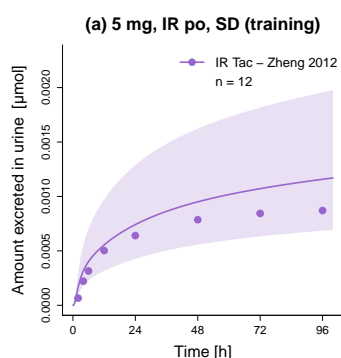


Figure S11: Cumulative amount excreted in urine of IR tacrolimus. Solid lines and ribbons represent population predictions ($n = 1000$; geometric mean and geometric standard deviation), while corresponding observed data are shown as dots [19]. IR: immediate-release, n: number of participants, po: oral, SD: single dose, Tac: tacrolimus.

S2.4 Whole Blood Concentration Goodness-of-Fit Plots

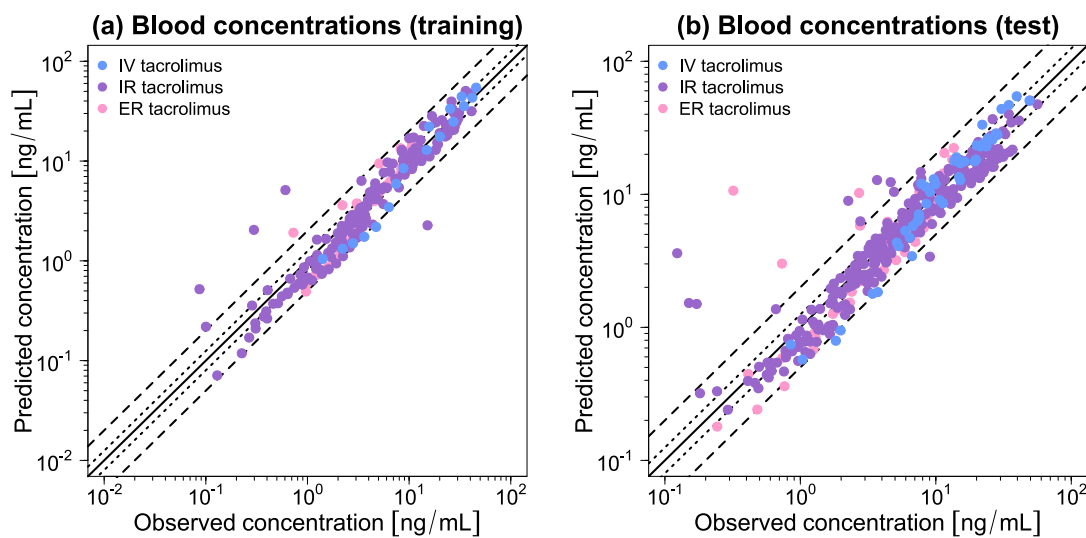


Figure S12: Goodness-of-fit plots of the final tacrolimus model. Stratified by training (a) and test dataset (b), predicted whole blood concentration measurements are plotted against corresponding observed data. The solid line represents the line of identity, while dotted lines indicate 1.25-fold and dashed lines 2-fold deviation from the respective observed value. ER: extended-release, IR: immediate-release, IV: intravenous.

S2.5 AUC_{last} and C_{max} Goodness-of-Fit Plots

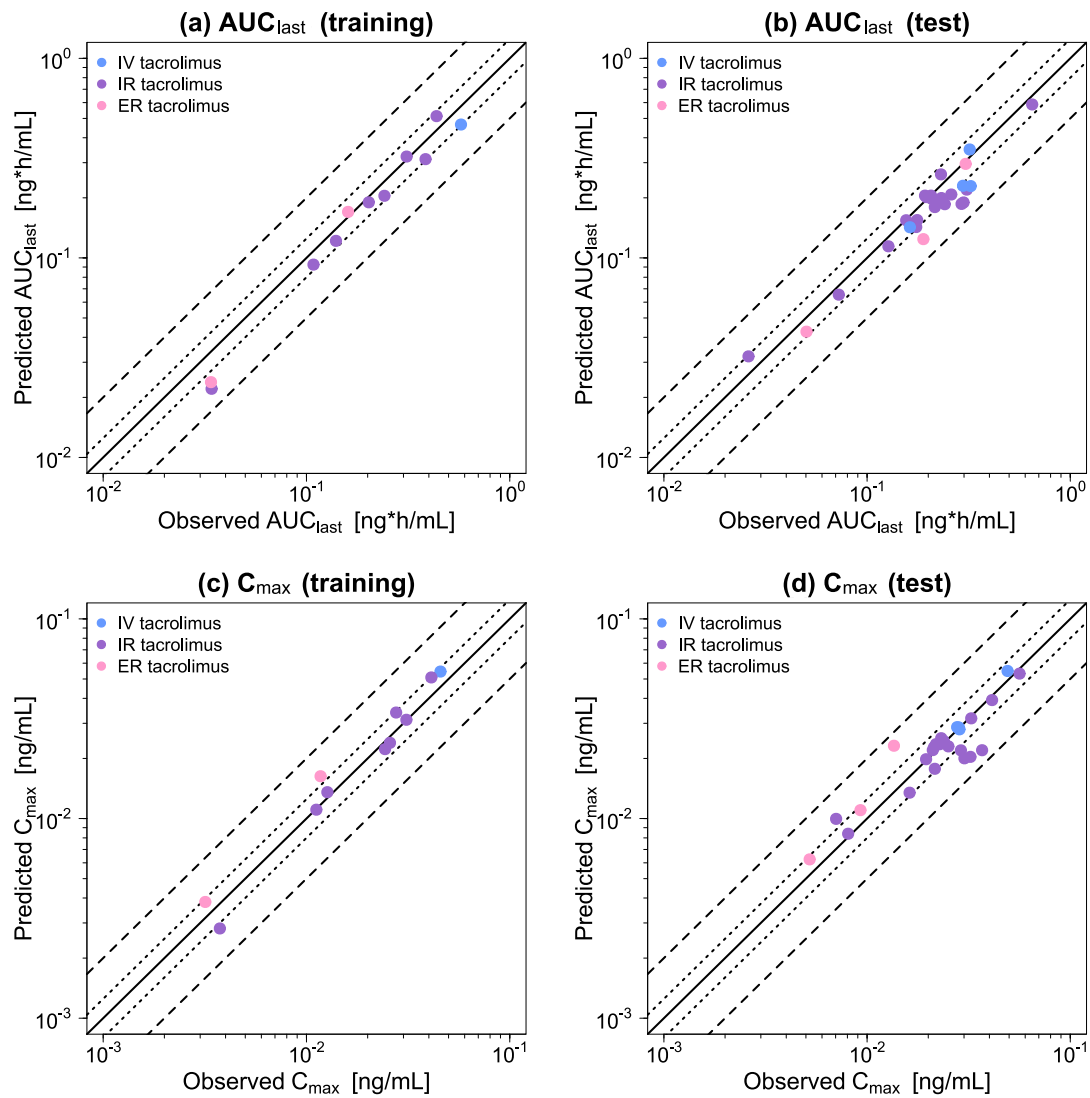


Figure S13: Goodness-of-fit plots of the final tacrolimus model. Stratified by training (left column) and test (right column) dataset, predicted AUC_{last} (a–b) and C_{max} (c–d) values are plotted against corresponding observed data. The solid line represents the line of identity, while dotted lines indicate 1.25-fold and dashed lines 2-fold deviation from the respective observed value. AUC_{last} : area under the whole blood concentration-time curve determined between first and last concentration measurements, C_{max} : maximum whole blood concentration, ER: extended-release, IR: immediate-release, IV: intravenous.

S2.6 MRD of Whole Blood Concentration Predictions

Table S5: MRD values of whole blood concentration predictions

Tacrolimus dosing regimen		n	Dataset	MRD	Reference
Route	Dose [mg]				
iv (inf, 4 h, SD)	0.015/kg	12	test	1.18	Mancinelli 2001 [9]
iv (inf, 4 h, SD)	0.015/kg	12	test	1.37	Mancinelli 2001 [9]
iv (inf, 4 h, SD)	0.015/kg	12	test	1.50	Mancinelli 2001 [9]
iv (inf, 4 h, SD)	0.025/kg	8	training	1.49	Bekersky 2001 [10]
iv (inf, 4 h, SD)	0.025/kg	1	test	1.35	Floren 1997 [11]
po (IR cap, SD)	0.5	36	training	1.81	Mathew 2011 [12]
po (IR cap, SD)	2	47	training	1.71	Kim 2017 [13]
po (IR cap, SD)	2	24	test	1.17	Wring 2019 [14]
po (IR cap, SD)	2	19	test	1.28	Itagaki 2004 [15]
po (IR cap, SD)	3	18	training	1.29	Bekersky 1999 [16]
po (IR cap, SD)	3	32	test	1.25	Bekersky 1998 [17]
po (IR cap, SD)	3.5	36	test	1.24	Sansone-Parsons 2007 [18]
po (IR cap, SD)	5	12	training	1.09	Zheng 2012 [19]
po (IR cap, SD)	5	109	training	1.68	Mathew 2011 [12]
po (IR cap, SD)	5	8	training	1.27	Bekersky 2001 [10]
po (IR cap, SD)	5	32	test	1.19	Bekersky 1999 [20]
po (IR cap, SD)	5	12	test	1.31	Mancinelli 2001 [9]
po (IR cap, SD)	5	12	test	1.53	Mancinelli 2001 [9]
po (IR cap, SD)	5	12	test	1.52	Mancinelli 2001 [9]
po (IR cap, SD)	5	41	test	1.59	Lainesse 2008 [21]
po (IR cap, SD)	5	32	test	1.17	Bekersky 1999 [20]
po (IR cap, SD)	5	15	test	1.25	Bekersky 2001 [22]
po (IR cap, SD)	5	24	test	1.27	Groll 2017 [23]
po (IR cap, SD)	5	36	test	1.32	Huppertz 2021 [24]
po (IR cap, SD)	5	36	test	1.20	Dowell 2007 [25]
po (IR cap, SD)	5	16	test	1.38	Bekersky 2001 [26]
po (IR cap, SD)	5	25	test	1.39	Alloway 2020 [27]
po (IR cap, SD)	7	18	training	1.25	Bekersky 1999 [16]
po (IR cap, SD)	7	18	test	1.57	Stift 2014 [28]
po (IR cap, SD)	8	1	test	1.28	Floren 1997 [11]
po (IR cap, SD)	10	18	training	1.75	Bekersky 1999 [16]
po (IR cap, SD)	10	27	test	1.52	Tortorici 2013 [29]
po (ER cap, SD)	2	21	training	1.73	Mercuri 2016 [30]
po (ER cap, SD)	3	16	test	1.70	Vanhove 2019 [31]
po (ER cap, MD, 10d)	5	93	training	1.31 (D10)	Gantar 2020 [32]
po (ER cap, SD)	5	113	test	2.46	Gantar 2020 [32]
po (ER cap, SD)	10	20	test	1.54	Undre 2017 [33]
Training dataset mean MRD (range)			1.49 (1.09–1.81)		
Test dataset mean MRD (range)			1.40 (1.17–2.46)		
Overall mean MRD (range)			1.43 (1.09–2.46)		
MRD \leq 2			36/37		

Cap: capsule, d: dosage period in days, D: day of pharmacokinetic sampling, ER: extended-release, inf: infusion, IR: immediate-release, iv: intravenous, MD: multiple dose (once daily), MRD: mean relative deviation, n: number of participants, po: oral, SD: single dose.

S2.7 Predicted and Observed AUC_{last} and C_{max} Values

Table S6: Predicted versus observed AUC_{last} and C_{max} values

Tacrolimus dosing regimen		n	Dataset	AUC _{last}			C _{max}			Reference
Route	Dose [mg]			Pred [$\frac{ng \cdot h}{mL}$]	Obs [$\frac{ng \cdot h}{mL}$]	Pred/Obs	Pred [$\frac{ng}{mL}$]	Obs [$\frac{ng}{mL}$]	Pred/Obs	
iv (inf, 4 h, SD)	0.015/kg	12	test	142.45	162.45	0.88	27.98	28.48	0.98	Mancinelli 2001 [9]
iv (inf, 4 h, SD)	0.015/kg	12	test	229.85	296.55	0.78	28.69	27.74	1.03	Mancinelli 2001 [9]
iv (inf, 4 h, SD)	0.015/kg	12	test	229.01	323.52	0.71	28.60	28.26	1.01	Mancinelli 2001 [9]
iv (inf, 4 h, SD)	0.025/kg	8	training	465.95	575.58	0.81	54.48	45.62	1.19	Bekersky 2001 [10]
iv (inf, 4 h, SD)	0.025/kg	1	test	349.43	319.86	1.09	54.84	49.13	1.12	Floren 1997 [11]
po (IR cap, SD)	0.5	36	training	22.08	34.14	0.65	2.82	3.75	0.75	Mathew 2011 [12]
po (IR cap, SD)	2	47	training	92.55	108.25	0.85	11.07	11.18	0.99	Kim 2017 [13]
po (IR cap, SD)	2	24	test	65.42	72.57	0.90	8.39	8.07	1.04	Wring 2019 [14]
po (IR cap, SD)	2	19	test	32.10	26.08	1.23	9.96	7.04	1.42	Itagaki 2004 [15]
po (IR cap, SD)	3	18	training	121.73	139.67	0.87	13.56	12.67	1.07	Bekersky 1999 [16]
po (IR cap, SD)	3	32	test	114.33	127.30	0.90	13.47	16.19	0.83	Bekersky 1998 [17]
po (IR cap, SD)	3.5	36	test	142.77	174.46	0.82	17.75	21.55	0.82	Sansone-Parsons 2007 [18]
po (IR cap, SD)	5	12	training	189.89	202.54	0.94	22.27	24.35	0.91	Zheng 2012 [19]
po (IR cap, SD)	5	109	training	312.54	385.23	0.81	31.24	31.01	1.01	Mathew 2011 [12]
po (IR cap, SD)	5	8	training	204.75	241.76	0.85	23.95	25.57	0.93	Bekersky 2001 [10]
po (IR cap, SD)	5	32	test	205.19	192.78	1.06	23.57	21.83	1.08	Bekersky 1999 [20]
po (IR cap, SD)	5	12	test	155.34	176.64	0.88	19.82	19.52	1.02	Mancinelli 2001 [9]
po (IR cap, SD)	5	12	test	190.20	298.74	0.64	21.99	36.81	0.60	Mancinelli 2001 [9]
po (IR cap, SD)	5	12	test	185.79	241.11	0.77	20.37	32.25	0.63	Mancinelli 2001 [9]
po (IR cap, SD)	5	41	test	186.43	291.67	0.64	20.03	30.13	0.66	Lainesse 2008 [21]
po (IR cap, SD)	5	32	test	205.20	192.78	0.99	23.57	22.79	1.03	Bekersky 1999 [20]
po (IR cap, SD)	5	15	test	199.51	232.19	0.86	22.02	21.05	1.05	Bekersky 2001 [22]
po (IR cap, SD)	5	24	test	181.67	216.42	0.84	22.98	25.12	0.91	Groll 2017 [23]
po (IR cap, SD)	5	36	test	201.69	195.87	1.03	24.46	23.80	1.03	Huppertz 2021 [24]
po (IR cap, SD)	5	36	test	154.44	155.78	0.99	25.26	23.17	1.09	Dowell 2007 [25]
po (IR cap, SD)	5	16	test	207.86	259.59	0.80	22.75	21.35	1.07	Bekersky 2001 [26]
po (IR cap, SD)	5	25	test	219.83	309.41	0.71	21.96	28.95	0.76	Alloway 2020 [27]

AUC_{last}: area under the whole blood concentration-time curve determined between first and last concentration measurements, cap: capsule, C_{max}: maximum whole blood concentration, d: dosage period in days, D: day of pharmacokinetic sampling, ER: extended-release, GMFE: geometric mean fold error, inf: infusion, IR: immediate-release, iv: intravenous, MD: multiple dose (once daily), n: number of participants, obs: observed, po: oral, pred: predicted, SD: single dose.

Table S6: Predicted versus observed AUC_{last} and C_{max} values (*continued*)

Tacrolimus dosing regimen		n	Dataset	AUC_{last}			C_{max}			Reference
Route	Dose [mg]			Pred [$\frac{ng \cdot h}{mL}$]	Obs [$\frac{ng \cdot h}{mL}$]	Pred/Obs	Pred [$\frac{ng}{mL}$]	Obs [$\frac{ng}{mL}$]	Pred/Obs	
po (IR cap, SD)	7	18	training	322.03	310.92	1.04	33.96	27.61	1.23	Bekersky 1999 [16]
po (IR cap, SD)	7	18	test	197.83	207.83	0.95	31.76	32.55	0.98	Stift 2014 [28]
po (IR cap, SD)	8	1	test	262.43	231.05	1.13	39.20	41.23	0.95	Floren 1997 [11]
po (IR cap, SD)	10	18	training	513.34	436.37	1.18	50.90	41.14	1.24	Bekersky 1999 [16]
po (IR cap, SD)	10	27	test	587.32	649.46	0.90	53.20	56.27	0.95	Tortorici 2013 [29]
po (ER cap, SD)	2	21	training	23.84	33.91	0.70	3.82	3.18	1.20	Mercuri 2016 [30]
po (ER cap, SD)	3	16	test	42.75	50.31	0.85	6.26	5.22	1.20	Vanhove 2019 [31]
po (ER cap, MD, 10d)	5	93	training	170.06	160.21	1.06 (D10)	16.29	11.73	1.39 (D10)	Gantar 2020 [32]
po (ER cap, SD)	5	113	test	124.18	189.24	0.66	11.02	9.28	1.19	Gantar 2020 [32]
po (ER cap, SD)	10	20	test	295.89	305.64	0.97	23.16	12.56	1.71	Undre 2017 [33]
Training dataset mean GMFE (range)				1.21 (1.04–1.55)			1.17 (1.01–1.39)			
Test dataset mean GMFE (range)				1.21 (1.01–1.57)			1.19 (1.01–1.71)			
Overall mean GMFE (range)				1.21 (1.01–1.57)			1.18 (1.01–1.71)			
GMFE ≤ 2				37/37			37/37			

AUC_{last} : area under the whole blood concentration-time curve determined between first and last concentration measurements, cap: capsule, C_{max} : maximum whole blood concentration, d: dosage period in days, D: day of pharmacokinetic sampling, ER: extended-release, GMFE: geometric mean fold error, inf: infusion, IR: immediate-release, iv: intravenous, MD: multiple dose (once daily), n: number of participants, obs: observed, po: oral, pred: predicted, SD: single dose.

S2.8 Local Sensitivity Analysis

S2.8.1 Methods

A local sensitivity analysis was performed for each modeled formulation, by calculating the sensitivity to single parameter changes according to Equation S2. A relative perturbation of 1000% was applied (variation range 10.0, maximum number of 9 steps) and parameters included were either optimized or assumed to affect AUC_{last} .

$$S = \frac{\Delta AUC_{last}}{\Delta p} \cdot \frac{p}{AUC_{last}} \quad (S2)$$

where S = sensitivity, ΔAUC_{last} = change of AUC_{last} , Δp = change of the analyzed parameter value, p = original parameter value, and AUC_{last} = simulated AUC_{last} with the original parameter value.

The threshold for sensitivity was set at $|0.5|$, which corresponds to a 50% change in simulated AUC_{last} given a 100% change in the parameter value examined.

S2.8.2 Results

Table S7: Parameters evaluated during the local sensitivity analyses

Parameter	Source	Parameter	Source
CYP3A4 K_i CI	Literature	Lipophilicity	Optimized
CYP3A4 K_I MBI	Literature	Solubility	Literature
CYP3A4 K_i MBI	Literature	GFR fraction	Assumed
CYP3A4 k_{inact} MBI	Literature	Dissolution shape IR Tac	Optimized
CYP3A5 K_I MBI	Literature	Dissolution time IR Tac	Literature
CYP3A5 K_i MBI	Literature	Dissolution shape ER Tac	Optimized
CYP3A5 k_{inact} MBI	Literature	Dissolution time ER Tac	Optimized
Intestinal permeability IR Tac	Optimized	CYP3A4 K_M	Literature
Intestinal permeability ER Tac	Optimized	CYP3A5 K_M	Literature
pKa, acid	Literature	CYP3A4 k_{cat}	Optimized
f_u	Literature	CYP3A5 k_{cat}	Optimized

CI: competitive inhibition, CYP: cytochrome P450, ER: extended-release, f_u : fraction unbound, GFR: glomerular filtration rate, IR: immediate-release, k_{cat} : catalytic rate constant, K_i : dissociation constant inhibitor-enzyme complex, K_I : concentration for half-maximal inactivation, k_{inact} : maximum inactivation rate constant, K_M : Michaelis-Menten constant, MBI: mechanism-based inactivation, pKa: acid dissociation constant, Tac: tacrolimus.

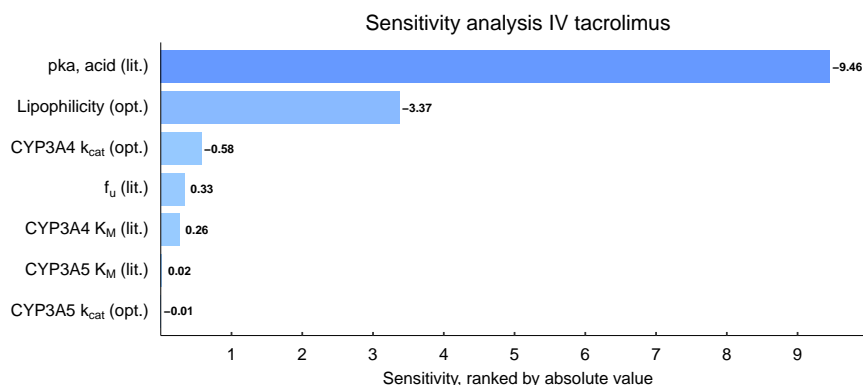


Figure S14: IV tacrolimus model sensitivity analysis (0.025 mg/kg body weight, 4 h infusion, single dose [10]). Presented are parameters with a calculated sensitivity different from 0.00. CYP: cytochrome P450, f_u : fraction unbound, IV: intravenous, k_{cat} : catalytic rate constant, K_M : Michaelis-Menten constant, lit.: literature, opt.: optimized, pKa: acid dissociation constant.

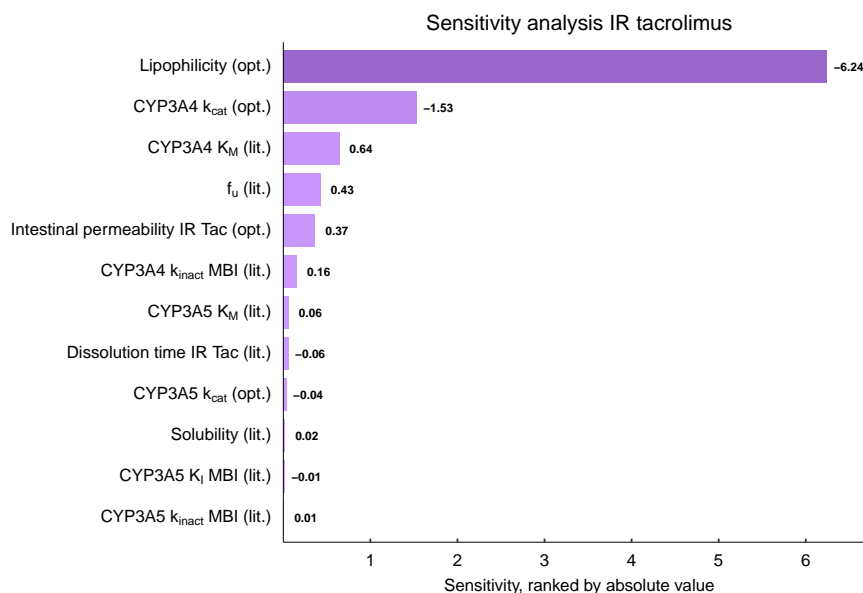


Figure S15: IR tacrolimus model sensitivity analysis (10 mg, single dose [16]). Presented are parameters with a calculated sensitivity different from 0.00. CYP: cytochrome P450, f_u : fraction unbound, IR: immediate-release, k_{cat} : catalytic rate constant, K_i : concentration for half-maximal inactivation, k_{inact} : maximum inactivation rate constant, K_M : Michaelis-Menten constant, lit.: literature, MBI: mechanism-based inactivation, opt.: optimized, Tac: tacrolimus.

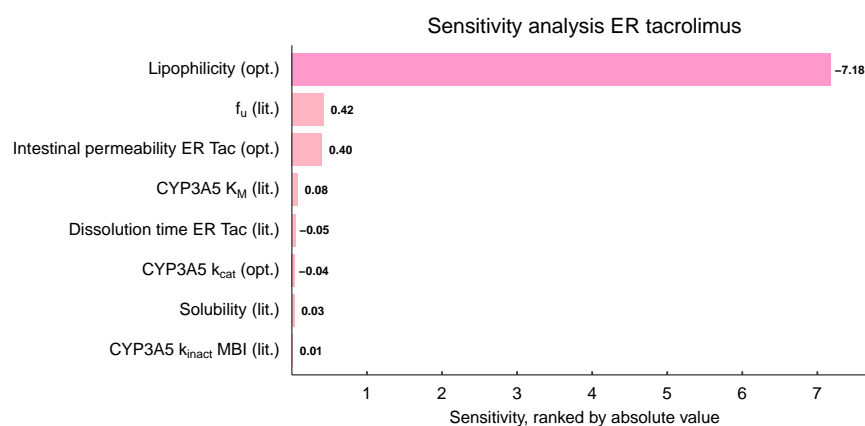


Figure S16: ER tacrolimus model sensitivity analysis (10 mg, single dose [33]). Presented are parameters with a calculated sensitivity different from 0.00. CYP: cytochrome P450, ER: extended-release, f_u : fraction unbound, k_{cat} : catalytic rate constant, k_{inact} : maximum inactivation rate constant, K_M : Michaelis-Menten constant, lit.: literature, MBI: mechanism-based inactivation, opt.: optimized, Tac: tacrolimus.

S3 Food-Drug Interaction Modeling

Modulated absorption and distribution of tacrolimus due to food intake was implemented via adjustment of the Weibull parameters time (50% dissolved) and shape, as well as the intestinal permeability. The final model parameters are listed in Table S3.

S3.1 Clinical Study Data

Table S8: Tacrolimus FDI model study table

Tacrolimus dosing regimen		n	Females	Ethnicity ^a	Frequency ^a of	Age	Weight	Height	Dataset	Reference
Route	Dose [mg]		[%]		<i>CYP3A5</i> *1 [%]	[years]	[kg]	[cm]		
po (IR cap, SD, fasted)	5	36	50	European	7.8	27±8.3	72±13	173±9	test	Huppertz 2021 [24]
po (IR cap, SD, fed) after 622 kcal	5	36	50	European	7.8	27±8.3	72±13	173±9	test	Huppertz 2021 [24]
po (IR cap, SD, fasted)	5	15	0	White American	7.8	32.6±10.1 (20–45)	85.2±9.42 (70.9–102)	179±5.77 (170–190)	test	Bekersky 2001 [22]
po (IR cap, SD, fed) 0.33 h after 668 kcal	5	15	0	White American	7.8	32.6±10.1 (20–45)	85.2±9.42 (70.9–102)	179±5.77 (170–190)	training	Bekersky 2001 [22]
po (IR cap, SD, fasted)	5	16	0	White American	7.8	34±9.23 (22–45)	82.5±10.3 (64.1–100)	183±6.48 (173–193)	test	Bekersky 2001 [26]
po (IR cap, SD, fed) 0.33 h after 848 kcal	5	16	0	White American	7.8	34±9.23 (22–45)	82.5±10.3 (64.1–100)	183±6.48 (173–193)	test	Bekersky 2001 [26]
po (IR cap, SD, fasted)	5	16	0	White American	7.8	34±9.23 (22–45)	82.5±10.3 (64.1–100)	183±6.48 (173–193)	test	Bekersky 2001 [26]
po (IR cap, SD, fed) 1.5 h after 848 kcal	5	16	0	White American	7.8	34±9.23 (22–45)	82.5±10.3 (64.1–100)	183±6.48 (173–193)	test	Bekersky 2001 [26]

^a: implemented, cap: capsule, CYP: cytochrome P450, FDI: food-drug interaction, IR: immediate-release, kcal: kilocalories, n: number of participants, po: oral, SD: single dose; values for age, weight and height are shown as mean ± standard deviation (range).

Table S8: Tacrolimus FDI study table (*continued*)

Tacrolimus dosing regimen		n	Females	Ethnicity ^a	Frequency ^a of <i>CYP3A5</i> *1 [%]	Age [years]	Weight [kg]	Height [cm]	Dataset	Reference
Route	Dose [mg]									
po (IR cap, SD, fasted)	5	15	0	White American	7.8	32.6±10.1 (20–45)	85.2±9.42 (70.9–102)	179±5.77 (170–190)	test	Bekersky 2001 [22]
po (IR cap, SD, fed) 0.33 h after 849 kcal	5	15	0	White American	7.8	32.6±10.1 (20–45)	85.2±9.42 (70.9–102)	179±5.77 (170–190)	training	Bekersky 2001 [22]
po (IR cap, SD, fasted)	5	41	81	White American	7.8	47±13 (21–66)	68.0±8.3 (53.1–85.5)	164.8±7.4 (151.5–180.5)	test	Lainesse 2008 [21]
po (IR cap, SD, fed) 0.5 h after 1000 kcal	5	46	61	White American	7.8	43±12 (19–61)	65.5±9.4 (45.6–85.6)	166.0±8.6 (149.0–181.5)	test	Lainesse 2008 [21]

^a: implemented, cap: capsule, CYP: cytochrome P450, FDI: food-drug interaction, IR: immediate-release, kcal: kilocalories, n: number of participants, po: oral, SD: single dose; values for age, weight and height are shown as mean ± standard deviation (range).

S3.2 Whole Blood Concentration-Time Profiles (Semilogarithmic)

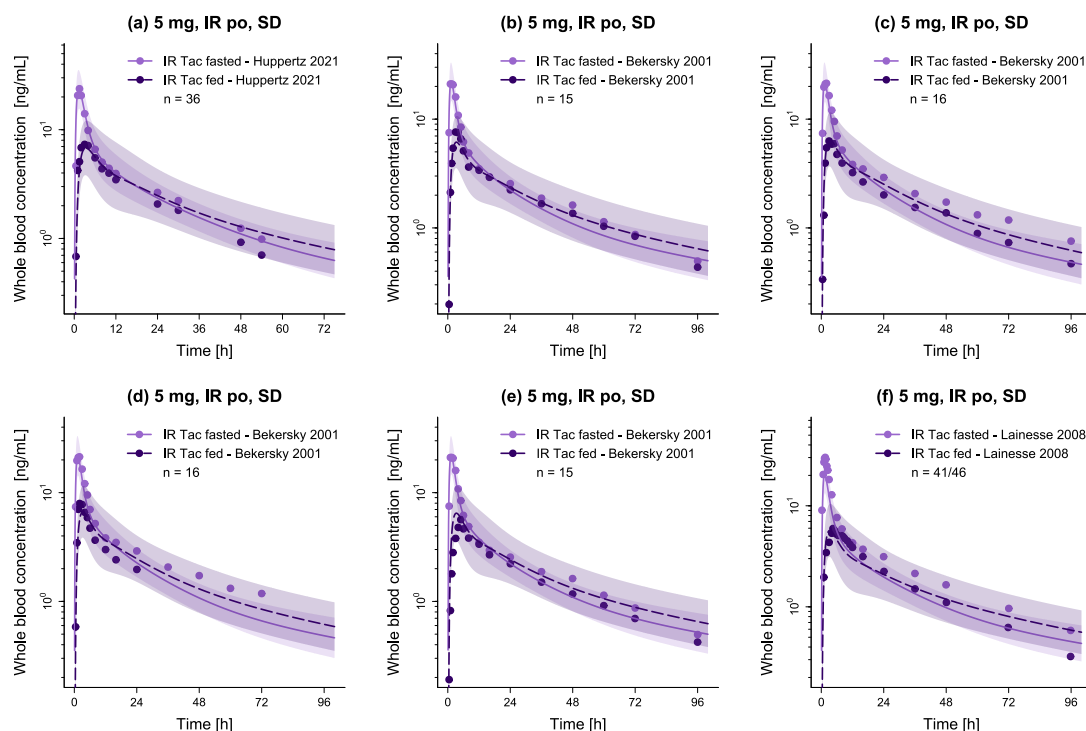


Figure S17: Evaluation of the modeled food-drug interactions. Presented are predicted whole blood concentration-time profiles (semilogarithmic plots) of IR tacrolimus under fed and fasted conditions, alongside corresponding observed data [21, 22, 24, 26]. Dashed (fed) and solid (fasted) lines and ribbons represent population predictions ($n = 1000$; geometric mean and geometric standard deviation), while corresponding observed data are shown as dots. n : number of participants, IR: immediate-release, po: oral, SD: single dose, Tac: tacrolimus.

S3.3 Whole Blood Concentration-Time Profiles (Linear)

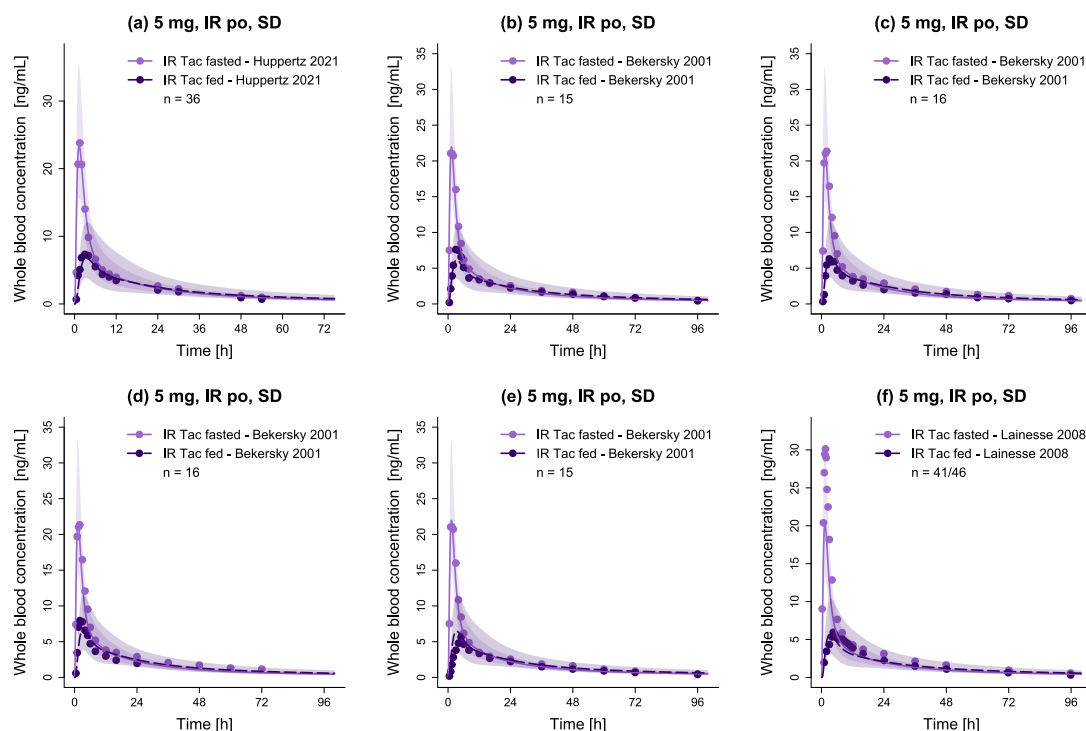


Figure S18: Evaluation of the modeled food-drug interactions. Presented are predicted whole blood concentration-time profiles (linear plots) of IR tacrolimus under fed and fasted conditions, alongside corresponding observed data [21, 22, 24, 26]. Dashed (fed) and solid (fasted) lines and ribbons represent population predictions (n = 1000; geometric mean and geometric standard deviation), while corresponding observed data are shown as dots. n: number of participants, IR: immediate-release, po: oral, SD: single dose, Tac: tacrolimus.

S3.4 FDI AUC_{last} and FDI C_{max} Ratio Goodness-of-Fit Plots

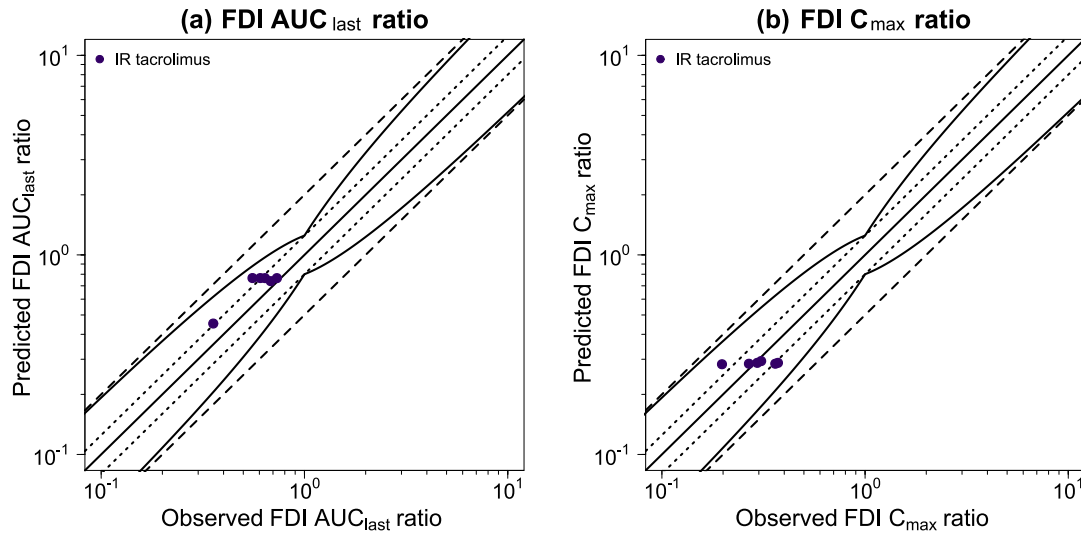


Figure S19: Evaluation of the modeled food-drug interactions. Presented are predicted versus observed FDI AUC_{last} (a) and FDI C_{max} (b) ratios with the solid line representing the line of identity, dotted lines indicating 1.25-fold and dashed lines 2-fold deviation from the respective observed value, along with the curved lines marking the prediction success limits proposed by Guest et al. [46] including 20%. AUC_{last} : area under the whole blood concentration-time curve determined between first and last concentration measurements, C_{max} : maximum whole blood concentration, FDI: food-drug interaction, n: number of participants, IR: immediate-release.

S3.5 Predicted and Observed FDI AUC_{last} and FDI C_{max} Ratios

Table S9: Predicted versus observed FDI AUC_{last} and FDI C_{max} ratios

Tacrolimus dosing regimen		n	Dataset	FDI AUC _{last} ratio			FDI C _{max} ratio			Reference
Route	Dose [mg]			Pred	Obs	Pred/Obs	Pred	Obs	Pred/Obs	
po (IR cap, SD) after 622 kcal	5	36 fasted/36 fed	test	0.74	0.68	1.08	0.29	0.31	0.95	Huppertz 2021 [24]
po (IR cap, SD) 0.33 h after 668 kcal	5	15 fasted/15 fed	training	0.76	0.73	1.05	0.28	0.36	0.79	Bekersky 2001 [22]
po (IR cap, SD) 0.33 h after 848 kcal	5	16 fasted/16 fed	test	0.77	0.61	1.26	0.29	0.29	0.98	Bekersky 2001 [26]
po (IR cap, SD) 1.5 h after 848 kcal	5	16 fasted/ 16 fed	test	0.45	0.36	1.27	0.29	0.37	0.77	Bekersky 2001 [26]
po (IR cap, SD) 0.33 h after 849 kcal	5	15 fasted/15 fed	training	0.76	0.64	1.20	0.28	0.27	1.06	Bekersky 2001 [22]
po (IR cap, SD) 0.5 h after 1000 kcal	5	41 fasted/46 fed	test	0.77	0.55	1.38	0.28	0.20	1.43	Lainesse 2008 [21]
Training Dataset mean GMFE (range)				1.12 (1.05–1.20)			1.17 (1.06–1.27)			
Test Dataset mean GMFE (range)				1.25 (1.08–1.38)			1.20 (1.02–1.43)			
Overall mean GMFE (range)				1.21 (1.05–1.38)			1.19 (1.02–1.43)			
GMFE ≤ 2				6/6			6/6			

AUC_{last}: area under the whole blood concentration-time curve determined between first and last concentration measurements, cap: capsule, C_{max}: maximum whole blood concentration, GMFE: geometric mean fold error, FDI: food-drug interaction, IR: immediate-release, kcal: kilocalories, n: number of participants, obs: observed, po: oral, pred: predicted, SD: single dose.

S4 Drug-Drug(-Gene) Interaction Modeling

S4.1 Types of Interactions Implemented

S4.1.1 Competitive Inhibition

Competitive inhibition (CI) involves reversible binding of an inhibitor to the respective enzyme, thus competing with substrates for the binding site, increasing the apparent Michaelis-Menten constant ($K_{M,app}$) while leaving the maximum reaction velocity (v_{max}) unaltered (Equations S3 and S4) [47]. Due to its reversibility, the inhibition can be overcome through an increase in substrate concentration (concentration-dependent inhibition).

$$v = \frac{v_{max} \cdot [S]}{K_{M,app} + [S]} \quad (S3)$$

$$K_{M,app} = K_M \cdot \left(1 + \frac{[I]}{K_i}\right) \quad (S4)$$

where v = reaction velocity, v_{max} = maximum reaction velocity, $[S]$ = free substrate concentration, $K_{M,app}$ = apparent Michaelis-Menten constant (inhibitor present), K_M = Michaelis-Menten constant (inhibitor absent), $[I]$ = free inhibitor concentration, and K_i = dissociation constant inhibitor-enzyme complex.

S4.1.2 Mechanism-Based Inactivation

In the case of mechanism-based inactivation (MBI), the inactivator, in addition to reversibly binding to the enzyme in question, is irreversibly converted into a reactive species that forms a covalent complex with the respective target (time-dependent inhibition). Due to the irreversibility, MBI can only be reversed by *de novo* synthesis of the relevant enzyme or transporter. In PK-Sim[®], MBI and its resulting impact on enzyme turnover is implemented according to Equation S5 [47].

$$\frac{d[T]}{dt} = k_{deg} \cdot [T]_0 - \left(k_{deg} + \frac{k_{inact} \cdot [I]}{K_I + [I]}\right) \cdot [T] \quad (S5)$$

where $d[T]/dt$ = enzyme turnover, k_{deg} = degradation rate constant, $[T]_0$ = initial enzyme concentration at time 0, k_{inact} = maximum inactivation rate constant, K_I = concentration for half-maximal inactivation, $[I]$ = free inactivator concentration, and $[T]$ = enzyme concentration.

S4.1.3 Induction

Induction of enzymes is usually caused by activation of specific nuclear receptors through binding of an inducer, resulting in increased *de novo* synthesis of the enzyme of interest. Equation S6 describes the correlation between maximum induction effect (E_{max}), concentration for half-maximal induction (EC_{50}) and the magnitude of induction, with the first two parameters used for implementation of an induction process in PK-Sim[®] [47, 48].

$$E = \frac{E_{max} \cdot [Ind]}{EC_{50} + [Ind]} \quad (S6)$$

where E = magnitude of induction, E_{max} = maximum induction effect, $[Ind]$ = free inducer concentration (steady-state), and EC_{50} = concentration for half-maximal induction.

S4.2 Clinical Study Data

Table S10: Tacrolimus DD(G)I model study table

Tacrolimus application [mg]	Perpetrator	Perpetrator application [mg]	n	Females [%]	Ethnicity ^a	Frequency ^a of <i>CYP3A5*1</i> [%]	Age [years]	Weight [kg]	Height [cm]	Reference
d4: 3 po (IR cap, SD)	Voriconazole	d1: 400 d2–4: 200 po (tab, BID)	6 NM CYP2C19	0	Japanese	25.8	27.7 (23–38)	63.9 (57.4–68.7)	172.7 (167.6–178.9)	Imamura 2016 [49]
d4: 3 po (IR cap, SD)	Voriconazole	d1: 400 d2–4: 200 po (tab, BID)	6 IM CYP2C19	0	Japanese	25.8	28.7 (22–37)	65.2 (57.0–74.3)	173.6 (170.0–178.5)	Imamura 2016 [49]
d4: 3 po (IR cap, SD)	Voriconazole	d1: 400 d2–4: 200 po (tab, BID)	6 PM CYP2C19	0	Japanese	25.8	27.7 (22–36)	61.3 (57.0–74.3)	174.3 (166.7–182.3)	Imamura 2016 [49]
d2: 3 po (IR cap, SD)	Voriconazole ^b	d1: 400 d2–4: 200 po (tab, BID)	18	0	European	16.7	34±11	82±13	182±8	Huppertz 2019 [50]
d5: 3 po (ER cap, SD)	Itraconazole ^c	d1–4: 200 po (cap, BID)	16	0	European	15.6	(18–28)	-	-	Vanhove 2019 [31]
d8: 0.025/kg iv (inf, 4 h, SD)	Rifampicin	d1–18: 600 po (cap, MD)	1	0	White American	100	-	-	-	Hebert 1999 [51]
d8: 8 po (IR cap, SD)	Rifampicin	d1–18: 600 po (cap, MD)	1	0	White American	100	-	-	-	Hebert 1999 [51]

-: not given, ^a: implemented, ^b: plus midazolam (not included in the model): d2; 0.03 mg; po (solution, SD), ^c: plus midazolam (not included in the model): d5; 2 mg; po (solution, SD), BID: multiple dose (twice daily), cap: capsule, CYP: cytochrome P450, d: day, DD(G)I: drug-drug(-gene) interaction, ER: extended-release, IM: intermediate metabolizer, inf: infusion, IR: immediate-release, iv: intravenous, MD: multiple dose (once daily), n: number of participants, NM: normal metabolizer, PM: poor metabolizer, po: oral, SD: single dose, tab: tablet; values for age, weight and height are presented as mean ± standard deviation (range).

S4.3 Drug-dependent Parameters DD(G)I Partner

S4.3.1 Voriconazole

Table S11: Drug-dependent parameters of the voriconazole PBPK model [52]

Parameter	Unit	Value	Source	Description
Voriconazole				
Molecular weight	g/mol	349.30	Lit.	Molecular weight
pKa, base		1.60	Lit.	Acid dissociation constant
Solubility (pH)	mg/L	3.20 (1.00), 2.70 (1.20), 0.10 (7.00)	Lit.	Solubility
Lipophilicity		1.80	Lit.	Lipophilicity
f_u	%	42.00	Lit.	Fraction unbound
CYP2C19 $K_M \rightarrow$ sink	$\mu\text{mol/L}$	3.50	Lit.	Michaelis-Menten constant
CYP2C19 $k_{\text{cat}} \rightarrow$ sink	1/min	1.19	Lit.	Catalytic rate constant
CYP3A4 $K_M \rightarrow$ sink	$\mu\text{mol/L}$	15.00	Lit.	Michaelis-Menten constant
CYP3A4 $k_{\text{cat}} \rightarrow$ sink	1/min	2.12	Opt.	Transport rate constant
GFR fraction		1 ^a	Asm.	Filtered drug in the urine
EHC continuous fraction		1	Asm.	Bile fraction continuously released
Intestinal permeability	cm/s	$2.71 \cdot 10^{-4}$	Opt.	Transcellular intestinal permeability
Cellular permeability	cm/min	PK-Sim Standard, $2.58 \cdot 10^{-3}$	Calc. [47]	Permeability into the cellular space
Partition coefficients		Poulin and Theil	Calc. [53–56]	Organ-plasma partition coefficients
Dissolution time (Weibull)	min	30.00	Opt.	Dissolution time (50%)
Dissolution shape (Weibull)		1.29	Opt.	Dissolution shape
CYP2C19 K_i	$\mu\text{mol/L}$	4.57	Lit.	Diss. const. inhibitor-enzyme complex (CI)
CYP3A4 K_i	$\mu\text{mol/L}$	9.33	Meas.	Conc. for half-maximal inactivation (MBI)
CYP3A4 k_{inact}	1/min	0.02	Opt.	Maximum inactivation rate constant (MBI)
CYP3A5 K_i	$\mu\text{mol/L}$	0.20 ^b	Lit. [57]	Diss. const. inhibitor-enzyme complex (CI)

^a: a GFR fraction of 1 corresponds to passive glomerular filtration of a compound, ^b: added to the original model, asm.: assumed, calc.: calculated, CI: competitive inhibition, conc.: concentration, const.: constant, CYP: cytochrome P450, diss.: dissociation, EHC: enterohepatic circulation, GFR: glomerular filtration rate, lit.: literature, meas.: measured, opt.: optimized. CYP2C19 drug-gene interactions were modeled by adjusting the reference concentration in the tissue of highest expression, i.e., for normal metabolizers 0.76 $\mu\text{mol protein/L}$ was implemented, for intermediate metabolizers 0.4 $\mu\text{mol protein/L}$, and for poor metabolizers 0.01 $\mu\text{mol protein/L}$.

S4.3.2 Itraconazole

Table S12: Drug-dependent parameters of the itraconazole PBPK model [7]

Parameter	Unit	Value	Source	Description
Itraconazole				
Molecular weight	g/mol	705.63	Lit.	Molecular weight
pKa, base		3.70	Lit.	Acid dissociation constant
Solubility (pH)	mg/L	8.00 (6.50)	Lit.	Solubility
Lipophilicity		4.62	Opt.	Lipophilicity
f_u	%	0.60	Lit.	Fraction unbound
CYP3A4 $K_M \rightarrow$ OH-Itra	nmol/L	2.07	Lit.	Michaelis-Menten constant
CYP3A4 $k_{cat} \rightarrow$ OH-Itra	1/min	0.04	Opt.	Transport rate constant
GFR fraction		1 ^a	Asm.	Filtered drug in the urine
EHC continuous fraction		1	Asm.	Bile fraction continuously released
Intestinal permeability	dm/min	$5.33 \cdot 10^{-5}$	Opt.	Transcellular intestinal permeability
Cellular permeability	cm/min	PK-Sim Standard, 0.01	Calc. [47]	Permeability into the cellular space
Partition coefficients		Rodgers + Rowland	Calc. [58, 59]	Organ-plasma partition coefficients
Dissolution time (Weibull)	min	406.30	Opt.	Dissolution time (50%)
Dissolution shape (Weibull)		1.43	Opt.	Dissolution shape
CYP3A4 K_i	nmol/L	1.30	Lit.	Diss. const. inhibitor-enzyme complex (CI)
CYP3A5 K_i	μ mol/L	0.94 ^b	Lit. [57]	Diss. const. inhibitor-enzyme complex (CI)
Hydroxy-Itraconazole				
Molecular weight	g/mol	721.63	Lit.	Molecular weight
pKa, base		3.70	Lit.	Acid dissociation constant

^a: a GFR fraction of 1 corresponds to passive glomerular filtration of a compound, ^b: added to the original model, asm.: assumed, calc.: calculated, CI: competitive inhibition, conc.: concentration, const.: constant, CYP: cytochrome P450, diss.: dissociation, EHC: entero-hepatic circulation, GFR: glomerular filtration rate, Keto-Itra: keto-itraconazole, lit.: literature, N-Des-Itra: N-desalkyl-itraconazole, OH-Itra: hydroxy-itraconazole, opt.: optimized.

Table S12: Drug-dependent parameters of the itraconazole PBPK model [7] (*continued*)

Parameter	Unit	Value	Source	Description
Solubility (pH)	mg/L	1.00 (7.00)	Asm.	Solubility
Lipophilicity		3.72	Opt.	Lipophilicity
f_u	%	1.70	Lit.	Fraction unbound
CYP3A4 $K_M \rightarrow$ Keto-Itra	nmol/L	4.17	Lit.	Michaelis-Menten constant
CYP3A4 $k_{cat} \rightarrow$ Keto-Itra	1/min	0.02	Opt.	Transport rate constant
GFR fraction		1 ^a	Asm.	Filtered drug in the urine
EHC continuous fraction		1	Asm.	Bile fraction continuously released
Intestinal permeability	cm/min	$1.52 \cdot 10^{-5}$	Calc.	Transcellular intestinal permeability
Cellular permeability	cm/min	PK-Sim Standard, $1.55 \cdot 10^{-3}$	Calc. [47]	Permeability into the cellular space
Partition coefficients		Rodgers + Roland	Calc. [58, 59]	Organ-plasma partition coefficients
CYP3A4 K_i	nmol/L	14.40	Lit.	Diss. const. inhibitor-enzyme complex (CI)
Keto-Itraconazole				
Molecular weight	g/mol	719.62	Lit.	Molecular weight
pKa, base		3.70	Lit.	Acid dissociation constant
Solubility (pH)	mg/L	1.00 (7.00)	Asm.	Solubility
Lipophilicity		4.21	Opt.	Lipophilicity
f_u	%	1.00	Lit.	Fraction unbound
CYP3A4 $K_M \rightarrow$ N-Des-Itra	nmol/L	2.22	Lit.	Michaelis-Menten constant
CYP3A4 $k_{cat} \rightarrow$ N-Des-Itra	1/min	0.39	Opt.	Transport rate constant
GFR fraction		1 ^a	Asm.	Filtered drug in the urine
EHC continuous fraction		1	Asm.	Bile fraction continuously released
Intestinal permeability	cm/min	$4.79 \cdot 10^{-5}$	Calc.	Transcellular intestinal permeability
Cellular permeability	cm/min	PK-Sim Standard, $4.92 \cdot 10^{-3}$	Calc. [47]	Permeability into the cellular space
Partition coefficients		Rodgers + Roland	Calc. [58, 59]	Organ-plasma partition coefficients
CYP3A4 K_i	nmol/L	5.12	Lit.	Diss. const. inhibitor-enzyme complex (CI)

^a: a GFR fraction of 1 corresponds to passive glomerular filtration of a compound, ^b: added to the original model, asm.: assumed, calc.: calculated, CI: competitive inhibition, conc.: concentration, const.: constant, CYP: cytochrome P450, diss.: dissociation, EHC: entero-hepatic circulation, GFR: glomerular filtration rate, Keto-Itra: keto-itraconazole, lit.: literature, N-Des-Itra: N-desalkyl-itraconazole, OH-Itra: hydroxy-itraconazole, opt.: optimized.

Table S12: Drug-dependent parameters of the itraconazole PBPK model [7] (*continued*)

Parameter	Unit	Value	Source	Description
N-Desalkyl-Itraconazole				
Molecular weight	g/mol	649.53	Lit.	Molecular weight
pKa, base		3.70	Lit.	Acid dissociation constant
Solubility (pH)	mg/L	1.00 (7.00)	Asm.	Solubility
Lipophilicity		5.18	Opt.	Lipophilicity
f_u	%	1.10	Lit.	Fraction unbound
CYP3A4 $K_M \rightarrow$ sink	nmol/L	0.63	Lit.	Michaelis-Menten constant
CYP3A4 $k_{cat} \rightarrow$ sink	1/min	0.06	Opt.	Transport rate constant
GFR fraction		1 ^a	Asm.	Filtered drug in the urine
EHC continuous fraction		1	Asm.	Bile fraction continuously released
Intestinal permeability	cm/min	$7.37 \cdot 10^{-4}$	Calc.	Transcellular intestinal permeability
Cellular permeability	cm/min	PK-Sim Standard, 0.09	Calc. [47]	Permeability into the cellular space
Partition coefficients		Rodgers + Roland	Calc. [58, 59]	Organ-plasma partition coefficients
CYP3A4 K_i	nmol/L	0.32	Lit.	Diss. const. inhibitor-enzyme complex (CI)

^a: a GFR fraction of 1 corresponds to passive glomerular filtration of a compound, ^b: added to the original model, asm.: assumed, calc.: calculated, CI: competitive inhibition, conc.: concentration, const.: constant, CYP: cytochrome P450, diss.: dissociation, EHC: entero-hepatic circulation, GFR: glomerular filtration rate, Keto-Itra: keto-itraconazole, lit.: literature, N-Des-Itra: N-desalkyl-itraconazole, OH-Itra: hydroxy-itraconazole, opt.: optimized.

S4.3.3 Rifampicin

Table S13: Drug-dependent parameters of the rifampicin PBPK model [7]

Parameter	Unit	Value	Source	Description
Rifampicin				
Molecular weight	g/mol	822.94	Lit.	Molecular weight
pKa, base		7.90	Lit.	Acid dissociation constant
pKa, acid		1.70	Lit.	Acid dissociation constant
Solubility (pH)	mg/L	2800.00 (7.5)	Lit.	Solubility
Lipophilicity		2.50	Opt.	Lipophilicity
f_u	%	17.00	Lit.	Fraction unbound
AADAC $K_M \rightarrow \text{sink}$	$\mu\text{mol/L}$	195.10	Lit.	Michaelis-Menten constant
AADAC $k_{\text{cat}} \rightarrow \text{sink}$	1/min	9.87	Opt.	Catalytic rate constant
OATP1B1 K_M	$\mu\text{mol/L}$	1.50	Lit.	Michaelis-Menten constant
OATP1B1 k_{cat}	1/min	74.43 ^a	Opt.	Transport rate constant
P-gp K_M	$\mu\text{mol/L}$	55.00	Lit.	Michaelis-Menten constant
P-gp k_{cat}	1/min	0.61	Opt.	Transport rate constant
GFR fraction		1 ^b	Asm.	Filtered drug in the urine
EHC continuous fraction		1	Asm.	Bile fraction continuously released
Intestinal permeability	cm/min	$1.24 \cdot 10^{-5}$	Opt.	Transcellular intestinal permeability
Cellular permeability	cm/min	PK-Sim Standard, $2.93 \cdot 10^{-5}$	Calc. [47]	Permeability into the cellular space
Partition coefficients		Rodgers + Rowland	Calc. [58, 59]	Organ-plasma partition coefficients
Formulation		Solution		Formulation used in predictions

^a: adjusted due to different reference concentrations in the original model and tacrolimus model, ^b: a GFR fraction of 1 corresponds to passive glomerular filtration of a compound, AADAC: arylacetamide deacetylase, asm.: assumed, calc.: calculated, CI: competitive inhibition, conc.: concentration, const.: constant, CYP: cytochrome P450, diss.: dissociation, EHC: enterohepatic circulation, GFR: glomerular filtration rate, lit.: literature, OATP: organic-anion-transporting polypeptide, opt.: optimized, P-gp: P-glycoprotein.

Table S13: Drug-dependent parameters of the rifampicin PBPK model [7] (*continued*)

Parameter	Unit	Value	Source	Description
Induction EC ₅₀	μmol/L	0.34	Lit.	Conc. for half-maximal induction
AADAC E _{max}		0.99	Opt.	Maximum induction effect
CYP3A4 E _{max}		9.00	Lit.	Maximum induction effect
CYP3A4 K _i	μmol/L	18.50	Lit.	Diss. const. inhibitor-enzyme complex (CI)
OATP1B1 E _{max}		0.38	Opt.	Maximum induction effect
OATP1B1 K _i	μmol/L	0.48	Lit.	Diss. const. inhibitor-enzyme complex (CI)
P-gp E _{max}		2.50	Lit.	Maximum induction effect
P-gp K _i	μmol/L	169.00	Lit.	Diss. const. inhibitor-enzyme complex (CI)

^a: adjusted due to different reference concentrations in the original model and tacrolimus model, ^b: a GFR fraction of 1 corresponds to passive glomerular filtration of a compound, AADAC: arylacetamide deacetylase, asm.: assumed, calc.: calculated, CI: competitive inhibition, conc.: concentration, const.: constant, CYP: cytochrome P450, diss.: dissociation, EHC: enterohepatic circulation, GFR: glomerular filtration rate, lit.: literature, OATP: organic-anion-transporting polypeptide, opt.: optimized, P-gp: P-glycoprotein.

S4.4 Whole Blood Concentration-Time Profiles (Semilogarithmic)

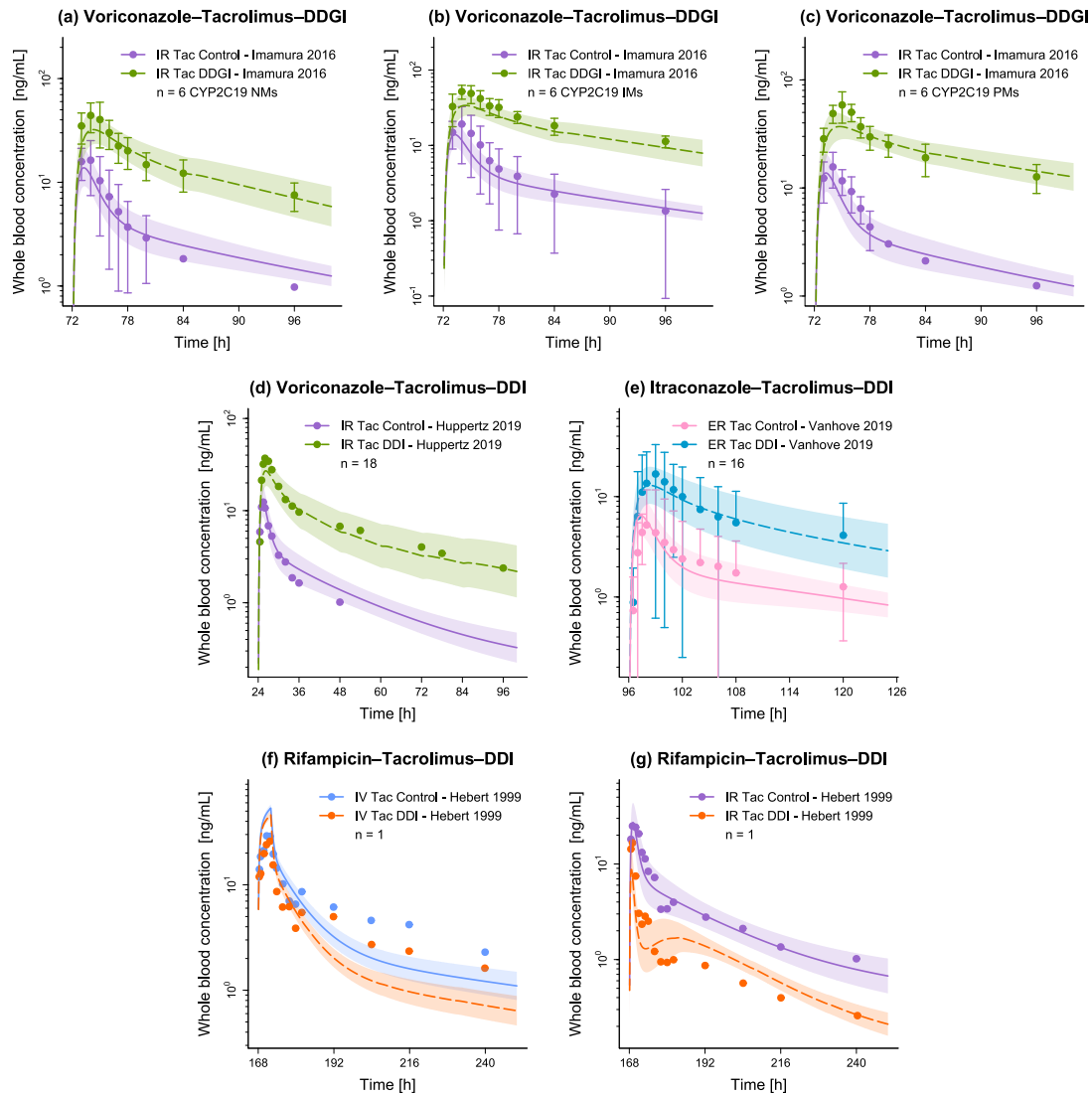


Figure S20: Evaluation of the modeled drug-drug(-gene) interactions. Presented are predicted whole blood concentration-time profiles (semilogarithmic plots) of tacrolimus without (Control) and with (DD(G)I) intake of the respective perpetrator drug (voriconazole (a-d), itraconazole (e), rifampicin (f-g)), alongside corresponding observed data [31, 49–51]. Solid (Control) and dashed (DD(G)I) lines and ribbons represent population predictions (n = 1000; geometric mean and geometric standard deviation), while corresponding observed data are shown as dots (\pm standard deviation, if available). CYP: cytochrome P450, DD(G)I: drug-drug(-gene) interaction, ER: extended-release, IM: intermediate metabolizer, IR: immediate-release, IV: intravenous, n: number of participants, NM: normal metabolizer, PM: poor metabolizer, Tac: tacrolimus.

S4.5 Whole Blood Concentration-Time Profiles (Linear)

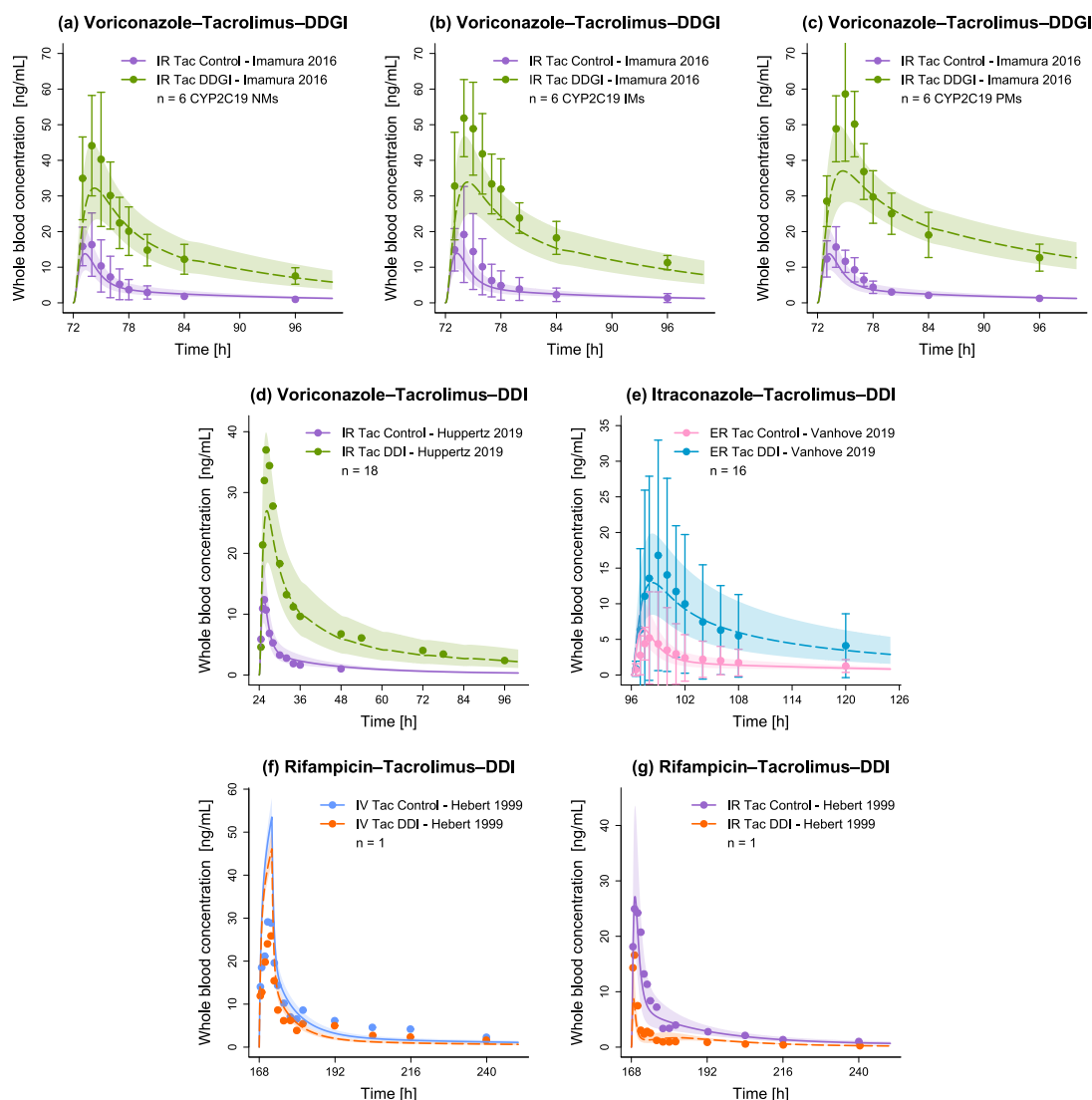


Figure S21: Evaluation of the modeled drug-drug(-gene) interactions. Presented are predicted whole blood concentration-time profiles (linear plots) of tacrolimus without (Control) and with (DD(G)I) intake of the respective perpetrator drug (voriconazole (a–d), itraconazole (e), rifampicin (f–g)), alongside corresponding observed data [31, 49–51]. Solid (Control) and dashed (DD(G)I) lines and ribbons represent population predictions ($n = 1000$; geometric mean and geometric standard deviation), while corresponding observed data are shown as dots (\pm standard deviation, if available). CYP: cytochrome P450, DD(G)I: drug-drug(-gene) interaction, ER: extended-release, IM: intermediate metabolizer, IR: immediate-release, IV: intravenous, n: number of participants, NM: normal metabolizer, PM: poor metabolizer, Tac: tacrolimus.

S4.6 DD(G)I AUC_{last} and DD(G)I C_{max} Ratio Goodness-of-Fit Plots

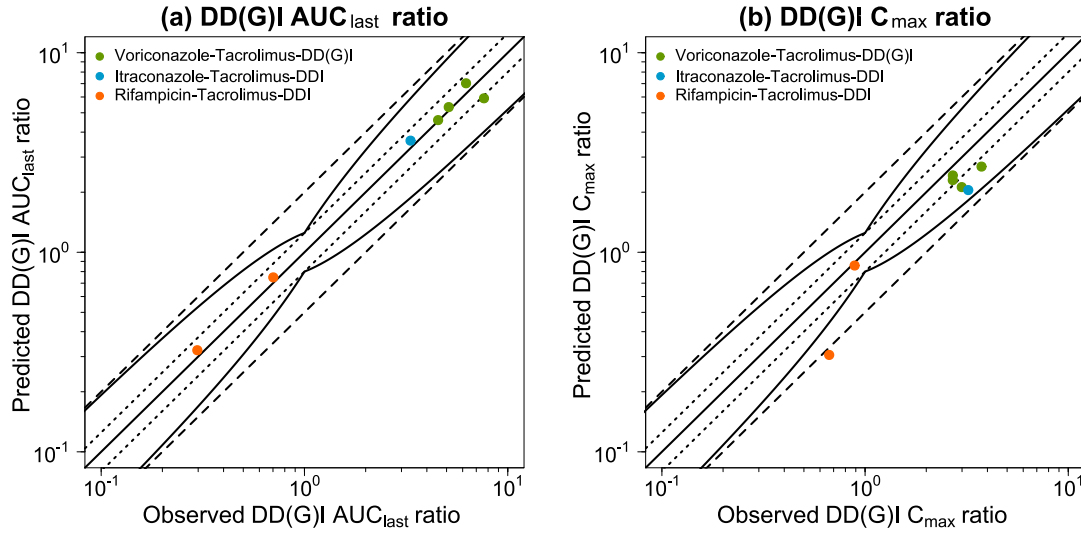


Figure S22: Evaluation of the modeled drug-drug(-gene) interactions. Predicted versus observed DD(G)I AUC_{last} (a) and DD(G)I C_{max} (b) ratios are shown with the solid line representing the line of identity, dotted lines indicating 1.25-fold and dashed lines 2-fold deviation from the respective observed value, along with the curved lines marking the prediction success limits proposed by Guest et al. [46] including 20% variability. AUC_{last} : area under the whole blood concentration-time curve determined between first and last concentration measurements, C_{max} : maximum whole blood concentration, DD(G)I: drug-drug(-gene) interaction.

S4.7 Predicted and Observed DD(G)I AUC_{last} and DD(G)I C_{max} Ratios

Table S14: Predicted versus observed DD(G)I AUC_{last} and DD(G)I C_{max} ratios

Tacrolimus application [mg]	Perpetrator	Perpetrator application [mg]	n	DD(G)I AUC _{last} ratio			DD(G)I C _{max} ratio			Reference
				Pred	Obs	Pred/Obs	Pred	Obs	Pred/Obs	
d4: 3 po (IR cap, SD)	Voriconazole	d1: 400, d2–4: 200 po (tab, BID)	6 NM CYP2C19	4.60	4.54	1.01	2.30	2.70	0.85	Imamura 2016 [49]
d4: 3 po (IR cap, SD)	Voriconazole	d1: 400, d2–4: 200 po (tab, BID)	6 IM CYP2C19	5.34	5.12	1.04	2.43	2.70	0.90	Imamura 2016 [49]
d4: 3 po (IR cap, SD)	Voriconazole	d1: 400, d2–4: 200 po (tab, BID)	6 PM CYP2C19	7.03	6.23	1.13	2.69	3.74	0.72	Imamura 2016 [49]
d2: 3 po (IR cap, SD)	Voriconazole ^a	d1: 400, d2–4: 200 po (tab, BID)	18	5.90	7.64	0.77	2.12	2.99	0.71	Huppertz 2019 [50]
d5: 3 po (ER cap, SD)	Itraconazole ^b	d1–4: 200 po (cap, BID)	16	3.63	3.32	1.09	2.05	3.22	0.64	Vanhove 2019 [31]
d8: 0.025/kg iv (inf, 4 h, SD)	Rifampicin	d1–18: 600 po (cap, MD)	1	0.75	0.70	1.07	0.86	0.89	0.97	Hebert 1999 [51]
d8: 8 po (IR cap, SD)	Rifampicin	d1–18: 600 po (cap, MD)	1	0.32	0.30	1.09	0.31	0.67	0.46	Hebert 1999 [51]
Overall mean GMFE (range) GMFE ≤ 2				1.10 (1.01–1.29) 7/7			1.41 (1.04–2.18) 6/7			

^a: plus midazolam (not included in the model): d2; 0.03 mg; po (solution, SD), ^b: plus midazolam (not included in the model): d5; 2 mg; po (solution, SD), AUC_{last}: area under the whole blood concentration-time curve determined between first and last concentration measurements, BID: multiple dose (twice daily), cap: capsule, C_{max}: maximum whole blood concentration, CYP: cytochrome P450, d: day, DD(G)I: drug-drug(-gene) interaction, ER: extended-release, IM: intermediate metabolizer, inf: infusion, iv: intravenous, GMFE: geometric mean fold error, IR: immediate-release, MD: multiple dose (once daily), n: number of participants, NM: normal metabolizer, PM: poor metabolizer, po: oral, pred: predicted, SD: single dose, tab: tablet.

Bibliography

- [1] M Nishimura and S Naito. Tissue-specific mRNA expression profiles of human phase I metabolizing enzymes except for cytochrome P450 and phase II metabolizing enzymes. *Drug metabolism and pharmacokinetics*, 21(5):357–374, 2006.
- [2] AD Rodrigues. Integrated cytochrome P450 reaction phenotyping. Attempting to bridge the gap between cDNA-expressed cytochromes P450 and native human liver microsomes. *Biochemical Pharmacology*, 57(5):465–480, 1999.
- [3] Open Systems Pharmacology Suite Community PK-Sim®Ontogeny Database Documentation, Available online (accessed on 30 April 2022). URL <https://github.com/Open-Systems-Pharmacology/OSPSuite.Documentation/blob/master/PK-SimOntogenyDatabaseVersion7.3.pdf>.
- [4] M Nishimura, H Yaguti, H Yoshitsugu, and S Naito. Tissue distribution of mRNA expression of human cytochrome P450 isoforms assessed by high-sensitivity real-time reverse transcription PCR. *Journal of the Pharmaceutical Society of Japan*, 123(5):369 – 375, 2003.
- [5] B Prasad, R Evers, A Gupta, CECA Hop, L Salphati, S Shukla, S Ambudkar, and JD Unadkat. Interindividual variability in hepatic OATPs and P-glycoprotein (ABCB1) protein expression: Quantification by LC-MS/MS and influence of genotype, age and sex. *Drug metabolism and disposition: the biological fate of chemicals*, 42(1):78–88, 2014.
- [6] M Nishimura and S Naito. Tissue-specific mRNA expression profiles of human ATP-binding cassette and solute carrier transporter superfamilies. *Drug metabolism and pharmacokinetics*, 20(6):452–477, 2005.
- [7] N Hanke, S Frechen, D Moj, H Britz, T Eissing, T Wendl, and T Lehr. PBPK models for CYP3A4 and P-gp DDI prediction: A modeling network of rifampicin, itraconazole, clarithromycin, midazolam, alfentanil, and digoxin. *CPT: Pharmacometrics and Systems Pharmacology*, 7(10):647–659, oct 2018.
- [8] M Meyer, S Schneckener, B Ludewig, L Kuepfer, and J Lippert. Using expression data for quantification of active processes in physiologically based pharmacokinetic modeling. *Drug metabolism and disposition: the biological fate of chemicals*, 40(5):892–901, may 2012.
- [9] LM Mancinelli, L Frassetto, LC Floren, D Dressler, S Carrier, I Bekersky, LZ Benet, and U Christians. The pharmacokinetics and metabolic disposition of tacrolimus: A comparison across ethnic groups. *Clinical Pharmacology and Therapeutics*, 69(1):24–31, 2001.
- [10] I Bekersky, D Dressler, A Alak, GW Boswell, and QA Mekki. Comparative tacrolimus pharmacokinetics: Normal versus mildly hepatically impaired subjects. *Journal of Clinical Pharmacology*, 41(6):628–635, 2001.
- [11] LC Floren, I Bekersky, LZ Benet, QA Mekki, D Dressier, JW Lee, JP Roberts, and MF Hebert. Tacrolimus oral bioavailability doubles with coadministration of ketoconazole. *Clinical Pharmacology and Therapeutics*, 62(1):41–49, 1997.
- [12] P Mathew, J Mandal, K Patel, K Soni, G Tangudu, R Patel, and P Kale. Bioequivalence of two tacrolimus formulations under fasting conditions in healthy male subjects. *Clinical Therapeutics*, 33(9):1105–1119, 2011.
- [13] YK Kim, A Kim, SJ Park, and H Lee. New tablet formulation of tacrolimus with smaller interindividual variability may become a better treatment option than the conventional capsule formulation in organ transplant patients. *Drug Design, Development and Therapy*, 11:2861–2869, 2017.

- [14] S Wring, G Murphy, G Atiee, C Corr, M Hyman, M Willett, and D Angulo. Clinical pharmacokinetics and drug-drug interaction potential for coadministered SCY-078, an oral fungicidal glucan synthase inhibitor, and tacrolimus. *Clinical Pharmacology in Drug Development*, 8(1): 60–69, 2019.
- [15] F Itagaki, M Homma, K Yuzawa, M Nishimura, S Naito, N Ueda, N Ohkohchi, and Y Kohda. Effect of lansoprazole and rabeprazole on tacrolimus pharmacokinetics in healthy volunteers with CYP2C19 mutations. *Journal of Pharmacy and Pharmacology*, 56(8):1055–1059, 2004.
- [16] I Bekersky, D Dressler, and QA Mekki. Dose linearity after oral administration of tacrolimus 1-mg capsules at doses of 3, 7, and 10 mg. *Clinical Therapeutics*, 21(12):2058–2064, 1999.
- [17] I Bekersky, D Dressler, GW Boswell, B Fergen, W Tracewell, and QA Mekki. Bioequivalence of a new strength tacrolimus capsule under development. *Transplantation Proceedings*, 30(4): 1457–1459, 1998.
- [18] A Sansone-Parsons, G Krishna, M Martinho, B Kantesaria, S Gelone, and TG Mant. Effect of oral posaconazole on the pharmacokinetics of cyclosporine and tacrolimus. *Pharmacotherapy*, 27(6):825–834, 2007.
- [19] S Zheng, Y Tasnif, MF Hebert, CL Davis, Y Shitara, JC Calamia, YS Lin, DD Shen, and KE Thummel. Measurement and compartmental modeling of the effect of CYP3A5 gene variation on systemic and intrarenal tacrolimus disposition. *Clinical Pharmacology and Therapeutics*, 92(6):737–745, 2012.
- [20] I Bekersky, D Dressler, W Colburn, and QA Mekki. Bioequivalence of 1 and 5 mg tacrolimus capsules using a replicate study design. *Journal of Clinical Pharmacology*, 39(10):1032–1037, 1999.
- [21] A Lainesse, S Hussain, T Monif, S Reyar, SK Tippabhotla, A Madan, and NR Thudi. Bioequivalence studies of tacrolimus capsule under fasting and fed conditions in healthy male and female subjects. *Arzneimittel-Forschung/Drug Research*, 58(5):242–247, 2008.
- [22] I Bekersky, D Dressler, and QA Mekki. Effect of low- and high-fat meals on tacrolimus absorption following 5 mg single oral doses to healthy human subjects. *Journal of Clinical Pharmacology*, 41(2):176–182, 2001.
- [23] AH Groll, A Desai, D Han, C Howieson, K Kato, S Akhtar, D Kowalski, C Lademacher, W Lewis, H Pearlman, D Mandarino, T Yamazaki, and R Townsend. Pharmacokinetic assessment of drug-drug interactions of isavuconazole with the immunosuppressants cyclosporine, mycophenolic acid, prednisolone, sirolimus, and tacrolimus in healthy adults. *Clinical Pharmacology in Drug Development*, 6(1):76–85, 2017.
- [24] A Huppertz, J Bollmann, R Behnisch, T Bruckner, M Zorn, J Burhenne, WE Haefeli, and D Czock. Differential effect of a continental breakfast on tacrolimus formulations with different release characteristics. *Clinical Pharmacology in Drug Development*, 10(8):899–907, 2021.
- [25] JA Dowell, M Stogniew, D Krause, T Henkel, and B Damle. Lack of pharmacokinetic interaction between anidulafungin and tacrolimus. *Journal of Clinical Pharmacology*, 47(3):305–314, 2007.
- [26] I Bekersky, D Dressler, and QA Mekki. Effect of time of meal consumption on bioavailability of a single oral 5 mg tacrolimus dose. *Journal of Clinical Pharmacology*, 41(3):289–297, 2001.
- [27] RR Alloway, J Trofe-Clark, DC Brennan, J Kerr, EA Cohen, U Meier-Kriesche, DR Stevens, MA Moten, and JD Momper. Chronopharmacokinetics and food effects of single-dose LCP-tacrolimus in healthy volunteers. *Therapeutic drug monitoring*, 42(5):679–685, 2020.

- [28] F Stiff, F Vanmolkot, I Scheffers, L Van Bortel, C Neef, and M Christiaans. Rectal and sublingual administration of tacrolimus: A single-dose pharmacokinetic study in healthy volunteers. *British Journal of Clinical Pharmacology*, 78(5):996–1004, 2014.
- [29] MA Tortorici, V Parks, K Matschke, J Korth-Bradley, and A Patat. The evaluation of potential pharmacokinetic interaction between sirolimus and tacrolimus in healthy volunteers. *European Journal of Clinical Pharmacology*, 69(4):835–842, 2013.
- [30] A Mercuri, S Wu, S Stranzinger, S Mohr, S Salar-Behzadi, M Bresciani, and E Fröhlich. In vitro and in silico characterisation of tacrolimus released under biorelevant conditions. *International Journal of Pharmaceutics*, 515(1-2):271–280, 2016.
- [31] T Vanhove, P Annaert, N Knops, H de Loor, J de Hoon, and DRJ Kuypers. In vivo CYP3A4 activity does not predict the magnitude of interaction between itraconazole and tacrolimus from an extended release formulation. *Basic and Clinical Pharmacology and Toxicology*, 124(1):50–55, 2019.
- [32] K Gantar, K Škerget, I Mochkin, and A Bajc. Meeting regulatory requirements for drugs with a narrow therapeutic index: Bioequivalence studies of generic once-daily tacrolimus. *Drug, Healthcare and Patient Safety*, 12:151–160, 2020.
- [33] N Undre and J Dickinson. Relative bioavailability of single doses of prolonged-release tacrolimus administered as a suspension, orally or via a nasogastric tube, compared with intact capsules: A phase 1 study in healthy participants. *BMJ Open*, 7(4):1–7, 2017.
- [34] RP Austin, P Barton, SL Cockcroft, MC Wenlock, and RJ Riley. The influence of nonspecific microsomal binding on apparent intrinsic clearance, and its prediction from physicochemical properties. *Drug Metabolism and Disposition*, 30(12):1497–1503, 2002.
- [35] F Langenbucher. Linearization of dissolution rate by the Weibull distribution. *J Pharm Pharmacol*, 24(12):979–981, 1972.
- [36] ChemAxon Tacrolimus, Available online (accessed on 23 April 2022). URL <https://chemicalize.com/app/calculation>.
- [37] AI Lauerma, C Surber, and HI Maibach. Absorption of topical tacrolimus (FK506) in vitro through human skin: Comparison with cyclosporin A. *Skin Pharmacology and Physiology*, 10(5-6):230–234, 1997.
- [38] SE Lucangioli, E Kenndler, A Carlucci, VP Tripodi, SL Scioscia, and CN Carducci. Relation between retention factors of immunosuppressive drugs in microemulsion electrokinetic chromatography with biosurfactants and octanol-water partition coefficients. *Journal of Pharmaceutical and Biomedical Analysis*, 33(5):871–878, 2003.
- [39] H Zahir, RA Nand, KF Brown, BN Tattam, and AJ McLachlan. Validation of methods to study the distribution and protein binding of tacrolimus in human blood. *Journal of Pharmacological and Toxicological Methods*, 46(1):27–35, 2001.
- [40] Y Dai, MF Hebert, N Isoherranen, CL Davis, C Marsh, DD Shen, and KE Thummel. Effect of CYP3A5 polymorphism on tacrolimus metabolic clearance in vitro. *Drug Metabolism and Disposition*, 34(5):836–847, 2006.
- [41] LK Kamdem, F Streit, UM Zanger, J Brockmöller, M Oellerich, VW Armstrong, and L Wojnowski. Contribution of CYP3A5 to the in vitro hepatic clearance of tacrolimus. *Clinical Chemistry*, 51(8):1374–1381, 2005.
- [42] R Kawai, M Lemaire, JL Steimer, A Bruehlisauer, W Niederberger, and M Rowland. Physiologically based pharmacokinetic study on a cyclosporin derivative, SDZ IMM 125. *Journal of Pharmacokinetics and Biopharmaceutics*, 22(5):327–365, 1994.

- [43] LM Berezhkovskiy. Volume of distribution at steady state for a linear pharmacokinetic system with peripheral elimination. *Journal of Pharmaceutical Sciences*, 93(6):1628–40, 2004.
- [44] JA Petan, N Undre, MR First, K Saito, T Ohara, O Iwabe, H Mimura, M Suzuki, and S Kitamura. Physiochemical properties of generic formulations of tacrolimus in mexico. *Transplantation Proceedings*, 40(5):1439–1442, 2008.
- [45] R Amundsen, A Åsberg, IK Ohm, and H Christensen. Cyclosporine A- and tacrolimus-mediated inhibition of CYP3A4 and CYP3A5 in vitro. 40(4):655–661, 2012.
- [46] EJ Guest, L Aarons, JB Houston, A Rostami-Hodjegan, and A Galetin. Critique of the two-fold measure of prediction success for ratios: Application for the assessment of drug-drug interactions. *Drug Metabolism and Disposition*, 39(2):170–173, 2011.
- [47] Open Systems Pharmacology Suite Community. Open Systems Pharmacology Suite Manual, Version 7.4 2018, Available online (accessed on 28 September 2021). URL <https://docs.open-systems-pharmacology.org/working-with-pk-sim/pk-sim-documentation>.
- [48] JH Lin. CYP induction-mediated drug interactions: In vitro assessment and clinical implications. *Pharmaceutical Research*, 23(6):1089–1116, 2006.
- [49] CK Imamura, K Furihata, S Okamoto, and Y Tanigawara. Impact of cytochrome P450 2C19 polymorphisms on the pharmacokinetics of tacrolimus when coadministered with voriconazole. *Journal of Clinical Pharmacology*, 56(4):408–413, 2016.
- [50] A Huppertz, C Ott, T Bruckner, KI Foerster, J Burhenne, J Weiss, M Zorn, WE Haefeli, and D Czock. Prolonged-release tacrolimus is less susceptible to interaction with the strong CYP3A inhibitor voriconazole in healthy volunteers. *Clinical Pharmacology and Therapeutics*, 106(6):1290–1298, 2019.
- [51] M F Hebert, R M Fisher, C L Marsh, D Dressler, and I Bekersky. Effects of rifampin on tacrolimus pharmacokinetics in healthy volunteers. *Journal of Clinical Pharmacology*, 39(1):91–96, 1999. doi: 10.1177/00912709922007499.
- [52] X Li, S Frechen, D Moj, T Lehr, M Taubert, CH Hsin, G Mikus, PJ Neuvonen, KT Olkkola, TI Saari, and U Fuhr. A physiologically based pharmacokinetic model of voriconazole integrating time-dependent inhibition of CYP3A4, genetic polymorphisms of CYP2C19 and predictions of drug-drug interactions. *Clinical Pharmacokinetics*, 59(6):781–808, 2020.
- [53] P Poulin, K Schoenlein, and PF Theil. Prediction of adipose tissue: plasma partition coefficients for structurally unrelated drugs. *Journal of pharmaceutical sciences*, 90(4):436–447, 2001.
- [54] P Poulin and FP Theil. A priori prediction of tissue:plasma partition coefficients of drugs to facilitate the use of physiologically-based pharmacokinetic models in drug discovery. *Journal of pharmaceutical sciences*, 89(1):16–35, 2000.
- [55] P Poulin and FP Theil. Prediction of pharmacokinetics prior to in vivo studies. 1. Mechanism-based prediction of volume of distribution. *Journal of pharmaceutical sciences*, 91(1):129–156, 2002.
- [56] P Poulin and FP Theil. Prediction of pharmacokinetics prior to in vivo studies. II. Generic physiologically based pharmacokinetic models of drug disposition. *Journal of pharmaceutical sciences*, 91(5):1358–1370, 2002.
- [57] H Yamazaki, M Nakamoto, M Shimizu, N Murayama, and T Niwa. Potential impact of cytochrome P450 3A5 in human liver on drug interactions with triazoles. *British Journal of Clinical Pharmacology*, 69(6):593–597, 2010.

- [58] T Rodgers, D Leahy, and M Rowland. Physiologically based pharmacokinetic modeling 1: predicting the tissue distribution of moderate-to-strong bases. *Journal of pharmaceutical sciences*, 94(6):1259–1276, 2005.
- [59] T Rodgers and M Rowland. Physiologically based pharmacokinetic modelling 2: predicting the tissue distribution of acids, very weak bases, neutrals and zwitterions. *Journal of pharmaceutical sciences*, 95(6):1238–1257, 2006.

B.2 PROJECT II: PBPK MODELING OF IMATINIB

CPT: PHARMACOMETRICS & SYSTEMS PHARMACOLOGY

Physiologically Based Pharmacokinetic Modeling of Imatinib and N-Desmethyl Imatinib for Drug-Drug Interaction Predictions

Supplement S1 - Model Information and Evaluation

Helena Leonie Hanae Loer¹, Christina Kovar^{1,2}, Simeon Rüdesheim^{1,2}, Fatima Zahra Marok¹, Laura Maria Fuhr¹, Dominik Selzer¹, Matthias Schwab^{2,3,4}, Thorsten Lehr¹

¹Clinical Pharmacy, Saarland University, 66123 Saarbrücken, Germany

²Dr. Margarete Fischer-Bosch-Institute of Clinical Pharmacology, 70376 Stuttgart, Germany

³Departments of Clinical Pharmacology, and Pharmacy and Biochemistry, University of Tübingen, 72076 Tübingen, Germany

⁴Cluster of Excellence iFIT (EXC2180), Image-Guided and Functionally Instructed Tumor Therapies, University of Tübingen, 69120 Tübingen, Germany

Funding:

Matthias Schwab was supported by the Robert Bosch Stiftung (Stuttgart, Germany), a grant from the German Federal Ministry of Education and Research (BMBF, 031L0188D, “GUIDE-IBD”) and the DFG im Rahmen der Exzellenzstrategie des Bundes und der Länder-EXC 2180-390900677.

Thorsten Lehr was supported by the German Federal Ministry of Education and Research (BMBF, Horizon 2020 INSPIRATION grant 643271), under the frame of ERACoSysMed and the European Union Horizon 2021 SafePolyMed (grant 101057639).

Conflict of Interest:

The authors declared no competing interests for this work.

Corresponding Author:

Thorsten Lehr, PhD
Clinical Pharmacy
Saarland University
Campus C4 3
66123 Saarbrücken
Germany

Contents

S1 Physiologically Based Pharmacokinetic Model Building	3
S1.1 System-Dependent Parameters	3
S1.2 Equations	6
S1.2.1 Weibull Function	6
S1.2.2 Michaelis-Menten Kinetics	6
S1.3 Clinical Study Data	7
S1.4 Drug-Dependent Parameters	9
S2 Physiologically Based Pharmacokinetic Model Evaluation	11
S2.1 Plasma Concentration-Time Profiles (Semilogarithmic)	11
S2.2 Plasma Concentration-Time Profiles (Linear)	16
S2.3 Urinary Excretion Profiles	20
S2.4 Goodness-of-Fit Plots	21
S2.5 MRD of Plasma Concentration Predictions	22
S2.6 Predicted and Observed AUC_{last} and C_{max} Values	24
S2.7 Local Sensitivity Analysis	26
S2.7.1 Methods	26
S2.7.2 Results	26
S3 Drug-Drug Interaction Modeling	28
S3.1 Clinical Study Data	28
S3.2 Drug-Dependent Parameters of DDI Partners	29
S3.2.1 Rifampicin	29
S3.2.2 Ketoconazole	30
S3.2.3 Gemfibrozil	32
S3.2.4 Simvastatin	33
S3.2.5 Metoprolol	34
S3.3 Plasma Concentration-Time Profiles (Semilogarithmic)	36
S3.4 Plasma Concentration-Time Profiles (Linear)	37
S3.5 DDI AUC_{last} and DDI C_{max} Ratio Goodness-of-Fit Plots	38
S3.6 Predicted and Observed DDI AUC_{last} and DDI C_{max} Ratios	39
S3.7 Comparison of CYP3A Perpetrator Effects – SD vs. MD Imatinib Administration . .	40
Bibliography	42

S1 Physiologically Based Pharmacokinetic Model Building

S1.1 System-Dependent Parameters

Table S1: System-dependent parameters

Enzyme/ Transporter	Reference concentration		Localization/ Direction	Half-life liver [h]	Half-life intestine [h]
	Mean ^a [μmol/L]	GeoSD ^b			
AADAC	1.00 ^c	1.40 ^d	intracellular	36	23
CYP2C8	2.56 [1]	2.05 [2]	intracellular	23	23
CYP2D6	0.40 [1]	2.49 [2]	intracellular	51	23
CYP3A4	4.32 [1]	1.18 (liver) [2] 1.45 (duodenum) [2]	intracellular	36	23
FMO3	1.00 ^c	1.40 ^d	intracellular	36	23
PON3	1.00 ^c	1.40 ^d	intracellular	36	23
UGT1A1	1.00 ^c	1.40 ^d	intracellular	36	23
UGT1A3	1.00 ^c	1.40 ^d	intracellular	36	23
UGT1A4	2.32 ^e [3]	1.07 [2]	intracellular	36	23
UGT2B7	2.78 [4]	1.60 [2]	intracellular	36	23
Chemical hydrolysis ^f	1.00 ^c	-	-	36	23
Liver lactonization ^g	1.00 ^c	1.40 ^d	-	36	23
Plasma hydrolysis ^f	1.00 ^c	1.40 ^d	-	36	23
BCRP	1.00 ^c	1.35 [5]	efflux	36	23
MRP2	1.00 ^c	1.49 [6]	efflux	36	23
OATP1B1	0.07 ^h [7]	1.54 [7]	influx	36	23
OATP1B3	1.00 ^c	1.54 [7]	influx	36	23
P-gp	1.41 [8]	1.60 [7]	efflux	36	23
Liver influx ⁱ	1.00 ^c	1.40 ^d	influx	36	23

AADAC: arylacetamide deacetylase, BCRP: breast cancer resistance protein, CYP: cytochrome P450, FMO: flavin-containing monooxygenase, MRP: multidrug resistance-associated protein, OATP: organic-anion-transporting polypeptide, P-gp: P-glycoprotein, PON: paraoxonase, UGT: uridine 5'-diphosphoglucuronosyltransferase.

^a: μmol protein/L in the tissue of highest expression

^b: geometric standard deviation of the reference concentration

^c: if no information was available, the mean reference concentration was set to 1.00 μmol/L and the catalytic rate constant was optimized according to [9]

^d: if no information was available, a moderate variability of 35% coefficient of variation was assumed

^e: calculated from protein per mg microsomal protein x 40.0 mg microsomal protein per g liver [10]

^f: simvastatin

^g: simvastatin hydroxy acid

^h: calculated from transporter per mg membrane protein x 37.0 mg membrane protein per g liver [7]

ⁱ: gemfibrozil

Table S2: Relative expression of implemented enzymes and transporters in organs and tissues [%]

	AADAC	CYP2C8	CYP2D6	CYP3A4	FMO3	PON3	UGT1A1	UGT1A3	UGT1A4	UGT2B7
Data source	RT-PCR [12]	RT-PCR [13]	RT-PCR [13]	RT-PCR [13]	RT-PCR [12]	Array [14]	RT-PCR [12]	RT-PCR [12]	RT-PCR [12]	EST [15]
Blood cells	0	0	0	0	0	0	0	0	0	0
Plasma	0	0	0	0	0	0	0	0	0	0
Bone	0	0	0	0	1	8	0	0	0	0
Brain	0	0	1	0	0	6	0	0	0	8
Fat	0	0	0	0	0	0	0	0	0	0
Gonads	0	1	77	0	0	15	0	0	0	13
Heart	0	0	0	0	0	5	0	0	0	0
Kidney	0	0	2	1	0	12	8	8	0	100
Liver periportal	100	100	100	100	100	100	100	100	100	23
Liver pericentral	100	100	100	100	100	100	100	100	100	23
Lung	3	0	2	0	2	18	0	0	0	0
Muscle	0	0	0	0	1	4	0	0	0	0
Pancreas	15	0	0	0	0	7	0	0	0	0
Skin	0	0	0	0	0	13	0	0	0	3
Spleen	0	0	0	0	0	6	0	0	0	0
Duodenum mucosa	25	0	9	7	0	9	32	32	0	4
Upper jejunum mucosa	25	0	9	7	0	9	32	32	0	4
Lower jejunum mucosa	25	0	9	7	0	9	32	32	0	4
Upper ileum mucosa	25	0	9	7	0	9	32	32	0	4
Lower ileum mucosa	25	0	9	7	0	9	32	32	0	4
Cecum mucosa	0	0	0	0	0	0	0	0	0	0
Colon ascendens mucosa	0	0	0	0	0	6	3	3	0	0
Colon transversum mucosa	0	0	0	0	0	6	3	3	0	0
Colon descendens mucosa	0	0	0	0	0	6	3	3	0	0
Colon sigmoid mucosa	0	0	0	0	0	6	3	3	0	0
Rectum mucosa	0	0	0	0	0	0	0	0	0	0
Stomach non-muc. tissue	8	0	0	0	1	9	2	2	0	13
Small intestine non-muc. tissue	25	0	9	7	0	9	32	32	0	4
Large intestine non-muc. tissue	0	0	0	0	0	6	3	3	0	0
Stomach lumen	0	0	0	0	0	0	0	0	0	0
Duodenum lumen	0	0	0	0	0	0	0	0	0	0
Upper jejunum lumen	0	0	0	0	0	0	0	0	0	0
Lower jejunum lumen	0	0	0	0	0	0	0	0	0	0
Upper ileum lumen	0	0	0	0	0	0	0	0	0	0
Lower ileum lumen	0	0	0	0	0	0	0	0	0	0
Cecum lumen	0	0	0	0	0	0	0	0	0	0
Colon ascendens lumen	0	0	0	0	0	0	0	0	0	0
Colon transversum lumen	0	0	0	0	0	0	0	0	0	0
Colon descendens lumen	0	0	0	0	0	0	0	0	0	0
Colon sigmoid lumen	0	0	0	0	0	0	0	0	0	0
Rectum lumen	0	0	0	0	0	0	0	0	0	0

^a: with the relative expression in blood cells set to 0.3046 [11], ^b: with the relative expression in intestinal mucosa increased by factor 3.57, ^c: gemfibrozil, AADAC: arylacetamide deacetylase, Array: microarray expression profile, BCRP: breast cancer resistance protein, CYP: cytochrome P450, EST: expressed sequence tags, FMO: flavin-containing monooxygenase, MRP: multidrug resistance-associated protein, muc.: mucosal, OATP: organic-anion-transporting polypeptide, P-gp: P-glycoprotein, PON: paraoxonase, RT-PCR: reverse transcription polymerase chain reaction, UGT: uridine 5'-diphospho-glucuronosyltransferase.

Table S2: Relative expression of implemented enzymes and transporters in organs and tissues [%] (*continued*)

	Chemical hydrolysis	Liver lactonization	Plasma hydrolysis	BCRP	MRP2	OATP1B1	OATP1B3	P-gp	Liver influx ^c
Data source	-	-	-	RT-PCR ^a [16]	Array [14]	RT-PCR [16]	Array [14]	RT-PCR ^b [16]	-
Blood cells	0	0	0	30	0	0	0	0	0
Plasma	0	0	100	-	-	-	-	-	-
Bone	66	0	0	21	7	0	3	2	0
Brain	73	0	0	46	6	0	3	8	0
Fat	73	0	0	0	0	0	0	0	0
Gonads	66	0	0	27	9	1	4	2	0
Heart	73	0	0	11	5	0	6	4	0
Kidney	82	0	0	9	59	0	2	71	0
Liver periportal	83	100	0	28	100	100	100	19	100
Liver pericentral	83	100	0	28	100	100	100	19	100
Lung	36	0	0	22	6	0	2	7	0
Muscle	52	0	0	3	31	0	2	1	0
Pancreas	96	0	0	1	56	0	1	1	0
Skin	66	0	0	0	3	0	1	0	0
Spleen	66	0	0	6	7	0	1	7	0
Duodenum mucosa	88	0	0	100	50	0	2	100	0
Upper jejunum mucosa	88	0	0	100	50	0	2	100	0
Lower jejunum mucosa	88	0	0	100	50	0	2	100	0
Upper ileum mucosa	88	0	0	100	50	0	2	100	0
Lower ileum mucosa	88	0	0	100	50	0	2	100	0
Cecum mucosa	88	0	0	0	0	0	0	0	0
Colon ascendens mucosa	88	0	0	16	12	0	1	40	0
Colon transversum mucosa	88	0	0	16	12	0	1	40	0
Colon descendens mucosa	88	0	0	16	12	0	1	40	0
Colon sigmoid mucosa	88	0	0	16	12	0	1	40	0
Rectum mucosa	88	0	0	0	0	0	0	0	0
Stomach non-muc. tissue	96	0	0	4	5	0	1	3	0
Small intestine non-muc. tissue	96	0	0	100	50	0	2	28	0
Large intestine non-muc. tissue	83	0	0	16	12	0	1	11	0
Stomach lumen	0	0	0	-	-	-	-	-	-
Duodenum lumen	10	0	0	-	-	-	-	-	-
Upper jejunum lumen	10	0	0	-	-	-	-	-	-
Lower jejunum lumen	60	0	0	-	-	-	-	-	-
Upper ileum lumen	100	0	0	-	-	-	-	-	-
Lower ileum lumen	81	0	0	-	-	-	-	-	-
Cecum lumen	10	0	0	-	-	-	-	-	-
Colon ascendens lumen	10	0	0	-	-	-	-	-	-
Colon transversum lumen	10	0	0	-	-	-	-	-	-
Colon descendens lumen	35	0	0	-	-	-	-	-	-
Colon sigmoid lumen	35	0	0	-	-	-	-	-	-
Rectum lumen	35	0	0	-	-	-	-	-	-

^a: with the relative expression in blood cells set to 0.3046 [11], ^b: with the relative expression in intestinal mucosa increased by factor 3.57, ^c: gemfibrozil, AADAC: arylacetamide deacetylase, Array: microarray expression profile, BCRP: breast cancer resistance protein, CYP: cytochrome P450, EST: expressed sequence tags, FMO: flavin-containing monooxygenase, MRP: multidrug resistance-associated protein, muc.: mucosal, OATP: organic-anion-transporting polypeptide, P-gp: P-glycoprotein, PON: paraoxonase, RT-PCR: reverse transcription polymerase chain reaction, UGT: uridine 5'-diphospho-glucuronosyltransferase.

S1.2 Equations

S1.2.1 Weibull Function

$$f_d(t) = 1 - \exp\left(\frac{-(t - t_{lag})^b}{a}\right) \quad (S1)$$

where $f_d(t)$ = fraction of administered dose dissolved at time t , t_{lag} = lag time between drug intake and start of the dissolution process, b = shape parameter, a = scale parameter.

S1.2.2 Michaelis-Menten Kinetics

$$v = \frac{v_{max} \cdot [S]}{K_M + [S]} = \frac{k_{cat} \cdot [E] \cdot [S]}{K_M + [S]} \quad (S2)$$

where v = reaction velocity, v_{max} = maximum reaction velocity, $[S]$ = free substrate concentration, K_M = Michaelis-Menten constant, k_{cat} = catalytic rate constant, and $[E]$ = enzyme concentration.

S1.3 Clinical Study Data

Table S3: Clinical studies of imatinib used for PBPK model development

Imatinib dosing regimen		n	Females [%]	Ethnicity ^a	Age [years]	Weight [kg]	Height [cm]	Compound(s) measured	Dataset	Reference
Route	Dose [mg]									
iv (inf, 1 h, SD)	100	17 (healthy)	18	White American	(40–58)	73.3±7 (62–88)	-	Ima	training	Peng 2004 [17]
po (-, QD)	25	3 (CML patients)	34	White American	53.11±12.99	80.05±17.72	-	Ima	test	Peng 2004 [18]
po (-, SD)	50	3 (CML patients)	34	White American	53.11±12.99	80.05±17.72	-	Ima	test	Peng 2004 [18]
po (-, QD)	50	3 (CML patients)	34	White American	53.11±12.99	80.05±17.72	-	Ima	test	Peng 2004 [18]
po (-, QD)	85	3 (CML patients)	34	White American	53.11±12.99	80.05±17.72	-	Ima	test	Peng 2004 [18]
po (tab, SD)	100	1 (healthy)	67	European	(25–34)	-	-	Ima	test	Zidan 2018 [19]
po (tab, SD)	100	1 (healthy)	67	European	(25–34)	-	-	Ima	test	Zidan 2018 [19]
po (tab, SD)	100	1 (healthy)	67	European	(25–34)	-	-	Ima	test	Zidan 2018 [19]
po (tab, SD)	100	37 (healthy)	-	European	32.4±9.84	75.0±7.63	177.4±7.12	Ima, NDMI	test	Ostrowicz 2014 [20]
po (tab, SD)	200	10 (healthy)	20	European	24±3	72±13	-	Ima, NDMI	training	Filppula 2013 [21]
po (tab, SD)	200	23 (healthy)	0	Asian	29±7	69.5±8.1	175.8±6	Ima	training	Jung 2014 [22]
po (cap, SD)	200	14 (healthy)	7	European	(35–59)	(64–103)	-	Ima, NDMI	test	Dutreix 2004 [23]
po (cap, SD)	200	4 (healthy)	0	European	-	(61.8–85.7)	-	Ima, NDMI	test	Gschwind 2005 [24]
po (tab, SD)	200	1 (healthy)	-	European	-	-	-	Ima, NDMI	test	Golabchifar 2011 [25]
po (-, SD)	200	27 (healthy)	-	Asian	-	-	-	Ima	test	Yang 2013 [26]
po (-, QD)	350	5 (CML patients)	34	White American	53.11±12.99	80.05±17.72	-	Ima	test	Peng 2004 [18]
po (-, SD)	400	12 (healthy)	50	White American	28.3±11.9 (21–57)	72.2±16.6 (50.9–101)	-	Ima, NDMI	training	Frye 2004 [27]
po (tab, SD)	400	33 (healthy)	18	White American	38.3±11.83 (19–60)	75.52±10.77 (57.6–101.7)	176.6±8.24 (161–194)	Ima, NDMI	training	Nikolova 2004 [28]
po (cap, SD)	400	17 (healthy)	18	White American	(40–58)	73.3±7 (62–88)	-	Ima	test	Peng 2004 [17]
po (cap, SD)	400	33 (healthy)	18	White American	38.3±11.83 (19–60)	75.52±10.77 (57.6–101.7)	176.6±8.24 (161–194)	Ima, NDMI	test	Nikolova 2004 [28]
po (tab, SD)	400	33 (healthy)	18	White American	38.3±11.83 (19–60)	75.52±10.77 (57.6–101.7)	176.6±8.24 (161–194)	Ima, NDMI	test	Nikolova 2004 [28]
po (-, SD)	400	26 (healthy)	31	European	24±3	72±12	175±8	Ima	test	Pena 2020 [29]

-: not given, ^a: implemented, BID: twice daily, cap: capsule, CML: chronic myeloid leukemia, GIST: gastrointestinal stromal tumor, Ima: imatinib, inf: infusion, iv: intravenous, n: number of participants, NDMI: N-desmethyl imatinib, po: oral, QD: once daily, SD: single dose, tab: tablet; values for age, weight, and height are shown as mean ± standard deviation (range).

Table S3: Clinical studies of imatinib used for PBPK model development (*continued*)

Imatinib dosing regimen		n	Females	Ethnicity ^a	Age	Weight	Height	Compound(s)	Dataset	Reference
Route	Dose [mg]		[%]		[years]	[kg]	[cm]	measured		
po (tab, SD)	400	30 (healthy)	0	Mexican American	27.8±6.5	71.2±9.8	171±9	Ima	test	Parrillo-Campiglia 2009 [30]
po (-, SD)	400	10 (healthy)	30	White American	43.7±6.4	80.5±6.0	-	Ima	test	Smith 2004 [31]
po (-, SD)	400	11 (healthy)	-	White American	-	-	-	Ima, NDMI	test	Tawbi 2014 [32]
po (cap, SD)	400	24 (healthy)	0	Asian	36.5±1.70	62.8±1.66 (60.0–66.5)	168 (163–173)	Ima, NDMI	test	Zhang 2014 [33]
po (-, SD)	400	12 (healthy)	50	White American	(20–51)	-	-	Ima, NDMI	test	Sparano 2009 [34]
po (cap, SD)	400	12 (CML patients)	46	European	43±10 (19–63)	69.2±8.2 (40.6–89.9)	174±12 (158–190)	Ima, NDMI	test	Mohajeri 2015 [35]
po (tab, SD)	400	12 (CML patients)	46	European	43±10 (19–63)	69.2±8.2 (40.6–89.9)	174±12 (158–190)	Ima, NDMI	test	Mohajeri 2015 [35]
po (tab, SD)	400	12 (CML patients)	46	European	43±10 (19–63)	69.2±8.2 (40.6–89.9)	174±12 (158–190)	Ima, NDMI	test	Mohajeri 2015 [35]
po (tab, SD)	400	21 (healthy)	0	European	39±11	78.7±9.4	175.4±7.4	Ima	test	Jawhari 2011 [36]
po (cap, SD)	400	14 (healthy)	7	European	49.8±8.2 (40–64)	74.4±8.1 (61.5–90.0)	172±6 (165–186)	Ima	test	Bolton 2004 [37]
po (tab, SD)	400	37 (healthy)	-	European	34.1±11.59	75.6±7.16	177.4±9.11	Ima, NDMI	test	Ostrowicz 2014 [20]
po (-, SD)	400	12 (healthy)	50	White American	-	-	-	Ima, NDMI	test	Egorin 2009 [38]
po (-, SD)	400	4 (CML patients)	34	White American	53.11±12.99	80.05±17.72	-	Ima	test	Peng 2004 [18]
po (tab, QD)	400	40 (CML patients)	20	Asian	40.95 (20–67)	58.21±8.41 (41–79)	163±8.07 (148–182)	Ima	test	Arora 2016 [39]
po (-, QD)	400	12 (GIST patients)	20	White American	-	-	-	Ima, NDMI	test	Eechoute 2011 [40]
po (-, QD)	400	5 (CML patients)	34	White American	53.11±12.99	80.05±17.72	-	Ima	test	Peng 2004 [18]
po (-, BID)	400	4 (CML patients)	34	White American	53.11±12.99	80.05±17.72	-	Ima	test	Peng 2004 [18]
po (-, BID)	500	6 (CML patients)	34	White American	53.11±12.99	80.05±17.72	-	Ima	test	Peng 2004 [18]
po (-, QD)	600	9 (CML patients)	34	White American	53.11±12.99	80.05±17.72	-	Ima	test	Peng 2004 [18]
po (-, SD)	750	6 (CML patients)	34	White American	53.11±12.99	80.05±17.72	-	Ima	test	Peng 2004 [18]

-: not given, ^a: implemented, BID: twice daily, cap: capsule, CML: chronic myeloid leukemia, GIST: gastrointestinal stromal tumor, Ima: imatinib, inf: infusion, iv: intravenous, n: number of participants, NDMI: N-desmethyl imatinib, po: oral, QD: once daily, SD: single dose, tab: tablet; values for age, weight, and height are shown as mean ± standard deviation (range).

S1.4 Drug-Dependent Parameters

Table S4: Drug-dependent parameters of the final imatinib PBPK model

Parameter	Unit	Value	Source	Literature	Reference	Description
Imatinib						
Molecular weight	g/mol	493.62	Lit.	493.62	[42]	Molecular weight
pKa ₁ , acid		12.69	Lit.	12.69	[42]	Acid dissociation constant
pKa ₂ , base		7.84	Lit.	7.84	[42]	Acid dissociation constant
pKa ₃ , base		4.27	Lit.	4.27	[42]	Acid dissociation constant
Solubility (pH)	mg/mL	0.04 (7.4)	Lit.	0.04 (7.4)	[42]	Solubility
Lipophilicity	log units	3.25	Opt.	2.89–4.53	[42–44]	Lipophilicity
f _u	%	3.0 (AGP)	Lit.	3.0–5.1	[31, 45, 46]	Fraction unbound
CYP2C8 K _M → NDMI	μmol/L	3.85	Lit.	3.85 ^a	[47]	Michaelis-Menten constant
CYP2C8 k _{cat} → NDMI	1/min	2.20	Opt.	4.07	[47]	Catalytic rate constant
CYP3A4 K _M → NDMI	μmol/L	12.96	Lit.	12.96 ^a	[47]	Michaelis-Menten constant
CYP3A4 k _{cat} → NDMI	1/min	2.59	Opt.	13.30	[47]	Catalytic rate constant
CYP3A4 CL → sink	1/min	0.42	Opt.	0.06	[47]	Clearance
P-gp K _M	μmol/L	4.09	Opt.	-	-	Michaelis-Menten constant
P-gp k _{cat}	1/min	2.98	Opt.	-	-	Transport rate constant
GFR fraction		1 ^b	Asm.	-	-	Filtered drug in the urine
EHC continuous fraction		1	Asm.	-	-	Bile fraction continuously released
Intestinal permeability	cm/min	3.52 · 10 ⁻⁵	Opt.	1.08±0.18 · 10 ⁻⁴	[48]	Transcellular intestinal permeability
Cellular permeability	cm/min	3.52 · 10 ⁻³	Calc.	PK-Sim Standard	[49]	Permeability into the cellular space
Partition coefficients			Calc.	Schmitt	[50]	Organ-plasma partition coefficients
Dissolution time (Weibull)	min	4.36	Lit.	4.36 ^c	[19]	Dissolution time (50%)
Dissolution shape (Weibull)		0.44	Lit.	0.44 ^c	[19]	Dissolution shape
CYP2C8 K _i	μmol/L	7.56	Lit.	7.56 ^a	[51]	Diss. const. inhibitor-enzyme complex (CI)
CYP2D6 K _i	μmol/L	6.75	Lit.	6.75 ^a	[51]	Diss. const. inhibitor-enzyme complex (CI)
CYP3A4 K _i	μmol/L	11.40	Lit.	11.40 ^a	[51]	Conc. for half-maximal inactivation (MBI)
CYP3A4 k _{inact}	1/min	0.07	Lit.	0.07	[51]	Maximum inactivation rate constant (MBI)
BCRP K _i	μmol/L	0.47	Lit.	0.47	[52]	Diss. const. inhibitor-transporter complex (CI)
P-gp K _i	μmol/L	8.00	Lit.	1.21–18.3	[44, 52, 53]	Diss. const. inhibitor-transporter complex (CI)

-: not available, ^a: *in vitro* values corrected for binding in the assay (f_{u,mic}), ^b: a GFR fraction of 1 corresponds to passive glomerular filtration of a compound,

^c: obtained from literature dissolution profile according to [41], AGP: α1-acid glycoprotein, asm.: assumed, BCRP: breast cancer resistance protein, calc.: calculated, CI: competitive inhibition, conc.: concentration, CYP: cytochrome P450, diss. const.: dissociation constant, EHC: enterohepatic circulation, GFR:

glomerular filtration rate, lit.: literature, MBI: mechanism-based inactivation, opt.: optimized, P-gp: P-glycoprotein.

Table S4: Drug-dependent parameters of the final imatinib PBPK model (*continued*)

Parameter	Unit	Value	Source	Literature	Reference	Description
N-Desmethyl Imatinib						
Molecular weight	g/mol	479.59	Lit.	479.59	[54]	Molecular weight
pKa ₁ , acid		12.69	Lit.	12.69	[54]	Acid dissociation constant
pKa ₂ , base		9.23	Lit.	9.23	[54]	Acid dissociation constant
pKa ₃ , base		4.45	Lit.	4.45	[54]	Acid dissociation constant
Solubility (pH)	mg/mL	0.37 (7.4)	Lit.	0.37 (7.4)	[54]	Solubility
Lipophilicity	log units	3.07	Opt.	4.00	[54]	Lipophilicity
f _u	%	3.6 (AGP)	Lit.	3.6–5	[45, 46]	Fraction unbound
CYP2C8 CL → sink	1/min	0.01	Opt.	$1.91 \cdot 10^{-3}$	[47]	Clearance
CYP3A4 CL → sink	1/min	$2.43 \cdot 10^{-5}$	Opt.	$7.21 \cdot 10^{-3}$	[47]	Clearance
CL _{hep} → sink	1/min	7.22	Opt.	-	-	Unspecific hepatic clearance
GFR fraction		1 ^b	Asm.	-	-	Filtered drug in the urine
EHC continuous fraction		1	Asm.	-	-	Bile fraction continuously released
Intestinal permeability	cm/min	$1.64 \cdot 10^{-5}$	Calc.			Transcellular intestinal permeability
Cellular permeability	cm/min	$2.81 \cdot 10^{-3}$	Calc.	PK-Sim Standard	[49]	Permeability into the cellular space
Partition coefficients			Calc.	PK-Sim Standard	[49]	Organ-plasma partition coefficients
CYP2C8 K _i	μmol/L	11.52	Lit.	11.52 ^a	[51]	Diss. const. inhibitor-enzyme complex (CI)
CYP2D6 K _i	μmol/L	12.15	Lit.	12.15 ^a	[51]	Diss. const. inhibitor-enzyme complex (CI)
CYP3A4 K _i	μmol/L	16.29	Lit.	16.29 ^a	[51]	Diss. const. inhibitor-enzyme complex (CI)

-: not available, ^a: *in vitro* values corrected for binding in the assay (f_{u,mic}), ^b: a GFR fraction of 1 corresponds to passive glomerular filtration of a compound, ^c: obtained from literature dissolution profile according to [41], AGP: α1-acid glycoprotein, asm.: assumed, BCRP: breast cancer resistance protein, calc.: calculated, CI: competitive inhibition, conc.: concentration, CYP: cytochrome P450, diss. const.: dissociation constant, EHC: enterohepatic circulation, GFR: glomerular filtration rate, lit.: literature, MBI: mechanism-based inactivation, opt.: optimized, P-gp: P-glycoprotein.

S2 Physiologically Based Pharmacokinetic Model Evaluation

S2.1 Plasma Concentration-Time Profiles (Semilogarithmic)

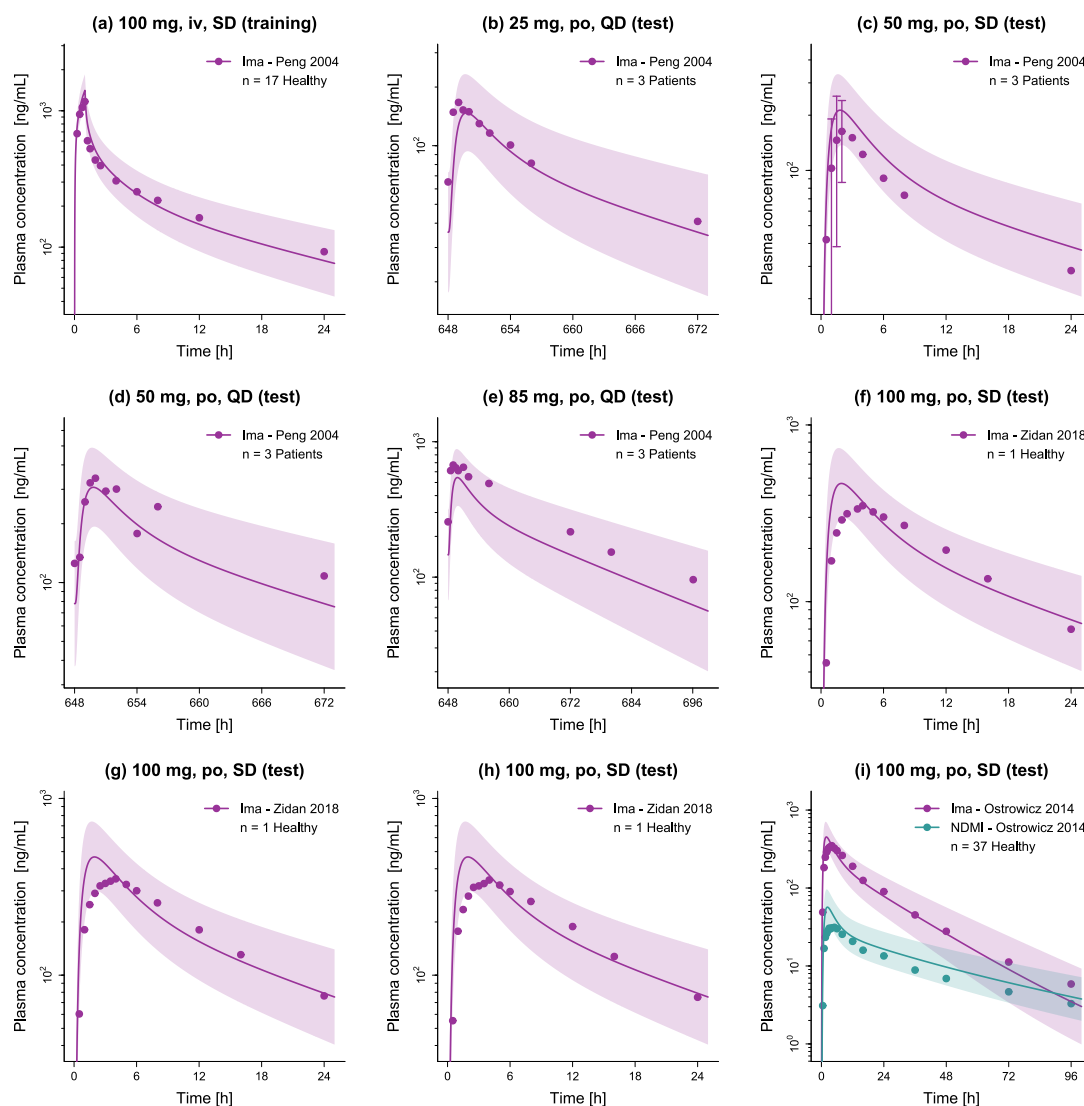


Figure S1: Semilogarithmic plots of predicted and observed plasma concentration-time profiles of imatinib and N-desmethyl imatinib. Solid lines and ribbons represent population predictions ($n = 1000$; geometric mean and geometric standard deviation), while corresponding observed data are shown as dots (\pm standard deviation, if available) [17–20]. Healthy: healthy subjects, Ima: imatinib, iv: intravenous, n: number of study participants, NDMI: N-desmethyl imatinib, Patients: cancer patients, po: oral, QD: once daily, SD: single dose.

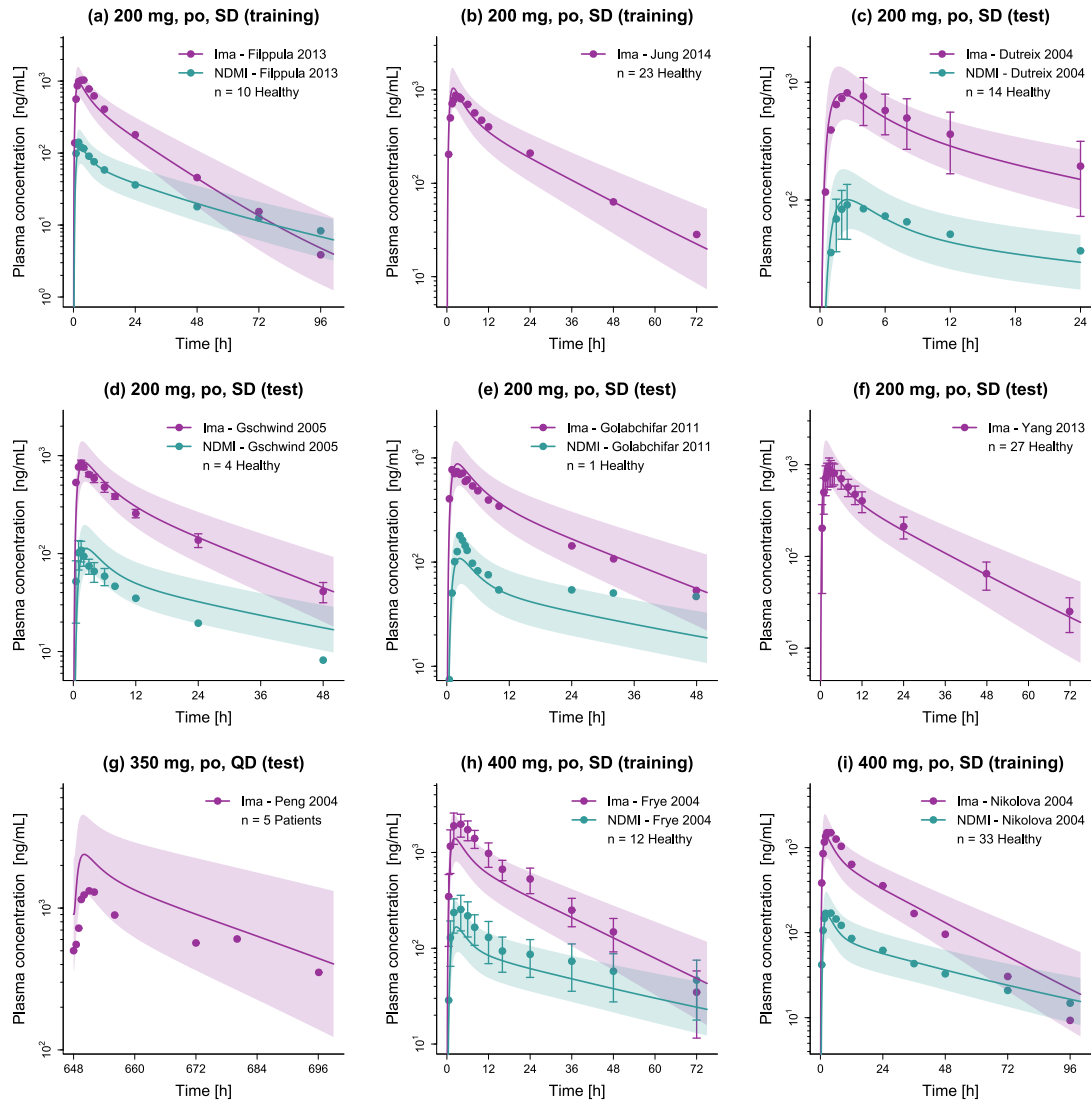


Figure S2: Semilogarithmic plots of predicted and observed plasma concentration-time profiles of imatinib and N-desmethyl imatinib. Solid lines and ribbons represent population predictions (n = 1000; geometric mean and geometric standard deviation), while corresponding observed data are shown as dots (\pm standard deviation, if available) [18, 21–28]. Healthy, healthy subjects, Ima: imatinib, n: number of study participants, NDMI: N-desmethyl imatinib, Patients: cancer patients, po: oral, QD: once daily, SD: single dose.

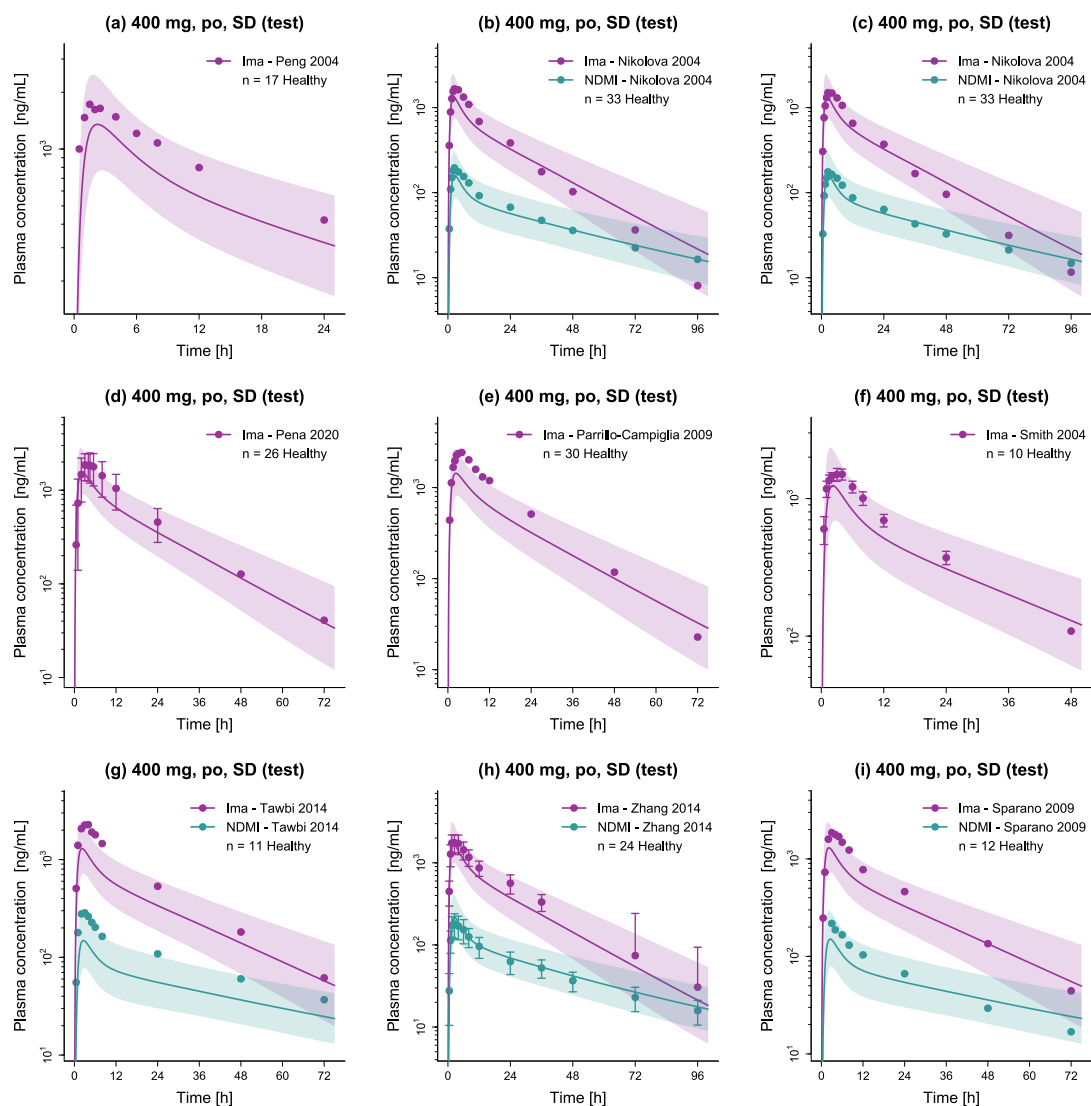


Figure S3: Semilogarithmic plots of predicted and observed plasma concentration-time profiles of imatinib and N-desmethyl imatinib. Solid lines and ribbons represent population predictions ($n = 1000$; geometric mean and geometric standard deviation), while corresponding observed data are shown as dots (\pm standard deviation, if available) [17, 28–34]. Healthy: healthy subjects, Ima: imatinib, n: number of study participants, NDMI: N-desmethyl imatinib, po: oral, SD: single dose.

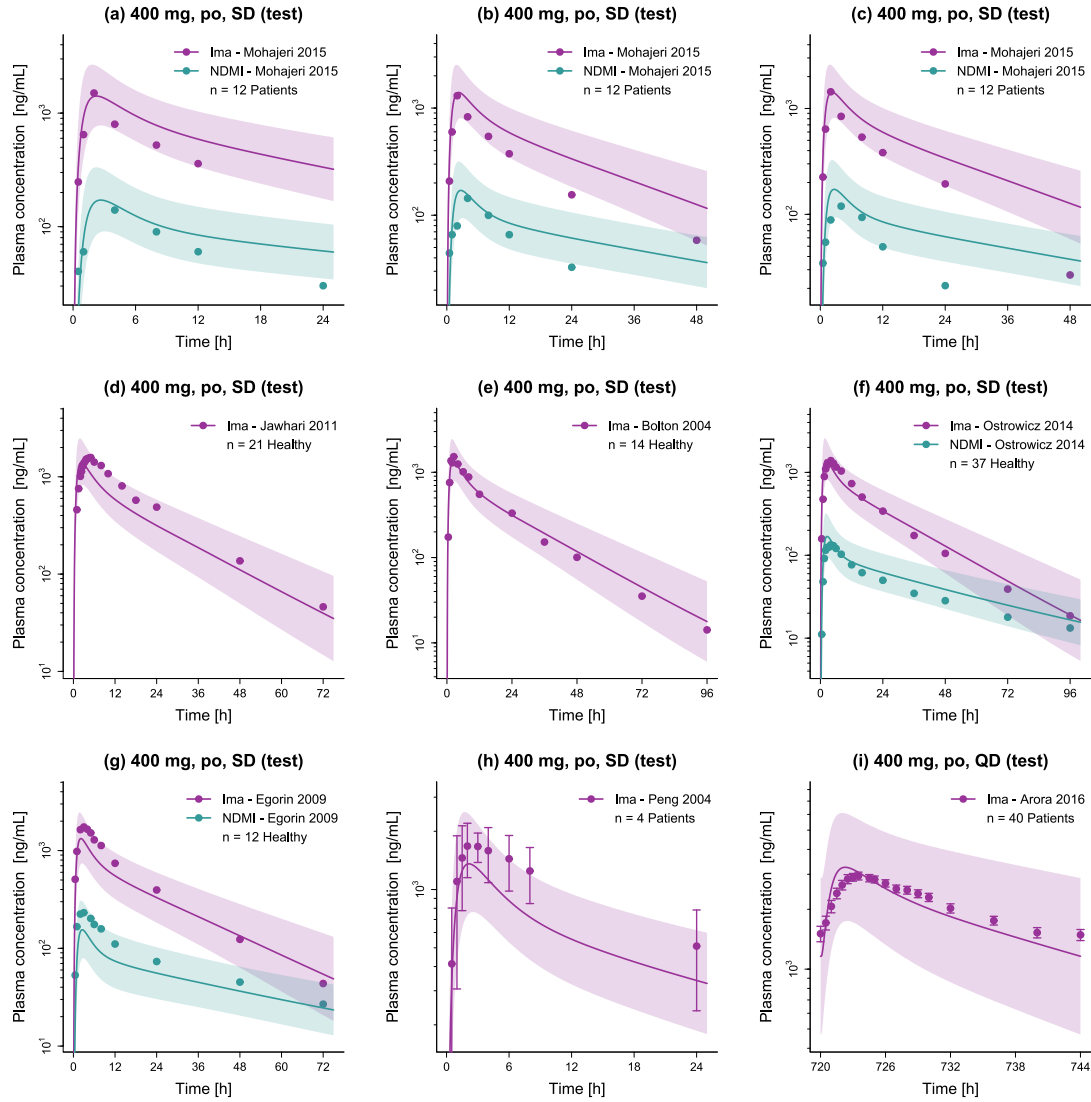


Figure S4: Semilogarithmic plots of predicted and observed plasma concentration-time profiles of imatinib and N-desmethyl imatinib. Solid lines and ribbons represent population predictions ($n = 1000$; geometric mean and geometric standard deviation), while corresponding observed data are shown as dots (\pm standard deviation, if available) [18, 20, 35–39]. Healthy: healthy subjects, Ima: imatinib, n: number of study participants, NDMI: N-desmethyl imatinib, Patients: cancer patients, po: oral, QD: once daily, SD: single dose.

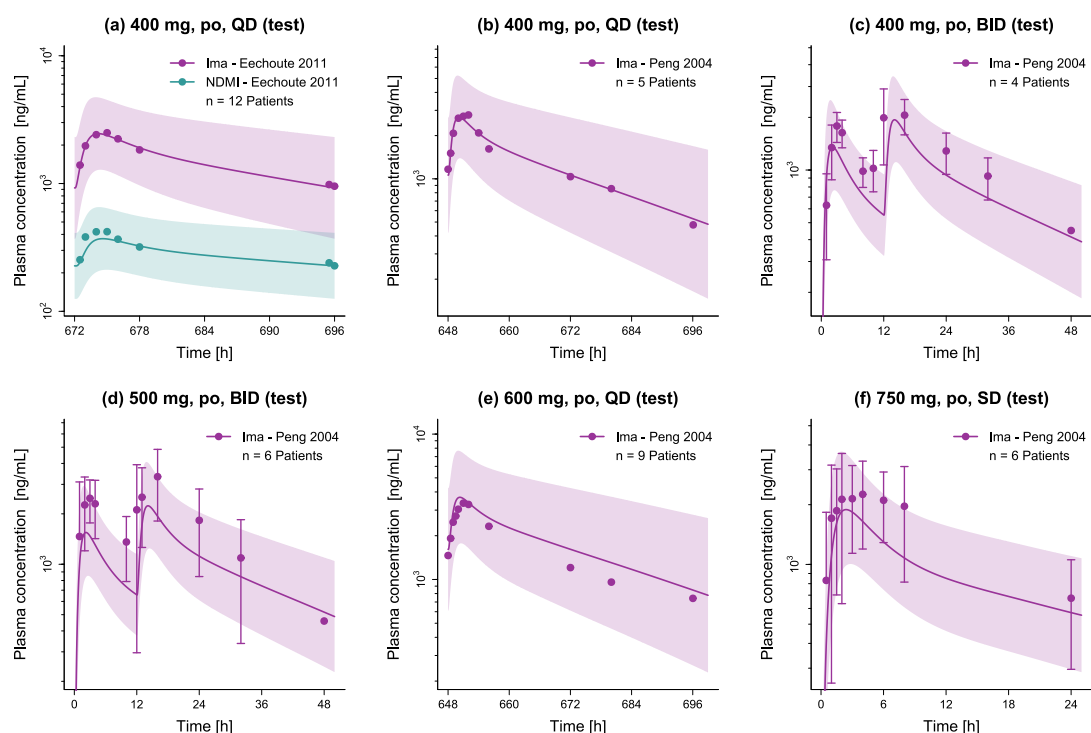


Figure S5: Semilogarithmic plots of predicted and observed plasma concentration-time profiles of imatinib and N-desmethyl imatinib. Solid lines and ribbons represent population predictions ($n = 1000$; geometric mean and geometric standard deviation), while corresponding observed data are shown as dots (\pm standard deviation, if available) [18, 40]. BID: twice daily, Ima: imatinib, n: number of study participants, NDMI: N-desmethyl imatinib, Patients: cancer patients, po: oral, QD: once daily, SD: single dose.

S2.2 Plasma Concentration-Time Profiles (Linear)

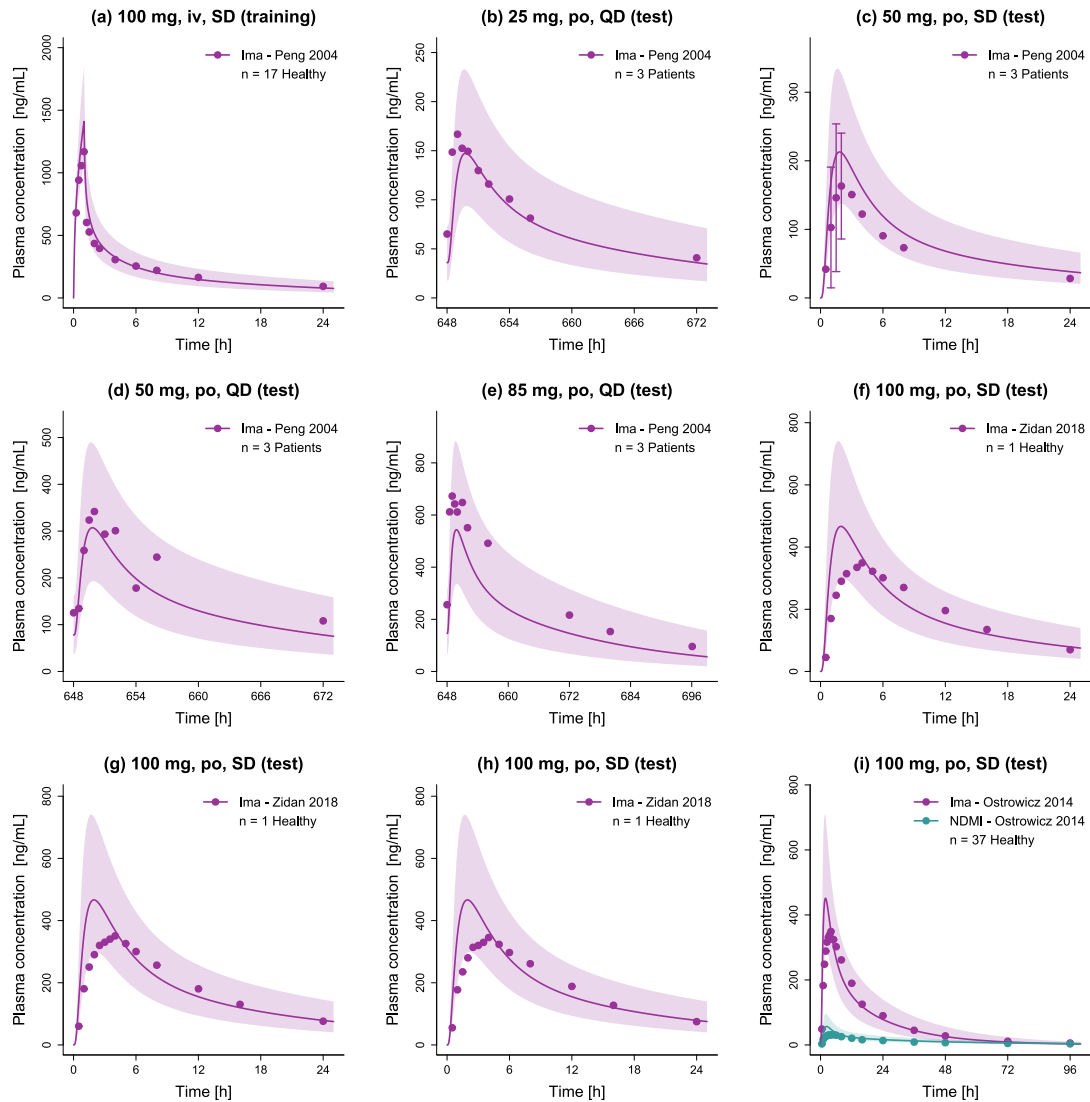


Figure S6: Linear plots of predicted and observed plasma concentration-time profiles of imatinib and N-desmethyl imatinib. Solid lines and ribbons represent population predictions ($n = 1000$; geometric mean and geometric standard deviation), while corresponding observed data are shown as dots (\pm standard deviation, if available) [17–20]. Healthy: healthy subjects, Ima: imatinib, iv: intravenous, n: number of study participants, NDMI: N-desmethyl imatinib, Patients: cancer patients, po: oral, QD: once daily, SD: single dose.

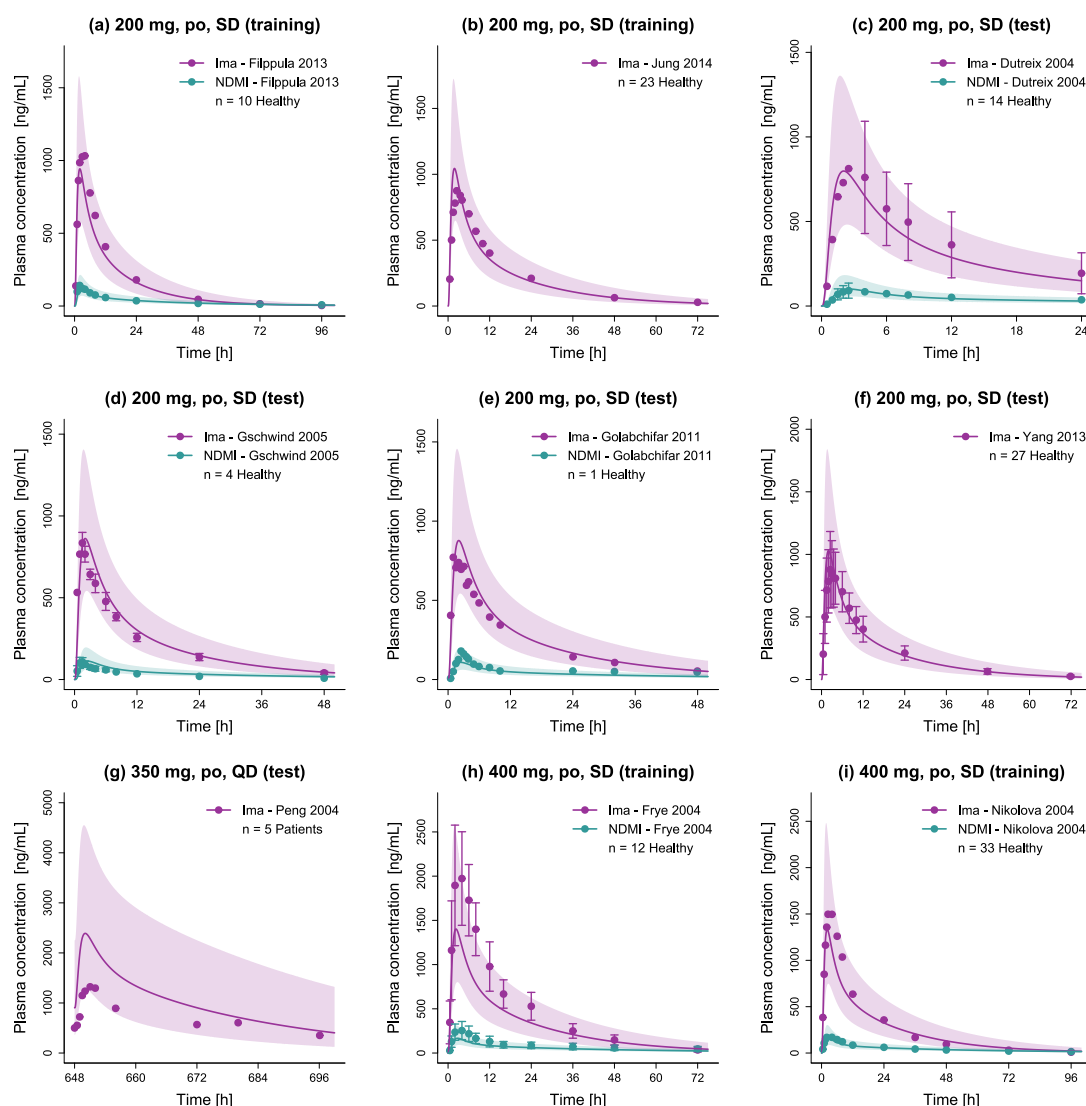


Figure S7: Linear plots of predicted and observed plasma concentration-time profiles of imatinib and N-desmethyl imatinib. Solid lines and ribbons represent population predictions ($n = 1000$; geometric mean and geometric standard deviation), while corresponding observed data are shown as dots (\pm standard deviation, if available) [18, 21–28]. Healthy: healthy subjects, Ima: imatinib, n: number of study participants, NDMI: N-desmethyl imatinib, Patients: cancer patients, po: oral, QD: once daily, SD: single dose.

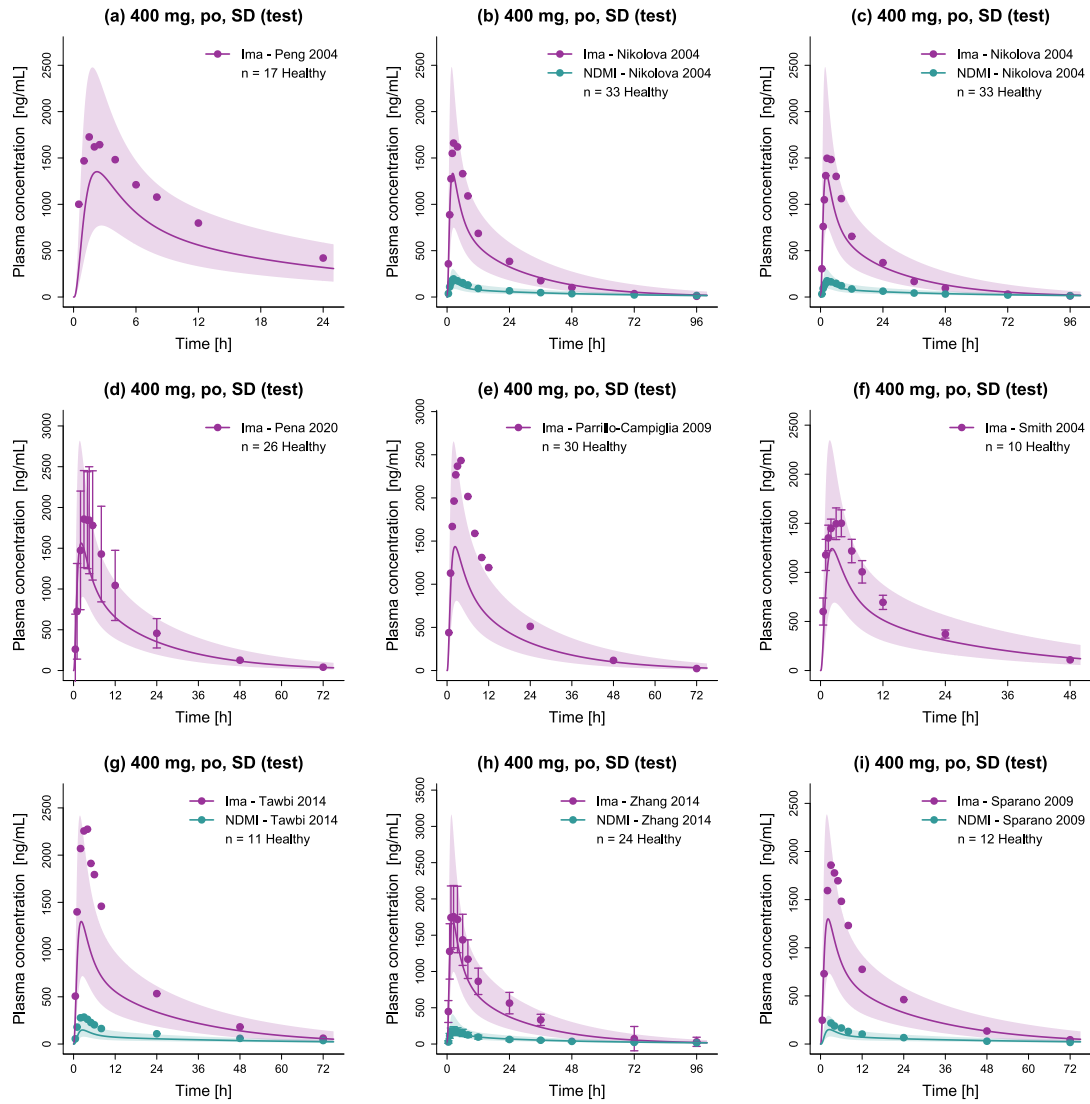


Figure S8: Linear plots of predicted and observed plasma concentration-time profiles of imatinib and N-desmethyl imatinib. Solid lines and ribbons represent population predictions ($n = 1000$; geometric mean and geometric standard deviation), while corresponding observed data are shown as dots (\pm standard deviation, if available) [17, 28–34]. Healthy: healthy subjects, Ima: imatinib, n: number of study participants, NDMI: N-desmethyl imatinib, po: oral, SD: single dose.

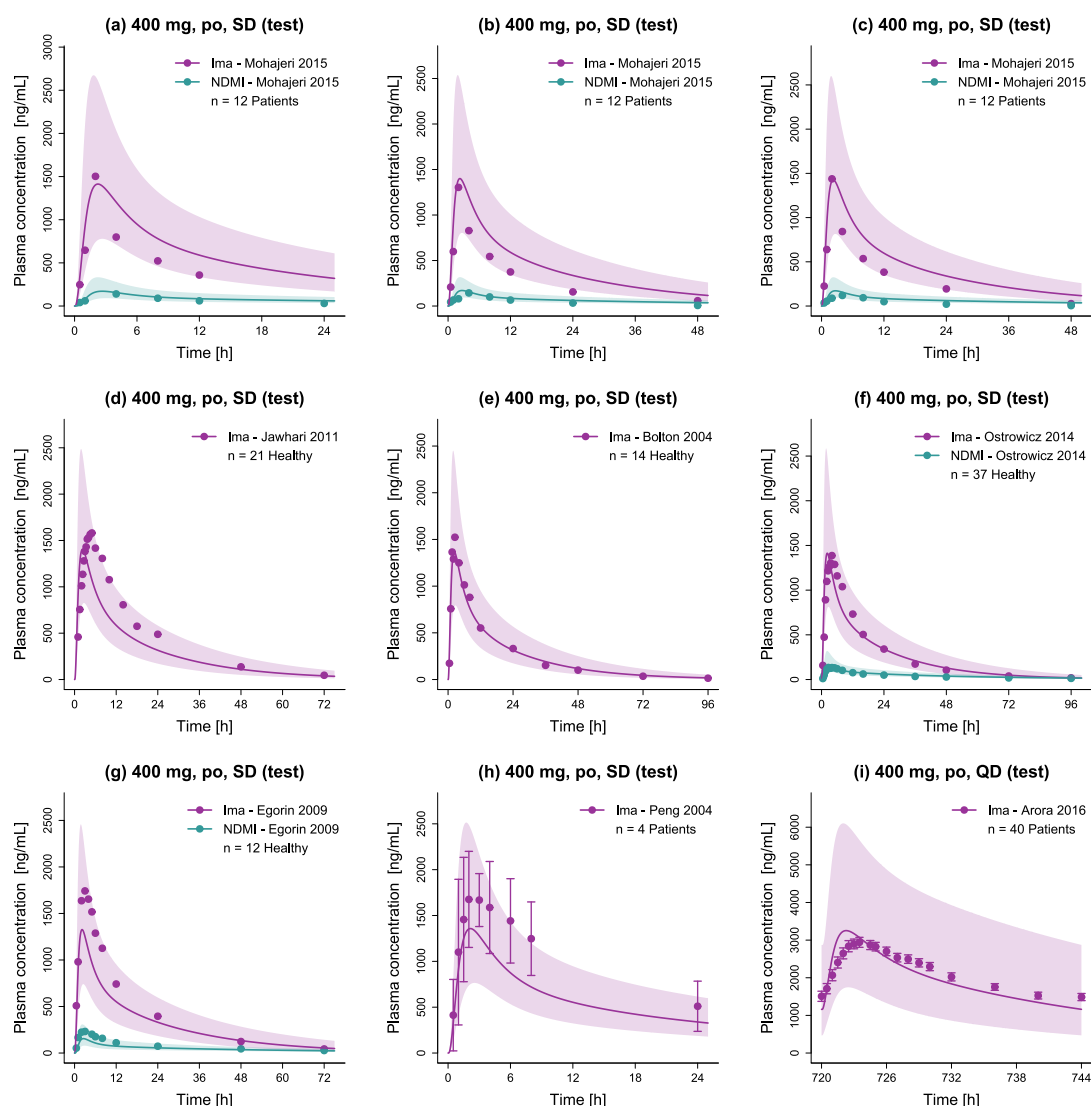


Figure S9: Linear plots of predicted and observed plasma concentration-time profiles of imatinib and N-desmethyl imatinib. Solid lines and ribbons represent population predictions ($n = 1000$; geometric mean and geometric standard deviation), while corresponding observed data are shown as dots (\pm standard deviation, if available) [18, 20, 35–39]. Healthy: healthy subjects, Ima: imatinib, n : number of study participants, NDMI: N-desmethyl imatinib, Patients: cancer patients, po: oral, QD: once daily, SD: single dose.

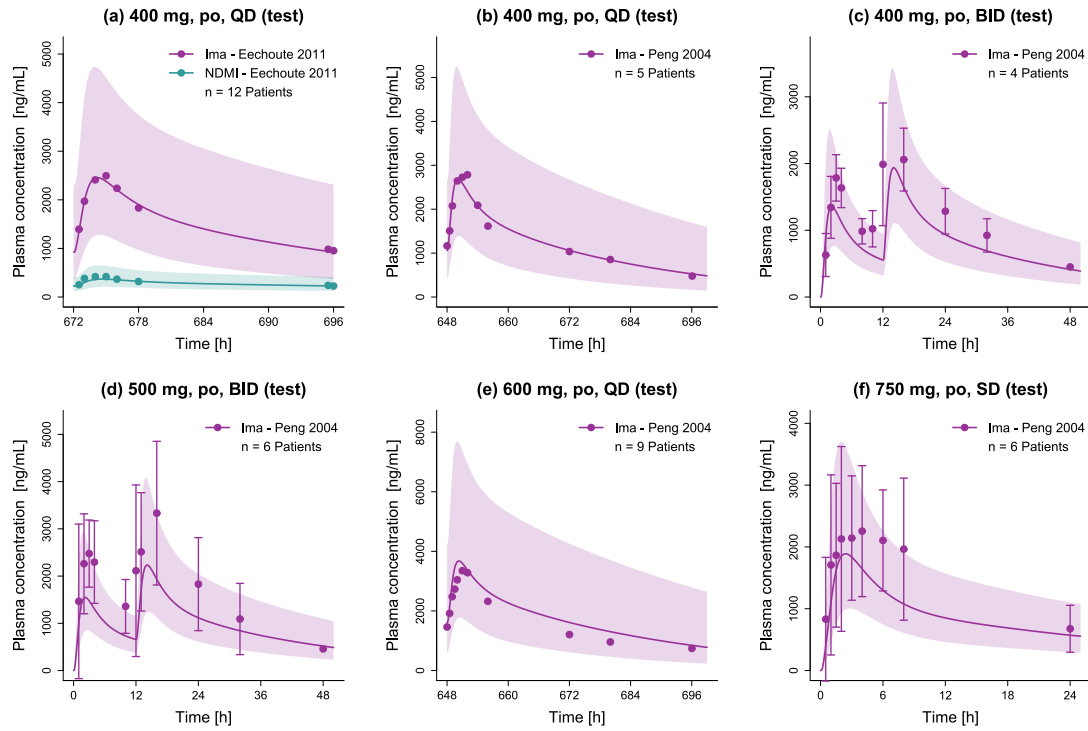


Figure S10: Linear plots of predicted and observed plasma concentration-time profiles of imatinib and N-desmethyl imatinib. Solid lines and ribbons represent population predictions ($n = 1000$; geometric mean and geometric standard deviation), while corresponding observed data are shown as dots (\pm standard deviation, if available) [18, 40]. BID: twice daily, Ima: imatinib, n: number of study participants, NDMI: N-desmethyl imatinib, Patients: cancer patients, po: oral, QD: once daily, SD: single dose.

S2.3 Urinary Excretion Profiles

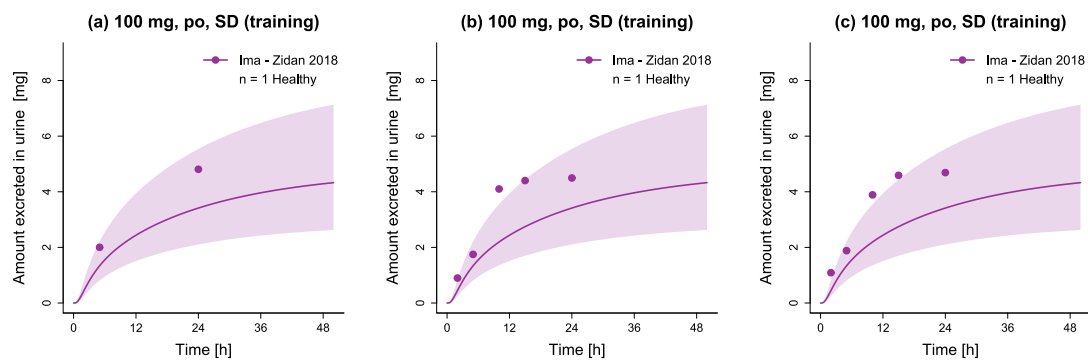


Figure S11: Cumulative amount excreted in urine of imatinib. Solid lines and ribbons represent population predictions ($n = 1000$; geometric mean and geometric standard deviation), while corresponding observed data are shown as dots [19]. Healthy: healthy subjects, Ima: imatinib, n: number of study participants, po: oral, SD: single dose.

S2.4 Goodness-of-Fit Plots

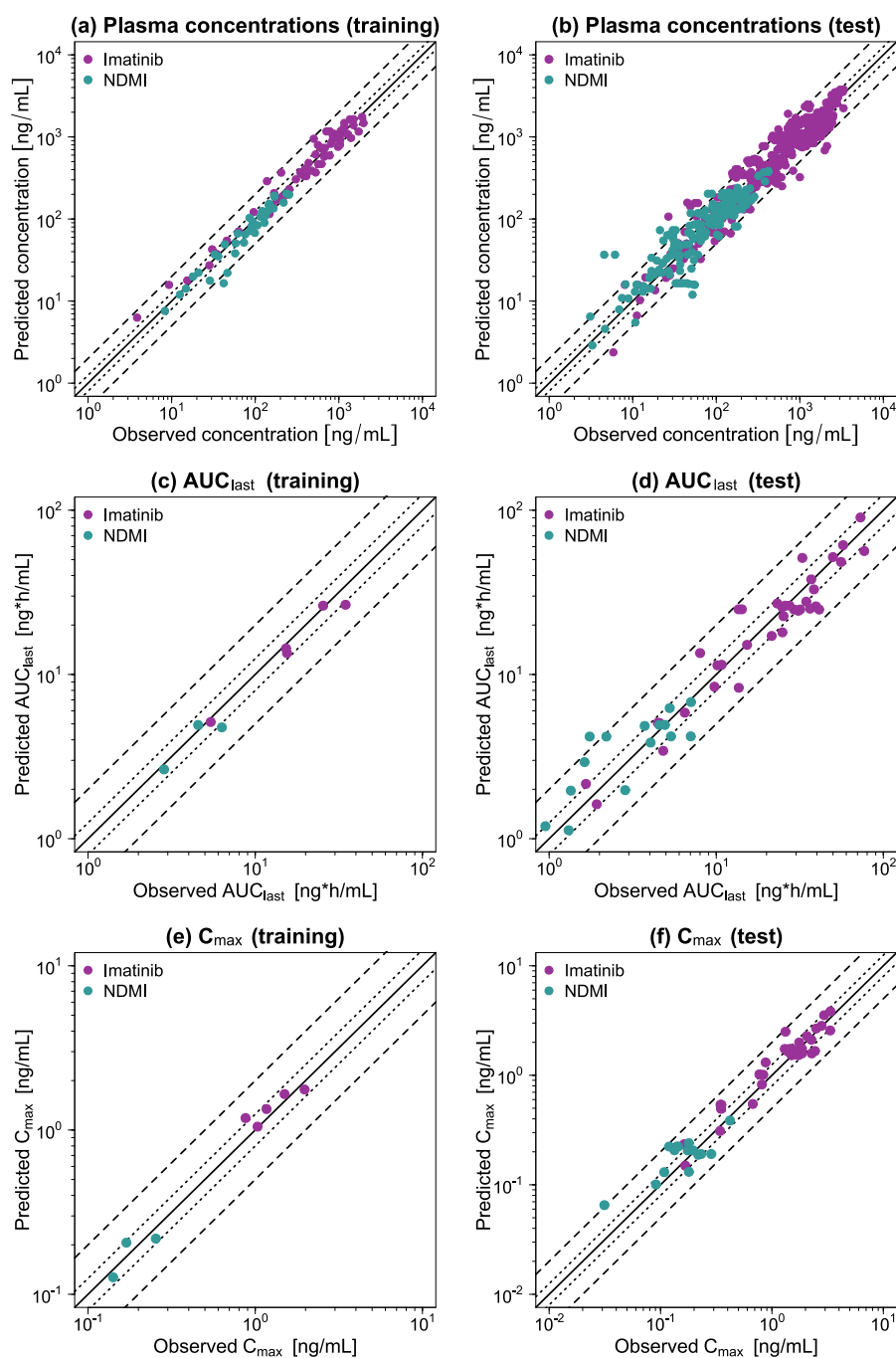


Figure S12: Goodness-of-fit plots of the final imatinib model. Stratified by training (left column) and test dataset (right column), predicted plasma concentration measurements (a–b) as well as AUC_{last} (c–d) and C_{max} (e–f) values are plotted against corresponding observed data. The solid line represents the line of identity, while dotted lines indicate 1.25-fold and dashed lines twofold deviation from the respective observed value. AUC_{last} : area under the curve determined between first and last plasma concentration measurements, C_{max} : maximum plasma concentration, NDMI: N-desmethyl imatinib.

S2.5 MRD of Plasma Concentration Predictions

Table S5: MRD values of plasma concentration predictions

Compound	Imatinib dosing regimen		n	Dataset	MRD	Reference
	Route	Dose [mg]				
Ima	iv (inf, 1 h, SD)	100	17 (healthy)	training	1.13	Peng 2004 [17]
Ima	po (-, QD)	25	3 (CML patients)	test	1.43	Peng 2004 [18]
Ima	po (-, SD)	50	3 (CML patients)	test	1.49	Peng 2004 [18]
Ima	po (-, QD)	50	3 (CML patients)	test	1.32	Peng 2004 [18]
Ima	po (-, QD)	85	3 (CML patients)	test	1.63	Peng 2004 [18]
Ima	po (tab, SD)	100	1 (healthy)	test	1.71	Zidan 2018 [19]
Ima	po (tab, SD)	100	1 (healthy)	test	1.59	Zidan 2018 [19]
Ima	po (tab, SD)	100	1 (healthy)	test	1.64	Zidan 2018 [19]
Ima	po (tab, SD)	100	37 (healthy)	test	1.61	Ostrowicz 2014 [20]
Ima	po (tab, SD)	200	10 (healthy)	training	1.36	Filppula 2013 [21]
Ima	po (tab, SD)	200	23 (healthy)	training	1.37	Jung 2014 [22]
Ima	po (cap, SD)	200	14 (healthy)	test	1.13	Duttreix 2004 [23]
Ima	po (cap, SD)	200	4 (healthy)	test	1.33	Gschwind 2005 [24]
Ima	po (tab, SD)	200	1 (healthy)	test	1.29	Golabchifar 2011 [25]
Ima	po (-, SD)	200	27 (healthy)	test	1.43	Yang 2013 [26]
Ima	po (-, QD)	350	5 (CML patients)	test	1.87	Peng 2004 [18]
Ima	po (-, SD)	400	12 (healthy)	training	1.28	Frye 2004 [27]
Ima	po (tab, SD)	400	33 (healthy)	training	1.25	Nikolova 2004 [28]
Ima	po (cap, SD)	400	17 (healthy)	test	1.52	Peng 2004 [17]
Ima	po (cap, SD)	400	33 (healthy)	test	1.25	Nikolova 2004 [28]
Ima	po (tab, SD)	400	33 (healthy)	test	1.23	Nikolova 2004 [28]
Ima	po (-, SD)	400	26 (healthy)	test	1.31	Pena 2020 [29]
Ima	po (tab, SD)	400	30 (healthy)	test	1.42	Parrillo-Campiglia [30]
Ima	po (-, SD)	400	10 (healthy)	test	1.28	Smith 2004 [31]
Ima	po (-, SD)	400	11 (healthy)	test	1.54	Tawbi 2014 [32]
Ima	po (cap, SD)	400	24 (healthy)	test	1.14	Zhang 2014 [33]
Ima	po (-, SD)	400	12 (healthy)	test	1.32	Sparano 2009 [34]
Ima	po (cap, SD)	400	12 (CML patients)	test	1.72	Mohajeri 2015 [35]
Ima	po (tab, SD)	400	12 (CML patients)	test	1.84	Mohajeri 2015 [35]
Ima	po (tab, SD)	400	12 (CML patients)	test	2.02	Mohajeri 2015 [35]
Ima	po (tab, SD)	400	21 (healthy)	test	1.40	Jawhari 2011 [36]
Ima	po (cap, SD)	400	14 (healthy)	test	1.31	Bolton 2004 [37]
Ima	po (tab, SD)	400	37 (healthy)	test	1.38	Ostrowicz 2014 [20]
Ima	po (-, SD)	400	12 (healthy)	test	1.23	Egorin 2009 [38]
Ima	po (-, SD)	400	4 (CML patients)	test	1.25	Peng 2004 [18]
Ima	po (tab, QD)	400	40 (CML patients)	test	1.15	Arora 2016 [39]
Ima	po (-, QD)	400	12 (GIST patients)	test	1.07	Eechoute 2011 [40]
Ima	po (-, QD)	400	5 (CML patients)	test	1.09	Peng 2004 [18]
Ima	po (-, BID)	400	4 (CML patients)	test	1.46	Peng 2004 [18]
Ima	po (-, BID)	500	6 (CML patients)	test	1.56	Peng 2004 [18]
Ima	po (-, QD)	600	9 (CML patients)	test	1.24	Peng 2004 [18]
Ima	po (-, SD)	750	6 (CML patients)	test	1.45	Peng 2004 [18]

-: not given, BID: twice daily, cap: capsule, CML: chronic myeloid leukemia, GIST: gastrointestinal stromal tumor, Ima: imatinib, inf: infusion, iv: intravenous, MRD: mean relative deviation, n: number of participants, NDMI: N-desmethyl imatinib, po: oral, QD: once daily, SD: single dose, tab: tablet.

Table S5: MRD values of plasma concentration predictions (*continued*)

Compound	Imatinib dosing regimen		n	Dataset	MRD	Reference
	Route	Dose [mg]				
NDMI	po (tab, SD)	100	37 (healthy)	test	1.71	Ostrowicz 2014 [20]
NDMI	po (tab, SD)	200	10 (healthy)	training	1.17	Filppula 2013 [21]
NDMI	po (cap, SD)	200	14 (healthy)	test	1.29	Dutreix 2004 [23]
NDMI	po (cap, SD)	200	4 (healthy)	test	1.85	Gschwind 2005 [24]
NDMI	po (tab, SD)	200	1 (healthy)	test	1.48	Golabchifar 2011 [25]
NDMI	po (-, SD)	400	12 (healthy)	training	1.42	Frye 2004 [27]
NDMI	po (tab, SD)	400	33 (healthy)	training	1.42	Nikolova 2004 [28]
NDMI	po (cap, SD)	400	33 (healthy)	test	1.27	Nikolova 2004 [28]
NDMI	po (tab, SD)	400	33 (healthy)	test	1.25	Nikolova 2004 [28]
NDMI	po (-, SD)	400	11 (healthy)	test	1.84	Tawbi 2014 [32]
NDMI	po (cap, SD)	400	24 (healthy)	test	1.21	Zhang 2014 [33]
NDMI	po (-, SD)	400	12 (healthy)	test	1.21	Sparano 2009 [34]
NDMI	po (cap, SD)	400	12 (CML patients)	test	1.92	Mohajeri 2015 [35]
NDMI	po (tab, SD)	400	12 (CML patients)	test	2.44	Mohajeri 2015 [35]
NDMI	po (tab, SD)	400	12 (CML patients)	test	2.81	Mohajeri 2015 [35]
NDMI	po (tab, SD)	400	37 (healthy)	test	1.44	Ostrowicz 2014 [20]
NDMI	po (-, SD)	400	12 (healthy)	test	1.61	Egorin 2009 [38]
NDMI	po (-, QD)	400	12 (GIST patients)	test	1.13	Eechoute 2011 [40]
Training dataset mean MRD (range)				1.29 (1.13–1.42)		
Test dataset mean MRD (range)				1.48 (1.07–2.81)		
Imatinib mean MRD (range)				1.41 (1.07–2.02)		
NDMI mean MRD (range)				1.58 (1.13–2.81)		
Overall mean MRD (range)				1.46 (1.07–2.81)		
MRD ≤ 2				57/60		

-: not given, BID: twice daily, cap: capsule, CML: chronic myeloid leukemia, GIST: gastrointestinal stromal tumor, Ima: imatinib, inf: infusion, iv: intravenous, MRD: mean relative deviation, n: number of participants, NDMI: N-desmethyl imatinib, po: oral, QD: once daily, SD: single dose, tab: tablet.

S2.6 Predicted and Observed AUC_{last} and C_{max} Values

Table S6: Predicted versus observed AUC_{last} and C_{max} values

Comp.	Imatinib dosing regimen		n	Dataset	AUC _{last}			C _{max}			Reference
	Route	Dose [mg]			Pred [$\frac{ng \cdot h}{mL}$]	Obs [$\frac{ng \cdot h}{mL}$]	Pred/Obs	Pred [$\frac{ng}{mL}$]	Obs [$\frac{ng}{mL}$]	Pred/Obs	
Ima	iv (inf, 1 h, SD)	100	17 (healthy)	training	5135.03	5413.67	0.95	1341.86	1168.54	1.15	Peng 2004 [17]
Ima	po (-, QD)	25	3 (CML patients)	test	1620.46	1925.88	0.84	149.64	166.80	0.90	Peng 2004 [18]
Ima	po (-, SD)	50	3 (CML patients)	test	2156.03	1659.50	1.30	234.92	163.17	1.44	Peng 2004 [18]
Ima	po (-, QD)	50	3 (CML patients)	test	3427.70	4812.66	0.71	309.81	341.81	0.91	Peng 2004 [18]
Ima	po (-, QD)	85	3 (CML patients)	test	8292.80	13640.36	0.61	546.95	672.65	0.81	Peng 2004 [18]
Ima	po (tab, SD)	100	1 (healthy)	test	5065.99	4567.07	1.11	537.48	349.13	1.54	Zidan 2018 [19]
Ima	po (tab, SD)	100	1 (healthy)	test	5066.65	4492.26	1.13	537.48	350.70	1.53	Zidan 2018 [19]
Ima	po (tab, SD)	100	1 (healthy)	test	5066.65	4472.12	1.13	537.48	345.41	1.56	Zidan 2018 [19]
Ima	po (tab, SD)	100	37 (healthy)	test	5850.56	6480.78	0.90	493.80	348.87	1.42	Ostrowicz 2014 [20]
Ima	po (tab, SD)	200	10 (healthy)	training	13491.87	15477.34	0.87	1048.55	1032.35	1.02	Filppula 2013 [21]
Ima	po (tab, SD)	200	23 (healthy)	training	14406.34	15278.67	0.94	1182.78	874.95	1.35	Jung 2014 [22]
Ima	po (cap, SD)	200	14 (healthy)	test	8422.16	9750.92	0.86	824.82	812.31	1.02	Duttreix 2004 [23]
Ima	po (cap, SD)	200	4 (healthy)	test	11361.68	10162.66	1.12	1011.29	834.99	1.21	Gschwind 2005 [24]
Ima	po (tab, SD)	200	1 (healthy)	test	11457.06	10770.52	1.06	1019.34	771.20	1.32	Golabchifar 2011 [25]
Ima	po (-, SD)	200	27 (healthy)	test	15141.20	15286.99	0.99	1310.48	877.81	1.49	Yang 2013 [26]
Ima	po (-, QD)	350	5 (CML patients)	test	51224.25	32731.62	1.56	2499.24	1322.70	1.89	Peng 2004 [18]
Ima	po (-, SD)	400	12 (healthy)	training	26558.01	34680.72	0.77	1765.16	1972.90	0.89	Frye 2004 [27]
Ima	po (tab, SD)	400	33 (healthy)	training	26233.38	25471.37	1.03	1654.84	1497.23	1.11	Nikolova 2004 [28]
Ima	po (cap, SD)	400	17 (healthy)	test	17158.16	21458.79	0.80	1525.15	1726.61	0.88	Peng 2004 [17]
Ima	po (cap, SD)	400	33 (healthy)	test	26231.76	27407.94	0.96	1654.84	1660.68	1.00	Nikolova 2004 [28]
Ima	po (tab, SD)	400	33 (healthy)	test	26231.72	25845.92	1.01	1654.84	1496.76	1.11	Nikolova 2004 [28]
Ima	po (-, SD)	400	26 (healthy)	test	27754.49	34577.78	0.80	1744.23	1857.26	0.94	Pena 2020 [29]
Ima	po (tab, SD)	400	30 (healthy)	test	25977.11	39524.46	0.66	1665.92	2432.85	0.68	Parrillo-Campiglia [30]
Ima	po (-, SD)	400	10 (healthy)	test	22647.09	25254.57	0.90	1522.71	1500.16	1.02	Smith 2004 [31]
Ima	po (-, SD)	400	11 (healthy)	test	24833.59	41273.28	0.60	1583.45	2274.30	0.70	Tawbi 2014 [32]
Ima	po (cap, SD)	400	24 (healthy)	test	32955.63	38422.97	0.86	1991.31	1755.60	1.13	Zhang 2014 [33]
Ima	po (-, SD)	400	12 (healthy)	test	24834.21	31739.96	0.78	1583.46	1858.33	0.85	Sparano 2009 [34]
Ima	po (cap, SD)	400	12 (CML patients)	test	13494.94	8003.87	1.69	1739.85	1502.51	1.16	Mohajeri 2015 [35]
Ima	po (tab, SD)	400	12 (CML patients)	test	24921.36	13603.14	1.83	1740.06	1303.70	1.33	Mohajeri 2015 [35]
Ima	po (tab, SD)	400	12 (CML patients)	test	24917.20	14231.96	1.75	1739.83	1437.86	1.21	Mohajeri 2015 [35]
Ima	po (tab, SD)	400	21 (healthy)	test	24426.74	30992.29	0.79	1558.62	1580.92	0.99	Jawhari 2011 [36]
Ima	po (cap, SD)	400	14 (healthy)	test	27039.91	23183.57	1.17	1602.67	1523.50	1.05	Bolton 2004 [37]
Ima	po (tab, SD)	400	37 (healthy)	test	25659.89	24839.39	1.03	1652.22	1386.64	1.19	Ostrowicz 2014 [20]
Ima	po (-, SD)	400	12 (healthy)	test	24830.21	29259.96	0.85	1583.31	1742.20	0.91	Egorin 2009 [38]
Ima	po (-, SD)	400	4 (CML patients)	test	18042.33	24873.97	0.73	1590.22	1675.79	0.95	Peng 2004 [18]

-: not given, AUC_{last}: area under the plasma concentration-time curve determined between first and last concentration measurements, BID: twice daily, cap: capsule, C_{max}: maximum plasma concentration, CML: chronic myeloid leukemia, comp.: compound, GST: gastrointestinal stromal tumor, GMFE: geometric mean fold error, Ima: imatinib, inf: infusion, iv: intravenous, NDMI: N-desmethyl imatinib, n: number of participants, obs: observed, po: oral, pred: predicted, QD: once daily, SD: single dose, tab: tablet.

Table S6: Predicted versus observed AUC_{last} and C_{max} values (*continued*)

Comp.	Imatinib dosing regimen		n	Dataset	AUC_{last}			C_{max}			Reference
	Route	Dose [mg]			Pred [$\frac{ng*h}{mL}$]	Obs [$\frac{ng*h}{mL}$]	Pred/Obs	Pred [$\frac{ng}{mL}$]	Obs [$\frac{ng}{mL}$]	Pred/Obs	
Ima	po (tab, QD)	400	40 (CML patients)	test	51824.07	49892.23	1.04	3536.39	2941.33	1.20	Arora 2016 [39]
Ima	po (-, QD)	400	12 (GIST patients)	test	37924.07	37036.92	1.02	2673.46	2495.52	1.07	Eechoute 2011 [40]
Ima	po (-, QD)	400	5 (CML patients)	test	61263.32	57407.51	1.07	2829.41	2784.60	1.02	Peng 2004 [18]
Ima	po (-, BID)	400	4 (CML patients)	test	48390.10	55826.05	0.87	2279.51	2059.17	1.11	Peng 2004 [18]
Ima	po (-, BID)	500	6 (CML patients)	test	56400.59	76859.29	0.73	2566.09	3332.50	0.77	Peng 2004 [18]
Ima	po (-, QD)	600	9 (CML patients)	test	90308.34	729947.50	1.24	3832.97	3350.20	1.14	Peng 2004 [18]
Ima	po (-, SD)	750	6 (CML patients)	test	25158.86	36417.12	0.69	2111.84	2255.24	0.94	Peng 2004 [18]
NDMI	po (tab, SD)	100	37 (healthy)	test	1191.65	948.99	1.26	65.20	31.30	2.08	Ostrowicz 2014 [20]
NDMI	po (tab, SD)	200	10 (healthy)	training	2642.06	2848.15	0.93	126.85	141.26	0.90	Filppula 2013 [21]
NDMI	po (cap, SD)	200	14 (healthy)	test	1125.55	1308.30	0.86	100.75	90.94	1.11	Duttreix 2004 [23]
NDMI	po (cap, SD)	200	4 (healthy)	test	1961.24	1347.14	1.46	130.29	107.86	1.21	Gschwind 2005 [24]
NDMI	po (tab, SD)	200	1 (healthy)	test	1975.89	2850.58	0.69	131.29	179.59	0.73	Golabchifar 2011 [25]
NDMI	po (-, SD)	400	12 (healthy)	training	4762.88	6313.61	0.75	218.23	254.29	0.86	Frye 2004 [27]
NDMI	po (tab, SD)	400	33 (healthy)	training	4925.99	4555.57	1.08	206.22	169.55	1.22	Nikolova 2004 [28]
NDMI	po (cap, SD)	400	33 (healthy)	test	4925.99	4927.30	1.00	206.22	195.45	1.06	Nikolova 2004 [28]
NDMI	po (tab, SD)	400	33 (healthy)	test	495.99	4565.31	1.08	206.22	175.30	1.18	Nikolova 2004 [28]
NDMI	po (-, SD)	400	11 (healthy)	test	4198.97	7038.25	0.60	191.02	285.15	0.67	Tawbi 2014 [32]
NDMI	po (cap, SD)	400	24 (healthy)	test	6239.45	5264.18	1.19	239.88	179.60	1.34	Zhang 2014 [33]
NDMI	po (-, SD)	400	12 (healthy)	test	3845.99	4044.45	0.95	187.88	218.01	0.86	Sparano 2009 [34]
NDMI	po (cap, SD)	400	12 (CML patients)	test	2927.40	1628.46	1.80	223.49	140.04	1.60	Mohajeri 2015 [35]
NDMI	po (tab, SD)	400	12 (CML patients)	test	4186.14	2199.09	1.90	223.51	143.83	1.55	Mohajeri 2015 [35]
NDMI	po (tab, SD)	400	12 (CML patients)	test	4185.71	1747.22	2.40	223.48	119.49	1.87	Mohajeri 2015 [35]
NDMI	po (tab, SD)	400	37 (healthy)	test	4859.00	3728.96	1.30	206.58	133.46	1.55	Ostrowicz 2014 [20]
NDMI	po (-, SD)	400	12 (healthy)	test	4198.54	5361.34	0.78	191.01	231.64	0.82	Egorin 2009 [38]
NDMI	po (-, QD)	400	12 (GIST patients)	test	6789.87	7060.68	0.96	386.00	420.01	0.92	Eechoute 2011 [40]
Training dataset mean GMFE (range)					1.14 (1.03–1.33)			1.18 (1.11–1.35)			
Test dataset mean GMFE (range)					1.31 (1.00–2.40)			1.27 (1.00–2.08)			
Imatinib mean GMFE (range)					1.25 (1.01–1.83)			1.22 (1.00–1.89)			
NDMI mean GMFE (range)					1.36 (1.00–2.40)			1.35 (1.06–2.08)			
Overall mean GMFE (range)					1.28 (1.00–2.40)			1.26 (1.00–2.08)			
GMFE ≤ 2					59/60			59/60			

–: not given, AUC_{last} : area under the plasma concentration-time curve determined between first and last concentration measurements, BID: twice daily, cap: capsule, C_{max} : maximum plasma concentration, CML: chronic myeloid leukemia, comp.: compound, GIST: gastrointestinal stromal tumor, GMFE: geometric mean fold error, Ima: imatinib, inf: infusion, iv: intravenous, NDMI: N-desmethyl imatinib, n: number of participants, obs: observed, po: oral, pred: predicted, QD: once daily, SD: single dose, tab: tablet.

S2.7 Local Sensitivity Analysis

S2.7.1 Methods

Local sensitivity analyses were performed for imatinib and N-desmethyl imatinib, by calculating the sensitivity to single parameter changes according to Equation S3. A relative perturbation of 10% was applied (variation range 0.1, maximum number of 2 steps) and parameters included were either optimized or assumed to affect AUC_{last} .

$$S = \frac{\Delta AUC_{last}}{\Delta p} \cdot \frac{p}{AUC_{last}} \quad (S3)$$

where S = sensitivity, ΔAUC_{last} = change of AUC_{last} , Δp = change of the analyzed parameter value, p = original parameter value, and AUC_{last} = simulated AUC_{last} with the original parameter value.

The threshold for sensitivity was set at $|0.5|$, which corresponds to a 50% change in simulated AUC_{last} given a 100% change in the parameter value examined.

S2.7.2 Results

Table S7: Parameters evaluated during the local sensitivity analyses

Compound	Parameter	Source	Compound	Parameter	Source
Ima	pKa ₁ , acid	Lit.	Ima	CYP3A4 K _i MBI	Lit.
Ima	pKa ₂ , base	Lit.	Ima	CYP3A4 K _I MBI	Lit.
Ima	pKa ₃ , base	Lit.	Ima	CYP3A4 k _{inact} MBI	Lit.
Ima	Solubility	Lit.	Ima	P-gp K _i CI	Lit.
Ima	Lipophilicity	Opt.	NDMI	pKa ₁ , acid	Lit.
Ima	Fraction unbound	Lit.	NDMI	pKa ₂ , base	Lit.
Ima	CYP2C8 K _M	Lit.	NDMI	pKa ₃ , base	Lit.
Ima	CYP2C8 k _{cat}	Opt.	NDMI	Solubility	Lit.
Ima	CYP3A4 K _M	Lit.	NDMI	Lipophilicity	Opt.
Ima	CYP3A4 k _{cat}	Opt.	NDMI	Fraction unbound	Lit.
Ima	CYP3A4 CL	Opt.	NDMI	CYP2C8 CL	Opt.
Ima	P-gp K _M	Opt.	NDMI	CYP3A4 CL	Opt.
Ima	P-gp k _{cat}	Opt.	NDMI	Hepatic CL	Opt.
Ima	GFR fraction	Asm.	NDMI	GFR fraction	Asm.
Ima	Intestinal permeability	Opt.	NDMI	CYP2C8 K _i CI	Lit.
Ima	CYP2C8 K _i CI	Lit.	NDMI	CYP3A4 K _i CI	Lit.

Asm.: assumed, CI: competitive inhibition, CYP: cytochrome P450, GFR: glomerular filtration rate, Ima: imatinib, k_{cat}: catalytic/transport rate constant, K_i: dissociation constant inhibitor-enzyme/transporter complex, K_I: concentration for half-maximal inactivation, k_{inact}: maximum inactivation rate constant, K_M: Michaelis-Menten constant, lit.: literature, MBI: mechanism-based inactivation, NDMI: N-desmethyl imatinib, opt.: optimized, pKa: acid dissociation constant, P-gp: P-glycoprotein.

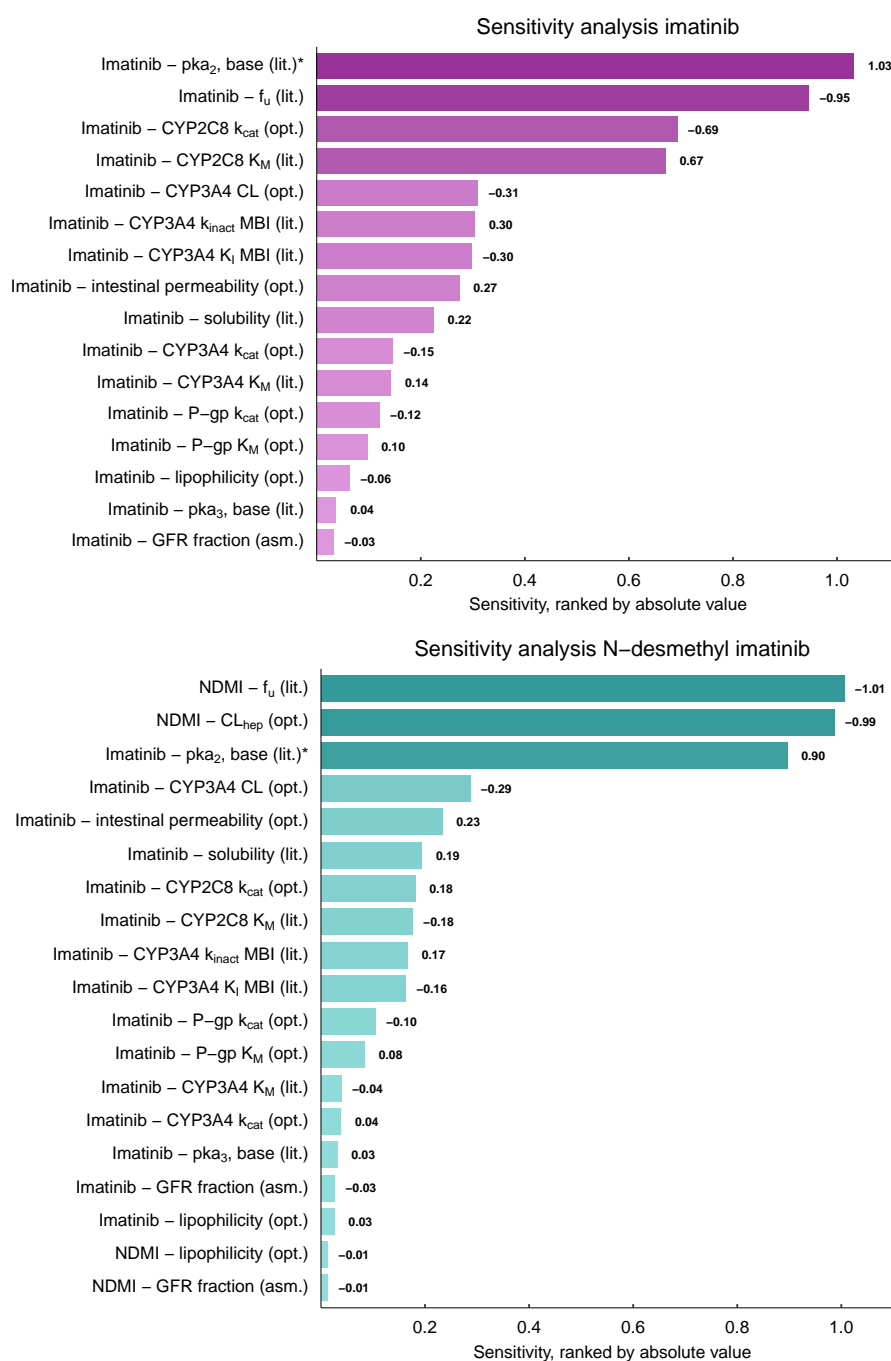


Figure S13: Imatinib model sensitivity analysis (400 mg, once daily [18]). Presented are parameters with a calculated sensitivity different from 0.00. Asm.: assumed, CI: competitive inhibition, CYP: cytochrome P450, f_u : fraction unbound, GFR: glomerular filtration rate, k_{cat} : catalytic/transport rate constant, K_i : dissociation constant inhibitor-enzyme/transporter complex, K_I : concentration for half-maximal inactivation, k_{inact} : maximum inactivation rate constant, K_M : Michaelis-Menten constant, lit.: literature, MBI: mechanism-based inactivation, NDMI: N-desmethyl imatinib, opt.: optimized, pKa: acid dissociation constant, P-gp: P-glycoprotein. *: Due to the proximity of the model parameter (7.84) to the physiological pH of 7.4, an increase of 10% causes only a small change in imatinib and NDMI AUC values, while a reduction of 10% is associated with a large decrease in exposure.

S3 Drug-Drug Interaction Modeling

S3.1 Clinical Study Data

Table S8: Imatinib DDI model study table

Victim application [mg]	Perpetrator application [mg]	n	Females [%]	Ethnicity ^a	Age [years]	Weight [kg]	Height [cm]	Compound(s) measured	Reference
Imatinib d8: 400 po (cap, SD)	Rifampicin d1–11: 600 po (-, QD)	14 (healthy)	7	European	49.8±8.2 (40–64)	74.4±8.1 (61.5–90.0)	172±6 (165–186)	Ima	Bolton 2004 [37]
Imatinib d1: 200 po (cap, SD)	Ketoconazole d1: 400 po (-, SD)	14 (healthy)	7	European	(35–59)	(64–103)	-	Ima, NDMI	Dutreix 2004 [23]
Imatinib d3: 200 po (tab, SD)	Gemfibrozil d1–6: 600 po (tab, BID)	10 (healthy)	20	European	24±3	72±13	-	Ima, NDMI	Filppula 2013 [21]
Simvastatin d7: 40 po (tab, SD)	Imatinib d1–7: 400 po (cap, QD)	20 (CML patients)	50	European	50.5±13.4	(53–111)	(158–192)	Simva, Simva-Acid	O’Brien 2003 [55]
Metoprolol d7: 100 po (tab, SD)	Imatinib d1–9: 400 po (cap, BID)	13 (CML patients) CYP2D6 NMs	-	Asian	40.6±13.2	73.7±12.6	-	Meto, OH-Meto	Wang 2008 [56]
Metoprolol d7: 100 po (tab, SD)	Imatinib d1–9: 400 po (cap, BID)	6 (CML patients) CYP2D6 IMs	-	Asian	39.8±6.1	72.3±8.0	-	Meto, OH-Meto	Wang 2008 [56]

-: not given, ^a: implemented, BID: twice daily, cap: capsule, CYP: cytochrome P450, d: day, DDI: drug-drug interaction, IM: intermediate metabolizer, Ima: imatinib, Meto: metoprolol, n: number of participants, NDMI: N-desmethyl imatinib, NM: normal metabolizer, OH-Meto: hydroxymetoprolol, po: oral, QD: once daily, SD: single dose, Simva: simvastatin, Simva-Acid: simvastatin hydroxy acid, tab: tablet; values for age, weight, and height are presented as mean ± standard deviation (range).

S3.2 Drug-Dependent Parameters of DDI Partners

S3.2.1 Rifampicin

Table S9: Drug-dependent parameters of the rifampicin PBPK model [8]

Parameter	Unit	Value	Description
Rifampicin			
Molecular weight	g/mol	822.94	Molecular weight
pKa ₁ , base		7.90	Acid dissociation constant
pKa ₂ , acid		1.70	Acid dissociation constant
Solubility (pH)	mg/L	2800.00 (7.5)	Solubility
Lipophilicity		2.50	Lipophilicity
f _u	%	17.00	Fraction unbound
AADAC K _M → sink	μmol/L	195.10	Michaelis-Menten constant
AADAC k _{cat} → sink	1/min	9.87	Catalytic rate constant
OATP1B1 K _M	μmol/L	1.50	Michaelis-Menten constant
OATP1B1 k _{cat}	1/min	74.43 ^a	Transport rate constant
P-gp K _M	μmol/L	55.00	Michaelis-Menten constant
P-gp k _{cat}	1/min	0.61	Transport rate constant
GFR fraction		1 ^b	Filtered drug in the urine
EHC continuous fraction		1	Bile fraction continuously released
Intestinal permeability	cm/min	1.24 · 10 ⁻⁵	Transcellular intestinal permeability
Cellular permeability	cm/min	PK-Sim Standard, 2.93 · 10 ⁻⁵	Permeability into the cellular space
Partition coefficients		Rodgers + Rowland	Organ-plasma partition coefficients
Formulation		Solution	Formulation used in predictions
Induction EC ₅₀	μmol/L	0.34	Conc. for half-maximal induction
AADAC E _{max}		0.99	Maximum induction effect
CYP2C8 E _{max}		3.20	Maximum induction effect
CYP2C8 K _i	μmol/L	30.20	Diss. const. inhibitor-enzyme complex
CYP3A4 E _{max}		9.00	Maximum induction effect
CYP3A4 K _i	μmol/L	18.50	Diss. const. inhibitor-enzyme complex
OATP1B1 E _{max}		0.38	Maximum induction effect
OATP1B1 K _i	μmol/L	0.48	Diss. const. inhibitor-transporter complex
P-gp E _{max}		2.50	Maximum induction effect
P-gp K _i	μmol/L	169.00	Diss. const. inhibitor-transporter complex

^a: adjusted due to different reference concentrations in the original model and imatinib model, ^b: a GFR fraction of 1 corresponds to passive glomerular filtration of a compound, AADAC: arylacetamide deacetylase, conc.: concentration, CYP: cytochrome P450, diss. const.: dissociation constant, EHC: enterohepatic circulation, GFR: glomerular filtration rate, OATP: organic-anion-transporting polypeptide, P-gp: P-glycoprotein.

S3.2.2 Ketoconazole

Table S10: Drug-dependent parameters of the ketoconazole PBPK model [58]

Parameter	Unit	Value	Description
Ketoconazole			
Molecular weight	g/mol	531.43	Molecular weight
pKa ₁ , base		6.51	Acid dissociation constant
pKa ₂ , base		2.94	Acid dissociation constant
Solubility (pH)	mg/L	4.34 (7.40)	Solubility
Lipophilicity	log units	2.52	Lipophilicity
f _u	%	1	Fraction unbound
AADAC K _M → ND-Keto	μmol/L	1.88	Michaelis-Menten constant
AADAC k _{cat} → ND-Keto	1/min	0.87	Catalytic rate constant
CYP3A4 K _M → sink	μmol/L	8.46 · 10 ⁻³	Michaelis-Menten constant
CYP3A4 k _{cat} → sink	1/min	0.10	Catalytic rate constant
UGT1A4 K _M → sink	μmol/L	7.00	Michaelis-Menten constant
UGT1A4 k _{cat} → sink	1/min	0.31	Catalytic rate constant
P-gp K _M	μmol/L	0.04	Michaelis-Menten constant
P-gp k _{cat}	1/min	0.33	Transport rate constant
GFR fraction		1 ^a	Filtered drug in the urine
EHC continuous fraction		1	Bile fraction continuously released
Intestinal permeability	cm/min	9.95 · 10 ⁻⁶ (fed)	Transcellular intestinal permeability
GET	min	45 (fed)	Gastric emptying time
Cellular permeability	cm/min	PK-Sim Standard	Permeability into the cellular space
		7.18 · 10 ⁻⁴	
Partition coefficients		Berezhkovskiy	Organ-plasma partition coefficients
Particle radius Bin1	nm	11.75	Particle dissolution radius
Particle radius Bin2	nm	111.06	Particle dissolution radius
Particle radius Bin3	nm	205.46	Particle dissolution radius
Density	g/cm ³	1.40	Density
Aqueous diffusion coefficient	dm ² /min	3.75 · 10 ⁻⁷	Aqueous diffusion coefficient
CYP2C8 K _i	μmol/L	2.50 ^b	Diss. const. inhibitor-enzyme complex
CYP3A4 K _i	μmol/L	8.46 · 10 ⁻³	Diss. const. inhibitor-enzyme complex
P-gp K _i	μmol/L	0.04	Diss. const. inhibitor-transporter complex
N-Deacetyl-Ketoconazole			
Molecular weight	g/mol	489.40	Molecular weight
pKa ₁ , base		8.90	Acid dissociation constant
pKa ₂ , base		6.42	Acid dissociation constant
pKa ₃ , base		0.20	Acid dissociation constant
Solubility (pH)	mg/mL	1.24 (6.50)	Solubility
Lipophilicity	log units	3.75	Lipophilicity
f _u	%	1	Fraction unbound
FMO3 K _M → OH-Keto	μmol/L	1.17	Michaelis-Menten constant
FMO3 k _{cat} → OH-Keto	1/min	378.65	Catalytic rate constant
GFR fraction		1 ^a	Filtered drug in the urine
EHC continuous fraction		1	Bile fraction continuously released
Intestinal permeability	cm/min	1.08 · 10 ⁻⁴	Transcellular intestinal permeability
Cellular permeability	cm/min	Charge dependent Schmitt, 0.02	Permeability into the cellular space
Partition coefficients		Rodgers + Rowland	Organ-plasma partition coefficients
CYP2C8 K _i	μmol/L	2.50 ^b	Diss. const. inhibitor-enzyme complex
CYP3A4 K _i	μmol/L	0.02	Diss. const. inhibitor-enzyme complex
P-gp K _i	μmol/L	0.12	Diss. const. inhibitor-transporter complex

^a: a GFR fraction of 1 corresponds to passive glomerular filtration of a compound, ^b: added to the model [57], AADAC: arylacetamide deacetylase, CYP: cytochrome P450, diss. const.: dissociation constant, EHC: enterohepatic circulation, FMO: flavin-containing monooxygenase, Gemfi-Glu: gemfibrozil-glucuronide, GFR: glomerular filtration rate, MBI: mechanism-based inactivation, MRP: multidrug resistance-associated protein, ND-Keto: N-deacetyl-ketoconazole, OATP: organic-anion-transporting polypeptide, OH-Keto: N-deacetyl-N-hydroxy-ketoconazole, P-gp: P-glycoprotein, UGT: uridine 5'-diphospho-glucuronosyltransferase.

Table S10: Drug-dependent parameters of the ketoconazole PBPK model [58] (*continued*)

Parameter	Unit	Value	Description
N-Deacetyl-N-Hydroxy-Ketoconazole			
Molecular weight	g/mol	505.40	Molecular weight
pKa ₁ , base		6.42	Acid dissociation constant
pKa ₂ , base		3.42	Acid dissociation constant
Solubility (pH)	mg/mL	4.40 · 10 ⁻³ (6.50)	Solubility
Lipophilicity	log units	4.20	Lipophilicity
f _u	%	1	Fraction unbound
FMO3 CL → sink	Lµmol/min	0.09	Clearance
GFR fraction		1 ^a	Filtered drug in the urine
EHC continuous fraction		1	Bile fraction continuously released
Intestinal permeability	cm/min	2.60 · 10 ⁻⁴	Transcellular intestinal permeability
Cellular permeability	cm/min	Charge dependent Schmitt, 0	Permeability into the cellular space
Partition coefficients		Berezhkovskiy	Organ-plasma partition coefficients
CYP2C8 K _i	µmol/L	2.50 ^b	Diss. const. inhibitor-enzyme complex
CYP3A4 K _i	µmol/L	0.02	Diss. const. inhibitor-enzyme complex
P-gp K _i	µmol/L	0.12	Diss. const. inhibitor-transporter complex

^a: a GFR fraction of 1 corresponds to passive glomerular filtration of a compound, ^b: added to the model [57], AADAC: arylacetamide deacetylase, CYP: cytochrome P450, diss. const.: dissociation constant, EHC: enterohepatic circulation, FMO: flavin-containing monooxygenase, Gemfi-Glu: gemfibrozil-glucuronide, GFR: glomerular filtration rate, MBI: mechanism-based inactivation, MRP: multidrug resistance-associated protein, ND-Keto: N-deacetyl-ketoconazole, OATP: organic-anion-transporting polypeptide, OH-Keto: N-deacetyl-N-hydroxy-ketoconazole, P-gp: P-glycoprotein, UGT: uridine 5'-diphospho-glucuronosyltransferase.

S3.2.3 Gemfibrozil

Table S11: Drug-dependent parameters of the gemfibrozil PBPK model [59]

Parameter	Unit	Value	Description
Gemfibrozil			
Molecular weight	g/mol	250.33	Molecular weight
pKa, acid		4.70	Acid dissociation constant
Solubility (pH)	mg/mL	0.17 (5.90)	Solubility
Lipophilicity	log units	2.80	Lipophilicity
f_u	%	0.65	Fraction unbound
UGT2B7 $K_M \rightarrow$ Gemfi-Glu	$\mu\text{mol/L}$	2.20	Michaelis-Menten constant
UGT2B7 $k_{\text{cat}} \rightarrow$ Gemfi-Glu	1/min	18.67 ^a	Catalytic rate constant
Liver influx K_M	$\mu\text{mol/L}$	2.39	Michaelis-Menten constant
Liver influx k_{cat}	1/min	39.26 ^b	Transport rate constant
GFR fraction		1 ^c	Filtered drug in the urine
EHC continuous fraction		1	Bile fraction continuously released
Intestinal permeability	cm/min	$6.62 \cdot 10^{-3}$	Transcellular intestinal permeability
Cellular permeability	cm/min	Charge dependent Schmitt 0.07	Permeability into the cellular space
Partition coefficients		Berezhkovskiy	Organ-plasma partition coefficients
Dissolution time (Weibull)	min	24.45	Dissolution time (50%)
Dissolution shape (Weibull)		1.56	Dissolution shape
CYP2C8 K_i	$\mu\text{mol/L}$	30.40	Diss. const. inhibitor-enzyme complex
OATP1B1 K_i	$\mu\text{mol/L}$	25.20	Diss. const. inhibitor-transporter complex
Gemfibrozil-Glucuronide			
Molecular weight	g/mol	426.46	Molecular weight
pKa, acid		2.68	Acid dissociation constant
Solubility (pH)	mg/L	789.00 (7.00)	Solubility
Lipophilicity	log units	1.41	Lipophilicity
f_u	%	12	Fraction unbound
MRP2 K_M	$\mu\text{mol/L}$	21.49	Michaelis-Menten constant
MRP2 k_{cat}	1/min	7.13	Transport rate constant
OATP1B1 K_M	$\mu\text{mol/L}$	0.43	Michaelis-Menten constant
OATP1B1 k_{cat}	1/min	147.00 ^b	Transport rate constant
GFR fraction		1 ^c	Filtered drug in the urine
EHC continuous fraction		1	Bile fraction continuously released
Intestinal permeability	cm/min	$5.98 \cdot 10^{-7}$	Transcellular intestinal permeability
Cellular permeability	cm/min	PK-Sim Standard, $1.22 \cdot 10^{-4}$	Permeability into the cellular space
Partition coefficients		PK-Sim Standard	Organ-plasma partition coefficients
CYP2C8 K_i	$\mu\text{mol/L}$	20.00	Conc. for half-maximal inactivation
CYP2C8 k_{inact}	1/min	0.21	Maximum inactivation rate constant
OATP1B1 K_i	$\mu\text{mol/L}$	22.60	Diss. const. inhibitor-transporter complex

^a: adjusted due to different reference concentrations in the original model and imatinib model, ^b: adapted when migrating the model from PK-Sim® version 9 to 10, ^c: a GFR fraction of 1 corresponds to passive glomerular filtration of a compound, conc.: concentration, CYP: cytochrome P450, diss. const.: dissociation constant, EHC: enterohepatic circulation, Gemfi-Glu: gemfibrozil-glucuronide, GFR: glomerular filtration rate, MRP: multidrug resistance-associated protein, OATP: organic-anion-transporting polypeptide, UGT: uridine 5'-diphospho-glucuronosyltransferase.

S3.2.4 Simvastatin

Table S12: Drug-dependent parameters of the simvastatin PBPK model (PK-Sim® V9) [60]

Parameter	Unit	Value	Description
Simvastatin			
Molecular weight	g/mol	418.57	Molecular weight
Solubility (pH)	mg/L	16.40 (5.00)	Solubility
Lipophilicity	log units	4.68	Lipophilicity
f_u	%	1.34	Fraction unbound
CYP3A4 $K_M \rightarrow$ sink	$\mu\text{mol/L}$	21.00	Michaelis-Menten constant
CYP3A4 $k_{\text{cat}} \rightarrow$ sink	1/min	5194.04	Catalytic rate constant
PON3 $K_M \rightarrow$ Simva-Acid	$\mu\text{mol/L}$	840.00	Michaelis-Menten constant
PON3 $k_{\text{cat}} \rightarrow$ Simva-Acid	1/min	4952.08	Catalytic rate constant
Chemical hydrolysis CL \rightarrow Simva-Acid	L/ $\mu\text{mol/min}$	$9.80 \cdot 10^{-4}$	Clearance
Plasma hydrolysis CL \rightarrow Simva-Acid	L/ $\mu\text{mol/min}$	0.06	Clearance
BCRP K_M	$\mu\text{mol/L}$	5.00	Michaelis-Menten constant
BCRP k_{cat}	1/min	7.50	Transport rate constant
GFR fraction		1 ^a	Filtered drug in the urine
EHC continuous fraction		1	Bile fraction continuously released
Intestinal permeability	cm/min	$1.08 \cdot 10^{-3}$	Transcellular intestinal permeability
Cellular permeability	cm/min	PK-Sim Standard	Permeability into the cellular space
		0.26	
Partition coefficients		Berezhkovskiy	Organ-plasma partition coefficients
Dissolution time (Weibull)	min	86.38	Dissolution time (50%)
Dissolution shape (Weibull)		1.30	Dissolution shape
CYP2C8 K_i	$\mu\text{mol/L}$	1.10	Diss. const. inhibitor-enzyme complex
CYP3A4 K_i	$\mu\text{mol/L}$	0.16	Diss. const. inhibitor-enzyme complex
OATP1B1 K_i	$\mu\text{mol/L}$	5.00	Diss. const. inhibitor-transporter complex
P-gp K_i	$\mu\text{mol/L}$	4.60	Diss. const. inhibitor-transporter complex
Simvastatin Hydroxy Acid			
Molecular weight	g/mol	436.60	Molecular weight
pKa, acid		4.20	Acid dissociation constant
Solubility (pH)	mg/L	13.09 (6.84)	Solubility
Lipophilicity	log units	1.45	Lipophilicity
f_u	%	5.68	Fraction unbound
CYP2C8 $K_M \rightarrow$ sink	$\mu\text{mol/L}$	36.00	Michaelis-Menten constant
CYP2C8 $k_{\text{cat}} \rightarrow$ sink	1/min	52.30	Catalytic rate constant
CYP3A4 $K_M \rightarrow$ sink	$\mu\text{mol/L}$	26.00	Michaelis-Menten constant
CYP3A4 $k_{\text{cat}} \rightarrow$ sink	1/min	31.00	Catalytic rate constant
UGT1A1 $K_M \rightarrow$ sink	$\mu\text{mol/L}$	349.00	Michaelis-Menten constant
UGT1A1 $k_{\text{cat}} \rightarrow$ sink	1/min	6.50	Catalytic rate constant
UGT1A3 $K_M \rightarrow$ sink	$\mu\text{mol/L}$	349.00	Michaelis-Menten constant
UGT1A3 $k_{\text{cat}} \rightarrow$ sink	1/min	6.50	Catalytic rate constant
Liver lactonization CL \rightarrow sink	L/ $\mu\text{mol/min}$	$2.43 \cdot 10^{-3}$	Clearance
OATP1B1 K_M	$\mu\text{mol/L}$	2.00	Michaelis-Menten constant
OATP1B1 k_{cat}	1/min	146.43 ^b	Transport rate constant
OATP1B3 K_M	$\mu\text{mol/L}$	2.00	Michaelis-Menten constant
OATP1B3 k_{cat}	1/min	2.15	Transport rate constant
P-gp K_M	$\mu\text{mol/L}$	10.00	Michaelis-Menten constant
P-gp k_{cat}	1/min	50.00	Transport rate constant
GFR fraction		1 ^a	Filtered drug in the urine
EHC continuous fraction		1	Bile fraction continuously released
Intestinal permeability	cm/min	$5.92 \cdot 10^{-7}$	Transcellular intestinal permeability
Cellular permeability	cm/min	Schmitt, $1.17 \cdot 10^{-4}$	Permeability into the cellular space
Partition coefficients		Charge dependent Schmitt normalized to PK-Sim	Organ-plasma partition coefficients
CYP2C8 K_i	$\mu\text{mol/L}$	41.10	Diss. const. inhibitor-enzyme complex
CYP3A4 K_i	$\mu\text{mol/L}$	69.60	Diss. const. inhibitor-enzyme complex
BCRP K_i	$\mu\text{mol/L}$	18.00	Diss. const. inhibitor-transporter complex
OATP1B1 K_i	$\mu\text{mol/L}$	3.60	Diss. const. inhibitor-transporter complex

^a: a GFR fraction of 1 corresponds to passive glomerular filtration of a compound, ^b: adjusted due to different reference concentrations in the original model and imatinib model, BCRP: breast cancer resistance protein, CYP: cytochrome P450, diss. const.: dissociation constant, EHC: enterohepatic circulation, GFR: glomerular filtration rate, MRP: multidrug resistance-associated protein, OATP: organic-anion-transporting polypeptide, P-gp: P-glycoprotein, PON: paraoxonase, Simva-Acid: simvastatin hydroxy acid, UGT: uridine 5'-diphospho-glucuronosyltransferase.

S3.2.5 Metoprolol

Table S13: Drug-dependent parameters of the metoprolol PBPK model [61]

Parameter	Unit	Value	Description
R-Metoprolol			
Molecular weight	g/mol	267.36	Molecular weight
pKa, base		9.70	Acid dissociation constant
Solubility (pH)	mg/mL	1000.00 (7.40)	Solubility
Lipophilicity	log units	1.77	Lipophilicity
f_u	%	88	Fraction unbound
CYP2D6 $K_M \rightarrow$ OH-Meto	$\mu\text{mol/L}$	10.08	Michaelis-Menten constant
CYP2D6 k_{cat} NM \rightarrow OH-Meto	1/min	5.73	Catalytic rate constant
CYP2D6 k_{cat} IM \rightarrow OH-Meto	1/min	1.65	Catalytic rate constant
CYP2D6 $K_M \rightarrow$ sink	$\mu\text{mol/L}$	8.82	Michaelis-Menten constant
CYP2D6 k_{cat} NM \rightarrow sink	1/min	9.40	Catalytic rate constant
CYP2D6 k_{cat} IM \rightarrow sink	1/min	2.70	Catalytic rate constant
CYP3A4 CL \rightarrow sink	1/min	0.02 ^a	Clearance
GFR fraction		1 ^b	Filtered drug in the urine
EHC continuous fraction		1	Bile fraction continuously released
Intestinal permeability	cm/min	$4.14 \cdot 10^{-5}$	Transcellular intestinal permeability
Cellular permeability	cm/min	PK-Sim Standard $4.64 \cdot 10^{-3}$	Permeability into the cellular space
Partition coefficients		Rodgers + Rowland	Organ-plasma partition coefficients
Dissolution time (Weibull)	min	12.31	Dissolution time (50%)
Dissolution shape (Weibull)		0.72	Dissolution shape
S-Metoprolol			
Molecular weight	g/mol	267.36	Molecular weight
pKa, base		9.70	Acid dissociation constant
Solubility (pH)	mg/mL	1000.00 (7.40)	Solubility
Lipophilicity	log units	1.77	Lipophilicity
f_u	%	88	Fraction unbound
CYP2D6 $K_M \rightarrow$ OH-Meto	$\mu\text{mol/L}$	10.75	Michaelis-Menten constant
CYP2D6 k_{cat} NM \rightarrow OH-Meto	1/min	6.30	Catalytic rate constant
CYP2D6 k_{cat} IM \rightarrow OH-Meto	1/min	1.82	Catalytic rate constant
CYP2D6 $K_M \rightarrow$ sink	$\mu\text{mol/L}$	12.43	Michaelis-Menten constant
CYP2D6 k_{cat} NM \rightarrow sink	1/min	7.89	Catalytic rate constant
CYP2D6 k_{cat} IM \rightarrow sink	1/min	2.27	Catalytic rate constant
CYP3A4 CL \rightarrow sink	1/min	0.02 ^a	Clearance
GFR fraction		1 ^b	Filtered drug in the urine
EHC continuous fraction		1	Bile fraction continuously released
Intestinal permeability	cm/min	$4.14 \cdot 10^{-5}$	Transcellular intestinal permeability
Cellular permeability	cm/min	PK-Sim Standard $4.64 \cdot 10^{-3}$	Permeability into the cellular space
Partition coefficients		Rodgers + Rowland	Organ-plasma partition coefficients
Dissolution time (Weibull)	min	12.31	Dissolution time (50%)
Dissolution shape (Weibull)		0.72	Dissolution shape

^a: included in the model instead of a non-specific hepatic clearance process, ^b: a GFR fraction of 1 corresponds to passive glomerular filtration of a compound, CYP: cytochrome P450, EHC: enterohepatic circulation, GFR: glomerular filtration rate, IM: intermediate metabolizer, NM: normal metabolizer, OH-Meto: hydroxymetoprolol.

Table S13: Drug-dependent parameters of the metoprolol PBPK model [61] (*continued*)

Parameter	Unit	Value	Description
Hydroxymetoprolol			
Molecular weight	g/mol	283.36	Molecular weight
pKa ₁ , base		9.67	Acid dissociation constant
pKa ₂ , acid		13.55	Acid dissociation constant
Solubility (pH)	mg/L	1430.00 (7.00)	Solubility
Lipophilicity	log units	0.87	Lipophilicity
f _u	%	63	Fraction unbound
Hepatic CL → sink	l/min	0.34	Clearance
GFR fraction		1 ^b	Filtered drug in the urine
EHC continuous fraction		1	Bile fraction continuously released
Intestinal permeability	cm/min	1.08 · 10 ⁻⁶	Transcellular intestinal permeability
Cellular permeability	cm/min	PK-Sim Standard 4.08 · 10 ⁻⁴	Permeability into the cellular space
Partition coefficients		Rodgers + Rowland	Organ-plasma partition coefficients

^a: included in the model instead of a non-specific hepatic clearance process, ^b: a GFR fraction of 1 corresponds to passive glomerular filtration of a compound, CYP: cytochrome P450, EHC: enterohepatic circulation, GFR: glomerular filtration rate, IM: intermediate metabolizer, NM: normal metabolizer, OH-Meto: hydroxymetoprolol.

S3.3 Plasma Concentration-Time Profiles (Semilogarithmic)

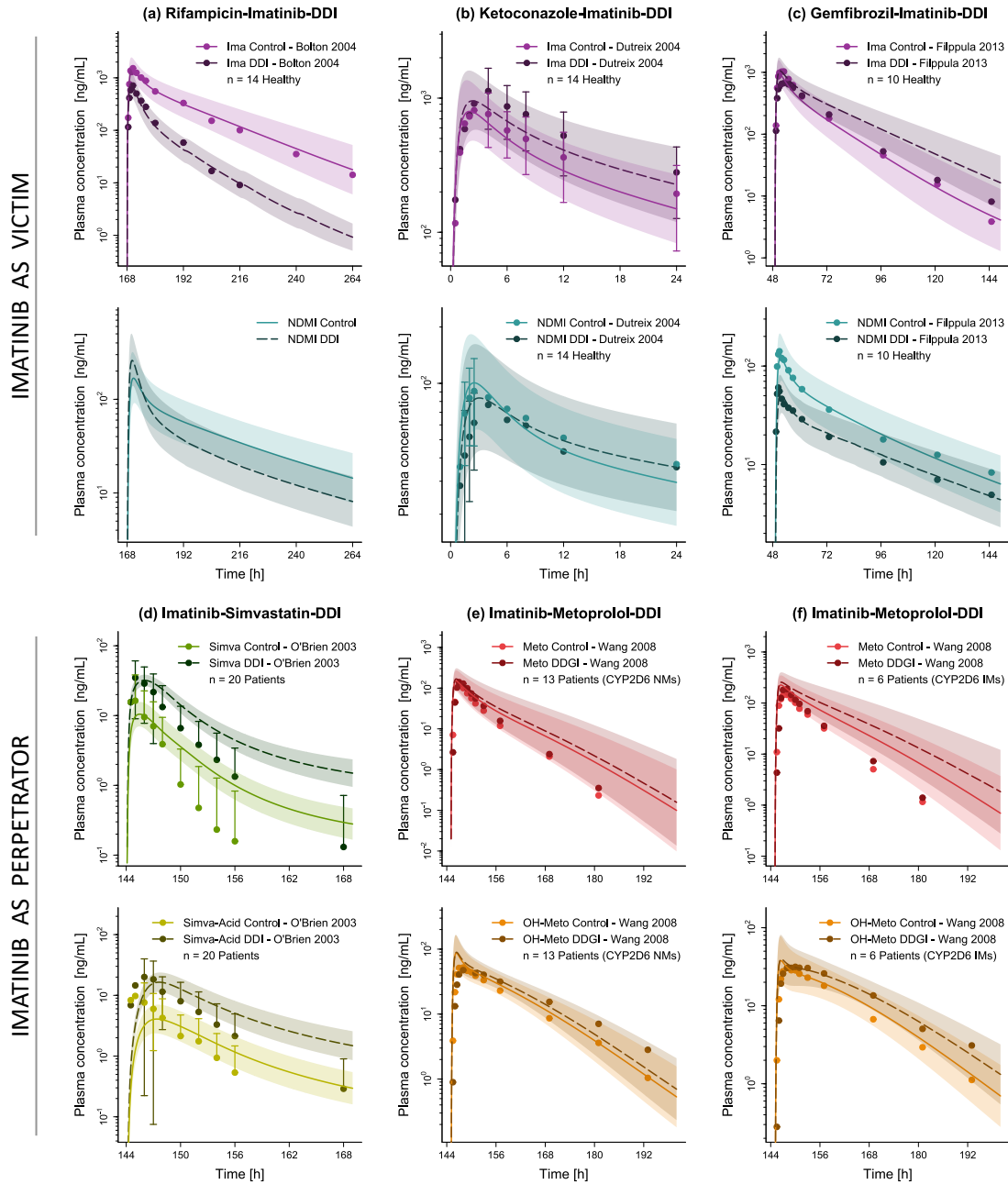


Figure S14: Evaluation of the modeled drug-drug interaction network. Presented are predicted plasma concentration-time profiles (semilogarithmic) of each victim drug (imatinib (a–c), simvastatin (d), metoprolol (e–f)) without (Control) and with (DDI) intake of the respective perpetrator drug (rifampicin (a), ketoconazole (b), gemfibrozil (c), imatinib (d–f)), alongside corresponding observed data [21, 23, 37, 55, 56]. Solid (Control) and dashed (DDI) lines and ribbons represent model population predictions ($n = 1000$; geometric mean and geometric standard deviation), while corresponding observed data are shown as dots (\pm standard deviation, if available). CYP: cytochrome P450, DDI: drug-drug interaction, Healthy: healthy subjects, IM: intermediate metabolizer, Ima: imatinib, Metro: metoprolol, n: number of study participants, NDMI: N-desmethyl imatinib, NM: normal metabolizer, OH-Meto: hydroxymetoprolol, Patients: cancer patients, Simva: simvastatin, Simva-Acid: simvastatin hydroxy acid.

S3.4 Plasma Concentration-Time Profiles (Linear)

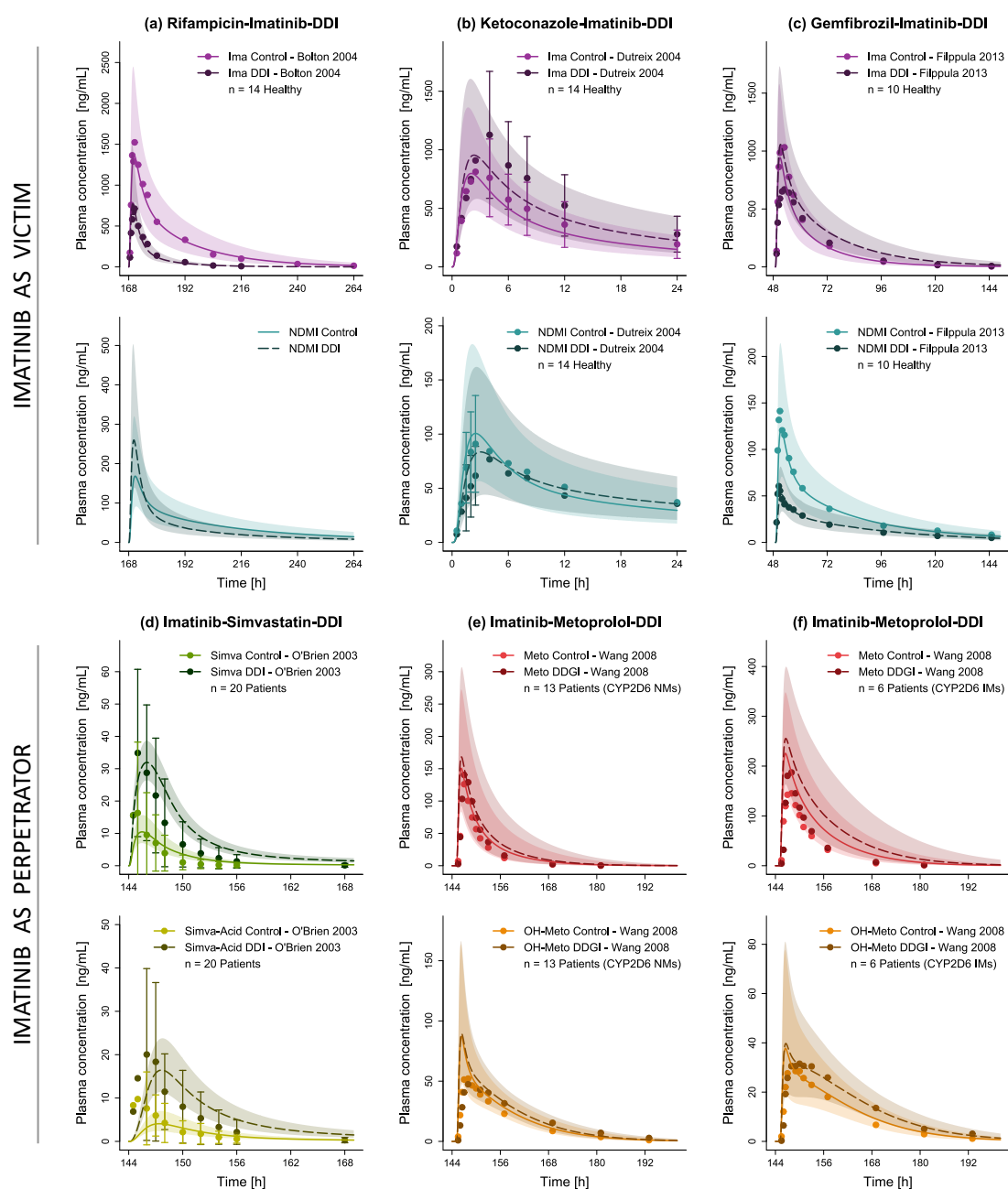


Figure S15: Evaluation of the modeled drug-drug interaction network. Presented are predicted plasma concentration-time profiles (linear) of each victim drug (imatinib (a-c), simvastatin (d), metoprolol (e-f)) without (Control) and with (DDI) intake of the respective perpetrator drug (rifampicin (a), ketoconazole (b), gemfibrozil (c), imatinib (d-f)), alongside corresponding observed data [21, 23, 37, 55, 56]. Solid (Control) and dashed (DDI) lines and ribbons represent model population predictions ($n = 1000$; geometric mean and geometric standard deviation), while corresponding observed data are shown as dots (\pm standard deviation, if available). CYP: cytochrome P450, DDI: drug-drug interaction, Healthy: healthy subjects, IM: intermediate metabolizer, Ima: imatinib, Meto: metoprolol, n: number of study participants, NDMI: N-desmethyl imatinib, NM: normal metabolizer, Patients: cancer patients, OH-Meto: hydroxymetoprolol, Simva: simvastatin, Simva-Acid: simvastatin hydroxy acid.

S3.5 DDI AUC_{last} and DDI C_{max} Ratio Goodness-of-Fit Plots

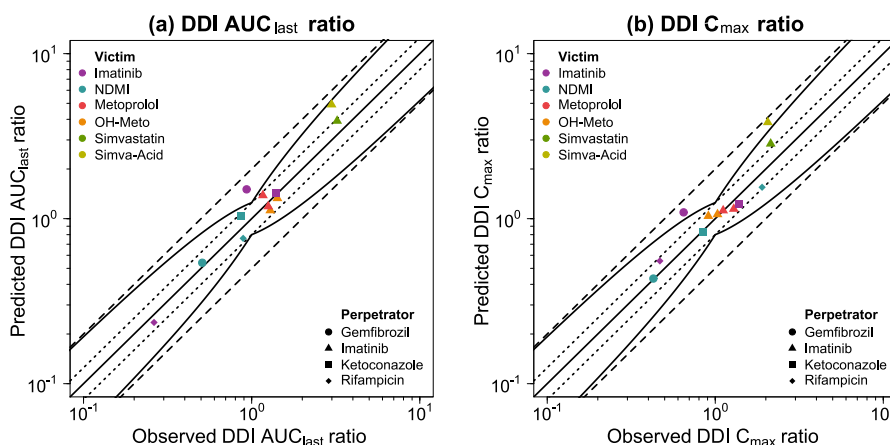


Figure S16: Evaluation of the modeled drug-drug interaction network. Predicted versus observed DDI AUC_{last} (a) and DDI C_{max} (b) ratios are shown with the solid line representing the line of identity, dotted lines indicating 1.25-fold and dashed lines twofold deviation from the respective observed value. Curved lines mark the prediction success limits proposed by Guest et al. [62] including 20% variability. AUC_{last} : area under the curve determined between first and last plasma concentration measurements, C_{max} : maximum plasma concentration, DDI: drug-drug interaction, NDMI: N-desmethyl imatinib, OH-Meto: hydroxymetoprolol, Simva-Acid: simvastatin hydroxy acid.

S3.6 Predicted and Observed DDI AUC_{last} and DDI C_{max} Ratios

Table S14: Predicted versus observed DDI AUC_{last} and DDI C_{max} ratios

Victim application [mg]	Perpetrator application [mg]	n	Compound	DDI AUC_{last} ratio			DDI C_{max} ratio			Reference
				Pred	Obs	Pred/Obs	Pred	Obs	Pred/Obs	
Imatinib d8: 400 po (cap, SD)	Rifampicin d1–11: 600 po (-, QD)	14 (healthy)	Ima NDMI	0.24 0.76	0.26 0.89	0.90 0.85	0.55 1.55	0.47 1.90	1.18 0.82	Bolton 2004 [37]
Imatinib d1: 200 po (cap, SD)	Ketoconazole d1: 400 po (-, SD)	14 (healthy)	Ima NDMI	1.44 1.04	1.40 0.86	1.02 1.21	1.24 0.83	1.39 0.84	0.89 0.99	Dutreix 2004 [23]
Imatinib d3: 200 po (tab, SD)	Gemfibrozil d1–6: 600 po (tab, BID)	10 (healthy)	Ima NDMI	1.51 0.54	0.93 0.51	1.61 1.06	1.09 0.43	0.65 0.43	1.68 1.01	Filppula 2013 [21]
Simvastatin d7: 40 po (tab, SD)	Imatinib d1–7: 400 po (cap, QD)	20 (CML patients)	Simva Simva-Acid	3.91 4.91	3.22 2.99	1.21 1.65	2.84 3.84	2.14 2.05	1.33 1.87	O'Brien 2003 [55]
Metoprolol d7: 100 po (tab, SD)	Imatinib d1–9: 400 po (cap, BID)	13 (CML patients) CYP2D6 NMs	Meto OH-Meto	1.19 1.12	1.26 1.29	0.94 0.87	1.12 1.04	1.11 0.91	1.01 1.14	Wang 2008 [56]
Metoprolol d7: 100 po (tab, SD)	Imatinib d1–9: 400 po (cap, BID)	6 (CML patients) CYP2D6 IMs	Meto OH-Meto	1.38 1.33	1.17 1.42	1.19 0.93	1.15 1.06	1.29 1.03	0.89 1.03	Wang 2008 [56]
Overall mean GMFE (range) GMFE ≤ 2				1.21 (1.02–1.65) 12/12			1.23 (1.01–1.87) 12/12			

-: not given, AUC_{last} : area under the plasma concentration-time curve determined between first and last concentration measurements, BID: twice daily, cap: capsule, C_{max} : maximum plasma concentration, CYP: cytochrome P450, d: day, DDI: drug-drug interaction, GMFE: geometric mean fold error, IM: intermediate metabolizer, Ima: imatinib, Meto: metoprolol, n: number of participants, NDMI: N-desmethyl imatinib, NM: normal metabolizer, OH-Meto: hydroxy-metoprolol, po: oral, QD: once daily, SD: single dose, Simva: simvastatin, Simva-Acid: simvastatin hydroxy acid, tab: tablet.

S3.7 Comparison of CYP3A Perpetrator Effects – SD vs. MD Imatinib Administration

In DDI studies involving CYP3A perpetrators, ketoconazole was observed to increase imatinib exposure by 40% after SD-administration, while ritonavir showed almost no effect on the steady-state AUC of imatinib [23, 63].

A detailed description and evaluation of the modeled ketoconazole-imatinib-DDI [23] can be found in Sections S3.1–S3.6.

The ritonavir-imatinib-DDI study by van Erp et al. [63] was not included in the developed DDI network due to limited reproducibility. Eleven patients were enrolled, six of whom were women, with an average age of 62 years. The influence of ritonavir on imatinib exposure at steady-state was investigated. Participants received imatinib doses equivalent to 100% on study days 1 and 5 and 50% on days 2, 3, and 4 of the doses given prior to participation in the study, which ranged from 400 to 800 mg once daily. Ritonavir was co-administered (600 mg once daily) on days 2, 3, and 4.

Since the AUC and C_{\max} values for imatinib and NDMI were reported as dose-normalized means for all patients and additionally the number of patients receiving each dose was not specified, the DDI study could not be accurately recreated in our model without bias. Here, we assumed a daily dose of 400 mg (100%) imatinib to simulate the ritonavir-imatinib-DDI and assessed the performance of our model in predicting the steady-state AUC of imatinib. The effect was compared to the impact of ketoconazole on imatinib SD-administration. For this, the imatinib model was coupled with a recently published ritonavir model [64]. Drug-dependent parameters of ritonavir are presented in Table S16. Figure S17 presents the goodness-of-fit plots of the ketoconazole-imatinib and ritonavir-imatinib DDI ratios, with respective values listed in Table S15.

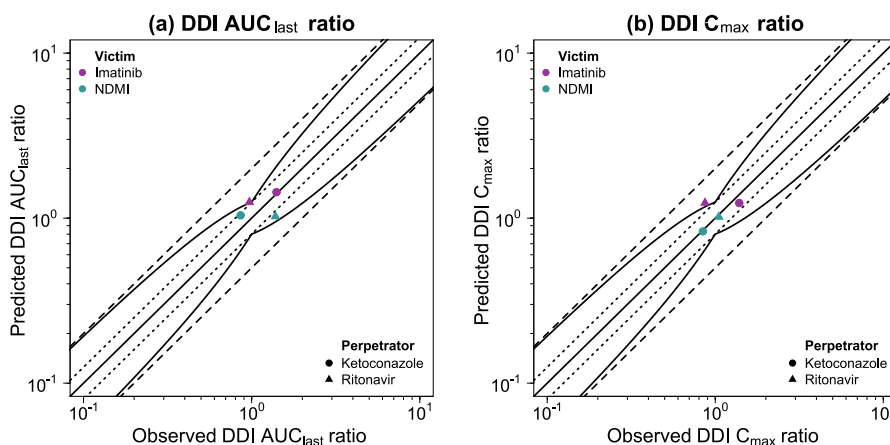


Figure S17: Predicted versus observed DDI AUC_{last} (a) and DDI C_{\max} (b) ratios are shown with the solid line representing the line of identity, dotted lines indicating 1.25-fold and dashed lines twofold deviation from the respective observed value. Curved lines mark the prediction success limits proposed by Guest et al. [62] including 20% variability. AUC_{last} : area under the curve determined between first and last plasma concentration measurements, C_{\max} : maximum plasma concentration, DDI: drug-drug interaction, NDMI: N-desmethyl imatinib.

Table S15: Predicted versus observed DDI AUC_{last} and DDI C_{max} ratios

Perpetrator	Compound	DDI AUC _{last} ratio			DDI C _{max} ratio			Reference
		Pred	Obs	Pred/Obs	Pred	Obs	Pred/Obs	
KET	Ima	1.44	1.40	1.02	1.24	1.39	0.89	Duttreix 2004 [23]
	NDMI	1.04	0.86	1.21	0.83	0.84	0.99	
RIT	Ima	1.25	0.97	1.29	1.24	0.87	1.42	van Erp 2007 [63]
	NDMI	1.02	1.39	0.74	1.02	1.05	0.97	
Overall mean GMFE (range)		1.22 (1.02–1.35)			1.15 (1.01–1.42)			
GMFE ≤ 2		4/4			4/4			

AUC_{last}: area under the plasma concentration-time curve determined between first and last concentration measurements, C_{max}: maximum plasma concentration, DDI: drug-drug interaction, GMFE: geometric mean fold error, Ima: imatinib, KET: ketoconazole, NDMI: N-desmethyl imatinib, RIT: ritonavir.

Table S16: Drug-dependent parameters of the ritonavir PBPK model [64]

Parameter	Unit	Value	Description
Ritonavir			
Molecular weight	g/mol	721.00	Molecular weight
pK _{a1} , base		1.90	Acid dissociation constant
pK _{a2} , base		2.60	Acid dissociation constant
Solubility (pH)	µg/mL	60.00 (7.0)	Solubility
Lipophilicity		3.90	Lipophilicity
f _u	%	2.00	Fraction unbound
CYP2D6 K _M → sink	µmol/L	1.00	Michaelis-Menten constant
CYP2D6 k _{cat} → sink	1/min	3.00	Catalytic rate constant
CYP3A4 K _M → sink	µmol/L	0.07	Michaelis-Menten constant
CYP3A4 k _{cat} → sink	1/min	1.10	Catalytic rate constant
P-gp K _M	µmol/L	0.13	Michaelis-Menten constant
P-gp k _{cat}	1/min	0.70	Transport rate constant
GFR fraction		1 ^a	Filtered drug in the urine
EHC continuous fraction		1	Bile fraction continuously released
Intestinal permeability	cm/min	6.50 · 10 ⁻⁵	Transcellular intestinal permeability
Cellular permeability	cm/min	PK-Sim Standard, 1.63 · 10 ⁻³	Permeability into the cellular space
Partition coefficients		Rodgers + Rowland	Organ-plasma partition coefficients
Particle radius	µm	10.00	Particle dissolution radius
Induction EC ₅₀	µmol/L	0.17	Conc. for half-maximal induction
CYP3A4 E _{max}		7.47	Maximum induction effect
CYP2D6 K _i	µmol/L	0.04	Diss. const. inhibitor-enzyme complex
CYP3A4 K _i	µmol/L	0.25	Diss. const. inhibitor-enzyme complex
CYP3A4 K _I	µmol/L	0.20	Conc. for half-maximal inactivation
CYP3A4 k _{inact}	1/min	0.40	Maximum inactivation rate constant
P-gp K _i	µmol/L	4.2 ^b	Diss. const. inhibitor-transporter complex

^a: a GFR fraction of 1 corresponds to passive glomerular filtration of a compound, ^b: added to the model [65], conc.: concentration, CYP: cytochrome P450, diss. const.: dissociation constant, EHC: enterohepatic circulation, GFR: glomerular filtration rate, P-gp: P-glycoprotein.

Bibliography

- [1] AD Rodrigues. Integrated cytochrome P450 reaction phenotyping. Attempting to bridge the gap between cDNA-expressed cytochromes P450 and native human liver microsomes. *Biochemical Pharmacology*, 57(5): 465–480, 1999. doi: 10.1016/s0006-2952(98)00268-8.
- [2] Open Systems Pharmacology Suite Community PK-Sim@Ontogeny Database Documentation, Available online (accessed on 30 April 2022). URL <https://github.com/Open-Systems-Pharmacology/OSPSuite.Documentation/blob/master/PK-SimOntogenyDatabaseVersion7.3.pdf>.
- [3] B Achour, A Dantonio, M Niosi, JJ Novak, JK Fallon, J Barber, PC Smith, A Rostami-Hodjegan, and TC Goosen. Quantitative characterization of major hepatic UDP-glucuronosyltransferase enzymes in human liver microsomes: Comparison of two proteomic methods and correlation with catalytic activity. *Drug metabolism and disposition: the biological fate of chemicals*, 45(10):1102–1112, 2017. doi: 10.1124/dmd.117.076703.
- [4] G Margaillan, M Rouleau, JK Fallon, P Caron, L Villeneuve, V Turcotte, PC Smith, MS Joy, and C Guillemette. Quantitative profiling of Human renal UDP-glucuronosyltransferases and glucuronidation activity: A comparison of normal and tumoral kidney tissues. *Drug Metabolism and Disposition*, 43(4):611–619, 2015. doi: 10.1124/dmd.114.062877.
- [5] B Prasad, Y Lai, Y Lin, and JD Unadkat. Interindividual variability in the hepatic expression of the human breast cancer resistance protein (BCRP/ABCG2): effect of age, sex, and genotype. *Journal of pharmaceutical sciences*, 102(3):787–793, 2013. doi: 10.1002/jps.23436.
- [6] AK Deo, B Prasad, L Balogh, Y Lai, and JD Unadkat. Interindividual variability in hepatic expression of the multidrug resistance-associated protein 2 (MRP2/ABCC2): quantification by liquid chromatography/tandem mass spectrometry. *Drug Metabolism and Disposition*, 40(5):852–855, 2012. doi: 10.1124/dmd.111.043810.
- [7] B Prasad, R Evers, A Gupta, CECA Hop, L Salphati, S Shukla, S Ambudkar, and JD Unadkat. Interindividual variability in hepatic OATPs and P-glycoprotein (ABCB1) protein expression: Quantification by LC-MS/MS and influence of genotype, age and sex. *Drug metabolism and disposition: the biological fate of chemicals*, 42(1):78–88, 2014. doi: 10.1124/dmd.113.053819.
- [8] N Hanke, S Frechen, D Moj, H Britz, T Eissing, T Wendl, and T Lehr. PBPK models for CYP3A4 and P-gp DDI prediction: A modeling network of rifampicin, itraconazole, clarithromycin, midazolam, alfentanil, and digoxin. *CPT: Pharmacometrics and Systems Pharmacology*, 7(10):647–659, 2018. doi: 10.1002/psp4.12343.
- [9] M Meyer, S Schneckener, B Ludewig, L Kuepfer, and J Lippert. Using expression data for quantification of active processes in physiologically based pharmacokinetic modeling. *Drug metabolism and disposition: the biological fate of chemicals*, 40(5):892–901, 2012. doi: 10.1124/dmd.111.043174.
- [10] D Scotcher, S Billington, J Brown, CR Jones, CDA Brown, A Rostami-Hodjegan, and A Galetin. Microsomal and cytosolic scaling factors in dog and human kidney cortex and application for in vitro-in vivo extrapolation of renal metabolic clearance. *Drug Metabolism and Disposition*, 45(5):556–568, 2017. doi: 10.1124/dmd.117.075242.
- [11] P Shi, M Liao, C Chuang, R Griffin, J Shi, M Hyer, JK Fallon, PC Smith, C Li, and CQ Xia. Efflux transporter breast cancer resistance protein dominantly expresses on the membrane of red blood cells, hinders partitioning of its substrates into the cells, and alters drug–drug interaction profiles. *Xenobiotica*, 48(11):1173–1183, 2018. doi: 10.1080/00498254.2017.1397812.
- [12] M Nishimura and S Naito. Tissue-specific mRNA expression profiles of human phase I metabolizing enzymes except for cytochrome P450 and phase II metabolizing enzymes. *Drug metabolism and pharmacokinetics*, 21(5):357–374, 2006. doi: 10.2133/dmpk.21.357.
- [13] M Nishimura, H Yaguti, H Yoshitsugu, and S Naito. Tissue distribution of mRNA expression of human cytochrome P450 isoforms assessed by high-sensitivity real-time reverse transcription PCR. *Journal of the Pharmaceutical Society of Japan*, 123(5):369–375, 2003. doi: 10.1248/yakushi.123.369.

- [14] N Kolesnikov, E Hastings, M Keays, O Melnichuk, YA Tang, E Williams, M Dylag, N Kurbatova, M Brandizi, T Burdett, K Megy, E Pilicheva, G Rustici, A Tikhonov, H Parkinson, R Petryszak, U Sarkans, and A Brazma. ArrayExpress update-simplifying data submissions. *Nucleic Acids Research*, 43(D1):D1113–D1116, 2015. doi: 10.1093/nar/gku1057.
- [15] National Center for Biotechnology Information (NCBI) (2010) Expressed Sequence Tags (EST) from UniGene.
- [16] M Nishimura and S Naito. Tissue-specific mRNA expression profiles of human ATP-binding cassette and solute carrier transporter superfamilies. *Drug metabolism and pharmacokinetics*, 20(6):452–477, 2005. doi: 10.2133/dmpk.20.452.
- [17] B Peng, C Dutreix, G Mehring, MJ Hayes, M Ben-Am, M Seiberling, R Pokorny, R Cupdeville, and P Lloyd. Absolute bioavailability of imatinib (Glivec®) orally versus intravenous infusion. *Journal of Clinical Pharmacology*, 44(2):158–162, 2004. doi: 10.1177/0091270003262101.
- [18] B Peng, M Hayes, D Resta, A Racine-Poon, BJ Druker, M Talpaz, CL Sawyers, M Rosamilia, J Ford, P Lloyd, and R Capdeville. Pharmacokinetics and pharmacodynamics of imatinib in a phase I trial with chronic myeloid leukemia patients. *Journal of Clinical Oncology*, 22(5):935–942, 2004. doi: 10.1200/JCO.2004.03.050.
- [19] DW Zidan, WS Hassan, MS Elmasry, and AA Shalaby. A novel spectrofluorimetric method for determination of imatinib in pure, pharmaceutical preparation, human plasma, and human urine. *Luminescence*, 33(1):232–242, 2018. doi: 10.1002/bio.3406.
- [20] A Ostrowicz, P Mikołajczak, M Wierzbička, and P Boguradzki. Bioequivalence study of 400 and 100 mg imatinib film-coated tablets in healthy volunteers. *Acta Poloniae Pharmaceutica - Drug Research*, 71(5): 843–854, 2014.
- [21] AM Filppula, A Tornio, M Niemi, PJ Neuvonen, and JT Backman. Gemfibrozil impairs imatinib absorption and inhibits the CYP2C8-mediated formation of its main metabolite. *Clinical Pharmacology and Therapeutics*, 94(3):383–393, 2013. doi: 10.1038/clpt.2013.92.
- [22] JA Jung, N Kim, JS Yang, TE Kim, JR Kim, GS Song, H Kim, JW Ko, and W Huh. Bioequivalence study of two imatinib formulations after single-dose administration in healthy Korean male volunteers. *Drug Research*, 64(12):651–655, 2014. doi: 10.1055/s-0034-1367059.
- [23] C Dutreix, B Peng, G Mehring, M Hayes, R Capdeville, R Pokorny, and M Seiberling. Pharmacokinetic interaction between ketoconazole and imatinib mesylate (Glivec) in healthy subjects. *Cancer Chemotherapy and Pharmacology*, 54(4):290–294, 2004. doi: 10.1007/s00280-004-0832-z.
- [24] HP Gschwind, U Pfaar, F Waldmeier, M Zollinger, C Sayer, P Zbinden, M Hayes, R Pokorny, M Seiberling, M Ben-Am, B Peng, and G Gross. Metabolism and disposition of imatinib mesylate in healthy volunteers. *Drug Metabolism and Disposition*, 33(10):1503–1512, 2005. doi: 10.1124/dmd.105.004283.
- [25] AA Golabchifar, MR Rouini, B Shafaghi, S Rezaee, A Foroumadi, and MR Khoshayand. Optimization of the simultaneous determination of imatinib and its major metabolite, CGP74588, in human plasma by a rapid HPLC method using D-optimal experimental design. *Talanta*, 85(5):2320–2329, 2011. doi: 10.1016/j.talanta.2011.07.093.
- [26] JS Yang, EG Cho, W Huh, JW Ko, JA Jung, and SY Lee. Rapid determination of imatinib in human plasma by liquid chromatography-tandem mass spectrometry: Application to a pharmacokinetic study. *Bulletin of the Korean Chemical Society*, 34(8):2425–2430, 2013. doi: 10.5012/bkcs.2013.34.8.2425.
- [27] RF Frye, SM Fitzgerald, TF Lagattuta, MW Hruska, and MJ Egorin. Effect of St John’s wort on imatinib mesylate pharmacokinetics. *Clinical Pharmacology and Therapeutics*, 76(4):323–329, 2004. doi: 10.1016/j.clpt.2004.06.007.
- [28] Z Nikolova, B Peng, M Hubert, M Seiberling, U Keller, YY Ho, H Schran, and R Capdeville. Bioequivalence, safety, and tolerability of imatinib tablets compared with capsules. *Cancer Chemotherapy and Pharmacology*, 53(5):433–438, 2004. doi: 10.1007/s00280-003-0756-z.
- [29] MA Pena, J Muriel, M Saiz-Rodríguez, AM Borobia, F Abad-Santos, J Frías, and AM Peiró. Effect of cytochrome P450 and ABCB1 polymorphisms on imatinib pharmacokinetics after single-dose administration to healthy subjects. *Clinical Drug Investigation*, 40(7):617–628, 2020. doi: 10.1007/s40261-020-00921-7.

- [30] S Parrillo-Campiglia, MC Ercoli, O Umpierrez, P Rodríguez, S Márquez, C Guarneri, FT Estevez-Parrillo, M Laurenz, and FE Estevez-Carrizo. Bioequivalence of two film-coated tablets of imatinib mesylate 400 mg: A randomized, open-label, single-dose, fasting, two-period, two-sequence crossover comparison in healthy male South American volunteers. *Clinical Therapeutics*, 31(10):2224–2232, 2009. doi: 10.1016/j.clinthera.2009.10.009.
- [31] P Smith, JM Bullock, BM Booker, CE Haas, CS Berenson, and WJ Jusko. The influence of St. John’s wort on the pharmacokinetics and protein binding of imatinib mesylate. *Pharmacotherapy*, 24(11):1508–1514, 2004. doi: 10.1592/phco.24.16.1508.50958.
- [32] H Tawbi, SM Christner, Y Lin, M Johnson, ET Mowrey, C Cherrin, E Chu, JJ Lee, S Puhalla, R Stoller, LR Appleman, BM Miller, and JH Beumer. Calcium carbonate does not affect imatinib pharmacokinetics in healthy volunteers. *Cancer Chemotherapy and Pharmacology*, 73(1):207–211, 2014. doi: 10.1007/s00280-013-2337-0.
- [33] Y Zhang, S Qiang, Z Yu, W Zhang, Z Xu, L Yang, A Wen, and T Hang. LC-MS-MS determination of imatinib and N-desmethyl imatinib in human plasma. *Journal of Chromatographic Science*, 52(4):344–350, 2014. doi: 10.1093/chromsci/bmt037.
- [34] BA Sparano, MJ Egorin, RA Parise, J Walters, KA Komazec, RL Redner, and JH Beumer. Effect of antacid on imatinib absorption. *Cancer Chemotherapy and Pharmacology*, 63(3):525–528, 2009. doi: 10.1007/s00280-008-0778-7.
- [35] E Mohajeri, B Kalantari-Khandani, A Pardakhty, M Safavi, and M Ansari. Comparative pharmacokinetic evaluation and bioequivalence study of three different formulations of imatinib mesylate in CML patients. *International Journal of Hematology-Oncology and Stem Cell Research*, 9(4):165–172, 2015.
- [36] D Jawhari, M Alswisi, and M Ghannam. Bioavailability of a new generic formulation of imatinib mesylate 400mg tablets versus glivec in healthy male adult volunteers. *Journal of Bioequivalence and Bioavailability*, 3(7):161–164, 2011. doi: 10.4172/jbb.1000077.
- [37] AE Bolton, B Peng, M Hubert, A Krebs-Brown, R Capdeville, U Keller, and M Seiberling. Effect of rifampicin on the pharmacokinetics of imatinib mesylate (Gleevec, STI571) in healthy subjects. *Cancer Chemotherapy and Pharmacology*, 53(2):102–106, 2004. doi: 10.1007/s00280-003-0722-9.
- [38] MJ Egorin, DD Shah, SM Christner, MA Yerik, KA Komazec, LR Appleman, RL Redner, BM Miller, and JH Beumer. Effect of a proton pump inhibitor on the pharmacokinetics of imatinib. *British Journal of Clinical Pharmacology*, 68(3):370–374, 2009. doi: 10.1111/j.1365-2125.2009.03466.x.
- [39] R Arora, M Sharma, T Monif, and S Iyer. A multi-centric bioequivalence trial in Ph+ chronic myeloid leukemia patients to assess bioequivalence and safety evaluation of generic imatinib mesylate 400 mg tablets. *Cancer Research and Treatment*, 48(3):1120–1129, 2016. doi: 10.4143/crt.2015.436.
- [40] K Eechoute, RM Franke, WJ Loos, LA Scherckenbach, I Boere, J Verweij, H Gurney, RB Kim, RG Tirona, RHJ Mathijssen, and A Sparreboom. Environmental and genetic factors affecting transport of imatinib by OATP1A2. *Clinical Pharmacology and Therapeutics*, 89(6):816–820, 2011. doi: 10.1038/clpt.2011.42.
- [41] F Langenbucher. Linearization of dissolution rate by the Weibull distribution. *J Pharm Pharmacol*, 24(12):979–981, 1972. doi: 10.1111/j.2042-7158.1972.tb08930.x.
- [42] ChemAxon Imatinib, Available online (accessed on 9 September 2022). URL <https://chemicalize.com/app/calculation>.
- [43] T Minematsu and KM Giacomini. Interactions of tyrosine kinase inhibitors with organic cation transporters and multidrug and toxic compound extrusion proteins. *Molecular Cancer Therapeutics*, 10(3):531–539, 2011. doi: 10.1158/1535-7163.MCT-10-0731.
- [44] T Hegedus, L Orfi, A Seprodi, A Váradi, B Sarkadi, and G Kéri. Interaction of tyrosine kinase inhibitors with the human multidrug transporter proteins, MDR1 and MRP1. *Biochimica et Biophysica Acta - Molecular Basis of Disease*, 1587(2-3):318–325, 2002. doi: 10.1016/S0925-4439(02)00095-9.
- [45] Fachinformation Glivec(R) Filmtabletten, Available online (accessed on 9 September 2022). URL <https://klinischeforschung.novartis.de/dokumente/fachinformationen-glivec-filmtabletten/>.

- [46] C Arellano, P Gandia, T Lafont, R Jongejan, and E Chatelut. Determination of unbound fraction of imatinib and N-desmethyl imatinib, validation of an UPLC-MS/MS assay and ultrafiltration method. *Journal of Chromatography B: Analytical Technologies in the Biomedical and Life Sciences*, 907:94–100, 2012. doi: 10.1016/j.jchromb.2012.09.007.
- [47] AM Filppula, M Neuvonen, J Laitila, PJ Neuvonen, and JT Backman. Autoinhibition of CYP3A4 leads to important role of CYP2C8 in imatinib metabolism: Variability in CYP2C8 activity may alter plasma concentrations and response. *Drug Metabolism and Disposition*, 41(1):50–59, 2013. doi: 10.1124/dmd.112.048017.
- [48] E Kralj, S Žakelj, J Trontelj, R Roškar, P Černelč, and A Kristl. Absorption and elimination of imatinib through the rat intestine in vitro. *International Journal of Pharmaceutics*, 460(1-2):144–149, 2014. doi: 10.1016/j.ijpharm.2013.10.054.
- [49] Open Systems Pharmacology Suite Community. Open Systems Pharmacology Suite Manual, Version 7.4 2018, Available online (accessed on 28 September 2021). URL <https://docs.open-systems-pharmacology.org/working-with-pk-sim/pk-sim-documentation>.
- [50] W Schmitt. General approach for the calculation of tissue to plasma partition coefficients. *Toxicology in Vitro*, 22(2):457–467, 2008. doi: 10.1016/j.tiv.2007.09.010.
- [51] AM Filppula, J Laitila, PJ Neuvonen, and Janne T Backman. Potent mechanism-based inhibition of CYP3A4 by imatinib explains its liability to interact with CYP3A4 substrates. *British Journal of Pharmacology*, 165(8):2787–2798, 2012. doi: 10.1111/j.1476-5381.2011.01732.x.
- [52] R D’Cunha, S Bae, DJ Murry, and G An. TKI combination therapy: strategy to enhance dasatinib uptake by inhibiting Pgp- and BCRP-mediated efflux. *Biopharmaceutics and drug disposition*, 37(7):397–408, 2016. doi: 10.1002/bdd.2022.
- [53] A Hamada, H Miyano, H Watanabe, and H Saito. Interaction of imatinib mesilate with human P-glycoprotein. *Journal of Pharmacology and Experimental Therapeutics*, 307(2):824–828, 2003. doi: 10.1124/jpet.103.055574.
- [54] ChemAxon N-Desmethyl Imatinib, Available online (accessed on 9 September 2022). URL <https://chemicalize.com/app/calculation>.
- [55] SG O’Brien, P Meinhardt, E Bond, J Beck, B Peng, C Dutreix, G Mehring, S Milosavljev, C Huber, R Capdeville, and T Fischer. Effects of imatinib mesylate (ST1571, Glivec) on the pharmacokinetics of simvastatin, a cytochrome P450 3A4 substrate, in patients with chronic myeloid leukaemia. *British Journal of Cancer*, 89(10):1855–1859, 2003. doi: 10.1038/sj.bjc.6601152.
- [56] Y Wang, L Zhou, C Dutreix, E Leroy, Q Yin, V Sethuraman, GJ Riviere, OQP Yin, H Schran, and ZX Shen. Effects of imatinib (Glivec) on the pharmacokinetics of metoprolol, a CYP2D6 substrate, in Chinese patients with chronic myelogenous leukaemia. *British Journal of Clinical Pharmacology*, 65(6):885–892, 2008. doi: 10.1111/j.1365-2125.2008.03150.x.
- [57] Chin Eng Ong, Sally Coulter, Donald J. Birkett, C. Ramana Bhasker, and John O. Miners. The xenobiotic inhibitor profile of cytochrome P4502C8. *British Journal of Clinical Pharmacology*, 50(6):573–580, 2000. doi: 10.1046/j.1365-2125.2000.00316.x.
- [58] FZ Marok, JG Wojtyniak, LM Fuhr, D Selzer, M Schwab, J Weiss, WE Haefeli, and Thorsten Lehr. A physiologically based pharmacokinetic model of ketoconazole and its metabolites as drug–drug interaction perpetrators. *Pharmaceutics*, 12(2):679, 2023. doi: 10.3390/pharmaceutics13030331.
- [59] D Türk, N Hanke, S Wolf, S Frechen, T Eissing, T Wendl, M Schwab, and T Lehr. Physiologically based pharmacokinetic models for prediction of complex CYP2C8 and OATP1B1 (SLCO1B1) drug–drug–gene interactions: a modeling network of gemfibrozil, repaglinide, pioglitazone, rifampicin, clarithromycin and itraconazole. *Clinical Pharmacokinetics*, 58(12):1595–1607, 2019. doi: 10.1007/s40262-019-00777-x.
- [60] JG Wojtyniak, D Selzer, M Schwab, and T Lehr. Physiologically based precision dosing approach for drug–drug–gene interactions: A simvastatin network analysis. *Clinical Pharmacology and Therapeutics*, 109(1):201–211, 2021. doi: 10.1002/cpt.2111.

- [61] S Rüdesheim, JG Wojtyniak, D Selzer, N Hanke, F Mahfoud, M Schwab, and T Lehr. Physiologically based pharmacokinetic modeling of metoprolol enantiomers and α -hydroxymetoprolol to describe CYP2D6 drug-gene interactions. *Pharmaceutics*, 12(12):1200, 2020. doi: 10.3390/pharmaceutics12121200.
- [62] EJ Guest, L Aarons, JB Houston, A Rostami-Hodjegan, and A Galetin. Critique of the two-fold measure of prediction success for ratios: Application for the assessment of drug-drug interactions. *Drug Metabolism and Disposition*, 39(2):170–173, 2011. doi: 10.1124/dmd.110.036103.
- [63] NP Van Erp, H Gelderblom, MO Karlsson, J Li, M Zhao, J Ouwerkerk, JW Nortier, HJ Guchelaar, SD Baker, and A Sparreboom. Influence of CYP3A4 inhibition on the steady-state pharmacokinetics of imatinib. *Clinical Cancer Research*, 13(24):7394–7400, 2007. ISSN 10780432. doi: 10.1158/1078-0432.CCR-07-0346.
- [64] L Zheng, W Zhang, KT Olkkola, A Dallmann, L Ni, Y Zhao, L Wang, Q Zhang, and W Hu. Physiologically based pharmacokinetic modeling of ritonavir-oxycodone drug interactions and its implication for dosing strategy. *European Journal of Pharmaceutical Sciences*, 194:106697, 2024. ISSN 18790720. doi: 10.1016/j.ejps.2024.106697.
- [65] Á Telbisz, C Ambrus, O Móznér, E Szabó, G Várady, É Bakos, B Sarkadi, and C Özvegy-Laczka. Interactions of potential anti-COVID-19 compounds with multispecific ABC and OATP drug transporters. *Pharmaceutics*, 13(1):81, 2021. ISSN 19994923. doi: 10.3390/pharmaceutics13010081.

B.3 PROJECT III: PBPK MODELING OF DASATINIB

CPT: Pharmacometrics & Systems Pharmacology

Supplementary Material: A Physiologically-Based Pharmacokinetic Precision Dosing Approach to Manage Dasatinib Drug–Drug Interactions

Christina Kovar^{1,2}, Helena Leonie Hanae Loer¹, Simeon Rüdesheim^{1,2}, Laura Maria Fuhr¹, Fatima Zahra Marok¹, Dominik Selzer¹, Matthias Schwab^{2,3,4} and Thorsten Lehr¹

¹Clinical Pharmacy, Saarland University, Saarbrücken, Germany

²Dr. Margarete Fischer-Bosch Institute of Clinical Pharmacology, Stuttgart, Germany

³Departments of Clinical Pharmacology, and Pharmacy and Biochemistry, University of Tübingen, Tübingen, Germany

⁴Cluster of Excellence iFIT (EXC2180), Image-Guided and Functionally Instructed Tumor Therapies, University of Tübingen, Tübingen, Germany

Funding

Matthias Schwab was supported by the Robert Bosch Stiftung (Stuttgart, Germany), a grant from the German Federal Ministry of Education and Research (BMBF, 031L0188D, “GUIDE-IBD”) and the DFG im Rahmen der Exzellenzstrategie des Bundes und der Länder-EXC 2180-390900677. Thorsten Lehr was supported by the German Federal Ministry of Education and Research (BMBF, Horizon 2020 INSPIRATION grant 643271), under the frame of ERACoSysMed and the European Union Horizon 2021 SafePolyMed (grant 101057639).

Conflict of Interest

The authors declared no competing interests for this work.

Corresponding Author

Prof. Dr. Thorsten Lehr
Clinical Pharmacy, Saarland University
Campus C5 3, 66123 Saarbrücken, Germany
ORCID: 0000-0002-8372-1465
Phone: +49 681 302 70255
Email: thorsten.lehr@mx.uni-saarland.de

Contents

S1 PBPK Model Building	3
S1.1 Assignment to Training and Test Dataset	3
S1.2 Virtual Individuals	3
S1.3 Virtual Populations	3
S1.4 Clinical Studies	4
S1.5 System-dependent Parameters	6
S1.6 Drug-dependent Parameter Table	8
S2 PBPK Model Evaluation	9
S2.1 Healthy Volunteers	9
S2.1.1 Plasma Profiles (Linear Scale)	9
S2.1.2 Plasma Profiles (Semilogarithmic Scale)	11
S2.2 Cancer Patients	13
S2.2.1 Plasma Profiles (Linear Scale)	13
S2.2.2 Plasma Profiles (Semilogarithmic Scale)	18
S2.2.3 Goodness-of-fit Plots	23
S2.2.4 Residual Plot	24
S2.3 Quantitative PBPK Model Evaluation	25
S2.3.1 Geometric Mean Fold Error (GMFE)	25
S2.3.2 Mean Relative Deviation (MRD)	27
S2.4 Local Sensitivity Analysis	29
S2.4.1 Mathematical Implementation	29
S2.4.2 Results of the Sensitivity Analysis	30
S3 PBPK Drug–Drug Interaction (DDI) Modeling	31
S3.1 Clinical DDI Studies	31
S3.2 DDI Model Evaluation	33
S3.2.1 Plasma Profiles of Enzyme-mediated DDIs (Semilogarithmic Scale)	33
S3.2.2 Plasma Profiles of pH-Dependent DDIs (Semilogarithmic Scale)	34
S3.2.3 Geometric Mean Fold Error (GMFE)	35
S4 PBPK Drug–Food Interaction (DFI) Modeling	36
S4.1 DFI Model Building	36
S4.1.1 Clinical DFI Studies	36
S4.2 DFI Model Evaluation	37
S4.2.1 Plasma Profiles And Goodness-of-Fit Plot of DFIs	37
S4.2.2 Geometric Mean Fold Error (GMFE)	39
S5 Model Application & Others	40
S5.1 Exposure Simulations for Model-Informed Precision Dosing	40
S5.1.1 Plasma Profiles of Simulated Single DDI Scenarios	43
S5.1.2 Plasma Profiles of Simulated Multiple DDI Scenarios	49
S5.2 CYP3A4 Autoinhibition	50
S5.3 Pharmacokinetic Parameters: Absolute Bioavailability, Fraction Absorbed, Fraction Metabolized, Fraction Escaping Gut Wall and Hepatic Elimination	50
References	51

S1 PBPK Model Building

S1.1 Assignment to Training and Test Dataset

Plasma profiles from the literature were divided into a training and a test dataset for model building (5 profiles) and evaluation (58 profiles), respectively. The plasma profiles were allocated to the training and test datasets using a non-randomized strategy to ensure comprehensive and varied data for model building. This data assortment encapsulated a wide spectrum of dosing ranges and an array of dosing regimens. In the process, we strived to maximize the number of plasma profiles for model evaluation. We specifically selected datasets with dense sampling intervals spanning a prolonged investigation period for the training dataset. An overview of all clinical studies is presented in [Table S1](#), [Table S7](#) and [Table S9](#).

S1.2 Virtual Individuals

Virtual “mean individuals” were created for each study based on mean or mode of age, sex, body weight, height, body mass index and ethnicity from the corresponding study reports. If demographic information was not provided for a study, either a 30-year-old white American male with a body weight of 80 kg and height of 1.78 m for healthy volunteers or a 64-year-old white American male with body weight of 82 kg and height of 1.75 m for cancer patients were used according to the third National Health and Nutrition Examination Survey (NHANES) database [1].

For each compartment expressing cytochrome P450 3A4 (CYP3A4), we applied uniform parameter values for the Michaelis-Menten kinetics—specifically, the Michaelis constant (K_m) and the catalytic constant (k_{cat})—to model CYP3A4-mediated metabolism. In general, enzyme and transporter expressions in different tissues were implemented according to the PK-Sim® expression database.

As CML is more prevalent in men, with an average diagnosis age of 64 years, a virtual 64-year-old European male individual was used for the dosing simulations [2]. Default values for body weight (64 kg) and height (1.70 m) were derived from the International Commission on Radiological Protection (ICRP) database [3].

S1.3 Virtual Populations

Virtual populations of 100 individuals were generated based on the respective study population demographics. Depending on the ethnicity and demographic characteristics, virtual individuals were varied by the implemented algorithm in PK-Sim® within the limits of the NHANES database for white Americans, the ICRP database for Europeans and the integrated database for Japanese population [4]. The corresponding algorithms for the generation of virtual populations have been reported by Willmann and coworkers [5].

For the studies CA180016 [6] and CA180032 [6] as well as the studies by Christopher et al. 2008 (a) [7], Vaidhyanathan et al. 2019 [8] and Vargas et al. 2016 [9] an age range of 20 to 50 years for healthy volunteers was assumed, while for the studies CA180005 and CA180009 as well as the studies by Christopher et al. 2008 (b) [7] and Luo et al. 2008 [10] an age range of 20 to 80 years for cancer patients was used since information about the study populations were not available. System-dependent parameters including reference concentrations and enzyme expression variabilities are listed in [Table S2](#).

S1.4 Clinical Studies

Table S1: Overview of clinical study data from the literature used for model development.

Clinical study	Dose [mg]	Route	N	Females [%]	Age [years]	Weight [kg]	BMI [kg/m ²]	Gastric pH	Fasted/Fed	Health Status	Dataset
Bioequivalence study [13]	140	po, tab, sd	122	-	- (18–48)	-	24.1 (-) ^a	2.0 ^b	fasted	healthy	training
Christopher 2008 (a) [7]	100	po, sol, sd	8	0	-	-	-	2.0 ^b	- ^c	healthy	test
Furlong 2012 [14]	100	po, tab, sd	20	-	-	-	-	2.0 ^b	fasted	healthy	training
Study CA180016 [6]	100	po, tab, sd	18	-	-	-	-	2.0 ^b	- ^c	healthy	test
Vaidhyanathan 2018 (a) [8]	70	po, tab, sd	64	-	-	-	-	2.0 ^b	fasted	healthy	training
Vaidhyanathan 2018 (b) [8]	100	po, PFOS, sd	-	-	-	-	-	2.0 ^b	fasted	healthy	test
Vaidhyanathan 2018 (c) [8]	100	po, dispersed tab, sd	-	-	-	-	-	2.0 ^b	fasted	healthy	test
Vaidhyanathan 2018 (d) [8]	100	po, tab, sd	-	-	-	-	-	2.0 ^b	fasted	healthy	test
Vargas 2016 [9]	100	po, tab, sd	-	-	28 (-) ^a	65 (-) ^a	22.7 (-) ^a	2.0 ^b	fasted	healthy	test
Araujo 2012 [15]	100	po, tab, qd, md	46	0	65 (48–83) ^{d,e}	-	-	2.0 ^b	- ^c	cancer	test
Christopher 2008 (b) [7]	180	po, tab, sd	3	-	-	-	-	2.0 ^b	- ^c	cancer	test
Demetri 2009 (a) [16]	35	po, tab, bid, md (B5D)	4	39.4 ^g	56 (32–81) ^{d,g}	-	-	2.0 ^b	fasted	cancer	test
Demetri 2009 (b) [16]	50	po, tab, bid, md (B5D)	3	39.4 ^g	56 (32–81) ^{d,g}	-	-	2.0 ^b	fasted	cancer	test
Demetri 2009 (c) [16]	70	po, tab, bid, md (B5D)	4	39.4 ^g	56 (32–81) ^{d,g}	-	-	2.0 ^b	fasted	cancer	test
Demetri 2009 (d) [16]	70	po, tab, bid, md (B7D)	3	47.1 ^g	59 (31–82) ^{d,g,e}	-	-	2.0 ^b	fasted	cancer	test
Demetri 2009 (e) [16]	90	po, tab, bid, md (B5D)	5	39.4 ^g	56 (32–81) ^{d,g}	-	-	2.0 ^b	fasted	cancer	test
Demetri 2009 (f) [16]	90	po, tab, bid, md (B7D)	5	47.1 ^g	59 (31–82) ^{d,g,e}	-	-	2.0 ^b	fasted	cancer	test
Demetri 2009 (g) [16]	100	po, tab, bid, md (B7D)	7	47.1 ^g	59 (31–82) ^{d,g,e}	-	-	2.0 ^b	fasted	cancer	test
Demetri 2009 (h) [16]	120	po, tab, bid, md (B5D)	7	39.4 ^g	56 (32–81) ^{d,g}	-	-	2.0 ^b	fasted	cancer	test
Demetri 2009 (i) [16]	120	po, tab, bid, md (B7D)	1	47.1 ^g	59 (31–82) ^{d,g,e}	-	-	2.0 ^b	fasted	cancer	test
Demetri 2009 (j) [16]	160	po, tab, bid, md (B5D)	1	39.4 ^g	56 (32–81) ^{d,g}	-	-	2.0 ^b	fasted	cancer	test
Luo 2008 [10]	90	po, tab, bid, md	-	-	-	-	-	2.0 ^b	- ^c	cancer	test
Study CA180002 (a) [6]	15	po, tab, qd, md (Q5D)	3	-	56 (15–79) ^{d,f}	-	-	2.0 ^b	fasted	cancer	test
Study CA180002 (b) [6]	25	po, tab, bid, md (B5D)	3	-	56 (15–79) ^{d,f}	-	-	2.0 ^b	fasted	cancer	test
Study CA180002 (c) [6]	30	po, tab, qd, md (Q5D)	3	-	56 (15–79) ^{d,f}	-	-	2.0 ^b	fasted	cancer	test
Study CA180002 (d) [6]	35	po, tab, bid, md (B5D)	8	-	56 (15–79) ^{d,f}	-	-	2.0 ^b	fasted	cancer	test
Study CA180002 (e) [6]	50	po, tab, bid, md (B5D)	3–5	-	56 (15–79) ^{d,f}	-	-	2.0 ^b	fasted	cancer	test
Study CA180002 (f) [6]	50	po, tab, bid, md (B7D)	6–8	-	56 (15–79) ^{d,f}	-	-	2.0 ^b	fasted	cancer	test
Study CA180002 (g) [6]	50	po, tab, qd, md (Q5D)	3	-	56 (15–79) ^{d,f}	-	-	2.0 ^b	fasted	cancer	test

–: unknown, **B5D**: five consecutive days bid dosing followed by two nontreatment days, **B7D**: continuous bid dosing, **bid**: twice a day, **BMI**: body mass index, **md**: multiple dose, **N**: number of participants, **PFOS**: powder for oral suspension, **po**: peroral, **Q5D**: five consecutive days once daily dosing followed by two nontreatment days, **qd**: once a day, **sd**: single dose, **sol**: solution, **tab**: tablet

^a Mean (range)

^b Default value in PK-Sim[®] for fasted state [11]

^c A light-fat breakfast or fasted state was assumed

^d Median (range)

^e Maximum age of the NHANES database is 81 years [1]

^f Values refer to the whole study population

^g Values refer to the whole study population (stratified by regimen)

^h Assumed (based on the reported age range of 12–17 [12])

Table S1: Overview of clinical study data from the literature used for model development (*continued*).

Clinical study	Dose [mg]	Route	N	Females [%]	Age [years]	Weight [kg]	BMI [kg/m ²]	Gastric pH	Fasted/ Fed	Health Status	Dataset
Study CA180002 (h) [6]	70	po, tab, bid, md (B5D)	6–9	-	56 (15–79) ^{d,f}	-	-	2.0 ^b	fasted	cancer	test
Study CA180002 (i) [6]	70	po, tab, bid, md (B7D)	11–14	-	56 (15–79) ^{d,f}	-	-	2.0 ^b	fasted	cancer	test
Study CA180002 (j) [6]	75	po, tab, qd, md (Q5D)	3	-	56 (15–79) ^{d,f}	-	-	2.0 ^b	fasted	cancer	test
Study CA180002 (k) [6]	90	po, tab, bid, md (B7D)	11	-	56 (15–79) ^{d,f}	-	-	2.0 ^b	fasted	cancer	test
Study CA180002 (l) [6]	105	po, tab, qd, md (Q5D)	3	-	56 (15–79) ^{d,f}	-	-	2.0 ^b	fasted	cancer	test
Study CA180002 (m) [6]	120	po, tab, bid, md (B7D)	7	-	56 (15–79) ^{d,f}	-	-	2.0 ^b	fasted	cancer	test
Study CA180002 (n) [6]	140	po, tab, qd, md (Q5D)	3	-	56 (15–79) ^{d,f}	-	-	2.0 ^b	fasted	cancer	test
Study CA180002 (o) [6]	180	po, tab, qd, md (Q5D)	3	-	56 (15–79) ^{d,f}	-	-	2.0 ^b	fasted	cancer	test
Study CA180005 (a) [6]	70	po, tab, bid, md (B5D)	-	-	-	-	-	2.0 ^b	- ^c	cancer	test
Study CA180005 (b) [6]	70	po, tab, bid, md (B7D)	-	-	-	-	-	2.0 ^b	- ^c	cancer	test
Takahashi 2011 (a) [17]	100	po, tab, qd, md	9	77.8	58 (33–65) ^d	-	-	2.0 ^b	fed ^c	cancer	test
Takahashi 2011 (b) [17]	150	po, tab, qd, md	3	33.3	55 (39–63) ^d	-	-	2.0 ^b	fed ^c	cancer	test
Takahashi 2011 (c) [17]	200	po, tab, qd, md	4	75.0	47.5 (33–53) ^d	-	-	2.0 ^b	fed ^c	cancer	test
Zwaan 2013 (a) [12]	100	po, tab, qd, sd	9	-	15 ^h (12–17)	-	-	2.0 ^b	- ^c	cancer	test
Zwaan 2013 (b) [12]	140	po, tab, qd, sd	8	-	15 ^h (12–17)	-	-	2.0 ^b	- ^c	cancer	test
Zwaan 2013 (c) [12]	170	po, tab, qd, sd	9	-	15 ^h (12–17)	-	-	2.0 ^b	- ^c	cancer	test
Zwaan 2013 (d) [12]	200	po, tab, qd, sd	2	-	15 ^h (12–17)	-	-	2.0 ^b	- ^c	cancer	test

–: unknown, **B5D**: five consecutive days bid dosing followed by two nontreatment days, **B7D**: continuous bid dosing, **bid**: twice a day, **BMI**: body mass index, **md**: multiple dose, **N**: number of participants, **PFOS**: powder for oral suspension, **po**: peroral, **Q5D**: five consecutive days once daily dosing followed by two nontreatment days, **qd**: once a day, **sd**: single dose, **sol**: solution, **tab**: tablet

^a Mean (range)

^b Default value in PK-Sim[®] for fasted state [11]

^c A light-fat breakfast or fasted state was assumed

^d Median (range)

^e Maximum age of the NHANES database is 81 years [1]

^f Values refer to the whole study population

^g Values refer to the whole study population (stratified by regimen)

^h Assumed (based on the reported age range of 12–17 [12])

S1.5 System-dependent Parameters

Table S2: System-dependent parameters and expression of relevant enzymes, transporters and processes.

Enzyme/Transporter/ Processes	Mean ref. conc. [$\mu\text{mol/L}$] ^a	GeoSD of the ref. conc. ^b	Relative expression in different organs ^c	Half-life liver [hours]	Half-life intestine [hours]
AADAC	1.00 ^d [18]	1.40 ^e	RT-PCR [26]	36	23
CYP1A2	1.80 [27]	1.63 (liver) [28]	RT-PCR [29]	39	23
CYP2A6	2.72 [27]	1.40 ^e	RT-PCR [29]	26	23
CYP2B6	1.56 [27]	1.40 ^e	RT-PCR [29]	32	23
CYP2C19	0.76 [27]	1.79 (liver) [28]	RT-PCR [29]	26	23
CYP2C8	2.56 [27]	2.05 (liver) [28]	RT-PCR [29]	23	23
CYP2D6	0.40 [27]	2.49 [28]	RT-PCR [29]	51	23
CYP3A4	4.32 [27]	1.18/1.46 (liver/duodenum) [28]	RT-PCR [29]	36 [30]	23 [31]
CYP3A5	0.04 [18]	1.40 ^e	RT-PCR [29]	36	23
EPHX1	1.00 ^d [18]	1.40 ^e	RT-PCR [26]	36	23
FMO3	1.00 ^d	1.00 [18]	RT-PCR [26]	-	23
PON3	1.00 ^d	1.40 ^e	Array [29]	36	23
UGT1A1	1.00 ^d	1.40 ^e	RT-PCR [26]	36	23
UGT1A3	1.00 ^d	1.40 ^e	RT-PCR [26]	36	23
UGT1A4	2.32 ^f	1.07 [28]	RT-PCR [26]	36	23
UGT2B7 ^g	2.78 ^f [32]	1.60 (liver) [28]	EST [33]	36	23
Unspecific liver lactonization	1.00 ^d	1.40 ^e	Liver only	36	23
Unspecific plasma hydrolysis	1.00 ^d	1.40 ^e	Plasma only	36	23
BCRP	1.00 ^d	1.35 [34]	RT-PCR ^h [35]	36	23
MRP2	1.00 ^d	1.49 [36]	Array [37]	36	23
OATP1B1	0.07 ^{i,j} [23]	1.54 [23]	RT-PCR [35]	36	-
OATP1B3	1.00 ^d [18]	1.54 [23]	Array [37]	36	23
P-gp	1.41 ^{optimized}	1.60 [23]	RT-PCR ^k [35]	36	23
Unspecific liver influx	1.00 ^d	1.40 ^e	Liver only	36	23
Unspecific hepatic clearance	-	-	-	-	-
Chemical hydrolysis	1.00	-	Ubiquitous	36	23

AADAC: arylacetamide deacetylase, **BCRP**: breast cancer resistance protein, **CYP**: cytochrome P450, **EST**: expressed sequence tag, **EPHX1**: epoxide hydroxylase 1, **FMO**: flavin-containing monooxygenase, **GeoSD**: geometric standard deviation, **MRP2**: multidrug resistance-associated protein 2, **OATP**: organic anion transporting polypeptide, **P-gp**: P-glycoprotein, **PON3**: paraoxonase 3, **ref. conc.**: reference concentration, **RT-PCR**: reverse transcription polymerase chain reaction, **UGT**: UDP-glucuronosyltransferase

^a $\mu\text{mol protein/L}$ in the tissue of highest expression

^b Geometric standard deviation of the reference concentration

^c In the different organs (PK-Sim[®] expression database profile)

^d If no information was available, the mean ref. conc. was set to 1.0 $\mu\text{mol/L}$ and the catalytic rate constant (k_{cat}) was optimized according to [18]

^e If no information was available a moderate variability of 35% CV was assumed ($= 1.40$ GSD)

^f Calculated from protein per mg microsomal protein $\times 40.0$ mg microsomal protein per g liver [19]

^g UGT2B7 enzyme for metabolism of fluconazole and simvastatin was implemented according to the respective publication [20, 21]

^h With relative expression in blood cells set to 0.3046 [22]

ⁱ Calculated from transporter per mg membrane protein $\times 37.0$ mg membrane protein per g liver [23]

^j Differences in the implementation of the OATP1B1 ref. conc. in the rifampicin [24], simvastatin [21] and erythromycin [25] PBPK model were compensated by using the concentration of 0.07 $\mu\text{mol/L}$ [23] and optimizing the k_{cat}

^k With relative expression in intestinal mucosa increased by factor 3.57 [24]

Table S3: Relative enzymes and transporters expression in organs and tissues implemented in the dasatinib PBPK model [%]

	CYP2C8	CYP3A4	OATP1B1	OATP1B3
Data source	RT-PCR [29]	RT-PCR [29]	RT-PCR [35]	Array [37]
Blood cells	0	0	0	0
Plasma	0	0	-	-
Bone	0	0	0	3
Brain	0	0	0	3
Fat	0	0	0	0
Gonads	1	0	1	4
Heart	0	0	0	6
Kidney	0	1	0	2
Liver periportal	100	100	100	100
Liver pericentral	100	100	100	100
Lung	0	0	0	2
Muscle	0	0	0	2
Pancreas	0	0	0	1
Skin	0	0	0	1
Spleen	0	0	0	1
Duodenum mucosa	0	7	0	2
Upper jejunum mucosa	0	7	0	2
Lower jejunum mucosa	0	7	0	2
Upper ileum mucosa	0	7	0	2
Lower ileum mucosa	0	7	0	2
Cecum mucosa	0	0	0	0
Colon ascendens mucosa	0	0	0	1
Colon transversum mucosa	0	0	0	1
Colon descendens mucosa	0	0	0	1
Colon sigmoid mucosa	0	0	0	1
Rectum mucosa	0	0	0	0
Stomach non-mucosal tissue	0	0	0	1
Small intestine non-mucosal tissue	0	7	0	2
Large intestine non-mucosal tissue	0	0	0	1
Stomach lumen	0	0	-	-
Duodenum lumen	0	0	-	-
Upper jejunum lumen	0	0	-	-
Lower jejunum lumen	0	0	-	-
Upper ileum lumen	0	0	-	-
Lower ileum lumen	0	0	-	-
Cecum lumen	0	0	-	-
Colon ascendens lumen	0	0	-	-
Colon transversum lumen	0	0	-	-
Colon descendens lumen	0	0	-	-
Colon sigmoid lumen	0	0	-	-
Rectum lumen	0	0	-	-

Array: microarray expression profile, **CYP:** cytochrome P450, **OATP:** organic anion transporting polypeptide

S1.6 Drug-dependent Parameter Table

Table S4: Drug-dependent parameters for dasatinib.

Parameter	Value [95% CI]	Unit	Source	Literature	Reference	Description
MW	488.01	g/mol	Literature	488.01	[39]	Molecular weight
pK _a (base)	3.10, 6.80	-	Literature	3.10, 6.80	[40]	Acid dissociation constant
pK _a (acid)	10.80	-	Literature	10.80	[40]	Acid dissociation constant
Solubility (pH 4.0)	0.04	mg/ml	Literature	0.04	[41]	Solubility
logP	3.59 [3.47, 3.71]	-	Optimized	2.71–4.01	[39, 40]	Lipophilicity
f _u	4.00	%	Literature	4.00	[42]	Fraction unbound
CYP3A4 K _m → M20 ^a	6.00	μmol/l	Literature	6.00	[43]	Michaelis-Menten constant
CYP3A4 k _{cat} → M20 ^a	58.38 [46.19, 70.57]	1/min	Optimized	-	-	Catalytic rate constant
CYP3A4 K _i	9.00	μmol/l	Literature	9.00	[44]	Inhibition Constant
CYP3A4 k _{inact}	0.02	1/min	Literature	0.02	[44]	Maximum rate of inactivation
CYP2C8 K _i	3.60	μmol/l	Literature	3.60	[44]	Dissociation Constant
OATP1B1 K _i	2.33	μmol/l	Literature	2.33	[45]	Dissociation Constant
OATP1B3 K _i	2.75	μmol/l	Literature	2.75	[45]	Dissociation Constant
Unspecific hepatic clearance	5.62 [3.17, 8.07]	1/min	Optimized	-	-	Elimination from plasma (first-order process in the liver)
GET (fasted)	15.00	min	Literature	15.00	[46]	Gastric emptying time
GET (fed)	103.44	min	Optimized	45–120	[47]	Gastric emptying time
GET (with Rabeprazole)	60.13	min	Optimized	-	-	Gastric emptying time
GET (with Maalox [®])	31.27	min	Optimized	-	-	Gastric emptying time
GFR fraction	1.00	-	Assumed	-	-	Fraction of filtered drug in the urine
EHC continuous fraction	1.00	-	Assumed	-	-	Fraction of bile continually released
Partition coefficients	Diverse ^b	-	Calculated	Schmitt	[48]	Cell to plasma partition coefficients
Cellular permeability	Diverse ^b	cm/min	Calculated	PK-Sim Standard	[46]	Permeability into the cellular space
Intestinal permeability	1.22·10 ⁻⁶ [6.42·10 ⁻⁷ , 1.80·10 ⁻⁶]	cm/s	Optimized	-	-	Transcellular intestinal permeability
Density	1.41	g/cm ³	Literature	1.41	[49]	Density
Aqueous diffusion coefficient	2.67·10 ⁻⁴	cm ² /min	Calculated	2.67·10 ⁻⁴	-	Aqueous diffusion coefficient
Particle dissolution radius (Bin1)	11.46	μm	Calculated	11.46 ^c	[8]	Mean Particle Radius
Particle dissolution radius (Bin2)	38.07	μm	Calculated	38.07 ^c	[8]	Mean Particle Radius
Particle dissolution radius (Bin3)	67.86	μm	Calculated	67.86 ^c	[8]	Mean Particle Radius

CI: confidence interval, CYP: cytochrome P450, EHC: enterohepatic circulation, GFR: glomerular filtration rate, OATP: organic anion transporting polypeptide

^a Metabolite was not included in the PBPK model

^b Values differ across the organs

^c Calculated according to [38]

S2 PBPK Model Evaluation

S2.1 Healthy Volunteers

S2.1.1 Plasma Profiles (Linear Scale)

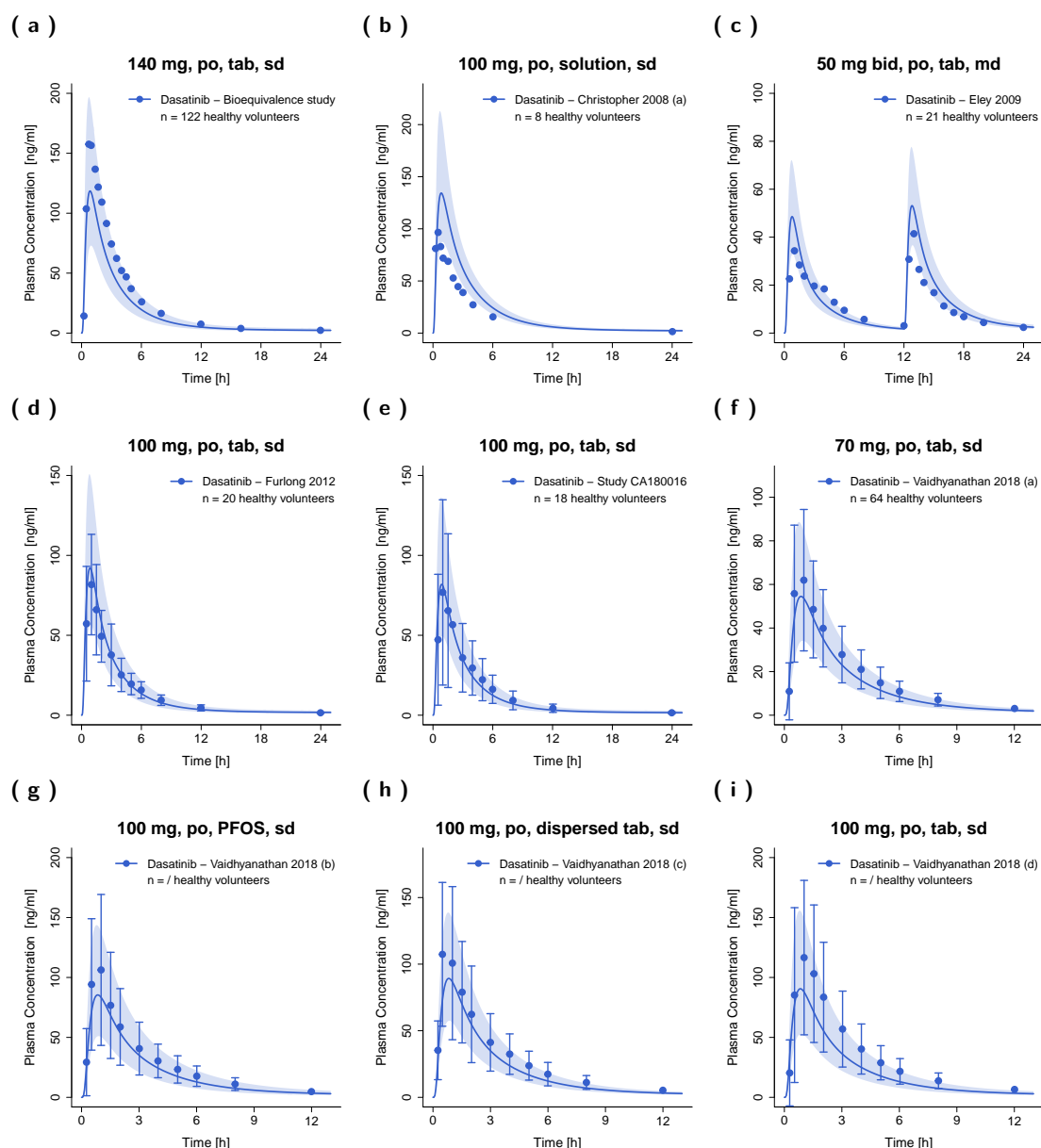


Figure S1: Predicted and observed dasatinib plasma concentration–time profiles in healthy volunteers on a linear scale. Solid lines show predicted geometric mean concentration–time profiles with ribbons illustrating the corresponding geometric standard deviation of the population simulations (n=100). Points demonstrate the mean observed data with the corresponding standard deviation of dasatinib (if depicted in the respective publication). /: no information available, **bid**: twice a day, **md**: multiple dose, **n**: number of participants, **PFOS**: powder for oral suspension, **po**: peroral, **qd**: once a day, **sd**: single dose, **tab**: tablet.

(j)

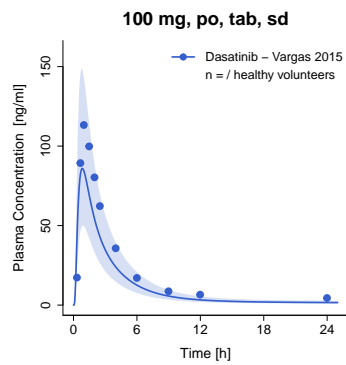


Figure S1: (*continued*) Predicted and observed dasatinib plasma concentration–time profiles in healthy volunteers on a linear scale. Solid lines show predicted geometric mean concentration–time profiles with ribbons illustrating the corresponding geometric standard deviation of the population simulations (n=100). Points demonstrate the mean observed data with the corresponding standard deviation of dasatinib (if depicted in the respective publication). /: no information available, **bid**: twice a day, **md**: multiple dose, **n**: number of participants, **PFOS**: powder for oral suspension, **po**: peroral, **qd**: once a day, **sd**: single dose, **tab**: tablet.

S2.1.2 Plasma Profiles (Semilogarithmic Scale)

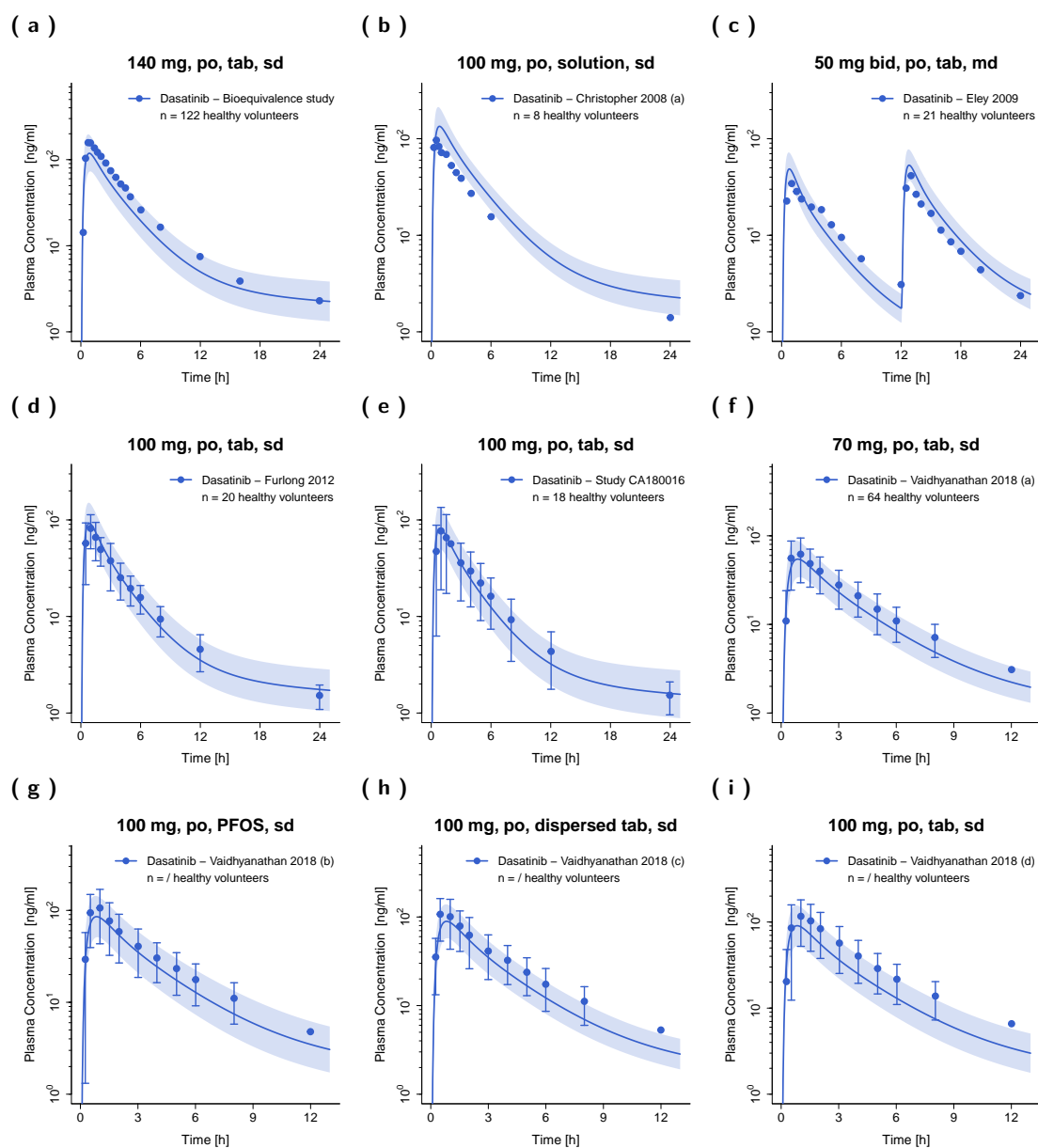


Figure S2: Predicted and observed dasatinib plasma concentration-time profiles in healthy volunteers on a semilogarithmic scale. Solid lines show predicted geometric mean concentration-time profiles with ribbons illustrating the corresponding geometric standard deviation of the population simulations (n=100). Points demonstrate the mean observed data with the corresponding standard deviation of dasatinib (if depicted in the respective publication). /: no information available, **bid**: twice a day, **md**: multiple dose, **n**: number of participants, **PFOS**: powder for oral suspension, **po**: peroral, **qd**: once a day, **sd**: single dose, **tab**: tablet.

(j)

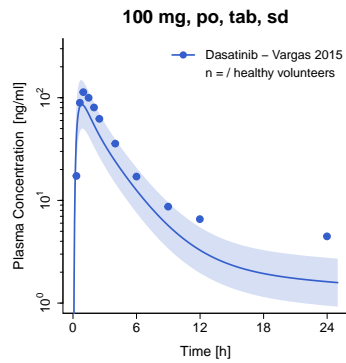


Figure S2: (continued) Predicted and observed dasatinib plasma concentration–time profiles in healthy volunteers on a semilogarithmic scale. Solid lines show predicted geometric mean concentration–time profiles with ribbons illustrating the corresponding geometric standard deviation of the population simulations ($n=100$). Points demonstrate the mean observed data with the corresponding standard deviation of dasatinib (if depicted in the respective publication). /: no information available, **bid**: twice a day, **md**: multiple dose, **n**: number of participants, **PFOS**: powder for oral suspension, **po**: peroral, **qd**: once a day, **sd**: single dose, **tab**: tablet.

S2.2 Cancer Patients

S2.2.1 Plasma Profiles (Linear Scale)

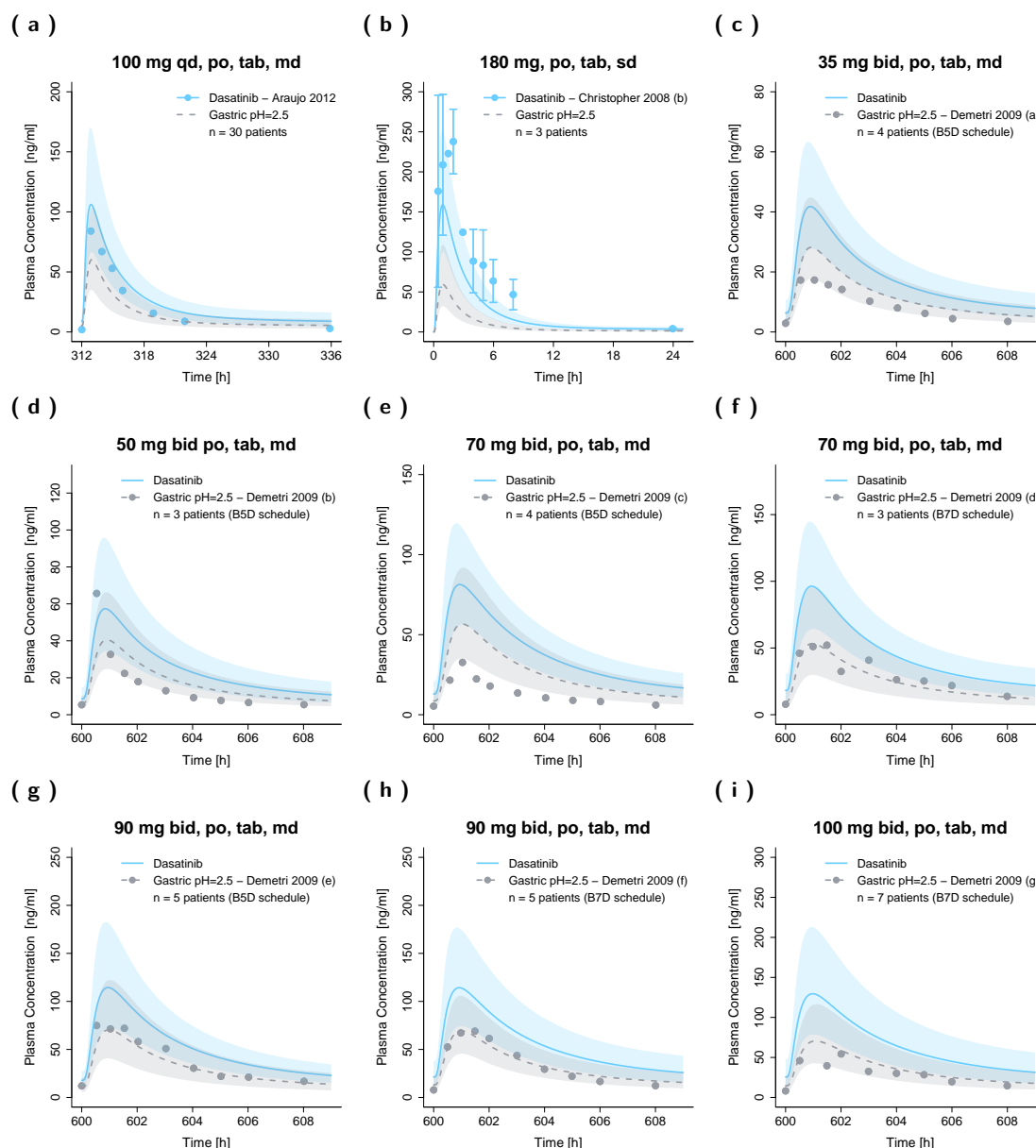


Figure S3: Predicted and observed dasatinib plasma concentration–time profiles in cancer patients on a linear scale. Solid and dashed lines show predicted geometric mean concentration–time profiles with gastric pH of 2.0 and 2.5, respectively, with ribbons illustrating the corresponding geometric standard deviation of the population simulations (n=100). Points demonstrate the mean observed data with the corresponding standard deviation of dasatinib (if depicted in the respective publication). /: no information available, **B5D**: five consecutive days bid dosing followed by two nontreatment days, **B7D**: seven consecutive days bid dosing, **bid**: twice a day, **md**: multiple dose, **n**: number of participants, **po**: peroral, **Q5D**: five consecutive days once daily dosing followed by two nontreatment days, **qd**: once a day, **sd**: single dose, **tab**: tablet.

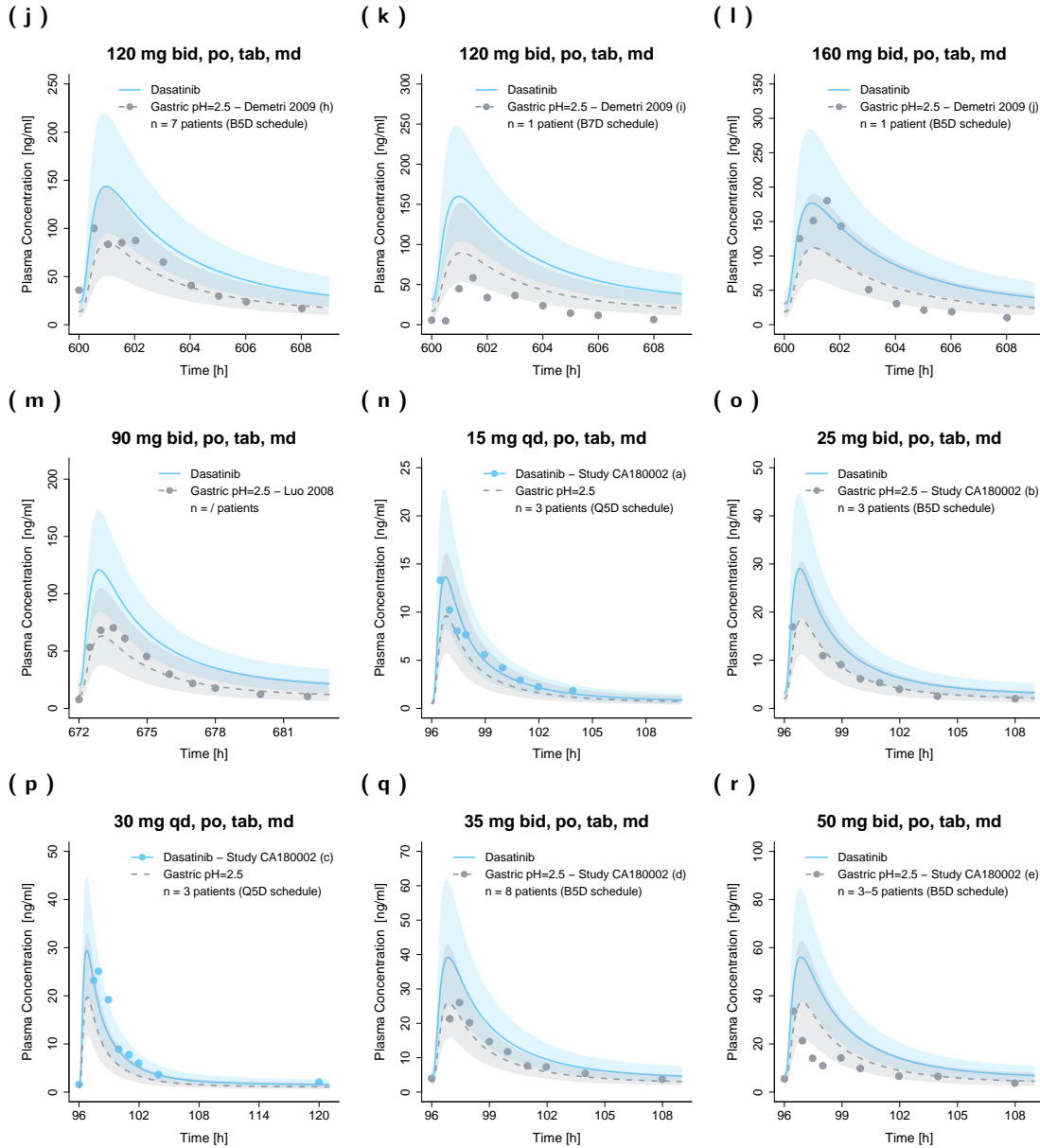


Figure S3: (continued) Predicted and observed dasatinib plasma concentration–time profiles in cancer patients on a linear scale. Solid and dashed lines show predicted geometric mean concentration–time profiles with gastric pH of 2.0 and 2.5, respectively, with ribbons illustrating the corresponding geometric standard deviation of the population simulations (n=100). Points demonstrate the mean observed data with the corresponding standard deviation of dasatinib (if depicted in the respective publication). /: no information available, **B5D**: five consecutive days bid dosing followed by two nontreatment days, **B7D**: seven consecutive days bid dosing, **bid**: twice a day, **md**: multiple dose, **n**: number of participants, **po**: peroral, **Q5D**: five consecutive days once daily dosing followed by two nontreatment days, **qd**: once a day, **sd**: single dose, **tab**: tablet.

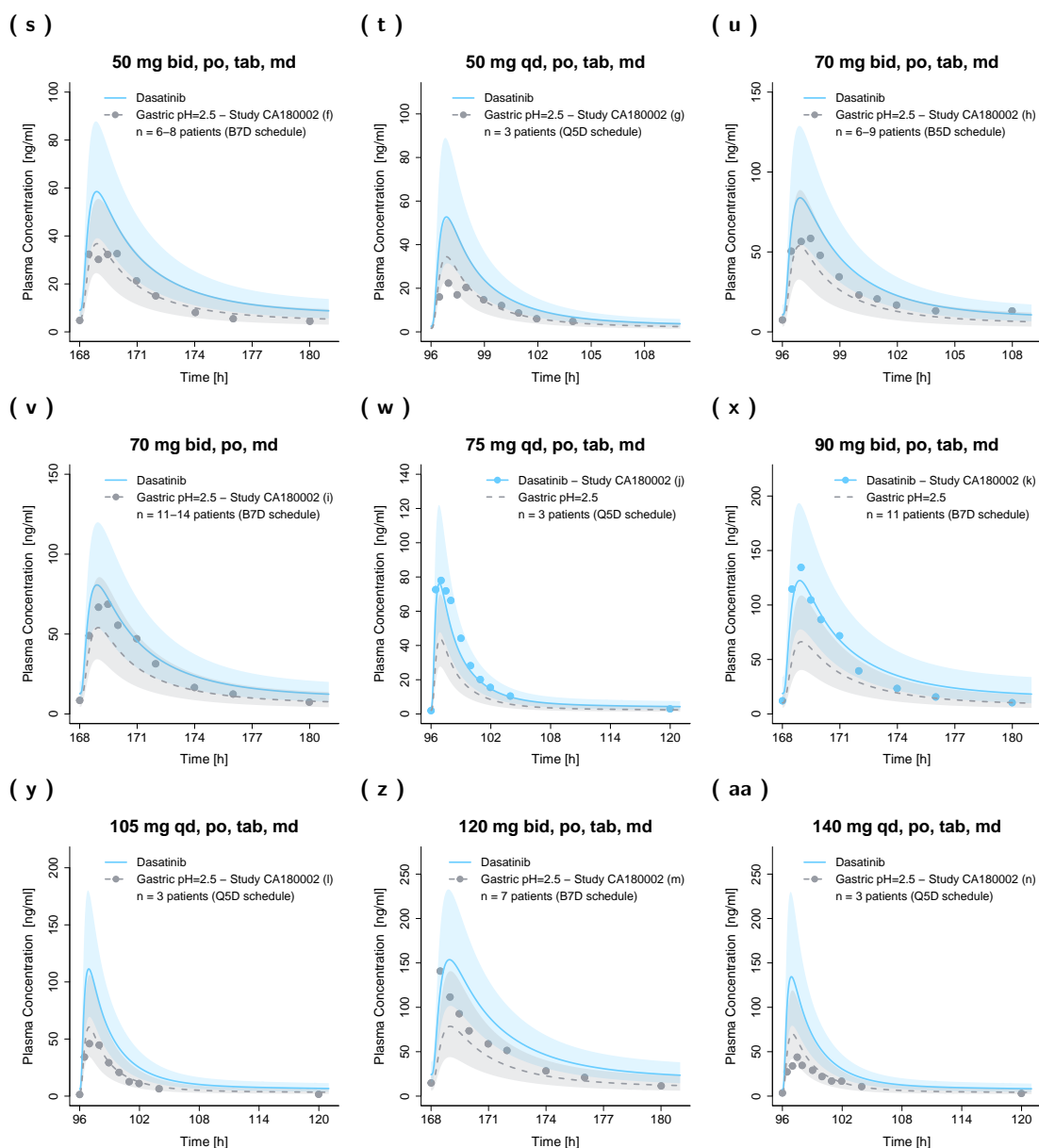


Figure S3: (continued) Predicted and observed dasatinib plasma concentration–time profiles in cancer patients on a linear scale. Solid and dashed lines show predicted geometric mean concentration–time profiles with gastric pH of 2.0 and 2.5, respectively, with ribbons illustrating the corresponding geometric standard deviation of the population simulations (n=100). Points demonstrate the mean observed data with the corresponding standard deviation of dasatinib (if depicted in the respective publication). /: no information available, **B5D**: five consecutive days bid dosing followed by two nontreatment days, **B7D**: seven consecutive days bid dosing, **bid**: twice a day, **md**: multiple dose, **n**: number of participants, **po**: peroral, **Q5D**: five consecutive days once daily dosing followed by two nontreatment days, **qd**: once a day, **sd**: single dose, **tab**: tablet.

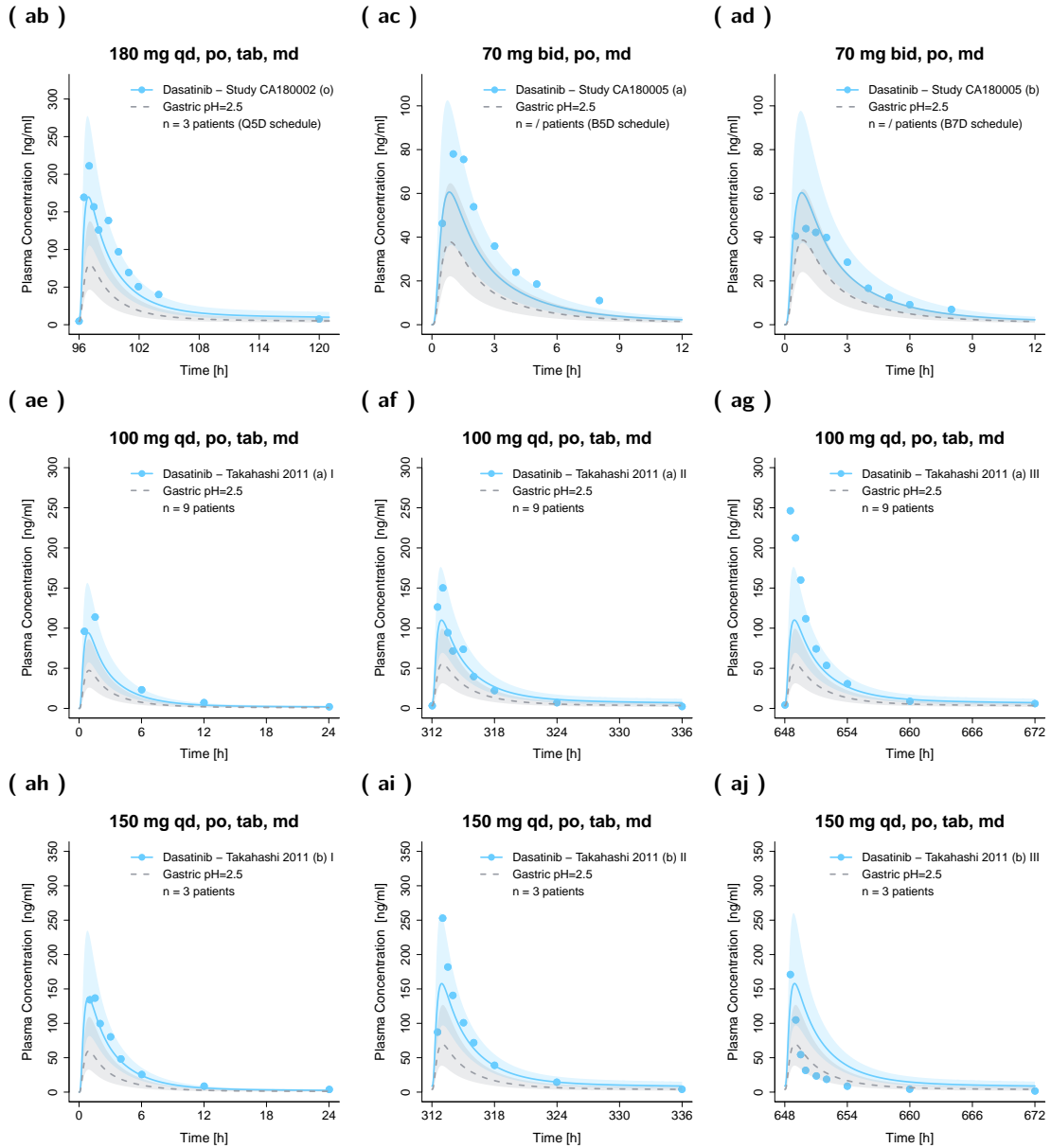


Figure S3: (continued) Predicted and observed dasatinib plasma concentration–time profiles in cancer patients on a linear scale. Solid and dashed lines show predicted geometric mean concentration–time profiles with gastric pH of 2.0 and 2.5, respectively, with ribbons illustrating the corresponding geometric standard deviation of the population simulations ($n=100$). Points demonstrate the mean observed data with the corresponding standard deviation of dasatinib (if depicted in the respective publication). /: no information available, **B5D**: five consecutive days bid dosing followed by two nontreatment days, **B7D**: seven consecutive days bid dosing, **bid**: twice a day, **md**: multiple dose, **n**: number of participants, **po**: peroral, **Q5D**: five consecutive days once daily dosing followed by two nontreatment days, **qd**: once a day, **sd**: single dose, **tab**: tablet.

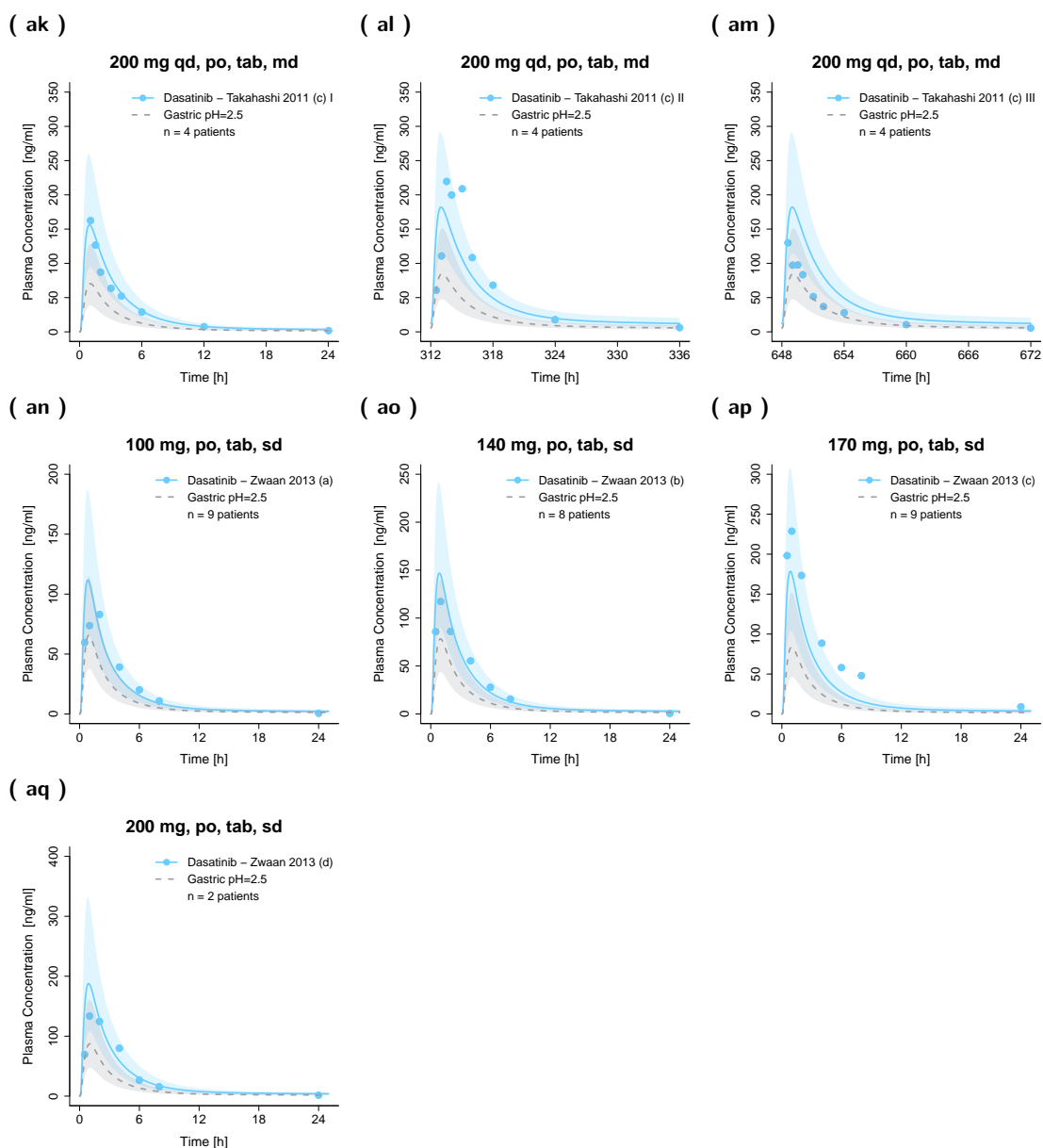


Figure S3: (continued) Predicted and observed dasatinib plasma concentration–time profiles in cancer patients on a linear scale. Solid and dashed lines show predicted geometric mean concentration–time profiles with gastric pH of 2.0 and 2.5, respectively, with ribbons illustrating the corresponding geometric standard deviation of the population simulations ($n=100$). Points demonstrate the mean observed data with the corresponding standard deviation of dasatinib (if depicted in the respective publication). /: no information available, **B5D**: five consecutive days bid dosing followed by two nontreatment days, **B7D**: seven consecutive days bid dosing, **bid**: twice a day, **md**: multiple dose, **n**: number of participants, **po**: peroral, **Q5D**: five consecutive days once daily dosing followed by two nontreatment days, **qd**: once a day, **sd**: single dose, **tab**: tablet.

S2.2.2 Plasma Profiles (Semilogarithmic Scale)

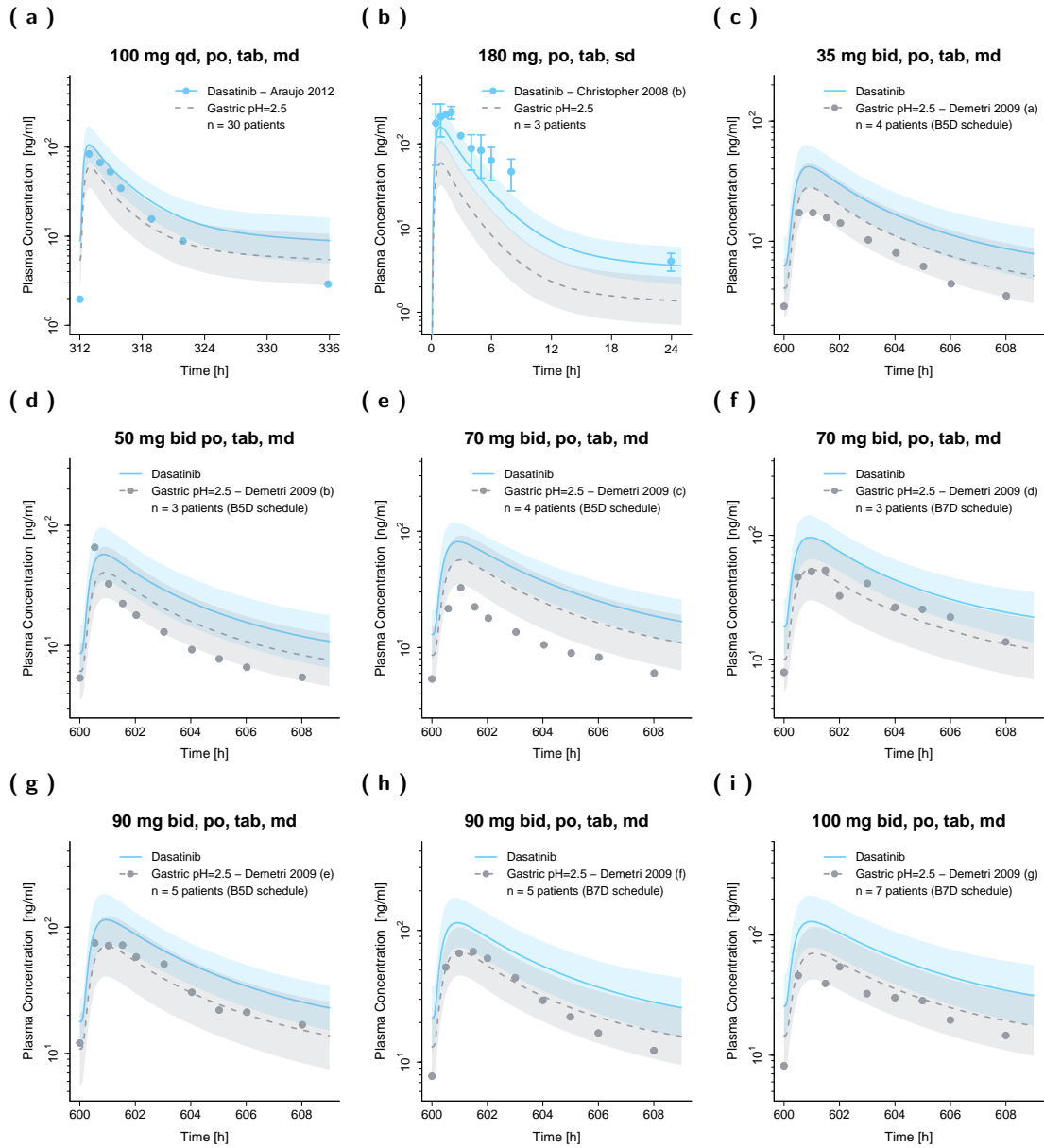


Figure S4: Predicted and observed dasatinib plasma concentration–time profiles in cancer patients on a semilogarithmic scale. Solid and dashed lines show predicted geometric mean concentration–time profiles with gastric pH of 2.0 and 2.5, respectively, with ribbons illustrating the corresponding geometric standard deviation of the population simulations ($n=100$). Points demonstrate the mean observed data with the corresponding standard deviation of dasatinib (if depicted in the respective publication). /: no information available, **B5D**: five consecutive days bid dosing followed by two nontreatment days, **B7D**: seven consecutive days bid dosing, **bid**: twice a day, **md**: multiple dose, **n**: number of participants, **po**: peroral, **Q5D**: five consecutive days once daily dosing followed by two nontreatment days, **qd**: once a day, **sd**: single dose, **tab**: tablet.

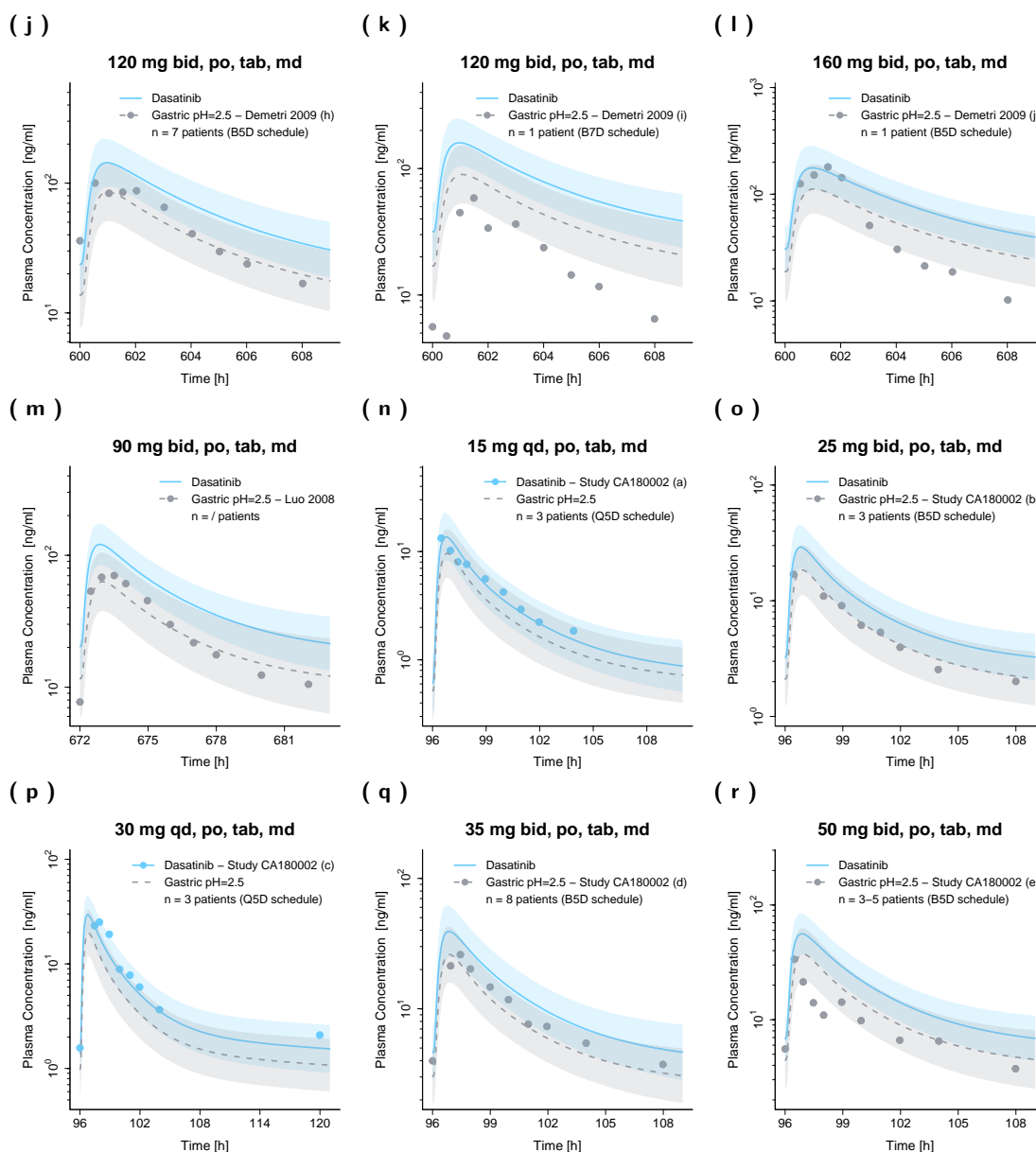


Figure S4: (continued) Predicted and observed dasatinib plasma concentration–time profiles in cancer patients on a semilogarithmic scale. Solid and dashed lines show predicted geometric mean concentration–time profiles with gastric pH of 2.0 and 2.5, respectively, with ribbons illustrating the corresponding geometric standard deviation of the population simulations ($n=100$). Points demonstrate the mean observed data with the corresponding standard deviation of dasatinib (if depicted in the respective publication). /: no information available, **B5D**: five consecutive days bid dosing followed by two nontreatment days, **B7D**: seven consecutive days bid dosing, **bid**: twice a day, **md**: multiple dose, **n**: number of participants, **po**: peroral, **Q5D**: five consecutive days once daily dosing followed by two nontreatment days, **qd**: once a day, **sd**: single dose, **tab**: tablet.

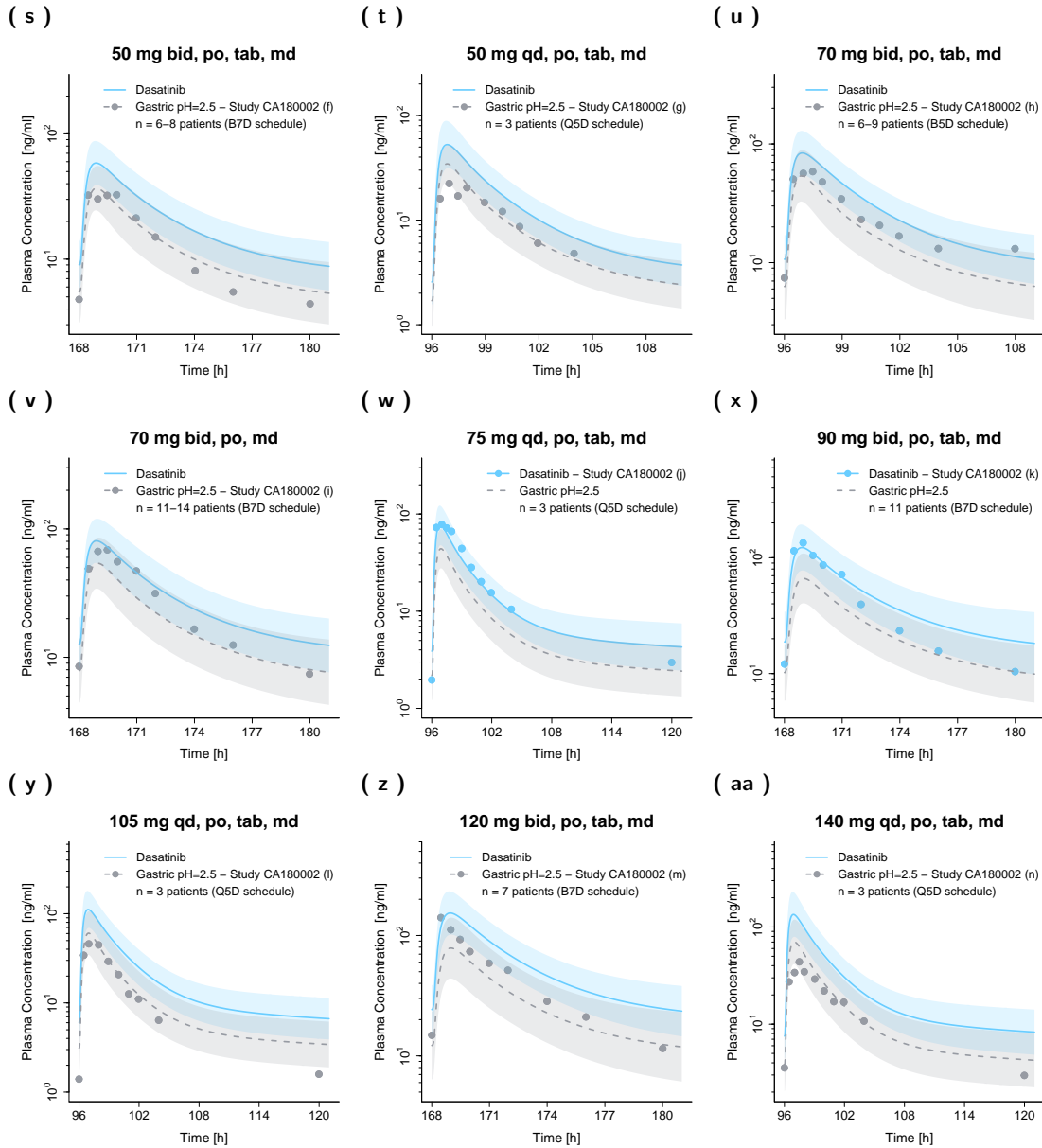


Figure S4: (continued) Predicted and observed dasatinib plasma concentration–time profiles in cancer patients on a semilogarithmic scale. Solid and dashed lines show predicted geometric mean concentration–time profiles with gastric pH of 2.0 and 2.5, respectively, with ribbons illustrating the corresponding geometric standard deviation of the population simulations ($n=100$). Points demonstrate the mean observed data with the corresponding standard deviation of dasatinib (if depicted in the respective publication). /: no information available, **B5D**: five consecutive days bid dosing followed by two nontreatment days, **B7D**: seven consecutive days bid dosing, **bid**: twice a day, **md**: multiple dose, **n**: number of participants, **po**: peroral, **Q5D**: five consecutive days once daily dosing followed by two nontreatment days, **qd**: once a day, **sd**: single dose, **tab**: tablet.

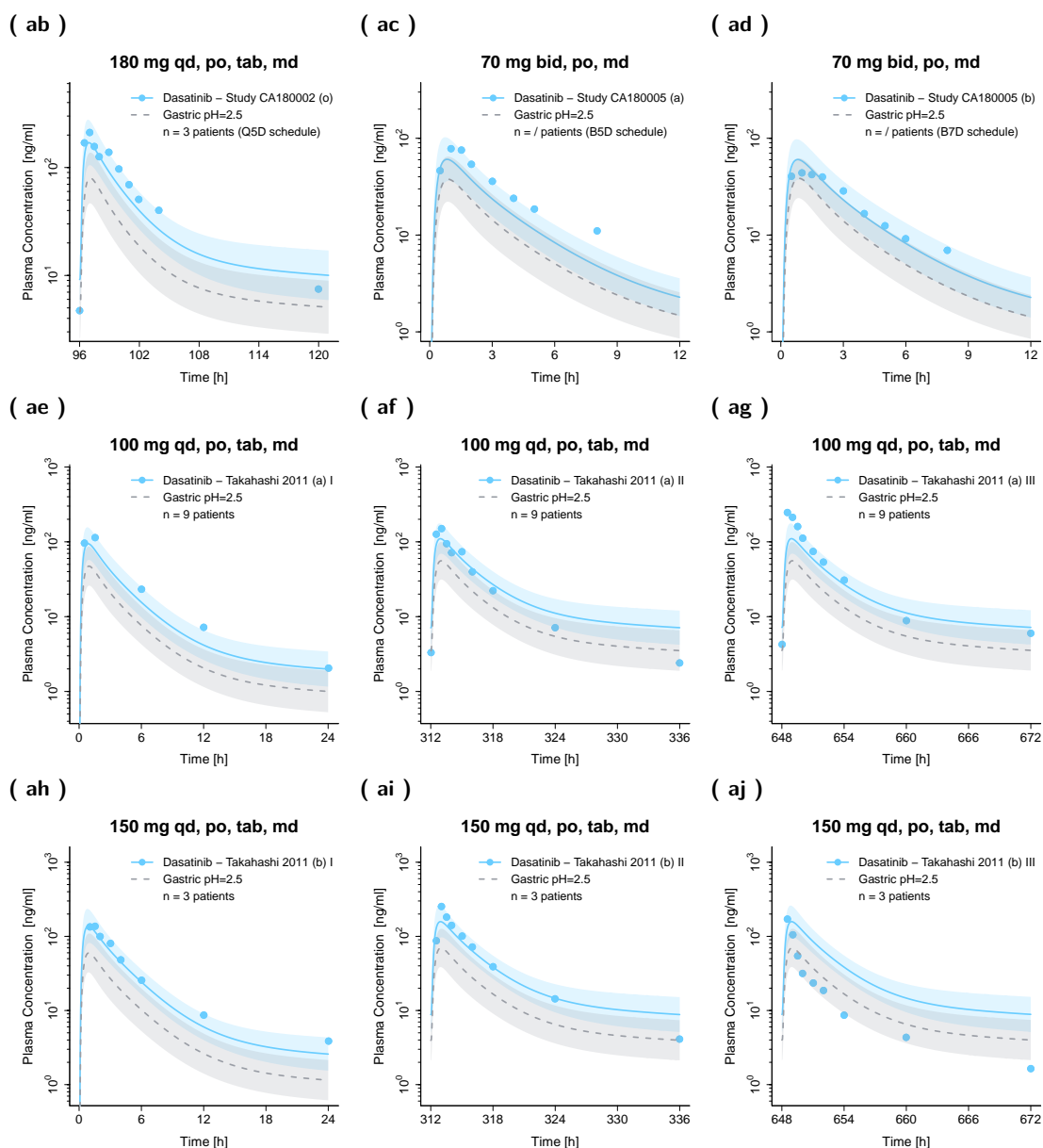


Figure S4: (continued) Predicted and observed dasatinib plasma concentration–time profiles in cancer patients on a semilogarithmic scale. Solid and dashed lines show predicted geometric mean concentration–time profiles with gastric pH of 2.0 and 2.5, respectively, with ribbons illustrating the corresponding geometric standard deviation of the population simulations ($n=100$). Points demonstrate the mean observed data with the corresponding standard deviation of dasatinib (if depicted in the respective publication). /: no information available, **B5D**: five consecutive days bid dosing followed by two nontreatment days, **B7D**: seven consecutive days bid dosing, **bid**: twice a day, **md**: multiple dose, **n**: number of participants, **po**: peroral, **Q5D**: five consecutive days once daily dosing followed by two nontreatment days, **qd**: once a day, **sd**: single dose, **tab**: tablet.

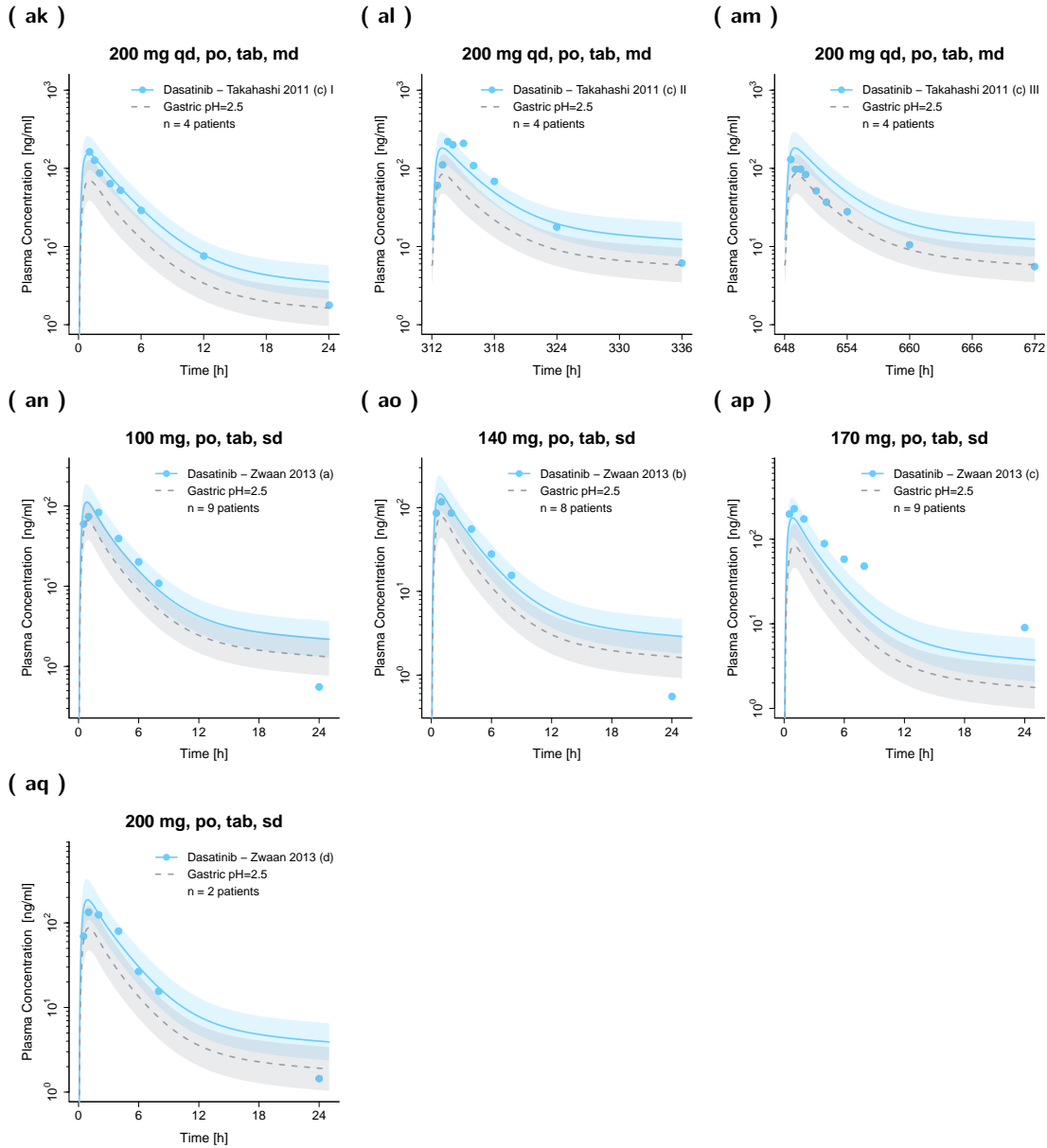


Figure S4: (continued) Predicted and observed dasatinib plasma concentration–time profiles in cancer patients on a semilogarithmic scale. Solid and dashed lines show predicted geometric mean concentration–time profiles with gastric pH of 2.0 and 2.5, respectively, with ribbons illustrating the corresponding geometric standard deviation of the population simulations ($n=100$). Points demonstrate the mean observed data with the corresponding standard deviation of dasatinib (if depicted in the respective publication). /: no information available, **B5D**: five consecutive days bid dosing followed by two nontreatment days, **B7D**: seven consecutive days bid dosing, **bid**: twice a day, **md**: multiple dose, **n**: number of participants, **po**: peroral, **Q5D**: five consecutive days once daily dosing followed by two nontreatment days, **qd**: once a day, **sd**: single dose, **tab**: tablet.

S2.2.3 Goodness-of-fit Plots

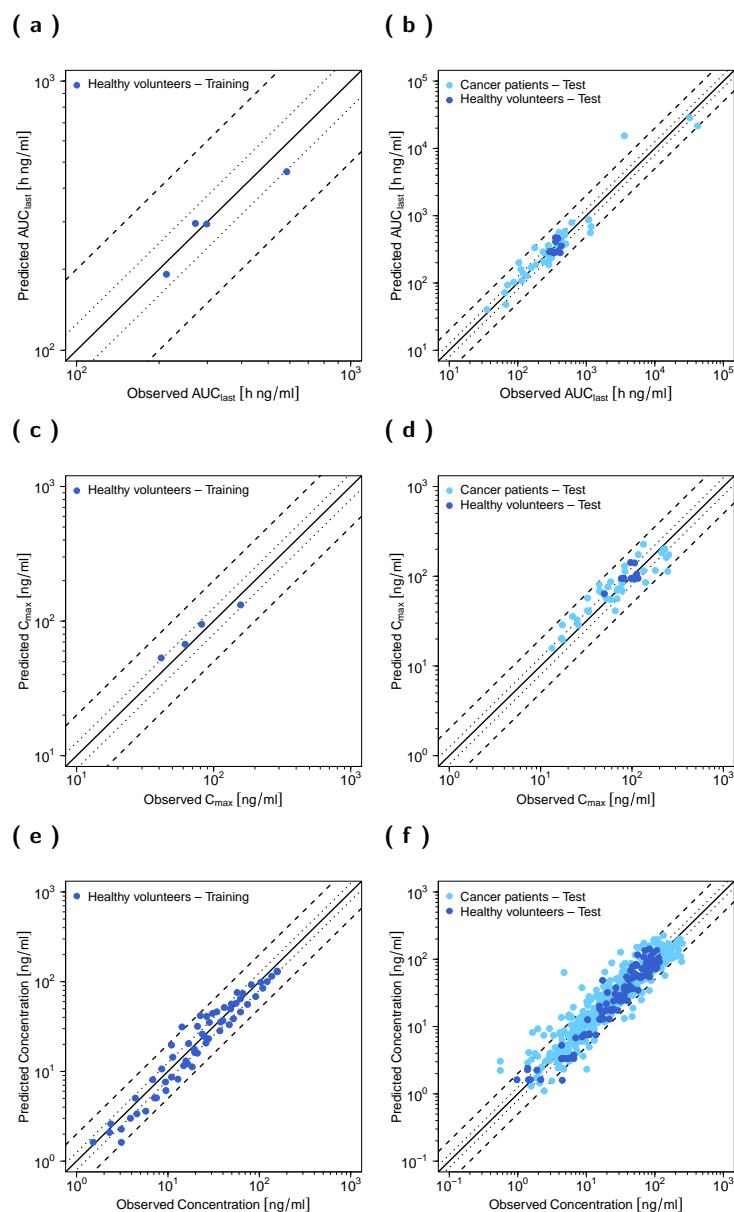


Figure S5: Goodness-of-fit plots of predicted versus observed AUC_{last} (a–b), C_{max} (c–d) and plasma concentrations (e–f) of the training (first column) and test dataset (second column). Solid lines mark the lines of identity, dotted lines indicate 1.25-fold and dashed lines two-fold deviation. AUC_{last} : areas under the plasma concentration–time curves from the first to the last time point of measurement, C_{max} : maximum plasma concentration.

S2.2.4 Residual Plot

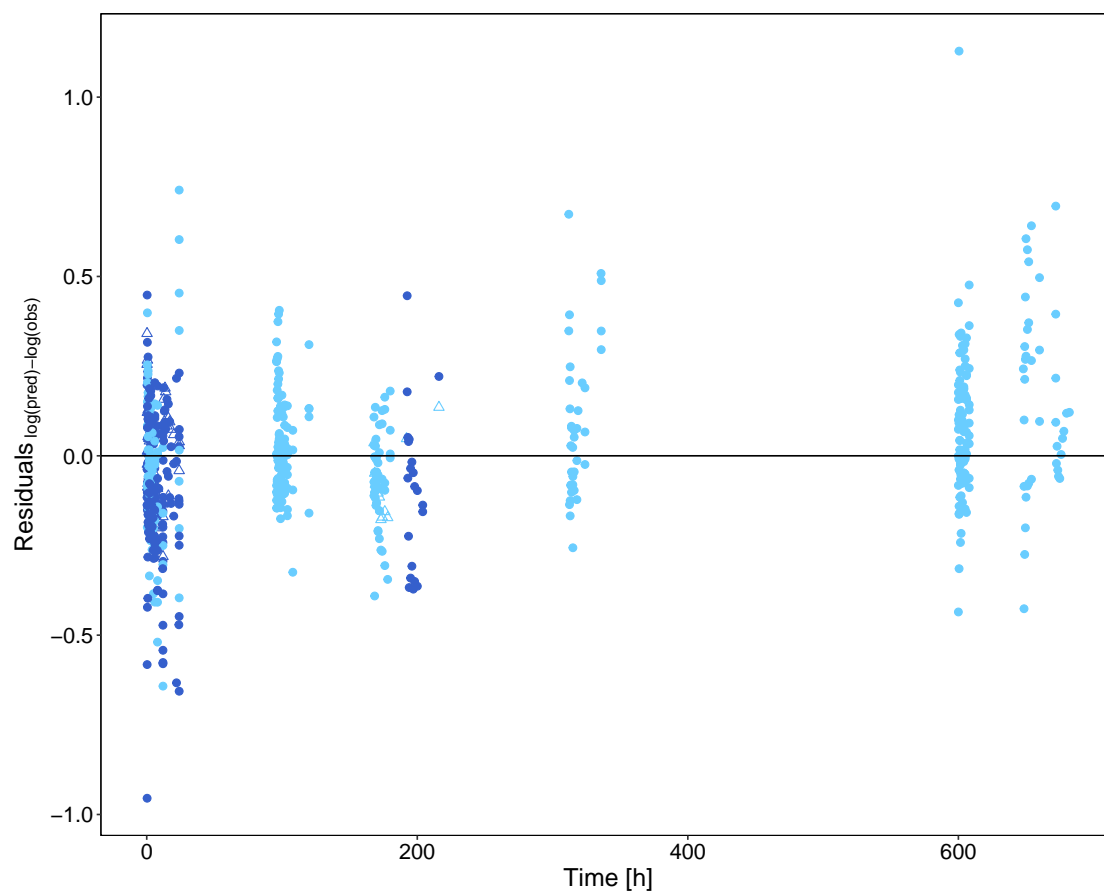


Figure S6: Residuals versus time. Blue and light blue symbols represent residuals from healthy volunteers and cancer patients, respectively. Triangles indicate residuals from the training dataset, while points indicate residuals from the test dataset. **Obs**: observed concentration, **pred**: predicted concentration.

S2.3 Quantitative PBPK Model Evaluation

S2.3.1 Geometric Mean Fold Error (GMFE)

Table S5: Geometric Mean Fold Error (GMFE) of C_{\max} and AUC_{last} Predictions.

Administration	Compound	C_{\max}			AUC_{last}			Reference
		Pred $\left[\frac{\text{ng}}{\text{ml}}\right]$	Obs $\left[\frac{\text{ng}}{\text{ml}}\right]$	Pred/Obs	Pred $\left[\frac{\text{ng}\cdot\text{h}}{\text{ml}}\right]$	Obs $\left[\frac{\text{ng}\cdot\text{h}}{\text{ml}}\right]$	Pred/Obs	
140 mg, po, tab, sd	Dasatinib	132.01	157.54	0.84	460.68	584.68	0.79	Bioequivalence study [13]
100 mg, po, sol, sd	Dasatinib	142.39	96.56	1.47	470.88	355.02	1.33	Christopher 2008 (a) [7]
50 mg, po, tab, bid, md	Dasatinib	53.24	41.43	1.29	295.99	271.31	1.09	Eley 2009 (control) [50]
100 mg, po, tab, sd	Dasatinib	94.78	81.72	1.16	294.52	298.60	0.99	Furlong 2012 [14]
100 mg, po, tab, sd	Dasatinib	140.72	106.81	1.32	461.41	387.37	1.19	Yago 2014 (control) [51]
100 mg, po, tab, sd	Dasatinib	94.78	81.31	1.17	292.05	323.65	0.90	Study CA180009 (fasted state (a)) [6]
100 mg, po, tab, sd	Dasatinib	63.76	49.78	1.28	410.28	357.61	1.15	Study CA180009 (with high-fat meal (b)) [6]
100 mg, po, tab, sd	Dasatinib	94.78	98.08	0.97	298.20	387.83	0.77	Study CA180009 (with light-fat meal (c)) [6]
100 mg, po, tab, sd	Dasatinib	94.78	76.82	1.23	293.25	301.65	0.97	Study CA180016 [6]
100 mg, po, tab, sd	Dasatinib	94.84	80.93	1.17	290.68	291.31	1.00	Study CA180032 (control) [6]
70 mg, po, tab, sd	Dasatinib	67.32	61.96	1.09	191.56	212.69	0.90	Vaidhyanathan 2018 (a) [8]
100 mg, po, PFOS, sd	Dasatinib	94.78	106.27	0.89	282.00	334.05	0.84	Vaidhyanathan 2018 (b) [8]
100 mg, po, dispersed tab, sd	Dasatinib	94.78	107.35	0.88	281.99	345.96	0.82	Vaidhyanathan 2018 (c) [8]
100 mg, po, tab, sd	Dasatinib	94.78	116.56	0.81	281.44	416.37	0.68	Vaidhyanathan 2018 (d) [8]
100 mg, po, tab, sd	Dasatinib	106.04	113.27	0.94	354.01	432.84	0.82	Vargas 2016 [9]
100 mg, po, tab, qd, md	Dasatinib	113.57	84.00	1.35	565.38	400.19	1.41	Araujo 2012 [15]
180 mg, po, tab, sd	Dasatinib	161.85	237.86	0.68	557.79	1149.40	0.49	Christopher 2008 (b) [7]
35 mg, po, tab, bid, md (B5D)	Dasatinib	28.74	17.28	1.66	93.48	71.05	1.32	Demetri 2009 (a) [16]
50 mg, po, tab, bid, md (B5D)	Dasatinib	41.23	65.65	0.63	139.03	120.09	1.16	Demetri 2009 (b) [16]
70 mg, po, tab, bid, md (B5D)	Dasatinib	57.16	32.64	1.75	199.85	103.69	1.93	Demetri 2009 (c) [16]
70 mg, po, tab, bid, md (B7D)	Dasatinib	56.47	52.12	1.08	207.76	238.01	0.87	Demetri 2009 (d) [16]
90 mg, po, tab, bid, md (B5D)	Dasatinib	72.10	74.88	0.96	258.15	307.42	0.84	Demetri 2009 (e) [16]
90 mg, po, tab, bid, md (B7D))	Dasatinib	69.87	69.03	1.01	263.07	273.55	0.96	Demetri 2009 (f) [16]
100 mg, po, tab, bid, md (B7D)	Dasatinib	75.90	54.40	1.40	284.12	240.30	1.18	Demetri 2009 (g) [16]
120 mg, po, tab, bid, md (B5D)	Dasatinib	92.46	100.07	0.92	339.75	396.39	0.86	Demetri 2009 (h) [16]
120 mg, po, tab, bid, md (B7D)	Dasatinib	86.73	58.42	1.48	334.03	177.28	1.88	Demetri 2009 (i) [16]
160 mg, po, tab, bid, md (B5D)	Dasatinib	116.02	180.29	0.64	413.91	433.80	0.95	Demetri 2009 (j) [16]
20 mg, po, tab, sd	Dasatinib	19.57	17.48	1.12	47.93	67.26	0.71	Johnson 2010 (control) [52]
90 mg, po, tab, bid, md	Dasatinib	72.47	70.28	1.03	306.38	301.74	1.02	Luo 2008 [10]

(continued)

Table S5: Geometric Mean Fold Error (GMFE) of C_{\max} and AUC_{last} Predictions (*continued*).

Administration	Compound	C_{\max}			AUC_{last}			Reference
		Pred $\left[\frac{\text{ng}}{\text{ml}}\right]$	Obs $\left[\frac{\text{ng}}{\text{ml}}\right]$	Pred/Obs	Pred $\left[\frac{\text{ng}\cdot\text{h}}{\text{ml}}\right]$	Obs $\left[\frac{\text{ng}\cdot\text{h}}{\text{ml}}\right]$	Pred/Obs	
15 mg, po, tab, qd, md (Q5D)	Dasatinib	15.77	13.30	1.19	40.22	35.50	1.13	Study CA180002 (a) [6]
25 mg, po, tab, bid, md (B5D)	Dasatinib	20.31	16.92	1.20	71.56	64.47	1.11	Study CA180002 (b) [6]
30 mg, po, tab, qd, md (Q5D)	Dasatinib	32.63	25.09	1.30	127.07	134.72	0.94	Study CA180002 (c) [6]
35 mg, po, tab, bid, md (B5D)	Dasatinib	28.55	26.02	1.10	107.80	114.35	0.94	Study CA180002 (d) [6]
50 mg, po, tab, bid, md (B5D)	Dasatinib	40.40	33.59	1.20	158.70	111.15	1.43	Study CA180002 (e) [6]
50 mg, po, tab, bid, md (B7D)	Dasatinib	41.34	32.63	1.27	169.28	156.54	1.08	Study CA180002 (f) [6]
50 mg, po, tab, qd, md (Q5D)	Dasatinib	35.72	22.36	1.60	102.44	87.51	1.17	Study CA180002 (g) [6]
70 mg, po, tab, bid, md (B5D)	Dasatinib	54.84	58.47	0.94	223.45	287.82	0.78	Study CA180002 (h) [6]
70 mg, po, tab, bid, md (B7D)	Dasatinib	56.15	68.66	0.82	237.56	311.15	0.76	Study CA180002 (i) [6]
75 mg, po, tab, qd, md (Q5D)	Dasatinib	83.54	78.00	1.07	363.20	380.49	0.95	Study CA180002 (j) [6]
90 mg, po, tab, bid, md (B7D)	Dasatinib	115.01	134.50	0.86	512.27	484.38	1.06	Study CA180002 (k) [6]
105 mg, po, tab, qd, md (Q5D)	Dasatinib	66.62	45.93	1.45	290.29	234.29	1.24	Study CA180002 (l) [6]
120 mg, po, tab, bid, md (B7D)	Dasatinib	85.07	140.79	0.60	378.38	503.90	0.75	Study CA180002 (m) [6]
140 mg, po, tab, qd, md (Q5D)	Dasatinib	80.35	43.84	1.83	360.80	278.94	1.29	Study CA180002 (n) [6]
180 mg, po, tab, qd, md (Q5D)	Dasatinib	182.78	211.15	0.87	868.30	1086.35	0.80	Study CA180002 (o) [6]
70 mg, po, tab, bid, md (B5D)	Dasatinib	68.62	78.02	0.88	187.28	283.48	0.66	Study CA180005 (a) [6]
70 mg, po, tab, bid, md (B7D)	Dasatinib	68.62	43.92	1.56	186.53	182.88	1.02	Study CA180005 (b) [6]
100 mg, po, tab, qd, md	Dasatinib	113.21	246.31	0.46	15399.80	3590.79	4.29	Takahashi 2011 (a) [17]
150 mg, po, tab, qd, md	Dasatinib	173.08	252.88	0.68	21560.86	42110.33	0.51	Takahashi 2011 (b) [17]
200 mg, po, tab, qd, md	Dasatinib	196.19	219.58	0.89	28503.51	32382.36	0.88	Takahashi 2011 (c) [17]
100 mg, po, tab, qd, sd	Dasatinib	130.21	83.05	1.57	419.24	370.40	1.13	Zwaan 2013 (a) [12]
140 mg, po, tab, qd, sd	Dasatinib	173.94	117.30	1.48	583.41	485.17	1.20	Zwaan 2013 (b) [12]
170 mg, po, tab, qd, sd	Dasatinib	202.39	228.72	0.88	688.11	1174.63	0.59	Zwaan 2013 (c) [12]
200 mg, po, tab, qd, sd	Dasatinib	226.89	133.54	1.70	789.00	613.16	1.29	Zwaan 2013 (d) [12]
		GMFE: 1.29 (1.01–2.18)			GMFE: 1.27 (1.00–4.29)			
		GMFE \leq 2: 52/53			GMFE \leq 2: 51/53			

AUC_{last} : area under the plasma concentration–time curve from the first to the last time point of measurement, **B5D**: five consecutive days bid dosing followed by two nontreatment days, **B7D**: continuous bid dosing, **bid**: twice a day, C_{\max} : maximum plasma concentration, **DFI**, drug–food interaction, **md**: multiple dose, **Obs**: observed, **PFOS**: powder for oral suspension, **po**: peroral, **Pred**: predicted, **Q5D**: five consecutive days once daily dosing followed by two nontreatment days, **qd**: once a day, **sd**: single dose, **sol**: solution, **tab**: tablet

S2.3.2 Mean Relative Deviation (MRD)

Table S6: Mean relative deviation (MRD) values of dasatinib plasma concentration predictions.

Administration	Compound	Health Status	MRD	Reference
140 mg, po, tab, sd	Dasatinib	Healthy	1.36	Bioequivalence study [13]
100 mg, po, sol, sd	Dasatinib	Healthy	1.54	Christopher 2008 (a) [7]
50 mg, po, tab, bid, md	Dasatinib	Healthy	1.43	Eley 2009 (control) [50]
100 mg, po, tab, sd	Dasatinib	Healthy	1.18	Furlong 2012 [14]
100 mg, po, tab, sd	Dasatinib	Healthy	1.37	Yago 2014 (control) [51]
100 mg, po, tab, sd	Dasatinib	Healthy	1.29	Study CA180009 (at fasted state (a)) [6]
100 mg, po, tab, sd	Dasatinib	Healthy	1.34	Study CA180009 (with high-fat meal (b)) [6]
100 mg, po, tab, sd	Dasatinib	Healthy	1.15	Study CA180009 (with light-fat meal (c)) [6]
100 mg, po, tab, sd	Dasatinib	Healthy	1.25	Study CA180016 [6]
100 mg, po, tab, sd	Dasatinib	Healthy	1.28	Study CA180032 (control) [6]
70 mg, po, tab, sd	Dasatinib	Healthy	1.31	Vaidhyanathan 2018 (a) [8]
100 mg, po, PFOS, sd	Dasatinib	Healthy	1.26	Vaidhyanathan 2018 (b) [8]
100 mg, po, dispersed tab, sd	Dasatinib	Healthy	1.32	Vaidhyanathan 2018 (c) [8]
100 mg, po, tab, sd	Dasatinib	Healthy	1.60	Vaidhyanathan 2018 (d) [8]
100 mg, po, tab, sd	Dasatinib	Healthy	1.63	Vargas 2016 [9]
100 mg, po, tab, qd, md	Dasatinib	Cancer	2.07	Araujo 2012 [15]
180 mg, po, tab, sd	Dasatinib	Cancer	2.01	Christopher 2008 (b) [7]
35 mg, po, tab, bid, md (B5D)	Dasatinib	Cancer	1.35	Demetri 2009 (a) [16]
50 mg, po, tab, bid, md (B5D)	Dasatinib	Cancer	1.49	Demetri 2009 (b) [16]
70 mg, po, tab, bid, md (B5D)	Dasatinib	Cancer	1.91	Demetri 2009 (c) [16]
70 mg, po, tab, bid, md (B7D)	Dasatinib	Cancer	1.26	Demetri 2009 (d) [16]
90 mg, po, tab, bid, md (B5D)	Dasatinib	Cancer	1.21	Demetri 2009 (e) [16]
90 mg, po, tab, bid, md (B7D))	Dasatinib	Cancer	1.19	Demetri 2009 (f) [16]
100 mg, po, tab, bid, md (B7D)	Dasatinib	Cancer	1.30	Demetri 2009 (g) [16]
120 mg, po, tab, bid, md (B5D)	Dasatinib	Cancer	1.44	Demetri 2009 (h) [16]
120 mg, po, tab, bid, md (B7D)	Dasatinib	Cancer	2.89	Demetri 2009 (i) [16]
160 mg, po, tab, bid, md (B5D)	Dasatinib	Cancer	1.66	Demetri 2009 (j) [16]
20 mg, po, tab, sd	Dasatinib	Cancer	1.64	Johnson 2010 (control) [52]
90 mg, po, tab, bid, md	Dasatinib	Cancer	1.24	Luo 2008 [10]
15 mg, po, tab, qd, md (Q5D)	Dasatinib	Cancer	1.21	Study CA180002 (a) [6]
25 mg, po, tab, bid, md (B5D)	Dasatinib	Cancer	1.13	Study CA180002 (b) [6]
30 mg, po, tab, qd, md (Q5D)	Dasatinib	Cancer	1.24	Study CA180002 (c) [6]
35 mg, po, tab, bid, md (B5D)	Dasatinib	Cancer	1.22	Study CA180002 (d) [6]
50 mg, po, tab, bid, md (B5D)	Dasatinib	Cancer	1.67	Study CA180002 (e) [6]
50 mg, po, tab, bid, md (B7D)	Dasatinib	Cancer	1.19	Study CA180002 (f) [6]
50 mg, po, tab, qd, md (Q5D)	Dasatinib	Cancer	1.33	Study CA180002 (g) [6]
70 mg, po, tab, bid, md (B5D)	Dasatinib	Cancer	1.37	Study CA180002 (h) [6]
70 mg, po, tab, bid, md (B7D)	Dasatinib	Cancer	1.30	Study CA180002 (i) [6]
75 mg, po, tab, qd, md (Q5D)	Dasatinib	Cancer	1.25	Study CA180002 (j) [6]
90 mg, po, tab, bid, md (B7D)	Dasatinib	Cancer	1.28	Study CA180002 (k) [6]
105 mg, po, tab, qd, md (Q5D)	Dasatinib	Cancer	1.47	Study CA180002 (l) [6]
120 mg, po, tab, bid, md (B7D)	Dasatinib	Cancer	1.42	Study CA180002 (m) [6]
140 mg, po, tab, qd, md (Q5D)	Dasatinib	Cancer	1.53	Study CA180002 (n) [6]
180 mg, po, tab, qd, md (Q5D)	Dasatinib	Cancer	1.34	Study CA180002 (o) [6]
70 mg, po, tab, bid, md (B5D)	Dasatinib	Cancer	1.89	Study CA180005 (a) [6]
70 mg, po, tab, bid, md (B7D)	Dasatinib	Cancer	1.36	Study CA180005 (b) [6]
100 mg, po, tab, qd, md	Dasatinib	Cancer	1.58	Takahashi 2011 (a) [17]
150 mg, po, tab, qd, md	Dasatinib	Cancer	2.08	Takahashi 2011 (b) [17]
200 mg, po, tab, qd, md	Dasatinib	Cancer	1.72	Takahashi 2011 (c) [17]

(continued)

Table S6: Mean relative deviation (MRD) values of dasatinib plasma concentration predictions (*continued*).

Study	Compound	Health Status	MRD	Reference
100 mg, po, tab, qd, sd	Dasatinib	Cancer	1.84	Zwaan 2013 (a) [12]
140 mg, po, tab, qd, sd	Dasatinib	Cancer	2.00	Zwaan 2013 (b) [12]
170 mg, po, tab, qd, sd	Dasatinib	Cancer	1.78	Zwaan 2013 (c) [12]
200 mg, po, tab, qd, sd	Dasatinib	Cancer	1.81	Zwaan 2013 (d) [12]
Overall MRD: 1.54 (1.13–2.89)				
49/53 MRD ≤ 2				
<p>B5D: five consecutive days bid dosing followed by two nontreatment days, B7D: continuous bid dosing, bid: twice a day, DFI: drug–food interaction, md: multiple dose, PFOS: powder for oral suspension, po: peroral, Q5D: five consecutive days once daily dosing followed by two nontreatment days, qd: once a day, sd: single dose, sol: solution, tab: tablet</p>				

S2.4 Local Sensitivity Analysis

S2.4.1 Mathematical Implementation

A sensitivity analysis was conducted by calculating the impact of single parameter changes (local sensitivity analysis) on the predicted AUC_{inf} . Here, the relative change of AUC_{inf} at steady-state after peroral administration of 100 mg dasatinib daily to the relative variation of model input parameters was calculated according to [Equation S1](#). Parameters were included in the sensitivity analysis, if they were optimized (I), assumed to affect AUC_{inf} (II) or might have a strong impact due to their use in the calculation of permeabilities or partition coefficients (III). A relative perturbation of 1000% (variation range 10.0, maximum number of 9 steps) was utilized. Parameters were considered sensitive if their sensitivity value was equal or greater than $|0.5|$. For instance, a sensitivity of $+0.5$ implies that a 100% increase of the examined parameter value leads to a 50% increase of the simulated AUC_{inf} .

$$S = \frac{\Delta AUC_{inf}}{\Delta p} \cdot \frac{p}{AUC_{inf}} \quad (S1)$$

S = sensitivity of the AUC_{inf} to the examined model parameter, ΔAUC_{inf} = change of the AUC_{inf} , AUC_{inf} = simulated AUC_{inf} with the original parameter value, p = original model parameter value, Δp = variation of the model parameter value

S2.4.2 Results of the Sensitivity Analysis

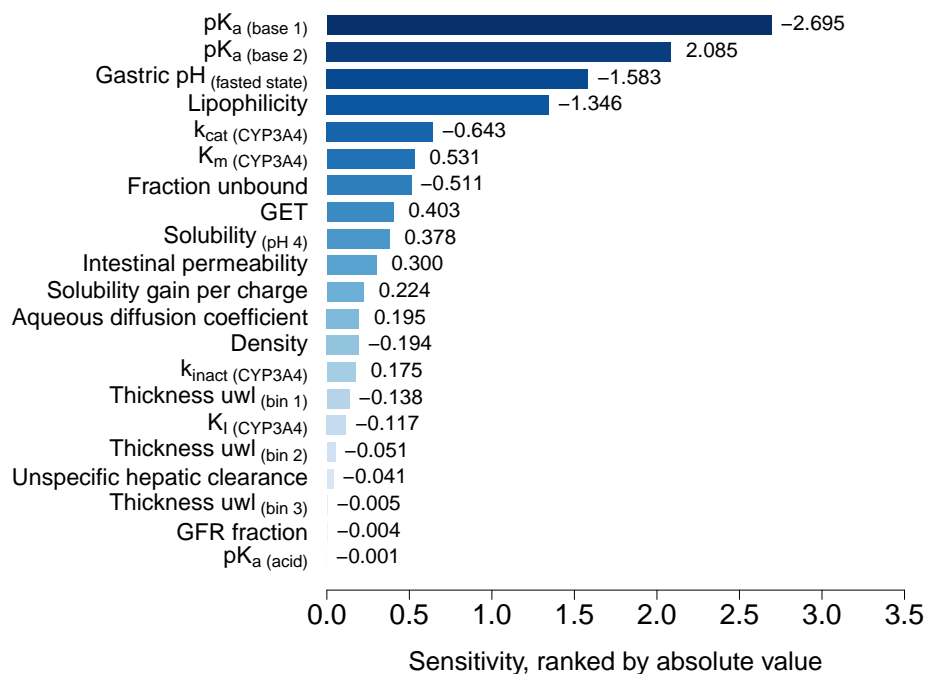


Figure S7: Sensitivity analysis of the dasatinib PBPK model. CYP: cytochrome P450, GET: gastric emptying time, GFR: glomerular filtration rate, k_{cat} : catalytic rate constant, K_i : inhibition constant, k_{inact} : maximum rate of inactivation, K_m : Michaelis-Menten constant, pK_a : acid dissociation constant, uwl : unstirred water layer.

S3 PBPK Drug–Drug Interaction (DDI) Modeling

S3.1 Clinical DDI Studies

Table S7: Overview of clinical study data from the literature used for DDI model development.

Clinical study	Dosing of Perpetrator Drug	Dosing of Victim Drug	Gastric pH	N	Females [%]	Age [years]	BMI [kg/m ²]	Health Status	Dataset
(a) Enzyme-mediated DDIs									
	<i>Ketoconazole</i>	<i>Dasatinib</i>							
Johnson 2010 (control) [52]		20 mg, tab, qd, md (D1–D8)	2.0 ^a	18	43	57.5 (23–80) ^b	-	cancer	test
Johnson 2010 (DDI) [52]	200 mg, tab, bid, md (D3–D8)	20 mg, tab, qd, md (D1–D8)	2.0 ^a	18	43	57.5 (23–80) ^b	-	cancer	training
	<i>Rifampicin</i>	<i>Dasatinib</i>							
Study CA180032 (control) [6]		100 mg, tab, sd (D1) ^c	2.0 ^a	20	-	-	-	healthy	test
Study CA180032 (DDI) [6]	600 mg, tab, qd, md (D2–D9) ^d	100 mg, tab, sd (D8) ^c	2.0 ^a	20	-	-	-	healthy	test
	<i>Dasatinib</i>	<i>Simvastatin</i>							
Study CA180022 (control) [6]		80 mg, tab, sd (D1)	2.0 ^a	48	58	40 (18–50) ^e	25.8 (20.9–31.7) ^e	healthy	test
Study CA180022 (DDI) [6]	100 mg, tab, sd (D8)	80 mg, tab, sd (D8)	2.0 ^a	48	58	40 (18–50) ^e	25.8 (20.9–31.7) ^e	healthy	test
(b) pH-dependent DDIs									
	<i>Rabeprazole</i>	<i>Dasatinib</i>							
Yago 2014 (control) [51]		100 mg, tab, sd	0.6 (0.5–1.8) ^b	10	10	38 (23–59) ^e	- (21.6–29.1)	healthy	test
Yago 2014 (DDI (a)) [51]	20 mg, tab, bid, md (D1–D4) ^f	100 mg, tab, sd (D4)	4.1 (2.8–5.2) ^e	10	10	38 (23–59) ^e	- (21.6–29.1)	healthy	test
Yago 2014 (DDI (b)) [51]	20 mg, tab, bid, md (D1–D4) ^f + 1500 mg BHC1	100 mg, tab, sd (D4) ^g	0.7 (0.5–3.6) ^e	10	10	38 (23–59) ^e	- (21.6–29.1)	healthy	test

–: unknown, **bid**: twice a day, **BHC1**: betaine hydrochloride, **BMI**: body mass index, **D**: day, **DDI**: drug–drug interaction, **md**: multiple dose, **N**: number of participants, **qd**: once a day, **sd**: single dose, **tab**: tablet

^a Default value in PK-Sim[®] for fasted state [11]

^b Median (range)

^c Administration of 100 mg dasatinib at 9:00 AM

^d Administration of 600 mg rifampicin at 9:00 PM

^e Mean (range)

^f Single dose rabeprazole at D4

^g Dasatinib administration following five minutes after BHC1 administration

^h Dasatinib was administered two hours before and ten hours after famotidine intake, respectively

ⁱ Dasatinib was administered two hours after and concomitantly with Maalox[®], respectively

Table S7: Overview of clinical study data from the literature used for DDI model development (*continued*).

Clinical study	Dosing of Perpetrator Drug	Dosing of Victim Drug	Gastric pH	N	Females [%]	Age [years]	BMI [kg/m ²]	Health Status	Dataset
	<i>Famotidine</i>	<i>Dasatinib</i>							
Eley 2009 (control) [50]		50 mg, tab, bid, md	2.0 ^a	22	0	29 (19–47) ^e	25.1 (18.8–29.6) ^e	healthy	training
Eley 2009 (DDI (a)) [50]	40 mg, tab, bid, md	50 mg, tab, bid, md ^h	2.8 [53]	22	0	29 (19–47) ^e	25.1 (18.8–29.6) ^e	healthy	test
	<i>Maalox</i> [®]	<i>Dasatinib</i>							
Eley 2009 (control) [50]		50 mg, tab, bid, md	2.0 ^a	22	0	29 (19–47) ^e	25.1 (18.8–29.6) ^e	healthy	training
Eley 2009 (DDI (b)) [50]	30 ml, liquid, bid, md	50 mg, tab, bid, md ⁱ	3.0 [54]	22	0	29 (19–47) ^e	25.1 (18.8–29.6) ^e	healthy	test

–: unknown, **bid**: twice a day, **BHCl**: betaine hydrochloride, **BMI**: body mass index, **D**: day, **DDI**: drug–drug interaction, **md**: multiple dose, **N**: number of participants, **qd**: once a day, **sd**: single dose, **tab**: tablet

^a Default value in PK-Sim[®] for fasted state [11]
^b Median (range)
^c Administration of 100 mg dasatinib at 9:00 AM
^d Administration of 600 mg rifampicin at 9:00 PM
^e Mean (range)
^f Single dose rabeprazole at D4
^g Dasatinib administration following five minutes after BHCl administration
^h Dasatinib was administered two hours before and ten hours after famotidine intake, respectively
ⁱ Dasatinib was administered two hours after and concomitantly with Maalox[®], respectively

S3.2 DDI Model Evaluation

S3.2.1 Plasma Profiles of Enzyme-mediated DDIs (Semilogarithmic Scale)

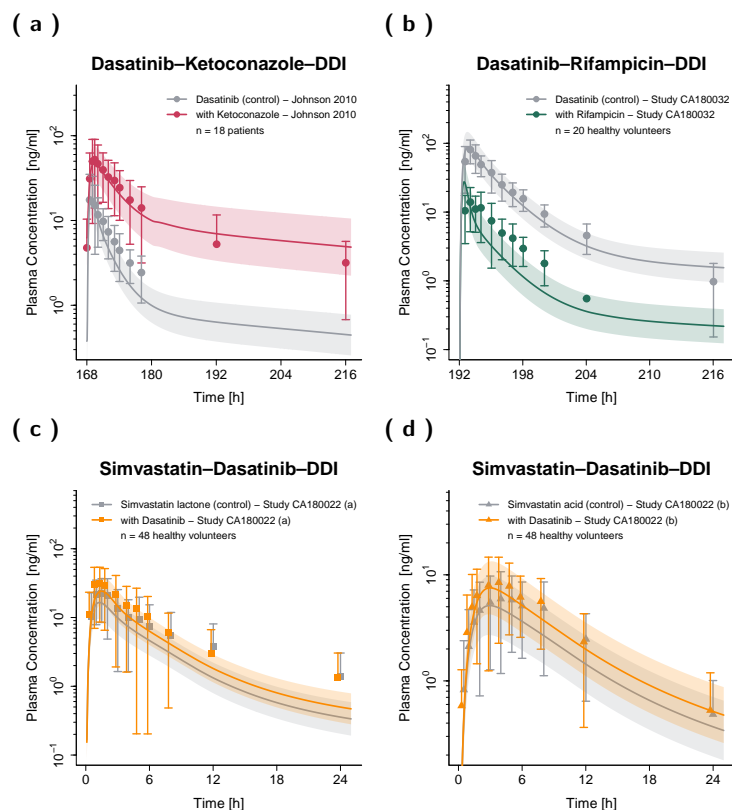


Figure S8: Predicted and observed plasma concentration-time profiles for enzyme-mediated DDIs with dasatinib acting as victim (a-b) and perpetrator drug (c-d) on a semilogarithmic scale. The solid lines show predicted geometric mean concentration-time profiles with and without intake of the perpetrator drug and ribbons show the corresponding geometric standard deviation of the population simulations (n=100). Points depict mean observed data and corresponding standard deviation of dasatinib, while squares and triangles depict the observed data and corresponding standard deviation of simvastatin lactone and simvastatin acid, respectively. /: no information available, DDIs: drug-drug interactions, n: number of participants.

S3.2.2 Plasma Profiles of pH-Dependent DDIs (Semilogarithmic Scale)

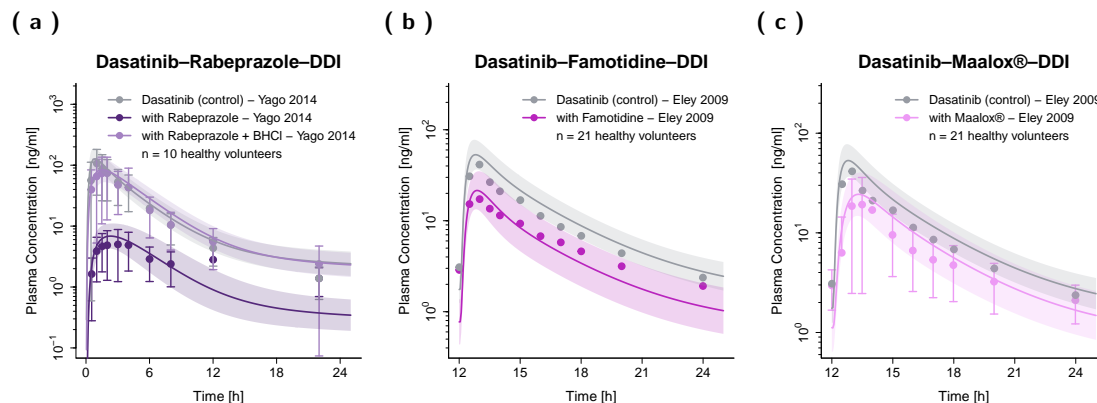


Figure S9: Predicted and observed plasma concentration–time profiles for the pH-dependent DDIs on a semilogarithmic scale. The solid lines show predicted geometric mean concentration–time profiles with and without the intake of perpetrator drug and ribbons show the corresponding geometric standard deviation of the population simulations ($n=100$). Points depict mean observed data and corresponding standard deviation of dasatinib (if depicted in the respective publication). **BHCl**: betaine hydrochloride, **DDIs**: drug–drug interactions, **n**: number of participants.

S3.2.3 Geometric Mean Fold Error (GMFE)

Table S8: Geometric Mean Fold Error (GMFE) of C_{\max} and AUC_{last} DDI ratios.

Administration	Compound	C_{\max} DDI Ratio			AUC_{last} DDI Ratio			Reference
		Pred [1]	Obs [1]	Pred/Obs	Pred [1]	Obs [1]	Pred/Obs	
Dasatinib–Ketoconazole–DDI	Dasatinib	2.17	2.99	0.73	9.14	7.65	1.19	Johnson 2010 [52]
Dasatinib–Rifampicin–DDI	Dasatinib	0.31	0.17	1.79	0.11	0.17	0.64	Study CA180032 [6]
Simvastatin–Dasatinib–DDI	Simvastatin lactone	1.48	1.38	1.07	1.47	1.23	1.20	Study CA180022 [6]
Simvastatin–Dasatinib–DDI	Simvastatin acid	1.52	1.43	1.06	1.45	1.19	1.22	Study CA180022 [6]
Dasatinib–Famotidine–DDI	Dasatinib	0.44	0.42	1.05	0.24	0.27	0.88	Eley 2009 [50]
Dasatinib–Maalox [®] –DDI	Dasatinib	0.45	0.46	0.97	0.31	0.28	1.09	Eley 2009 [50]
Dasatinib–Rabeprazole–DDI	Dasatinib	0.05	0.05	1.16	0.10	0.15	0.68	Yago 2014 [51]
Dasatinib–Rabeprazole–BHCl–DDI	Dasatinib	0.66	0.69	0.95	1.02	0.92	1.10	Yago 2014 [51]
		GMFE: 1.18 (1.03–1.79)			GMFE: 1.24 (1.09–1.57)			
		GMFE \leq 2: 08/08			GMFE \leq 2: 08/08			
		Guest limits: 08/08			Guest limits: 08/08			

AUC_{last} : area under the plasma concentration–time curve from the first to the last time point of measurement, **BHCl**: betaine hydrochloride,

C_{\max} : maximum plasma concentration, **DDI**: drug–drug interaction, **Obs**: observed, **Pred**: predicted

S4 PBPK Drug–Food Interaction (DFI) Modeling

S4.1 DFI Model Building

Studies have shown that the intake of both light and high-fat meals only marginally influences the pharmacokinetics (PK) of dasatinib. During light-fat meal ingestion, the maximum concentration (C_{\max}) and area under the concentration–time curve (AUC) increased by 22% and 21%, respectively. The time to peak concentration (T_{\max}) remained unaffected. In contrast, high-fat meal consumption led to a 24% decrease in C_{\max} and a 14% increase in AUC, along with a one-hour delay in T_{\max} , when compared to a fasted state [6]. The plasma concentration–time profiles of the DFI study investigating dasatinib exposure in the fasted state, after light-fat and high-fat breakfast were included in the model development (Table S9). The observed dasatinib data during ingestion of a light-fat meal (which only slightly impacted the PK of dasatinib) could be well predicted using the dasatinib model parameters of the fasted state, while the delay in T_{\max} after a high-fat meal intake could be covered by prolonging the gastric emptying time from 15.0 minutes (default setting in PK-Sim[®] for the fasted state) to 103.4 minutes.

S4.1.1 Clinical DFI Studies

Table S9: Overview of clinical study data from the literature used for DFI model development.

Clinical study	Dosing of dasatinib	Meal	N	Females [%]	Age [years]	BMI [kg/m ²]	Health Status	Dataset
Study CA180009 (control) [6]	100 mg, tab, qd, sd	Fasted state	48	-	-	-	healthy	test
Study CA180009 (DFI (a)) [6]	100 mg, tab, qd, sd	Light breakfast (319 kcal)	48	-	-	-	healthy	test
Study CA180009 (DFI (b)) [6]	100 mg, tab, qd, sd	High-fat breakfast (985 kcal)	48	-	-	-	healthy	test

BMI: body mass index, **D:** day, **DFI:** drug–food interaction, **N:** number of subjects, **qd:** once a day, **sd:** single dose, **tab:** tablet

S4.2 DFI Model Evaluation

S4.2.1 Plasma Profiles And Goodness-of-Fit Plot of DFIs

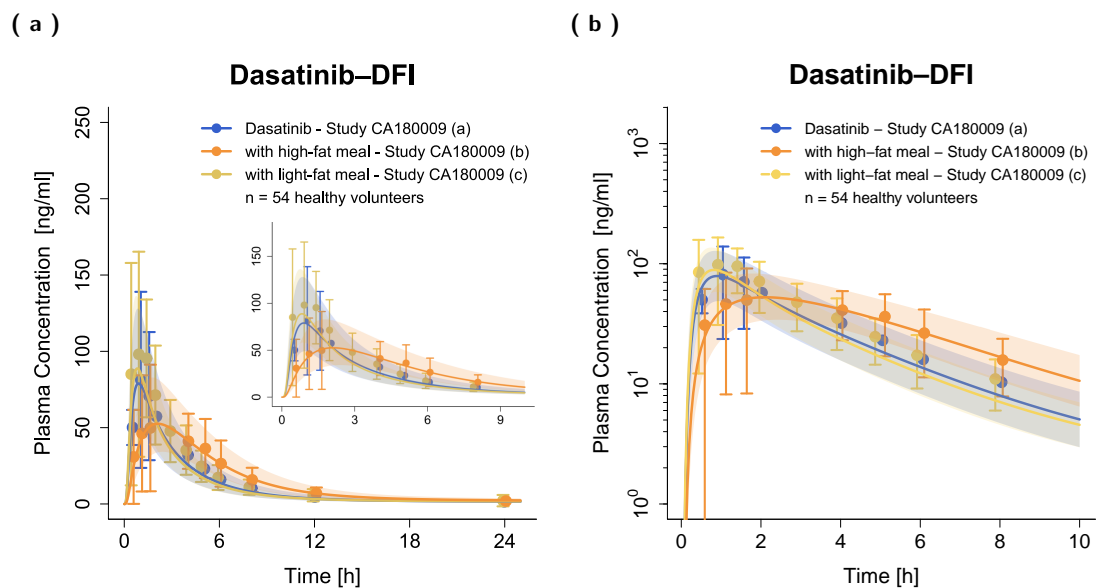


Figure S10: Predicted and observed plasma concentration-time profiles for the DFIs. Blue, yellow and orange lines show predicted geometric mean concentration-time profiles at fasted state, after light-fat and after high-fat breakfast, respectively. Ribbons show the corresponding geometric standard deviation of the population simulations (n=100). Points depict mean observed data and corresponding standard deviation of dasatinib. **DFI:** drug-food interaction, **n:** number of participants.

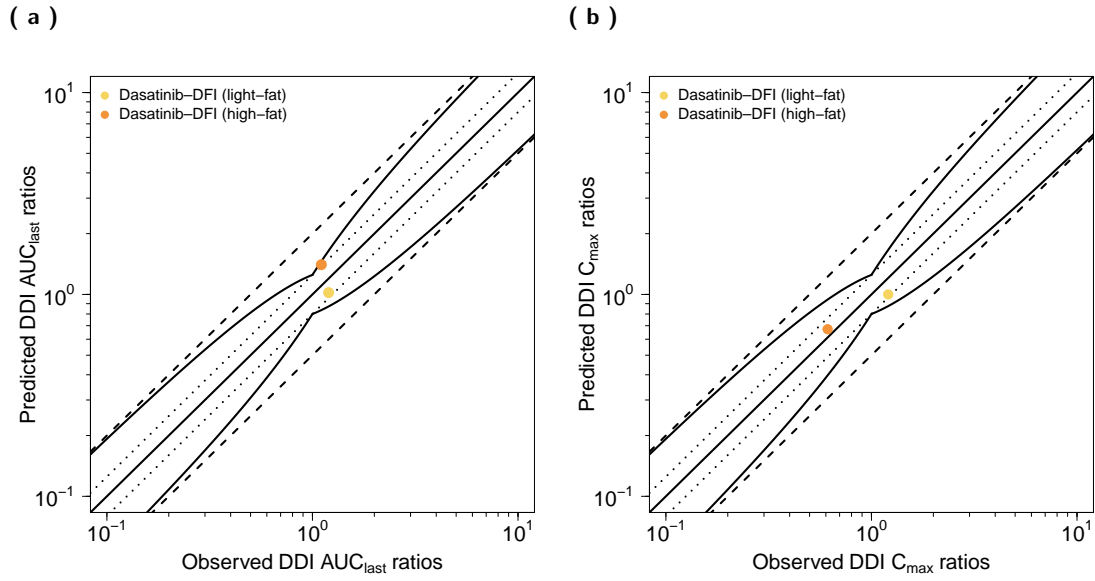


Figure S11: Predicted versus observed DFI AUC_{last} ratios (a) and DFI C_{max} ratios (b) of dasatinib. The straight solid lines mark the lines of identity, the curved lines show the limits of the predictive measure proposed by Guest et al. with 1.25-fold variability [55]. Dotted lines indicate 1.25-fold and dashed lines two-fold deviation. AUC_{last} : area under the plasma concentration–time curve from the first to the last time point of measurement, C_{max} : maximum plasma concentration, **DFI**: drug–food interaction.

S4.2.2 Geometric Mean Fold Error (GMFE)

Table S10: Geometric Mean Fold Error (GMFE) of C_{\max} and AUC_{last} DFI ratios.

Administration	Compound	C_{\max} DFI Ratio			AUC_{last} DFI Ratio			Reference
		Pred [1]	Obs [1]	Pred/Obs	Pred [1]	Obs [1]	Pred/Obs	
100 mg, po, tab, sd	Dasatinib	0.67	0.61	1.10	1.40	1.10	1.27	Study CA180009 (b) [6]
100 mg, po, tab, sd	Dasatinib	1.00	1.21	0.83	1.02	1.20	0.85	Study CA180009 (c) [6]
GMFE: 1.15 (1.21–1.10)				GMFE: 1.22 (1.17–1.27)				
GMFE \leq 2: 02/02				GMFE \leq 2: 02/02				
Guest limits: 02/02				Guest limits: 02/02				

AUC_{last} : area under the plasma concentration–time curve from the first to the last time point of measurement,

C_{\max} : maximum plasma concentration, **DFI**, drug–food interaction, **Obs**: observed, **Pred**: predicted

S5 Model Application & Others

S5.1 Exposure Simulations for Model-Informed Precision Dosing

The developed PBPK model of dasatinib was coupled with previously published PBPK models of carbamazepine [56] (version 11), clarithromycin [24] (version 11), efavirenz [56, 57] (version 11), erythromycin [25] (version 11), fluconazole [20] (version 11), fluvoxamine [58] (version 11), grapefruit juice [59] (version 11), itraconazole [24] (version 11), ketoconazole [60] (version 11), rifampicin [24] (version 11), simvastatin [21] (version 9) and voriconazole [61] (version 11). The drug-dependent parameters of the compounds were adapted from the respective publications. Modifications of drug-dependent parameters are shown in Table S11.

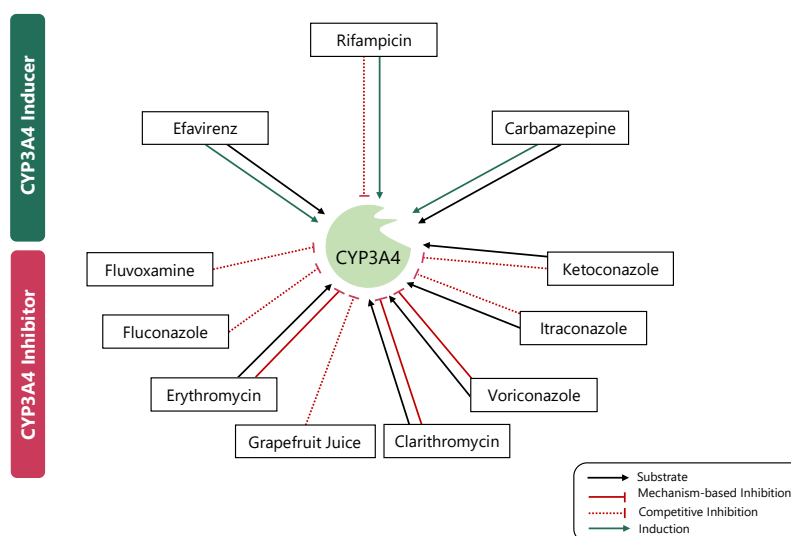


Figure S12: Overview of investigated DDI scenarios. The developed dasatinib PBPK model was coupled with previously published PBPK perpetrator models of clarithromycin, erythromycin, fluconazole, fluvoxamine, grapefruit juice, itraconazole, ketoconazole and voriconazole as CYP3A4 inhibitors as well as of carbamazepine, efavirenz and rifampicin as CYP3A4 inducers. **DDI**: drug–drug interaction, **PBPK**: physiologically based pharmacokinetic.

Table S11: Modified drug-dependent parameters of the PBPK models from the literature.

PBPK model	Modified parameter	Published parameter	Reason for Modification
Efavirenz [56, 57]	modified according to [56]	see [57]	-
Erythromycin [25]	OATP1B1 $k_{cat} = 19.29$ 1/min	OATP1B1 $k_{cat} = 1.35$ 1/min	Different OATP1B1 ref. conc.
Rifampicin [24]	OATP1B1 $k_{cat} = 74.43$ 1/min	OATP1B1 $k_{cat} = 5.21$ 1/min	Different OATP1B1 ref. conc.
Simvastatin [21]	OATP1B1 $k_{cat} = 146.41$ 1/min	OATP1B1 $k_{cat} = 10.25$ 1/min	Different OATP1B1 ref. conc.

k_{cat} : catalytic rate constant, **OATP**: organic anion transporting polypeptide, **ref. conc.**: reference concentration

Table S12: Overview of model-based dose adaptations for dasatinib within various DDI scenarios based on the exposure matching principle.

Perpetrator	Dosing of Perpetrator	Dosing of Dasatinib	AUC _{ss} Ratio ¹	AUC _{ss} Ratio ² (adapted)	Adapted Dasatinib Dose
Strong CYP3A4 Inhibitors					
Clarithromycin	250 mg, bid	100 mg, qd	1.85	0.99	50 mg, qd
	250 mg, bid	140 mg, qd	1.76	0.96	70 mg, qd
Clarithromycin	500 mg, bid	100 mg, qd	3.37	1.11	30 mg, qd
	500 mg, bid	140 mg, qd	3.21	1.05	40 mg, qd
Itraconazole (fed state)	200 mg, bid	100 mg, qd	4.59	1.03	20 mg, qd
	200 mg, bid	140 mg, qd	4.36	1.09	30 mg, qd
Ketoconazole	200 mg, bid	100 mg, qd	3.75	0.84	20 mg, qd
	200 mg, bid	140 mg, qd	3.59	0.88	30 mg, qd
Voriconazole	400 mg, qd (D1) + 200 mg, bid	100 mg, qd	3.01	0.98	30 mg, qd
	400 mg, qd (D1) + 200 mg, bid	140 mg, qd	2.87	0.93	40 mg, qd
Moderate CYP3A4 Inhibitors					
Erythromycin	500 mg, tid	100 mg, qd	2.12	0.93	40 mg, qd
	500 mg, tid	140 mg, qd	1.84	0.97	60 mg, qd
Erythromycin	500 mg, qid	100 mg, qd	2.31	1.01	40 mg, qd
	500 mg, qid	140 mg, qd	2.19	1.05	60 mg, qd
Fluconazole	200 mg, qd	100 mg, qd	2.11	1.09	50 mg, qd
	200 mg, qd	140 mg, qd	2.04	0.93	60 mg, qd
Fluconazole	400 mg, qd	100 mg, qd	2.70	0.87	30 mg, qd
	400 mg, qd	140 mg, qd	2.59	1.01	50 mg, qd
Fluvoxamine (+0 h)	100 mg, qd	100 mg, qd	1.15	1.04	90 mg, qd
	100 mg, qd	140 mg, qd	1.12	0.98	120 mg, qd

–: Dose adaptations could not be provided, **AUC_{ss}**: steady state area under the concentration–time curve, **bid**: twice a day, **D**: day, **IR**: immediate release, **qd**: once daily, **qid**: four times a day, **sd**: single dose, **tab**: tablet, **tid**: three times a day

¹ AUC_{ss} Ratio was calculated dividing AUC_{ss} of the DDI setting (with 100 or 140 mg dasatinib) by the corresponding AUC_{ss} of the control scenario.

² AUC_{ss} Ratio (adapted) was calculated dividing AUC_{ss} of the DDI setting using the model-based adapted dose of dasatinib by the corresponding AUC_{ss} of the control scenario.

³ Rifampicin is also a weak CYP3A4 inhibitor; administrations were simulated to be concomitantly with dasatinib administrations.

Table S12: Overview of model-based dose adaptations for dasatinib within various DDI scenarios based on the exposure matching principle.

Perpetrator	Dosing of Perpetrator	Dosing of Dasatinib	AUC _{ss} Ratio	AUC _{ss} Ratio (adapted)	Adapted Dasatinib Dose
Fluvoxamine (+12 h)	100 mg, qd	100 mg, qd	1.02	1.02	100 mg, qd
	100 mg, qd	140 mg, qd	1.02	1.02	140 mg, qd
Grapefruit Juice	250 ml, qd	100 mg, qd	1.40	1.02	70 mg, qd
	250 ml, qd	140 mg, qd	1.33	1.00	100 mg, qd
Grapefruit Juice	250 ml, sd	100 mg, qd	1.13	1.02	90 mg, qd
	250 ml, sd	140 mg, qd	1.10	1.03	130 mg, qd
Strong CYP3A4 Inducers					
Carbamazepine (IR tab, fed state)	400 mg, tid	100 mg, qd	0.30	1.01	250 mg, qd
	400 mg, tid	140 mg, qd	0.35	0.99	340 mg, qd
Rifampicin ³	600 mg, qd	100 mg, qd	0.50	1.01	230 mg, qd
	600 mg, qd	140 mg, qd	0.48	1.00	360 mg, qd
Moderate CYP3A4 Inducers					
Efavirenz (+ 0 h)	600 mg, qd	100 mg, qd	0.34	0.99	240 mg, qd
	600 mg, qd	140 mg, qd	0.37	1.00	340 mg, qd
Efavirenz (+12 h)	600 mg, qd	100 mg, qd	0.23	1.00	310 mg, qd
	600 mg, qd	140 mg, qd	-	-	-

-: Dose adaptations could not be provided, **AUC_{ss}**: steady state area under the concentration–time curve, **bid**: twice a day, **D**: day, **IR**: immediate release, **qd**: once daily, **qid**: four times a day, **sd**: single dose, **tab**: tablet, **tid**: three times a day

¹ AUC_{ss} Ratio was calculated dividing AUC_{ss} of the DDI setting (with 100 or 140 mg dasatinib) by the corresponding AUC_{ss} of the control scenario.

² AUC_{ss} Ratio (adapted) was calculated dividing AUC_{ss} of the DDI setting using the model-based adapted dose of dasatinib by the corresponding AUC_{ss} of the control scenario.

³ Rifampicin is also a weak CYP3A4 inhibitor; administrations were simulated to be concomitantly with dasatinib administrations.

S5.1.1 Plasma Profiles of Simulated Single DDI Scenarios

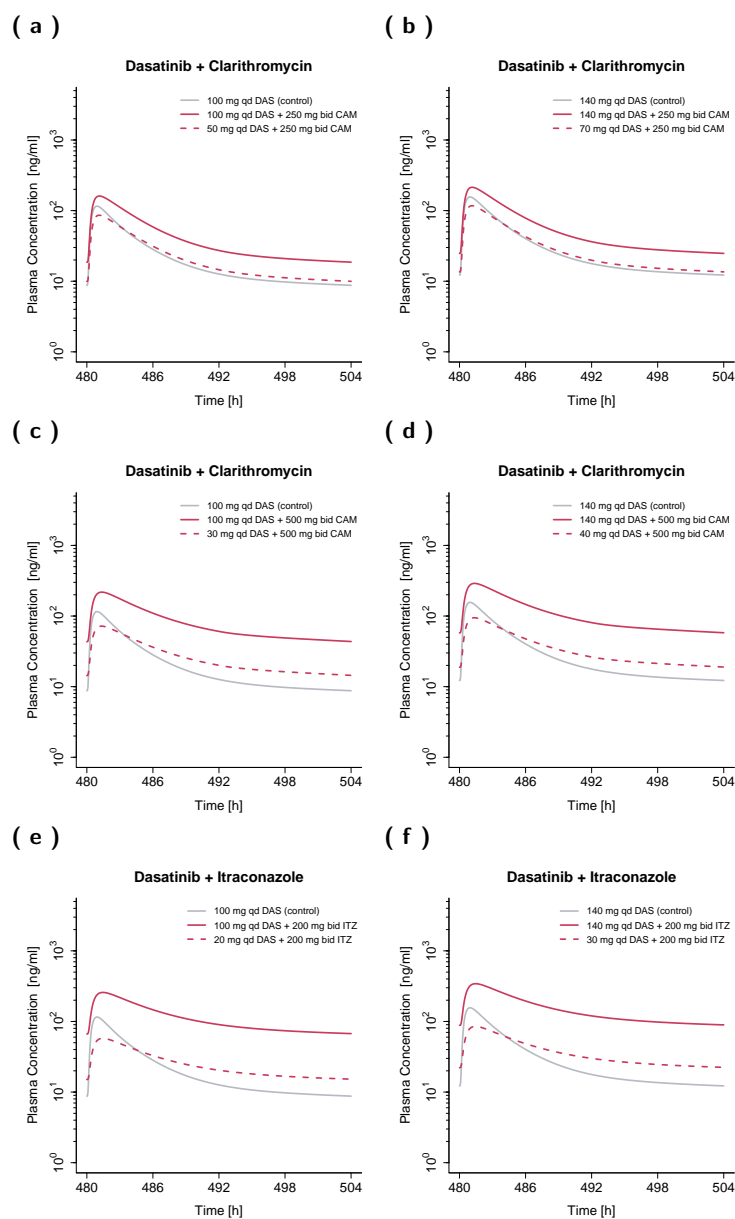


Figure S13: Model-based dose adaptations for dasatinib within various single DDI scenarios including moderate and strong CYP3A4 inhibitors and inducers. The first and second column represent the simulation results after administration of 100 mg and 140 mg dasatinib daily, respectively. Colored and grey solid lines show simulated mean concentration–time profiles with and without intake of a perpetrator drug, respectively. Dashed lines represent the simulated mean concentration–time profiles in presence of a perpetrator drug, using an adapted dose of dasatinib. **Bid:** twice a day, **CAM:** clarithromycin, **CBZ:** carbamazepine, **D:** day, **DAS:** dasatinib, **DDI:** drug–drug interaction, **EFV:** efavirenz, **ERY:** erythromycin, **FLV:** fluvoxamine, **FLZ:** fluconazole, **GFJ:** grapefruit juice, **ITZ:** itraconazole, **KCZ:** ketoconazole, **qd:** once a day, **qid:** four times a day, **RIF:** rifampicin, **sd:** single dose, **tid:** three times a day, **VRC:** voriconazole.

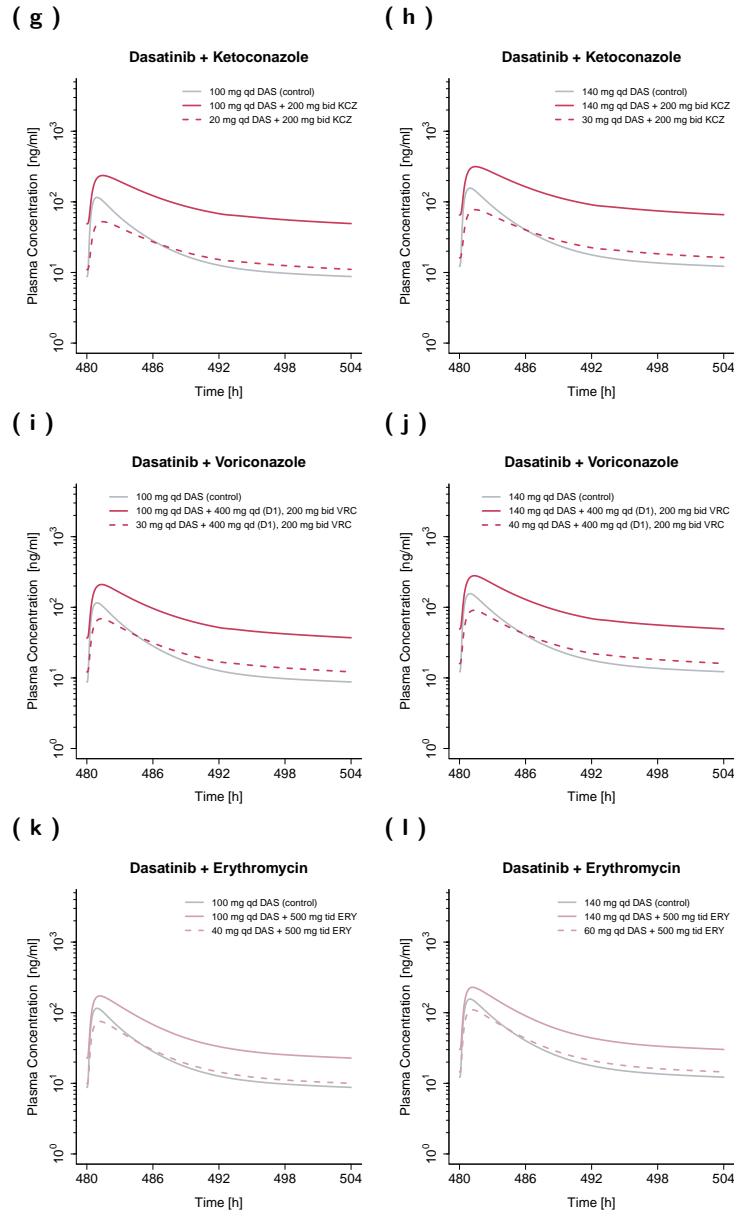


Figure S13: (continued) Model-based dose adaptations for dasatinib within various single DDI scenarios including moderate and strong CYP3A4 inhibitors and inducers. The first and second column represent the simulation results after administration of 100 mg and 140 mg dasatinib daily, respectively. Colored and grey solid lines show simulated mean concentration–time profiles with and without intake of a perpetrator drug, respectively. Dashed lines represent the simulated mean concentration–time profiles in presence of a perpetrator drug, using an adapted dose of dasatinib. **Bid**: twice a day, **CAM**: clarithromycin, **CBZ**: carbamazepine, **D**: day, **DAS**: dasatinib, **DDI**: drug–drug interaction, **EFV**: efavirenz, **ERY**: erythromycin, **FLV**: fluvoxamine, **FLZ**: fluconazole, **GFJ**: grapefruit juice, **ITZ**: itraconazole, **KCZ**: ketoconazole, **qd**: once a day, **qid**: four times a day, **RIF**: rifampicin, **sd**: single dose, **tid**: three times a day, **VRC**: voriconazole.

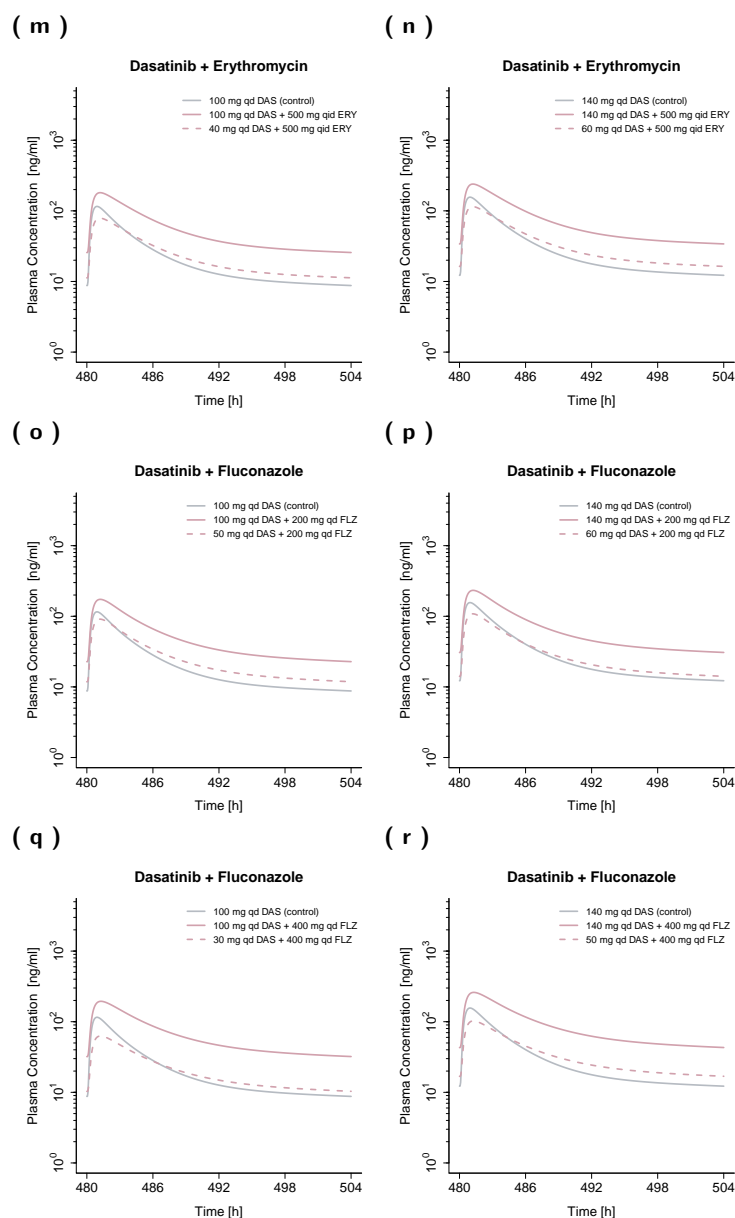


Figure S13: (continued) Model-based dose adaptations for dasatinib within various single DDI scenarios including moderate and strong CYP3A4 inhibitors and inducers. The first and second column represent the simulation results after administration of 100 mg and 140 mg dasatinib daily, respectively. Colored and grey solid lines show simulated mean concentration-time profiles with and without intake of a perpetrator drug, respectively. Dashed lines represent the simulated mean concentration-time profiles in presence of a perpetrator drug, using an adapted dose of dasatinib. **Bid:** twice a day, **CAM:** clarithromycin, **CBZ:** carbamazepine, **D:** day, **DAS:** dasatinib, **DDI:** drug-drug interaction, **EFV:** efavirenz, **ERY:** erythromycin, **FLV:** fluvoxamine, **FLZ:** fluconazole, **GFJ:** grapefruit juice, **ITZ:** itraconazole, **KCZ:** ketoconazole, **qd:** once a day, **qid:** four times a day, **RIF:** rifampicin, **sd:** single dose, **tid:** three times a day, **VRC:** voriconazole.

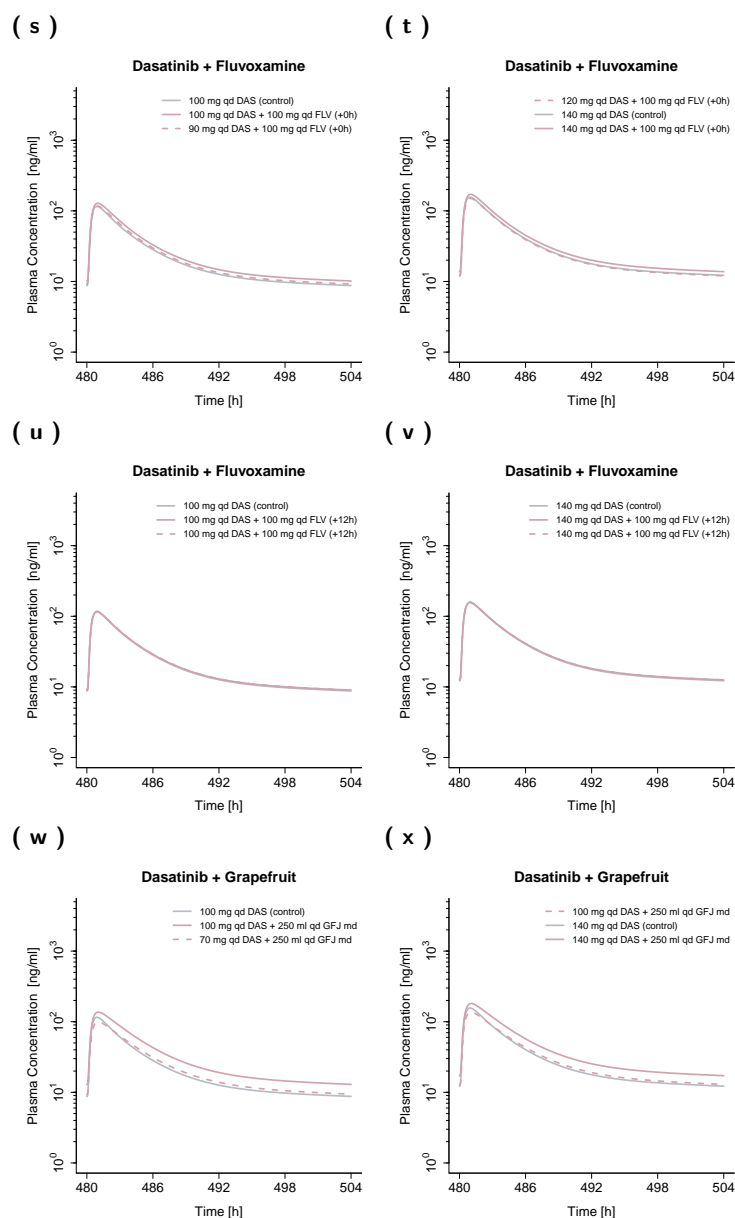


Figure S13: (continued) Model-based dose adaptations for dasatinib within various single DDI scenarios including moderate and strong CYP3A4 inhibitors and inducers. The first and second column represent the simulation results after administration of 100 mg and 140 mg dasatinib daily, respectively. Colored and grey solid lines show simulated mean concentration–time profiles with and without intake of a perpetrator drug, respectively. Dashed lines represent the simulated mean concentration–time profiles in presence of a perpetrator drug, using an adapted dose of dasatinib. **Bid:** twice a day, **CAM:** clarithromycin, **CBZ:** carbamazepine, **D:** day, **DAS:** dasatinib, **DDI:** drug–drug interaction, **EFV:** efavirenz, **ERY:** erythromycin, **FLV:** fluvoxamine, **FLZ:** fluconazole, **GFJ:** grapefruit juice, **ITZ:** itraconazole, **KCZ:** ketoconazole, **qd:** once a day, **qid:** four times a day, **RIF:** rifampicin, **sd:** single dose, **tid:** three times a day, **VRC:** voriconazole.

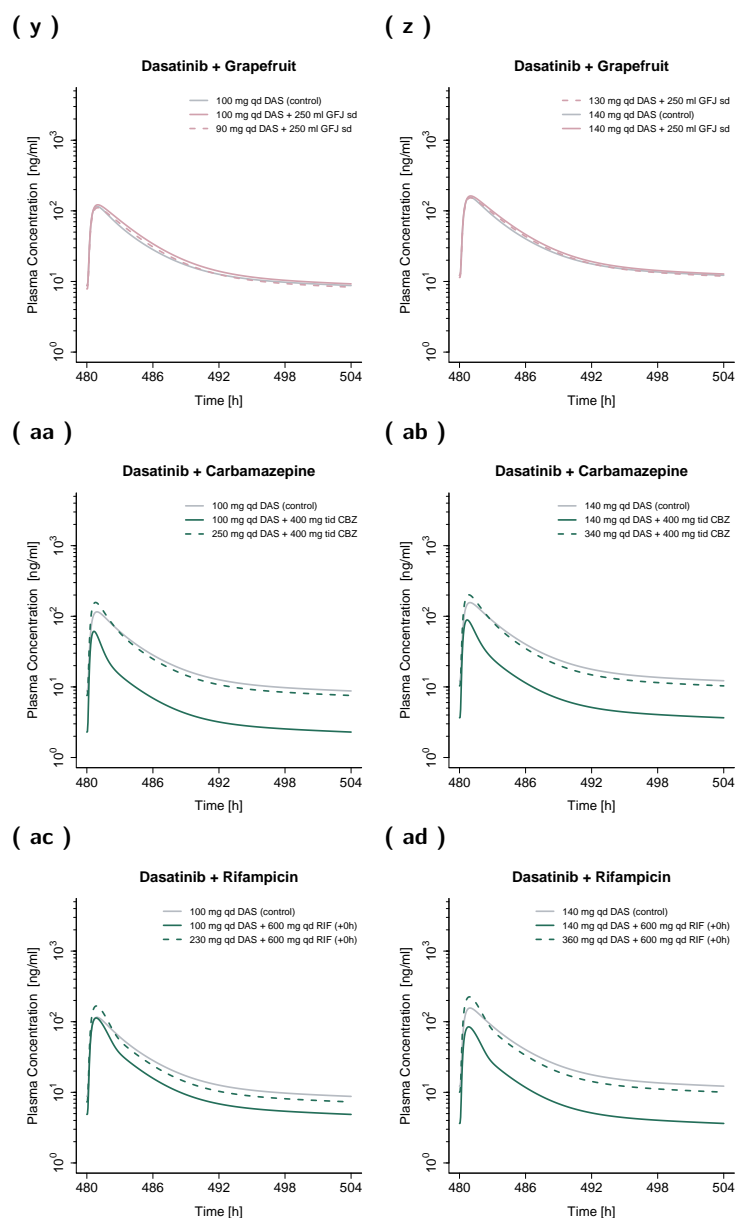


Figure S13: (continued) Model-based dose adaptations for dasatinib within various single DDI scenarios including moderate and strong CYP3A4 inhibitors and inducers. The first and second column represent the simulation results after administration of 100 mg and 140 mg dasatinib daily, respectively. Colored and grey solid lines show simulated mean concentration-time profiles with and without intake of a perpetrator drug, respectively. Dashed lines represent the simulated mean concentration-time profiles in presence of a perpetrator drug, using an adapted dose of dasatinib. **Bid**: twice a day, **CAM**: clarithromycin, **CBZ**: carbamazepine, **D**: day, **DAS**: dasatinib, **DDI**: drug-drug interaction, **EFV**: efavirenz, **ERY**: erythromycin, **FLV**: fluvoxamine, **FLZ**: fluconazole, **GFJ**: grapefruit juice, **ITZ**: itraconazole, **KCZ**: ketoconazole, **qd**: once a day, **qid**: four times a day, **RIF**: rifampicin, **sd**: single dose, **tid**: three times a day, **VRC**: voriconazole.

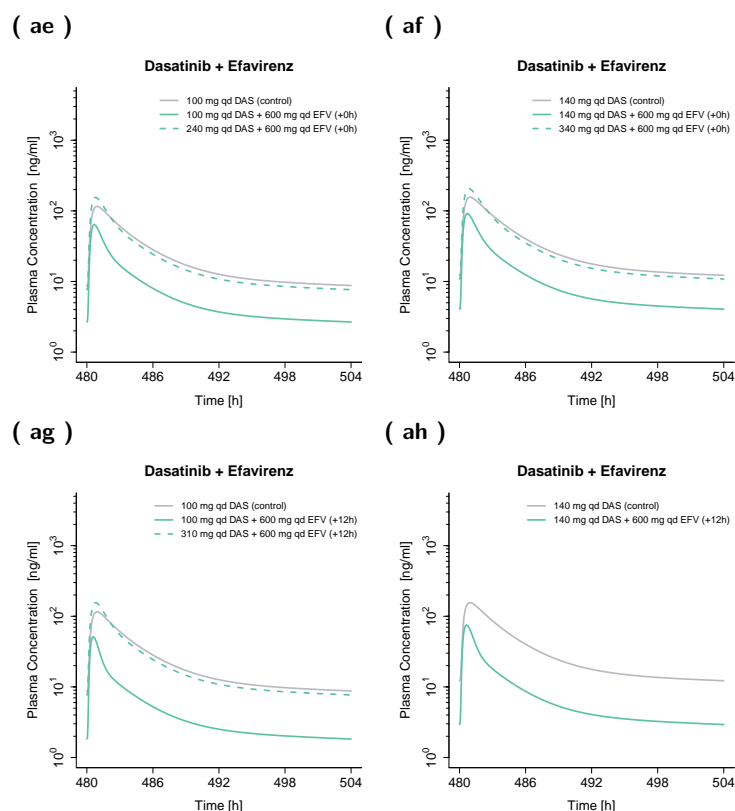


Figure S13: (continued) Model-based dose adaptations for dasatinib within various single DDI scenarios including moderate and strong CYP3A4 inhibitors and inducers. The first and second column represent the simulation results after administration of 100 mg and 140 mg dasatinib daily, respectively. Colored and grey solid lines show simulated mean concentration–time profiles with and without intake of a perpetrator drug, respectively. Dashed lines represent the simulated mean concentration–time profiles in presence of a perpetrator drug, using an adapted dose of dasatinib. **Bid:** twice a day, **CAM:** clarithromycin, **CBZ:** carbamazepine, **D:** day, **DAS:** dasatinib, **DDI:** drug–drug interaction, **EFV:** efavirenz, **ERY:** erythromycin, **FLV:** fluvoxamine, **FLZ:** fluconazole, **GFJ:** grapefruit juice, **ITZ:** itraconazole, **KCZ:** ketoconazole, **qd:** once a day, **qid:** four times a day, **RIF:** rifampicin, **sd:** single dose, **tid:** three times a day, **VRC:** voriconazole.

S5.1.2 Plasma Profiles of Simulated Multiple DDI Scenarios

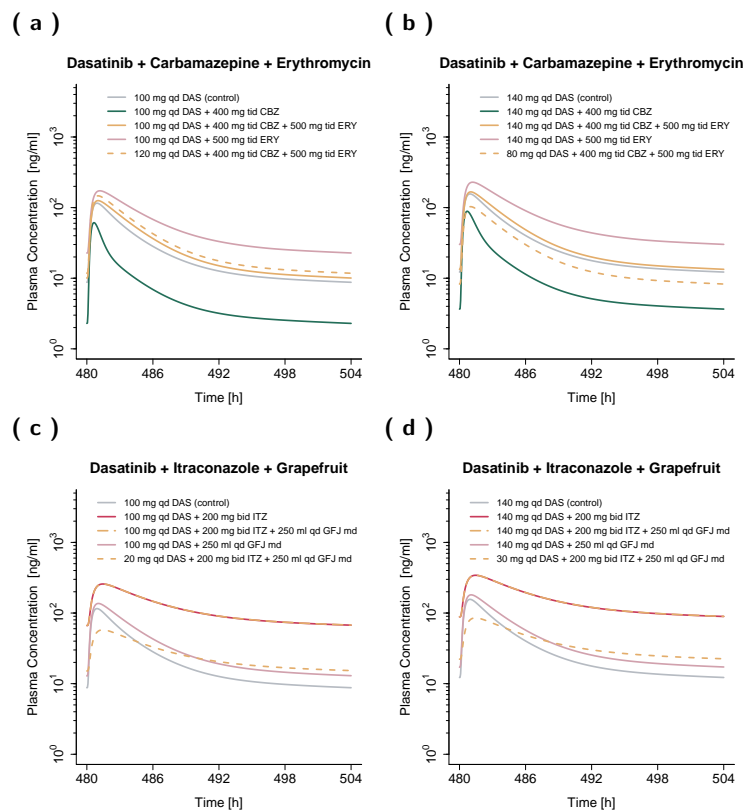


Figure S14: Model-based dose adaptations for dasatinib within multiple DDIs. The first and second column represent the simulation results after administration of 100 mg and 140 mg dasatinib daily, respectively. Colored and grey solid lines show simulated mean concentration–time profiles with and without intake of perpetrator drug(s), respectively. Dashed lines represent the simulated mean concentration–time profiles in presence of perpetrator drug(s), using an adapted dose of dasatinib. **Bid:** twice a day, **CBZ:** carbamazepine, **DAS:** dasatinib, **DDI:** drug–drug interaction, **ERY:** erythromycin, **GFJ:** grapefruit juice, **ITZ:** itraconazole, **qd:** once a day, **tid:** three times a day.

S5.2 CYP3A4 Autoinhibition

Dasatinib exhibits time-dependent inhibition of CYP3A4 according to *in vitro* studies [44, 62] affecting the exposure of CYP3A4 substrates (e.g., simvastatin) [6], but also its own metabolism. CYP3A4 time-dependent inhibition by dasatinib results in a slight supra-proportional increase in exposure of 16% comparing area under the concentration–time curve (AUC) from zero to infinity after single dose administration and AUC steady state (AUC_{ss}) (see Table S13). Moreover, the time-dependent inhibition showed no or only minor effects on the performed prospective DDI simulations with dasatinib as victim drug (e.g., no impact on AUC_{ss} during itraconazole DDI and 7% higher AUC_{ss} during fluvoxamine DDI).

Table S13: Impact of CYP3A4 autoinhibition on dasatinib exposure.

Dasatinib Dosing Regimen	AUC _{inf}	AUC _{ss}	AUC _{ss} /AUC _{inf}
20 mg, sd	0.19	-	1.07
20 mg, qd	-	0.20	1.07
100 mg, sd	1.06	-	1.16
100 mg, qd	-	1.24	1.16
140 mg, sd	1.51	-	1.15
140 mg, qd	-	1.73	1.15
360 mg, sd	3.09	-	1.11
360 mg, qd	-	3.42	1.11
420 mg, sd	3.26	-	1.10
420 mg, qd	-	3.58	1.10

AUC_{inf}: area under the concentration–time curve from zero to infinity,

AUC_{ss}: steady state area under the concentration–time curve,

CYP: cytochrome P450, qd: once a day, sd: single dose

S5.3 Pharmacokinetic Parameters: Absolute Bioavailability, Fraction Absorbed, Fraction Metabolized, Fraction Escaping Gut Wall and Hepatic Elimination

Table S14: Overview of simulated F_a, F_g, F_h, F_m and BA.

Dasatinib Dosing Regimen	F _a (%)	F _g (%)	F _h (%)	F _m (%)	BA (%)
20 mg, sd	80	47	64	94	24
100 mg, sd	69	64	63	93	28
140 mg, sd	65	68	63	92	28
360 mg, sd	45	79	62	91	22
420 mg, sd	41	79	62	90	20

BA: absolute bioavailability, CYP: cytochrome P450, F_a: fraction absorbed,

F_g: fraction escaping gut wall elimination, F_h: fraction escaping hepatic elimination

F_m: fraction metabolized via CYP3A4, sd: single dose

References

- [1] National Center for Health Statistics (1997) Third National Health and Nutrition Examination Survey (NHANES III). Tech. rep., Hyattsville, MD 20782
- [2] American Cancer Society (2022) Cancer Facts and Figures. <https://www.cancer.org/cancer/chronic-myeloid-leukemia/about/statistics.html>, available online (accessed: 2023-02-01)
- [3] Valentin J (2002) Basic anatomical and physiological data for use in radiological protection: reference values. A report of age- and gender-related differences in the anatomical and physiological characteristics of reference individuals. ICRP Publication 89. *Annals of the ICRP* 32(3-4):5–265
- [4] Schlender J (2015) A report including the description of the physiology base of the Japanese population implemented in PK-Sim®. https://github.com/Open-Systems-Pharmacology/OSPSuite.Documentation/blob/master/Japanese_Population/Report.md, available online (accessed: 2022-08-04)
- [5] Willmann S, Höhn K, Edginton A, Sevestre M, Solodenko J, Weiss W, Lippert J, Schmitt W (2007) Development of a physiology-based whole-body population model for assessing the influence of individual variability on the pharmacokinetics of drugs. *Journal of pharmacokinetics and pharmacodynamics* 34(3):401–31
- [6] Center for Drug Evaluation (2005) Clinical Pharmacology and Biopharmaceutics Review(s): NDA Review - Dasatinib. https://www.accessdata.fda.gov/drugsatfda_docs/nda/2006/021986s000_Sprycel_ClinPharmR.pdf, available online (accessed: 2022-08-04)
- [7] Christopher LJ, Cui D, Wu C, Luo R, Manning JA, Bonacorsi SJ, Lago M, Allentoff A, Lee FYF, McCann B, Galbraith S, Reitberg DP, He K, Barros A, Blackwood-Chirchir A, Humphreys WG, Iyer RA (2008) Metabolism and disposition of dasatinib after oral administration to humans. *Drug metabolism and disposition: the biological fate of chemicals* 36(7):1357–64
- [8] Vaidhyanathan S, Wang X, Crison J, Varia S, Gao JZH, Saxena A, Good D (2019) Bioequivalence Comparison of Pediatric Dasatinib Formulations and Elucidation of Absorption Mechanisms Through Integrated PBPK Modeling. *Journal of pharmaceutical sciences* 108(1):741–749
- [9] Vargas M, Villarraga E (2016) Bioequivalence Study of Two Dasatinib 100 mg Formulations in Healthy Colombians. *Journal of Bioequivalence & Bioavailability* 09(01):302–305
- [10] Luo FR, Barrett YC, Yang Z, Camuso A, McGlinchey K, Wen ML, Smykla R, Fager K, Wild R, Palme H, Galbraith S, Blackwood-Chirchir A, Lee FY (2008) Identification and validation of phospho-SRC, a novel and potential pharmacodynamic biomarker for dasatinib (SPRYCEL), a multi-targeted kinase inhibitor. *Cancer chemotherapy and pharmacology* 62(6):1065–74
- [11] Willmann S, Schmitt W, Keldenich J, Lippert J, Dressman JB (2004) A physiological model for the estimation of the fraction dose absorbed in humans. *Journal of medicinal chemistry* 47(16):4022–31
- [12] Zwaan CM, Rizzari C, Mechinaud F, Lancaster DL, Lehrnbecher T, van der Velden VHJ, Beverloo BB, den Boer ML, Pieters R, Reinhardt D, Dworzak M, Rosenberg J, Manos G, Agrawal S, Strauss L, Baruchel A, Kearns PR (2013) Dasatinib in children and adolescents with relapsed or refractory leukemia: results of the CA180-018 phase I dose-escalation study of the Innovative Therapies for Children with Cancer Consortium. *Journal of clinical oncology : official journal of the American Society of Clinical Oncology* 31(19):2460–8

- [13] Synthon Hispania SL (2019) Public Assessment Report (Decentralised Procedure): Dasatinib Synthon Hispania 20 mg ; 50 mg ; 70 mg ; 80 mg ; 100 mg ; 140 mg Filmtabletten. https://file.wuxuwang.com/hma/DE_H_5896_003_PAR.pdf, available online (accessed: 2022-05-05)
- [14] Furlong MT, Agrawal S, Hawthorne D, Lago M, Unger S, Krueger L, Stouffer B (2012) A validated LC-MS/MS assay for the simultaneous determination of the anti-leukemic agent dasatinib and two pharmacologically active metabolites in human plasma: application to a clinical pharmacokinetic study. *Journal of pharmaceutical and biomedical analysis* 58(1):130–5
- [15] Araujo JC, Mathew P, Armstrong AJ, Braud EL, Posadas E, Lonberg M, Gallick GE, Trudel GC, Paliwal P, Agrawal S, Logothetis CJ (2012) Dasatinib combined with docetaxel for castration-resistant prostate cancer: results from a phase 1-2 study. *Cancer* 118(1):63–71
- [16] Demetri GD, Lo Russo P, MacPherson IRJ, Wang D, Morgan JA, Brunton VG, Paliwal P, Agrawal S, Voi M, Evans TRJ (2009) Phase I dose-escalation and pharmacokinetic study of dasatinib in patients with advanced solid tumors. *Clinical cancer research : an official journal of the American Association for Cancer Research* 15(19):6232–40
- [17] Takahashi S, Miyazaki M, Okamoto I, Ito Y, Ueda K, Seriu T, Nakagawa K, Hatake K (2011) Phase I study of dasatinib (BMS-354825) in Japanese patients with solid tumors. *Cancer science* 102(11):2058–64
- [18] Meyer M, Schneckener S, Ludewig B, Kuepfer L, Lippert J (2012) Using expression data for quantification of active processes in physiologically based pharmacokinetic modeling. *Drug metabolism and disposition: the biological fate of chemicals* 40(5):892–901
- [19] Scotcher D, Billington S, Brown J, Jones CR, Brown CDA, Rostami-Hodjegan A, Galetin A (2017) Microsomal and Cytosolic Scaling Factors in Dog and Human Kidney Cortex and Application for In Vitro-In Vivo Extrapolation of Renal Metabolic Clearance. *Drug metabolism and disposition: the biological fate of chemicals* 45(5):556–568
- [20] Eriksson J, Solodenko J (2021) Building and evaluation of a PBPK model for Fluconazole in healthy adults. <https://github.com/Open-Systems-Pharmacology/OSP-PBPK-Model-Library/tree/master/Fluconazole>, available online (accessed: 2023-08-17)
- [21] Wojtyniak JG, Selzer D, Schwab M, Lehr T (2021) Physiologically Based Precision Dosing Approach for Drug-Drug-Gene Interactions: A Simvastatin Network Analysis. *Clinical pharmacology and therapeutics* 109(1):201–211
- [22] Shi P, Liao M, Chuang BC, Griffin R, Shi J, Hyer M, Fallon JK, Smith PC, Li C, Xia CQ (2018) Efflux transporter breast cancer resistance protein dominantly expresses on the membrane of red blood cells, hinders partitioning of its substrates into the cells, and alters drug-drug interaction profiles. *Xenobiotica; the fate of foreign compounds in biological systems* 48(11):1173–1183
- [23] Prasad B, Evers R, Gupta A, Hop CECA, Salphati L, Shukla S, Ambudkar SV, Unadkat JD (2014) Interindividual variability in hepatic organic anion-transporting polypeptides and P-glycoprotein (ABCB1) protein expression: quantification by liquid chromatography tandem mass spectroscopy and influence of genotype, age, and sex. *Drug metabolism and disposition: the biological fate of chemicals* 42(1):78–88
- [24] Hanke N, Frechen S, Moj D, Britz H, Eissing T, Wendl T, Lehr T (2018) PBPK Models for CYP3A4 and P-gp DDI Prediction: A Modeling Network of Rifampicin, Itraconazole, Clarithromycin, Midazolam, Alfentanil, and Digoxin. *CPT: pharmacometrics & systems pharmacology* 7(10):647–659

- [25] Dallmann A, Solodenko J, Wendl T, Frechen S (2022) Building and Evaluation of a PBPK Model for Erythromycin in Healthy Adults. https://github.com/Open-Systems-Pharmacology/OSP-PBPK-Model-Library/blob/master/Erythromycin/Erythromycin_evaluation_report.pdf, available online (accessed: 2022-10-18)
- [26] Nishimura M, Naito S (2006) Tissue-specific mRNA expression profiles of human phase I metabolizing enzymes except for cytochrome P450 and phase II metabolizing enzymes. *Drug metabolism and pharmacokinetics* 21(5):357–74
- [27] Rodrigues AD (1999) Integrated cytochrome P450 reaction phenotyping: attempting to bridge the gap between cDNA-expressed cytochromes P450 and native human liver microsomes. *Biochemical pharmacology* 57(5):465–80
- [28] Open Systems Pharmacology Suite Community (2018) PK-Sim® Ontogeny Database Documentation, Version 7.3. <https://github.com/Open-Systems-Pharmacology/OSPSuite.Documentation/blob/master/PK-SimOntogenyDatabaseVersion7.3.pdf>, available online (accessed: 2020-03-25)
- [29] Nishimura M, Yaguti H, Yoshitsugu H, Naito S, Satoh T (2003) Tissue distribution of mRNA expression of human cytochrome P450 isoforms assessed by high-sensitivity real-time reverse transcription PCR. *Yakugaku zasshi : Journal of the Pharmaceutical Society of Japan* 123(5):369–75
- [30] Rowland Yeo K, Walsky RL, Jamei M, Rostami-Hodjegan A, Tucker GT (2011) Prediction of time-dependent CYP3A4 drug-drug interactions by physiologically based pharmacokinetic modelling: impact of inactivation parameters and enzyme turnover. *European journal of pharmaceutical sciences : official journal of the European Federation for Pharmaceutical Sciences* 43(3):160–73
- [31] Greenblatt DJ, von Moltke LL, Harmatz JS, Chen G, Weemhoff JL, Jen C, Kelley CJ, LeDuc BW, Zinny MA (2003) Time course of recovery of cytochrome p450 3A function after single doses of grapefruit juice. *Clinical pharmacology and therapeutics* 74(2):121–9
- [32] Margailan G, Rouleau M, Klein K, Fallon JK, Caron P, Villeneuve L, Smith PC, Zanger UM, Guillemette C (2015) Multiplexed Targeted Quantitative Proteomics Predicts Hepatic Glucuronidation Potential. *Drug metabolism and disposition: the biological fate of chemicals* 43(9):1331–5
- [33] National Center for Biotechnology Information (NCBI) (2010) Expressed Sequence Tags (EST) from UniGene.
- [34] Prasad B, Lai Y, Lin Y, Unadkat JD (2013) Interindividual variability in the hepatic expression of the human breast cancer resistance protein (BCRP/ABCG2): effect of age, sex, and genotype. *Journal of pharmaceutical sciences* 102(3):787–93
- [35] Nishimura M, Naito S (2005) Tissue-specific mRNA expression profiles of human ATP-binding cassette and solute carrier transporter superfamilies. *Drug metabolism and pharmacokinetics* 20(6):452–77
- [36] Deo AK, Prasad B, Balogh L, Lai Y, Unadkat JD (2012) Interindividual variability in hepatic expression of the multidrug resistance-associated protein 2 (MRP2/ABCC2): quantification by liquid chromatography/tandem mass spectrometry. *Drug metabolism and disposition: the biological fate of chemicals* 40(5):852–5

- [37] Kolesnikov N, Hastings E, Keays M, Melnichuk O, Tang YA, Williams E, Dylag M, Kurbatova N, Brandizi M, Burdett T, Megy K, Pilicheva E, Rustici G, Tikhonov A, Parkinson H, Petryszak R, Sarkans U, Brazma A (2015) ArrayExpress update—simplifying data submissions. *Nucleic acids research* 43(Database issue):D1113–6
- [38] Andre Dallmann (2021) IVIC with the particle dissolution module implemented in OSP. <https://github.com/AndreDlm/IVIC-with-particle-dissolution-module-in-OSP>, available online (accessed: 2023-01-05)
- [39] Developed by ChemAxon (2009) Chemicalize was used for prediction of dasatinib properties. <https://chemicalize.com/>, available online (accessed: 2022-05-03)
- [40] Hořínková J, Šíma M, Slanař O (2019) Pharmacokinetics of Dasatinib. *Prague medical report* 120(2-3):52–63
- [41] Tsume Y, Takeuchi S, Matsui K, Amidon GE, Amidon GL (2015) In vitro dissolution methodology, mini-Gastrointestinal Simulator (mGIS), predicts better in vivo dissolution of a weak base drug, dasatinib. *European journal of pharmaceutical sciences : official journal of the European Federation for Pharmaceutical Sciences* 76:203–12
- [42] Watanabe R, Esaki T, Kawashima H, Natsume-Kitatani Y, Nagao C, Ohashi R, Mizuguchi K (2018) Predicting Fraction Unbound in Human Plasma from Chemical Structure: Improved Accuracy in the Low Value Ranges. *Molecular pharmaceutics* 15(11):5302–5311
- [43] Wang L, Christopher LJ, Cui D, Li W, Iyer R, Humphreys WG, Zhang D (2008) Identification of the human enzymes involved in the oxidative metabolism of dasatinib: an effective approach for determining metabolite formation kinetics. *Drug metabolism and disposition: the biological fate of chemicals* 36(9):1828–39
- [44] Chang M, Bathena S, Christopher LJ, Shen H, Roy A (2022) Prediction of drug-drug interaction potential mediated by transporters between dasatinib and metformin, pravastatin, and rosuvastatin using physiologically based pharmacokinetic modeling. *Cancer chemotherapy and pharmacology* 89(3):383–392
- [45] Pahwa S, Alam K, Crowe A, Farasyn T, Neuhoﬀ S, Hatley O, Ding K, Yue W (2017) Pre-treatment With Rifampicin and Tyrosine Kinase Inhibitor Dasatinib Potentiates the Inhibitory Effects Toward OATP1B1- and OATP1B3-Mediated Transport. *Journal of pharmaceutical sciences* 106(8):2123–2135
- [46] Open Systems Pharmacology Suite Community (2021) Open Systems Pharmacology Suite Manual. <https://raw.githubusercontent.com/Open-Systems-Pharmacology/OSPSuite.Documentation/master/OpenSystemsPharmacologySuite.pdf>, available online (accessed: 2023-05-04)
- [47] Fisher RS, Rock E, Malmud LS (1987) Effects of meal composition on gallbladder and gastric emptying in man. *Digestive diseases and sciences* 32(12):1337–44
- [48] Schmitt W (2008) General approach for the calculation of tissue to plasma partition coefficients. *Toxicology in vitro : an international journal published in association with BIBRA* 22(2):457–67
- [49] ChemicalBook (2006) ChemicalBook was used for collection of chemical information of dasatinib. <https://www.chemicalbook.com/>, available online (accessed: 2023-01-05)

- [50] Eley T, Luo FR, Agrawal S, Sanil A, Manning J, Li T, Blackwood-Chirchir A, Bertz R (2009) Phase I study of the effect of gastric acid pH modulators on the bioavailability of oral dasatinib in healthy subjects. *Journal of clinical pharmacology* 49(6):700–9
- [51] Yago MR, Frymoyer A, Benet LZ, Smelick GS, Frassetto LA, Ding X, Dean B, Salphati L, Budha N, Jin JY, Dresser MJ, Ware JA (2014) The use of betaine HCl to enhance dasatinib absorption in healthy volunteers with rabeprazole-induced hypochlorhydria. *The AAPS journal* 16(6):1358–65
- [52] Johnson FM, Agrawal S, Burris H, Rosen L, Dhillon N, Hong D, Blackwood-Chirchir A, Luo FR, Sy O, Kaul S, Chiappori AA (2010) Phase 1 pharmacokinetic and drug-interaction study of dasatinib in patients with advanced solid tumors. *Cancer* 116(6):1582–91
- [53] Okada M, Yao T, Sakurai T, Arita M, Okabe N, Iida M, Okada Y, Koga T (1992) A comparative study of once-a-day morning and once-a-day bedtime administration of 40 mg famotidine in treating gastric ulcers. *The American journal of gastroenterology* 87(8):1009–13
- [54] Dennis L Decktor, Malcolm Robinson SG (1995) Comparative Effects of Liquid Antacids on Esophageal and Gastric pH in Patients with Heartburn. *American journal of therapeutics* 2(7):481–486
- [55] Guest EJ, Aarons L, Houston JB, Rostami-Hodjegan A, Galetin A (2011) Critique of the two-fold measure of prediction success for ratios: application for the assessment of drug-drug interactions. *Drug metabolism and disposition: the biological fate of chemicals* 39(2):170–3
- [56] Fuhr LM, Marok FZ, Hanke N, Selzer D, Lehr T (2021) Pharmacokinetics of the CYP3A4 and CYP2B6 Inducer Carbamazepine and Its Drug-Drug Interaction Potential: A Physiologically Based Pharmacokinetic Modeling Approach. *Pharmaceutics* 13(2):1–21
- [57] Wendl T, Frechen S, Solodenko J, Dallmann A (2021) Building and Evaluation of a PBPK Model for Efavirenz in Healthy Adults. https://github.com/Open-Systems-Pharmacology/OSP-PBPK-Model-Library/blob/master/Efavirenz/efavirenz_evaluation_report.pdf, available online (accessed: 2022-10-18)
- [58] Britz H, Hanke N, Volz AK, Spigset O, Schwab M, Eissing T, Wendl T, Frechen S, Lehr T (2019) Physiologically-Based Pharmacokinetic Models for CYP1A2 Drug–Drug Interaction Prediction: A Modeling Network of Fluvoxamine, Theophylline, Caffeine, Rifampicin, and Midazolam. *CPT: Pharmacometrics and Systems Pharmacology* 8(5):296–307
- [59] Fuhr LM, Marok FZ, Fuhr U, Selzer D, Lehr T (2023) Physiologically based pharmacokinetic modeling of bergamottin and 6,7-dihydroxybergamottin to describe CYP3A4 mediated grapefruit-drug interactions. *Clinical pharmacology and therapeutics* (031):0–2
- [60] Marok FZ, Wojtyniak JG, Fuhr LM, Selzer D, Schwab M, Weiss J, Haefeli WE, Lehr T (2023) A Physiologically Based Pharmacokinetic Model of Ketoconazole and Its Metabolites as Drug–Drug Interaction Perpetrators. *Pharmaceutics* 15(2)
- [61] Li X, Frechen S, Moj D, Lehr T, Taubert M, Hsin CH, Mikus G, Neuvonen PJ, Olkkola KT, Saari TI, Fuhr U (2020) A Physiologically Based Pharmacokinetic Model of Voriconazole Integrating Time-Dependent Inhibition of CYP3A4, Genetic Polymorphisms of CYP2C19 and Predictions of Drug–Drug Interactions. *Clinical pharmacokinetics* 59(6):781–808
- [62] Li X, He Y, Ruiz CH, Koenig M, Cameron MD, Vojkovsky T (2009) Characterization of dasatinib and its structural analogs as CYP3A4 mechanism-based inactivators and the proposed bioactivation pathways. *Drug metabolism and disposition: the biological fate of chemicals* 37(6):1242–50

B.4 PROJECT IV: CYP2D6 DDGI NETWORK MODELING

Clinical Pharmacology & Therapeutics

A Comprehensive CYP2D6 Drug-Drug-Gene Interaction Network for Application in Precision Dosing and Drug Development

Supplement S1 - Model Information and Evaluation

Simeon Rüdesheim^{1,2*}, Helena Leonie Hanae Loer^{1*}, Denise Feick^{1,3}, Fatima Zahra Marok¹, Laura Maria Fuhr¹, Dominik Selzer¹, Donato Teutonico⁴, Annika R. P. Schneider⁵, Juri Solodenko⁵, Sebastian Frechen⁵, Maaïke van der Lee⁶, Dirk Jan A. R. Moes⁶, Jesse J. Swen⁶, Matthias Schwab^{2,7,8}, and Thorsten Lehr¹

* Authors contributed equally

¹ Clinical Pharmacy, Saarland University, Saarbrücken, Germany

² Dr. Margarete Fischer-Bosch-Institute of Clinical Pharmacology, Stuttgart, Germany

³ Drug Metabolism and Pharmacokinetics, Sanofi R&D, Frankfurt am Main, Germany

⁴ Translational Medicine & Early Development, Sanofi R&D, Vitry-sur-Seine, France

⁵ Bayer AG, Pharmaceuticals, Research & Development, Model-informed drug development, Leverkusen, Germany

⁶ Department of Clinical Pharmacy & Toxicology, Leiden University Medical Center, Leiden, The Netherlands

⁷ Departments of Clinical Pharmacology, Pharmacy and Biochemistry, University of Tübingen, Tübingen, Germany

⁸ Cluster of Excellence iFIT (EXC2180) "Image-guided and Functionally Instructed Tumor Therapies", University of Tübingen, Tübingen, Germany

Corresponding Author:

Prof. Dr. Thorsten Lehr, Clinical Pharmacy, Saarland University, Campus C4 3, 66123 Saarbrücken, Germany, Phone: +49 681 302 70255, Email: thorsten.lehr@mx.uni-saarland.de

Contents

S1 Desipramine PBPK Model Development	2
S1.1 PBPK Model Building	2
S1.2 PBPK Model Evaluation	2
S2 Desipramine Base Model Results	3
S2.1 Clinical Studies	4
S2.2 Drug-Dependent Parameters	5
S2.3 Plasma Concentration-Time Profiles (Semilogarithmic Representation)	6
S2.4 Plasma Concentration-Time Profiles (Linear Representation)	8
S2.5 Predicted Compared to Observed Concentrations	10
S2.6 Mean Relative Deviation of Plasma Concentration Predictions	11
S2.7 Predicted Compared to Observed AUC _{last} and C _{max} Values	12
S2.8 Geometric Mean Fold Errors of Predicted AUC _{last} and C _{max} Values	13
S2.9 Sensitivity Analysis	15
S3 Desipramine DGI Model Results	17
S3.1 Clinical Studies	17
S3.2 Plasma Concentration-Time Profiles (Semilogarithmic Representation)	18
S3.3 Plasma Concentration-Time Profiles (Linear Representation)	20
S3.4 DGI AUC _{last} and C _{max} Ratios	22
S4 DD(G)I Network Development	24
S4.1 System-Dependent Parameters	24
S4.2 Types of Interaction	28
S4.3 Published PBPK DDI Models	29
S5 DGI Model Evaluation	35
S5.1 DGI AUC _{last} and C _{max} Ratios	35
S5.2 Geometric Mean Fold Errors of Predicted DGI AUC _{last} and C _{max} Ratios	36
S6 DDI Model Evaluation	39
S6.1 Alprazolam	39
S6.2 Atomoxetine	43
S6.3 (E)-Clomiphen	48
S6.4 Desipramine	68
S6.5 Dextromethorphan	73
S6.6 Digoxin	78
S6.7 Metoprolol	82
S6.8 Mexiletine	89
S6.9 Midazolam	93
S6.10 Paroxetine	97
S6.11 Quinidine	101
S6.12 Risperidone	106
S6.13 DDI AUC _{last} and C _{max} Ratios	111
S7 DDGI Model Evaluation	112
S7.1 DDGI AUC _{last} and C _{max} Ratios	112
S7.2 Geometric Mean Fold Errors of Predicted DDGI AUC _{last} and C _{max} Ratios	113
S8 Model-Informed Dose Adaptations	115
References	117

S1 Desipramine PBPK Model Development

S1.1 PBPK Model Building

Physiologically based pharmacokinetic (PBPK) model development for the desipramine parent-metabolite model was initiated with an extensive literature search for physicochemical parameters as well as information on absorption, distribution, metabolism and excretion processes. Moreover, plasma concentration-time profiles of desipramine and 2-hydroxydesipramine after intravenous and oral administrations of desipramine, as well as important meta data such as information on study subjects and administration protocols were collected. Plasma concentration-time profiles were split into a training dataset for model development and a test dataset for model evaluation. Studies for the training dataset were selected to include various routes of administration (i.e., intravenous and oral) and a wide dosing range. To determine appropriate quantitative structure-activity relationship (QSAR) techniques for computing partition coefficients and cellular permeabilities, parameter optimizations were conducted. Additionally, using the Monte Carlo algorithm, model parameter values that were not available in the literature, such as relevant catalytic and transport rate constants (k_{cat}) and intestinal permeability, were optimized by fitting model simulations to all studies of the training dataset.

For drug-gene interaction (DGI) modeling, the cytochrome P450 (CYP) 2D6 Michaelis-Menten constant (K_M) values for desipramine 2-hydroxylation were kept constant for all modeled phenotypes. CYP2D6 k_{cat} values were adjusted separately for the different phenotypes: CYP2D6 poor metabolizers were assumed to show no CYP2D6 activity ($k_{cat} = 0$ 1/min) whereas the k_{cat} value for normal metabolizers (NMs) was optimized. Of note, the “fast NM” phenotype is singular to the studies conducted by Brøsen et al. and does not directly correspond to any traditional phenotype category. Rather, the authors grouped NM individuals with a particularly low sparteine metabolic ratio within the NM category into a category separate to the broad NM category. Modeling of the corresponding CYP2D6 metabolism was complicated by the fact that no CYP2D6 genotypes or activity scores (ASs) were reported for any of the respective study cohorts. To reflect the higher activity of the fast NMs compared to NMs, fast NM was assumed to correspond to an AS of 2, with the respective CYP2D6 k_{cat} value used for fast NMs.

S1.2 PBPK Model Evaluation

Model performance of the desipramine PBPK model was evaluated graphically by comparison of population predicted (1000 individuals) and observed desipramine and 2-hydroxydesipramine plasma concentration-time profiles. Additionally, predicted plasma concentrations for mean individuals, area under the plasma concentration-time curve calculated from the first to the last concentration measurement (AUC_{last}) and maximum plasma concentration (C_{max}) values were compared to observed values in goodness-of-fit plots. Mean relative deviations (MRDs) for all predicted concentration time-profiles as well as geometric mean fold errors (GMFEs) for all predicted AUC_{last} and C_{max} values were calculated as previously described [1].

Sensitivity of the parent-metabolite model to single model parameters was calculated, determined as relative change of AUC_{0-24h} at steady state according to Equation S1. A relative perturbation of 1000% (variation range 10.0, maximum number of 2 steps) was applied. Parameters were included into the analysis if (i) they have been optimized, (ii) they are associated with optimized parameters or (iii) they could have a strong impact due to their use in the calculation of permeabilities or partition coefficients. Parameters were considered sensitive, if their sensitivity value was equal or greater than 0.5.

$$S = \frac{\Delta AUC}{AUC} \cdot \frac{p}{\Delta p} \quad (S1)$$

S = sensitivity of the AUC to the examined model parameter, ΔAUC = change of the AUC, AUC = simulated AUC with the original parameter value, Δp = change of the examined parameter value and p = original parameter value.

DGI prediction performance was evaluated by comparing population predicted (1000 individuals) and observed plasma concentration-time profiles of the different phenotypes. Predicted DGI AUC_{last} and C_{max} ratios were calculated relative to normal metabolizers as previously described [1] with subsequent comparison to the corresponding observed ratios in goodness-of-fit plots. The limits proposed by Guest et al. were applied to determine prediction accuracy (including 20% variability) [2]. Quantitative assessment was conducted by calculating GMFE values for all predicted DGI AUC_{last} and C_{max} ratios as previously described [1].

S2 Desipramine Base Model Results

Whole-body PBPK models for desipramine and its metabolite 2-hydroxydesipramine were developed in PK-Sim® using a total of 39 plasma concentration-time profiles of desipramine (28 profiles) and 2-hydroxydesipramine (11 profiles) from 20 clinical studies. Here, plasma concentration-time profiles were reported after intravenous administrations of 50 mg desipramine hydrochloride as well as single and multiple oral administrations of 25–100 mg desipramine hydrochloride. Comprehensive information on clinical studies used for model building and evaluation is given in Table S1. The main metabolic pathway of desipramine, its 2-hydroxylation to its main metabolite 2-hydroxydesipramine, was incorporated via CYP2D6. Residual metabolism and 2-hydroxydesipramine clearance was implemented via an unspecific hepatic clearance process. Additionally, passive glomerular filtration was incorporated in the model for both compounds. All relevant drug-dependent parameters for desipramine and 2-hydroxydesipramine are listed in Table S2. Information on the expression and localization of relevant proteins is provided in Tables S8–S10. Population predictions of all modeled plasma concentration-time profiles of desipramine and 2-hydroxydesipramine in semilogarithmic and linear representations are shown in Sections S2.3–S2.4.

Figures S5–S6 display the good descriptive and predictive performance of the desipramine parent-metabolite model. Overall, regarding the predicted plasma concentrations, AUC_{last} and C_{max} values, 96%, 100% and 100% of the desipramine training dataset, 91%, 100% and 100% of the desipramine test dataset, 100%, 100% and 100% of the 2-hydroxydesipramine training dataset as well as 90%, 100% and 100% of the 2-hydroxydesipramine test dataset were within two-fold of the corresponding observed values, respectively. Values for MRD, as well as AUC_{last} and C_{max} values of all profiles are provided in Tables S3–S4.

A local sensitivity analysis using a multiple dose simulation of 50 mg desipramine hydrochloride revealed that the desipramine model is sensitive to perturbation of the CYP2D6 k_{cat} and lipophilicity of desipramine (both optimized), as well as the fraction unbound of desipramine and CYP2D6 K_M (both implemented as fixed literature values). The 2-hydroxydesipramine model is sensitive to changes of the fraction unbound of 2-hydroxydesipramine (fixed value from the literature) and its unspecific hepatic clearance process (optimized). Table S5 provides a list of parameters evaluated during the local sensitivity analysis with its results visualized in Figure S7.

S2.1 Clinical Studies

Table S1: Clinical study data used for desipramine model development

Dose [mg] ^a	Route	n	Population ^b	Fem. [%]	Age [years]	Weight [kg]	BMI [kg/m ²]	Phenotype/AS	Molecule	Dataset	Reference
Intravenous											
50 (44)	s.d. iv 60 min inf	3	European [3]	33	29 (24–35)	-	-	PM	DES	training	Brøsen 1988 [4]
50 (44)	s.d. iv 60 min inf	4	European [3]	75	29.75 (22–37)	-	-	NM	DES	training	Brøsen 1988 [4]
50 (44)	s.d. iv 60 min inf	4	European [3]	50	23.75 (22–27)	-	-	fast NM	DES	training	Brøsen 1988 [4]
Oral											
25 (22)	s.d. po	6	European [3]	21	(27–51)	-	-	PM	DES	training	Spina 1987 [5]
25 (22)	s.d. po	8	European [3]	21	(27–51)	-	-	NM	DES	training	Spina 1987 [5]
50 (44)	s.d. po	13	European [3]	0	26 (20–56)	84 (69–93)	-	-	DES	training	Aarnoutse 2005 [6]
50 (44)	s.d. po	6	American [7]	0	44 (35–53)	78.2 (60.3–92.8)	-	-	DES	test	Bergstrom 1992 [8]
50 (44)	s.d. po	26	American [7]	4	33.6±7.2	80.9±11.2	26.4±2.8	-	DES, OHD	training	Boni 2009 [9]
50 (44)	s.d. po	17	American [7]	53	31.5±10.8	-	24.6±3.19	-	DES	training	Harris 2007 [10]
50 (44)	s.d. po	20	European [3]	55	58.3±9.9	84.3±28.5	29.3±10.1	-	DES, OHD	test	Hynes 2015 [11]
50 (44)	s.d. po	24	European [3]	-	(18–45)	-	-	-	DES	training	Madani 2002 [12]
50 (44)	s.d. po	20	American [7]	15	35.0±7.7	79.9±9.8	-	-	DES, OHD	test	Nichols 2009 [13]
50 (44)	s.d. po	38	American [7]	-	(18–45)	above 60	(18–30)	-	DES	test	Nichols 2013 [14]
50 (44)	s.d. po	20	American [7]	-	(18–55)	above 50	(18–30)	-	DES, OHD	test	Patroneva 2008 [15]
50 (44)	s.d. po	15	American [7]	0	-	-	-	-	DES	test	Reese 2008 [16]
50 (44)	s.d. po	22	American [7]	50	(26–55)	-	(18.8–30.4)	-	DES	test	Sauer 2004 [17]
50 (44)	s.d. po	16	American [7]	56	42 (21–63)	71.4	-	-	DES	test	Skinner 2003 [18]
50 (44)	q.d. po	6	American [7]	0	30.4±5.2	73.3±8.5	-	-	DES	test	Alderman 1997 [19]
100 (88)	s.d. po	6	European [3]	83	26.8 (24–33)	-	-	AS = 2	DES, OHD	test	Bergmann 2001 [20]
100 (88)	s.d. po	6	European [3]	33	36.7 (22–54)	-	-	AS = 2.5	DES, OHD	test	Bergmann 2001 [20]
100 (88)	s.d. po	6	European [3]	50	28.8 (23–34)	-	-	PM	DES	training	Brøsen 1986 [21]
100 (88)	s.d. po	6	European [3]	50	28.3 (21–36)	-	-	NM	DES, OHD	training	Brøsen 1986 [21]
100 (88)	s.d. po	6	European [3]	50	24.1 (21–30)	-	-	fast NM	DES, OHD	training	Brøsen 1986 [21]
100 (88)	s.d. po	8	European [3]	0	(22–24)	-	-	PM	DES	test	Brøsen 1993 [22]
100 (88)	s.d. po	5	European [3]	0	(22–24)	-	-	NM	DES, OHD	test	Brøsen 1993 [22]
100 (88)	s.d. po	4	European [3]	0	(22–24)	-	-	fast NM	DES, OHD	test	Brøsen 1993 [22]
100 (88)	s.d. po	6	European [3]	50	27.7 (23–38)	-	-	-	DES, OHD	test	Brøsen 1989 [23]
100 (88)	s.d. po	6	European [3]	0	(24–38)	(67–81)	-	-	DES	test	Spina 1995 [24]

AS: CYP2D6 activity score, BMI: body mass index, DES: desipramine, fem: females, inf: infusion, iv: intravenous, n: number of study participants, NM: CYP2D6 normal metabolizer, OHD: 2-hydroxydesipramine, PM: CYP2D6 poor metabolizer, po: oral, q.d.: once daily, -: not available. Values are given as mean (range). Respective doses of desipramine base were calculated and incorporated in simulations. ^a Dose given as desipramine hydrochloride (desipramine base). ^b Population used in simulations.

S2.2 Drug-Dependent Parameters

Table S2: Drug-dependent parameters of the desipramine model

Parameter	Desipramine			2-Hydroxydesipramine			Description
	Value	Source	Literature	Value	Source	Literature	
MW [g/mol]	266.4	Lit.	266.4 [25]	282.4	Lit.	282.4 [25]	Molecular weight of desipramine base
pK _a (base 1)	2.84	Lit.	2.84 [26]	4.51	Lit.	4.51 [26]	Acid dissociation constant
pK _a (base 2)	10.02	Lit.	10.02 [27]	9.90	Lit.	9.90 [26]	Acid dissociation constant
pK _a (acid)	-	-	-	10.63	Lit.	10.63 [26]	Acid dissociation constant
Solubility (pH 6.5) [mg/L]	214.29	Lit.	214.29 [26]	282.39	Lit.	282.39 [26]	Solubility
Lipophilicity	3.52	Opt.	3.90, 4.90 [26, 27]	2.33	Opt.	3.17 [26]	Lipophilicity
f _{u,p} [%]	14	Lit.	14 ^a [28]	12	Lit.	12 ^a [28]	Fraction unbound plasma
CYP2D6 (DES → OHD) K _M [μmol/L]	0.73	Lit.	6.1 × 0.12 ^b [29, 30]	-	-	-	Michaelis-Menten constant
CYP2D6 (DES → OHD) k _{cat} [1/min]	5.03 ^d	Opt.	-	-	-	-	Catalytic rate constant (NM)
CYP2D6 (DES → OHD) k _{cat} [1/min]	9.86	Opt.	-	-	-	-	Catalytic rate constant (AS = 2)
CYP2D6 (DES → OHD) k _{cat} [1/min]	28.88	Opt.	-	-	-	-	Catalytic rate constant (AS = 2.5)
CYP2D6 (DES → OHD) k _{cat} [1/min]	0	Opt.	-	-	-	-	Catalytic rate constant (PM)
CL _{hep} [1/min]	0.54	Opt.	-	9.93	Opt.	-	Hepatic metabolic clearance
GFR fraction	1	Asm.	-	1	Asm.	-	Fraction of filtered drug in the urine
EHC continuous fraction	1	Asm.	-	1	Asm.	-	Fraction of bile continually released
Partition coefficients	Diverse	Calc.	R & R [31, 32]	Diverse	Calc.	R & R [31, 32]	Cell to plasma partition coefficients
Cellular perm. [cm/min]	0.27	Calc.	PK-Sim [33]	0.01	Calc.	PK-Sim [33]	Permeability into the cellular space
Intestinal perm. [cm/min]	1.14 · 10 ⁻⁵	Opt.	6.44 · 10 ⁻⁴	3.19 · 10 ⁻⁵	Calc.	3.19 · 10 ⁻⁵ (calc.)	Transcellular intestinal permeability
Formulation	Solution	Asm.	-	-	-	-	Formulation used in predictions

AS: CYP2D6 activity score, asm.: assumed, calc.: calculated, CYP: cytochrome P450, DES: desipramine, EHC: enterohepatic circulation, GFR: glomerular filtration rate, lit.: literature, NM: CYP2D6 normal metabolizer, OHD: 2-hydroxydesipramine, opt.: optimized, PK-Sim: PK-Sim calculation method, PM: CYP2D6 poor metabolizer, R & R: Rodgers & Rowland calculation method, -: not implemented/not available. ^a Calculated with f_{u,p} predictor [28]. ^b Reported K_M values adjusted for fraction unbound in the incubation (f_{u,inc}) = 12% (calculated) [30]. ^d Also assumed for studies where no information about CYP2D6 polymorphism was provided.

S2.3 Plasma Concentration-Time Profiles (Semilogarithmic Representation)

Profiles from DGI studies in semilogarithmic representation can be found in Subsection S3.2 of the separate Section S3 "Desipramine DGI Model Results".

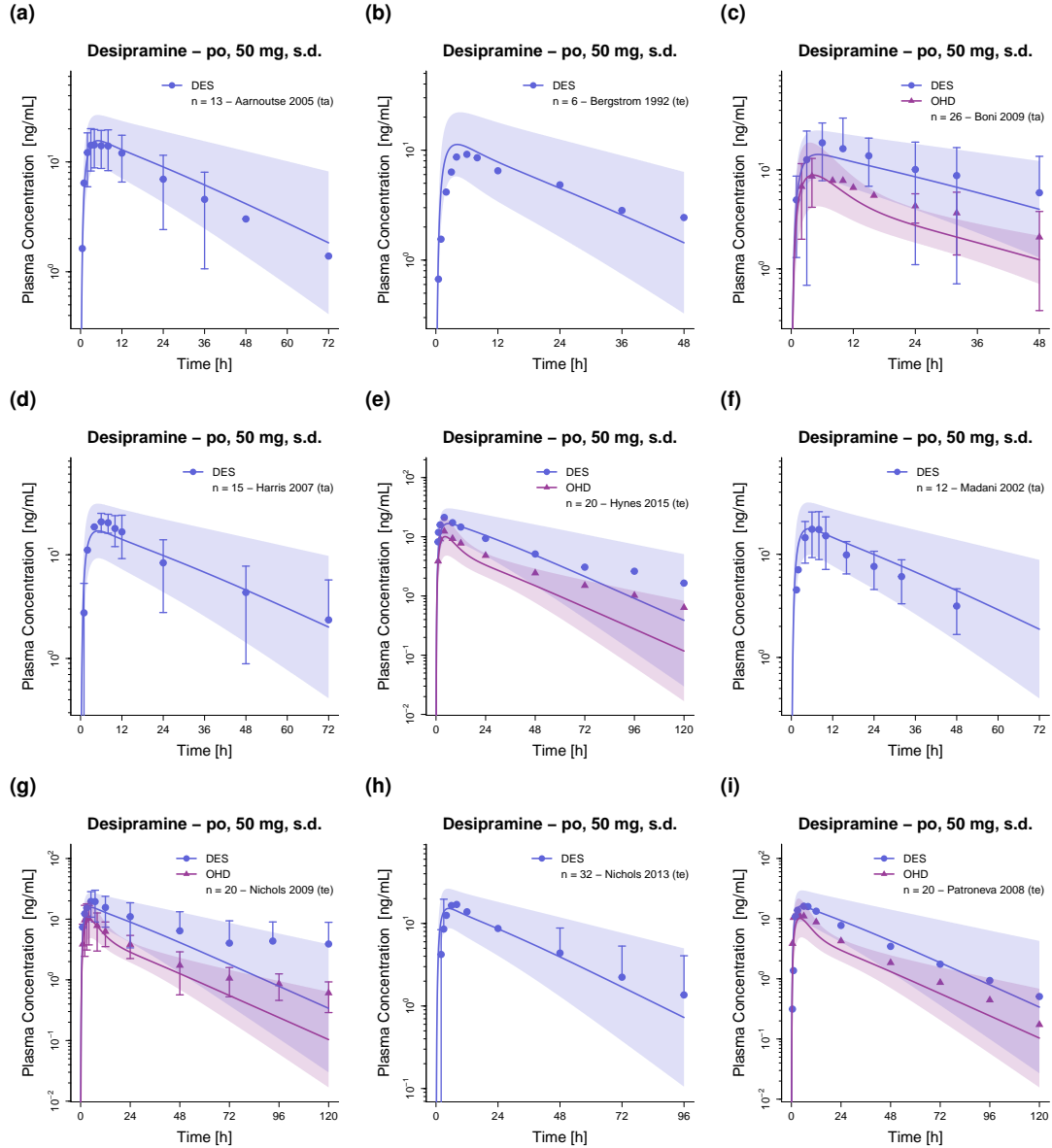


Figure S1: Predicted compared to observed plasma concentration-time profiles of desipramine and 2-hydroxydesipramine. Population predicted (1000 individuals) geometric means are shown as lines, corresponding geometric standard deviations as shaded areas and observed data as dots/triangles (\pm standard deviation, if reported) [6, 8–15]. DES: desipramine n: number of study participants, OHD: 2-hydroxydesipramine, po: oral, s.d.: single dose, ta: training dataset, te: test dataset.

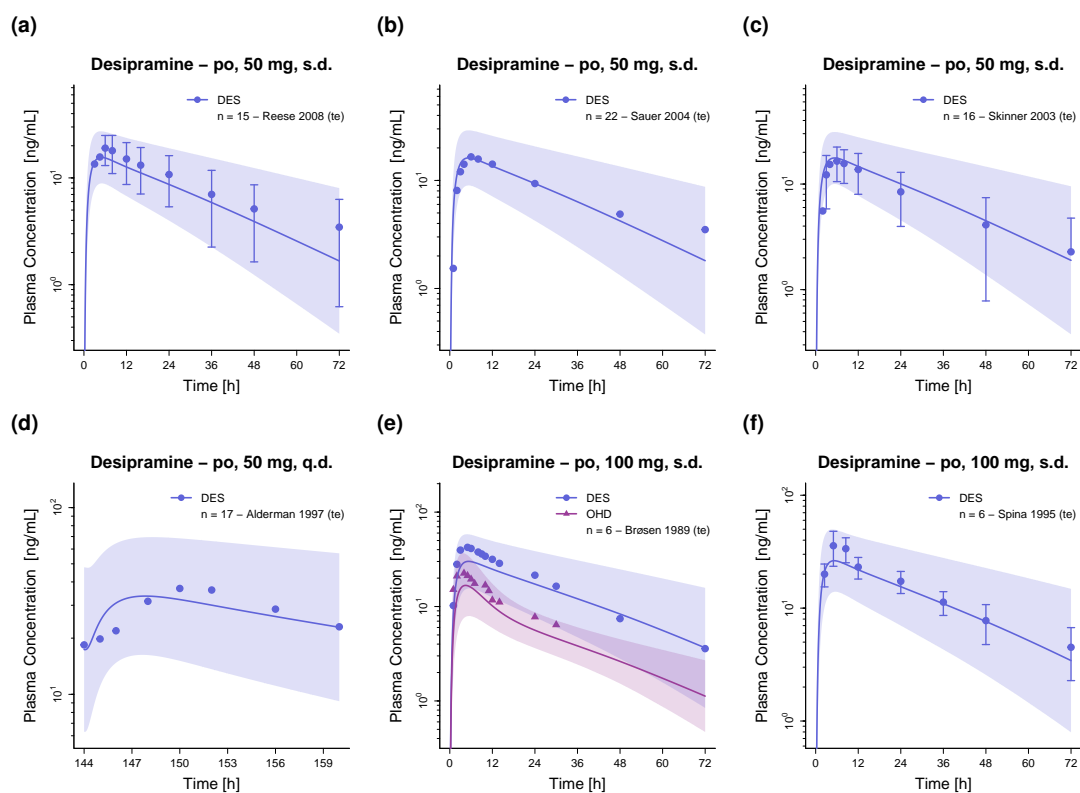


Figure S2: Predicted compared to observed plasma concentration-time profiles of desipramine and 2-hydroxydesipramine. Population predicted (1000 individuals) geometric means are shown as lines, corresponding geometric standard deviations as shaded areas and observed data as dots/triangles (\pm standard deviation, if reported) [16–19, 23, 24]. DES: desipramine n: number of study participants, OHD: 2-hydroxydesipramine, po: oral, q.d.: once daily, s.d.: single dose, te: test dataset.

S2.4 Plasma Concentration-Time Profiles (Linear Representation)

Profiles from DGI studies in semilogarithmic representation can be found in Subsection S3.3 of the separate Section S3 "Desipramine DGI Model Results".

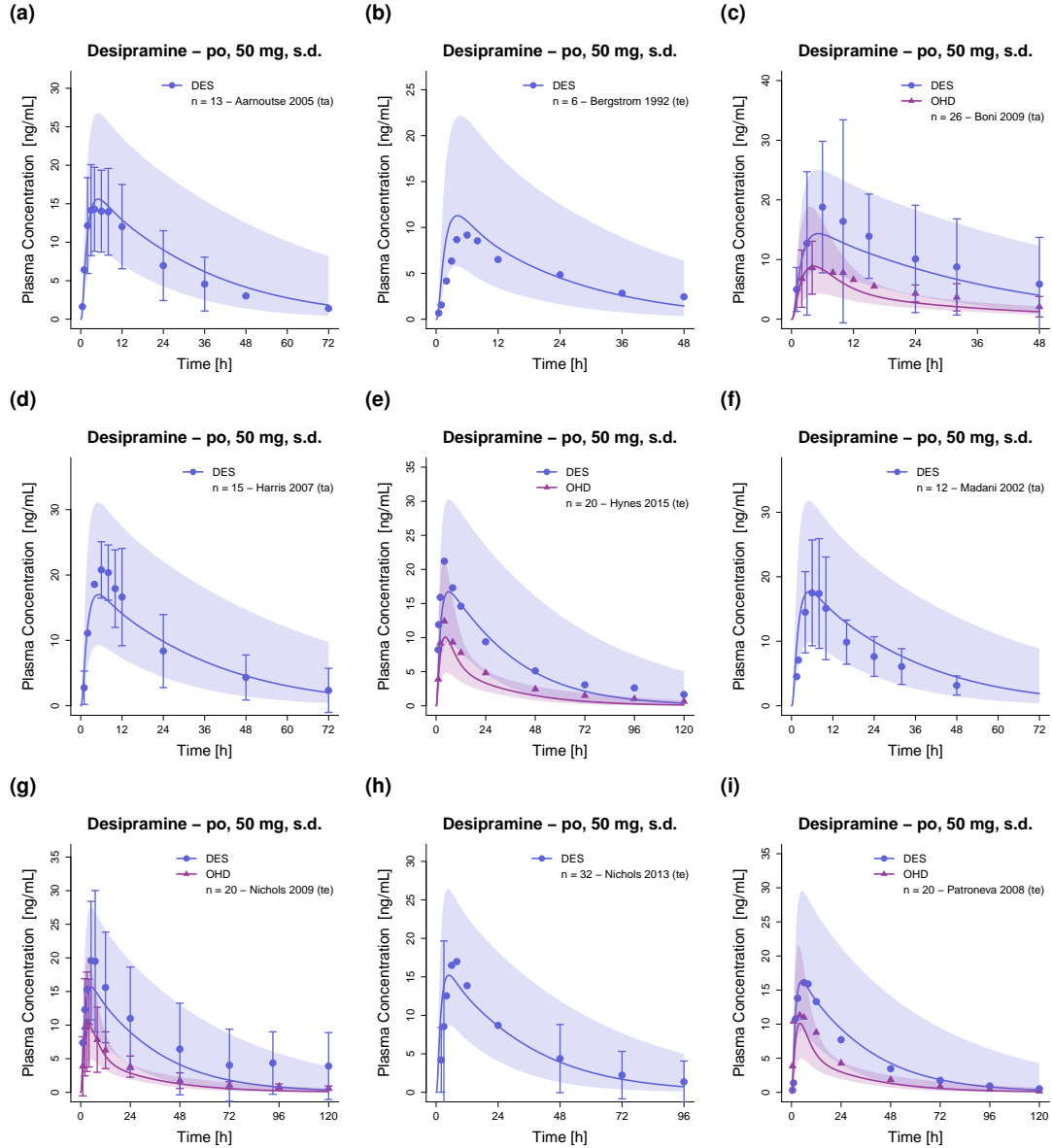


Figure S3: Predicted compared to observed plasma concentration-time profiles of desipramine and 2-hydroxydesipramine. Population predicted (1000 individuals) geometric means are shown as lines, corresponding geometric standard deviations as shaded areas and observed data as dots/triangles (\pm standard deviation, if reported) [6, 8–15]. DES: desipramine n: number of study participants, OHD: 2-hydroxydesipramine, po: oral, s.d.: single dose, ta: training dataset, te: test dataset.

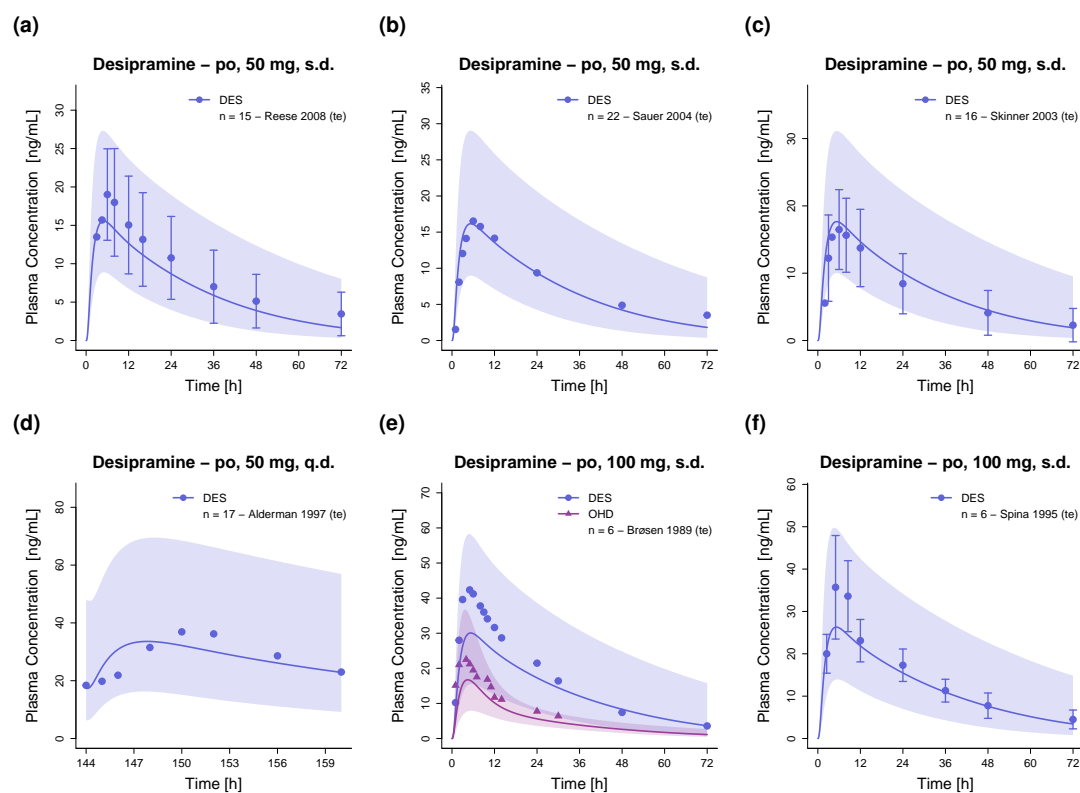


Figure S4: Predicted compared to observed plasma concentration-time profiles of desipramine and 2-hydroxydesipramine. Population predicted (1000 individuals) geometric means are shown as lines, corresponding geometric standard deviations as shaded areas and observed data as dots/triangles (\pm standard deviation, if reported) [16–19, 23, 24]. DES: desipramine n: number of study participants, OHD: 2-hydroxydesipramine, po: oral, q.d.: once daily, s.d.: single dose, te: test dataset.

S2.5 Predicted Compared to Observed Concentrations

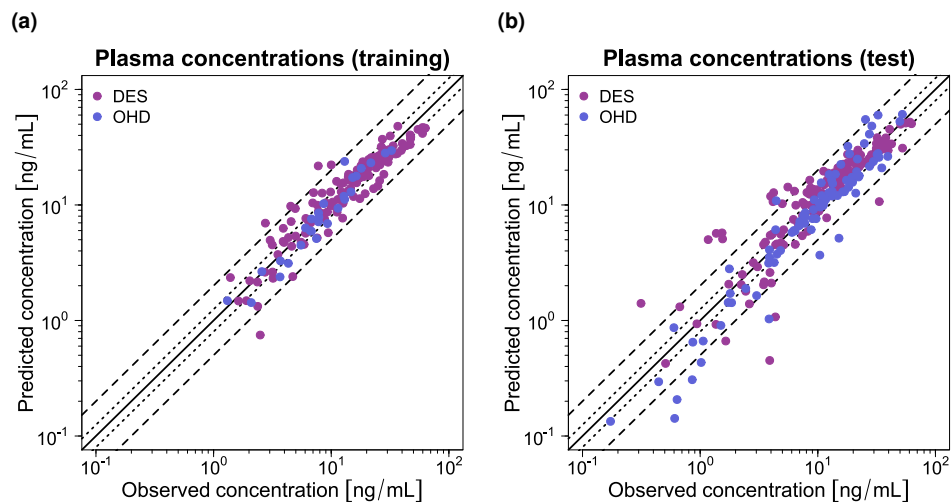


Figure S5: Goodness-of-fit plots comparing predicted and observed plasma concentration values of desipramine and 2-hydroxydesipramine. The solid line marks the line of identity. Dotted lines indicate 1.25-fold, dashed lines indicate 2-fold deviation. DES: desipramine, OHD: 2-hydroxydesipramine.

S2.6 Mean Relative Deviation of Plasma Concentration Predictions

Table S3: MRD values of desipramine plasma concentration predictions

Dose [mg] ^a	Route	MRD DES	MRD OHD	Phenotype/AS	Dataset	Reference
Intravenous						
50 (44)	s.d. iv 60 min inf	1.20	-	PM	training	Brøsen 1988 [4]
50 (44)	s.d. iv 60 min inf	1.16	-	NM	training	Brøsen 1988 [4]
50 (44)	s.d. iv 60 min inf	1.72	-	fast NM	training	Brøsen 1988 [4]
Oral						
25 (22)	s.d. po	1.11	-	PM	training	Spina 1987 [5]
25 (22)	s.d. po	1.23	-	NM	training	Spina 1987 [5]
50 (44)	s.d. po	1.37	-	-	training	Aarnoutse 2005 [6]
50 (44)	s.d. po	1.84	-	-	test	Bergstrom 1992 [8]
50 (44)	s.d. po	1.14	1.28	-	training	Boni 2009 [9]
50 (44)	s.d. po	1.45	-	-	training	Harris 2007 [10]
50 (44)	s.d. po	1.50	1.63	-	test	Hynes 2015 [11]
50 (44)	s.d. po	1.44	-	-	training	Madani 2002 [12]
50 (44)	s.d. po	2.26	1.76	-	test	Nichols 2009 [13]
50 (44)	s.d. po	1.56	-	-	test	Nichols 2013 [14]
50 (44)	s.d. po	1.85	1.80	-	test	Patroneva 2008 [15]
50 (44)	s.d. po	1.21	-	-	test	Reese 2008 [16]
50 (44)	s.d. po	1.63	-	-	test	Sauer 2004 [17]
50 (44)	s.d. po	1.55	-	-	test	Skinner 2003 [18]
50 (44)	q.d. po	1.15	-	-	test	Alderman 1997 [19]
100 (88)	s.d. po	1.13	1.29	AS = 2	test	Bergmann 2001 [20]
100 (88)	s.d. po	1.09	1.46	AS = 2.5	test	Bergmann 2001 [20]
100 (88)	s.d. po	1.34	-	PM	training	Brøsen 1986 [21]
100 (88)	s.d. po	1.39	1.22	NM	training	Brøsen 1986 [21]
100 (88)	s.d. po	1.44	1.24	fast NM	training	Brøsen 1986 [21]
100 (88)	s.d. po	1.58	-	PM	test	Brøsen 1993 [22]
100 (88)	s.d. po	1.54	1.31	NM	test	Brøsen 1993 [22]
100 (88)	s.d. po	1.95	1.60	fast NM	test	Brøsen 1993 [22]
100 (88)	s.d. po	1.22	1.45	-	test	Brøsen 1989 [23]
100 (88)	s.d. po	1.20	-	-	test	Spina 1995 [24]
Mean DES MRD training dataset (range):		1.33 (1.11–1.72), 12/12 with MRD ≤ 2				
Mean DES MRD test dataset (range):		1.52 (1.09–2.26), 15/16 with MRD ≤ 2				
Overall DES MRD (range):		1.44 (1.09–2.26), 27/28 with MRD ≤ 2				
Mean OHD MRD training dataset (range):		1.24 (1.22–1.28), 3/3 with MRD ≤ 2				
Mean OHD MRD test dataset (range):		1.54 (1.29–1.80), 8/8 with MRD ≤ 2				
Overall OHD MRD (range):		1.46 (1.22–1.80), 11/11 with MRD ≤ 2				
Overall MRD training dataset (range):		1.32 (1.11–1.72), 15/15 with MRD ≤ 2				
Overall MRD test dataset (range):		1.52 (1.09–2.26), 23/24 with MRD ≤ 2				
Overall MRD (range):		1.44 (1.09–2.26), 38/39 with MRD ≤ 2				

AS: CYP2D6 activity score, DES: desipramine, inf: infusion, iv: intravenous, MRD: mean relative deviation, NM: CYP2D6 normal metabolizer, OHD: 2-hydroxydesipramine, PM: CYP2D6 poor metabolizer, po: oral, q.d.: once daily, s.d.: single dose. Respective doses of desipramine base were calculated and incorporated in simulations. ^a Dose given as desipramine hydrochloride (desipramine base).

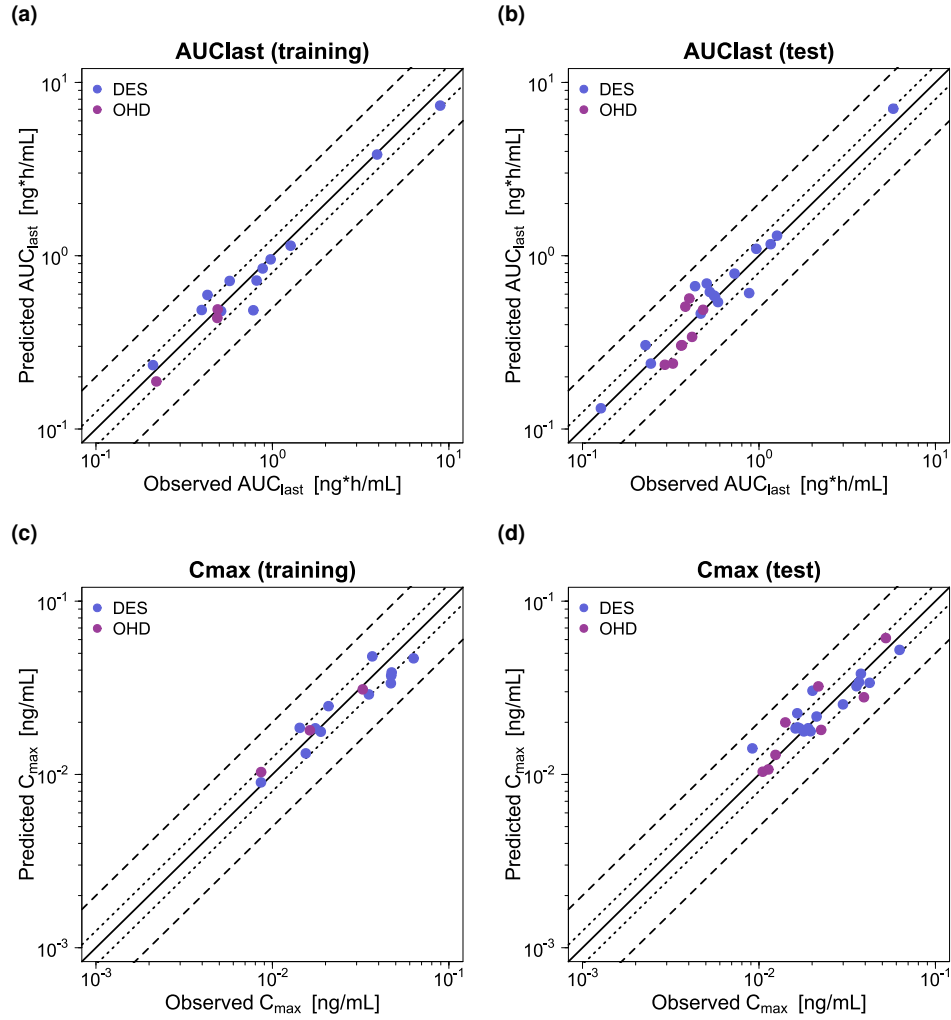
S2.7 Predicted Compared to Observed AUC_{last} and C_{max} Values

Figure S6: Goodness-of-fit plots comparing predicted and observed AUC_{last} and C_{max} values of desipramine and 2-hydroxydesipramine. The solid line marks the line of identity. Dotted lines indicate 1.25-fold, dashed lines indicate 2-fold deviation. AUC_{last} : area under the plasma concentration-time curve calculated between the first and last concentration measurement, C_{max} : maximum plasma concentration, DES: desipramine, OHD: 2-hydroxydesipramine.

S2.8 Geometric Mean Fold Errors of Predicted AUC_{last} and C_{max} ValuesTable S4: Predicted and observed desipramine AUC_{last} and C_{max} values

Dose [mg] ^a	Route	t _{last} [h]	AUC _{last}			C _{max}			Phenotype/AS	Molecule	Dataset	Reference
			Pred [ng•h/mL]	Obs [ng•h/mL]	Pred/Obs	Pred [ng/mL]	Obs [ng/mL]	Pred/Obs				
Desipramine												
50 (44)	s.d. iv 60 min inf	432	3836.62	3918.10	0.98	38.77	47.40	0.82	PM	DES	training	Brøsen 1988 [4]
50 (44)	s.d. iv 60 min inf	72	844.06	880.83	0.96	48.00	36.80	1.30	NM	DES	training	Brøsen 1988 [4]
50 (44)	s.d. iv 60 min inf	72	484.37	779.40	0.62	37.17	47.10	0.79	fast NM	DES	training	Brøsen 1988 [4]
25 (22)	s.d. po	96	952.76	976.94	0.98	13.23	15.46	0.86	PM	DES	training	Spina 1987 [5]
25 (22)	s.d. po	48	233.63	210.49	1.11	9.00	8.61	1.05	NM	DES	training	Spina 1987 [5]
50 (44)	s.d. po	72	593.82	428.44	1.39	18.57	14.28	1.30	-	DES	training	Aarnoutse 2005 [6]
50 (44)	s.d. po	48	304.54	227.47	1.34	14.14	9.17	1.54	-	DES	test	Bergstrom 1992 [8]
50 (44)	s.d. po	48	479.07	511.64	0.94	17.65	18.80	0.94	-	DES	training	Boni 2009 [9]
50 (44)	s.d. po	72	715.30	572.38	1.25	24.78	20.78	1.19	-	DES	training	Harris 2007 [10]
50 (44)	s.d. po	120	788.64	726.71	1.09	21.59	21.20	1.02	-	DES	test	Hynes 2015 [11]
50 (44)	s.d. po	48	486.19	397.47	1.22	18.46	17.50	1.05	-	DES	training	Madani 2002 [12]
50 (44)	s.d. po	120	608.65	879.27	0.69	17.75	19.60	0.91	-	DES	test	Nichols 2009 [13]
50 (44)	s.d. po	96	589.25	555.75	1.06	18.46	16.98	1.09	-	DES	test	Nichols 2013 [14]
50 (44)	s.d. po	120	617.53	526.28	1.17	18.43	16.10	1.14	-	DES	test	Patroneva 2008 [15]
50 (44)	s.d. po	72	540.00	585.45	0.92	18.48	19.01	0.97	-	DES	test	Reese 2008 [16]
50 (44)	s.d. po	72	581.05	563.27	1.03	18.69	16.53	1.13	-	DES	test	Sauer 2004 [17]
50 (44)	s.d. po	72	691.11	505.75	1.37	22.54	16.48	1.37	-	DES	test	Skinner 2003 [18]
50 (44)	q.d. po	24	463.40	467.65	0.99	34.09	36.90	0.92	-	DES	test	Alderman 1997 [19]
100 (88)	s.d. po	14	238.61	243.94	0.98	25.37	29.92	0.85	AS = 2	DES	test	Bergmann 2001 [20]
100 (88)	s.d. po	14	131.70	127.07	1.04	17.71	17.96	0.99	AS = 2.5	DES	test	Bergmann 2001 [20]
100 (88)	s.d. po	408	7352.29	8926.66	0.82	46.79	63.10	0.74	PM	DES	training	Brøsen 1986 [21]
100 (88)	s.d. po	72	1142.66	1267.39	0.90	33.58	46.90	0.72	NM	DES	training	Brøsen 1986 [21]
100 (88)	s.d. po	72	719.20	813.04	0.88	28.96	35.20	0.82	fast NM	DES	training	Brøsen 1986 [21]
100 (88)	s.d. po	240	7052.91	5765.12	1.22	52.33	62.60	0.84	PM	DES	test	Brøsen 1993 [22]
100 (88)	s.d. po	72	1305.38	1265.24	1.03	38.11	37.80	1.01	NM	DES	test	Brøsen 1993 [22]
100 (88)	s.d. po	48	667.02	434.27	1.54	30.42	20.10	1.51	fast NM	DES	test	Brøsen 1993 [22]
100 (88)	s.d. po	72	1165.41	1164.85	1.00	33.79	42.35	0.80	-	DES	test	Brøsen 1989 [23]
100 (88)	s.d. po	72	1096.07	965.43	1.14	32.29	35.70	0.90	-	DES	test	Spina 1995 [24]
Mean DES GMFE training dataset (range):			1.18 (1.02–1.61), 12/12 with GMFE ≤ 2			1.22 (1.05–1.40), 12/12 with GMFE ≤ 2						
Mean DES GMFE test dataset (range):			1.16 (1.00–1.54), 16/16 with GMFE ≤ 2			1.17 (1.01–1.54), 16/16 with GMFE ≤ 2						
Overall DES GMFE (range):			1.17 (1.00–1.61), 28/28 with GMFE ≤ 2			1.19 (1.01–1.54), 28/28 with GMFE ≤ 2						

AS: CYP2D6 activity score, AUC_{last}: area under the plasma concentration-time curve calculated between the first and last concentration measurement, C_{max}: maximum plasma concentration, DES: desipramine, GMFE: geometric mean fold error, inf: infusion, iv: intravenous, obs: observed, NM: CYP2D6 normal metabolizer, OHD: 2-hydroxydesipramine, PM: CYP2D6 poor metabolizer, po: oral, q.d.: once daily, s.d.: single dose, t_{last}: time of the last concentration measurement, -: not available. Respective doses of desipramine base were calculated and incorporated in simulations. ^a Dose given as desipramine hydrochloride (desipramine base).

Table S4: Predicted and observed desipramine AUC_{last} and C_{max} values (*continued*)

Dose [mg] ^a	Route	t _{last} [h]	AUC _{last}			C _{max}			Phenotype/AS	Molecule	Dataset	Reference
			Pred [ng*h/mL]	Obs [ng*h/mL]	Pred/Obs	Pred [ng/mL]	Obs [ng/mL]	Pred/Obs				
2-Hydroxydesipramine												
50 (44)	s.d. po	48	188.12	219.93	0.86	10.32	8.63	1.20	-	OHD	training	Boni 2009 [9]
50 (44)	s.d. po	120	304.64	365.80	0.83	12.97	12.40	1.05	-	OHD	test	Hynes 2015 [11]
50 (44)	s.d. po	120	234.84	292.76	0.80	10.37	10.50	0.99	-	OHD	test	Nichols 2009 [13]
50 (44)	s.d. po	120	238.64	325.03	0.73	10.69	11.30	0.95	-	OHD	test	Patroneva 2008 [15]
100 (88)	s.d. po	24	340.07	417.57	0.81	27.89	39.33	0.71	AS = 2	OHD	test	Bergmann 2001 [20]
100 (88)	s.d. po	24	508.29	382.58	1.33	61.22	52.34	1.17	AS = 2.5	OHD	test	Bergmann 2001 [20]
100 (88)	s.d. po	72	437.29	487.03	0.90	17.98	16.30	1.10	NM	OHD	training	Brøsen 1986 [21]
100 (88)	s.d. po	48	490.01	489.54	1.00	30.96	32.50	0.95	fast NM	OHD	training	Brøsen 1986 [21]
100 (88)	s.d. po	72	487.49	482.02	1.01	19.96	14.10	1.42	NM	OHD	test	Brøsen 1993 [22]
100 (88)	s.d. po	72	566.50	402.70	1.41	32.22	21.70	1.48	fast NM	OHD	test	Brøsen 1993 [22]
100 (88)	s.d. po	30	303.09	362.43	0.84	18.07	22.50	0.80	-	OHD	test	Brøsen 1989 [23]
Mean OHD GMFE training dataset (range):			1.09 (1.00–1.17), 3/3 with GMFE ≤ 2			1.12 (1.05–1.20), 3/3 with GMFE ≤ 2						
Mean OHD GMFE test dataset (range):			1.25 (1.01–1.41), 8/8 with GMFE ≤ 2			1.23 (1.01–1.48), 8/8 with GMFE ≤ 2						
Overall OHD GMFE (range):			1.21 (1.00–1.41), 11/11 with GMFE ≤ 2			1.20 (1.01–1.48), 11/11 with GMFE ≤ 2						
Mean GMFE training dataset (range):			1.16 (1.00–1.61), 15/15 with GMFE ≤ 2			1.20 (1.05–1.40), 15/15 with GMFE ≤ 2						
Mean GMFE test dataset (range):			1.19 (1.00–1.54), 24/24 with GMFE ≤ 2			1.19 (1.01–1.54), 24/24 with GMFE ≤ 2						
Overall GMFE (range):			1.18 (1.00–1.61), 39/39 with GMFE ≤ 2			1.19 (1.01–1.54), 39/39 with GMFE ≤ 2						

AS: CYP2D6 activity score, AUC_{last}: area under the plasma concentration-time curve calculated between the first and last concentration measurement, C_{max}: maximum plasma concentration, DES: desipramine, GMFE: geometric mean fold error, inf: infusion, iv: intravenous, obs: observed, NM: CYP2D6 normal metabolizer, OHD: 2-hydroxydesipramine, PM: CYP2D6 poor metabolizer, po: oral, q.d.: once daily, s.d.: single dose, t_{last}: time of the last concentration measurement, -: not available. Respective doses of desipramine base were calculated and incorporated in simulations. ^a Dose given as desipramine hydrochloride (desipramine base).

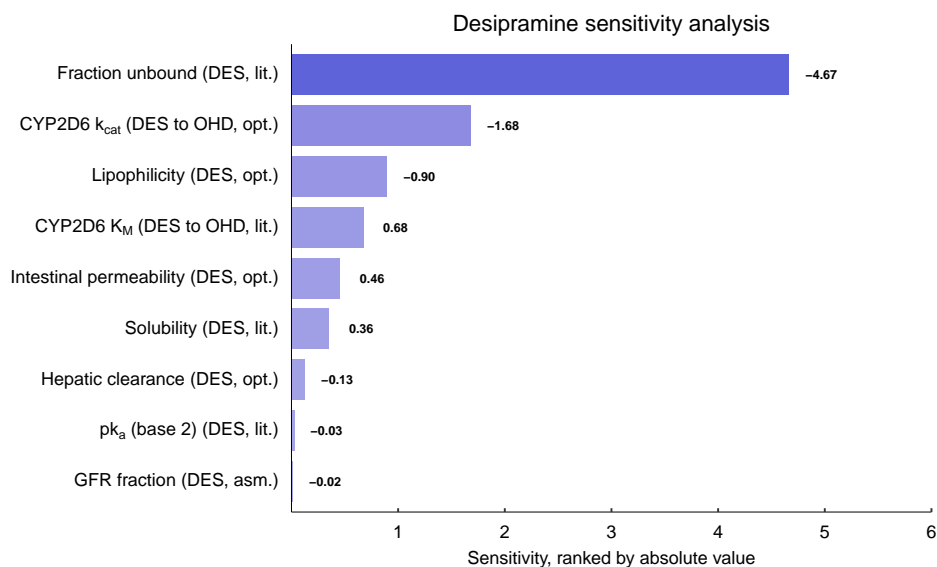
S2.9 Sensitivity Analysis

Table S5: Parameters evaluated during desipramine and 2-hydroxydesipramine sensitivity analysis

Parameter	Desipramine		2-Hydroxydesipramine	
	Value	Source	Value	Source
pK _a (base 1)	2.84	Literature	4.51	Literature
pK _a (base 2)	10.02	Literature	9.90	Literature
pK _a (acid)	-	-	10.63	Literature
Solubility (pH 6.5) [mg/L]	214.29	Literature	282.39	Literature
Lipophilicity	3.52	Optimized	2.33	Optimized
f _{u,p} [%]	14	Literature	12	Literature
CYP2D6 (DES → OHD) K _M [μmol/L]	0.73	Literature	-	-
CYP2D6 (DES → OHD) k _{cat} [1/min]	5.03	Optimized	-	-
CL _{hep} [1/min]	0.54	Optimized	9.93	Optimized
GFR fraction	1	Assumed	1	Assumed
Intestinal permeability [cm/min]	1.14 · 10 ⁻⁵	Optimized	-	-

CL_{hep}: hepatic metabolic clearance, CYP: cytochrome P450, DES: desipramine, f_{u,p}: fraction unbound plasma, k_{cat}: catalytic or transport rate constant, K_i: concentration for 50% inhibition (competitive), K_M: Michaelis-Menten constant, OHD: 2-hydroxydesipramine, pK_a: acid dissociation constant, -: parameter not included.

(a)



(b)

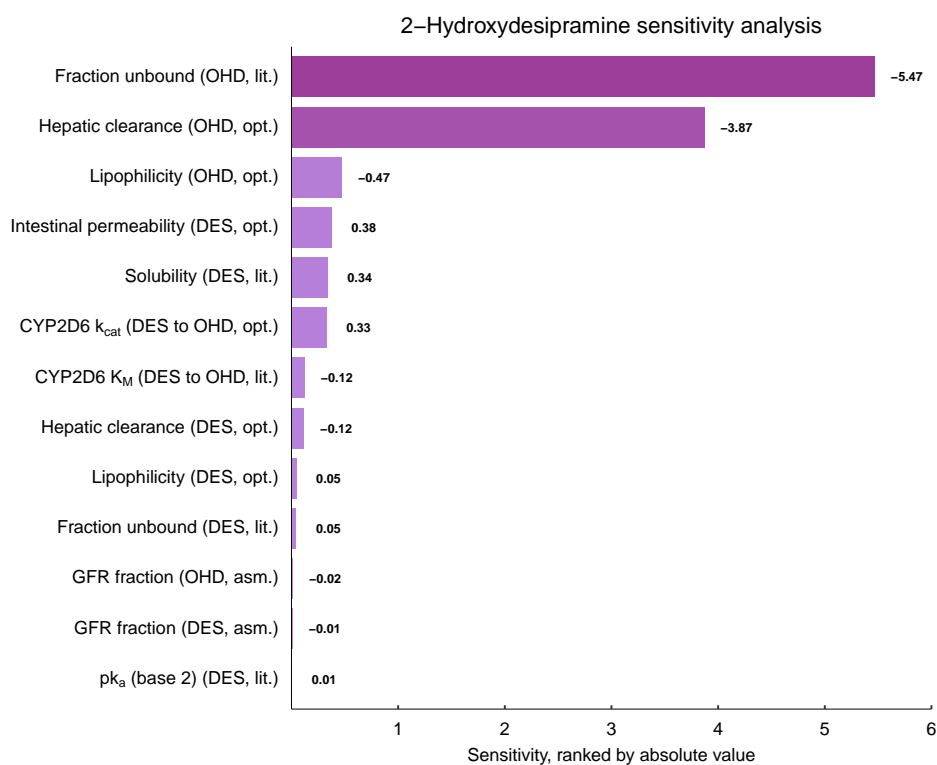


Figure S7: Local sensitivity analysis results of the desipramine PBPK model ((a) desipramine and (b) 2-hydroxydesipramine), determined as relative change of AUC_{0-24h} at steady state in a once daily regimen of 50 mg desipramine hydrochloride. Asm.: assumed, CYP: cytochrome P450, DES: desipramine, k_{cat} : catalytic or transport rate constant, K_M : Michaelis-Menten constant, lit.: literature value, OHD: 2-hydroxydesipramine, opt.: optimized, pK_a : acid dissociation constant.

S3 Desipramine DGI Model Results

Desipramine DGI modeling was performed using five DGI studies providing a total of thirteen desipramine and six 2-hydroxydesipramine plasma-concentration-time profiles. Comprehensive information on the DGI studies used is given in Table S6.

Predicted and observed plasma concentration-time profiles of desipramine and 2-hydroxydesipramine are shown in semilogarithmic and linear representations in Sections S3.2–S3.3. Overall, predicted AUC_{last} and C_{max} ratios were in good agreement with observed DGI ratios, highlighting the good performance of the desipramine DGI model with 8/11 DGI AUC_{last} and 8/11 C_{max} ratios within the prediction success limits proposed by Guest et al. [2] as depicted in Figure S12. All predicted and observed DGI AUC_{last} and C_{max} ratios are listed in Table S7.

S3.1 Clinical Studies

Table S6: Clinical study data used for desipramine DGI model development

Dose [mg] ^a	Route	n	Population ^b	Fem. [%]	Age [years]	Weight [kg]	BMI [kg/m ²]	Phenotype/AS	Molecule	Reference
Intravenous										
50 (44)	s.d. iv 60 min inf	3	European [3]	33	29 (24–35)	-	-	PM	DES	Brøsen 1988 [4]
50 (44)	s.d. iv 60 min inf	4	European [3]	75	29.75 (22–37)	-	-	NM	DES	Brøsen 1988 [4]
50 (44)	s.d. iv 60 min inf	4	European [3]	50	23.75 (22–27)	-	-	fast NM	DES	Brøsen 1988 [4]
Oral										
25 (22)	s.d. po	6	European [3]	21	(27–51)	-	-	PM	DES	Spina 1987 [5]
25 (22)	s.d. po	8	European [3]	21	(27–51)	-	-	NM	DES	Spina 1987 [5]
100 (88)	s.d. po	6	European [3]	83	26.8 (24–33)	-	-	AS = 2	DES, OHD	Bergmann 2001 [20]
100 (88)	s.d. po	6	European [3]	33	36.7 (22–54)	-	-	AS = 2.5	DES, OHD	Bergmann 2001 [20]
100 (88)	s.d. po	6	European [3]	50	28.8 (23–34)	-	-	PM	DES	Brøsen 1986 [21]
100 (88)	s.d. po	6	European [3]	50	28.3 (21–36)	-	-	NM	DES, OHD	Brøsen 1986 [21]
100 (88)	s.d. po	6	European [3]	50	24.1 (21–30)	-	-	fast NM	DES, OHD	Brøsen 1986 [21]
100 (88)	s.d. po	8	European [3]	0	(22–24)	-	-	PM	DES	Brøsen 1993 [22]
100 (88)	s.d. po	5	European [3]	0	(22–24)	-	-	NM	DES, OHD	Brøsen 1993 [22]
100 (88)	s.d. po	4	European [3]	0	(22–24)	-	-	fast NM	DES, OHD	Brøsen 1993 [22]

AS: CYP2D6 activity score, BMI: body mass index, calc: calculated, DES: desipramine, DGI: drug-gene interaction, fem: females, inf: infusion, iv: intravenous, n: number of study participants, NM: CYP2D6 normal metabolizer, OHD: 2-hydroxydesipramine, PM: CYP2D6 poor metabolizer, po: oral, -: not available. Values are given as mean (range). Respective doses of desipramine base were calculated and incorporated in simulations. ^a Dose given as desipramine hydrochloride (desipramine base). ^b Population used in simulations.

S3.2 Plasma Concentration-Time Profiles (Semilogarithmic Representation)

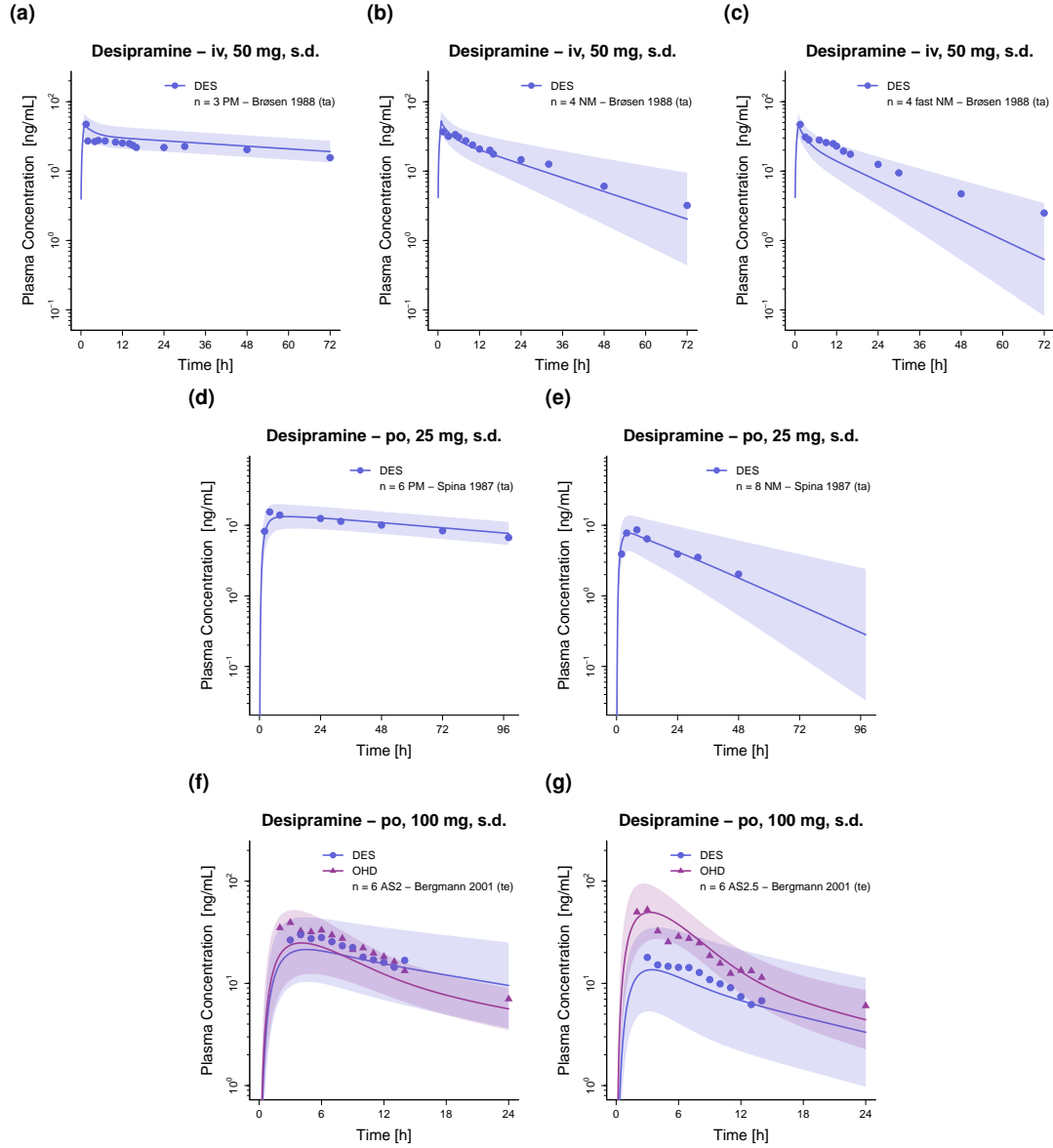


Figure S8: Predicted compared to observed plasma concentration-time profiles of desipramine and 2-hydroxydesipramine at varying CYP2D6 activity levels. Population predicted (1000 individuals) geometric means are shown as lines, corresponding geometric standard deviations as shaded areas and observed data as dots/triangles [4, 5, 20]. AS: CYP2D6 activity score, DES: desipramine, iv: intravenous, n: number of study participants, NM: CYP2D6 normal metabolizer, OHD: 2-hydroxydesipramine, PM: CYP2D6 poor metabolizer, po: oral, s.d.: single dose, ta: training dataset, te: test dataset.

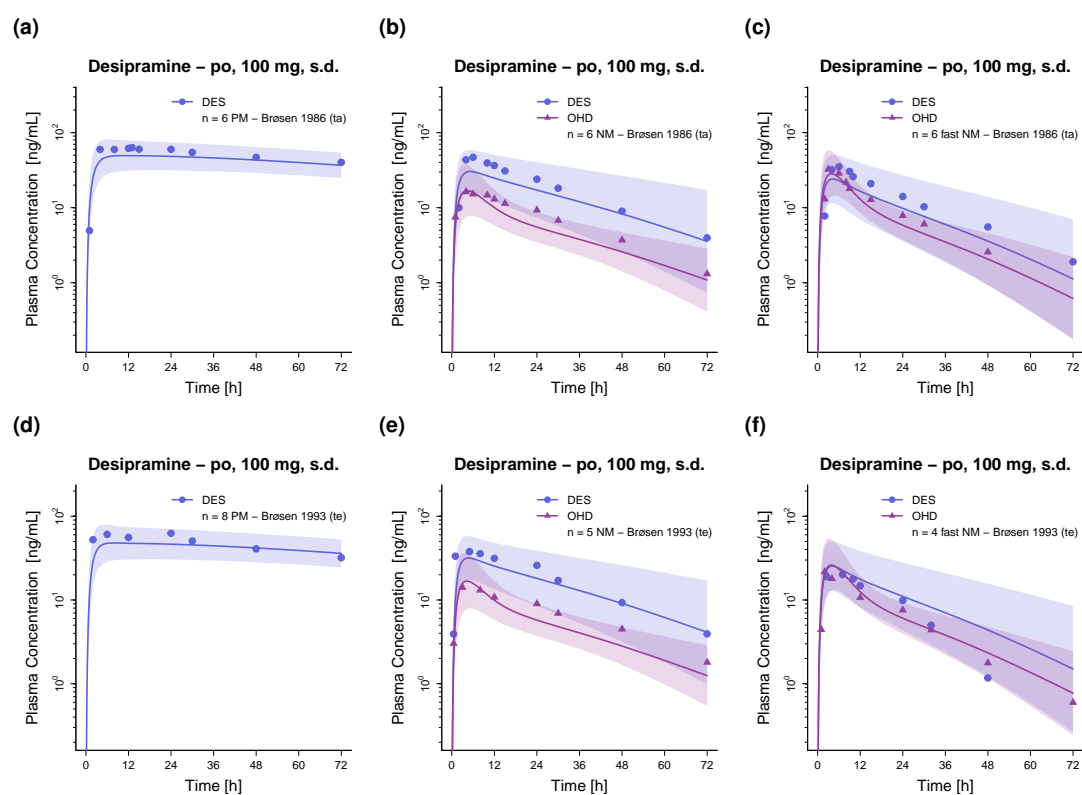


Figure S9: Predicted compared to observed plasma concentration-time profiles of desipramine and 2-hydroxydesipramine at varying CYP2D6 activity levels. Population predicted (1000 individuals) geometric means are shown as lines, corresponding geometric standard deviations as shaded areas and observed data as dots/triangles [21, 22]. AS: CYP2D6 activity score, DES: desipramine n: number of study participants, NM: CYP2D6 normal metabolizer, OHD: 2-hydroxydesipramine, PM: CYP2D6 poor metabolizer, po: oral, s.d.: single dose, ta: training dataset, te: test dataset.

S3.3 Plasma Concentration-Time Profiles (Linear Representation)

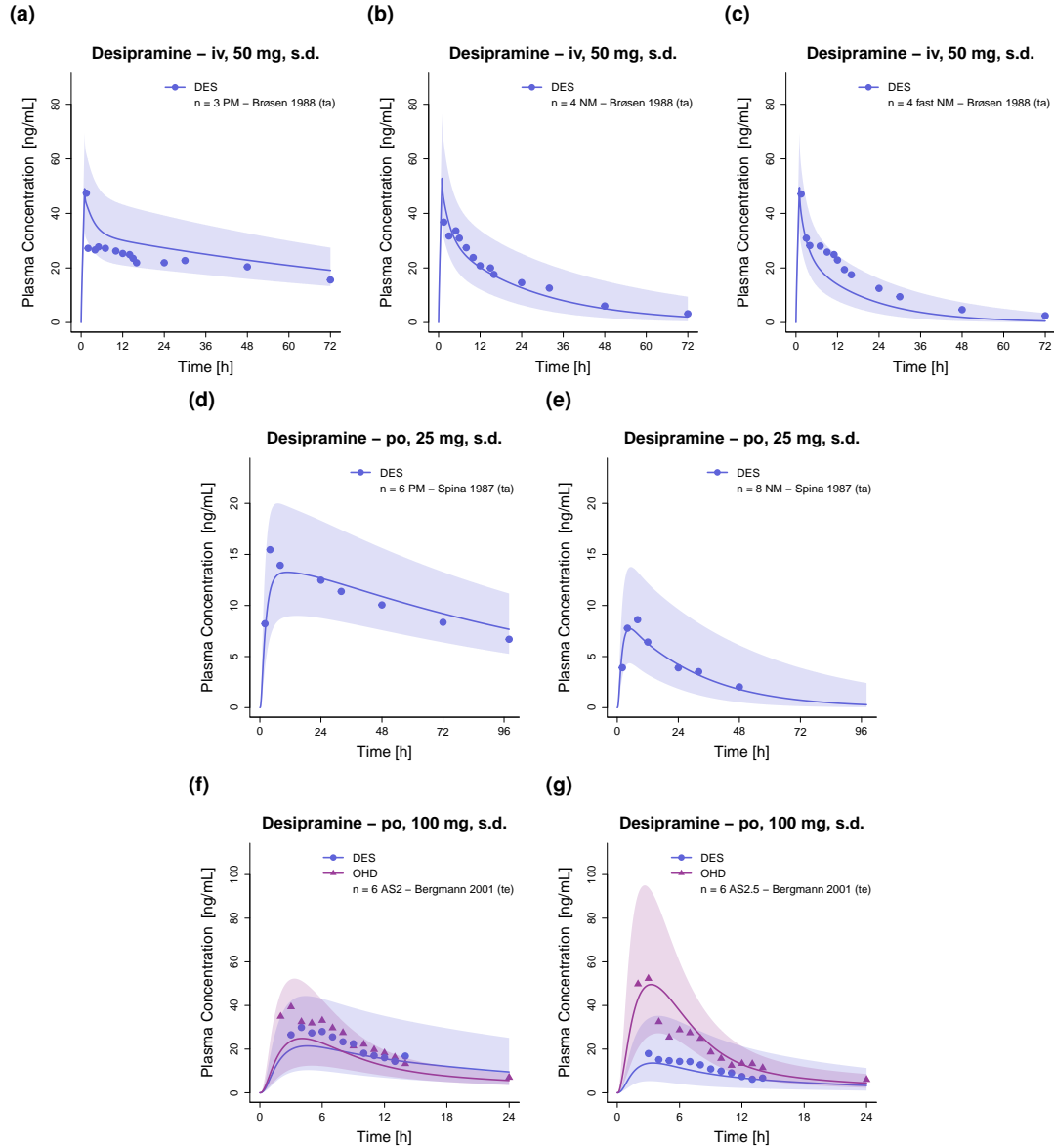


Figure S10: Predicted compared to observed plasma concentration-time profiles of desipramine and 2-hydroxydesipramine at varying CYP2D6 activity levels. Population predicted (1000 individuals) geometric means are shown as lines, corresponding geometric standard deviations as shaded areas and observed data as dots/triangles [4, 5, 20]. AS: CYP2D6 activity score, DES: desipramine, iv: intravenous, n: number of study participants, NM: CYP2D6 normal metabolizer, OHD: 2-hydroxydesipramine, PM: CYP2D6 poor metabolizer, po: oral, s.d.: single dose, ta: training dataset, te: test dataset.

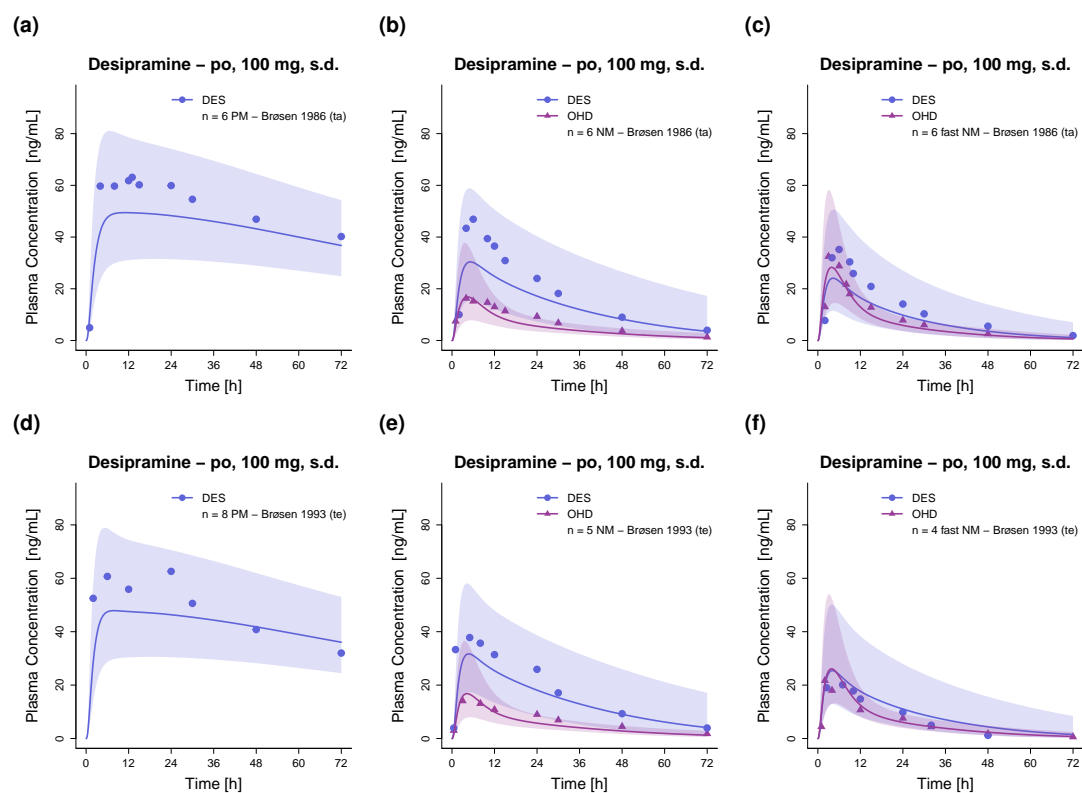


Figure S11: Predicted compared to observed plasma concentration-time profiles of desipramine and 2-hydroxydesipramine at varying CYP2D6 activity levels. Population predicted (1000 individuals) geometric means are shown as lines, corresponding geometric standard deviations as shaded areas and observed data as dots/triangles [21, 22]. AS: CYP2D6 activity score, DES: desipramine n: number of study participants, NM: CYP2D6 normal metabolizer, OHD: 2-hydroxydesipramine, PM: CYP2D6 poor metabolizer, po: oral, s.d.: single dose, ta: training dataset, te: test dataset.

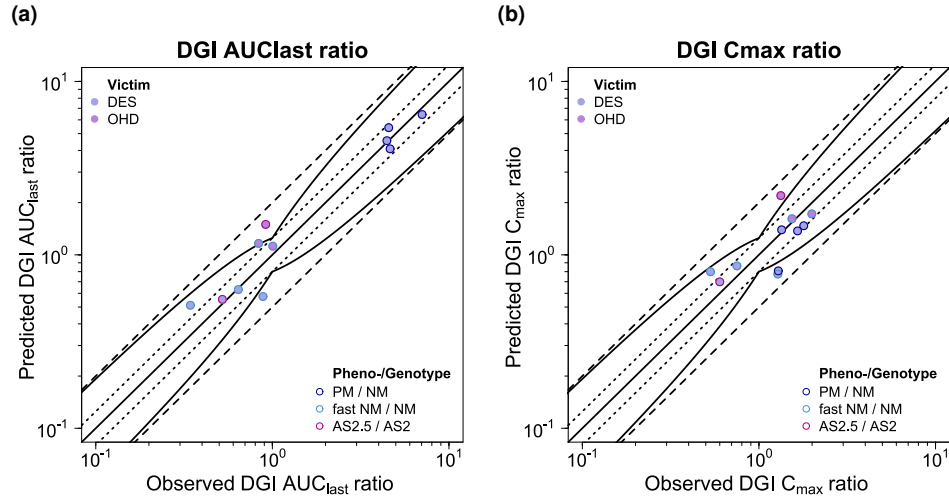
S3.4 DGI AUC_{last} and C_{max} Ratios

Figure S12: Goodness-of-fit plots comparing predicted and observed DGI AUC_{last} and C_{max} ratios for victim drug desipramine. The solid line marks the line of identity. Dotted lines indicate 1.25-fold, dashed lines indicate 2-fold deviation. Prediction success limits proposed by Guest et al. [2] are shown as curved lines (including 20% variability). AS: CYP2D6 activity score, AUC_{last} : area under the plasma concentration-time curve calculated between the first and last concentration measurement, C_{max} : maximum plasma concentration, DES: desipramine, DGI: drug-gene interaction, NM: CYP2D6 normal metabolizer, OHD: 2-hydroxydesipramine, PM: CYP2D6 poor metabolizer.

S3.4.1 Geometric Mean Fold Errors of Predicted DGI AUC_{last} and C_{max} RatiosTable S7: Predicted and observed DGI AUC_{last} and C_{max} ratios involving **desipramine** as victim drug

Dose [mg] ^a	Route	t _{last} [h]	DGI AUC _{last} ratio			DGI C _{max} ratio			Phenotype/AS	Molecule	Reference
			Pred	Obs	Pred/Obs	Pred	Obs	Pred/Obs			
Intravenous											
50 (44)	s.d. iv 60 min inf	432 / 72	4.55	4.45	1.02	0.81	1.29	0.63	PM / NM	DES	Brøsen 1988 [4]
50 (44)	s.d. iv 60 min inf	72 / 72	0.57	0.88	0.65	0.77	1.28	0.60	fast NM / NM	DES	Brøsen 1988 [4]
Mean GMFE (range):			1.28 (1.02–1.54), 2/2 with GMFE ≤ 2			1.62 (1.59–1.65), 2/2 with GMFE ≤ 2					
Oral											
25 (22)	s.d. po	96 / 48	4.08	4.64	0.88	1.47	1.80	0.82	PM / NM	DES	Spina 1987 [5]
100 (88)	s.d. po	14 / 14	0.55	0.52	1.06	0.70	0.60	1.16	AS2.5 / AS2	DES	Bergmann 2001 [20]
100 (88)	s.d. po	24 / 24	1.49	0.92	1.63	2.19	1.33	1.65	AS2.5 / AS2	OHD	Bergmann 2001 [20]
100 (88)	s.d. po	408 / 72	6.43	7.04	0.91	1.39	1.35	1.04	PM / NM	DES	Brøsen 1986 [21]
100 (88)	s.d. po	72 / 72	0.63	0.64	0.98	0.86	0.75	1.15	fast NM / NM	DES	Brøsen 1986 [21]
100 (88)	s.d. po	48 / 72	1.12	1.01	1.11	1.72	1.99	0.86	fast NM / NM	OHD	Brøsen 1986 [21]
100 (88)	s.d. po	240 / 72	5.40	4.56	1.19	1.37	1.66	0.83	PM / NM	DES	Brøsen 1993 [22]
100 (88)	s.d. po	48 / 72	0.51	0.34	1.49	0.80	0.53	1.50	fast NM / NM	DES	Brøsen 1993 [22]
100 (88)	s.d. po	72 / 72	1.16	0.84	1.39	1.61	1.54	1.05	fast NM / NM	OHD	Brøsen 1993 [22]
Mean GMFE (range):			1.24 (1.02–1.63), 9/9 with GMFE ≤ 2			1.24 (1.04–1.65), 9/9 with GMFE ≤ 2					
Overall GMFE (range):			1.24 (1.02–1.63), 11/11 with GMFE ≤ 2			1.31 (1.04–1.65), 11/11 with GMFE ≤ 2					

AS: CYP2D6 activity score, AUC_{last}: area under the plasma concentration-time curve calculated between the first and last concentration measurement, C_{max}: maximum plasma concentration, DES: desipramine, DGI: drug-gene interaction, GMFE: geometric mean fold error, inf: infusion, iv: intravenous, NM: CYP2D6 normal metabolizer, obs: observed, OHD: 2-hydroxydesipramine, PM: CYP2D6 poor metabolizer, po: oral, pred: predicted, s.d.: single dose, t_{last}: time of the last concentration measurement. Respective doses of desipramine base were calculated and incorporated in simulations. ^a Dose given as desipramine hydrochloride (desipramine base).

S4 DD(G)I Network Development

S4.1 System-Dependent Parameters

Table S8: Relevant enzymes, transporters and binding proteins

Protein	Relevant model(s)	Highest expression	Reference concentration [μmol/L]	
			Mean ^a	GSD
Enzymes				
AADAC	KET, RIF	Liver [34]	1.00 ^b [35]	1.40 ^c
CYP1A2	FLV, MEX	Liver [36]	1.80 [37]	1.63 [38]
CYP2B6	BUP, CBZ, CLO	Liver [34]	1.56 [37]	1.56 [38]
CYP2C8	CBZ	Liver [36]	2.56 [37]	2.05 [38]
CYP2C19	ATO, BUP, OME	Liver [36]	0.76 [37]	1.80 [38]
CYP2D6	ATO, DES, DEX, CLO, FLV, MET, MEX, PAR, RIS	Liver [36]	0.40 [37]	2.49 [38]
CYP3A4	ALP, CBZ, CLA, CLO, DEX, ERY, ITR, KET, MET, MID, OME, PAR, QUI, RIS, VER	Liver [36]	4.32 [37]	1.18 liver, 1.46 int. [38]
EPHX1	CBZ	Liver [34]	1.00 ^b [35]	1.40 ^c
FMO3	KET	Liver [39]	1.00 ^b [35]	1.40 ^c
HSD11B1	BUP	Liver [39]	1.00 ^b [35]	1.40 ^c
UGT1A4	KET, MID	Liver [34]	2.32 ^d [40, 41]	1.51 [40]
UGT2B7	CBZ, BUP	Kidney [42]	2.78 [43]	1.60 [38]
UGT2B15	DEX	Liver [34]	2.48 ^d [40, 41]	1.26 [40]
Transporters				
MATE1	CIM	Kidney [44, 45]	0.13 ^e [41, 46]	1.53 [46]
OAT3	CIM	Kidney [47]	0.09 ^e [41, 46]	1.53 [46]
OATP1B1	ERY, RIF	Liver [47]	0.07 ^f [48]	1.54 [48]
OCT1	CIM	Liver [39]	0.16 ^f [48, 49]	1.50 [49]
P-gp	DIG, KET, QUI, RIF, RIS, VER	Duodenum mucosa, Upper jejunum mucosa, Lower jejunum mucosa, Upper ileum mucosa Lower ileum mucosa [47]	1.41 ^g [50]	1.60 [48]
Binding proteins				
ATP1A2	DIG	Brain [39]	0.48 ^g [50]	1.40 ^c
Bp ^h	BUP	Brain [42]	1.00 ^b [35]	1.40 ^c
GABRG2	MID	Brain [39]	1.04 [51]	1.40 ^c

AADAC: arylacetamide deacetylase, ALP: alprazolam, ATO: atomoxetine, ATP1A2: ATPase Na⁺/K⁺ transporting subunit alpha 2, BP: binding partner, BUP: bupropion, CBZ: carbamazepine, CIM: cimetidine, CLA: clarithromycin, CLO: *E*-clomiphene, CYP: cytochrome P450, DES: desipramine, DEX: dextromethorphan, DIG: digoxin, EPHX: epoxide hydrolase, ERY: erythromycin, FLV: fluvoxamine, FMO: flavin-containing monooxygenase, GABRG: gamma-aminobutyric acid (GABA) A receptor gamma, GSD: geometric standard deviation, HSD: hydroxysteroid dehydrogenase, int: intestine, ITR: itraconazole, KET: ketoconazole, MATE: multidrug and toxin extrusion protein, MET: metoprolol, MEX: mexiletine, MID: midazolam, OAT: organic anion transporter, OATP: organic anion transporting polypeptide, OCT: organic cation transporter, OME: omeprazole, PAR: paroxetine, P-gp: P-glycoprotein, QUI: quinidine, RIF: rifampicin, RIS: risperidone, UGT: uridine 5'-diphospho-glucuronosyltransferase, VER: verapamil. ^a In the tissue of highest expression. ^b If no information was available, the mean reference concentration was set to 1.00 $\mu\text{mol/L}$ and the catalytic rate constant was optimized according to [35]. ^c A moderate variability of 35% CV was assumed (= 1.40 GSD). ^d Protein per mg microsomal protein x 40 mg microsomal protein per g liver [41]. ^e Transporter per mg membrane protein x 26.2 mg human kidney microsomal protein per g kidney [41]. ^f Transporter per mg membrane protein x 37.0 mg membrane protein per g liver [48]. ^g Optimized by Hanke et al. [50]. ^h Binding partner representing various neurotransmitter transporters (therapeutic target).

Table S9: Expression data of relevant enzymes

	AADAC	CYP1A2	CYP2B6	CYP2C8	CYP2C19	CYP2D6	CYP3A4
Properties							
Localization	Intracellular	Intracellular	Intracellular	Intracellular	Intracellular	Intracellular	Intracellular
Half-life liver/intestine [h]^a	36/23	39/23	32/23	23/23	26/23	51/23	36/23 [52, 53]
Relative expression in various organs and tissues [%]							
Data source	RT-PCR [34]	RT-PCR [36]	RT-PCR [34]	RT-PCR [36]	RT-PCR [36, 54]	RT-PCR [36]	RT-PCR [36]
Blood Cells	0	0	0	0	0	0	0
Plasma	0	0	0	0	0	0	0
Bone	0	0	0	0	0	0	0
Brain	0	0	0	0	0	1	0
Fat	0	0	0	0	0	0	0
Gonads	0	0	1	1	0	77	0
Heart	0	0	0	0	0	0	0
Kidney	0	0	10	0	0	2	1
Liver Periportal	100	100	100	100	100	100	100
Liver Pericentral	100	100	100	100	100	100	100
Lung	3	0	60	0	0	2	0
Muscle	0	0	0	0	0	0	0
Pancreas	15	0	0	0	0	0	0
Skin	0	0	0	0	0	0	0
Spleen	0	0	0	0	0	0	0
Duodenum mucosa	25	0	7	0	2	9	7
Upper jejunum mucosa	25	0	7	0	1	9	7
Lower jejunum mucosa	25	0	7	0	1	9	7
Upper ileum mucosa	25	0	7	0	1	9	7
Lower ileum mucosa	25	0	7	0	1	9	7
Colon ascendens mucosa	0	0	0	0	0	0	0
Colon transversum mucosa	0	0	0	0	0	0	0
Colon descendens mucosa	0	0	0	0	0	0	0
Colon sigmoid mucosa	0	0	0	0	0	0	0
Stomach non-mucosal tissue	8	0	0	0	0	0	0
Small intestine non-mucosal tissue	25	0	7	0	1	9	7
Large intestine non-mucosal tissue	0	0	0	0	0	0	0

AADAC: arylacetamide deacetylase, Array: microarray expression profile, CYP: cytochrome P450, EPHX: epoxide hydrolase, EST: expressed sequence tag, FMO: flavin-containing monooxygenase, HSD: hydroxysteroid dehydrogenase, RT-PCR: reverse transcription-polymerase chain reaction measured expression profile, UGT: uridine 5'-diphospho-glucuronosyltransferase. ^a Information from PK-Sim[®] expression database.

Table S9: Expression data of relevant enzymes (*continued*)

	EPHX1	FMO3	HSD11B1	UGT1A4	UGT2B7	UGT2B15
Properties						
Localization	Intracellular	Intracellular	Intracellular	Intracellular	Intracellular	Intracellular
Half-life liver/intestine [h] ^a	36/23	36/23	36/23	36/23	36/23	36/23
Relative expression in various organs and tissues [%]						
Data source	RT-PCR [34]	Array [39]	Array [39]	RT-PCR [34]	EST [42]	RT-PCR [34]
Blood Cells	1	0	0	0	0	0
Plasma	1	0	0	0	0	0
Bone	2	1	4	0	0	0
Brain	4	0	9	0	8	0
Fat	0	0	0	0	0	0
Gonads	18	0	21	0	13	0
Heart	12	0	0	0	0	0
Kidney	15	0	7	0	100	0
Liver Periportal	100	100	100	100	23	100
Liver Pericentral	100	100	100	100	23	100
Lung	14	2	8	0	0	0
Muscle	36	1	6	0	0	0
Pancreas	10	0	7	0	0	2
Skin	0	0	30	0	3	0
Spleen	6	0	10	0	0	0
Duodenum mucosa	6	0	9	0	4	0
Upper jejunum mucosa	6	0	9	0	4	0
Lower jejunum mucosa	6	0	9	0	4	0
Upper ileum mucosa	6	0	9	0	4	0
Lower ileum mucosa	6	0	9	0	4	0
Colon ascendens mucosa	4	0	4	0	0	0
Colon transversum mucosa	4	0	4	0	0	0
Colon descendens mucosa	4	0	4	0	0	0
Colon sigmoid mucosa	4	0	4	0	0	0
Stomach non-mucosal tissue	5	1	4	0	13	3
Small intestine non-mucosal tissue	6	0	9	0	4	0
Large intestine non-mucosal tissue	4	0	4	0	0	0

AADAC: arylacetamide deacetylase, Array: microarray expression profile, CYP: cytochrome P450, EPX: epoxide hydrolase, EST: expressed sequence tag, FMO: flavin-containing monooxygenase, HSD: hydroxysteroid dehydrogenase, RT-PCR: reverse transcription-polymerase chain reaction measured expression profile, UGT: uridine 5'-diphospho-glucuronosyltransferase. ^a Information from PK-Sim[®] expression database.

Table S10: Expression data of relevant transporters and binding proteins

	MATE1	OAT3	OATP1B1	OCT1	P-gp	ATP1A2	BP ^a	GABRG2
Properties								
Localization	Cell membrane	Cell membrane	Cell membrane	Cell membrane	Cell membrane	Interstitial	Interstitial	Interstitial
Direction	Efflux	Influx	Influx	Influx	Efflux	n.a.	n.a.	n.a.
Half-life liver/intestine [h]^b	n.a./n.a.	n.a./n.a.	36/23	36/23	36/23	36/23	36/23	36/23
Relative expression in various organs and tissues [%]								
Data source	[44, 45]	RT-PCR [47]	RT-PCR [47]	Array [39]	RT-PCR [47, 50]	Array [39]	EST [42]	[51]
Blood Cells	0	0	0	0	0	0	0	0
Plasma	0	0	0	0	0	0	0	0
Bone	0	0	0	2	2	1	0	0
Brain	0	0	0	1 (BBB)	8 (BBB)	100	100	100
Fat	0	0	0	0	0	0	0	0
Gonads	0	0	1	0	2	5	28	0
Heart	0	0	0	1	4	32	0	0
Kidney	100 (apical)	100 (basolateral)	0	3 (basolateral)	71 (apical)	2	42	0
Liver Periportal	0	0	100 (basolateral)	100 (basolateral)	19 (apical)	2	0	0
Liver Pericentral	0	0	100 (basolateral)	100 (basolateral)	19 (apical)	2	0	0
Lung	0	0	0	1	7	3	0	0
Muscle	0	0	0	4	1	70	12	0
Pancreas	0	0	0	1	1	1	0	0
Skin	0	0	0	1	0	4	0	0
Spleen	0	0	0	0	7	1	0	0
Duodenum mucosa	0	0	0	2 (apical)	100 (apical)	5	18	0
Upper jejunum musoca	0	0	0	2 (apical)	100 (apical)	5	18	0
Lower jejunum mucosa	0	0	0	2 (apical)	100 (apical)	5	18	0
Upper ileum mucosa	0	0	0	2 (apical)	100 (apical)	5	18	0
Lower ileum mucosa	0	0	0	2 (apical)	100 (apical)	5	18	0
Colon ascendens mucosa	0	0	0	0	40 (apical)	8	0	0
Colon transversum mucosa	0	0	0	0	40 (apical)	8	0	0
Colon descendens mucosa	0	0	0	0	40 (apical)	8	0	0
Colon sigmoid mucosa	0	0	0	0	40 (apical)	8	0	0
Stomach non-mucosal tissue	0	0	0	1	3	3	0	0
Small intestine non-mucosal tissue	0	0	0	2	28	5	18	0
Large intestine non-mucosal tissue	0	0	0	3	11	8	0	0

Array: microarray expression profile, ATP1A2: ATPase Na⁺/K⁺ transporting subunit alpha 2, BBB: blood-brain barrier, BP: binding partner, EST: expressed sequence tag, GABRG: gamma-aminobutyric acid (GABA) A receptor gamma, MATE: multidrug and toxin extrusion, protein, n.a.: not applicable, OAT: organic anion transporter, OATP: organic anion transporting polypeptide, OCT: organic cation transporter, P-gp: P-glycoprotein, RT-PCR: reverse transcription-polymerase chain reaction measured expression profile. ^a Binding partner representing various neurotransmitter transporters (therapeutic target). ^b Information from PK-Sim[®] expression database.

S4.2 Types of Interaction

S4.2.1 Competitive Inhibition

$$K_{M,app} = K_M * (1 + \frac{[I]}{K_i}) \quad (S2)$$

$$v = \frac{v_{max} * [S]}{K_{M,app} + [S]} = \frac{k_{cat} * [E] * [S]}{K_{M,app} + [S]} \quad (S3)$$

$K_{M,app}$ = Michaelis-Menten constant in the presence of inhibitor, K_M = Michaelis-Menten constant, $[I]$ = free inhibitor concentration, K_i = dissociation constant of the inhibitor-enzyme/transporter complex, v = reaction velocity, $[S]$ = free substrate concentration, k_{cat} = catalytic or transport rate constant and $[E]$ = enzyme concentration.

S4.2.2 Non-Competitive Inhibition

$$v_{max,app} = \frac{v_{max}}{1 + \frac{[I]}{K_i}} \quad (S4)$$

$$v = \frac{v_{max,app} * [S]}{K_M + [S]} \quad (S5)$$

$v_{max,app}$ = maximum reaction velocity in the presence of inhibitor, v_{max} = maximum reaction velocity, $[I]$ = free inhibitor concentration, K_i = dissociation constant of the inhibitor-enzyme/transporter complex, v = reaction velocity, $[S]$ = free substrate concentration and K_M = Michaelis-Menten constant.

S4.2.3 Mechanism-Based Inactivation

$$\frac{d[E]}{dt} = k_{deg} * E_0 - \frac{k_{deg} + k_{inact} * [I]}{K_I + [I]} * [E] \quad (S6)$$

$\frac{d[E]}{dt}$ = enzyme turnover, k_{deg} = degradation rate constant, E_0 = enzyme concentration at time 0, $[I]$ = free mechanism-based inactivator concentration, k_{inact} = maximum inactivation rate constant, K_I = concentration for half-maximal inactivation and $[E]$ = enzyme concentration.

S4.2.4 Induction

$$\frac{d[E]}{dt} = k_{deg} * E_0 * \frac{1 + (E_{max} * [Ind])}{EC50 + [Ind]} \quad (S7)$$

$\frac{d[E]}{dt}$ = enzyme turnover, k_{deg} = degradation rate constant, E_0 = enzyme concentration at time 0, E_{max} = maximal induction effect *in vivo*, $[Ind]$ = free inducer concentration and $EC50$ = concentration for half maximal induction *in vivo*.

S4.2.5 Down Regulation

$$\frac{d[E]}{dt} = k_{deg} * E_0 * \frac{1 + (E_{max} * [Ind])}{EC50 + [Ind]} \quad (S8)$$

$\frac{d[E]}{dt}$ = enzyme turnover, k_{deg} = degradation rate constant, E_0 = enzyme concentration at time 0, E_{max} = maximal induction effect *in vivo*, $[Ind]$ = free inducer concentration and $EC50$ = concentration for half maximal induction *in vivo*.

S4.3 Published PBPK DDI Models

Interaction parameters added to the original model during the network development process are indicated by citing the corresponding references.

Table S11: Published perpetrator models and included relevant interaction constants

Model (PK-Sim® Version)	Mechanism	Parameter	Value	Publication	Model repository
Atomoxetine (V11)				Rüdesheim et al. 2022 [1]	Atomoxetine-Model
Atomoxetine	Competitive inhibition	CYP3A4 K_i [$\mu\text{mol/L}$]	34.00	[17]	
	Competitive inhibition	CYP2D6 K_i [$\mu\text{mol/L}$]	3.60	[17]	
Bupropion (V11)				Marok et al. 2021 [55]	Bupropion-DDGI-Model
Bupropion	Down regulation	CYP2D6 E_{max}	-0.63	[56, 57]	
	Down regulation	CYP2D6 EC_{50}	0.61	[56, 57]	
	Competitive inhibition	CYP2D6 K_i	21	[16]	
Hydroxybupropion	Down regulation	CYP2D6 E_{max}	-0.96	[56, 57]	
	Down regulation	CYP2D6 EC_{50}	1.78	[56, 57]	
	Competitive inhibition	CYP2D6 EC_i	13.30	[16]	
Erythrohydrobupropion	Down regulation	CYP2D6 E_{max}	-0.23	[56, 57]	
	Down regulation	CYP2D6 EC_{50}	2.30	[56, 57]	
	Competitive inhibition	CYP2D6 EC_i	1.70	[16]	
Threohydrobupropion	Down regulation	CYP2D6 E_{max}	-0.53	[56, 57]	
	Down regulation	CYP2D6 EC_{50}	0.10	[56, 57]	
	Competitive inhibition	CYP2D6 EC_i	5.40	[16]	
Carbamazepine (V11)				Fuhr et al. 2021 [58]	Carbamazepine-Model (OSP, v1.0) ^a
Carbamazepine	Induction	CYP3A4 E_{max}	6.00		
	Induction	CYP3A4 EC_{50} [$\mu\text{mol/L}$]	20.00		
Carbamazepine-10,11-epoxide	-	-	-		
Cimetidine (V11)				Hanke et al. 2020 [59]	Cimetidine-Model (OSP, v1.1) ^a
Cimetidine	Competitive inhibition	CYP3A4 K_i [$\mu\text{mol/L}$]	268.00	[60]	
	Competitive inhibition	CYP2D6 K_i [$\mu\text{mol/L}$]	38.00		
Clarithromycin (V11)				Hanke et al. 2018 [50]	Clarithromycin-Model (OSP, v1.2) ^a
Clarithromycin	Mechanism-based inactivation	CYP3A4 K_I	6.04		
	Mechanism-based inactivation	CYP3A4 k_{inact} [$\mu\text{mol/L}$]	0.04		

CYP: cytochrome P450, EC_{50} : concentration for half maximal induction, E_{max} : maximal induction effect, K_i : dissociation constant of the inhibitor-enzyme/transporter (competitive) and inhibitor-enzyme/transporter(-substrate) complex (non-competitive), K_I : concentration for 50% inactivation (mechanism-based inactivation), k_{inact} : maximum inactivation rate (mechanism-based inactivation), OSP: Open Systems Pharmacology, P-gp: P-glycoprotein. If not otherwise indicated, interaction constants were adopted from the respective published models. Hyperlinks refer to the respective model repositories. ^a Open Systems Pharmacology model repository (<https://github.com/Open-Systems-Pharmacology>). ^b modification by Feick et al. [66].

Table S11: Published perpetrator models and included relevant interaction constants (*continued*)

Model (PK-Sim® Version)	Mechanism	Parameter	Value	Publication	Model repository
Erythromycin (V11)					Erythromycin-Model (OSP, v1.3) ^a
Erythromycin	Mechanism-based inactivation	CYP3A4 K _i	7.60		
	Mechanism-based inactivation	CYP3A4 k _{inact} [μmol/L]	0.03		
Fluvoxamine (V11)					Fluvoxamine-Model (OSP, v1.2) ^a
Fluvoxamine	Competitive inhibition	CYP3A4 K _i [μmol/L]	1.60	Britz et al. 2019 [61]	
	Competitive inhibition	CYP2D6 K _i [μmol/L]	8.2	[62]	
	Competitive inhibition	CYP2C19 K _i [nmol/L]	3.60	[63]	
Itraconazole (V11)					Itraconazole-Model (OSP, v1.3) ^a
Itraconazole	Competitive inhibition	CYP3A4 K _i [nmol/L]	1.30	Hanke et al. 2018 [50]	
	Competitive inhibition	P-gp K _i [nmol/L]	8.00		
Hydroxy-itraconazole	Competitive inhibition	CYP3A4 K _i [nmol/L]	14.40		
Keto-itraconazole	Competitive inhibition	CYP3A4 K _i [nmol/L]	5.12		
N-Desalkyl-itraconazole	Competitive inhibition	CYP3A4 K _i [nmol/L]	0.32		
Ketoconazole (V11)					Ketoconazole-DDI-Model
Ketoconazole	Competitive inhibition	CYP3A4 K _i [μmol/L]	0.008	Marok et al. 2023 [64]	
	Competitive inhibition	P-gp K _i [μmol/L]	0.035		
N-Deacetylketoconazole	Competitive inhibition	CYP3A4 K _i [μmol/L]	0.022		
	Competitive inhibition	P-gp K _i [μmol/L]	0.119		
N-Deacetyl-N-Hydroxyketoconazole	Competitive inhibition	CYP3A4 K _i [μmol/L]	0.022		
	Competitive inhibition	P-gp K _i [μmol/L]	0.119		
Omeprazole (V11)					Omeprazole-Model (OSP, v1.1) ^a
R-Omeprazole	Competitive inhibition	CYP3A4 K _i [μmol/L]	44.50 ^b	Kanacher et al. 2020 [54]	
S-Omeprazole	Competitive inhibition	CYP3A4 K _i [μmol/L]	46.60 ^b		
Paroxetine (V11)					Paroxetine-Model
Paroxetine	Mechanism-based inactivation	CYP2D6 K _i [μmol/L]	0.17	Rüdesheim et al. 2022 [1]	
	Mechanism-based inactivation	CYP2D6 k _{inact} [1/min]	0.17		
	Mechanism-based inactivation	CYP3A4 K _i [μmol/L]	4.48		
	Mechanism-based inactivation	CYP3A4 k _{inact} [1/min]	0.01		

CYP: cytochrome P450, EC₅₀: concentration for half maximal induction, E_{max}: maximal induction effect, K_i : dissociation constant of the inhibitor-enzyme/transporter (competitive) and inhibitor-enzyme/transporter(-substrate) complex (non-competitive), KI: concentration for 50% inactivation (mechanism-based inactivation), k_{inact} : maximum inactivation rate (mechanism-based inactivation), OSP: Open Systems Pharmacology, P-gp: P-glycoprotein. If not otherwise indicated, interaction constants were adopted from the respective published models. Hyperlinks refer to the respective model repositories. ^a Open Systems Pharmacology model repository (<https://github.com/Open-Systems-Pharmacology>). ^b modification by Feick et al. [66].

Table S11: Published perpetrator models and included relevant interaction constants (*continued*)

Model (PK-Sim® Version)	Mechanism	Parameter	Value	Publication	Model repository
Quinidine (V11)				Feick et al. 2023 [66]	Quinidine-Model
Quinidine	Competitive inhibition	CYP2D6 K_i [$\mu\text{mol/L}$]	0.017		
	Competitive inhibition	P-gp K_i [$\mu\text{mol/L}$]	0.10		
	Competitive inhibition	CYP2D6 K_i [$\mu\text{mol/L}$]	2.30		
Rifampicin (V11)				Hanke et al. 2018 [50]	Rifampicin-Model (OSP, v1.2) ^a
Rifampicin	Induction	CYP3A4 E_{max}	9.00		
	Induction	CYP3A4 EC_{50} [$\mu\text{mol/L}$]	0.34		
	Competitive inhibition	CYP3A4 K_i [$\mu\text{mol/L}$]	18.50		
	Induction	P-gp E_{max}	2.50		
	Induction	P-gp EC_{50} [$\mu\text{mol/L}$]	0.34		
	Competitive inhibition	P-gp K_i [$\mu\text{mol/L}$]	169.00		
Verapamil (V11)				Hanke et al. 2020a [67]	Verapamil-Norverapamil-Model
R-Verapamil	Mechanism-based inactivation	CYP3A4 K_I [$\mu\text{mol/L}$]	27.63		
	Mechanism-based inactivation	CYP3A4 k_{inact} [1/min]	0.038		
	Non-competitive inhibition	P-gp K_i [$\mu\text{mol/L}$]	0.038		
S-Verapamil	Mechanism-based inactivation	CYP3A4 K_I [$\mu\text{mol/L}$]	3.85		
	Mechanism-based inactivation	CYP3A4 k_{inact} [1/min]	0.034		
	Non-competitive inhibition	P-gp K_i [$\mu\text{mol/L}$]	0.038		
R-Norverapamil	Mechanism-based inactivation	CYP3A4 K_I [$\mu\text{mol/L}$]	6.10		
	Mechanism-based inactivation	CYP3A4 k_{inact} [1/min]	0.048		
	Non-competitive inhibition	P-gp K_i [$\mu\text{mol/L}$]	0.038		
S-Norverapamil	Mechanism-based inactivation	CYP3A4 K_I [$\mu\text{mol/L}$]	2.90		
	Mechanism-based inactivation	CYP3A4 k_{inact} [1/min]	0.080		
	Non-competitive inhibition	P-gp K_i [$\mu\text{mol/L}$]	0.038		

CYP: cytochrome P450, EC_{50} : concentration for half maximal induction, E_{max} : maximal induction effect, K_i : dissociation constant of the inhibitor-enzyme/transporter (competitive) and inhibitor-enzyme/transporter(-substrate) complex (non-competitive), K_I : concentration for 50% inactivation (mechanism-based inactivation), k_{inact} : maximum inactivation rate (mechanism-based inactivation), OSP: Open Systems Pharmacology, P-gp: P-glycoprotein. If not otherwise indicated, interaction constants were adopted from the respective published models. Hyperlinks refer to the respective model repositories. ^a Open Systems Pharmacology model repository (<https://github.com/Open-Systems-Pharmacology>). ^b modification by Feick et al. [66].

Table S12: Published victim models and affected metabolism and transport pathways

Model (PK-Sim® Version)	Mechanism	Parameter	Value	Publication	Model repository
Alprazolam (V11)					Alprazolam-Model (OSP, v1.1) ^a
Alprazolam	Metabolism to 4-OHA	CYP3A4 K_M [μmol/L]	704.00		
	Metabolism to 4-OHA	CYP3A4 k_{cat} [1/min]	13.73		
	Metabolism to α-OHA	CYP3A4 K_M [μmol/L]	269.00		
	Metabolism to α-OHA	CYP3A4 k_{cat} [1/min]	0.81		
Atomoxetine (V11)				Rüdesheim et al. 2022 [1]	Atomoxetine-Model
Atomoxetine	Metabolism	CYP2D6 K_M [μmol/L]	2.30		
	Metabolism	CYP2D6 k_{cat} [1/min] (NM)	37.44		
(E)-Clomiphene (V11)				Kovar et al. 2022 [68]	E-clomiphene-Model
(E)-clomiphene	Metabolism to OHC	CYP2D6 K_M [μmol/L]	0.13		
	Metabolism to OHC	CYP2D6 k_{cat} [1/min] (NM)	306.38		
	Metabolism to NDC	CYP2D6 K_M [μmol/L]	0.78		
	Metabolism to NDC	CYP2D6 k_{cat} [1/min] (NM)	121.36		
	Metabolism	CYP2D6 K_M [μmol/L]	0.03		
	Metabolism	CYP2D6 k_{cat} [1/min] (NM)	130.35		
	Metabolism to NDC	CYP3A4 K_M [μmol/L]	0.78		
	Metabolism to NDC	CYP3A4 k_{cat} [1/min]	44.95		
(E)-4-hydroxyclophene	Metabolism	CYP2D6 K_M [μmol/L]	3.60		
	Metabolism	CYP2D6 k_{cat} [1/min] (NM)	8.55.17		
	Metabolism to HDC	CYP3A4 K_M [μmol/L]	3.40		
	Metabolism to HDC	CYP3A4 k_{cat} [1/min]	19.52		
(E)-N-desethylclomiphene	Metabolism to HDC	CYP2D6 K_M [μmol/L]	0.49		
	Metabolism to HDC	CYP2D6 k_{cat} [1/min] (NM)	64.52		
	Metabolism	CYP2D6 K_M [μmol/L]	0.97		
	Metabolism	CYP2D6 k_{cat} [1/min] (NM)	5.84		
	Metabolism	CYP3A4 K_M [μmol/L]	0.97		
	Metabolism	CYP3A4 k_{cat} [1/min]	0.78		
(E)-4-OH-DE-clomiphene	Metabolism	CYP2D6 K_M [μmol/L]	8.86		
	Metabolism	CYP2D6 k_{cat} [1/min] (NM)	211.71		

α -OHA: α -hydroxylalprazolam, CL: clearance, CYP: cytochrome P450, DXT: dextrorphan, HDC/(E)-4-OH-DE-clomiphene:(E)-4-hydroxy-N-desethylclomiphene, k_{cat} : catalytic or transport rate constant, K_M : Michaelis-Menten constant, NDC: (E)-N-desethylclomiphene, NM: CYP2D6 normal metabolizer, 4-OHA: 4-hydroxylalprazolam, OHC: (E)-4-hydroxyclophene, OHM: α -hydroxymetoprolol, OHQ: 3-hydroxyquinidine, OHR: 9-hydroxyrisperidone, OSP: Open Systems Pharmacology, P-gp: P-glycoprotein. If not otherwise indicated, process parameters were adopted from the respective published models. CYP2D6 NM kcat values were adjusted according to the respective publications to account for varying CYP2D6 activity levels. Hyperlinks refer to the respective model repositories. ^a Open Systems Pharmacology model repository (<https://github.com/Open-Systems-Pharmacology>). ^b Replacement of original unspecific hepatic metabolic clearance process.

Table S12: Published victim models and affected metabolism and transport pathways (*continued*)

Model (PK-Sim® Version)	Mechanism	Parameter	Value	Publication	Model repository
Dextromethorphan (V11)				Rüdesheim et al. 2022 [69]	Dextromethorphan-Model
Dextromethorphan	Metabolism to DXT	CYP2D6 K_M [$\mu\text{mol/L}$]	4.65		
	Metabolism to DXT	CYP2D6 k_{cat} [1/min] (NM)	90.89		
	Metabolism	CYP4A4 K_M [$\mu\text{mol/L}$]	176.80		
	Metabolism	CYP3A4 k_{cat} [1/min]	5.65		
Dextrorphan	Metabolism	CYP4A4 K_M [$\mu\text{mol/L}$]	910.00		
	Metabolism	CYP3A4 k_{cat} [1/min]	7.41		
Dextrorphan-O-glucuronide	-	-	-		
Digoxin (V11)				Hanke et al. 2018 [50]	Digoxin-Model (OSP) ^a
Digoxin	Transport	P-gp K_M [$\mu\text{mol/L}$]	177.00		
	Transport	P-gp k_{cat} [1/min]	71.16		
Metoprolol (V11)				Rüdesheim et al. 2020 [70]	Metoprolol-Model
R-Metoprolol	Metabolism to OHM	CYP2D6 K_M [$\mu\text{mol/L}$]	10.08		
	Metabolism to OHM	CYP2D6 k_{cat} [1/min] (NM)	6.02		
	Metabolism	CYP2D6 K_M [$\mu\text{mol/L}$]	8.82		
	Metabolism	CYP2D6 k_{cat} [1/min] (NM)	9.87		
	Metabolism	CYP3A4 CL [1/min]	0.02 ^b		
S-Metoprolol	Metabolism to OHM	CYP2D6 K_M [$\mu\text{mol/L}$]	10.75		
	Metabolism to OHM	CYP2D6 k_{cat} [1/min] (NM)	8.27		
	Metabolism	CYP2D6 K_M [$\mu\text{mol/L}$]	12.43		
	Metabolism	CYP2D6 k_{cat} [1/min] (NM)	10.37		
	Metabolism	CYP3A4 CL [1/min]	0.02 ^b		
α -Hydroxymetoprolol	-	-	-		
Mexiletine (V11)				Kanacher et al. 2020 [54]	Mexiletine-Model (OSP, v1.1) ^a
Mexiletine	Metabolism	CYP2D6 CL [1/min] (NM)	0.46		
Midazolam (V11)				Hanke et al. 2018 [50]	Midazolam-Model (OSP, v1.1) ^a
Midazolam	Metabolism	CYP3A4 K_M [$\mu\text{mol/L}$]	4.00		
	Metabolism	CYP3A4 k_{cat} [1/min]	8.76		

α -OHA: α -hydroxyalprazolam, CL: clearance, CYP: cytochrome P450, DXT: dextrorphan, HDC/(E)-4-OH-DE-clomiphene:(E)-4-hydroxy-N-desethylclomiphene, k_{cat} : catalytic or transport rate constant, K_M : Michaelis-Menten constant, NDC: (E)-N-desethylclomiphene, NM: CYP2D6 normal metabolizer, 4-OHA: 4-hydroxyalprazolam, OHC: (E)-4-hydroxyclophene, OHM: α -hydroxymetoprolol, OHQ: 3-hydroxyquinidine, OHR: 9-hydroxyrisperidone, OSP: Open Systems Pharmacology, P-gp: P-glycoprotein. If not otherwise indicated, process parameters were adopted from the respective published models. CYP2D6 NM k_{cat} values were adjusted according to the respective publications to account for varying CYP2D6 activity levels. Hyperlinks refer to the respective model repositories. ^a Open Systems Pharmacology model repository (<https://github.com/Open-Systems-Pharmacology>). ^b Replacement of original unspecific hepatic metabolic clearance process.

Table S12: Published victim models and affected metabolism and transport pathways (*continued*)

Model (PK-Sim® Version)	Mechanism	Parameter	Value	Publication	Model repository
Paroxetine (V11)				Rüdesheim et al. 2022 [1]	Paroxetine-Model
Paroxetine	Metabolism	CYP2D6 K_M [$\mu\text{mol/L}$]	0.03		
	Metabolism	CYP2D6 k_{cat} [1/min] (NM)	1.37		
	Metabolism	CYP3A4 K_M [$\mu\text{mol/L}$]	4.70		
	Metabolism	CYP3A4 k_{cat} [1/min]	1.01		
Quinidine (V11)				Feick et al. 2023 [66]	Quinidine-Model
Quinidine	Metabolism to OHQ	CYP3A4 K_M [$\mu\text{mol/L}$]	51.80		
	Metabolism to OHQ	CYP3A4 k_{cat} [1/min]	2.21		
	Metabolism	CYP3A4 K_M [$\mu\text{mol/L}$]	65.03		
	Metabolism	CYP3A4 k_{cat} [1/min]	3.84		
	Transport	P-gp K_M [$\mu\text{mol/L}$]	0.23		
	Transport	P-gp k_{cat} [1/min]	0.77		
3-Hydroxyquinidine	Metabolism	CYP3A4 CL [1/min]	0.08		
Risperidone (V11)				Rüdesheim et al. 2022 [1]	Risperidone-Model
Risperidone	Metabolism to OHR	CYP2D6 K_M [$\mu\text{mol/L}$]	1.10		
	Metabolism to OHR	CYP2D6 k_{cat} [1/min] (NM)	1.04		
	Metabolism	CYP2D6 K_M [$\mu\text{mol/L}$]	1.10		
	Metabolism	CYP2D6 k_{cat} [1/min] (NM)	0.63		
	Metabolism to OHR	CYP3A4 K_M [$\mu\text{mol/L}$]	61.00		
	Metabolism to OHR	CYP3A4 k_{cat} [1/min]	0.70		
	Metabolism	CYP3A4 K_M [$\mu\text{mol/L}$]	61.00		
	Metabolism	CYP3A4 k_{cat} [1/min]	0.15		
	Transport	P-gp K_M [$\mu\text{mol/L}$]	26.30		
	Transport	P-gp k_{cat} [1/min]	12.72		
9-Hydroxyrisperidone	Transport	P-gp K_M [$\mu\text{mol/L}$]	149.60		
	Transport	P-gp k_{cat} [1/min]	$5.70 \cdot 10^{-3}$		

α -OHA: α -hydroxyalprazolam, CL: clearance, CYP: cytochrome P450, DXT: dextrorphan, HDC/(E)-4-OH-DE-clomiphene:(E)-4-hydroxy-N-desethylclomiphene, k_{cat} : catalytic or transport rate constant, K_M : Michaelis-Menten constant, NDC: (E)-N-desethylclomiphene, NM: CYP2D6 normal metabolizer, 4-OHA: 4-hydroxyalprazolam, OHC: (E)-4-hydroxyclophene, OHM: α -hydroxymetoprolol, OHQ: 3-hydroxyquinidine, OHR: 9-hydroxyrisperidone, OSP: Open Systems Pharmacology, P-gp: P-glycoprotein. If not otherwise indicated, process parameters were adopted from the respective published models. CYP2D6 NM kcat values were adjusted according to the respective publications to account for varying CYP2D6 activity levels. Hyperlinks refer to the respective model repositories. ^a Open Systems Pharmacology model repository (<https://github.com/Open-Systems-Pharmacology>). ^b Replacement of original unspecific hepatic metabolic clearance process.

S5 DGI Model Evaluation

S5.1 DGI AUC_{last} and C_{max} Ratios

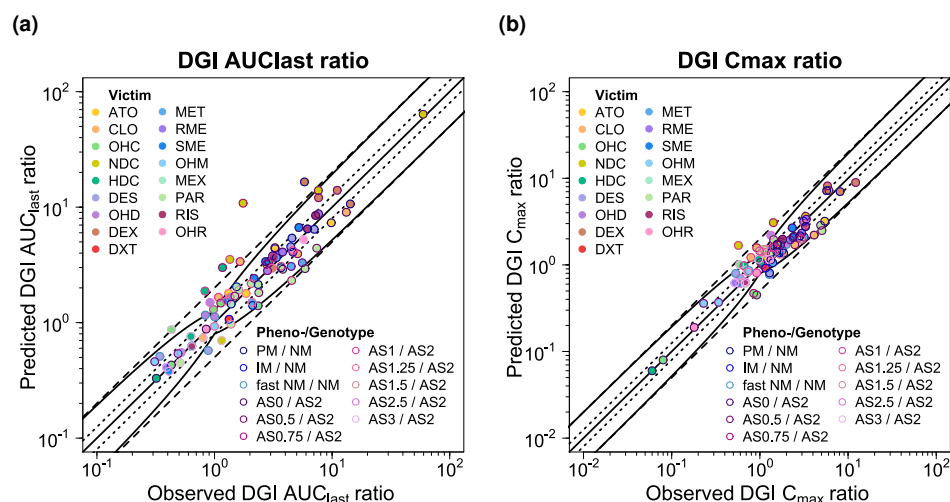


Figure S13: Goodness-of-fit plots comparing predicted and observed DGI AUC_{last} and C_{max} ratios. The solid line marks the line of identity. Dotted lines indicate 1.25-fold, dashed lines indicate 2-fold deviation. Prediction success limits proposed by Guest et al. [2] are shown as curved lines (including 20% variability). AS: CYP2D6 activity score, ATO: atomoxetine, AUC_{last} : area under the plasma concentration-time curve calculated between the first and last concentration measurement, CLO: (*E*)-clomiphene, C_{max} : maximum plasma concentration, DES: desipramine, DEX: dextromethorphan, DGI: drug-gene interaction, DXT: dextrorphan, HDC: (*E*)-4-hydroxy-N-desethylclomiphene, IM: CYP2D6 intermediate metabolizer, MET: metoprolol, MEX: mexiletine, NDC: (*E*)-N-desethylclomiphene, NM: CYP2D6 normal metabolizer, OHC: (*E*)-4-hydroxyclophene, OHD: 2-hydroxydesipramine, OHM: α -hydroxymetoprolol, OHR: 9-hydroxyrisperidone, PAR: paroxetine, PM: CYP2D6 poor metabolizer, RIS: risperidone, RME: R-metoprolol, SME: S-metoprolol.

S5.2 Geometric Mean Fold Errors of Predicted DGI AUC_{last} and C_{max} RatiosTable S13: Predicted and observed DGI AUC_{last} and C_{max} ratios

Drug administration	t _{last} [h]	DGI AUC _{last} ratio			DGI C _{max} ratio			Phenotype/AS	Molecule	Reference
		Pred	Obs	Pred/Obs	Pred	Obs	Pred/Obs			
Atomoxetine										
20 mg s.d. po	24 / 24	4.47	3.26	1.37	1.71	1.57	0.86	AS0 / AS2	ATO	Jung 2020 [71]
20 mg s.d. po	24 / 24	1.79	1.86	0.96	1.17	1.21	1.09	AS1.25 / AS2	ATO	Jung 2020 [71]
20 mg s.d. po	24 / 24	3.20	2.78	1.15	1.71	1.61	1.06	AS0.5 / AS2	ATO	Kim 2018 [72]
20 mg b.i.d. po	216 / 72	7.33	9.84	0.74	3.20	5.43	0.59	PM / NM	ATO	Sauer 2003 [73]
25 mg s.d. po	48 / 48	2.99	3.68	0.81	1.37	1.86	0.74	PM / NM	ATO	Todor 2016 [74]
40 mg s.d. po	24 / 24	3.41	2.89	1.18	1.83	1.74	1.05	AS0.5 / AS2	ATO	Byeon 2015 [75]
40 mg s.d. po	24 / 24	1.80	1.32	1.36	1.40	1.15	1.22	AS1.25 / AS2	ATO	Byeon 2015 [75]
Mean GMFE (range):		1.24 (1.04–1.37), 7/7 with GMFE ≤ 2			1.22 (1.03–1.70), 7/7 with GMFE ≤ 2					
(E)-Clomiphene										
42 mg s.d. po	168 / 72	9.04	13.21	0.68	2.21	4.12	0.54	AS0 / AS2	CLO	Mürdter 2016 [76]
42 mg s.d. po	168 / 168	0.43	0.43	1.01	0.08	0.08	0.99	AS0 / AS2	OHC	Mürdter 2016 [76]
42 mg s.d. po	168 / 72	63.77	59.41	1.07	7.23	6.07	1.19	AS0 / AS2	NDC	Mürdter 2016 [76]
42 mg s.d. po	168 / 168	0.33	0.32	1.03	0.06	0.06	1.04	AS0 / AS2	HDC	Mürdter 2016 [76]
42 mg s.d. po	168 / 72	3.95	5.09	0.78	1.71	2.49	0.69	AS0.5 / AS2	CLO	Mürdter 2016 [76]
42 mg s.d. po	168 / 168	1.40	2.35	0.59	0.45	0.92	0.48	AS0.5 / AS2	OHC	Mürdter 2016 [76]
42 mg s.d. po	168 / 72	13.95	7.64	1.83	3.64	3.30	1.10	AS0.5 / AS2	NDC	Mürdter 2016 [76]
42 mg s.d. po	168 / 168	3.29	2.90	1.13	1.07	1.02	1.05	AS0.5 / AS2	HDC	Mürdter 2016 [76]
42 mg s.d. po	168 / 72	3.39	1.65	2.05	1.58	0.92	1.72	AS0.75 / AS2	CLO	Mürdter 2016 [76]
42 mg s.d. po	168 / 168	1.48	1.13	1.31	0.47	0.85	0.55	AS0.75 / AS2	OHC	Mürdter 2016 [76]
42 mg s.d. po	168 / 72	10.83	1.75	6.19	3.08	1.42	2.17	AS0.75 / AS2	NDC	Mürdter 2016 [76]
42 mg s.d. po	168 / 168	3.00	1.17	2.57	1.01	1.07	0.94	AS0.75 / AS2	HDC	Mürdter 2016 [76]
42 mg s.d. po	72 / 72	1.66	1.08	1.54	1.22	0.79	1.55	AS1 / AS2	CLO	Mürdter 2016 [76]
42 mg s.d. po	168 / 168	1.30	0.98	1.32	0.61	0.59	1.03	AS1 / AS2	OHC	Mürdter 2016 [76]
42 mg s.d. po	72 / 168	3.53	1.35	2.61	1.68	0.57	2.92	AS1 / AS2	NDC	Mürdter 2016 [76]
42 mg s.d. po	168 / 168	1.88	0.83	2.25	0.98	0.66	1.49	AS1 / AS2	HDC	Mürdter 2016 [76]
42 mg s.d. po	72 / 72	0.74	0.80	0.93	0.88	0.71	1.23	AS3 / AS2	CLO	Mürdter 2016 [76]
42 mg s.d. po	168 / 168	0.87	0.43	2.00	1.01	0.59	1.72	AS3 / AS2	OHC	Mürdter 2016 [76]
42 mg s.d. po	72 / 72	0.70	1.15	0.61	1.17	1.19	0.98	AS3 / As2	NDC	Mürdter 2016 [76]
42 mg s.d. po	168 / 168	0.76	0.63	1.20	1.16	0.97	1.19	AS3 / AS2	HDC	Mürdter 2016 [76]
Mean GMFE (range):		1.83 (1.03–6.19), 14/20 with GMFE ≤ 2			1.46 (1.02–2.95), 17/20 with GMFE ≤ 2					
Desipramine										
50 mg s.d. iv	432 / 72	4.55	4.45	1.02	0.81	1.29	0.63	PM / NM	DES	Brøsen 1988 [4]
50 mg s.d. iv	72 / 72	0.57	0.88	0.65	0.77	1.28	0.60	fast NM / NM	DES	Brøsen 1988 [4]
25 mg s.d. po	96 / 48	4.08	4.64	0.88	1.47	1.80	0.82	PM / NM	DES	Spina 1987 [5]
100 mg s.d. po	240 / 72	5.40	4.56	1.19	1.37	1.66	0.83	PM / NM	DES	Brøsen 1993 [22]
100 mg s.d. po	48 / 72	0.51	0.34	1.49	0.80	0.53	1.50	fast NM / NM	DES	Brøsen 1993 [22]
100 mg s.d. po	72 / 72	1.16	0.84	1.39	1.61	1.54	1.05	fast NM / NM	OHD	Brøsen 1993 [22]

AS: CYP2D6 activity score, ATO: atomoxetine, AUC_{last}: area under the plasma concentration-time curve calculated between the first and last concentration measurement, b.i.d.: twice daily, CLO: (E)-clomiphene, C_{max}: maximum plasma concentration, DES: desipramine, DEX: dextromethorphan, DGI: drug-gene interaction, DXT: dextropropan, GMFE: geometric mean fold error, HDC: (E)-4-hydroxy-N-desethylclomiphene, IM: CYP2D6 intermediate metabolizer, iv: intravenous, MET: metoprolol, MEX: mexiletine, NDC: (E)-N-desethylclomiphene, NM: CYP2D6 normal metabolizer, obs: observed, OHC: (E)-4-hydroxyclophene, OHD: 2-hydroxydesipramine, OHM: α-hydroxymetoprolol, OHR: 9-hydroxyrisperidone, PAR: paroxetine, PM: CYP2D6 poor metabolizer, RIS: risperidone, RME: R-metoprolol, SME: S-metoprolol, po: oral, pred: predicted, q.d.: once daily, s.d.: single dose, t_{last}: time of the last concentration measurement. If perpetrator or victim drugs were applied in form of salts, the respective dose of base was calculated and incorporated in simulations.

Table S13: Predicted and observed DGI AUC_{last} and C_{max} ratios (*continued*)

Drug administration	t _{last} [h]	DGI AUC _{last} ratio			DGI C _{max} ratio			Phenotype/AS	Molecule	Reference
		Pred	Obs	Pred/Obs	Pred	Obs	Pred/Obs			
100 mg s.d. po	14 / 14	0.55	0.52	1.06	0.70	0.60	1.16	AS2.5 / AS2	DES	Bergmann 2001 [20]
100 mg s.d. po	24 / 24	1.49	0.92	1.63	2.19	1.33	1.65	AS2.5 / AS2	OHD	Bergmann 2001 [20]
100 mg s.d. po	408 / 72	6.43	7.04	0.91	1.39	1.35	1.04	PM / NM	DES	Brøsen 1986 [21]
100 mg s.d. po	72 / 72	0.63	0.64	0.98	0.86	0.75	1.15	fast NM / NM	DES	Brøsen 1986 [21]
100 mg s.d. po	48 / 72	1.12	1.01	1.11	1.72	1.99	0.86	fast NM / NM	OHD	Brøsen 1986 [21]
Mean GMFE (range):		1.24 (1.02–1.63), 11/11 with GMFE ≤ 2			1.31 (1.04–1.65), 11/11 with GMFE ≤ 2					
Dextromethorphan										
5 mg s.d. po	24 / 24	4.37	3.27	1.34	3.20	3.13	1.34	IM / NM	DEX	Storelli 2018 [77]
5 mg s.d. po	24 / 24	1.07	1.33	0.80	0.92	1.16	0.80	IM / NM	DXT	Storelli 2018 [77]
15 mg s.d. po	24 / 12	14.01	11.06	1.27	8.94	12.17	0.73	AS0.5 / AS2	DEX	Qiu 2016 [78]
15 mg s.d. po	24 / 12	2.97	3.10	0.96	2.94	3.23	0.91	AS1.25 / AS2	DEX	Qiu 2016 [78]
30 mg s.d. po	24 / 24	12.07	7.67	1.57	8.17	5.84	1.40	AS0.5 / AS2	DEX	Yamazaki 2017 [79]
30 mg s.d. po	168 / 48	16.55	5.82	2.84	7.20	5.71	1.26	PM / NM	DEX	Capon 1996 [80]
30 mg s.d. po	12 / 12	10.67	14.29	0.75	7.02	8.11	0.87	PM / NM	DEX	Gorski 2004 [81]
Mean GMFE (range):		1.52 (1.04–2.84), 6/7 with GMFE ≤ 2			1.22 (1.02–1.40), 7/7 with GMFE ≤ 2					
Metoprolol										
20 mg s.d. iv	8 / 8	1.41	2.11	0.67	1.06	1.40	0.76	PM / NM	MET	Leemann 1993 [82]
100 mg s.d. po	24 / 12	0.46	0.31	1.46	0.36	0.23	1.56	AS0.5 / AS2	MET	Bae 2014 [83]
100 mg s.d. po	24 / 24	3.302	5.58	1.69	2.08	2.77	0.75	AS0.5 / AS2	OHM	Bae 2014 [83]
100 mg s.d. po	24 / 12	3.07	4.49	0.68	2.09	3.18	0.66	AS0.5 / AS2	MET	Jin 2008 [84]
100 mg s.d. po	24 / 24	0.54	0.49	1.09	0.37	0.34	1.06	AS0.5 / AS2	OHM	Jin 2008 [84]
100 mg s.d. po	24 / 12	1.50	2.08	0.72	1.33	1.70	0.78	AS1.25 / AS2	MET	Jin 2008 [84]
100 mg s.d. po	24 / 24	0.93	1.00	0.92	0.83	0.73	1.14	AS1.25 / AS2	OHM	Jin 2008 [84]
100 mg s.d. po	48 / 24	3.66	3.36	1.09	2.17	2.86	0.76	PM / NM	MET	Hamelin 2000 [85]
100 mg s.d. po	48 / 12	3.79	3.12	1.22	2.14	2.44	0.88	AS0 / AS2	MET	Sharma 2005 [86]
100 mg s.d. po	48 / 12	4.09	3.79	1.08	2.33	2.98	0.78	AS0 / AS2	RME	Sharma 2005 [86]
100 mg s.d. po	48 / 12	3.38	2.72	1.25	2.07	2.38	0.87	AS0 / AS2	SME	Sharma 2005 [86]
100 mg s.d. po	12 / 12	2.82	2.82	1.00	1.95	2.21	0.89	AS0.5 / AS2	RME	Huang 1999 [87]
100 mg s.d. po	12 / 12	2.42	2.17	1.11	1.71	1.72	0.99	AS0.5 / AS2	SME	Huang 1999 [87]
100 mg s.d. po	12 / 12	1.65	1.36	1.22	1.52	1.19	1.28	AS1.25 / AS2	RME	Huang 1999 [87]
100 mg s.d. po	12 / 12	1.54	1.27	1.21	1.41	1.05	1.34	AS1.25 / AS2	SME	Huang 1999 [87]
100 mg s.d. po	24 / 24	8.76	7.67	1.14	3.37	3.36	1.00	AS0 / AS2	RME	Seeringer 2008 [88]
100 mg s.d. po	24 / 24	6.67	5.22	1.28	2.68	2.33	1.15	AS0 / AS2	SME	Seeringer 2008 [88]
100 mg s.d. po	10 / 24	0.41	0.39	1.04	0.62	0.52	1.18	AS3 / AS2	RME	Seeringer 2008 [88]
100 mg s.d. po	10 / 24	0.38	0.41	0.93	0.61	0.59	1.02	AS3 / AS2	SME	Seeringer 2008 [88]
Mean GMFE (range):		1.23 (1.00–1.69), 19/19 with GMFE ≤ 2			1.22 (1.00–1.57), 19/19 with GMFE ≤ 2					

AS: CYP2D6 activity score, ATO: atomoxetine, AUC_{last}: area under the plasma concentration-time curve calculated between the first and last concentration measurement, b.i.d.: twice daily, CLO: (E)-clomiphene, C_{max}: maximum plasma concentration, DES: desipramine, DEX: dextromethorphan, DGI: drug-gene interaction, DXT: dextrorphan, GMFE: geometric mean fold error, HDC: (E)-4-hydroxy-N-desethylclomiphene, IM: CYP2D6 intermediate metabolizer, iv: intravenous, MET: metoprolol, MEX: mexiletine, NDC: (E)-N-desethylclomiphene, NM: CYP2D6 normal metabolizer, obs: observed, OHC: (E)-4-hydroxyclophene, OHD: 2-hydroxydesipramine, OHM: α-hydroxymetoprolol, OHR: 9-hydroxyrisperidone, PAR: paroxetine, PM: CYP2D6 poor metabolizer, RIS: risperidone, RME: R-metoprolol, SME: S-metoprolol, po: oral, pred: predicted, q.d.: once daily, s.d.: single dose, t_{last}: time of the last concentration measurement. If perpetrator or victim drugs were applied in form of salts, the respective dose of base was calculated and incorporated in simulations.

Table S13: Predicted and observed DGI AUC_{last} and C_{max} ratios (*continued*)

Drug administration	t _{last} [h]	DGI AUC _{last} ratio			DGI C _{max} ratio			Phenotype/AS	Molecule	Reference
		Pred	Obs	Pred/Obs	Pred	Obs	Pred/Obs			
Mexiletine										
100 mg b.i.d. po	12 / 12	2.05	1.54	1.32	1.33	1.40	0.96	PM / NM	MEX	Labbé 2000 [89]
200 mg s.d. po	48 / 48	1.45	1.39	1.05	1.15	1.33	0.86	PM / NM	MEX	Abolfathi 1993 [90]
Mean GMFE (range):		1.19 (1.05–1.33), 2/2 with GMFE ≤ 2			1.11 (1.05–1.16), 2/2 with GMFE ≤ 2					
Paroxetine										
25 mg s.d. po	96 / 48	4.42	7.40	0.60	2.49	5.05	0.49	AS0.5 / AS2	PAR	Chen 2015 [91]
25 mg s.d. po	72 / 48	3.08	3.68	0.84	1.98	2.96	0.67	AS1 / AS2	PAR	Chen 2015 [91]
25 mg s.d. po	72 / 48	1.92	1.61	1.19	1.51	1.10	1.37	AS1.5 / AS2	PAR	Chen 2015 [91]
30 mg q.d. po	96 / 96	2.14	2.35	0.91	1.431	1.55	0.92	PM / NM	PAR	Sindrup 1992 [92]
40 mg s.d. po	144 / 144	2.90	3.80	0.76	1.74	1.57	1.11	AS0 / AS2	PAR	Mürdter 2016 [76]
40 mg s.d. po	144 / 144	1.82	2.38	0.76	1.60	1.41	1.13	AS0.5 / AS2	PAR	Mürdter 2016 [76]
40 mg s.d. po	144 / 144	2.32	4.53	0.51	1.52	1.57	0.97	AS0.75 / AS2	PAR	Mürdter 2016 [76]
40 mg s.d. po	144 / 144	2.18	2.05	1.06	1.45	0.99	1.46	AS1 / AS2	PAR	Mürdter 2016 [76]
40 mg s.d. po	144 / 144	0.45	0.51	0.88	0.61	0.68	0.90	AS3 / AS2	PAR	Mürdter 2016 [76]
40 mg s.d. po	240 / 48	2.94	5.89	0.50	2.87	4.88	0.59	AS0 / AS2	PAR	Yoon 2000 [93]
40 mg s.d. po	192 / 48	1.70	1.49	1.14	1.96	1.43	1.37	AS0.5 / AS2	PAR	Yoon 2000 [93]
40 mg s.d. po	96 / 24	0.97	1.38	0.70	1.32	1.38	0.96	AS1.25 / AS2	PAR	Yoon 2000 [93]
Mean GMFE (range):		1.33 (1.03–2.00), 12/12 with GMFE ≤ 2			1.35 (1.05–2.03), 11/12 with GMFE ≤ 2					
Risperidone										
1 mg q.d. po	48 / 24	8.47	7.24	1.17	1.98	1.81	1.09	AS0 / AS2	RIS	Novalbos 2010 [94]
1 mg q.d. po	48 / 48	0.88	0.85	1.04	0.19	0.18	1.06	AS0 / AS2	OHR	Novalbos 2010 [94]
1 mg q.d. po	24 / 24	3.68	3.16	1.16	1.59	1.44	1.10	AS1 / AS2	RIS	Novalbos 2010 [94]
1 mg q.d. po	48 / 48	4.21	4.64	0.91	0.81	0.92	0.88	AS1 / AS2	OHR	Novalbos 2010 [94]
1 mg q.d. po	12 / 24	0.62	0.64	0.97	0.64	0.68	0.94	AS3 / AS2	RIS	Novalbos 2010 [94]
1 mg q.d. po	48 / 48	5.23	5.74	0.91	1.16	1.28	0.91	AS3 / AS2	OHR	Novalbos 2010 [94]
2 mg q.d. po	24 / 24	6.49	6.18	1.05	2.77	3.29	0.84	PM / NM	RIS	Bondolfi 2002 [95]
Mean GMFE (range):		1.09 (1.03–1.17), 7/7 with GMFE ≤ 2			1.11 (1.06–1.19), 7/7 with GMFE ≤ 2					
Overall GMFE (range):		1.40 (1.00–6.19), 78/85 with GMFE ≤ 2			1.29 (1.00–2.95), 81/85 with GMFE ≤ 2					

AS: CYP2D6 activity score, ATO: atomoxetine, AUC_{last}: area under the plasma concentration-time curve calculated between the first and last concentration measurement, b.i.d.: twice daily, CLO: (E)-clomiphene, C_{max}: maximum plasma concentration, DES: desipramine, DEX: dextromethorphan, DGI: drug-gene interaction, DXT: dextrorphan, GMFE: geometric mean fold error, HDC: (E)-4-hydroxy-N-desethylclomiphene, IM: CYP2D6 intermediate metabolizer, iv: intravenous, MET: metoprolol, MEX: mexiletine, NDC: (E)-N-desethylclomiphene, NM: CYP2D6 normal metabolizer, obs: observed, OHC: (E)-4-hydroxyclophene, OHD: 2-hydroxydesipramine, OHM: α -hydroxymetoprolol, OHR: 9-hydroxyrisperidone, PAR: paroxetine, PM: CYP2D6 poor metabolizer, RIS: risperidone, RME: R-metoprolol, SME: S-metoprolol, po: oral, pred: predicted, q.d.: once daily, s.d.: single dose, t_{last}: time of the last concentration measurement. If perpetrator or victim drugs were applied in form of salts, the respective dose of base was calculated and incorporated in simulations.

S6 DDI Model Evaluation

S6.1 Alprazolam

S6.1.1 Clinical Studies

Table S14: Clinical study data used for DDI model development with **alprazolam** as victim

Drug administration		n	Population ^a	Fem. [%]	Age [years]	Weight [kg]	BMI [kg/m ²]	Molecule	Reference
Perpetrator	Alprazolam								
<i>Paroxetine</i>									
20 mg q.d. po	1 mg q.d. po	22	European [3]	64	26±4	64±9	168±7 ^b	ALP, PAR	Calvo 2004 [96]

ALP: alprazolam, BMI: body mass index, DDI: drug-drug interaction, fem: females, n: number of study participants, PAR: paroxetine, po: oral, q.d.: once daily. Values are given as mean (range). If perpetrator or victim drugs were applied in form of salts, the respective dose of base was calculated and incorporated in simulations. ^a Population used in simulations. ^b Height of subjects [cm].

S6.1.2 Plasma Concentration-Time Profiles (Semilogarithmic Representation)

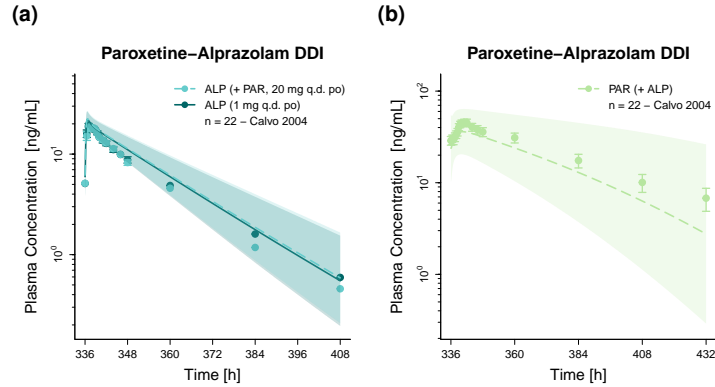


Figure S14: Predicted compared to observed plasma concentration-time profiles of alprazolam alone (solid line) and after pretreatment and/or concomitant administration (dashed line) of (a) paroxetine (semilogarithmic representation). Population predicted (1000 individuals) geometric means are shown as lines, corresponding geometric standard deviations as shaded areas and observed data as dots (\pm standard deviation, if reported) [96]. ALP: alprazolam, DDI: drug-drug interaction, n: number of study participants, PAR: paroxetine, po: oral, q.d.: once daily.

S6.1.3 Plasma Concentration-Time Profiles (Linear Representation)

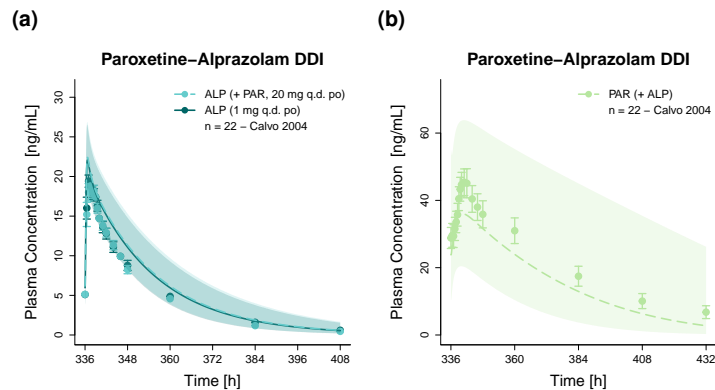


Figure S15: Predicted compared to observed plasma concentration-time profiles of (a) alprazolam alone (solid line) and after pretreatment (dashed line) with paroxetine (linear representation). Population predicted (1000 individuals) geometric means are shown as lines, corresponding geometric standard deviations as shaded areas and observed data as dots (\pm standard deviation, if reported) [96]. ALP: alprazolam, DDI: drug-drug interaction, n: number of study participants, PAR: paroxetine, po: oral, q.d.: once daily.

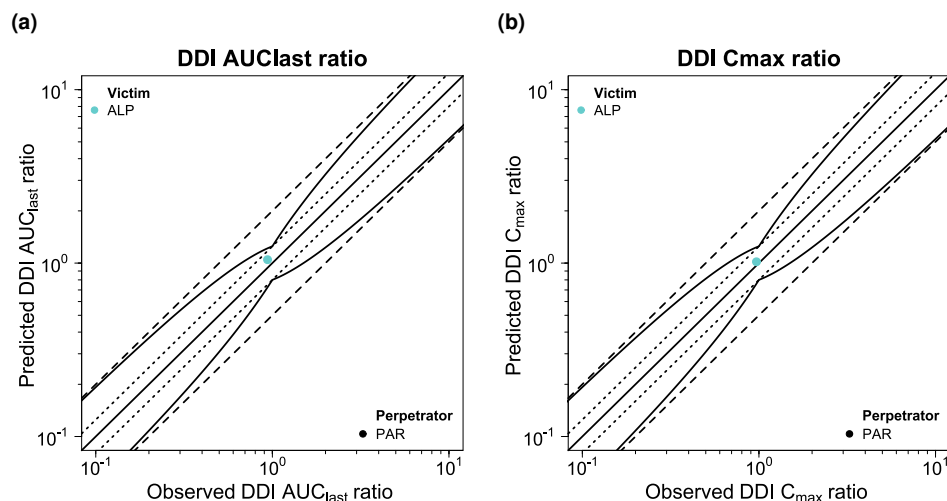
S6.1.4 DDI AUC_{last} and C_{max} Ratios

Figure S16: Goodness-of-fit plots comparing predicted and observed DDI AUC_{last} and C_{max} ratios for victim drug alprazolam. The solid line marks the line of identity. Dotted lines indicate 1.25-fold, dashed lines indicate 2-fold deviation. Prediction success limits proposed by Guest et al. [2] are shown as curved lines (including 20% variability). ALP: alprazolam, AUC_{last} : area under the plasma concentration-time curve calculated between the first and last concentration measurement, C_{max} : maximum plasma concentration, DDI: drug-drug interaction, PAR: paroxetine.

S6.1.5 Geometric Mean Fold Errors of Predicted DDI AUC_{last} and C_{max} Ratios

Table S15: Predicted and observed DDI AUC_{last} and C_{max} ratios involving **alprazolam** as victim drug

Drug administration			DDI AUC _{last} ratio			DDI C _{max} ratio			Molecule	Reference
Perpetrator	Alprazolam	t _{last} [h]	Pred	Obs	Pred/Obs	Pred	Obs	Pred/Obs		
<i>Paroxetine</i>										
20 mg q.d. po	1 mg q.d. po	72	1.05	0.94	1.11	1.02	0.97	1.05	ALP	Calvo 2004 [96]
Overall GMFE (range):			1.11 (-), 1/1 with GMFE ≤ 2			1.05 (-), 1/1 with GMFE ≤ 2				

ALP: alprazolam, AUC_{last}: area under the plasma concentration-time curve calculated between the first and last concentration measurement, C_{max}: maximum plasma concentration, DDI: drug-drug interaction, GMFE: geometric mean fold error, obs: observed, PAR: paroxetine, po: oral, pred: predicted, q.d.: once daily, t_{last}: time of the last concentration measurement. If perpetrator or victim drugs were applied in form of salts, the respective dose of base was calculated and incorporated in simulations.

S6.2 Atomoxetine

S6.2.1 Clinical Studies

Table S16: Clinical study data used for DD(G)I model development with **atomoxetine** as victim

Drug administration		n	Population ^a	Fem. [%]	Age [years]	Weight [kg]	BMI [kg/m ²]	Phenotype/AS	Molecule	Reference
Perpetrator	Atomoxetine									
Bupropion										
150/300 mg q.d. po	25 mg s.d. po	2	European [3]	-	(18–55)	-	-	PM	ATO	Todor 2016 [74]
150/300 mg q.d. po	25 mg s.d. po	18	European [3]	-	(18–55)	-	-	NM	ATO	Todor 2016 [74]
Fluvoxamine										
50/100 mg q.d. po	25 mg s.d. po	18	European [3]	-	(18–55)	-	(19–25)	NM	ATO	Todor 2017 [97]
Paroxetine										
20 mg q.d. po	20 mg s.d. po	7	Asian [98]	8	22.7±1.9	-	21.4±1.6	AS = 0	ATO	Jung 2020 [71]
20 mg q.d. po	20 mg s.d. po	9	Asian [98]	8	23.2±1.4	-	21.3±1.3	AS = 1.25	ATO	Jung 2020 [71]
20 mg q.d. po	20 mg s.d. po	10	Asian [98]	8	22±1.8	-	21.8±1.8	AS = 2	ATO	Jung 2020 [71]
20 mg b.i.d./q.d. po	25 mg s.d. po	22	European [3]	32	25.3±2.3	-	24.1±3.1	-	ATO	Todor 2015 [99]
20 mg q.d. po	20 mg b.i.d. po	22	American [7]	23	38 (20–49)	-	23.8 (fem.) 24.4 (male)	NM	ATO, PAR	Belle 2002 [100]

AS: CYP2D6 activity score, ATO: atomoxetine, b.i.d.: twice daily, BMI: body mass index, DD(G)I: drug-drug(-gene) interaction, fem: females, n: number of study participants, NM: CYP2D6 normal metabolizer, PAR: paroxetine, PM: CYP2D6 poor metabolizer, po: oral, q.d.: once daily, s.d: single dose, -: not available. Values are given as mean (range). If perpetrator or victim drugs were applied in form of salts, the respective dose of base was calculated and incorporated in simulations. ^a Population used in simulations.

S6.2.2 Plasma Concentration-Time Profiles (Semilogarithmic Representation)

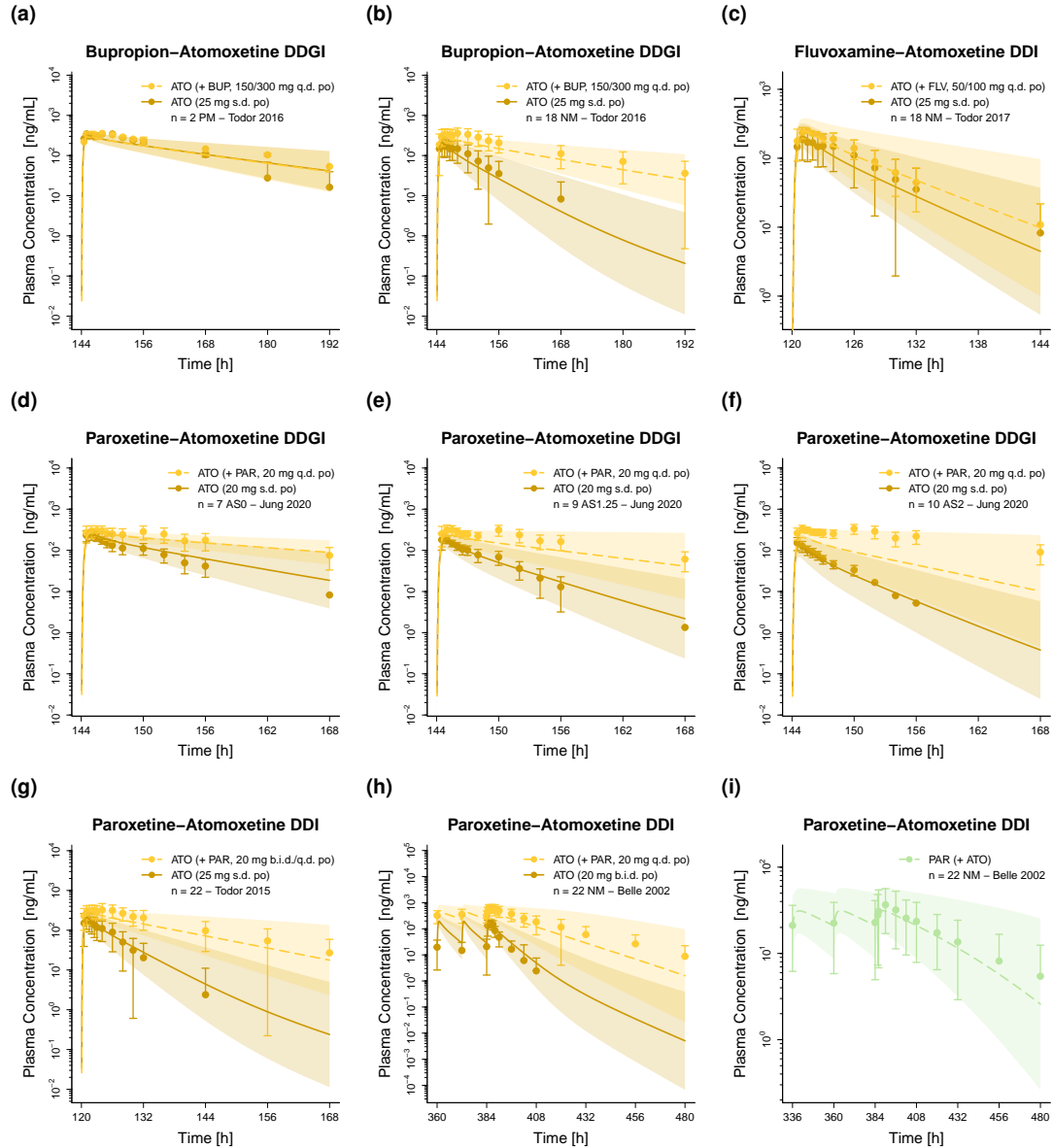


Figure S17: Predicted compared to observed plasma concentration-time profiles of atomoxetine alone (solid line) and after pretreatment and/or concomitant administration (dashed line) of (a–b) bupropion, (c) fluvoxamine and (d–h) paroxetine (semilogarithmic representation). Population predicted (1000 individuals) geometric means are shown as lines, corresponding geometric standard deviations as shaded areas and observed data as dots (\pm standard deviation, if reported) [71, 74, 97, 99, 100]. AS: CYP2D6 activity score, b.i.d.: twice daily, BUP: bupropion, DD(G)I: drug-drug(-gene) interaction, FLV: fluvoxamine, n: number of study participants, NM: CYP2D6 normal metabolizer, PAR: paroxetine, PM: CYP2D6 poor metabolizer, po: oral, q.d.: once daily, s.d.: single dose.

S6.2.3 Plasma Concentration-Time Profiles (Linear Representation)

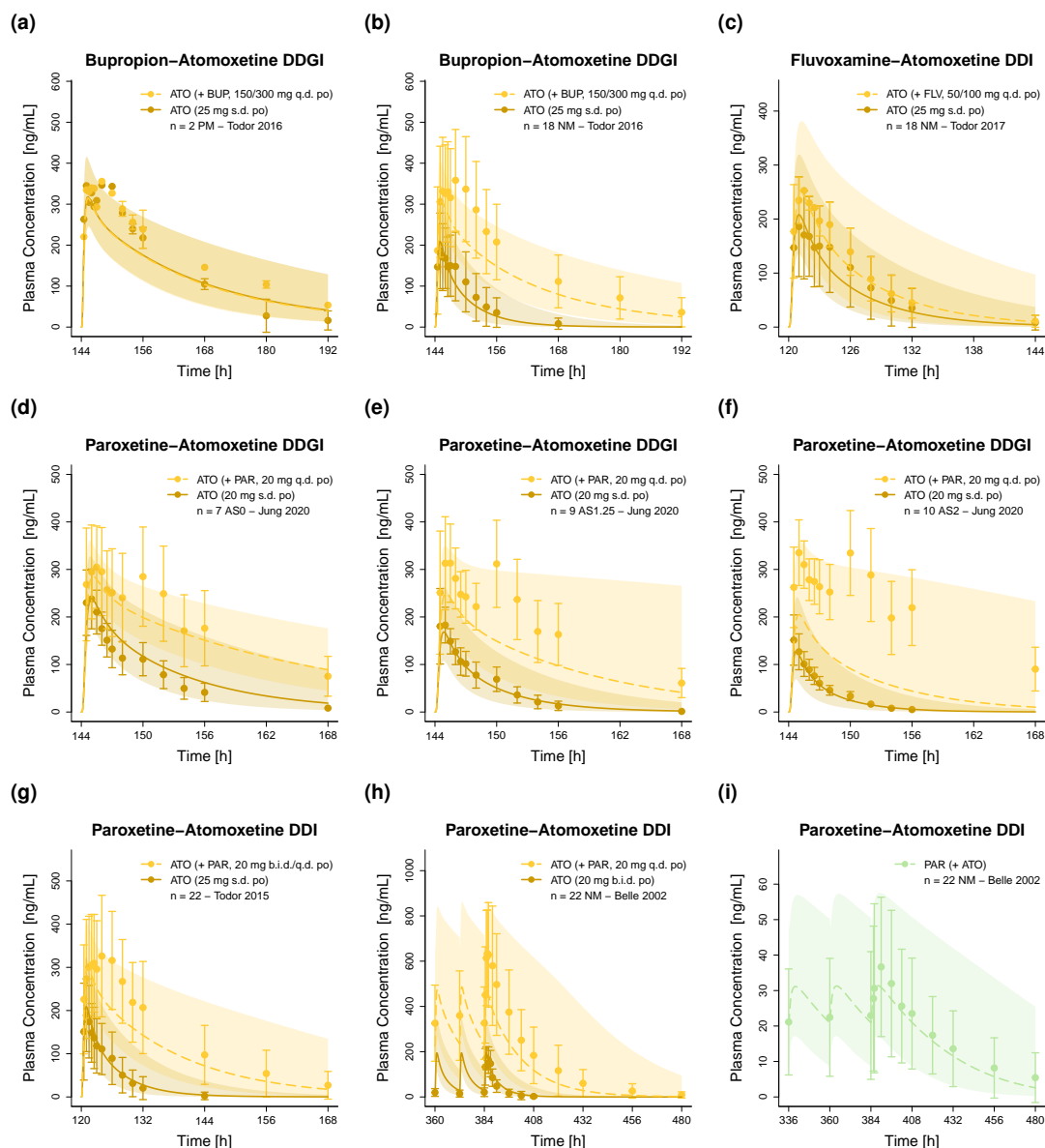


Figure S18: Predicted compared to observed plasma concentration-time profiles of atomoxetine alone (solid line) and after pretreatment and/or concomitant administration (dashed line) of (a–b) bupropion, (c) fluvoxamine and (d–h) paroxetine (linear representation). Population predicted (1000 individuals) geometric means are shown as lines, corresponding geometric standard deviations as shaded areas and observed data as dots (\pm standard deviation, if reported) [71, 74, 97, 99, 100]. AS: CYP2D6 activity score, b.i.d.: twice daily, BUP: bupropion, DD(G)I: drug-drug(-gene) interaction, FLV: fluvoxamine, n: number of study participants, NM: CYP2D6 normal metabolizer, PAR: paroxetine, PM: CYP2D6 poor metabolizer, po: oral, q.d.: once daily, s.d.: single dose.

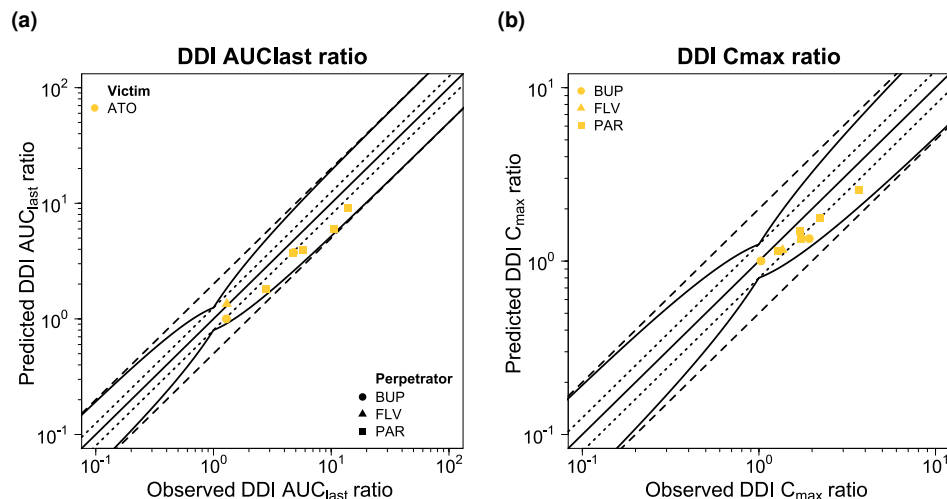
S6.2.4 DDI AUC_{last} and C_{max} Ratios

Figure S19: Goodness-of-fit plots comparing predicted and observed DDI AUC_{last} and C_{max} ratios for victim drug atomoxetine. The solid line marks the line of identity. Dotted lines indicate 1.25-fold, dashed lines indicate 2-fold deviation. Prediction success limits proposed by Guest et al. [2] are shown as curved lines (including 20% variability). ATO: atomoxetine, AUC_{last} : area under the plasma concentration-time curve calculated between the first and last concentration measurement, BUP: bupropion, C_{max} : maximum plasma concentration, FLV: fluvoxamine, PAR: paroxetine.

S6.2.5 Geometric Mean Fold Errors of Predicted DDI AUC_{last} and C_{max} RatiosTable S17: Predicted and observed DDI AUC_{last} and C_{max} ratios involving **atomoxetine** as victim drug

Drug administration			DDI AUC _{last} ratio			DDI C _{max} ratio			Phenotype/AS	Molecule	Reference
Perpetrator	Atomoxetine	t _{last} [h]	Pred	Obs	Pred/Obs	Pred	Obs	Pred/Obs			
Bupropion											
150/300 mg q.d. po	25 mg s.d. po	48	1.00	1.29	0.78	1.00	1.03	0.98	PM	ATO	Todor 2016 [74]
150/300 mg q.d. po	25 mg s.d. po	48	3.75	4.80	0.78	1.35	1.93	0.70	NM	ATO	Todor 2016 [74]
Mean GMFE (range):			1.32 (1.28–1.36), 2/2 with GMFE ≤ 2			1.19 (1.02–1.6), 2/2 with GMFE ≤ 2					
Fluvoxamine											
50/100 mg q.d. po	25 mg s.d. po	24	1.35	1.30	1.04	1.16	1.36	0.85	NM	ATO	Todor 2017 [97]
Mean GMFE (range):			1.04 (-), 1/1 with GMFE ≤ 2			1.17 (-), 1/1 with GMFE ≤ 2					
Paroxetine											
20 mg q.d. po	20 mg s.d. po	24	1.80	2.80	0.64	1.15	1.28	0.90	AS = 0	ATO	Jung 2020 [71]
20 mg q.d. po	20 mg s.d. po	24	3.69	4.70	0.79	1.49	1.71	0.87	AS = 1.25	ATO	Jung 2020 [71]
20 mg q.d. po	20 mg s.d. po	24	5.98	10.57	0.57	1.78	2.21	0.87	AS = 2	ATO	Jung 2020 [71]
20 mg b.i.d./q.d. po	25 mg s.d. po	48	3.96	5.73	0.69	1.34	1.73	0.78	-	ATO	Todor 2015 [99]
20 mg q.d. po	20 mg b.i.d. po	96	9.04	13.87	0.65	2.58	3.70	0.70	NM	ATO	Belle 2002 [100]
Mean GMFE (range):			1.52 (1.27–1.77), 5/5 with GMFE ≤ 2			1.25 (1.12–1.43), 5/5 with GMFE ≤ 2					
Overall GMFE (range):			1.41 (1.04–1.77), 8/8 with GMFE ≤ 2			1.22 (1.02–1.43), 8/8 with GMFE ≤ 2					

AS: CYP2D6 activity score, ATO: atomoxetine, AUC_{last} : area under the plasma concentration-time curve calculated between the first and last concentration measurement, b.i.d.: twice daily, C_{max} : maximum plasma concentration, DDI: drug-drug interaction, GMFE: geometric mean fold error, NM: CYP2D6 normal metabolizer, obs: observed, PM: CYP2D6 poor metabolizer, po: oral, pred: predicted, q.d.: once daily, s.d.: single dose, t_{last} : time of the last concentration measurement. If perpetrator or victim drugs were applied in form of salts, the respective dose of base was calculated and incorporated in simulations.

S6.3 (E)-Clomiphene

S6.3.1 Clinical Studies

Table S18: Clinical study data used for DD(G)I model development with **(E)-clomiphene** as victim

Drug administration		n	Population ^a	Fem. [%]	Age [years]	Weight [kg]	BMI [kg/m ²]	AS	Molecule	Reference
Perpetrator	(E)-Clomiphene									
Clarithromycin										
500 mg b.i.d po	42 mg s.d. po	5	European [3]	100	25.0 (22–29)	61.1 (50.0–70.0)	21.4 (20.6–22.9)	AS = 0	CLO, OHC, NDC, HDC	Mürdter 2016 [76]
500 mg b.i.d po	42 mg s.d. po	4	European [3]	100	24.3 (21–30)	59.3 (55.5–64.0)	21.1 (20.3–22.0)	AS = 0.5	CLO, OHC, NDC, HDC	Mürdter 2016 [76]
500 mg b.i.d po	42 mg s.d. po	2	European [3]	100	25.5 (23–28)	68.8 (63.5–74.0)	23.6 (22.5–24.7)	AS = 1	CLO, OHC, NDC, HDC	Mürdter 2016 [76]
500 mg b.i.d po	42 mg s.d. po	3	European [3]	100	32.3 (26–43)	56.5 (48.0–63.5)	21.3 (18.8–24.2)	AS = 2	CLO, OHC, NDC, HDC	Mürdter 2016 [76]
500 mg b.i.d po	42 mg s.d. po	3	European [3]	100	25.7 (22–28)	61.7 (54.0–73.0)	22.6 (20.3–23.8)	AS = 3	CLO, OHC, NDC, HDC	Mürdter 2016 [76]
Paroxetine										
40 mg q.d. po	42 mg s.d. po	4	European [3]	100	24.8 (22–29)	60.5 (50.0–70.0)	21.5 (20.6–22.9)	AS = 0	CLO, OHC, NDC, HDC	Mürdter 2016 [76]
40 mg q.d. po	42 mg s.d. po	4	European [3]	100	24.3 (21–30)	59.3 (55.5–64.0)	21.1 (20.3–22.0)	AS = 0.5	CLO, OHC, NDC, HDC	Mürdter 2016 [76]
40 mg q.d. po	42 mg s.d. po	2	European [3]	100	25.5 (23–28)	68.8 (63.5–74.0)	23.6 (22.5–24.7)	AS = 1	CLO, OHC, NDC, HDC	Mürdter 2016 [76]
40 mg q.d. po	42 mg s.d. po	3	European [3]	100	32.3 (26–43)	56.5 (48.0–63.5)	21.3 (18.8–24.2)	AS = 2	CLO, OHC, NDC, HDC	Mürdter 2016 [76]
40 mg q.d. po	42 mg s.d. po	3	European [3]	100	25.7 (22–28)	61.7 (54.0–73.0)	22.6 (20.3–23.8)	AS = 3	CLO, OHC, NDC, HDC	Mürdter 2016 [76]

AS: CYP2D6 activity score, b.i.d.: twice daily, BMI: body mass index, CLO: (E)-clomiphene, DD(G)I: drug-drug(-gene) interaction, fem: females, HDC: (E)-4-hydroxy-N-desethylclomiphene, n: number of study participants, NDC: (E)-N-desethylclomiphene, OHC: (E)-4-hydroxyclophene, po: oral, q.d.: once daily, s.d.: single dose. Values are given as mean (range). If perpetrator or victim drugs were applied in form of salts, the respective dose of base was calculated and incorporated in simulations. ^a Population used in simulations.

S6.3.2 Plasma Concentration-Time Profiles (Semilogarithmic Representation)

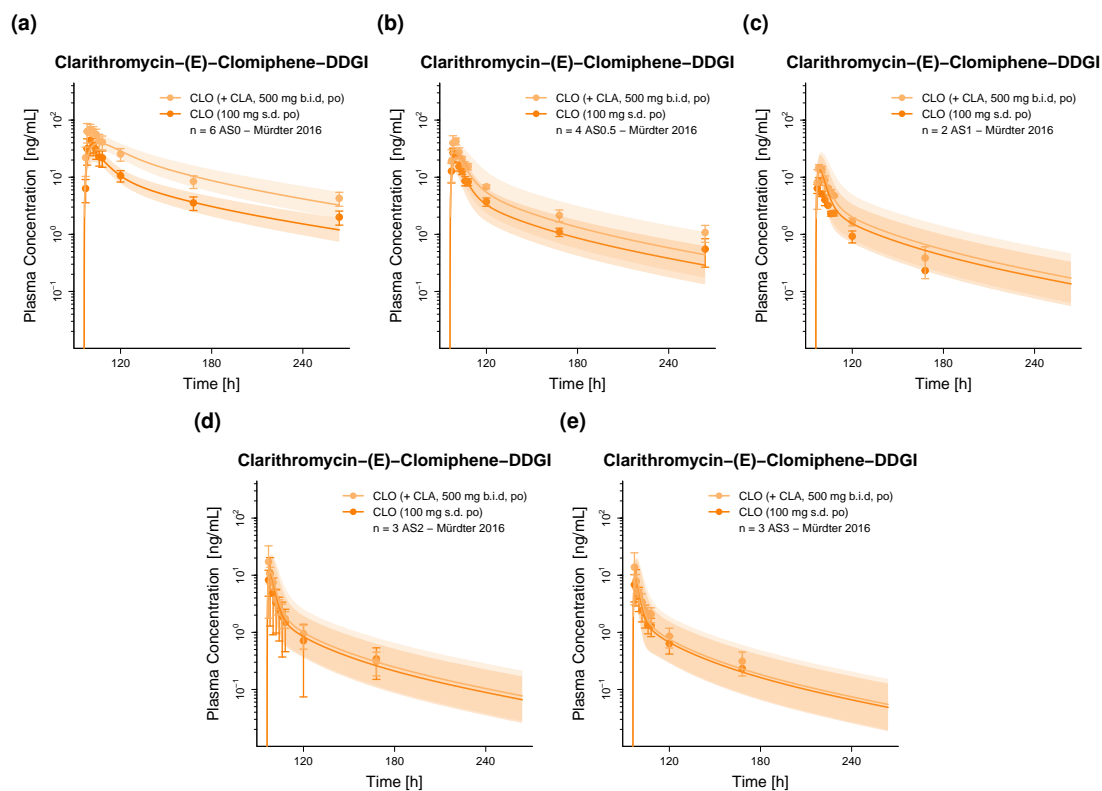


Figure S20: Predicted compared to observed plasma concentration-time profiles of (*E*)-clomiphene alone (solid line) and after pretreatment and concomitant administration (dashed line) of clarithromycin (semilogarithmic representation). Population predicted (1000 individuals) geometric means are shown as lines, corresponding geometric standard deviations as shaded areas and observed data as dots (\pm standard deviation, if reported) [76]. AS: CYP2D6 activity score, b.i.d.: twice daily, CLA: clarithromycin, CLO: (*E*)-clomiphene, DDGI: drug-drug-gene interaction, n: number of study participants, po: oral, s.d.: single dose.

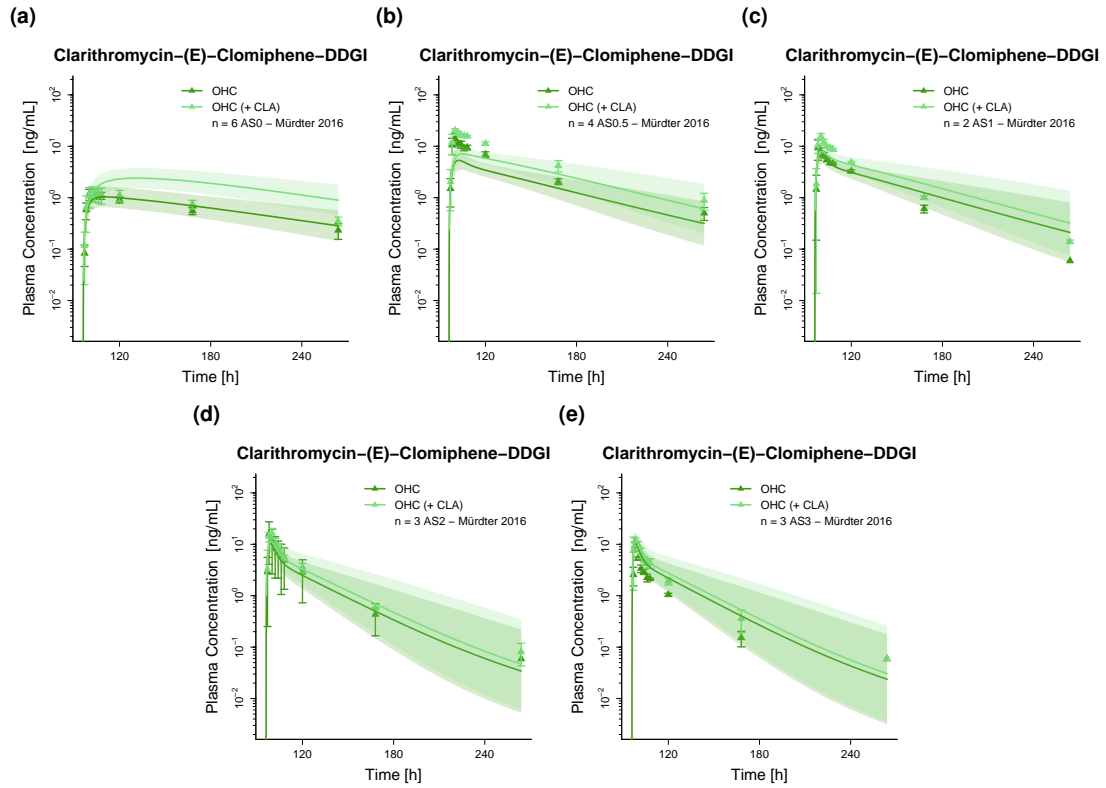


Figure S21: Predicted compared to observed plasma concentration-time profiles of (E)-4-hydroxyclophene alone (solid line) and after pretreatment and concomitant administration (dashed line) of clarithromycin (semilogarithmic representation). Population predicted (1000 individuals) geometric means are shown as lines, corresponding geometric standard deviations as shaded areas and observed data as triangles (\pm standard deviation, if reported) [76]. AS: CYP2D6 activity score, CLA: clarithromycin, DDGI: drug-drug-gene interaction, n: number of study participants, OHC: (E)-4-hydroxyclophene.

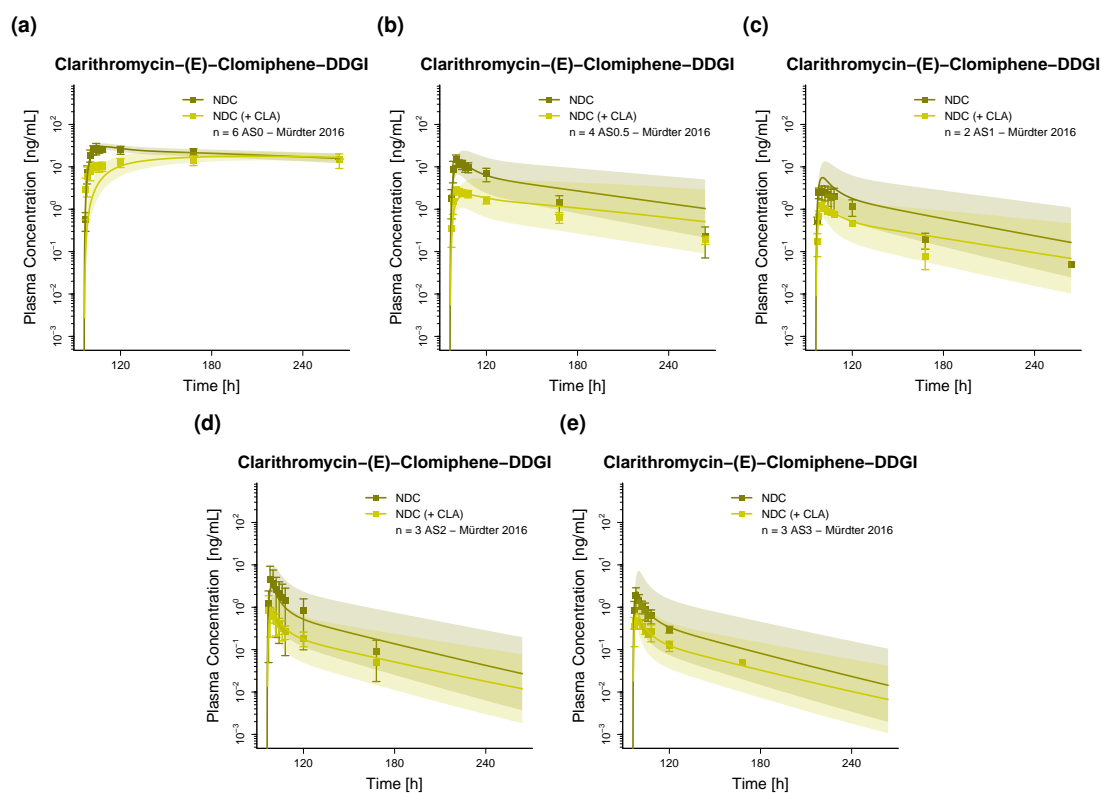


Figure S22: Predicted compared to observed plasma concentration-time profiles of (*E*)-N-desethylclomiphene alone (solid line) and after pretreatment and concomitant administration (dashed line) of clarithromycin (semilogarithmic representation). Population predicted (1000 individuals) geometric means are shown as lines, corresponding geometric standard deviations as shaded areas and observed data as triangles (\pm standard deviation, if reported) [76]. AS: CYP2D6 activity score, CLA: clarithromycin, DDGI: drug-drug-gene interaction, n: number of study participants, NDC: (*E*)-N-desethylclomiphene.

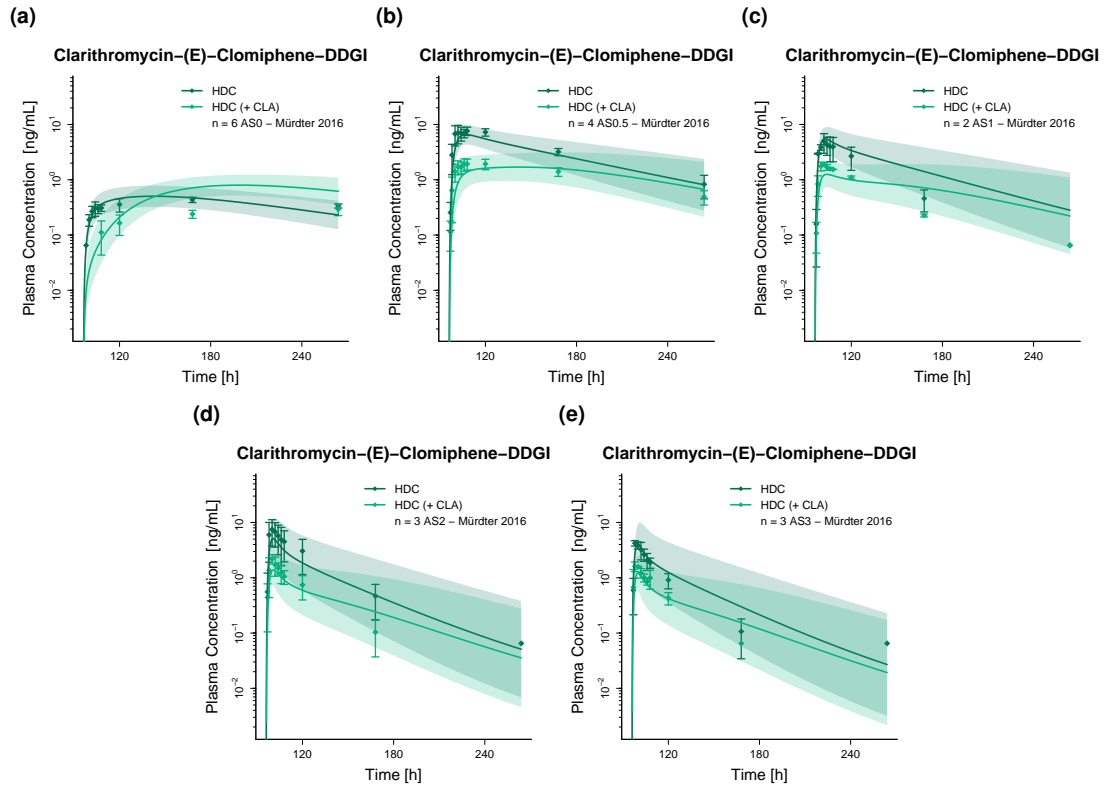


Figure S23: Predicted compared to observed plasma concentration-time profiles of (*E*)-4-hydroxy-N-desethylclomiphene alone (solid line) and after pretreatment and concomitant administration (dashed line) of clarithromycin (semilogarithmic representation). Population predicted (1000 individuals) geometric means are shown as lines, corresponding geometric standard deviations as shaded areas and observed data as triangles (\pm standard deviation, if reported) [76]. AS: CYP2D6 activity score, CLA: clarithromycin, DDGI: drug-drug-gene interaction, HDC: (*E*)-4-hydroxy-N-desethylclomiphene, n: number of study participants.

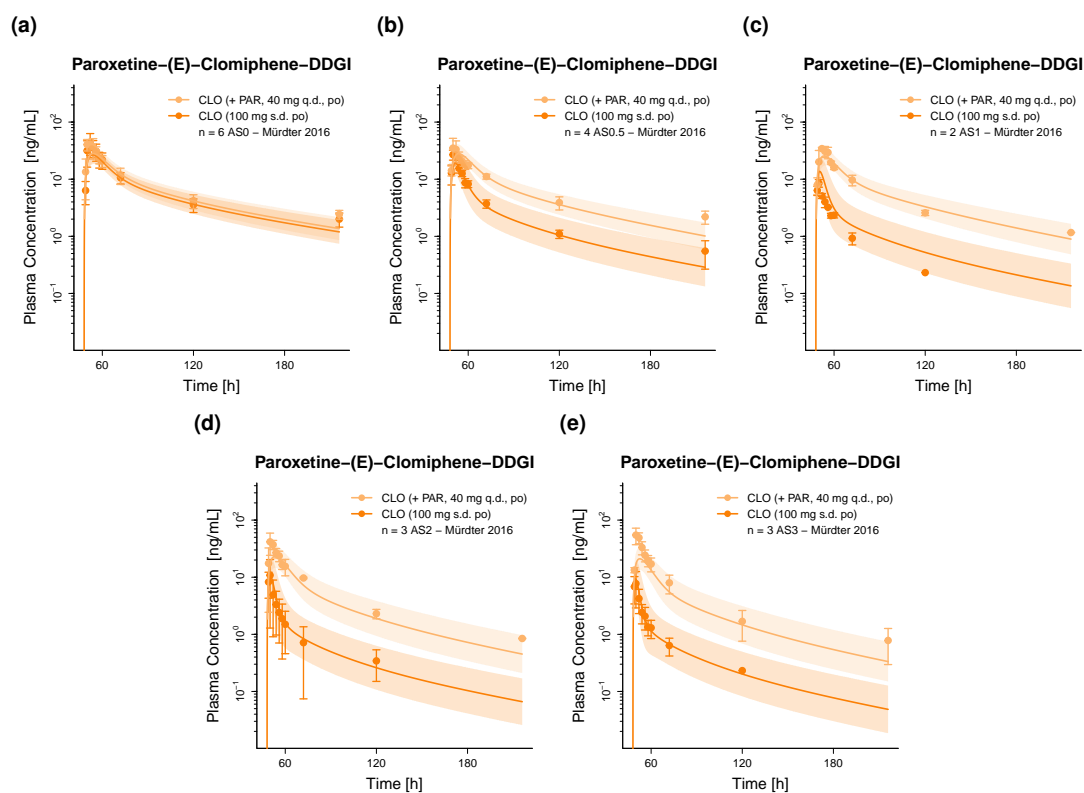


Figure S24: Predicted compared to observed plasma concentration-time profiles of (E)-clomiphene alone (solid line) and after pretreatment and concomitant administration (dashed line) of paroxetine (semilogarithmic representation). Population predicted (1000 individuals) geometric means are shown as lines, corresponding geometric standard deviations as shaded areas and observed data as dots (\pm standard deviation, if reported) [76]. AS: CYP2D6 activity score, CLO: (E)-clomiphene, DDGI: drug-drug-gene interaction, n: number of study participants, PAR: paroxetine, po: oral, q.d.: once daily, s.d.: single dose.

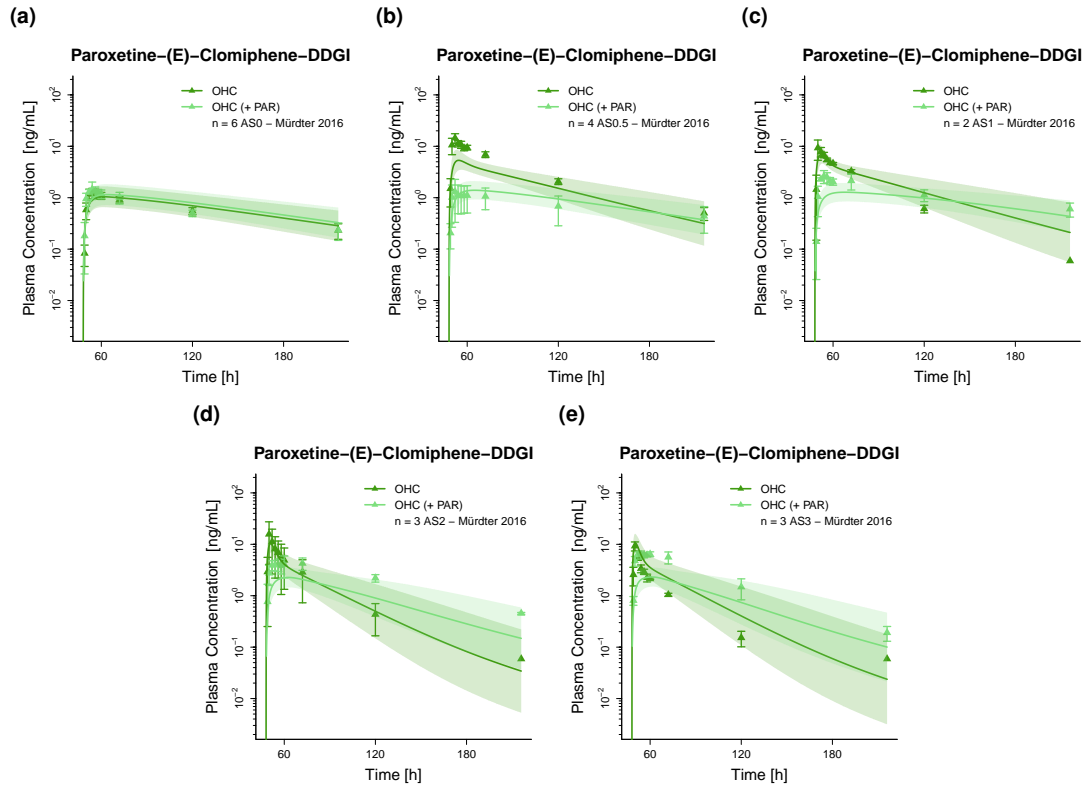


Figure S25: Predicted compared to observed plasma concentration-time profiles of (E)-4-hydroxyclophene alone (solid line) and after pretreatment and concomitant administration (dashed line) of paroxetine (semilogarithmic representation). Population predicted (1000 individuals) geometric means are shown as lines, corresponding geometric standard deviations as shaded areas and observed data as triangles (\pm standard deviation, if reported) [76]. AS: CYP2D6 activity score, DDGI: drug-drug-gene interaction, n: number of study participants, OHC: (E)-4-hydroxyclophene, PAR: paroxetine.

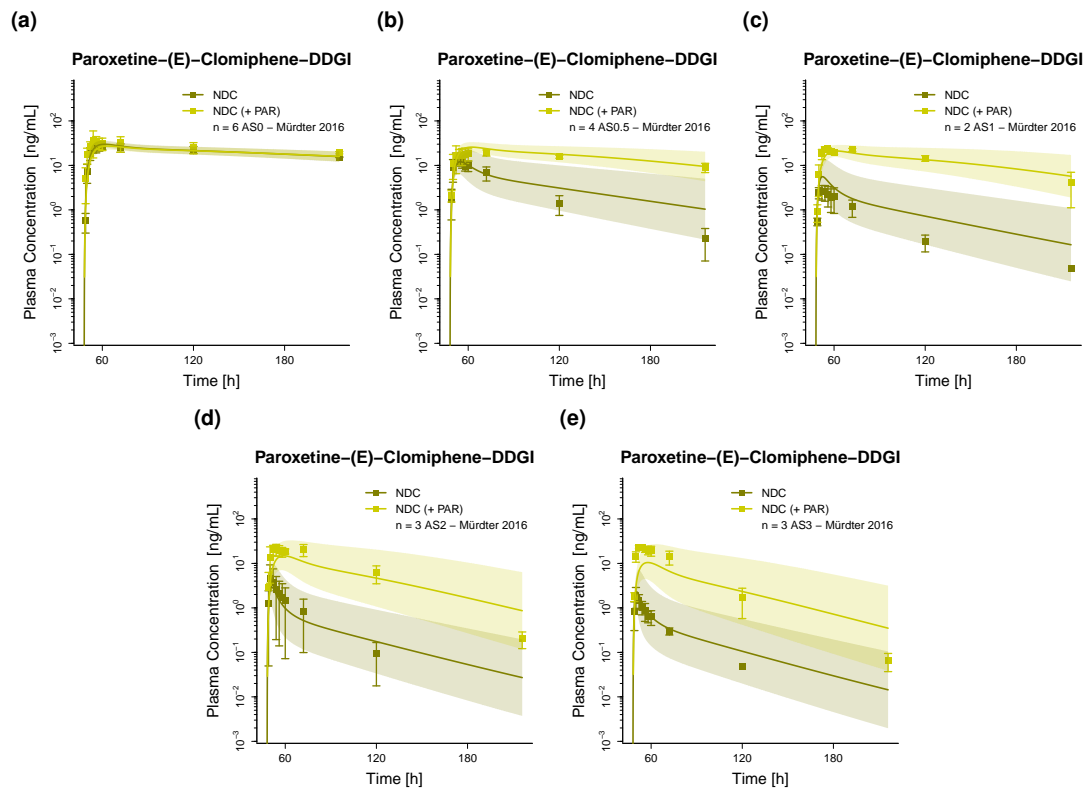


Figure S26: Predicted compared to observed plasma concentration-time profiles of (E)-N-desethylclomiphene alone (solid line) and after pretreatment and concomitant administration (dashed line) of paroxetine (semilogarithmic representation). Population predicted (1000 individuals) geometric means are shown as lines, corresponding geometric standard deviations as shaded areas and observed data as triangles (\pm standard deviation, if reported) [76]. AS: CYP2D6 activity score, DDGI: drug-drug-gene interaction, n: number of study participants, NDC: (E)-N-desethylclomiphene, PAR: paroxetine.

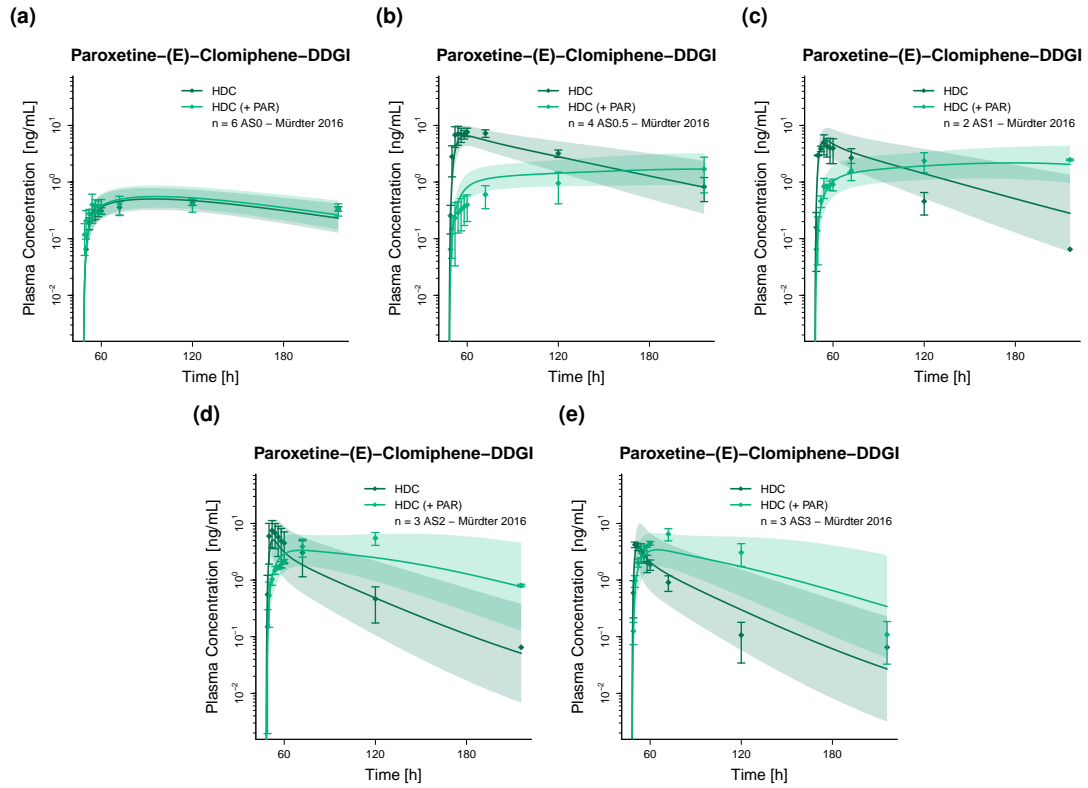


Figure S27: Predicted compared to observed plasma concentration-time profiles of (E)-4-hydroxy-N-desethylclomiphene alone (solid line) and after pretreatment and concomitant administration (dashed line) of paroxetine (semilogarithmic representation). Population predicted (1000 individuals) geometric means are shown as lines, corresponding geometric standard deviations as shaded areas and observed data as triangles (\pm standard deviation, if reported) [76]. AS: CYP2D6 activity score, DDGI: drug-drug-gene interaction, HDC: (E)-4-hydroxy-N-desethylclomiphene, n: number of study participants, PAR: paroxetine.

S6.3.3 Plasma Concentration-Time Profiles (Linear Representation)

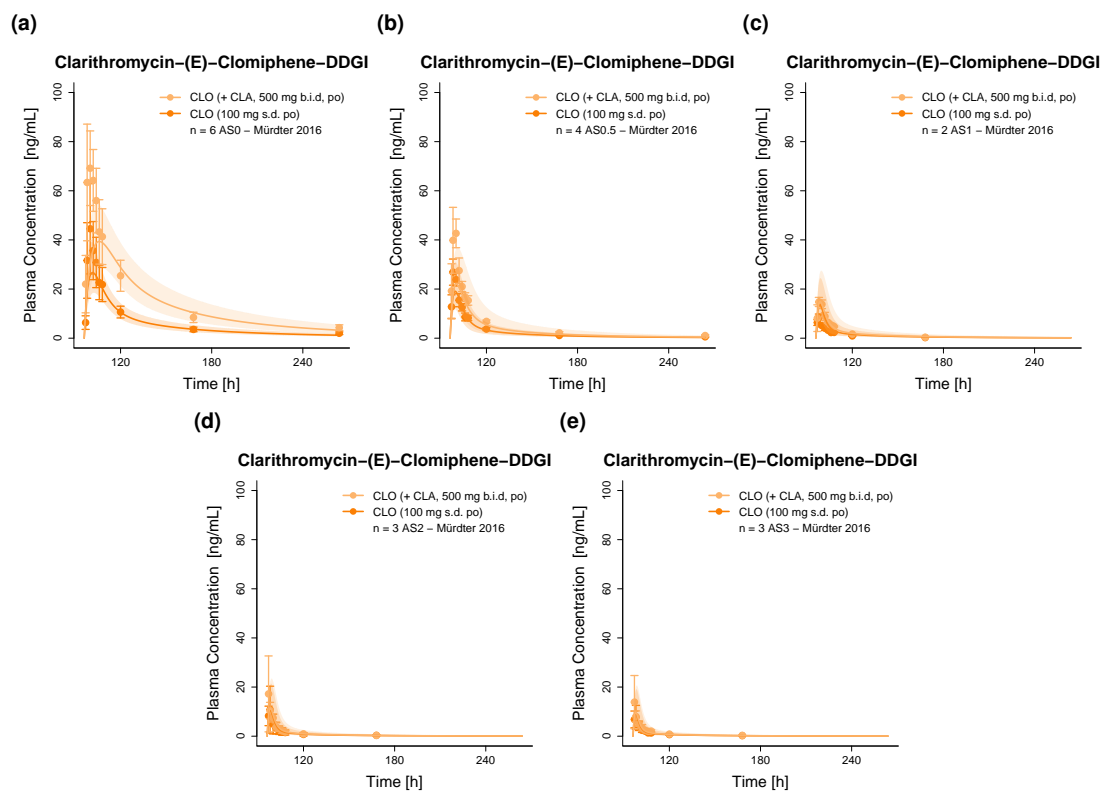


Figure S28: Predicted compared to observed plasma concentration-time profiles of (E)-clomiphene alone (solid line) and after pretreatment and concomitant administration (dashed line) of clarithromycin (linear representation). Population predicted (1000 individuals) geometric means are shown as lines, corresponding geometric standard deviations as shaded areas and observed data as dots (\pm standard deviation, if reported) [76]. AS: CYP2D6 activity score, b.i.d.: twice daily, CLA: clarithromycin, CLO: (E)-clomiphene, DDGI: drug-drug-gene interaction, n: number of study participants, po: oral, s.d.: single dose.

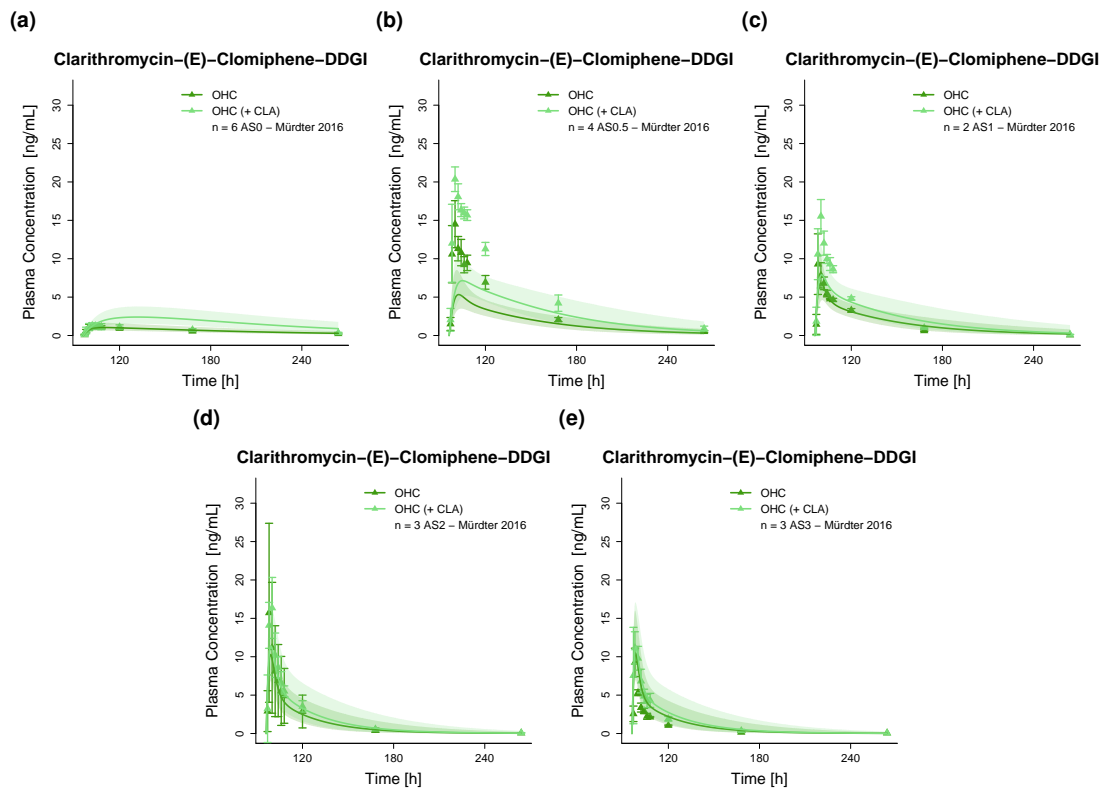


Figure S29: Predicted compared to observed plasma concentration-time profiles of (E)-4-hydroxyclophene alone (solid line) and after pretreatment and concomitant administration (dashed line) of clarithromycin (linear representation). Population predicted (1000 individuals) geometric means are shown as lines, corresponding geometric standard deviations as shaded areas and observed data as triangles (\pm standard deviation, if reported) [76]. AS: CYP2D6 activity score, CLA: clarithromycin, DDGI: drug-drug-gene interaction, n: number of study participants, OHC: (E)-4-hydroxyclophene.

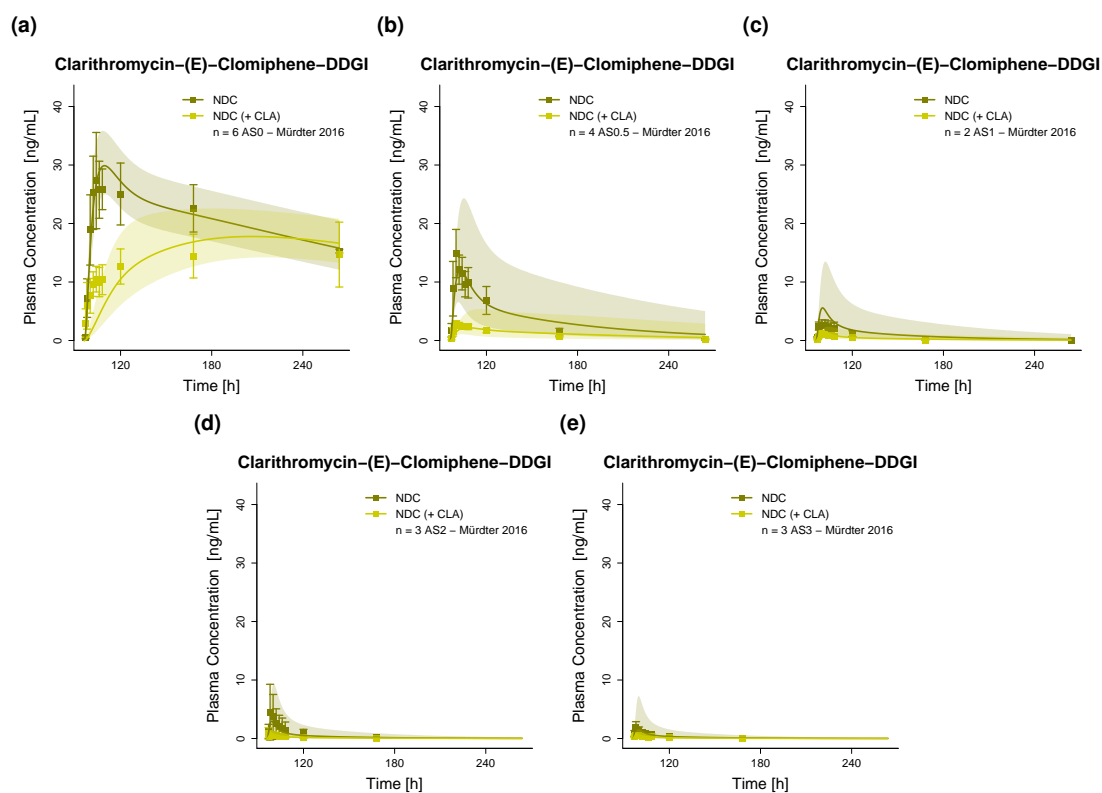


Figure S30: Predicted compared to observed plasma concentration-time profiles of (*E*)-N-desethylclomiphene alone (solid line) and after pretreatment and concomitant administration (dashed line) of clarithromycin (linear representation). Population predicted (1000 individuals) geometric means are shown as lines, corresponding geometric standard deviations as shaded areas and observed data as triangles (± standard deviation, if reported) [76]. AS: CYP2D6 activity score, CLA: clarithromycin, DDGI: drug-drug-gene interaction, n: number of study participants, NDC: (*E*)-N-desethylclomiphene.

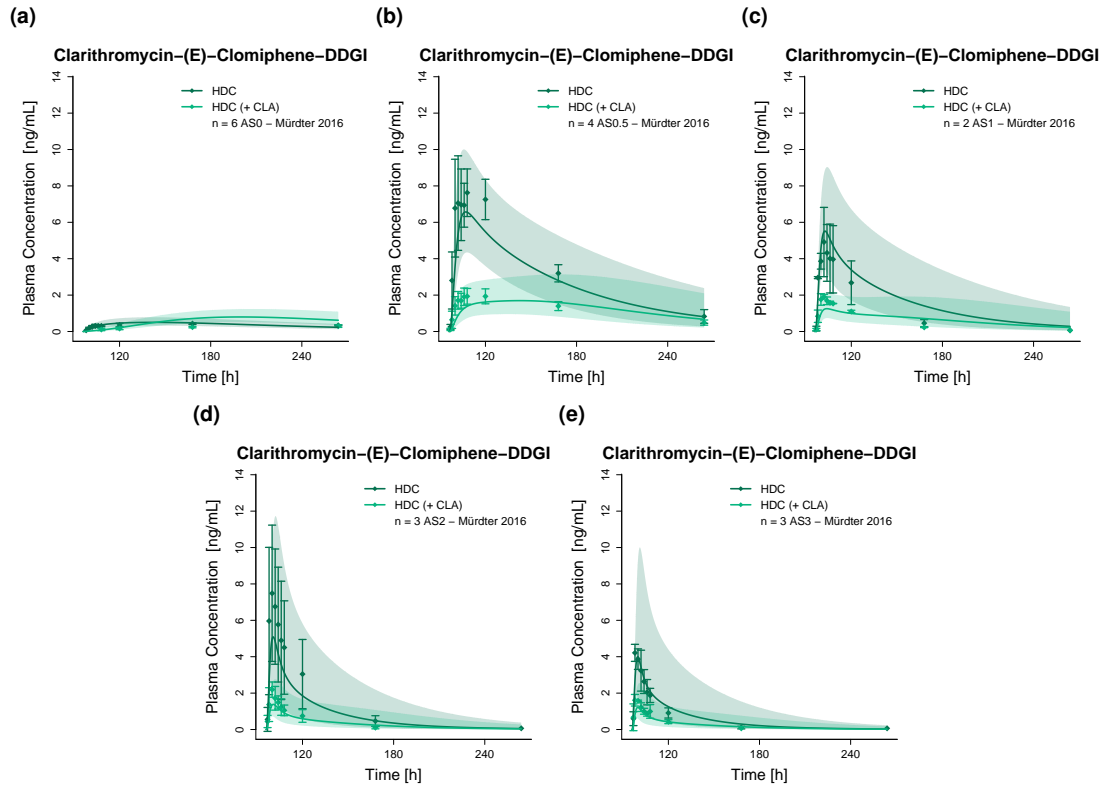


Figure S31: Predicted compared to observed plasma concentration-time profiles of (*E*)-4-hydroxy-N-desethylclomiphene alone (solid line) and after pretreatment and concomitant administration (dashed line) of clarithromycin (linear representation). Population predicted (1000 individuals) geometric means are shown as lines, corresponding geometric standard deviations as shaded areas and observed data as triangles (\pm standard deviation, if reported) [76]. AS: CYP2D6 activity score, CLA: clarithromycin, DDGI: drug-drug-gene interaction, HDC: (*E*)-4-hydroxy-N-desethylclomiphene, n: number of study participants.

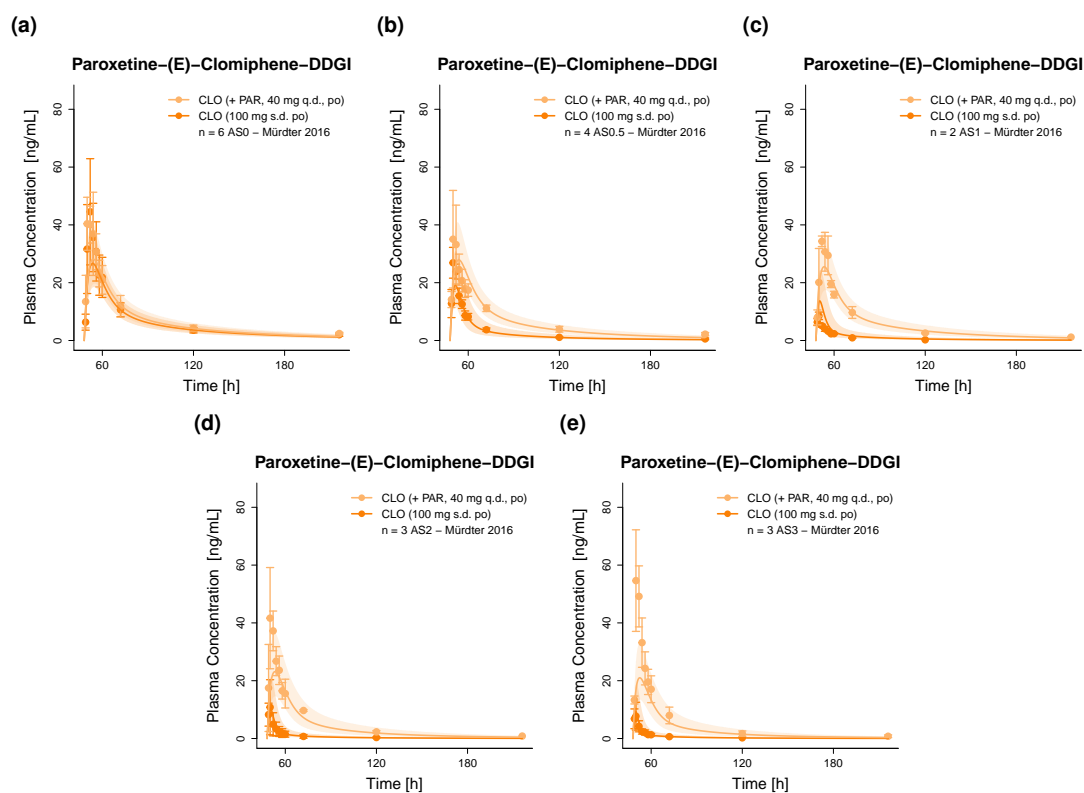


Figure S32: Predicted compared to observed plasma concentration-time profiles of (E)-clomiphene alone (solid line) and after pretreatment and concomitant administration (dashed line) of paroxetine (linear representation). Population predicted (1000 individuals) geometric means are shown as lines, corresponding geometric standard deviations as shaded areas and observed data as dots (\pm standard deviation, if reported) [76]. AS: CYP2D6 activity score, CLO: (E)-clomiphene, DDGI: drug-drug-gene interaction, n: number of study participants, PAR: paroxetine, po: oral, q.d.: once daily, s.d.: single dose.

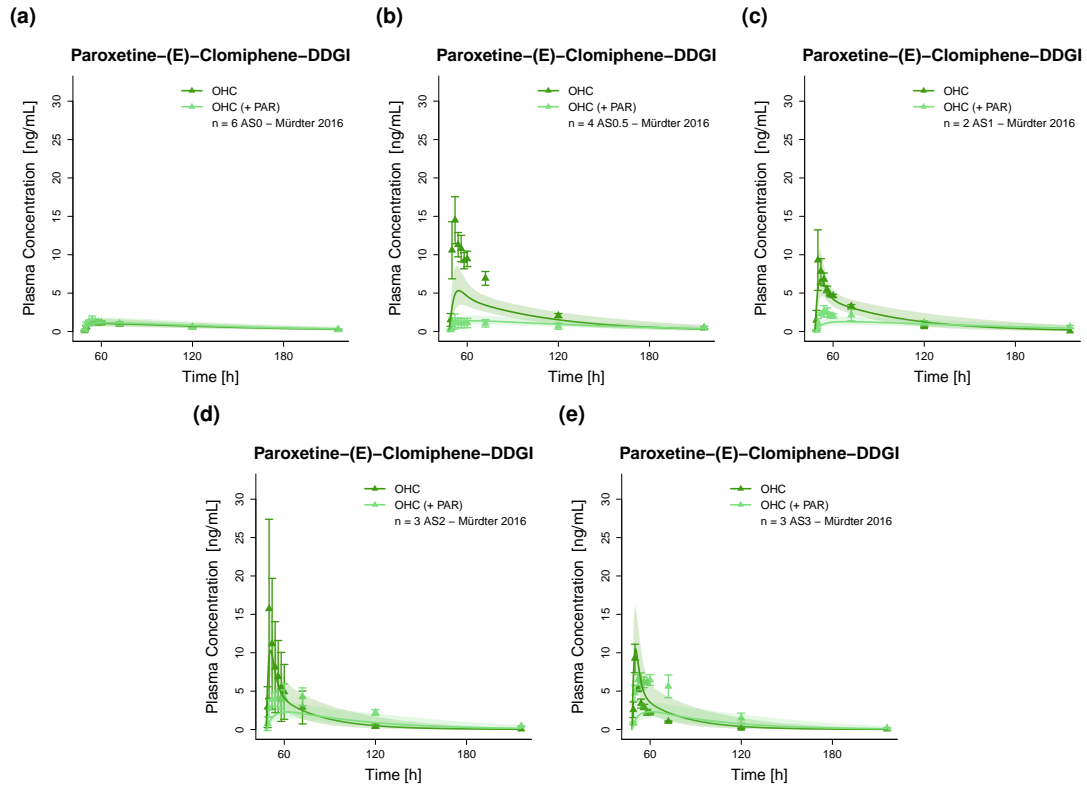


Figure S33: Predicted compared to observed plasma concentration-time profiles of (E)-4-hydroxyclophene alone (solid line) and after pretreatment and concomitant administration (dashed line) of paroxetine (linear representation). Population predicted (1000 individuals) geometric means are shown as lines, corresponding geometric standard deviations as shaded areas and observed data as triangles (\pm standard deviation, if reported) [76]. AS: CYP2D6 activity score, DDGI: drug-drug-gene interaction, n: number of study participants, OHC: (E)-4-hydroxyclophene, PAR: paroxetine.

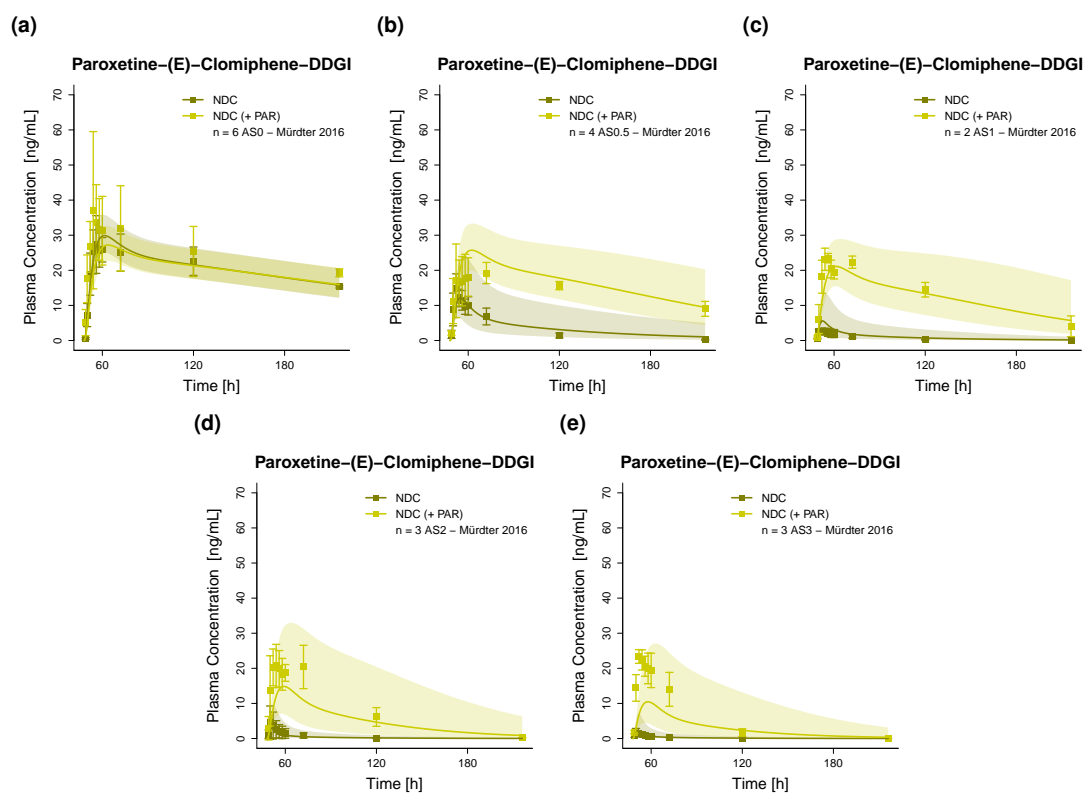


Figure S34: Predicted compared to observed plasma concentration-time profiles of (E)-N-desethylclomiphene alone (solid line) and after pretreatment and concomitant administration (dashed line) of paroxetine (linear representation). Population predicted (1000 individuals) geometric means are shown as lines, corresponding geometric standard deviations as shaded areas and observed data as triangles (\pm standard deviation, if reported) [76]. AS: CYP2D6 activity score, DDGI: drug-drug-gene interaction, n: number of study participants, NDC: (E)-N-desethylclomiphene, PAR: paroxetine.

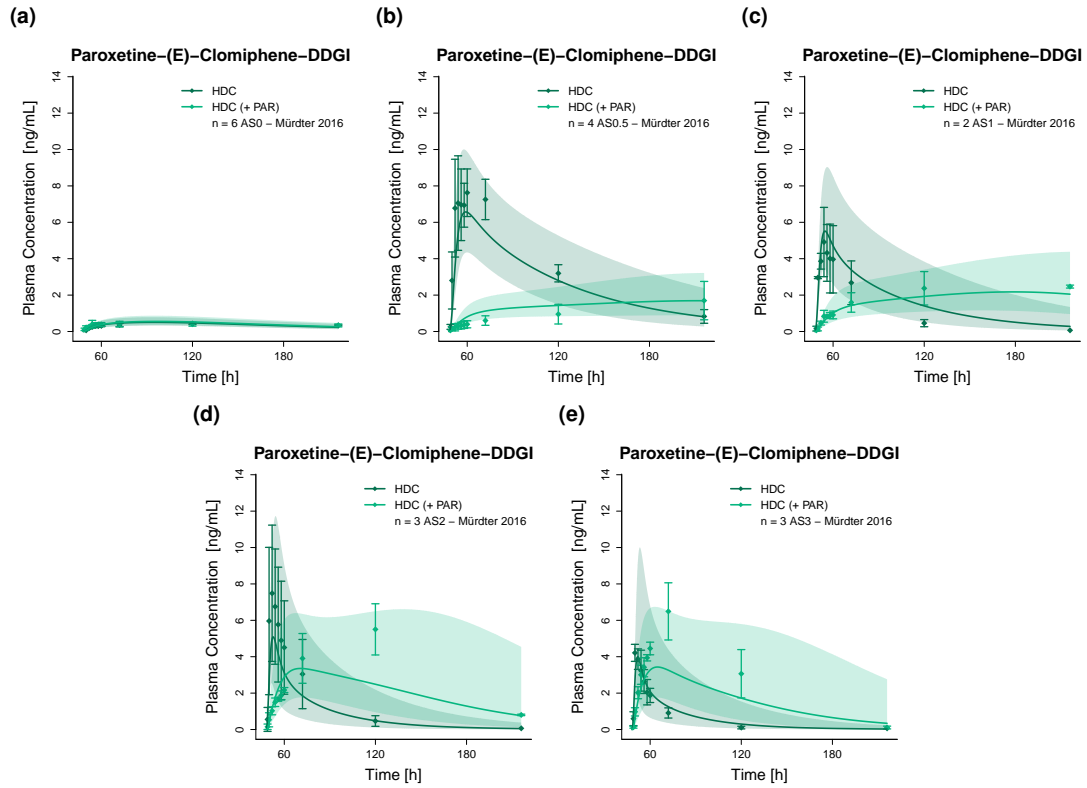


Figure S35: Predicted compared to observed plasma concentration-time profiles of (E)-4-hydroxy-N-desethylclomiphene alone (solid line) and after pretreatment and concomitant administration (dashed line) of paroxetine (linear representation). Population predicted (1000 individuals) geometric means are shown as lines, corresponding geometric standard deviations as shaded areas and observed data as triangles (\pm standard deviation, if reported) [76]. AS: CYP2D6 activity score, DDGI: drug-drug-gene interaction, HDC: (E)-4-hydroxy-N-desethylclomiphene, n: number of study participants, PAR: paroxetine.

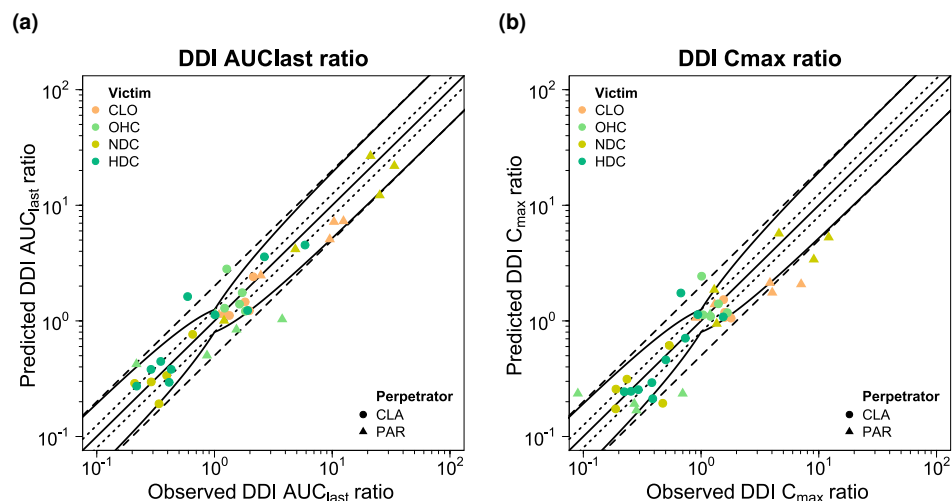
S6.3.4 DDI AUC_{last} and C_{max} Ratios

Figure S36: Goodness-of-fit plots comparing predicted and observed DDI AUC_{last} and C_{max} ratios for victim drug clomiphen. The solid line marks the line of identity. Dotted lines indicate 1.25-fold, dashed lines indicate 2-fold deviation. Prediction success limits proposed by Guest et al. [2] are shown as curved lines (including 20% variability). AUC_{last} : area under the plasma concentration-time curve calculated between the first and last concentration measurement, CLO: (*E*)-clomiphen, CLA: clarithromycin, C_{max} : maximum plasma concentration, HDC: (*E*)-4-hydroxy-*N*-desethylclomiphen, NDC: (*E*)-*N*-desethylclomiphen, OHC: (*E*)-4-hydroxyclophen, PAR: paroxetine.

S6.3.5 Geometric Mean Fold Errors of Predicted DDI AUC_{last} and C_{max} RatiosTable S19: Predicted and observed DDI AUC_{last} and C_{max} ratios involving (*E*)-clomiphene as victim drug

Drug administration			DDI AUC_{last} ratio			DDI C_{max} ratio			AS	Molecule	Reference
Perpetrator	(E)-Clomiphene	t_{last} [h]	Pred	Obs	Pred/Obs	Pred	Obs	Pred/Obs			
Clarithromycin											
500 mg b.i.d po	42 mg s.d. po	168	2.41	2.13	1.13	1.53	1.55	0.98	AS = 0	CLO	Mürdter 2016 [76]
500 mg b.i.d po	42 mg s.d. po	168	2.81	1.27	2.21	2.44	1.01	2.41	AS = 0	OHC	Mürdter 2016 [76]
500 mg b.i.d po	42 mg s.d. po	168	0.76	0.65	1.17	0.61	0.54	1.14	AS = 0	NDC	Mürdter 2016 [76]
500 mg b.i.d po	42 mg s.d. po	168	1.62	0.59	2.75	1.74	0.67	2.59	AS = 0	HDC	Mürdter 2016 [76]
500 mg b.i.d po	42 mg s.d. po	168	1.46	1.82	0.80	1.18	1.59	0.75	AS = 0.5	CLO	Mürdter 2016 [76]
500 mg b.i.d po	42 mg s.d. po	168	1.75	1.72	1.02	1.41	1.40	1.00	AS = 0.5	OHC	Mürdter 2016 [76]
500 mg b.i.d po	42 mg s.d. po	168	0.30	0.29	1.02	0.17	0.19	0.92	AS = 0.5	NDC	Mürdter 2016 [76]
500 mg b.i.d po	42 mg s.d. po	168	0.45	0.35	1.28	0.25	0.25	0.97	AS = 0.5	HDC	Mürdter 2016 [76]
500 mg b.i.d po	42 mg s.d. po	72	1.22	1.98	0.62	1.10	1.73	0.63	AS = 1	CLO	Mürdter 2016 [76]
500 mg b.i.d po	42 mg s.d. po	168	1.40	1.63	0.86	1.18	1.67	0.70	AS = 1	OHC	Mürdter 2016 [76]
500 mg b.i.d po	42 mg s.d. po	72	0.19	0.34	0.57	0.19	0.47	0.41	AS = 1	NDC	Mürdter 2016 [76]
500 mg b.i.d po	42 mg s.d. po	168	0.38	0.43	0.89	0.21	0.39	0.55	AS = 1	HDC	Mürdter 2016 [76]
500 mg b.i.d po	42 mg s.d. po	72	1.15	1.23	0.94	1.07	1.59	0.67	AS = 2	CLO	Mürdter 2016 [76]
500 mg b.i.d po	42 mg s.d. po	168	1.29	1.22	1.06	1.13	1.04	1.09	AS = 2	OHC	Mürdter 2016 [76]
500 mg b.i.d po	42 mg s.d. po	72	0.29	0.21	1.38	0.26	0.19	1.36	AS = 2	NDC	Mürdter 2016 [76]
500 mg b.i.d po	42 mg s.d. po	72	0.27	0.22	1.25	0.25	0.29	0.87	AS = 2	HDC	Mürdter 2016 [76]
500 mg b.i.d po	42 mg s.d. po	72	1.34	1.06	0.83	1.06	1.80	0.59	AS = 3	CLO	Mürdter 2016 [76]
500 mg b.i.d po	42 mg s.d. po	168	1.21	1.83	0.66	1.09	1.20	0.91	AS = 3	OHC	Mürdter 2016 [76]
500 mg b.i.d po	42 mg s.d. po	72	0.34	0.39	0.86	0.31	0.23	1.34	AS = 3	NDC	Mürdter 2016 [76]
500 mg b.i.d po	42 mg s.d. po	72	0.29	0.41	0.72	0.29	0.38	0.77	AS = 3	HDC	Mürdter 2016 [76]

Mean GMFE (range): 1.43 (1.08–2.34), 19/20 with GMFE ≤ 2 1.54 (1.06–2.55), 18/20 with GMFE ≤ 2

AUC_{last} : area under the plasma concentration-time curve calculated between the first and last concentration measurement, AS: CYP2D6 activity score, b.i.d.: twice daily, CLO: (*E*)-clomiphene, C_{max} : maximum plasma concentration, DDI: drug-drug interaction, GMFE: geometric mean fold error, HDC: (*E*)-4-hydroxy-N-desethylclomiphene, NDC: (*E*)-N-desethylclomiphene, obs: observed, OHC: (*E*)-4-hydroxyclophene, po: oral, pred: predicted, q.d.: once daily, s.d: single dose, t_{last} : time of the last concentration measurement. If perpetrator or victim drugs were applied in form of salts, the respective dose of base was calculated and incorporated in simulations.

Table S19: Predicted and observed DDI AUC_{last} and C_{max} ratios involving (*E*)-clomiphene as victim drug (*continued*)

Drug administration			DDI AUC _{last} ratio			DDI C _{max} ratio			AS	Molecule	Reference
Perpetrator	(E)-Clomiphene	t _{last} [h]	Pred	Obs	Pred/Obs	Pred	Obs	Pred/Obs			
Paroxetine											
40 mg q.d. po	42 mg s.d. po	168	1.13	1.09	1.03	1.06	0.91	1.17	AS = 0	CLO	Mürdter 2016 [76]
40 mg q.d. po	42 mg s.d. po	168	1.15	1.02	1.13	1.13	1.19	0.95	AS = 0	OHC	Mürdter 2016 [76]
40 mg q.d. po	42 mg s.d. po	168	1.00	1.21	0.83	0.94	1.36	0.70	AS = 0	NDC	Mürdter 2016 [76]
40 mg q.d. po	42 mg s.d. po	168	1.13	1.01	1.12	1.13	0.94	1.21	AS = 0	HDC	Mürdter 2016 [76]
40 mg q.d. po	42 mg s.d. po	168	2.47	2.47	1.00	1.39	1.30	1.07	AS = 0.5	CLO	Mürdter 2016 [76]
40 mg q.d. po	42 mg s.d. po	168	0.42	0.22	1.95	0.24	0.09	2.62	AS = 0.5	OHC	Mürdter 2016 [76]
40 mg q.d. po	42 mg s.d. po	168	4.17	4.86	0.86	1.86	1.29	1.44	AS = 0.5	NDC	Mürdter 2016 [76]
40 mg q.d. po	42 mg s.d. po	168	0.38	0.29	1.32	0.24	0.22	1.10	AS = 0.5	HDC	Mürdter 2016 [76]
40 mg q.d. po	42 mg s.d. po	168	5.08	9.53	0.53	1.76	4.02	0.44	AS = 1	CLO	Mürdter 2016 [76]
40 mg q.d. po	42 mg s.d. po	168	0.50	0.86	0.58	0.17	0.28	0.60	AS = 1	OHC	Mürdter 2016 [76]
40 mg q.d. po	42 mg s.d. po	168	12.21	25.32	0.48	3.40	9.07	0.37	AS = 1	NDC	Mürdter 2016 [76]
40 mg q.d. po	42 mg s.d. po	168	1.23	1.91	0.64	0.46	0.50	0.92	AS = 1	HDC	Mürdter 2016 [76]
40 mg q.d. po	42 mg s.d. po	168	7.19	10.35	0.69	2.13	3.85	0.55	AS = 2	CLO	Mürdter 2016 [76]
40 mg q.d. po	42 mg s.d. po	168	0.84	1.54	0.55	0.19	0.27	0.71	AS = 2	OHC	Mürdter 2016 [76]
40 mg q.d. po	42 mg s.d. po	168	26.72	21.14	1.26	5.70	4.59	1.24	AS = 2	NDC	Mürdter 2016 [76]
40 mg q.d. po	42 mg s.d. po	168	3.58	2.65	1.35	0.71	0.74	0.96	AS = 2	HDC	Mürdter 2016 [76]
40 mg q.d. po	42 mg s.d. po	168	7.29	12.47	0.59	2.08	7.08	0.29	AS = 3	CLO	Mürdter 2016 [76]
40 mg q.d. po	42 mg s.d. po	168	1.03	3.76	0.27	0.24	0.70	0.34	AS = 3	OHC	Mürdter 2016 [76]
40 mg q.d. po	42 mg s.d. po	168	21.91	33.72	0.65	5.28	12.14	0.43	AS = 3	NDC	Mürdter 2016 [76]
40 mg q.d. po	42 mg s.d. po	168	4.53	5.87	0.77	1.08	1.54	0.70	AS = 3	HDC	Mürdter 2016 [76]
Mean GMFE (range):			1.56 (1.00–3.64), 18/20 with GMFE ≤ 2			1.72 (1.04–3.41), 15/20 with GMFE ≤ 2					
Overall GMFE (range):			1.49 (1.00–3.64), 37/40 with GMFE ≤ 2			1.63 (1.04–3.41), 33/40 with GMFE ≤ 2					

AUC_{last}: area under the plasma concentration-time curve calculated between the first and last concentration measurement, AS: CYP2D6 activity score, b.i.d.: twice daily, CLO: (*E*)-clomiphene, C_{max}: maximum plasma concentration, DDI: drug-drug interaction, GMFE: geometric mean fold error, HDC: (*E*)-4-hydroxy-N-desethylclomiphene, NDC: (*E*)-N-desethylclomiphene, obs: observed, OHC: (*E*)-4-hydroxyclophene, po: oral, pred: predicted, q.d.: once daily, s.d.: single dose, t_{last}: time of the last concentration measurement. If perpetrator or victim drugs were applied in form of salts, the respective dose of base was calculated and incorporated in simulations.

S6.4 Desipramine

S6.4.1 Clinical Studies

Table S20: Clinical study data used for DD(G)I model development with **desipramine** as victim

Drug administration		n	Population ^a	Fem. [%]	Age [years]	Weight [kg]	BMI [kg/m²]	Phenotype	Molecule	Reference
Perpetrator	Desipramine									
Atomoxetine										
40/60 mg b.i.d. po	50 mg s.d. po	22	American [7]	50	(26–55)	-	(18.8–30.4)	-	DES	Sauer 2004 [17]
Bupropion										
150 mg q.d./b.i.d. po	50 mg s.d. po	15	American [7]	0	-	-	-	-	DES	Reese 2008 [16]
Paroxetine										
20 mg q.d. po	50 mg s.d. po	20	American [7]	15	35.0±7.7	79.9±9.8	-	-	DES, OHD	Nichols 2009 [13]
20 mg q.d. po	100 mg s.d. po	8	European [3]	0	(22–24)	-	-	PM	DES	Brøsen 1993 [22]
20 mg q.d. po	100 mg s.d. po	5	European [3]	0	(22–24)	-	-	NM	DES	Brøsen 1993 [22]
20 mg q.d. po	100 mg s.d. po	4	European [3]	0	(22–24)	-	-	fast NM	DES	Brøsen 1993 [22]
20/30 mg q.d. po	50 mg q.d. po	6	American [7]	0	30.4±5.2	73.3±8.5	-	-	DES	Alderman 1997 [19]
Quinidine										
200 mg q.d. po	100 mg s.d. po	6	European [3]	50	27.7 (23–38)	-	-	-	DES, OHD, QUI, OHQ	Brøsen 1989 [23]

b.i.d.: twice daily, BMI: body mass index, DD(G)I: drug-drug(-gene) interaction, DES: desipramine, fem: females, n: number of study participants, NM: CYP2D6 normal metabolizer, OHD: 2-hydroxydesipramine, OHQ: 3-hydroxyquinidine, PM: CYP2D6 poor metabolizer, po: oral, q.d.: once daily, QUI: quinidine, s.d: single dose, -: not available. Values are given as mean (range). If perpetrator or victim drugs were applied in form of salts, the respective dose of base was calculated and incorporated in simulations. ^a Population used in simulations.

S6.4.2 Plasma Concentration-Time Profiles (Semilogarithmic Representation)

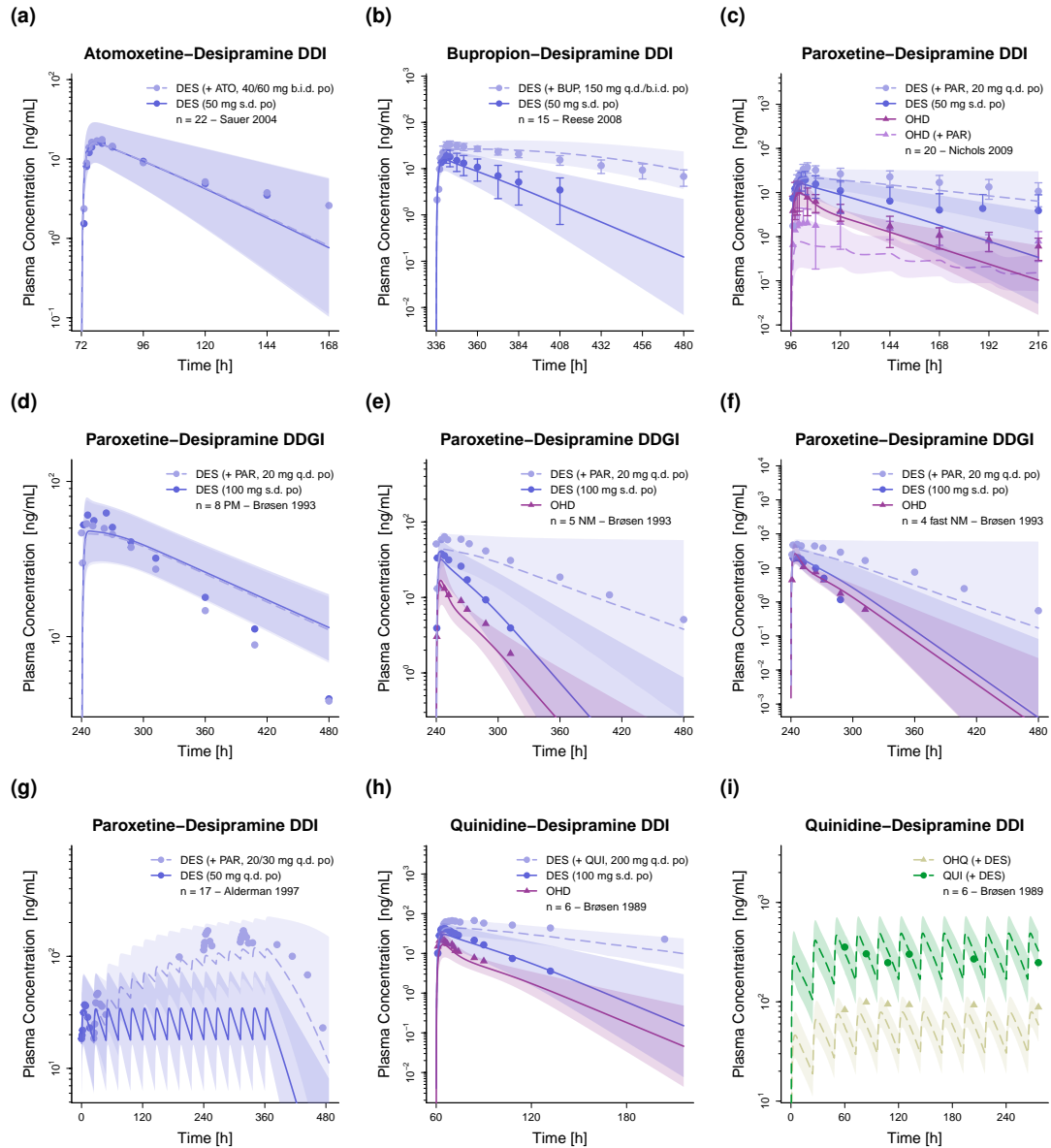


Figure S37: Predicted compared to observed plasma concentration-time profiles of desipramine alone (solid line) and after pretreatment and/or concomitant administration (dashed line) of (a) atomoxetine, (b) bupropion, (c–g) paroxetine and (h) quinidine (semilogarithmic representation). Population predicted (1000 individuals) geometric means are shown as lines, corresponding geometric standard deviations as shaded areas and observed data as dots/triangles (\pm standard deviation, if reported) [13, 16, 17, 19, 22, 23]. ATO: atomoxetine, b.i.d.: twice daily, BUP: bupropion, DD(G)I: drug-drug(-gene) interaction, DES: desipramine, n: number of study participants, NM: CYP2D6 normal metabolizer, OHD: 2-hydroxydesipramine, OHQ: 3-hydroxydesipramine, PAR: paroxetine, PM: CYP2D6 poor metabolizer, po: oral, q.d.: once daily, QUI: quinidine, s.d.: single dose.

S6.4.3 Plasma Concentration-Time Profiles (Linear Representation)

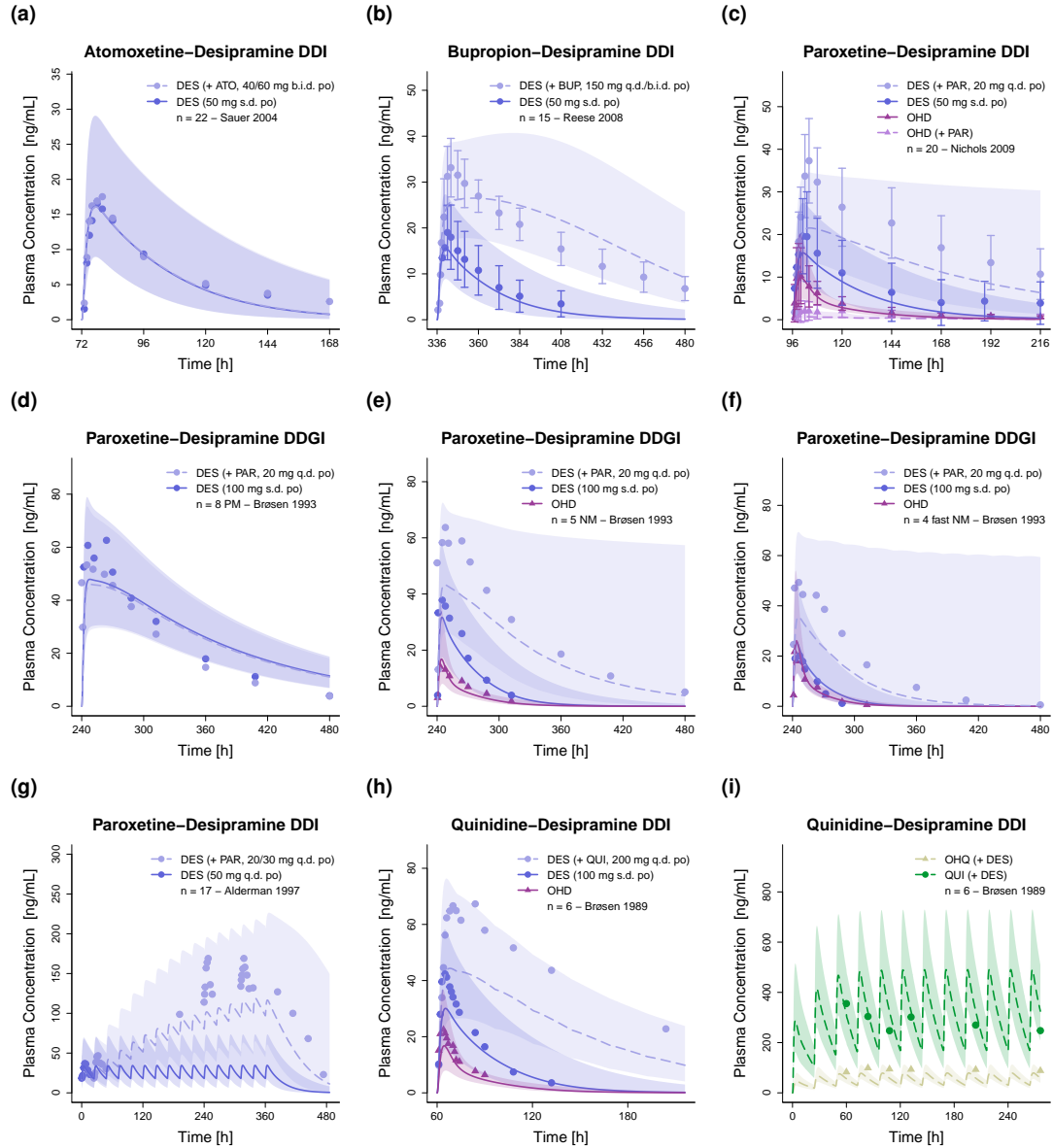


Figure S38: Predicted compared to observed plasma concentration-time profiles of desipramine alone (solid line) and after pretreatment and/or concomitant administration (dashed line) of (a) atomoxetine, (b) bupropion, (c–g) paroxetine and (h) quinidine (linear representation). Population predicted (1000 individuals) geometric means are shown as lines, corresponding geometric standard deviations as shaded areas and observed data as dots/triangles (\pm standard deviation, if reported) [13, 16, 17, 19, 22, 23]. ATO: atomoxetine, b.i.d.: twice daily, BUP: bupropion, DD(G)I: drug-drug(-gene) interaction, DES: desipramine, n: number of study participants, NM: CYP2D6 normal metabolizer, OHD: 2-hydroxydesipramine, OHQ: 3-hydroxydesipramine, PAR: paroxetine, PM: CYP2D6 poor metabolizer, po: oral, q.d.: once daily, QUI: quinidine, s.d.: single dose.

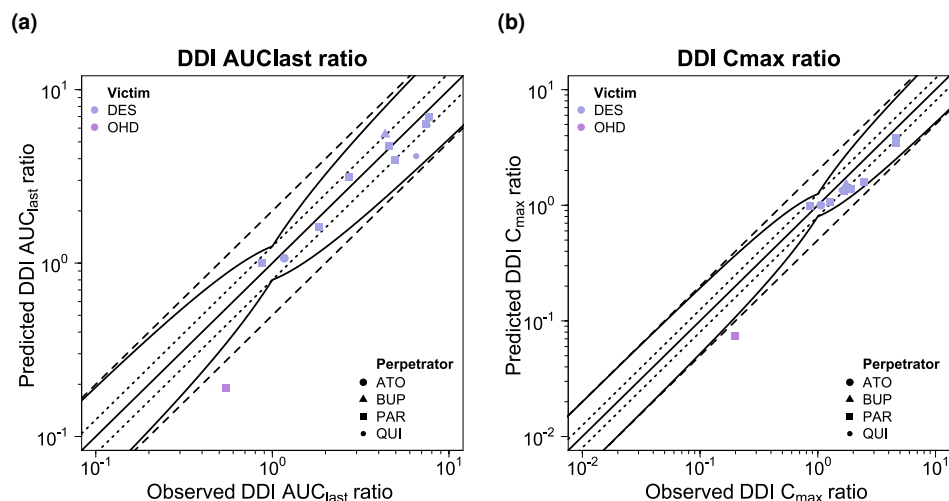
S6.4.4 DDI AUC_{last} and C_{max} Ratios

Figure S39: Goodness-of-fit plots comparing predicted and observed DDI AUC_{last} and C_{max} ratios for victim drug desipramine. The solid line marks the line of identity. Dotted lines indicate 1.25-fold, dashed lines indicate 2-fold deviation. Prediction success limits proposed by Guest et al. [2] are shown as curved lines (including 20% variability). ATO: atomoxetine, BUP: bupropion, AUC_{last} : area under the plasma concentration-time curve calculated between the first and last concentration measurement, C_{max} : maximum plasma concentration, DES: desipramine, DDI: drug-drug interaction, OHD: 2-hydroxydesipramine, PAR: paroxetine, QUI: quinidine.

S6.4.5 Geometric Mean Fold Errors of Predicted DDI AUC_{last} and C_{max} RatiosTable S21: Predicted and observed DDI AUC_{last} and C_{max} ratios involving **desipramine** as victim drug

Drug administration			DDI AUC _{last} ratio			DDI C _{max} ratio			Phenotype	Molecule	Reference
Perpetrator	Desipramine	t _{last} [h]	Pred	Obs	Pred/Obs	Pred	Obs	Pred/Obs			
Atomoxetine											
40/60 mg b.i.d. po	50 mg s.d. po	96	1.07	1.17	0.91	1.00	1.06	0.95	-	DES	Sauer 2004 [17]
Mean GMFE (range):			1.09 (-), 1/1 with GMFE ≤ 2			1.06 (-), 1/1 with GMFE ≤ 2					
Bupropion											
150 mg q.d./b.i.d. po	50 mg s.d. po	168	5.52	4.35	1.27	1.51	1.74	0.87	-	DES	Reese 2008 [16]
Mean GMFE (range):			1.27 (-), 1/1 with GMFE ≤ 2			1.15 (-), 1/1 with GMFE ≤ 2					
Paroxetine											
20 mg q.d. po	50 mg s.d. po	120	3.13	2.71	1.16	1.37	1.90	0.72	-	DES	Nichols 2009 [13]
20 mg q.d. po	50 mg s.d. po	120	0.19	0.55	0.35	0.07	0.20	0.37	-	OHD	Nichols 2009 [13]
20 mg q.d. po	100 mg s.d. po	239	1.00	0.87	1.15	0.99	0.85	1.16	PM	DES	Brøsen 1993 [22]
20 mg q.d. po	100 mg s.d. po	234	4.76	4.60	1.04	1.33	1.90	0.79	NM	DES	Brøsen 1993 [22]
20 mg q.d. po	100 mg s.d. po	233	6.96	7.76	0.90	1.61	2.45	0.65	fast NM	DES	Brøsen 1993 [22]
20/30 mg q.d. po	50 mg q.d. po (D1)	24	1.60	1.84	0.87	1.06	1.27	0.84	-	DES	Alderman 1997 [19]
20/30 mg q.d. po	50 mg q.d. po (D10)	16	3.93	4.96	0.79	3.48	4.58	0.76	-	DES	Alderman 1997 [19]
20/30 mg q.d. po	50 mg q.d. po (D13)	16	6.37	7.40	0.86	3.83	4.58	0.84	-	DES	Alderman 1997 [19]
Mean GMFE (range):			1.37 (1.04–2.86), 7/8 with GMFE ≤ 2			1.47 (1.16–2.68), 7/8 with GMFE ≤ 2					
Quinidine											
200 mg q.d. po	100 mg s.d. po	213	4.14	6.52	0.63	1.35	1.59	0.85	-	DES	Brøsen 1989 [23]
Mean GMFE (range):			1.58 (-), 1/1 with GMFE ≤ 2			1.18 (-), 1/1 with GMFE ≤ 2					
Overall GMFE (range):			1.35 (1.04–2.86), 10/11 with GMFE ≤ 2			1.38 (1.06–2.68), 10/11 with GMFE ≤ 2					

AUC_{last} : area under the plasma concentration-time curve calculated between the first and last concentration measurement, b.i.d.: twice daily, C_{max} : maximum plasma concentration, D: day, DDI: drug-drug interaction, DES: desipramine, GMFE: geometric mean fold error, NM: CYP2D6 normal metabolizer, obs: observed, OHD: 2-hydroxydesipramine, PM: CYP2D6 poor metabolizer, po: oral, pred: predicted, q.d.: once daily, s.d.: single dose, t_{last} : time of the last concentration measurement. If perpetrator or victim drugs were applied in form of salts, the respective dose of base was calculated and incorporated in simulations.

S6.5 Dextromethorphan

S6.5.1 Clinical Studies

Table S22: Clinical study data used for DD(G)I model development with **dextromethorphan** as victim

Drug administration		n	Population ^a	Fem. [%]	Age [years]	Weight [kg]	BMI [kg/m ²]	Phenotype	Molecule	Reference
Perpetrator	Dextromethorphan									
<i>Paroxetine</i>										
20 mg b.i.d. po	5 mg s.d. po	16	European [3]	75	24 (21–27)	-	22 (19–26)	IM	DEX, DXT, PAR	Storelli 2018 [77]
20 mg b.i.d. po	5 mg s.d. po	17	European [3]	53	27 (18–42)	-	23 (19–26)	NM	DEX, DXT, PAR	Storelli 2018 [77]
30 mg q.d. po	30 mg b.i.d. po ^b	13	American [7]	14.3	33.5 (23–50)	73.3	25.1	NM	DEX	Schoedel 2012 [101]
<i>Quinidine</i>										
50 mg s.d. po	30 mg s.d. po	6	European [3]	33.3	22.4 (20–26)	70 (49–86)	-	NM	DEX, DTT	Capon 1996 [80]
100 mg s.d. po	30 mg s.d. po	5	American [7]	80	26.4 (20–31)	-	-	NM	DEX, DXT, DXG	Schadel 1995 [102]

b.i.d.: twice daily, BMI: body mass index, DD(G)I: drug-drug(-gene) interaction, DEX: dextromethorphan, DTT: total dextrorphan, DXG: dextrorphan-O-glucuronide, DXT: dextrorphan, fem: females, IM: CYP2D6 intermediate metabolizer, n: number of study participants, NM: CYP2D6 normal metabolizer, PAR: paroxetine, po: oral, s.d: single dose, -: not available. Values are given as mean (range). If perpetrator or victim drugs were applied in form of salts, the respective dose of base was calculated and incorporated in simulations. ^a Population used in simulations. ^b: plus quinidine (30 mg b.i.d. po)

S6.5.2 Plasma Concentration-Time Profiles (Semilogarithmic Representation)

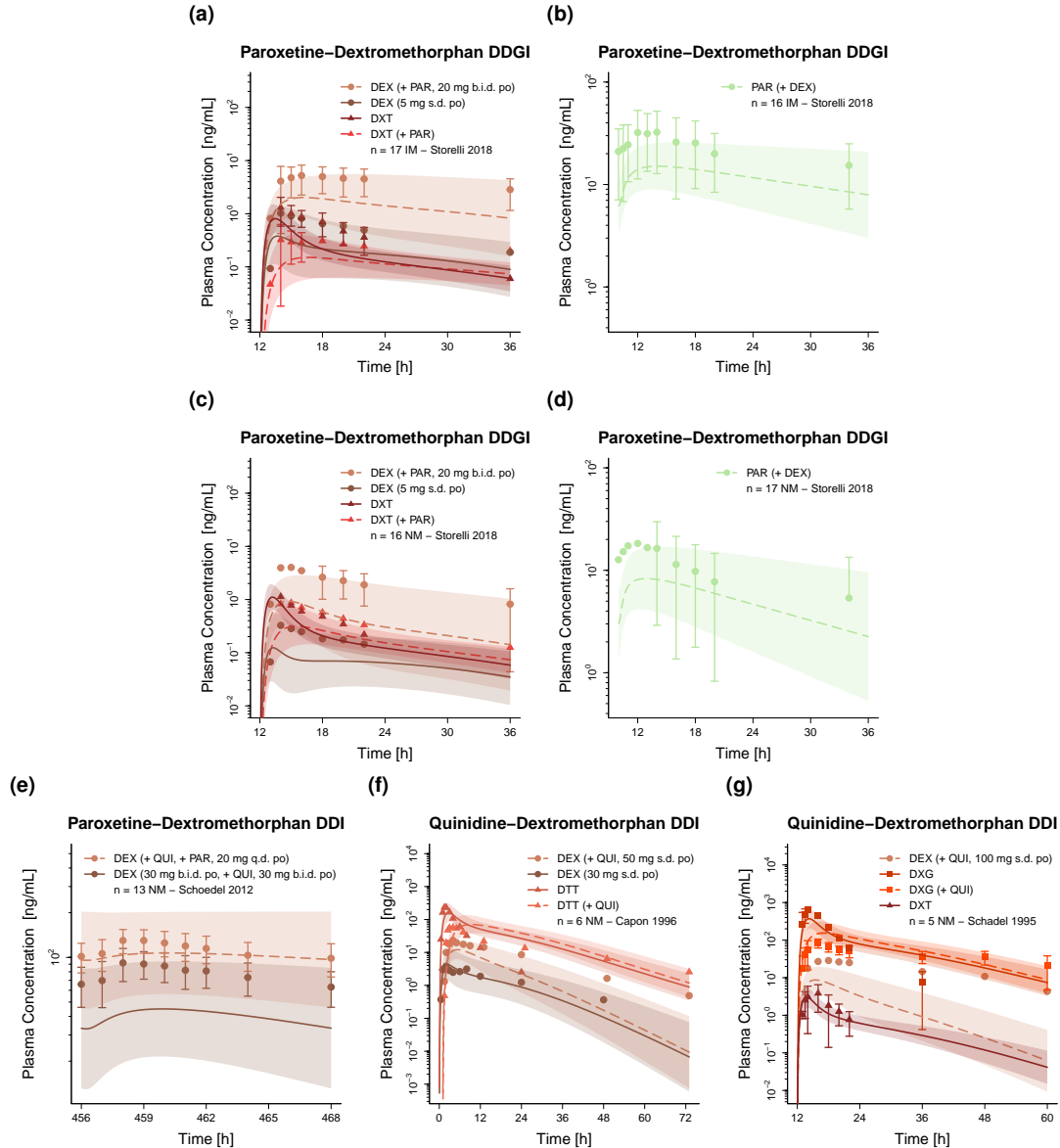


Figure S40: Predicted compared to observed plasma concentration-time profiles of dextromethorphan alone (solid line) and after pretreatment and/or concomitant administration (dashed line) of (a,c,e) paroxetine and (f–g) quinidine (semilogarithmic representation). Population predicted (1000 individuals) geometric means are shown as lines, corresponding geometric standard deviations as shaded areas and observed data as dots/triangles/squares (\pm standard deviation, if reported) [77, 80, 101, 102]. b.i.d.: twice daily, DD(G)I: drug-drug(-gene) interaction, DEX: dextromethorphan, DTT: total dextromethorphan, DXG: dextromethorphan-O-glucuronide, DXT: dextromethorphan, IM: CYP2D6 intermediate metabolizer, n: number of study participants, NM: CYP2D6 normal metabolizer, PAR: paroxetine, po: oral, q.d.: once daily, QUI: quinidine, s.d.: single dose.

S6.5.3 Plasma Concentration-Time Profiles (Linear Representation)

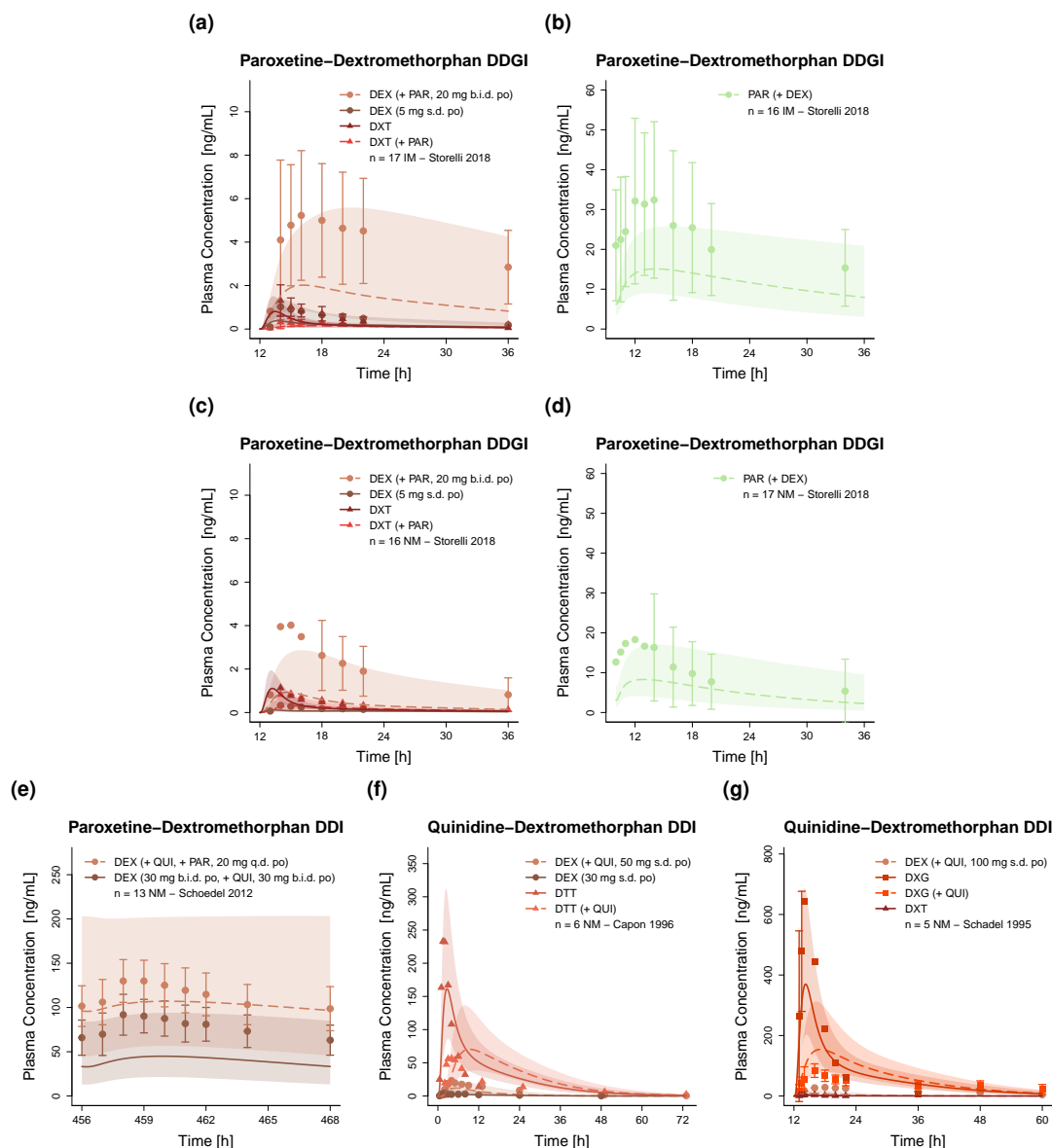


Figure S41: Predicted compared to observed plasma concentration-time profiles of dextromethorphan alone (solid line) and after pretreatment and/or concomitant administration (dashed line) of (a,c,e) paroxetine and (f-g) quinidine (linear representation). Population predicted (1000 individuals) geometric means are shown as lines, corresponding geometric standard deviations as shaded areas and observed data as dots/triangles/squares (\pm standard deviation, if reported) [77, 80, 101, 102]. b.i.d.: twice daily, DD(G)I: drug-drug(-gene) interaction, DEX: dextromethorphan, DTT: total dextromethorphan, DXG: dextromethorphan-O-glucuronide, DXT: dextromethorphan, IM: CYP2D6 intermediate metabolizer, n: number of study participants, NM: CYP2D6 normal metabolizer, PAR: paroxetine, po: oral, q.d.: once daily, QUI: quinidine, s.d.: single dose.

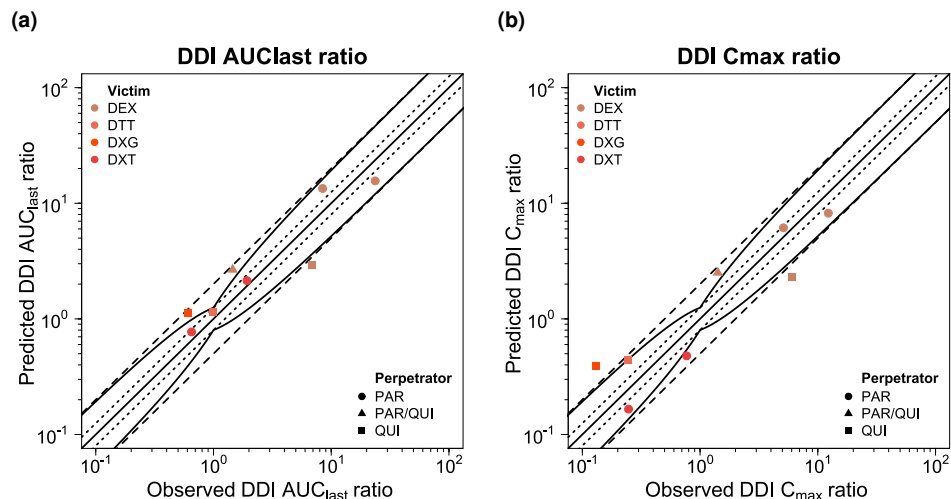
S6.5.4 DDI AUC_{last} and C_{max} Ratios

Figure S42: Goodness-of-fit plots comparing predicted and observed DDI AUC_{last} and C_{max} ratios for victim drug dextromethorphan. The solid line marks the line of identity. Dotted lines indicate 1.25-fold, dashed lines indicate 2-fold deviation. Prediction success limits proposed by Guest et al. [2] are shown as curved lines (including 20% variability). AUC_{last} : area under the plasma concentration-time curve calculated between the first and last concentration measurement, C_{max} : maximum plasma concentration, DEX: dextromethorphan, DTT: total dextrophan, DXG: dextrophan O-glucuronide, DXT: dextrophan, PAR: paroxetine, QUI: quinidine.

S6.5.5 Geometric Mean Fold Errors of Predicted DDI AUC_{last} and C_{max} RatiosTable S23: Predicted and observed DDI AUC_{last} and C_{max} ratios involving **dextromethorphan** as victim drug

Drug administration			DDI AUC _{last} ratio			DDI C _{max} ratio			Phenotype	Molecule	Reference
Perpetrator	Dextromethorphan	t _{last} [h]	Pred	Obs	Pred/Obs	Pred	Obs	Pred/Obs			
Paroxetine											
20 mg b.i.d. po	5 mg s.d. po	24	13.43	8.45	1.59	6.14	5.11	1.20	IM	DEX	Storelli 2018 [77]
20 mg b.i.d. po	5 mg s.d. po	24	0.77	0.65	1.18	0.17	0.25	0.67	IM	DXT	Storelli 2018 [77]
20 mg b.i.d. po	5 mg s.d. po	24	15.63	23.61	0.66	8.21	12.29	0.67	NM	DEX	Storelli 2018 [77]
20 mg b.i.d. po	5 mg s.d. po	24	2.14	1.92	1.11	0.48	0.77	0.62	NM	DXT	Storelli 2018 [77]
20 mg q.d. po	30 mg b.i.d. po ^a	12	2.66	1.45	1.83	2.51	1.42	1.77	NM	DEX	Schoedel 2012 [101]
Mean GMFE (range):			1.52 (1.11–1.88), 5/5 with GMFE ≤ 2			1.61 (1.20–1.98), 5/5 with GMFE ≤ 2					
Quinidine											
50 mg s.d. po	30 mg s.d. po	72	2.93	6.84	0.43	2.32	6.07	0.38	NM	DEX	Capon 1996 [80]
50 mg s.d. po	30 mg s.d. po	96	1.15	0.99	1.16	0.44	0.24	1.83	NM	DTT	Capon 1996 [80]
100 mg s.d. po	30 mg s.d. po	48	1.12	0.61	1.85	0.39	0.13	3.03	NM	DXG	Schadel 1995 [102]
Mean GMFE (range):			1.78 (1.16–2.33), 2/3 with GMFE ≤ 2			2.49 (1.83–3.03), 1/3 with GMFE ≤ 2					
Overall GMFE (range):			1.62 (1.11–2.33), 7/8 with GMFE ≤ 2			1.94 (1.20–3.03), 6/8 with GMFE ≤ 2					

AUC_{last} : area under the plasma concentration-time curve calculated between the first and last concentration measurement, b.i.d.: twice daily, C_{max} : maximum plasma concentration, DDI: drug-drug interaction, DEX: dextromethorphan, DTT: total dextrophan, DXG: dextrophan-O-glucuronide, DXT: dextrophan, GMFE: geometric mean fold error, obs: observed, PAR: paroxetine, po: oral, pred: predicted, q.d.: once daily, s.d.: single dose, t_{last} : time of the last concentration measurement. If perpetrator or victim drugs were applied in form of salts, the respective dose of base was calculated and incorporated in simulations. ^a: plus quinidine (30 mg b.i.d. po)

S6.6 Digoxin

S6.6.1 Clinical Studies

Table S24: Clinical study data used for DDI model development with **digoxin** as victim

Drug administration		n	Population ^a	Fem. [%]	Age [years]	Weight [kg]	BMI [kg/m ²]	Molecule	Reference
Perpetrator	Digoxin								
Quinidine									
200 mg b.i.d. po	10 µg/kg s.d. iv	6	European [3]	33	(21–28)	-	-	DIG	Steiness 1980 [103]
200 mg q.i.d. po	1 mg s.d. iv	7	European [3]	-	-	-	-	DIG	Ochs 1981 [104]

b.i.d.: twice daily, BMI: body mass index, DDI: drug-drug interaction, DIG: digoxin, fem: females, iv: intravenous, n: number of study participants, po: oral, q.i.d.: four times daily, s.d: single dose, -: not available. Values are given as mean (range). If perpetrator or victim drugs were applied in form of salts, the respective dose of base was calculated and incorporated in simulations. ^a Population used in simulations.

S6.6.2 Plasma Concentration-Time Profiles (Semilogarithmic Representation)

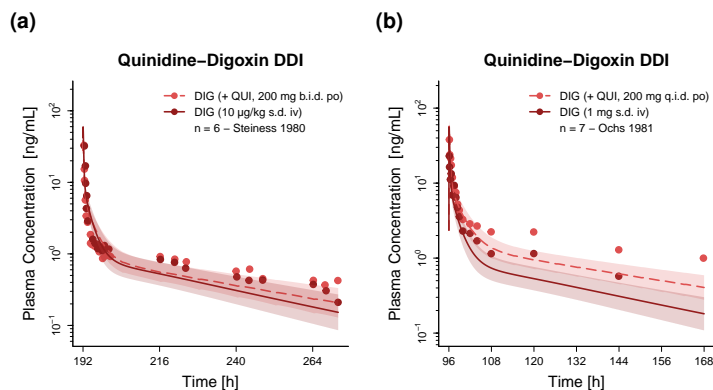


Figure S43: Predicted compared to observed plasma concentration-time profiles of digoxin alone (solid line) and after pretreatment and/or concomitant administration (dashed line) of (a–b) quinidine (semilogarithmic representation). Population predicted (1000 individuals) geometric means are shown as lines, corresponding geometric standard deviations as shaded areas and observed data as dots [103, 104]. b.i.d.: twice daily, DDI: drug-drug interaction, DIG: digoxin, iv: intravenous, n: number of study participants, po: oral, q.i.d.: four times daily, QUI: quinidine, s.d.: single dose.

S6.6.3 Plasma Concentration-Time Profiles (Linear Representation)

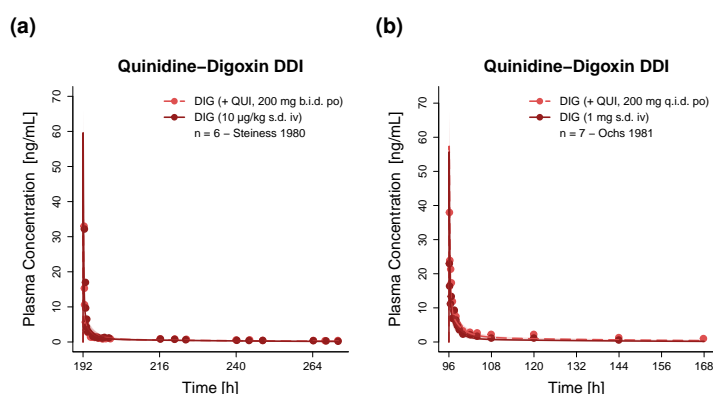


Figure S44: Predicted compared to observed plasma concentration-time profiles of digoxin alone (solid line) and after pretreatment and/or concomitant administration (dashed line) of (a–b) quinidine (linear representation). Population predicted (1000 individuals) geometric means are shown as lines, corresponding geometric standard deviations as shaded areas and observed data as dots [103, 104]. b.i.d.: twice daily, DDI: drug-drug interaction, DIG: digoxin, iv: intravenous, n: number of study participants, po: oral, q.i.d.: four times daily, QUI: quinidine, s.d.: single dose.

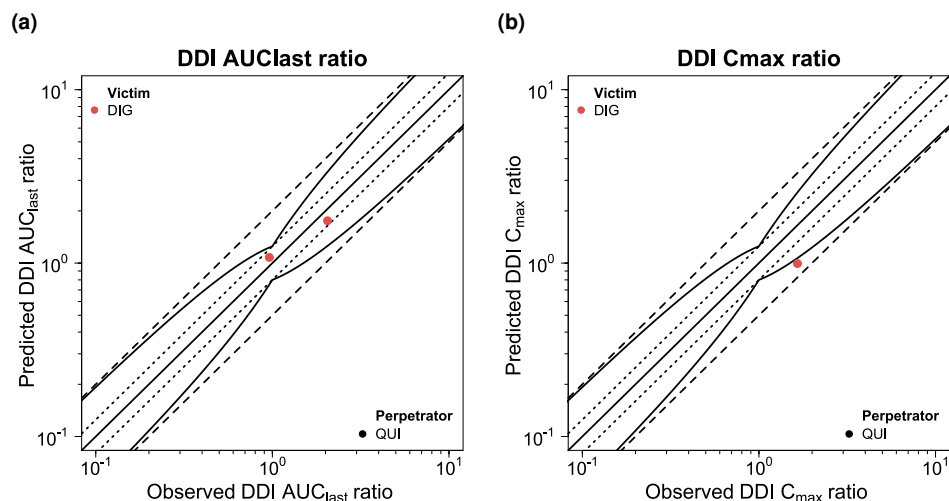
S6.6.4 DDI AUC_{last} and C_{max} Ratios

Figure S45: Goodness-of-fit plots comparing predicted and observed DDI AUC_{last} and C_{max} ratios for victim drug digoxin. The solid line marks the line of identity. Dotted lines indicate 1.25-fold, dashed lines indicate 2-fold deviation. Prediction success limits proposed by Guest et al. [2] are shown as curved lines (including 20% variability). AUC_{last} : area under the plasma concentration-time curve calculated between the first and last concentration measurement, C_{max} : maximum plasma concentration, DIG: digoxin, QUI: quinidine.

S6.6.5 Geometric Mean Fold Errors of Predicted DDI AUC_{last} and C_{max} RatiosTable S25: Predicted and observed DDI AUC_{last} and C_{max} ratios involving **digoxin** as victim drug

Drug administration			DDI AUC _{last} ratio			DDI C _{max} ratio			Molecule	Reference
Perpetrator	Digoxin	t _{last} [h]	Pred	Obs	Pred/Obs	Pred	Obs	Pred/Obs		
Quinidine										
200 mg b.i.d. po	10 µg/kg s.d. iv	80	1.08	0.96	1.12	-	-	-	DIG	Steiness 1980 [103]
200 mg q.i.d. po	1 mg s.d. iv	72	1.75	2.05	0.85	0.99	1.65	0.60	DIG	Ochs 1981 [104]
Mean GMFE (range):			1.15 (1.12–1.17), 2/2 with GMFE ≤ 2			1.66 (-), 1/1 with GMFE ≤ 2				

AUC_{last} : area under the plasma concentration-time curve calculated between the first and last concentration measurement, b.i.d.: twice daily, C_{max} : maximum plasma concentration, DDI: drug-drug interaction, DIG: digoxin, GMFE: geometric mean fold error, obs: observed, po: oral, pred: predicted, q.i.d. four times daily, s.d.: single dose, t_{last} : time of the last concentration measurement, -: not available. If perpetrator or victim drugs were applied in form of salts, the respective dose of base was calculated and incorporated in simulations.

S6.7 Metoprolol

S6.7.1 Clinical Studies

Table S26: Clinical study data used for DD(G)I model development with **metoprolol** as victim

Drug administration		n	Population ^a	Fem. [%]	Age [years]	Weight [kg]	BMI [kg/m ²]	Phenotype	Molecule	Reference
Perpetrator	Metoprolol									
Cimetidine										
800 mg q.d. po	100 mg s.d. po (IR)	12	European [3]	50	21.8 (19–34)	-	-	-	MET	Chellingsworth 1988 [105]
800 mg q.d. po	100 mg b.i.d. po (IR)	12	European [3]	0	23.2 (19–32)	-	-	-	MET	Chellingsworth 1988 [105]
800 mg q.d. po	100 mg b.i.d. po (IR)	12	European [3]	0	25 (20–33)	71 (63–84)	180 (171–191) ^b	-	MET	Toon 1988 [106]
200/400 mg q.i.d. po	100 mg b.i.d. po (IR)	6	European [3]	0	23.6±1.9	68.7±5.1	-	-	MET	Kirch 1982 [107]
Paroxetine										
10 mg b.i.d. po	50 mg s.d. po (IR)	10	American [7]	0	28±10	81.6±9.9	179.0±6.0 ^b	NM	MET	Stout 2011 [108]
10 mg b.i.d. po	100 mg s.d. po (ER)	10	American [7]	0	28±10	81.6±9.9	179.0±6.0 ^b	NM	MET	Stout 2011 [108]
20 mg q.d. po	100 mg s.d. po (IR)	12	American [7]	27	(21–45)	-	-	NM	RME, SME	Parker 2011 [109]
20 mg q.d. po	100 mg b.i.d. po (IR)	12	American [7]	27	(21–45)	-	-	NM	RME, SME	Parker 2011 [109]
20 mg q.d. po	200 mg s.d. po (ER)	12	American [7]	27	(21–45)	-	-	NM	RME, SME	Parker 2011 [109]
10 mg b.i.d. po	100 mg s.d. po (IR)	8	European [3]	0	(20–29)	-	-	-	RME, SME	Hemeryck 2000 [110]
Quinidine										
50 mg s.d. po	20 mg s.d. iv	3	European [3]	0	(22–34)	(58–80)	-	PM	MET	Leemann 1993 [82]
50 mg s.d. po	20 mg s.d. iv	4	European [3]	0	(22–34)	(58–80)	-	NM	MET	Leemann 1993 [82]
250 mg b.i.d. po	20 mg s.d. iv	3	European [3]	0	(22–34)	(58–80)	-	PM	MET	Leemann 1993 [82]
250 mg b.i.d. po	20 mg s.d. iv	4	European [3]	0	(22–34)	(58–80)	-	NM	MET	Leemann 1993 [82]
100 mg q.d. po	200 mg s.d. po	10	American [7]	0	28.9 (24–40)	85.2	-	NM	RME, SME	Johnson 1996 [111]
100 mg q.d. po	200 mg s.d. po	10	American [7]	0	28.5 (24–36)	82.2	-	NM	RME, SME	Johnson 1996 [111]
Rifampicin										
600 mg q.d. po	100 mg s.d. po	12	European [3]	0	28 (21–35)	71 (62–82)	-	-	MET	Bennett 1982 [112]

b.i.d.: twice daily, BMI: body mass index, DD(G)I: drug-drug(-gene) interaction, ER: extended release formulation, fem: females, IR: immediate release formulation, iv: intravenous, MET: metoprolol, n: number of study participants, NM: CYP2D6 normal metabolizer, PM: CYP2D6 poor metabolizer, po: oral, q.d.: once daily, q.i.d.: four times daily, RME: R-metoprolol, s.d: single dose, SME: S-metoprolol, -: not available. Values are given as mean (range). If perpetrator or victim drugs were applied in form of salts, the respective dose of base was calculated and incorporated in simulations.

^a Population used in simulations. ^b Height of subjects [cm].

S6.7.2 Plasma Concentration-Time Profiles (Semilogarithmic Representation)

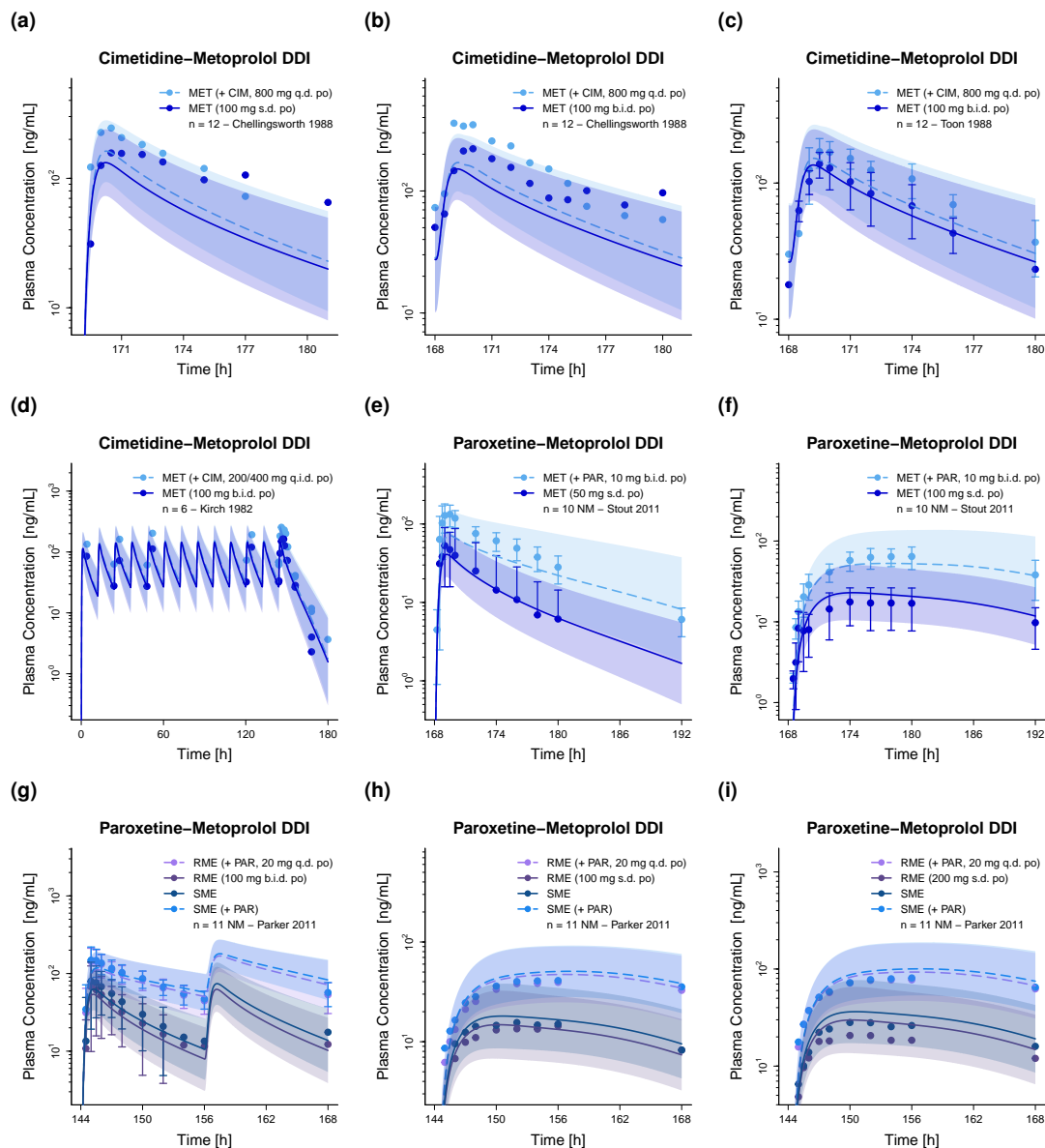


Figure S46: Predicted compared to observed plasma concentration-time profiles of metoprolol alone (solid line) and after pretreatment and/or concomitant administration (dashed line) of (a–d) cimetidine (e–i) paroxetine (semilogarithmic representation). Population predicted (1000 individuals) geometric means are shown as lines, corresponding geometric standard deviations as shaded areas and observed data as dots (\pm standard deviation, if reported) [105–109]. b.i.d.: twice daily, CIM: cimetidine, DDI: drug-drug interaction, MET: metoprolol, n: number of study participants, NM: CYP2D6 normal metabolizer, PAR: paroxetine, po: oral, q.d.: once daily, RME: R-metoprolol, s.d.: single dose, SME: S-metoprolol.

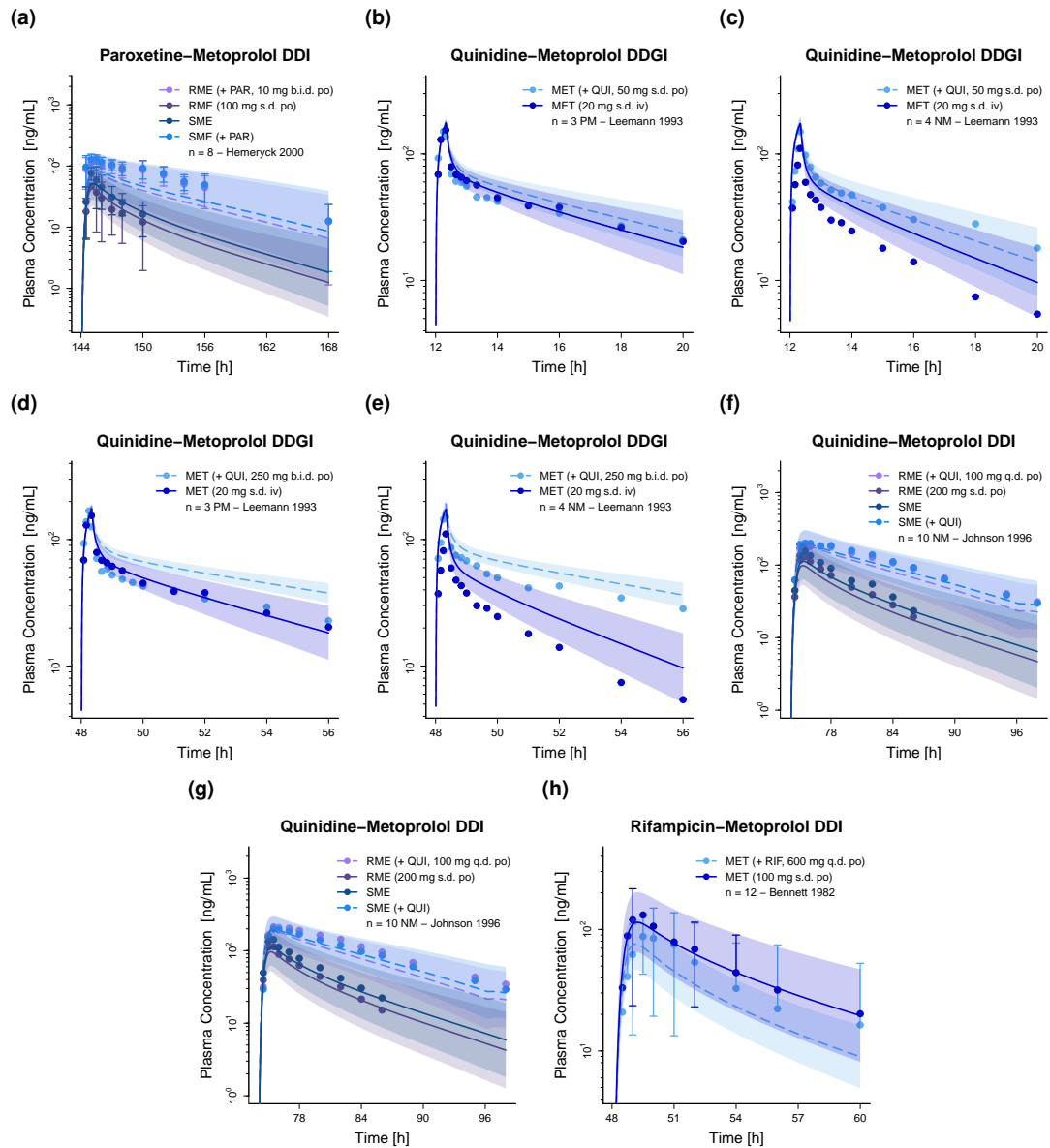


Figure S47: Predicted compared to observed plasma concentration-time profiles of metoprolol alone (solid line) and after pretreatment and/or concomitant administration (dashed line) of (a) paroxetine, (b–g) quinidine and (h) rifampicin (semilogarithmic representation). Population predicted (1000 individuals) geometric means are shown as lines, corresponding geometric standard deviations as shaded areas and observed data as dots (\pm standard deviation, if reported) [82, 110–112]. b.i.d.: twice daily, DD(G)I: drug-drug(-gene) interaction, iv: intravenous, MET: metoprolol, n: number of study participants, NM: CYP2D6 normal metabolizer, PAR: paroxetine, po: oral, q.d.: once daily, QUI: quinidine, RIF: rifampicin, RME: R-metoprolol, s.d.: single dose, SME: S-metoprolol.

S6.7.3 Plasma Concentration-Time Profiles (Linear Representation)

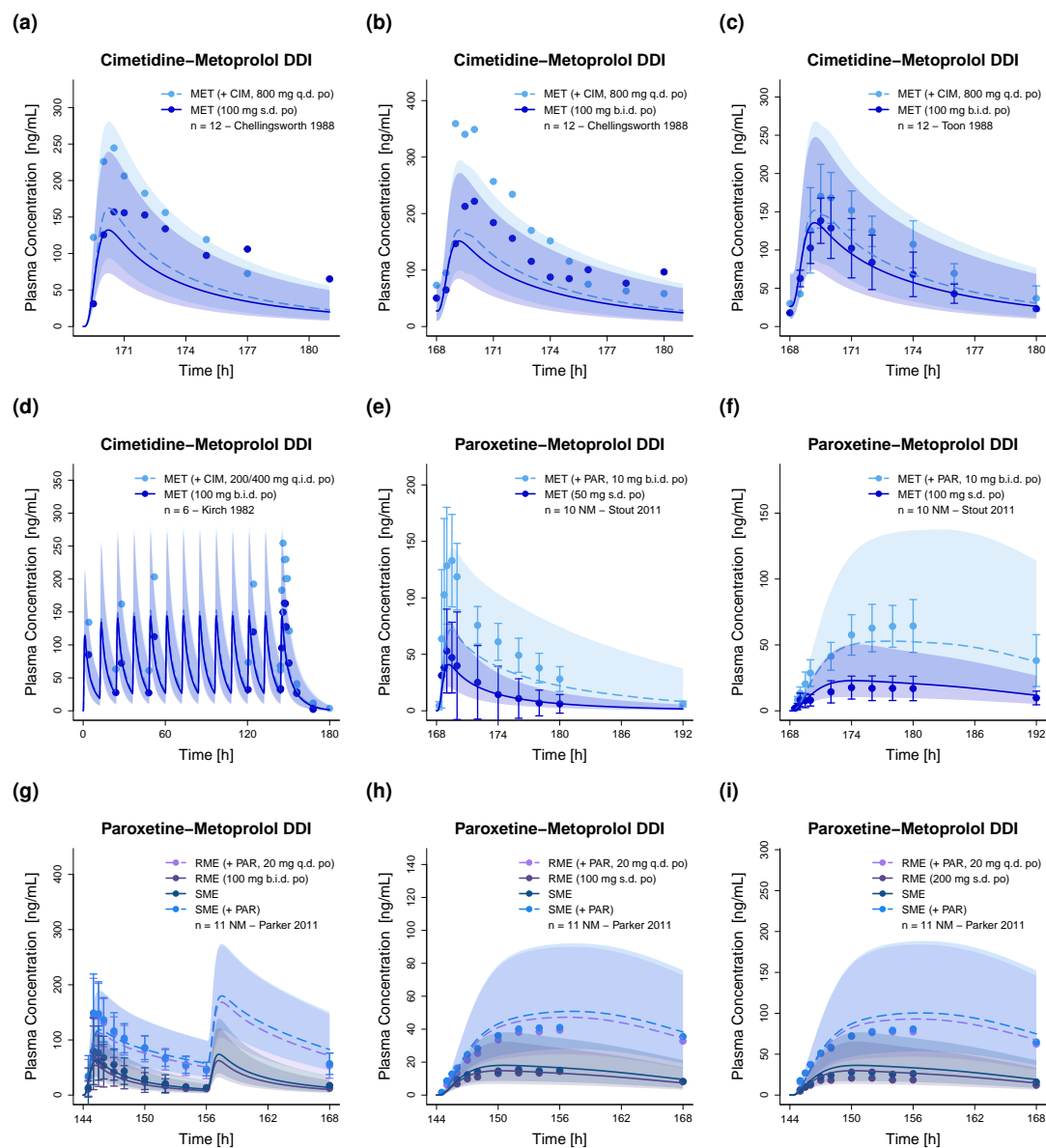


Figure S48: Predicted compared to observed plasma concentration-time profiles of metoprolol alone (solid line) and after pretreatment and/or concomitant administration (dashed line) of (a–d) cimetidine (e–i) paroxetine (linear representation). Population predicted (10000 individuals) geometric means are shown as lines, corresponding geometric standard deviations as shaded areas and observed data as dots (\pm standard deviation, if reported) [105–109]. b.i.d.: twice daily, CIM: cimetidine, DDI: drug-drug interaction, MET: metoprolol, n: number of study participants, NM: CYP2D6 normal metabolizer, PAR: paroxetine, po: oral, q.d.: once daily, RME: R-metoprolol, s.d.: single dose, SME: S-metoprolol.

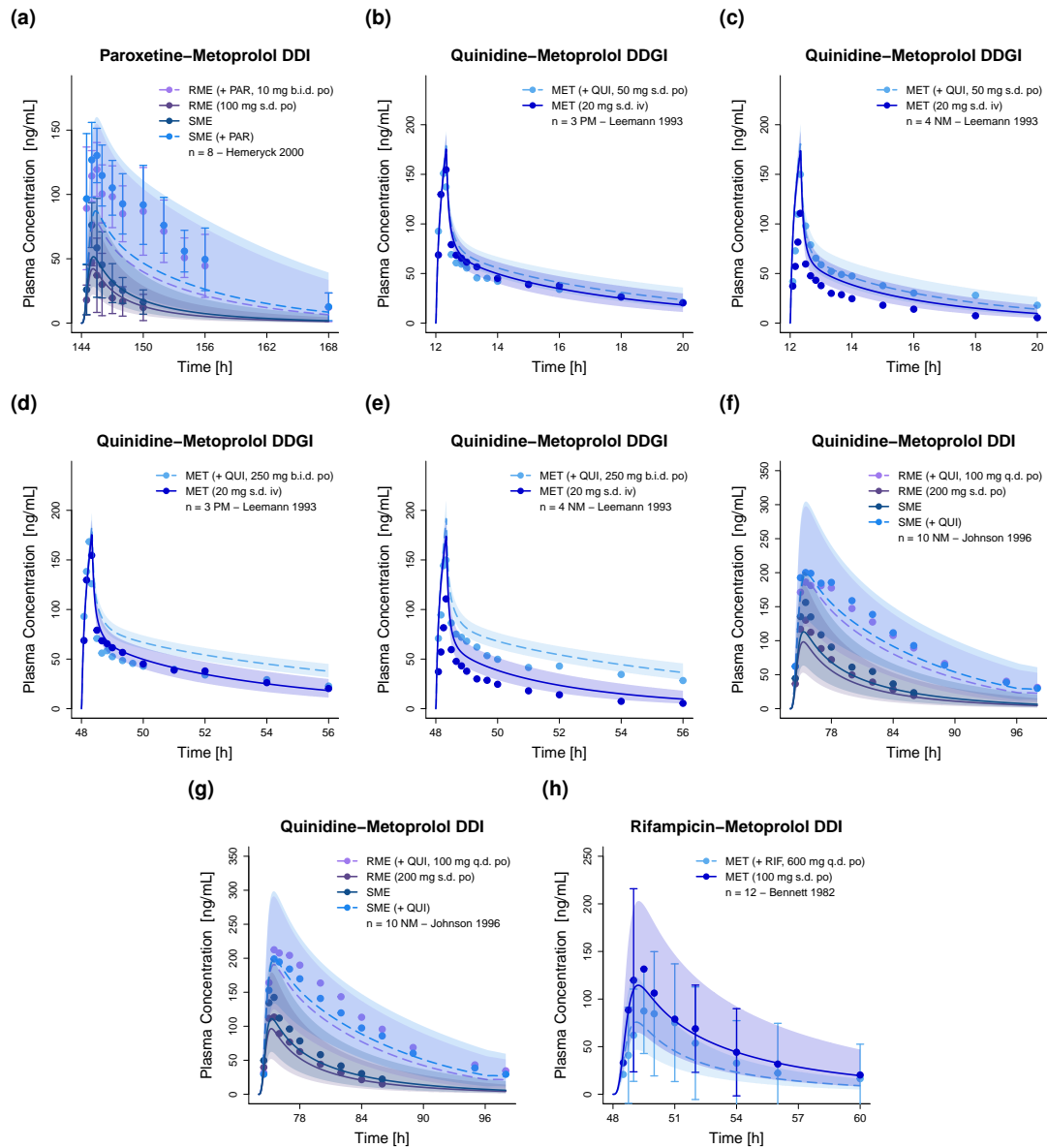


Figure S49: Predicted compared to observed plasma concentration-time profiles of metoprolol alone (solid line) and after pretreatment and/or concomitant administration (dashed line) of (a) paroxetine, (b–g) quinidine and (h) rifampicin (linear representation). Population predicted (1000 individuals) geometric means are shown as lines, corresponding geometric standard deviations as shaded areas and observed data as dots (\pm standard deviation, if reported) [82, 110–112]. b.i.d.: twice daily, DD(G)I: drug-drug(-gene) interaction, iv: intravenous, MET: metoprolol, n: number of study participants, NM: CYP2D6 normal metabolizer, PAR: paroxetine, po: oral, q.d.: once daily, QUI: quinidine, RIF: rifampicin, RME: R-metoprolol, s.d.: single dose, SME: S-metoprolol.

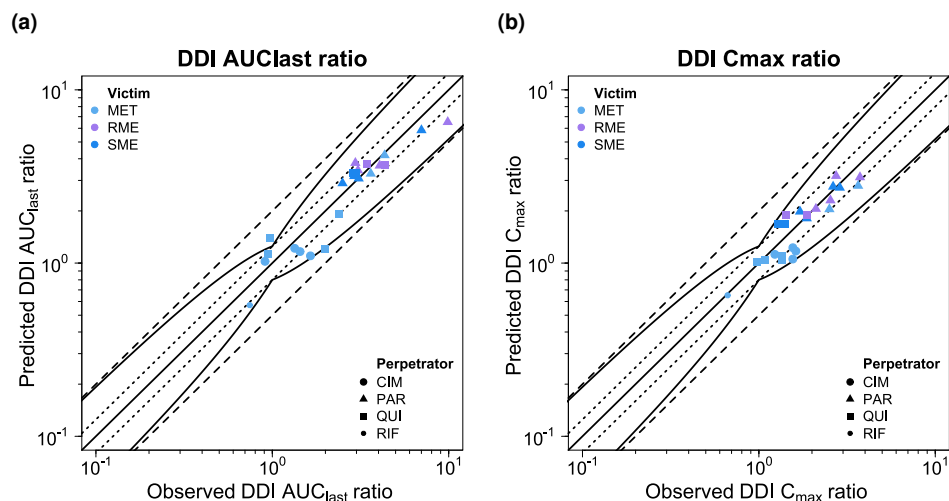
S6.7.4 DDI AUC_{last} and C_{max} Ratios

Figure S50: Goodness-of-fit plots comparing predicted and observed DDI AUC_{last} and C_{max} ratios for victim drug metoprolol. The solid line marks the line of identity. Dotted lines indicate 1.25-fold, dashed lines indicate 2-fold deviation. Prediction success limits proposed by Guest et al. [2] are shown as curved lines (including 20% variability). AUC_{last} : area under the plasma concentration-time curve calculated between the first and last concentration measurement, CIM: cimetidine, C_{max} : maximum plasma concentration, MET: metoprolol racemate, RME: (*R*-metoprolol, SME: (*S*-metoprolol, PAR: paroxetine, QUI: quinidine.

S6.7.5 Geometric Mean Fold Errors of Predicted DDI AUC_{last} and C_{max} RatiosTable S27: Predicted and observed DDI AUC_{last} and C_{max} ratios involving **metoprolol** as victim drug

Drug administration			DDI AUC _{last} ratio			DDI C _{max} ratio			Phenotype	Molecule	Reference
Perpetrator	Metoprolol	t _{last} [h]	Pred	Obs	Pred/Obs	Pred	Obs	Pred/Obs			
Cimetidine											
800 mg q.d. po	100 mg s.d. po	12	1.02	0.91	1.13	1.23	1.56	0.79		MET	Chellingsworth 1988 [105]
800 mg q.d. po	100 mg b.i.d. po	12	1.22	1.34	0.91	1.17	1.62	0.72		MET	Chellingsworth 1988 [105]
800 mg q.d. po	100 mg b.i.d. po	12	1.16	1.44	0.81	1.12	1.23	0.91	-	MET	Toon 1988 [106]
200/400 mg q.i.d. po	100 mg b.i.d. po	36	1.10	1.64	0.67	1.05	1.56	0.68	-	MET	Kirch 1982 [107]
Mean GMFE (range):			1.24 (1.10–1.49), 4/4 with GMFE ≤ 2			1.31 (1.10–1.48), 4/4 with GMFE ≤ 2					
Paroxetine											
10 mg b.i.d. po	50 mg s.d. po	24	4.20	4.33	0.97	2.05	2.51	0.81	NM	MET	Stout 2011 [108]
10 mg b.i.d. po	100 mg s.d. po	24	3.28	3.62	0.91	2.79	3.65	0.76	NM	MET	Stout 2011 [108]
20 mg q.d. po	100 mg s.d. po	24	3.79	2.96	1.28	3.18	2.74	1.16	NM	RME	Parker 2011 [109]
20 mg q.d. po	100 mg s.d. po	24	3.18	2.91	1.09	2.76	2.64	1.05	NM	SME	Parker 2011 [109]
20 mg q.d. po	100 mg b.i.d. po	12	3.43	3.06	1.12	2.06	2.11	0.98	NM	RME	Parker 2011 [109]
20 mg q.d. po	100 mg b.i.d. po	12	2.89	2.50	1.16	1.81	1.87	0.97	NM	SME	Parker 2011 [109]
20 mg q.d. po	200 mg s.d. po	24	3.65	4.06	0.90	3.13	3.74	0.84	NM	RME	Parker 2011 [109]
20 mg q.d. po	200 mg s.d. po	24	3.08	3.09	1.00	2.72	2.88	0.95	NM	SME	Parker 2011 [109]
10 mg b.i.d. po	100 mg s.d. po	24	6.52	9.88	0.66	2.30	2.55	0.90	-	RME	Hemeryck 2000 [110]
10 mg b.i.d. po	100 mg s.d. po	24	5.85	7.01	0.83	1.98	1.71	1.16	-	SME	Hemeryck 2000 [110]
Mean GMFE (range):			1.16 (1.00–1.51), 10/10 with GMFE ≤ 2			1.13 (1.02–1.31), 10/10 with GMFE ≤ 2					
Quinidine											
50 mg s.d. po	20 mg s.d. iv	8	1.13	0.95	1.19	1.02	0.98	1.04	PM	MET	Leemann 1993 [82]
50 mg s.d. po	20 mg s.d. iv	8	1.20	2.00	0.60	1.04	1.35	0.77	NM	MET	Leemann 1993 [82]
250 mg b.i.d. po	20 mg s.d. iv	8	1.39	0.97	1.43	1.04	1.09	0.95	PM	MET	Leemann 1993 [82]
250 mg b.i.d. po	20 mg s.d. iv	8	1.91	2.38	0.80	1.09	1.35	0.81	NM	MET	Leemann 1993 [82]
100 mg q.d. po	200 mg s.d. po	24	3.71	3.44	1.08	1.88	1.43	1.32	NM	RME	Johnson 1996 [111]
100 mg q.d. po	200 mg s.d. po	24	3.33	2.87	1.16	1.69	1.28	1.32	NM	SME	Johnson 1996 [111]
100 mg q.d. po	200 mg s.d. po	24	3.69	4.35	0.85	1.89	1.87	1.01	NM	RME	Johnson 1996 [111]
100 mg q.d. po	200 mg s.d. po	24	3.31	2.99	1.11	1.69	1.40	1.21	NM	SME	Johnson 1996 [111]
Mean GMFE (range):			1.27 (1.08–1.66), 8/8 with GMFE ≤ 2			1.19 (1.01–1.32), 8/8 with GMFE ≤ 2					
Rifampicin											
600 mg q.d. po	100 mg s.d. po	12	0.57	0.74	0.77	0.65	0.66	0.98	-	MET	Bennett 1982 [112]
Mean GMFE (range):			1.30 (-), 1/1 with GMFE ≤ 2			1.02 (-), 1/1 with GMFE ≤ 2					
Overall GMFE (range):			1.22 (1.00–1.66), 23/23 with GMFE ≤ 2			1.18 (1.01–1.48), 23/23 with GMFE ≤ 2					

AUC_{last} : area under the plasma concentration-time curve calculated between the first and last concentration measurement, b.i.d.: twice daily, C_{max} : maximum plasma concentration, DDI: drug-drug interaction, GMFE: geometric mean fold error, iv: intravenous, MET: metoprolol, NM: CYP2D6 normal metabolizer, obs: observed, PM: CYP2D6 poor metabolizer, po: oral, pred: predicted, q.d.: once daily, RME: R-metoprolol, s.d.: single dose, SME: S-metoprolol, t_{last} : time of the last concentration measurement, -: not available. If perpetrator or victim drugs were applied in form of salts, the respective dose of base was calculated and incorporated in simulations.

S6.8 Mexiletine

S6.8.1 Clinical Studies

Table S28: Clinical study data used for DD(G)I model development with **mexiletine** as victim

Drug administration		n	Population ^a	Fem. [%]	Age [years]	Weight [kg]	BMI [kg/m ²]	Phenotype	Molecule	Reference
Perpetrator	Mexiletine									
Quinidine										
50 mg q.i.d. po	200 mg s.d. po	4	American [7]	7	26	74	-	PM	MEX	Abolfathi 1993 [90]
50 mg q.i.d. po	200 mg s.d. po	10	American [7]	7	26	74	-	NM	MEX	Abolfathi 1993 [90]

BMI: body mass index, DD(G)I: drug-drug(-gene) interaction, fem: females, n: number of study participants, MEX: mexiletine, NM: CYP2D6 normal metabolizer, PM: CYP2D6 poor metabolizer, po: oral, q.i.d.: four times daily, s.d: single dose, -: not available. Values are given as mean (range). If perpetrator or victim drugs were applied in form of salts, the respective dose of base was calculated and incorporated in simulations. ^a Population used in simulations.

S6.8.2 Plasma Concentration-Time Profiles (Semilogarithmic Representation)

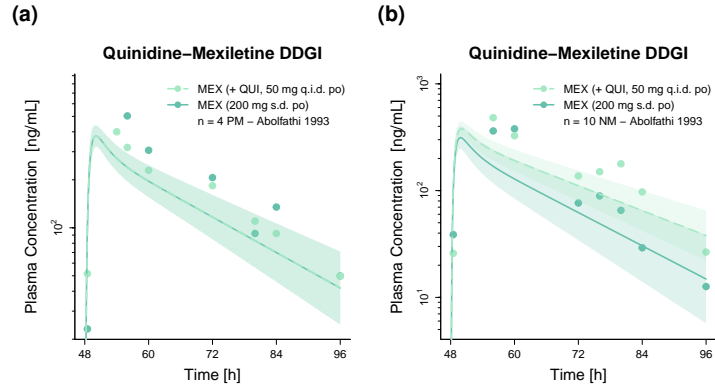


Figure S51: Predicted compared to observed plasma concentration-time profiles of mexiletine alone (solid line) and after pretreatment and/or concomitant administration (dashed line) of quinidine (semilogarithmic representation). Population predicted (1000 individuals) geometric means are shown as lines, corresponding geometric standard deviations as shaded areas and observed data as dots [90]. DDGI: drug-drug-gene interaction, MEX: mexiletine, n: number of study participants, NM: CYP2D6 normal metabolizer, PM: CYP2D6 poor metabolizer, po: oral, q.i.d.: four times daily, QUI: quinidine, s.d.: single dose.

S6.8.3 Plasma Concentration-Time Profiles (Linear Representation)

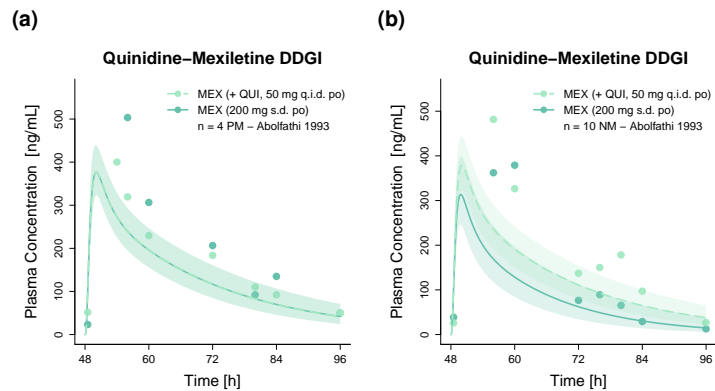


Figure S52: Predicted compared to observed plasma concentration-time profiles of mexiletine alone (solid line) and after pretreatment and/or concomitant administration (dashed line) of quinidine (linear representation). Population predicted (1000 individuals) geometric means are shown as lines, corresponding geometric standard deviations as shaded areas and observed data as dots [90]. DDGI: drug-drug-gene interaction, MEX: mexiletine, n: number of study participants, NM: CYP2D6 normal metabolizer, PM: CYP2D6 poor metabolizer, po: oral, q.i.d.: four times daily, QUI: quinidine, s.d.: single dose.

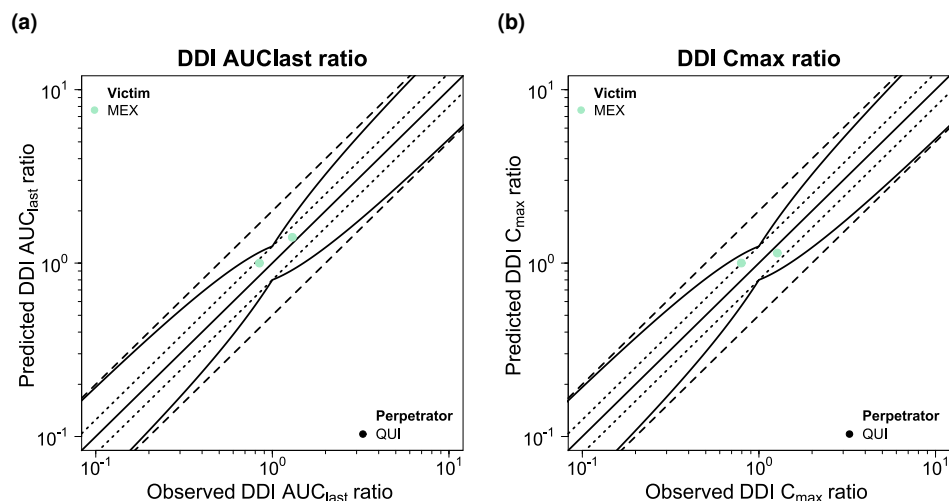
S6.8.4 DDI AUC_{last} and C_{max} Ratios

Figure S53: Goodness-of-fit plots comparing predicted and observed DDI AUC_{last} and C_{max} ratios for victim drug mexiletine. The solid line marks the line of identity. Dotted lines indicate 1.25-fold, dashed lines indicate 2-fold deviation. Prediction success limits proposed by Guest et al. [2] are shown as curved lines (including 20% variability). AUC_{last} : area under the plasma concentration-time curve calculated between the first and last concentration measurement, C_{max} : maximum plasma concentration, MEX: mexiletine, QUI: quinidine.

S6.8.5 Geometric Mean Fold Errors of Predicted DDI AUC_{last} and C_{max} Ratios

Table S29: Predicted and observed DDI AUC_{last} and C_{max} ratios involving **mexiletine** as victim drug

Drug administration			DDI AUC _{last} ratio			DDI C _{max} ratio			Phenotype	Molecule	Reference
Perpetrator	Mexiletine	t _{last} [h]	Pred	Obs	Pred/Obs	Pred	Obs	Pred/Obs			
Quinidine											
50 mg q.i.d. po	200 mg s.d. po	48	1.00	0.85	1.18	1.00	0.79	1.26	PM	MEX	Abolfathi 1993 [90]
50 mg q.i.d. po	200 mg s.d. po	48	1.41	1.30	1.08	1.14	1.27	0.90	NM	MEX	Abolfathi 1993 [90]
Overall GMFE (range):			1.13 (1.08–1.18), 2/2 with GMFE ≤ 2			1.19 (1.11– 1.26), 2/2 with GMFE ≤ 2					

AUC_{last} : area under the plasma concentration-time curve calculated between the first and last concentration measurement, DDI: drug-drug interaction, GMFE: geometric mean fold error, MEX: mexiletine, NM: CYP2D6 normal metabolizer, obs: observed, PM: CYP2D6 poor metabolizer, po: oral, pred: predicted, q.i.d. four times daily, q.d.: once daily, s.d.: single dose, t_{last} : time of the last concentration measurement. If perpetrator or victim drugs were applied in form of salts, the respective dose of base was calculated and incorporated in simulations.

S6.9 Midazolam

S6.9.1 Clinical Studies

Table S30: Clinical study data used for DDI model development with **midazolam** as victim

Drug administration		n	Population ^a	Fem. [%]	Age [years]	Weight [kg]	BMI [kg/m ²]	Phenotype	Molecule	Reference
Perpetrator	Midazolam									
<i>Atomoxetine</i>										
60 mg b.i.d. po	5 mg s.d. po	8	American [7]	50	27 (20–35)	-	(18.1–25.1)	PM	MID	Sauer 2004 [17]

b.i.d.: twice daily, BMI: body mass index, DDI: drug-drug interaction, fem: females, n: number of study participants, PM: CYP2D6 poor metabolizer, po: oral, MID: midazolam -: not available. Values are given as mean (range). If perpetrator or victim drugs were applied in form of salts, the respective dose of base was calculated and incorporated in simulations. ^a Population used in simulations.

S6.9.2 Plasma Concentration-Time Profiles (Semilogarithmic Representation)

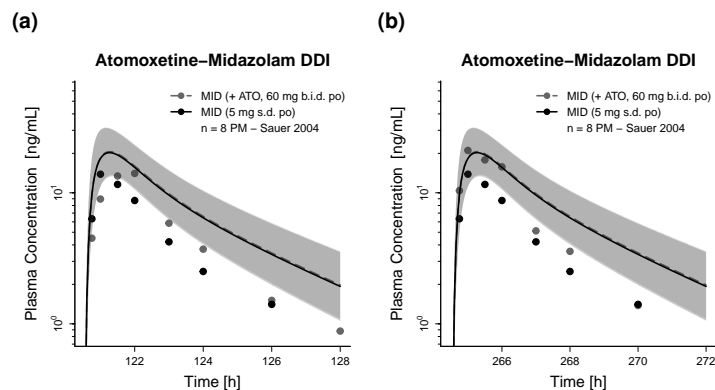


Figure S54: Predicted compared to observed plasma concentration-time profiles of midazolam alone (solid line) and after pretreatment and/or concomitant administration (dashed line) of atomoxetine (semilogarithmic representation). Population predicted (1000 individuals) geometric means are shown as lines, corresponding geometric standard deviations as shaded areas and observed data as dots [17]. ATO: atomoxetine, b.i.d.: twice daily, DDI: drug-drug interaction, MID: midazolam, n: number of study participants, PM: CYP2D6 poor metabolizer, po: oral, s.d.: single dose.

S6.9.3 Plasma Concentration-Time Profiles (Linear Representation)

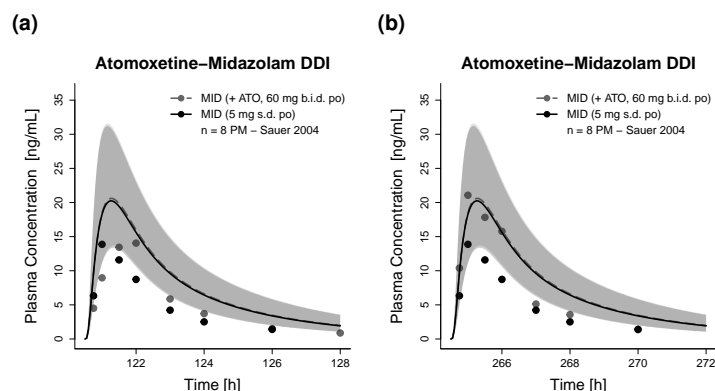


Figure S55: Predicted compared to observed plasma concentration-time profiles of midazolam alone (solid line) and after pretreatment and/or concomitant administration (dashed line) of atomoxetine (linear representation). Population predicted (1000 individuals) geometric means are shown as lines, corresponding geometric standard deviations as shaded areas and observed data as dots [17]. ATO: atomoxetine, b.i.d.: twice daily, DDI: drug-drug interaction, MID: midazolam, n: number of study participants, PM: CYP2D6 poor metabolizer, po: oral, s.d.: single dose.

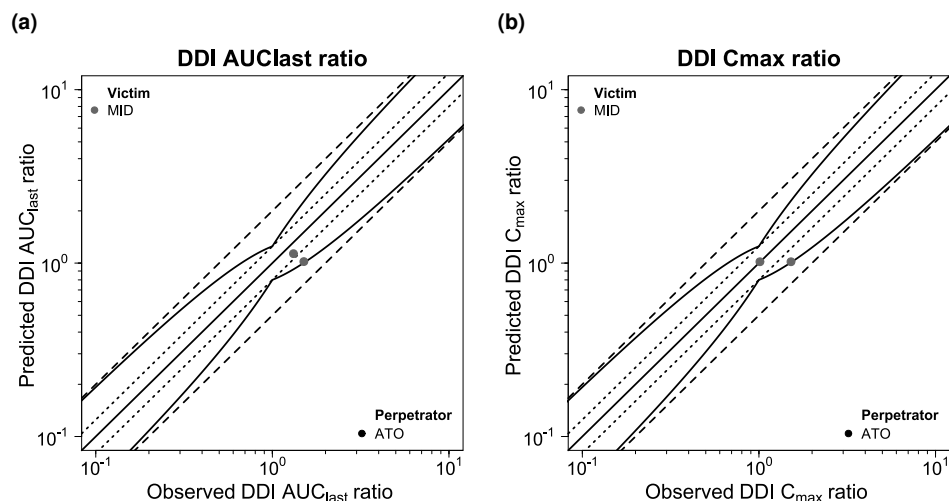
S6.9.4 DDI AUC_{last} and C_{max} Ratios

Figure S56: Goodness-of-fit plots comparing predicted and observed DDI AUC_{last} and C_{max} ratios for victim drug midazolam. The solid line marks the line of identity. Dotted lines indicate 1.25-fold, dashed lines indicate 2-fold deviation. Prediction success limits proposed by Guest et al. [2] are shown as curved lines (including 20% variability). ATO: atomoxetine, AUC_{last} : area under the plasma concentration-time curve calculated between the first and last concentration measurement, C_{max} : maximum plasma concentration, MID: midazolam.

S6.9.5 Geometric Mean Fold Errors of Predicted DDI AUC_{last} and C_{max} Ratios

Table S31: Predicted and observed DDI AUC_{last} and C_{max} ratios involving **midazolam** as victim drug

Drug administration			DDI AUC _{last} ratio			DDI C _{max} ratio			Phenotype	Molecule	Reference
Perpetrator	Midazolam	t _{last} [h]	Pred	Obs	Pred/Obs	Pred	Obs	Pred/Obs			
Atomoxetine											
60 mg b.i.d. po	5 mg s.d. po (D6)	5	1.13	1.32	0.86	1.02	1.01	1.00	PM	MID	Sauer 2004 [17]
60 mg b.i.d. po	5 mg s.d. po (D12)	5	1.02	1.51	0.68	1.02	1.52	0.67	PM	MID	Sauer 2004 [17]
Overall GMFE (range):			1.39 (1.31–1.48), 2/2 with GMFE ≤ 2			1.36 (1.22–1.49), 2/2 with GMFE ≤ 2					

AUC_{last} : area under the plasma concentration-time curve calculated between the first and last concentration measurement, b.i.d.: twice daily, C_{max} : maximum plasma concentration, D: day, DDI: drug-drug interaction, GMFE: geometric mean fold error, MID: midazolam, obs: observed, PM: CYP2D6 poor metabolizer, po: oral, pred: predicted, s.d.: single dose, t_{last} : time of the last concentration measurement. If perpetrator or victim drugs were applied in form of salts, the respective dose of base was calculated and incorporated in simulations.

S6.10 Paroxetine

S6.10.1 Clinical Studies

Table S32: Clinical study data used for DDI model development with **paroxetine** as victim

Drug administration		n	Population ^a	Fem. [%]	Age [years]	Weight [kg]	BMI [kg/m ²]	Phenotype	Molecule	Reference
Perpetrator	Paroxetine									
<i>Itraconazole</i>										
100 mg b.i.d. po	20 mg s.d. po	13	Japanese [113]	77	24.2±3.5	57.3±7.2	-	-	PAR	Yasui-Furukori 2007 [114]
<i>QUI/DEX</i>										
30 mg b.i.d. po	20 mg q.d. po	14	American [7]	14.3	33.6 (19–55)	75.3	25.3	NM	PAR	Schoedel 2012 [101]

b.i.d.: twice daily, BMI: body mass index, DDI: drug-drug interaction, DEX: dextromethorphan, fem: females, n: number of study participants, NM: CYP2D6 normal metabolizer, PAR: paroxetine, po: oral, q.d.: once daily, QUI: quinidine, s.d: single dose, -: not available. Values are given as mean (range). If perpetrator or victim drugs were applied in form of salts, the respective dose of base was calculated and incorporated in simulations. ^a Population used in simulations.

S6.10.2 Plasma Concentration-Time Profiles (Semilogarithmic Representation)

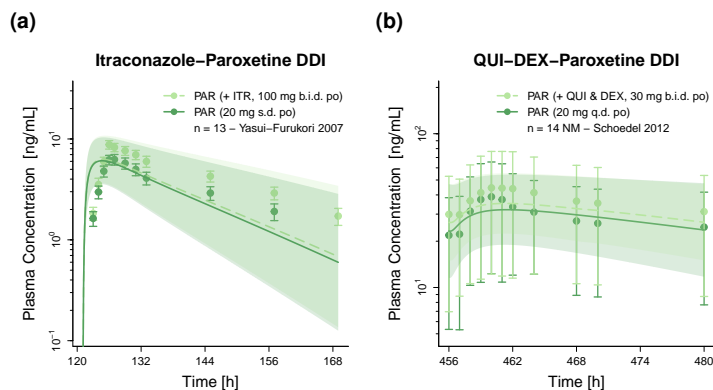


Figure S57: Predicted compared to observed plasma concentration-time profiles of paroxetine alone (solid line) and after pretreatment and/or concomitant administration (dashed line) of (a) itraconazole and (b) quinidine plus dextromethorphan (semilogarithmic representation). Population predicted (1000 individuals) geometric means are shown as lines, corresponding geometric standard deviations as shaded areas and observed data as dots (\pm standard deviation, if reported) [101, 114]. b.i.d.: twice daily, DDI: drug-drug interaction, DEX: dextromethorphan, ITR: itraconazole, n: number of study participants, PAR: paroxetine, po: oral, q.d.: once daily, QUI: quinidine, s.d.: single dose.

S6.10.3 Plasma Concentration-Time Profiles (Linear Representation)

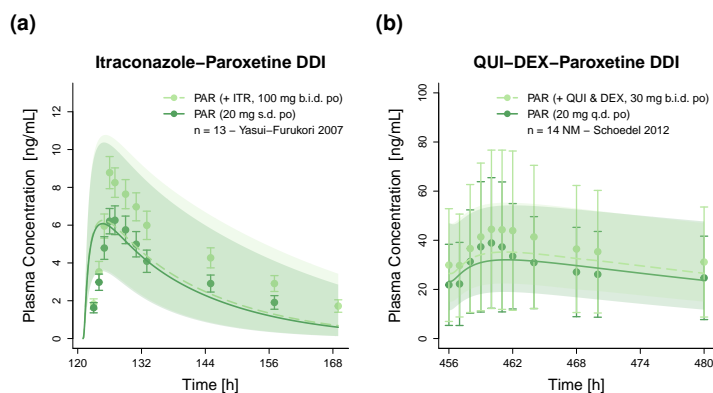


Figure S58: Predicted compared to observed plasma concentration-time profiles of paroxetine alone (solid line) and after pretreatment and/or concomitant administration (dashed line) of (a) itraconazole and (b) quinidine plus dextromethorphan (linear representation). Population predicted (1000 individuals) geometric means are shown as lines, corresponding geometric standard deviations as shaded areas and observed data as dots (\pm standard deviation, if reported) [101, 114]. b.i.d.: twice daily, DDI: drug-drug interaction, DEX: dextromethorphan, ITR: itraconazole, n: number of study participants, PAR: paroxetine, po: oral, q.d.: once daily, QUI: quinidine, s.d.: single dose.

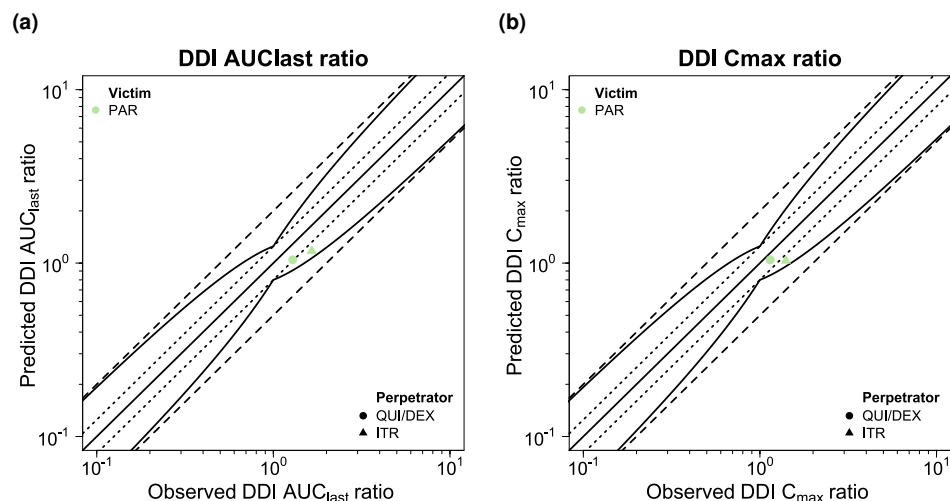
S6.10.4 DDI AUC_{last} and C_{max} Ratios

Figure S59: Goodness-of-fit plots comparing predicted and observed DDI AUC_{last} and C_{max} ratios for victim drug paroxetine. The solid line marks the line of identity. Dotted lines indicate 1.25-fold, dashed lines indicate 2-fold deviation. Prediction success limits proposed by Guest et al. [2] are shown as curved lines (including 20% variability). AUC_{last} : area under the plasma concentration-time curve calculated between the first and last concentration measurement, C_{max} : maximum plasma concentration, DEX: dextromethorphan, ITR: itraconazole, PAR: paroxetine, QUI: quinidine.

S6.10.5 Geometric Mean Fold Errors of Predicted DDI AUC_{last} and C_{max} Ratios

Table S33: Predicted and observed DDI AUC_{last} and C_{max} ratios involving **paroxetine** as victim drug

Drug administration			DDI AUC _{last} ratio			DDI C _{max} ratio			Phenotype	Molecule	Reference
Perpetrator	Paroxetine	t _{last} [h]	Pred	Obs	Pred/Obs	Pred	Obs	Pred/Obs			
<i>Itraconazole</i>											
100 mg b.i.d. po	20 mg s.d. po	36	1.17	1.65	0.81	1.03	1.40	0.74	-	PAR	Yasui-Furukori 2007 [114]
Mean GMFE (range):			1.41 (-), 1/1 with GMFE ≤ 2			1.36 (-), 1/1 with GMFE ≤ 2					
<i>QUI/DEX</i>											
30 mg b.i.d. po	20 mg q.d. po	24	1.04	1.29	0.81	1.04	1.14	0.91	NM	PAR	Schoedel 2012 [101]
Mean GMFE:			1.23 (-), 1/1 with GMFE ≤ 2			1.10 (-), 1/1 with GMFE ≤ 2					
Overall GMFE (range):			1.32 (1.23–1.41), 2/2 with GMFE ≤ 2			1.23 (1.10–1.36), 2/2 with GMFE ≤ 2					

AUC_{last}: area under the plasma concentration-time curve calculated between the first and last concentration measurement, b.i.d.: twice daily, C_{max}: maximum plasma concentration, DDI: drug-drug interaction, DEX: dextromethorphan, GMFE: geometric mean fold error, obs: observed, PAR: paroxetine, po: oral, pred: predicted, q.d.: once daily, QUI: quinidine, s.d.: single dose, t_{last}: time of the last concentration measurement. If perpetrator or victim drugs were applied in form of salts, the respective dose of base was calculated and incorporated in simulations.

S6.11 Quinidine

S6.11.1 Clinical Studies

Table S34: Clinical study data used for DDI model development with **quinidine** as victim

Drug administration		n	Population ^a	Fem. [%]	Age [years]	Weight [kg]	BMI [kg/m ²]	Molecule	Reference
Perpetrator	Quinidine								
Carbamazepine									
200/400 mg b.i.d. po	200 mg s.d. po	10	European [3]	0	(21–26)	(62–85)	(19–26)	QUI, OHQ	Andreasen 2007 [115]
Cimetidine									
300 mg q.d. po	400 mg s.d. po	9	American [7]	0	(21–35)	-	-	QUI	Kolb 1984 [116]
300 mg q.i.d. po	400 mg s.d. po	9	American [7]	0	(21–35)	-	-	QUI	Hardy 1983 [117]
Erythromycin									
250 mg q.i.d. po	200 mg s.d. po	6	European [3]	0	(20–35)	-	-	QUI	Damkier 1999b [118]
Fluvoxamine									
100 mg q.d. po	200 mg s.d. po	6	American [7]	0	-	-	-	QUI, OHQ	Damkier 1999a [122]
Itraconazole									
200 mg q.d. po	100 mg s.d. po	9	European [3]	56	25 (21–32)	64 (41–80)	-	QUI	Kaukonen 1997 [120]
100 mg q.d. po	200 mg s.d. po	6	European [3]	0	(20–35)	-	-	QUI	Damkier 1999b [118]
Omeprazole									
40 mg q.d. po	400 mg s.d. po	8	European [3]	0	(22–29)	(60–94)	-	QUI, OHQ	Ching 1991 [121]
Rifampicin									
600 mg q.d. po	200 mg s.d. po	6	European [3]	0	-	-	-	QUI, OHQ	Damkier 1999 [119]
Verapamil									
80 mg t.i.d. po	400 mg s.d. po	6	European [3]	0	(23–34)	-	-	QUI	Edwards 1987 [123]
120 mg t.i.d. po	400 mg s.d. po	6	European [3]	0	(23–34)	-	-	QUI	Edwards 1987 [123]

b.i.d.: twice daily, BMI: body mass index, DDI: drug-drug interaction, fem: females, n: number of study participants, OHQ: 3-hydroxyquinidine, po: oral, q.d.: once daily, q.i.d.: four times daily, QUI: quinidine, s.d: single dose, t.i.d.: three times daily, -: not available. Values are given as mean (range). If perpetrator or victim drugs were applied in form of salts, the respective dose of base was calculated and incorporated in simulations. ^a Population used in simulations.

S6.11.2 Plasma Concentration-Time Profiles (Semilogarithmic Representation)

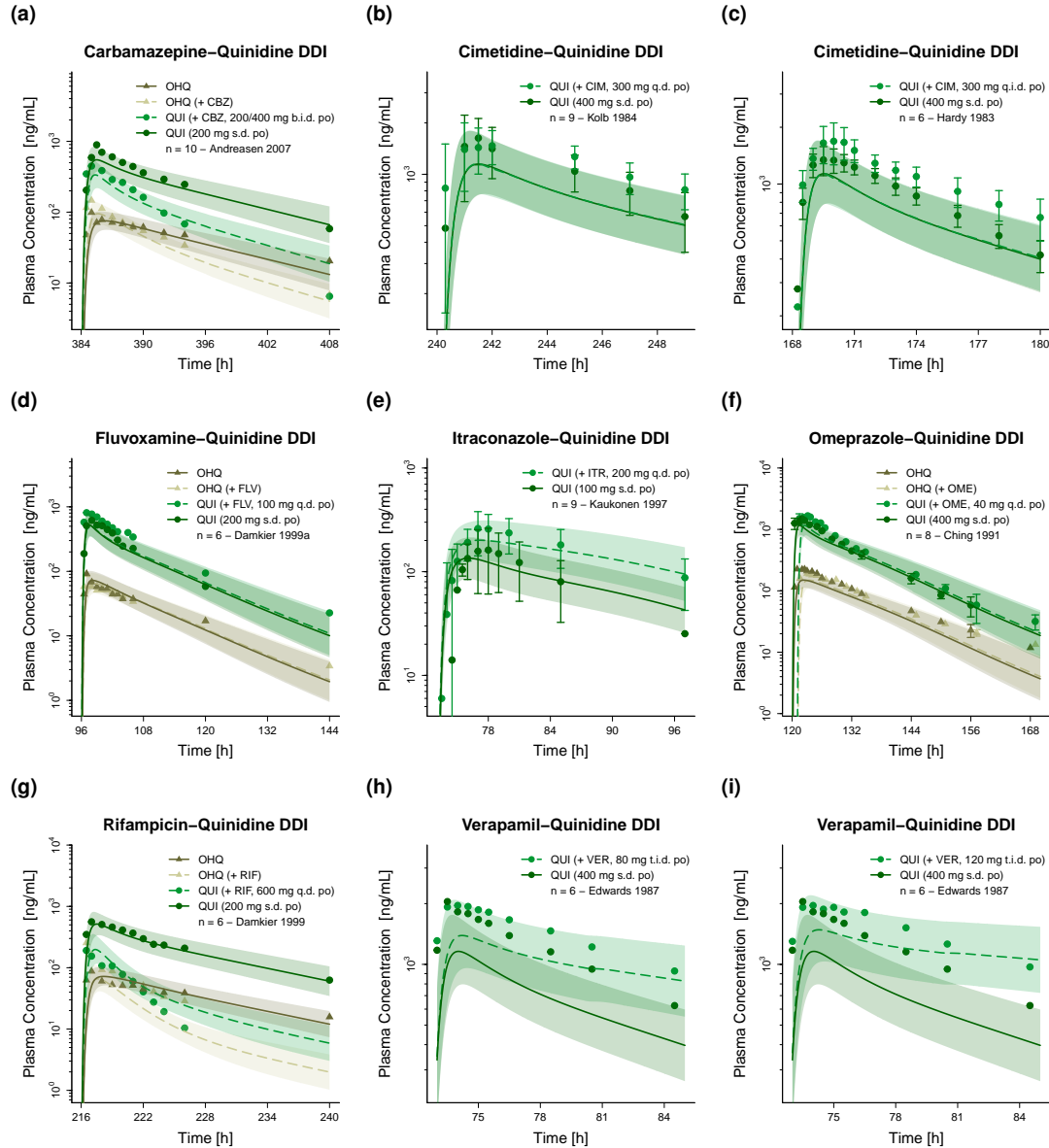


Figure S60: Predicted compared to observed plasma concentration-time profiles of quinidine alone (solid line) and after pretreatment and/or concomitant administration (dashed line) of (a) carbamazepine, (b–c) cimetidine, (d) fluvoxamine, (e) itraconazole, (f) omeprazole, (g) rifampicin and (h–i) verapamil (semilogarithmic representation). Population predicted (1000 individuals) geometric means are shown as lines, corresponding geometric standard deviations as shaded areas and observed data as dots/triangles (\pm standard deviation, if reported) [115–117, 119–123]. b.i.d.: twice daily, CBZ: carbamazepine, CIM: cimetidine, DDI: drug-drug interaction, FLV: fluvoxamine, ITR: itraconazole, n: number of study participants, OHQ: 3-hydroxyquinidine, OME: omeprazole, po: oral, q.d.: once daily, q.i.d.: four times daily, QUI: quinidine, RIF: rifampicin, s.d.: single dose, t.i.d.: three times daily, VER: verapamil.

S6.11.3 Plasma Concentration-Time Profiles (Linear Representation)

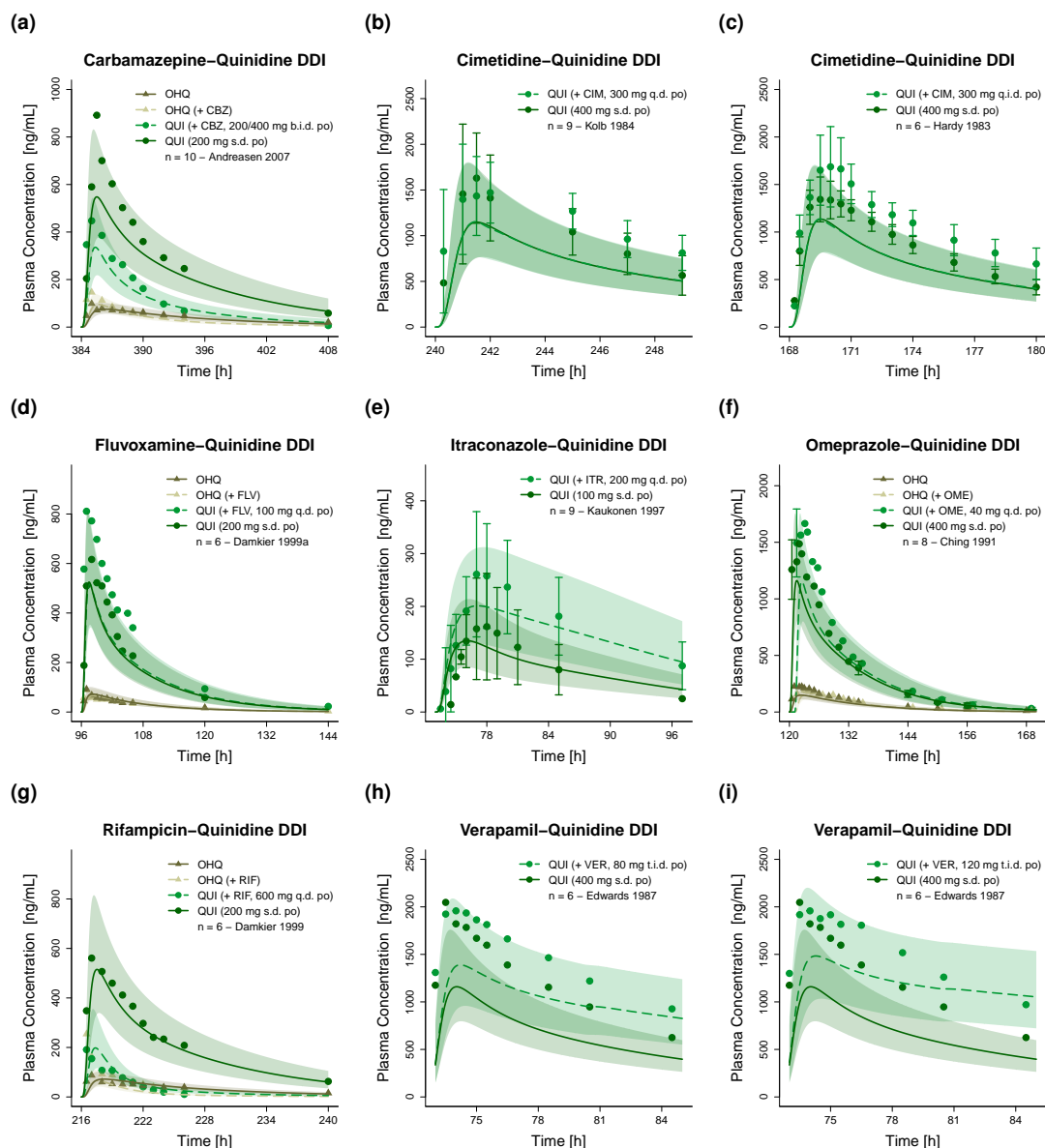


Figure S61: Predicted compared to observed plasma concentration-time profiles of quinidine alone (solid line) and after pretreatment and/or concomitant administration (dashed line) of (a) carbamazepine, (b–c) cimetidine, (d) fluvoxamine, (e) itraconazole, (f) omeprazole, (g) rifampicin and (h–i) verapamil (linear representation). Population predicted (1000 individuals) geometric means are shown as lines, corresponding geometric standard deviations as shaded areas and observed data as dots/triangles (\pm standard deviation, if reported) [115–117, 119–123]. b.i.d.: twice daily, CBZ: carbamazepine, CIM: cimetidine, DDI: drug-drug interaction, FLV: fluvoxamine, ITR: itraconazole, n: number of study participants, OHQ: 3-hydroxyquinidine, OME: omeprazole, po: oral, q.d.: once daily, q.i.d.: four times daily, QUI: quinidine, RIF: rifampicin, s.d.: single dose, t.i.d.: three times daily, VER: verapamil.

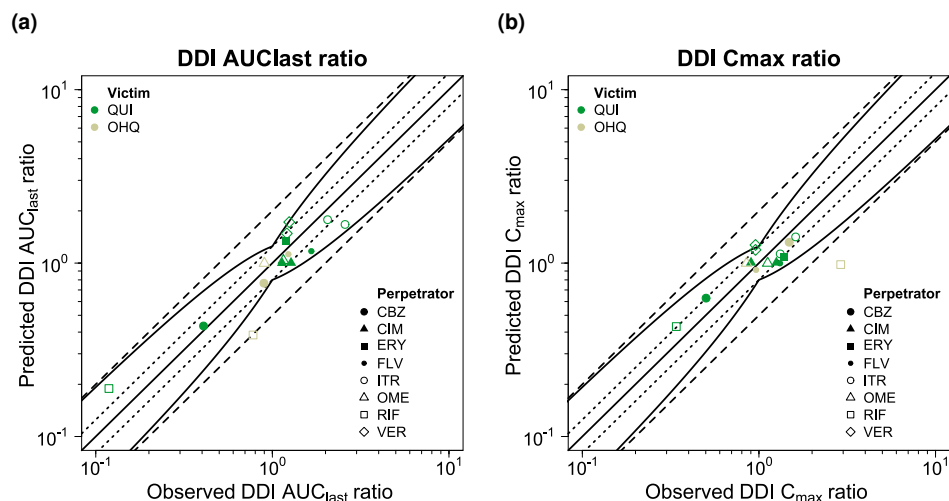
S6.11.4 DDI AUC_{last} and C_{max} Ratios

Figure S62: Goodness-of-fit plots comparing predicted and observed DDI AUC_{last} and C_{max} ratios for victim drug quinidine. The solid line marks the line of identity. Dotted lines indicate 1.25-fold, dashed lines indicate 2-fold deviation. Prediction success limits proposed by Guest et al. [2] are shown as curved lines (including 20% variability). AUC_{last} : area under the plasma concentration-time curve calculated between the first and last concentration measurement, CBZ: carbamazepine, CIM: cimetidine, C_{max} : maximum plasma concentration, ERY: erythromycin, FLV: fluvoxamine, ITR: itraconazole, OHQ: 3-hydroxyquinidine, OME: omeprazole, QUI: quinidine, RIF: rifampicin, VER: verapamil.

S6.11.5 Geometric Mean Fold Errors of Predicted DDI AUC_{last} and C_{max} RatiosTable S35: Predicted and observed DDI AUC_{last} and C_{max} ratios involving **quinidine** as victim drug

Drug administration			DDI AUC_{last} ratio			DDI C_{max} ratio			Molecule	Reference
Perpetrator	Quinidine	t_{last} [h]	Pred	Obs	Pred/Obs	Pred	Obs	Pred/Obs		
Carbamazepine										
200/400 mg b.i.d. po	200 mg s.d. po	24	0.43	0.41	1.06	0.63	0.50	1.25	QUI	Andreasen 2007 [115]
200/400 mg b.i.d. po	200 mg s.d. po	24	0.77	0.90	0.86	1.32	1.48	0.89	OHQ	Andreasen 2007 [115]
Mean GMFE (range):			1.12 (1.06–1.17), 2/2 with GMFE ≤ 2			1.19 (1.12–1.25), 2/2 with GMFE ≤ 2				
Cimetidine										
300 mg q.d. po	400 mg s.d. po	9	1.00	1.13	0.88	1.01	0.90	1.11	QUI	Kolb 1984 [116]
300 mg q.i.d. po	400 mg s.d. po	12	1.00	1.28	0.79	1.01	1.26	0.80	QUI	Hardy 1983 [117]
Mean GMFE (range):			1.20 (1.13–1.27), 2/2 with GMFE ≤ 2			1.18 (1.11–1.25), 2/2 with GMFE ≤ 2				
Erythromycin										
250 mg q.i.d. po	200 mg s.d. po	inf	1.34	1.19	1.13	1.08	1.39	0.78	QUI	Damkier 1999b [118]
Mean GMFE (range):			1.32 (-), 1/1 with GMFE ≤ 2			1.23 (-), 1/1 with GMFE ≤ 2				
Fluvoxamine										
100 mg q.d. po	200 mg s.d. po	48	1.17	1.66	0.70	1.00	1.32	0.76	QUI	Damkier 1999a [122]
100 mg q.d. po	200 mg s.d. po	48	1.12	1.23	0.91	0.91	0.96	0.95	OHQ	Damkier 1999a [122]
Mean GMFE (range):			1.26 (1.09–1.42), 2/2 with GMFE ≤ 2			1.19 (1.05–1.32), 2/2 with GMFE ≤ 2				
Itraconazole										
200 mg q.d. po	100 mg s.d. po	24	1.78	2.05	0.87	1.42	1.61	0.88	QUI	Kaukonen 1997 [120]
100 mg q.d. po	200 mg s.d. po	inf	1.67	2.58	0.65	1.13	1.32	0.86	QUI	Damkier 1999b [118]
Mean GMFE:			1.24 (1.15–1.32), 2/2 with GMFE ≤ 2			1.18 (1.14–1.23), 2/2 with GMFE ≤ 2				
Omeprazole										
40 mg q.d. po	400 mg s.d. po	48	1.04	1.15	0.90	1.00	1.12	0.89	QUI	Ching 1991 [121]
40 mg q.d. po	400 mg s.d. po	48	1.00	0.90	1.11	1.00	0.85	1.17	OHQ	Ching 1991 [121]
Mean GMFE (range):			1.11 (1.11–1.12), 2/2 with GMFE ≤ 2			1.15 (1.12–1.17), 2/2 with GMFE ≤ 2				
Rifampicin										
600 mg q.d. po	200 mg s.d. po	10	0.19	0.12	1.59	0.43	0.34	1.26	QUI	Damkier 1999 [119]
600 mg q.d. po	200 mg s.d. po	10	0.38	0.78	0.50	0.98	2.90	0.34	OHQ	Damkier 1999 [119]
Mean GMFE (range):			1.81 (1.59–2.02), 1/2 with GMFE ≤ 2			2.11 (1.26–2.96), 1/2 with GMFE ≤ 2				
Verapamil										
80 mg t.i.d. po	400 mg s.d. po	12	1.48	1.21	1.23	1.19	0.96	1.25	QUI	Edwards 1987 [123]
120 mg t.i.d. po	400 mg s.d. po	12	1.72	1.25	1.38	1.27	0.96	1.33	QUI	Edwards 1987 [123]
Mean GMFE (range):			1.30 (1.23–1.38), 2/2 with GMFE ≤ 2			1.29 (1.25–1.33), 2/2 with GMFE ≤ 2				
Overall GMFE (range):			1.29 (1.06–2.02), 14/15 with GMFE ≤ 2			1.32 (1.05–2.96), 14/15 with GMFE ≤ 2				

AUC_{last} : area under the plasma concentration-time curve calculated between the first and last concentration measurement, b.i.d.: twice daily, C_{max} : maximum plasma concentration, DDI: drug-drug interaction, GMFE: geometric mean fold error, obs: observed, OHQ: 3-hydroxyquinidine, po: oral, pred: predicted, q.d.: once daily, q.i.d.: four times daily, QUI: quinidine, s.d.: single dose, t.i.d.: three times daily, t_{last} : time of the last concentration measurement. If perpetrator or victim drugs were applied in form of salts, the respective dose of base was calculated and incorporated in simulations.

S6.12 Risperidone

S6.12.1 Clinical Studies

Table S36: Clinical study data used for DDI model development with **risperidone** as victim

Drug administration		n	Population ^a	Fem. [%]	Age [years]	Weight [kg]	BMI [kg/m ²]	AS	Molecule	Reference
Perpetrator	Risperidone									
<i>Ketoconazole</i>										
200 mg q.d. po	2 mg s.d. po	10	Asian [98]	0	33.3±8.1	64.1±5.8	165.8±7.3 ^b	-	RIS, OHR	Mahatthanatrakul 2012 [124]
<i>Rifampicin</i>										
600 mg q.d. po	1 mg s.d po	10	Asian [98]	0	(23–38)	(65–80)	-	AS = 1.25	RIS, OHR	Kim 2018 [125]
600 mg q.d. po	4 mg s.d. po	10	Asian [98]	0	30.5±6.5	(55–76)	22.1±2.2	-	RIS	Mahatthanatrakul 2007 [126]
<i>Verapamil</i>										
80 mg t.i.d. po	1 mg s.d. po	12	Japanese [113]	0	24.0±2.0	64.8±6.2	-	AS = 1	RIS, OHR	Nakagami 2005 [127]

AS: CYP2D6 activity score, BMI: body mass index, DDI: drug-drug interaction, fem: females, n: number of study participants, OHR: 9-hydroxyrisperidone, po: oral, q.d.: once daily, RIS: risperidone, s.d: single dose, t.i.d.: three times daily, -: not available. Values are given as mean (range). If perpetrator or victim drugs were applied in form of salts, the respective dose of base was calculated and incorporated in simulations. ^a Population used in simulations. ^b Height of subjects [cm].

S6.12.2 Plasma Concentration-Time Profiles (Semilogarithmic Representation)

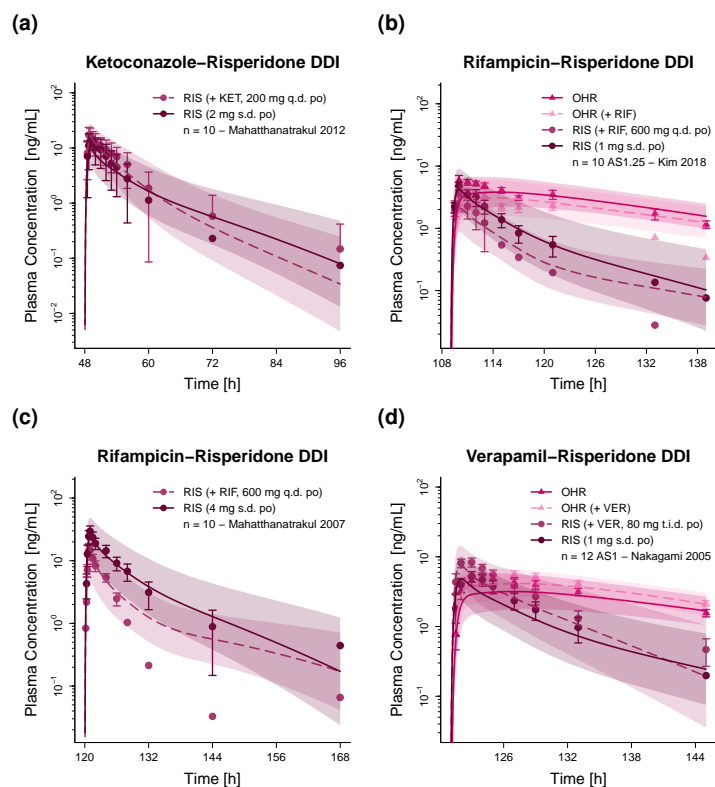


Figure S63: Predicted compared to observed plasma concentration-time profiles of risperidone alone (solid line) and after pretreatment and/or concomitant administration (dashed line) of (a) ketoconazole, (b–c) rifampicin and (d) verapamil (semilogarithmic representation). Population predicted (1000 individuals) geometric means are shown as lines, corresponding geometric standard deviations as shaded areas and observed data as dots/triangles (\pm standard deviation, if reported) [124–127]. AS: CYP2D6 activity score, DDI: drug-drug interaction, KET: ketoconazole, n : number of study participants, OHR: 9-hydroxyrisperidone, po: oral, q.d.: once daily, RIF: rifampicin, s.d.: single dose, t.i.d.: three times daily, VER: verapamil.

S6.12.3 Plasma Concentration-Time Profiles (Linear Representation)

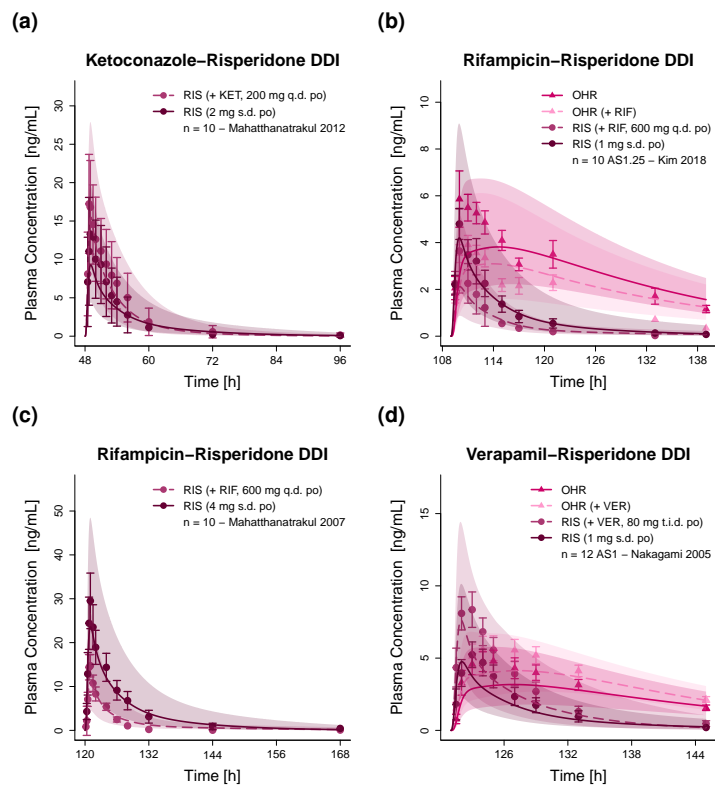


Figure S64: AS: CYP2D6 activity score, Predicted compared to observed plasma concentration-time profiles of risperidone alone (solid line) and after pretreatment and/or concomitant administration (dashed line) of (a) ketoconazole, (b–c) rifampicin and (d) verapamil (linear representation). Population predicted (1000 individuals) geometric means are shown as lines, corresponding geometric standard deviations as shaded areas and observed data as dots/triangles (\pm standard deviation, if reported) [124–127]. DDI: drug-drug interaction, KET: ketoconazole, n: number of study participants, OHR: 9-hydroxyrisperidone, po: oral, q.d.: once daily, RIF: rifampicin, s.d.: single dose, t.i.d.: three times daily, VER: verapamil.

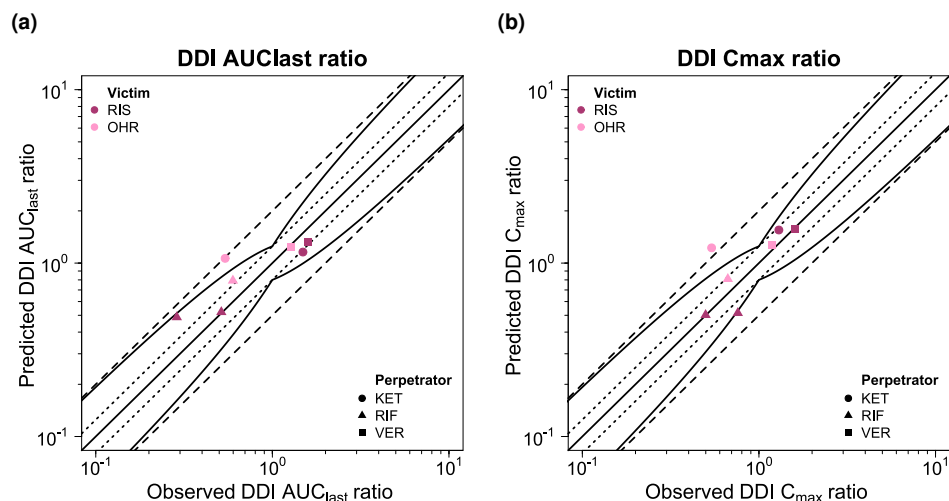
S6.12.4 DDI AUC_{last} and C_{max} Ratios

Figure S65: Goodness-of-fit plots comparing predicted and observed DDI AUC_{last} and C_{max} ratios for victim drug risperidone. The solid line marks the line of identity. Dotted lines indicate 1.25-fold, dashed lines indicate 2-fold deviation. Prediction success limits proposed by Guest et al. [2] are shown as curved lines (including 20% variability). AUC_{last} : area under the plasma concentration-time curve calculated between the first and last concentration measurement, C_{max} : maximum plasma concentration, KET: ketoconazole, OHR: 9-hydroxyrisperidone, RIF: rifampicin, RIS: risperidone, VER: verapamil.

S6.12.5 Geometric Mean Fold Errors of Predicted DDI AUC_{last} and C_{max} RatiosTable S37: Predicted and observed DDI AUC_{last} and C_{max} ratios involving **risperidone** as victim drug

Drug administration			DDI AUC_{last} ratio			DDI C_{max} ratio			AS	Molecule	Reference
Perpetrator	Risperidone	t_{last} [h]	Pred	Obs	Pred/Obs	Pred	Obs	Pred/Obs			
Ketoconazole											
200 mg q.d. po	2 mg s.d. po	48	1.16	1.49	0.78	1.55	1.30	1.20	-	RIS	Mahatthanatrakul 2012 [124]
200 mg q.d. po	2 mg s.d. po	96	1.06	0.54	1.97	1.22	0.54	2.27	-	OHR	Mahatthanatrakul 2012 [124]
Mean GMFE (range):			1.63 (1.29–1.97), 2/2 with GMFE ≤ 2			1.73 (1.20–2.27), 1/2 with GMFE ≤ 2					
Rifampicin											
600 mg q.d. po	1 mg s.d po	24	0.52	0.51	1.02	0.52	0.76	0.68	AS = 1.25	RIS	Kim 2018 [125]
600 mg q.d. po	1 mg s.d po	30	0.79	0.60	1.33	0.81	0.67	1.21	AS = 1.25	OHR	Kim 2018 [125]
600 mg q.d. po	4 mg s.d. po	48	0.49	0.29	1.69	0.50	0.50	1.01		RIS	Mahatthanatrakul 2007 [126]
Mean GMFE (range):			1.35 (1.02–1.69), 3/3 with GMFE ≤ 2			1.23 (1.01–1.47), 3/3 with GMFE ≤ 2					
Verapamil											
80 mg t.i.d. po	1 mg s.d. po	24	1.32	1.58	0.83	1.58	1.59	0.99	AS = 1	RIS	Nakagami 2005 [127]
80 mg t.i.d. po	1 mg s.d. po	24	1.23	1.28	0.96	1.27	1.19	1.07	AS = 1	OHR	Nakagami 2005 [127]
Mean GMFE (range):			1.12 (1.04–1.20), 2/2 with GMFE ≤ 2			1.04 (1.01–1.07), 2/2 with GMFE ≤ 2					
Overall GMFE (range):			1.36 (1.02–1.97), 7/7 with GMFE ≤ 2			1.32 (1.01–2.27), 6/7 with GMFE ≤ 2					

AS: CYP2D6 activity score, AUC_{last} : area under the plasma concentration-time curve calculated between the first and last concentration measurement, C_{max} : maximum plasma concentration, DDI: drug-drug interaction, GMFE: geometric mean fold error, obs: observed, OHR: 9-hydroxyrisperidone, po: oral, pred: predicted, q.d.: once daily, RIS: risperidone, s.d.: single dose, t.i.d.: three times daily, t_{last} : time of the last concentration measurement. If perpetrator or victim drugs were applied in form of salts, the respective dose of base was calculated and incorporated in simulations.

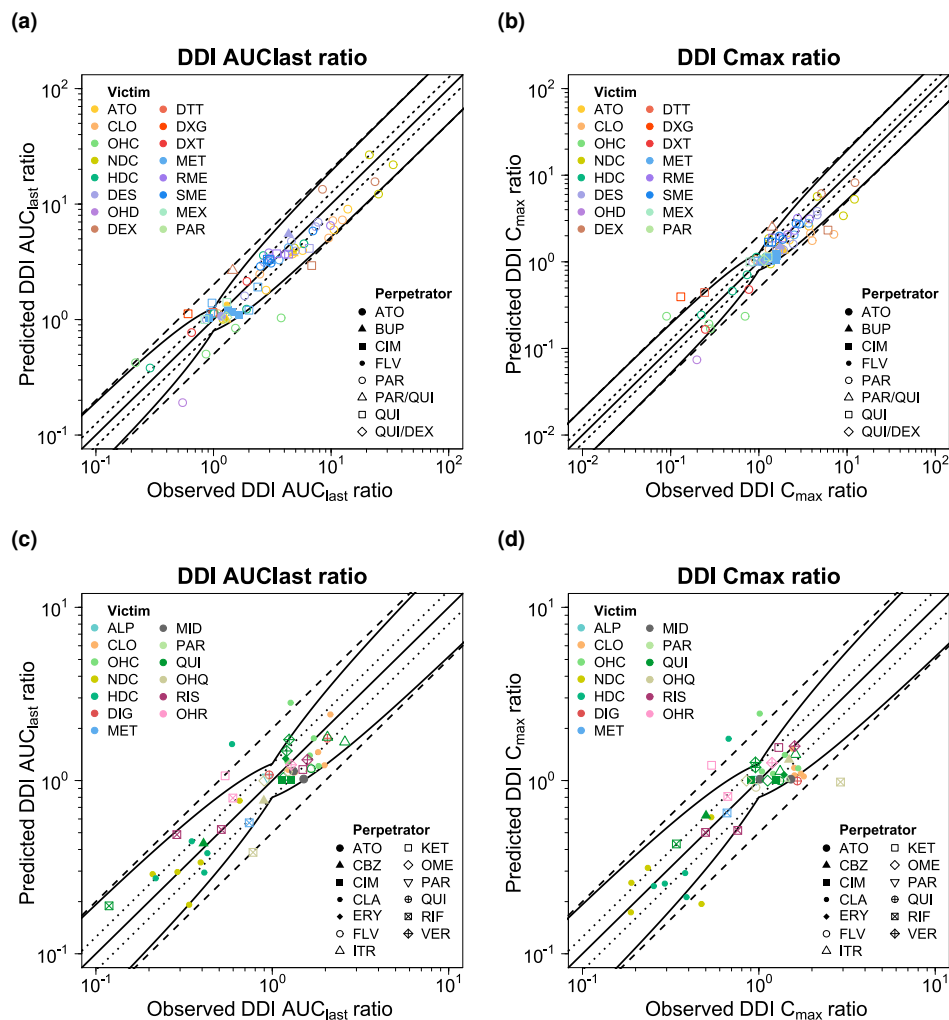
S6.13 DDI AUC_{last} and C_{max} Ratios

Figure S66: Goodness-of-fit plots comparing predicted and observed DDI AUC_{last} and C_{max} ratios. The solid line marks the line of identity. Dotted lines indicate 1.25-fold, dashed lines indicate 2-fold deviation. Prediction success limits proposed by Guest et al. [2] are shown as curved lines (including 20% variability). ALP: alprazolam, ATO: atomoxetine, AUC_{last} : area under the plasma concentration-time curve calculated between the first and last concentration measurement, BUP: bupropion, CBZ: carbamazepine, CIM: cimetidine, CLA: clarithromycin, CLO: (*E*)-clomiphene, C_{max} : maximum plasma concentration, DES: desipramine, DEX: dextromethorphan, DGI: drug-gene interaction, DIG: digoxin, DTT: total dextropropranolol, DXG: dextropropranolol-O-glucuronide, DXT: dextropropranolol, ERY: erythromycin, FLV: fluvoxamine, HDC: (*E*)-4-hydroxy-N-desethylclomiphene, ITR: itraconazole, KET: ketoconazole, MET: metoprolol, MEX: mexiletine, MID: midazolam, NDC: (*E*)-N-desethylclomiphene, OHC: (*E*)-4-hydroxyclophene, OHD: 2-hydroxydesipramine, OHM: alpha-hydroxymetoprolol, OHQ: 3-hydroxyquinidine, OHR: 9-hydroxyrisperidone, OME: omeprazole, PAR: paroxetine, QUI: quinidine, RIF: rifampicin, RIS: risperidone, RME: R-metoprolol, SME: S-metoprolol, VER: verapamil.

S7 DDGI Model Evaluation

Comprehensive information on the modeled DDGI studies as well as respective predicted and observed plasma concentration-time profiles in semilogarithmic and linear representations can be found in Section S6 "DDI Model Evaluation".

S7.1 DDGI AUC_{last} and C_{max} Ratios

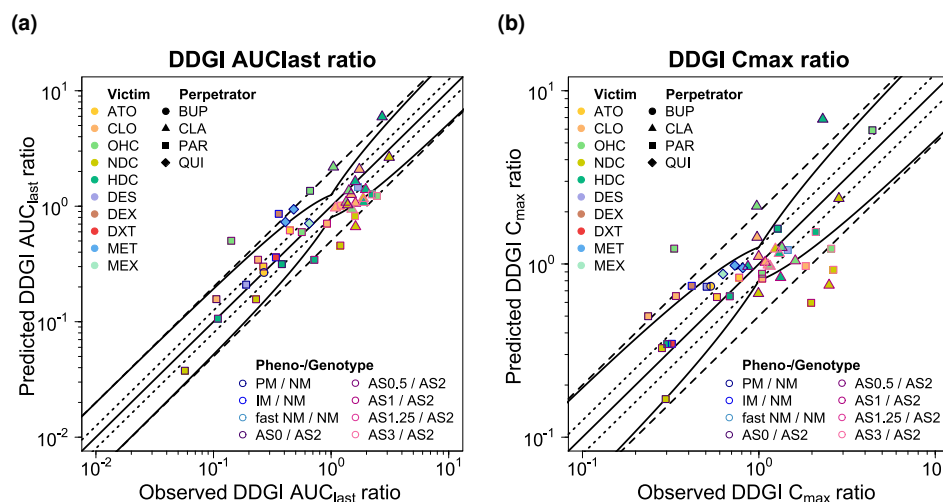


Figure S67: Goodness-of-fit plots comparing predicted and observed DDGI AUC_{last} and C_{max} ratios. The solid line marks the line of identity. Dotted lines indicate 1.25-fold, dashed lines indicate 2-fold deviation. Prediction success limits proposed by Guest et al. [2] are shown as curved lines (including 20% variability). AS: CYP2D6 activity score, ATO: atomoxetine, AUC_{last} : area under the plasma concentration-time curve calculated between the first and last concentration measurement, BUP: bupropion, CLA: clarithromycin, CLO: (*E*)-clomiphene, C_{max} : maximum plasma concentration, DES: desipramine, DEX: dextromethorphan, DDGI: drug-drug-gene interaction, DXT: dextropropion, HDC: (*E*)-4-hydroxy-N-desethylclomiphene, IM: CYP2D6 intermediate metabolizer, MET: metoprolol, MEX: mexiletine, NDC: (*E*)-N-desethylclomiphene, NM: CYP2D6 normal metabolizer, OHC: (*E*)-4-hydroxyclophene, PAR: paroxetine, PM: CYP2D6 poor metabolizer, QUI: quinidine.

S7.2 Geometric Mean Fold Errors of Predicted DDGI AUC_{last} and C_{max} RatiosTable S38: Predicted and observed DDGI AUC_{last} and C_{max} ratios

Drug administration			DDGI AUC _{last} ratio			DDGI C _{max} ratio			Phenotype/AS	Molecule	Reference
Victim	Perpetrator	t _{last} [h]	Pred	Obs	Pred/Obs	Pred	Obs	Pred/Obs			
Atomoxetine	Bupropion										
25 mg s.d. po	150/300 mg q.d. po	48 / 48	0.27	0.27	0.99	0.74	0.53	1.39	PM / NM	ATO	Todor 2016 [74]
Mean GMFE (range):			1.01 (-), 1/1 with GMFE ≤ 2			1.39 (-), 1/1 with GMFE ≤ 2					
Atomoxetine	Paroxetine										
20 mg s.d. po	20 mg q.d. po	24 / 24	0.30	0.26	1.13	0.64	0.58	1.11	AS0 / AS2	ATO	Jung 2020 [71]
20 mg s.d. po	20 mg q.d. po	24 / 24	0.62	0.45	1.39	0.83	0.77	1.08	AS1.25 / AS2	ATO	Jung 2020 [71]
Mean GMFE (range):			1.26 (1.13–1.39), 2/2 with GMFE ≤ 2			1.10 (1.08–1.11), 2/2 with GMFE ≤ 2					
(E)-Clomiphene	Clarithromycin										
42 mg s.d. po	500 mg b.i.d po	168 / 72	2.09	1.74	1.20	1.43	0.98	1.46	AS0 / AS2	CLO	Mürdter 2016 [76]
42 mg s.d. po	500 mg b.i.d po	168 / 168	2.18	1.04	2.09	2.16	0.97	2.22	AS0 / AS2	OHC	Mürdter 2016 [76]
42 mg s.d. po	500 mg b.i.d po	168 / 72	2.65	3.11	0.85	2.39	2.84	0.84	AS0 / AS2	NDC	Mürdter 2016 [76]
42 mg s.d. po	500 mg b.i.d po	168 / 72	5.95	2.71	2.20	6.86	2.30	2.98	AS0 / AS2	HDC	Mürdter 2016 [76]
42 mg s.d. po	500 mg b.i.d po	168 / 72	1.26	1.48	0.86	1.11	1.00	1.11	AS0.5 / AS2	CLO	Mürdter 2016 [76]
42 mg s.d. po	500 mg b.i.d po	168 / 168	1.36	1.41	0.96	1.24	1.35	0.92	AS0.5 / AS2	OHC	Mürdter 2016 [76]
42 mg s.d. po	500 mg b.i.d po	168 / 72	1.03	1.38	0.74	0.68	0.99	0.68	AS0.5 / AS2	NDC	Mürdter 2016 [76]
42 mg s.d. po	500 mg b.i.d po	168 / 72	1.64	1.60	1.02	0.97	0.87	1.12	AS0.5 / AS2	HDC	Mürdter 2016 [76]
42 mg s.d. po	500 mg b.i.d po	72 / 72	1.06	1.61	0.66	1.02	1.09	0.94	AS1 / AS2	CLO	Mürdter 2016 [76]
42 mg s.d. po	500 mg b.i.d po	168 / 168	1.08	1.34	0.81	1.04	1.61	0.65	AS1 / AS2	OHC	Mürdter 2016 [76]
42 mg s.d. po	500 mg b.i.d po	72 / 72	0.67	1.61	0.41	0.75	2.50	0.30	AS1 / AS2	NDC	Mürdter 2016 [76]
42 mg s.d. po	500 mg b.i.d po	168 / 72	1.40	1.96	0.71	0.84	1.33	0.63	AS1 / AS2	HDC	Mürdter 2016 [76]
42 mg s.d. po	500 mg b.i.d po	72 / 72	0.97	1.09	0.89	0.99	1.13	0.87	AS3 / AS2	CLO	Mürdter 2016 [76]
42 mg s.d. po	500 mg b.i.d po	168 / 168	0.94	1.50	0.63	0.97	1.16	0.84	AS3 / AS2	OHC	Mürdter 2016 [76]
42 mg s.d. po	500 mg b.i.d po	72 / 72	1.17	1.87	0.62	1.22	1.24	0.98	AS3 / AS2	NDC	Mürdter 2016 [76]
42 mg s.d. po	500 mg b.i.d po	72 / 72	1.08	1.89	0.57	1.15	1.30	0.88	AS3 / AS2	HDC	Mürdter 2016 [76]
Mean GMFE (range):			1.49 (1.02–2.42), 13/16 with GMFE ≤ 2			1.54 (1.02–3.31), 13/16 with GMFE ≤ 2					
(E)-Clomiphene	Paroxetine										
42 mg s.d. po	40 mg q.d. po	168 / 168	0.16	0.11	1.48	0.50	0.24	2.12	AS0 / AS2	CLO	Mürdter 2016 [76]
42 mg s.d. po	40 mg q.d. po	168 / 168	1.36	0.66	2.06	5.92	4.40	1.34	AS0 / AS2	OHC	Mürdter 2016 [76]
42 mg s.d. po	40 mg q.d. po	168 / 168	0.04	0.06	0.66	0.17	0.30	0.56	AS0 / AS2	NDC	Mürdter 2016 [76]
42 mg s.d. po	40 mg q.d. po	168 / 168	0.31	0.38	0.83	1.60	1.28	1.25	AS0 / AS2	HDC	Mürdter 2016 [76]
42 mg s.d. po	40 mg q.d. po	168 / 168	0.34	0.24	1.44	0.65	0.34	1.93	AS0.5 / AS2	CLO	Mürdter 2016 [76]
42 mg s.d. po	40 mg q.d. po	168 / 168	0.50	0.14	3.55	1.23	0.33	3.71	AS0.5 / AS2	OHC	Mürdter 2016 [76]
42 mg s.d. po	40 mg q.d. po	168 / 168	0.16	0.23	0.68	0.33	0.28	1.16	AS0.5 / AS2	NDC	Mürdter 2016 [76]
42 mg s.d. po	40 mg q.d. po	168 / 168	0.11	0.11	0.98	0.34	0.30	1.14	AS0.5 / AS2	HDC	Mürdter 2016 [76]
42 mg s.d. po	40 mg q.d. po	168 / 168	0.71	0.92	0.77	0.82	1.04	0.79	AS1 / AS2	CLO	Mürdter 2016 [76]
42 mg s.d. po	40 mg q.d. po	168 / 168	0.60	0.56	1.06	0.88	1.04	0.84	AS1 / AS2	OHC	Mürdter 2016 [76]
42 mg s.d. po	40 mg q.d. po	168 / 168	0.46	1.20	0.38	0.60	1.98	0.30	AS1 / AS2	NDC	Mürdter 2016 [76]
42 mg s.d. po	40 mg q.d. po	168 / 168	0.34	0.72	0.48	0.65	0.68	0.95	AS1 / AS2	HDC	Mürdter 2016 [76]

AS: CYP2D6 activity score, ATO: atomoxetine, AUC_{last}: area under the plasma concentration-time curve calculated between the first and last concentration measurement, b.i.d.: twice daily, CLO: (E)-clomiphene, C_{max}: maximum plasma concentration, DES: desipramine, DEX: dextromethorphan, DDGI: drug-drug-gene interaction, DXT: dextrorphan, GMFE: geometric mean fold error, HDC: (E)-4-hydroxy-N-desethylclomiphene, IM: CYP2D6 intermediate metabolizer, iv: intravenous, MET: metoprolol, MEX: mexiletine, NDC: (E)-N-desethylclomiphene, NM: CYP2D6 normal metabolizer, obs: observed, OHC: (E)-4-hydroxyclophene, PM: CYP2D6 poor metabolizer, po: oral, pred: predicted, q.d.: once daily, s.d.: single dose, t_{last}: time of the last concentration measurement. If perpetrator or victim drugs were applied in form of salts, the respective dose of base was calculated and incorporated in simulations.

Table S38: Predicted and observed DDGI AUC_{last} and C_{max} ratios (*continued*)

Drug administration			DDGI AUC _{last} ratio			DDGI C _{max} ratio			Phenotype/AS	Molecule	Reference
Victim	Perpetrator	t _{last} [h]	Pred	Obs	Pred/Obs	Pred	Obs	Pred/Obs			
42 mg s.d. po	40 mg q.d. po	168 / 168	1.01	1.20	0.84	0.97	1.84	0.53	AS3 / AS2	CLO	Mürdter 2016 [76]
42 mg s.d. po	40 mg q.d. po	168 / 168	1.23	2.45	0.50	1.23	2.57	0.48	AS3 / AS2	OHC	Mürdter 2016 [76]
42 mg s.d. po	40 mg q.d. po	168 / 168	0.82	1.59	0.51	0.93	2.65	0.35	AS3 / AS2	NDC	Mürdter 2016 [76]
42 mg s.d. po	40 mg q.d. po	168 / 168	1.26	2.21	0.57	1.53	2.10	0.73	AS3 / AS2	HDC	Mürdter 2016 [76]
Mean GMFE (range):			1.73 (1.02–3.55), 12/16 with GMFE ≤ 2			1.84 (1.05–3.71), 11/16 with GMFE ≤ 2					
Desipramine	Paroxetine										
100 mg s.d. po	20 mg q.d. po	239 / 234	0.21	0.19	1.11	0.74	0.51	1.46	PM / NM	DES	Brøsen 1993 [22]
100 mg s.d. po	20 mg q.d. po	233 / 234	1.46	1.69	0.87	1.20	1.46	0.83	fast NM / NM	DES	Brøsen 1993 [22]
Mean GMFE (range):			1.13 (1.11–1.16), 2/2 with GMFE ≤ 2			1.34 (1.21–1.46), 2/2 with GMFE ≤ 2					
Dextromethorphan	Paroxetine										
5 mg s.d. po	20 mg b.i.d. po	24 / 24	0.86	0.36	2.40	0.75	0.42	1.80	IM / NM	DEX	Storelli 2018 [77]
5 mg s.d. po	20 mg b.i.d. po	24 / 24	0.36	0.34	1.06	0.35	0.32	1.08	IM / NM	DXT	Storelli 2018 [77]
Mean GMFE (range):			1.73 (1.06–2.40), 1/2 with GMFE ≤ 2			1.44 (1.08–1.80), 2/2 with GMFE ≤ 2					
Metoprolol	Quinidine										
20 mg s.d. iv	50 mg s.d. po	8 / 8	0.94	0.48	1.98	0.98	0.73	1.35	PM / NM	MET	Leemann 1993 [82]
20 mg s.d. iv	250 mg b.i.d. po	8 / 8	0.73	0.41	1.79	0.95	0.81	1.18	PM / NM	MET	Leemann 1993 [82]
Mean GMFE (range):			1.87 (1.79–1.96), 2/2 with GMFE ≤ 2			1.26 (1.17–1.34), 2/2 with GMFE ≤ 2					
Mexiletine	Quinidine										
200 mg s.d. po	50 mg q.i.d. po	48 / 48	0.71	0.65	1.09	0.88	0.63	1.40	PM / NM	MEX	Abolfathi 1993 [90]
Mean GMFE (range):			1.09 (-), 1/1 with GMFE ≤ 2			1.40 (-), 1/1 with GMFE ≤ 2					
Overall GMFE (range):			1.56 (1.01–3.55), 34/42 with GMFE ≤ 2			1.60 (1.02–3.71), 34/42 with GMFE ≤ 2					

AS: CYP2D6 activity score, ATO: atomoxetine, AUC_{last}: area under the plasma concentration-time curve calculated between the first and last concentration measurement, b.i.d.: twice daily, CLO: (*E*)-clomiphene, C_{max}: maximum plasma concentration, DES: desipramine, DEX: dextromethorphan, DDGI: drug-drug-gene interaction, DXT: dextrorphan, GMFE: geometric mean fold error, HDC: (*E*)-4-hydroxy-*N*-desethylclomiphene, IM: CYP2D6 intermediate metabolizer, iv: intravenous, MET: metoprolol, MEX: mexiletine, NDC: (*E*)-*N*-desethylclomiphene, NM: CYP2D6 normal metabolizer, obs: observed, OHC: (*E*)-4-hydroxyclophene, PM: CYP2D6 poor metabolizer, po: oral, pred: predicted, q.d.: once daily, s.d.: single dose, t_{last}: time of the last concentration measurement. If perpetrator or victim drugs were applied in form of salts, the respective dose of base was calculated and incorporated in simulations.

S8 Model-Informed Dose Adaptations

Table S39: Administration protocols used for model-informed dose adaptations

	Compound	Drug administration	Reference
Victim drugs	Atomoxetine	40 mg b.i.d. po	[128]
	Metoprolol	100 mg b.i.d. po	[129]
Perpetrator drugs	Cimetidine	200 mg b.i.d. po	[130]
	Itraconazole	200 mg q.d. po	[131]
	Paroxetine	20 mg q.d. po	[132]
	Quinidine	400 mg q.i.d. po	[133]

b.i.d.: twice daily, po: oral, q.d.: once daily, q.i.d.: four times daily. If perpetrator or victim drugs are clinically applied in form of salts, the respective dose of base was calculated and incorporated in simulations.

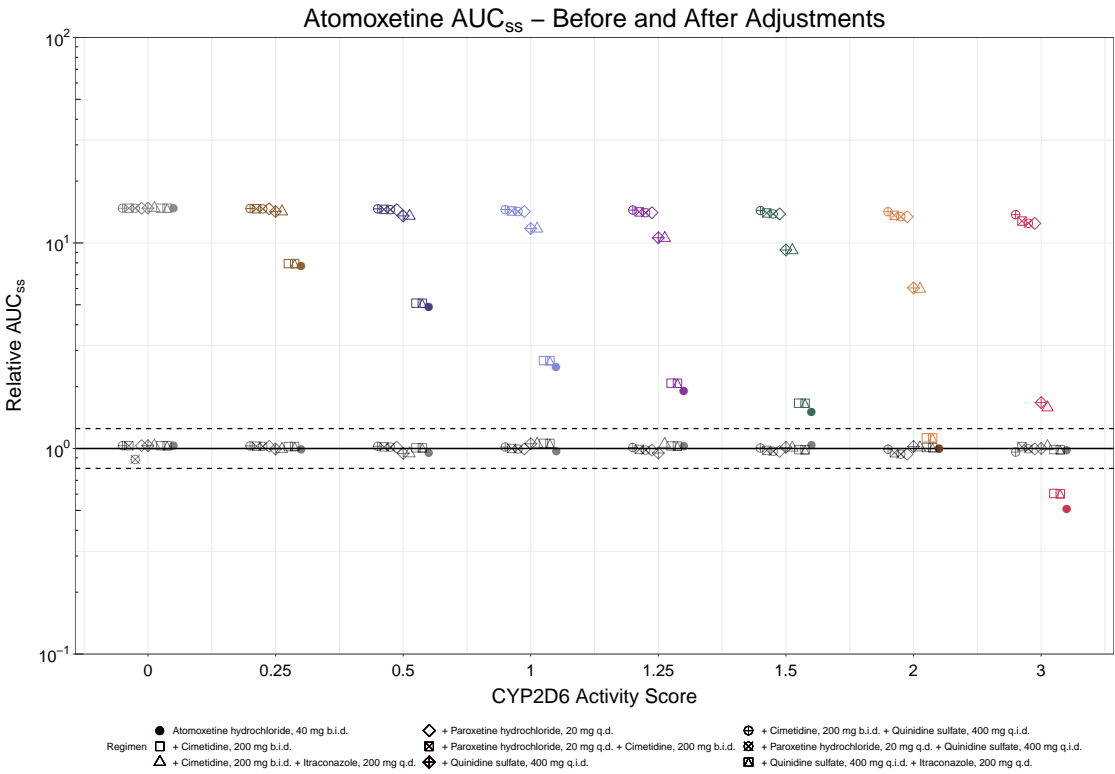


Figure S68: Dose adjustments for atomoxetine using the matching exposure strategy. Colored symbols indicate the AUC_{ss} before dose adjustments for the respective D(D)GI scenario. The corresponding black symbols indicate the matched AUC_{ss} after atomoxetine dose adjustments. Solid black lines show the respective reference AUC_{ss} (activity score 2, no DDI) and dashed black lines mark 80% and 125% of the reference AUC_{ss}. AUC_{ss}: area under the concentration–time curve during steady state, b.i.d.: twice a day, CYP: cytochrome P450, D(D)GI: drug-(drug)-gene interaction, q.d.: once daily, q.i.d.: four times a day.

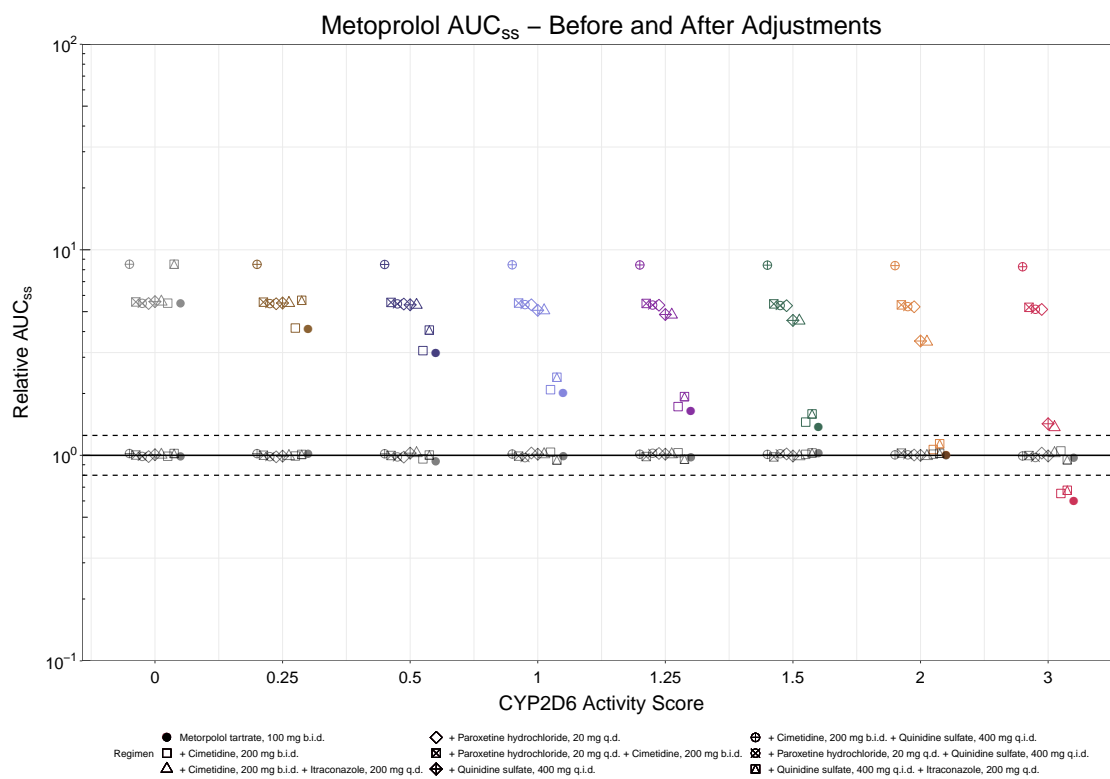


Figure S69: Dose adjustments for metoprolol using the matching exposure strategy. Colored symbols indicate the AUC_{ss} before dose adjustments for the respective D(D)GI scenario. The corresponding black symbols indicate the matched AUC_{ss} after metoprolol dose adjustments. Solid black lines show the respective reference AUC_{ss} (activity score 2, no DDI) and dashed black lines mark 80% and 125% of the reference AUC_{ss}. AUC_{ss}: area under the concentration–time curve during steady state, b.i.d.: twice a day, CYP: cytochrome P450, D(D)GI: drug(-drug)-gene interaction, q.d.: once daily, q.i.d.: four times a day.

References

- [1] S. Rüdesheim, D. Selzer, T. Mürdter, S. Igel, R. Kerb, M. Schwab, and T. Lehr. Physiologically Based Pharmacokinetic Modeling to Describe the CYP2D6 Activity Score-Dependent Metabolism of Paroxetine, Atomoxetine and Risperidone. *Pharmaceutics*, 14(8), 2022. doi: 10.3390/pharmaceutics14081734.
- [2] E. J. Guest, L. Aarons, J. B. Houston, A. Rostami-Hodjegan, and A. Galetin. Critique of the two-fold measure of prediction success for ratios: application for the assessment of drug-drug interactions. *Drug metabolism and disposition: the biological fate of chemicals*, 39(2):170–3, 2011. doi: 10.1124/dmd.110.036103.
- [3] ICRP Publication 89. Third National Health and Nutrition Examination Survey (NHANES III). *Annals of the ICRP*, 3–4(32):5–265, 2014.
- [4] K. Brøsen and L. F. Gram. First-pass metabolism of imipramine and desipramine: Impact of the sparteine oxidation phenotype. *Clinical Pharmacology and Therapeutics*, 43(4):400–406, 1988. doi: 10.1038/clpt.1988.50.
- [5] E. Spina, E. Steiner, Ö. Ericsson, and F. Sjöqvist. Hydroxylation of desmethylinipramine: Dependence on the debrisoquin hydroxylation phenotype. *Clinical Pharmacology and Therapeutics*, 41(3):314–319, 1987. doi: 10.1038/clpt.1987.33.
- [6] R. E. Aarnoutse, J. Kleinnijenhuis, P. P. Koopmans, D. J. Touw, J. Wieling, Y. A. Hekster, and D. M. Burger. Effect of low-dose ritonavir (100 mg twice daily) on the activity of cytochrome P450 2D6 in healthy volunteers. *Clinical pharmacology and therapeutics*, 78(6):664–74, 2005. doi: 10.1016/j.clpt.2005.09.001.
- [7] National Center for Health Statistics Hyattsville, MS 20782. Basic anatomical and physiological data for use in radiological protection: reference values. A report of age- and gender-related differences in the anatomical and physiological characteristics of reference individuals. 1997.
- [8] R. F. Bergstrom, A. L. Peyton, and L. Lemberger. Quantification and mechanism of the fluoxetine and tricyclic antidepressant interaction. *Clinical pharmacology and therapeutics*, 51(3):239–48, 1992. doi: 10.1038/clpt.1992.18.
- [9] J. Boni, R. Abbas, C. Leister, J. Burns, R. Jordan, M. Hoffmann, W. DeMaio, and B. Hug. Disposition of desipramine, a sensitive cytochrome P450 2D6 substrate, when coadministered with intravenous temsirolimus. *Cancer chemotherapy and pharmacology*, 64(2):263–70, 2009. doi: 10.1007/s00280-008-0865-9.
- [10] R. Z. Harris, M. Salfi, E. Posvar, D. Hoelscher, and D. Padhi. Pharmacokinetics of desipramine HCl when administered with cinacalcet HCl. *European journal of clinical pharmacology*, 63(2):159–63, 2007. doi: 10.1007/s00228-006-0129-8.
- [11] S. M. Hynes, E. Wickremsinhe, W. Zhang, R. Decker, J. Ott, J. Chandler, and M. Mitchell. Evaluation of the likelihood of a selective CHK1 inhibitor (LY2603618) to inhibit CYP2D6 with desipramine as a probe substrate in cancer patients. *Biopharmaceutics & Drug Disposition*, 36(1):49–63, 2015. doi: 10.1002/bdd.1922.
- [12] S. Madani, D. Barilla, J. Cramer, Y. Wang, and C. Paul. Effect of terbinafine on the pharmacokinetics and pharmacodynamics of desipramine in healthy volunteers identified as cytochrome P450 2D6 (CYP2D6) extensive metabolizers. *Journal of clinical pharmacology*, 42(11):1211–8, 2002. doi: 10.1177/009127002762491299.
- [13] A. I. Nichols, P. Fatato, M. Shenouda, J. Paul, J. A. Isler, R. D. Pedersen, Q. Jiang, S. Ahmed, and A. Patroneva. The effects of desvenlafaxine and paroxetine on the pharmacokinetics of the cytochrome P450 2D6 substrate desipramine in healthy adults. *Journal of clinical pharmacology*, 49(2):219–28, 2009. doi: 10.1177/0091270008326716.
- [14] A. I. Nichols, A. Madelyn, Y. Chen, J. A. Behrle, G. Frick, and J. Paul. Effects of desvenlafaxine on the pharmacokinetics of desipramine in healthy adults. *International Clinical Psychopharmacology*, 28(2):99–105, 2013. doi: 10.1097/YIC.0b013e32835c1f49.
- [15] A. Patroneva, S. M. Connolly, P. Fatato, R. Pedersen, Q. Jiang, J. Paul, C. Guico-Pabia, J. A. Isler, M. E. Burczynski, and A. I. Nichols. An assessment of drug-drug interactions: the effect of desvenlafaxine and duloxetine on the pharmacokinetics of the CYP2D6 probe desipramine in healthy subjects. *Drug metabolism and disposition: the biological fate of chemicals*, 36(12):2484–2491, 2008. doi: 10.1124/dmd.108.021527.

- [16] M. J. Reese, R. M. Wurm, K. T. Muir, G. T. Generaux, L. St John-Williams, and D. J. McConn. An in vitro mechanistic study to elucidate the desipramine/bupropion clinical drug-drug interaction. *Drug metabolism and disposition: the biological fate of chemicals*, 36(7):1198–201, 2008. doi: 10.1124/dmd.107.020198.
- [17] J.-M. Sauer, A. J. Long, B. Ring, J. S. Gillespie, N. P. Sanburn, K. A. DeSante, D. Petullo, M. R. VandenBranden, C. B. Jensen, S. A. Wrighton, B. P. Smith, H. A. Read, and J. W. Witcher. Atomoxetine Hydrochloride: Clinical Drug-Drug Interaction Prediction and Outcome. *Journal of Pharmacology and Experimental Therapeutics*, 308(2): 410–418, 2004. doi: 10.1124/jpet.103.058727.
- [18] M. H. Skinner, H.-Y. Kuan, A. Pan, K. Sathirakul, M. P. Knadler, C. R. Gonzales, K. P. Yeo, S. Reddy, M. Lim, M. Ayan-Oshodi, and S. D. Wise. Duloxetine is both an inhibitor and a substrate of cytochrome P4502D6 in healthy volunteers. *Clinical pharmacology and therapeutics*, 73(3):170–7, 2003. doi: 10.1067/mcp.2003.28.
- [19] J. Alderman, S. H. Preskorn, D. J. Greenblatt, W. Harrison, D. Penenberg, J. Allison, and M. Chung. Desipramine pharmacokinetics when coadministered with paroxetine or sertraline in extensive metabolizers. *Journal of clinical psychopharmacology*, 17(4):284–91, 1997. doi: 10.1097/00004714-199708000-00008.
- [20] T. K. Bergmann, L. Bathum, and K. Brosen. Duplication of CYP2D6 predicts high clearance of desipramine but high clearance does not predict duplication of CYP2D6. *European journal of clinical pharmacology*, 57(2):123–7, 2001. doi: 10.1007/s002280100284.
- [21] K. Brøsen, S. Victoria Otton, and L. F. Gram. Imipramine demethylation and hydroxylation: Impact of the sparteine oxidation phenotype. *Clinical Pharmacology and Therapeutics*, 40(5):543–549, 1986. doi: 10.1038/clpt.1986.221.
- [22] K. Brøsen, J. G. Hansen, K. K. Nielsen, S. H. Sindrup, and L. F. Gram. Inhibition by paroxetine of desipramine metabolism in extensive but not in poor metabolizers of sparteine. *European journal of clinical pharmacology*, 44(4):349–55, 1993. doi: 10.1007/BF00316471.
- [23] K. Brøsen and L. F. Gram. Quinidine inhibits the 2-hydroxylation of imipramine and desipramine but not the demethylation of imipramine. *European Journal of Clinical Pharmacology*, 37(2):155–160, 1989. doi: 10.1007/BF00558224.
- [24] E. Spina, A. Avenoso, G. M. Campo, A. P. Caputi, and E. Perucca. The effect of carbamazepine on the 2-hydroxylation of desipramine. *Psychopharmacology*, 117(4):413–6, 1995. doi: 10.1007/BF02246212.
- [25] S. Kim, J. Chen, T. Cheng, A. Gindulyte, J. He, S. He, Q. Li, B. A. Shoemaker, P. A. Thiessen, B. Yu, L. Zaslavsky, J. Zhang, and E. E. Bolton. PubChem 2019 update: improved access to chemical data. *Nucleic acids research*, 47(D1):D1102–D1109, 2019.
- [26] ChemAxon. Chemicalize, 2023. URL <https://chemicalize.com>.
- [27] D. S. Wishart, C. Knox, A. C. Guo, S. Shrivastava, M. Hassanali, P. Stothard, Z. Chang, and J. Woolsey. DrugBank: a comprehensive resource for in silico drug discovery and exploration. *Nucleic acids research*, 34(Database issue): D668–72, 2006. doi: 10.1093/nar/gkj067.
- [28] R. Watanabe, T. Esaki, H. Kawashima, Y. Natsume-Kitatani, C. Nagao, R. Ohashi, and K. Mizuguchi. Predicting Fraction Unbound in Human Plasma from Chemical Structure: Improved Accuracy in the Low Value Ranges. *Molecular Pharmaceutics*, 15(11):5302–5311, 2018. doi: 10.1021/acs.molpharmaceut.8b00785.
- [29] S. E. Ball, D. Ahern, J. Scatina, and J. Kao. Venlafaxine: In vitro inhibition of CYP2D6 dependent imipramine and desipramine metabolism; comparative studies with selected SSRIs, and effects on human hepatic CYP3A4, CYP2C9 and CYP1A2. *British Journal of Clinical Pharmacology*, 43(6):619–626, 1997. doi: 10.1046/j.1365-2125.1997.00591.x.
- [30] R. P. Austin, P. Barton, S. L. Cockroft, M. C. Wenlock, and R. J. Riley. The influence of nonspecific microsomal binding on apparent intrinsic clearance, and its prediction from physicochemical properties. *Drug Metabolism and Disposition*, 30(12):1497–1503, 2002. doi: 10.1124/dmd.30.12.1497.
- [31] T. Rodgers, D. Leahy, and M. Rowland. Physiologically based pharmacokinetic modeling 1: Predicting the tissue distribution of moderate-to-strong bases. *Journal of Pharmaceutical Sciences*, 94(6):1259–1276, 2005. doi: 10.1002/jps.20322.

- [32] T. Rodgers and M. Rowland. Physiologically based pharmacokinetic modelling 2: Predicting the tissue distribution of acids, very weak bases, neutrals and zwitterions. *Journal of Pharmaceutical Sciences*, 95(6):1238–57, 2006. doi: 10.1002/jps.20502.
- [33] Open Systems Pharmacology Suite Community. Open Systems Pharmacology Documentation., 2018. URL <https://docs.open-systems-pharmacology.org/working-with-pk-sim/pk-sim-documentation>.
- [34] M. Nishimura and S. Naito. Tissue-specific mRNA expression profiles of human phase I metabolizing enzymes except for cytochrome P450 and phase II metabolizing enzymes. *Drug metabolism and pharmacokinetics*, 21(5): 357–74, 2006. doi: 10.2133/dmpk.21.357.
- [35] M. Meyer, S. Schneckener, B. Ludewig, L. Kuepfer, and J. Lippert. Using expression data for quantification of active processes in physiologically based pharmacokinetic modeling. *Drug metabolism and disposition: the biological fate of chemicals*, 40(5):892–901, 2012. doi: 10.1124/dmd.111.043174.
- [36] M. Nishimura, H. Yaguti, H. Yoshitsugu, S. Naito, and T. Satoh. Tissue distribution of mRNA expression of human cytochrome P450 isoforms assessed by high-sensitivity real-time reverse transcription PCR. *Journal of the Pharmaceutical Society of Japan*, 123(5):369–75, 2003. doi: 10.1248/yakushi.123.369.
- [37] A. D. Rodrigues. Integrated cytochrome P450 reaction phenotyping: attempting to bridge the gap between cDNA-expressed cytochromes P450 and native human liver microsomes. *Biochemical pharmacology*, 57(5): 465–80, 1999. doi: 10.1016/S0006-2952(98)00268-8.
- [38] Open Systems Pharmacology Suite Community. Open Systems Pharmacology Suite Manual, 2018. URL <https://docs.open-systems-pharmacology.org/>.
- [39] N. Kolesnikov, E. Hastings, M. Keays, O. Melnichuk, Y. A. Tang, E. Williams, M. Dylag, N. Kurbatova, M. Brandizi, T. Burdett, K. Megy, E. Pilicheva, G. Rustici, A. Tikhonov, H. Parkinson, R. Petryszak, U. Sarkans, and A. Brazma. ArrayExpress update-simplifying data submissions. *Nucleic Acids Research*, 43(D1):D1113–D1116, 2015. doi: 10.1093/nar/gku1057.
- [40] B. Achour, M. R. Russell, J. Barber, and A. Rostami-Hodjegan. Simultaneous quantification of the abundance of several cytochrome P450 and uridine 5'-diphospho-glucuronosyltransferase enzymes in human liver microsomes using multiplexed targeted proteomics. *Drug metabolism and disposition: the biological fate of chemicals*, 42(4): 500–510, 2014. doi: 10.1124/dmd.113.055632.
- [41] D. Scotcher, S. Billington, J. Brown, C. R. Jones, C. D. Brown, A. Rostami-Hodjegan, and A. Galetin. Microsomal and cytosolic scaling factors in dog and human kidney cortex and application for in vitro-in vivo extrapolation of renal metabolic clearance. *Drug Metabolism and Disposition*, 45(5):556–568, 2017. doi: 10.1124/dmd.117.075242.
- [42] National Center for Biotechnology Information (NCBI). Expressed Sequence Tags (EST) from UniGene, 2019.
- [43] G. Margaillan, M. Rouleau, J. K. Fallon, P. Caron, L. Villeneuve, V. Turcotte, P. C. Smith, M. S. Joy, and C. Guillemette. Quantitative profiling of human renal UDP-glucuronosyltransferases and glucuronidation activity: A comparison of normal and tumoral kidney tissues. *Drug Metabolism and Disposition*, 43(4):611–19, 2015. doi: 10.1124/dmd.114.062877.
- [44] M. Otsuka, T. Matsumoto, R. Morimoto, S. Arioka, H. Omote, and Y. Moriyama. A human transporter protein that mediates the final excretion step for toxic organic cations. *Proceedings of the National Academy of Sciences of the United States of America*, 102(50):17923–8, 2005. doi: 10.1073/pnas.0506483102.
- [45] S. Masuda, T. Terada, A. Yonezawa, Y. Tanihara, K. Kishimoto, T. Katsura, O. Ogawa, and K.-i. Inui. Identification and functional characterization of a new human kidney-specific H⁺/organic cation antiporter, kidney-specific multidrug and toxin extrusion 2. *Journal of the American Society of Nephrology : JASN*, 17(8):2127–35, 2006. doi: 10.1681/ASN.2006030205.
- [46] B. Prasad, K. Johnson, S. Billington, C. Lee, G. W. Chung, C. D. Brown, E. J. Kelly, J. Himmelfarb, and J. D. Unadkat. Abundance of drug transporters in the human kidney cortex as quantified by quantitative targeted proteomics. *Drug Metabolism and Disposition*, 44(12):1920–1924, 2016. doi: 10.1124/dmd.116.072066.

- [47] M. Nishimura and S. Naito. Tissue-specific mRNA expression profiles of human ATP-binding cassette and solute carrier transporter superfamilies. *Drug metabolism and pharmacokinetics*, 20(6):452–77, 2005. doi: 10.2133/dmpk.20.452.
- [48] B. Prasad, R. Evers, A. Gupta, C. E. C. A. Hop, L. Salphati, S. Shukla, S. V. Ambudkar, and J. D. Unadkat. Interindividual variability in hepatic organic anion - transporting polypeptides and P-glycoprotein (ABCB1) protein expression: quantification by liquid chromatography tandem mass spectroscopy and influence of genotype, age, and sex. *Drug metabolism and disposition: the biological fate of chemicals*, 42(1):78–88, 2014. doi: 10.1124/dmd.113.053819.
- [49] L. Wang, B. Prasad, L. Salphati, X. Chu, A. Gupta, C. E. Hop, R. Evers, and J. D. Unadkat. Interspecies variability in expression of hepatobiliary transporters across human, dog, monkey, and rat as determined by quantitative proteomics. *Drug Metabolism and Disposition*, 43(3):367–74, 2015. doi: 10.1124/dmd.114.061580.
- [50] N. Hanke, S. Frechen, D. Moj, H. Britz, T. Eissing, T. Wendl, and T. Lehr. PBPK models for CYP3A4 and P-gp DDI prediction: A modeling network of rifampicin, itraconazole, clarithromycin, midazolam, alfentanil, and digoxin. *CPT: Pharmacometrics & Systems Pharmacology*, 7(10):647–59, 2018. doi: 10.1002/psp4.12343.
- [51] Midazolam OSP Repository, 2023. URL <https://github.com/Open-Systems-Pharmacology/Midazolam-Model>.
- [52] K. Rowland Yeo, R. L. Walsky, M. Jamei, A. Rostami-Hodjegan, and G. T. Tucker. Prediction of time-dependent CYP3A4 drug-drug interactions by physiologically based pharmacokinetic modelling: Impact of inactivation parameters and enzyme turnover. *European Journal of Pharmaceutical Sciences*, 43(3):160–73, 2011. doi: 10.1016/j.ejps.2011.04.008.
- [53] D. J. Greenblatt, L. L. von Moltke, J. S. Harmatz, G. Chen, J. L. Weemhoff, C. Jen, C. J. Kelley, B. W. LeDuc, and M. A. Zinny. Time course of recovery of cytochrome P450 3A function after single doses of grapefruit juice. *Clinical Pharmacology and Therapeutics*, 74(2):121–29, 2003. doi: 10.1016/S0009-9236(03)00118-8.
- [54] T. Kanacher, A. Lindauer, E. Mezzalana, I. Michon, C. Veau, J. D. G. Mantilla, V. Nock, and A. Fleury. A Physiologically-Based Pharmacokinetic (PBPK) Model Network for the Prediction of CYP1A2 and CYP2C19 Drug-Drug-Gene Interactions with Fluvoxamine, Omeprazole, S-mephenytoin, Moclobemide, Tizanidine, Mexiletine, Ethinylestradiol, and Caffeine. *Pharmaceutics*, 12(12):1–15, 2020. doi: 10.3390/pharmaceutics12121191.
- [55] F. Z. Marok, L. M. Fuhr, N. Hanke, D. Selzer, and T. Lehr. Physiologically Based Pharmacokinetic Modeling of Bupropion and Its Metabolites in a CYP2B6 Drug-Drug-Gene Interaction Network. *Pharmaceutics*, 13(3), 2021. doi: 10.3390/pharmaceutics13030331.
- [56] J. E. Sager, S. Tripathy, L. S. Price, A. Nath, J. Chang, A. Stephenson-Famy, and N. Isoherranen. In vitro to in vivo extrapolation of the complex drug-drug interaction of bupropion and its metabolites with CYP2D6; simultaneous reversible inhibition and CYP2D6 downregulation. *Biochemical Pharmacology*, 123:85–96, 2017. ISSN 18732968. doi: 10.1016/j.bcp.2016.11.007. URL <http://dx.doi.org/10.1016/j.bcp.2016.11.007>.
- [57] J. E. Sager, S. Tripathy, L. S. Price, A. Nath, J. Chang, A. Stephenson-Famy, and N. Isoherranen. Corrigendum to “In vitro to in vivo extrapolation of the complex drug-drug interaction of bupropion and its metabolites with CYP2D6; simultaneous reversible inhibition and CYP2D6 downregulation” [Biochem. Pharmacol. 123(2017)85–96] (Biochemical Pharmacology. *Biochemical Pharmacology*, 183(November 2020):114306, 2021. ISSN 18732968. doi: 10.1016/j.bcp.2020.114306. URL <https://doi.org/10.1016/j.bcp.2020.114306>.
- [58] L. M. Fuhr, F. Z. Marok, N. Hanke, D. Selzer, and T. Lehr. Pharmacokinetics of the CYP3A4 and CYP2B6 Inducer Carbamazepine and Its Drug-Drug Interaction Potential: A Physiologically Based Pharmacokinetic Modeling Approach. *Pharmaceutics*, 13(2), 2021. doi: 10.3390/pharmaceutics13020270.
- [59] N. Hanke, D. Türk, D. Selzer, N. Ishiguro, T. Ebner, S. Wiebe, F. Müller, P. Stopfer, V. Nock, and T. Lehr. A Comprehensive Whole-Body Physiologically Based Pharmacokinetic Drug-Drug-Gene Interaction Model of Metformin and Cimetidine in Healthy Adults and Renally Impaired Individuals. *Clinical pharmacokinetics*, 59(11): 1419–1431, 2020. doi: 10.1007/s40262-020-00896-w.
- [60] M. Madeira, M. Levine, T. K. H. Chang, A. Mirfazaian, and G. D. Bellward. The effect of cimetidine on

- dextromethorphan O-demethylase activity of human liver microsomes and recombinant CYP2D6. *Drug metabolism and disposition: the biological fate of chemicals*, 32(4):460–7, 2004. doi: 10.1124/dmd.32.4.460.
- [61] H. Britz, N. Hanke, A.-K. Volz, O. Spigset, M. Schwab, T. Eissing, T. Wendl, S. Frechen, and T. Lehr. Physiologically-Based Pharmacokinetic Models for CYP1A2 Drug-Drug Interaction Prediction: A Modeling Network of Fluvoxamine, Theophylline, Caffeine, Rifampicin, and Midazolam. *CPT: pharmacometrics & systems pharmacology*, 8(5):296–307, 2019. doi: 10.1002/psp4.12397.
- [62] H. K. Crewe, M. S. Lennard, G. T. Tucker, F. R. Woods, and R. E. Haddock. The effect of selective serotonin re-uptake inhibitors on cytochrome P4502D6 (CYP2D6) activity in human liver microsomes. *British journal of clinical pharmacology*, 34(3):262–5, sep 1992. ISSN 0306-5251. doi: 10.1111/j.1365-2125.1992.tb04134.x. URL <https://bpspubs.onlinelibrary.wiley.com/doi/10.1111/j.1365-2125.1992.tb04134.x> <http://www.ncbi.nlm.nih.gov/pubmed/1389951> <http://www.pubmedcentral.nih.gov/articlerender.fcgi?artid=PMC1381398>.
- [63] K. Iga. Dynamic and Static Simulations of Fluvoxamine-Perpetrated Drug-Drug Interactions Using Multiple Cytochrome P450 Inhibition Modeling, and Determination of Perpetrator-Specific CYP Isoform Inhibition Constants and Fractional CYP Isoform Contributions to Victim Clearance. *Journal of Pharmaceutical Sciences*, 105(3): 1307–1317, mar 2016. ISSN 0022-3549. doi: 10.1016/J.XPHS.2015.11.044.
- [64] F. Z. Marok, J.-G. Wojtyniak, L. M. Fuhr, D. Selzer, M. Schwab, J. Weiss, W. E. Haefeli, and T. Lehr. A Physiologically Based Pharmacokinetic Model of Ketoconazole and Its Metabolites as Drug-Drug Interaction Perpetrators. *Pharmaceutics*, 15(2), 2023. doi: 10.3390/pharmaceutics15020679.
- [65] X. Q. Li, T. B. Andersson, M. Ahlström, and L. Weidolf. Comparison of inhibitory effects of the proton pump-inhibiting drugs omeprazole, esomeprazole, lansoprazole, pantoprazole, and rabeprazole on human cytochrome P450 activities. *Drug Metabolism and Disposition*, 32(8):821–827, 2004. doi: 10.1124/dmd.32.8.821.
- [66] D. Feick, S. Rüdeshiem, F. Z. Marok, D. Selzer, H. L. H. Loer, D. Teutonico, S. Frechen, M. van der Lee, D. J. A. R. Moes, J. J. Swen, M. Schwab, and T. Lehr. Physiologically Based Pharmacokinetic Modeling of Quinidine to Establish a CYP3A4, P-gp and CYP2D6 Drug-Drug-Gene Interaction Network. *CPT: pharmacometrics & systems pharmacology*, 2023. doi: 10.1002/psp4.12981.
- [67] N. Hanke, D. Türk, D. Selzer, S. Wiebe, É. Fernandez, P. Stopfer, V. Nock, and T. Lehr. A Mechanistic, Enantioselective, Physiologically Based Pharmacokinetic Model of Verapamil and Norverapamil, Built and Evaluated for Drug-Drug Interaction Studies. *Pharmaceutics*, 12(6), 2020. doi: 10.3390/pharmaceutics12060556.
- [68] C. Kovar, L. Kovar, S. Rüdeshiem, D. Selzer, B. Ganchev, P. Kröner, S. Igel, R. Kerb, E. Schaeffeler, T. E. Mürdter, M. Schwab, and T. Lehr. Prediction of Drug-Drug-Gene Interaction Scenarios of (E)-Clomiphene and Its Metabolites Using Physiologically Based Pharmacokinetic Modeling. *Pharmaceutics*, 14(12), 2022. doi: 10.3390/pharmaceutics14122604.
- [69] S. Rüdeshiem, D. Selzer, U. Fuhr, M. Schwab, and T. Lehr. Physiologically-based pharmacokinetic modeling of dextromethorphan to investigate interindividual variability within CYP2D6 activity score groups. *CPT: pharmacometrics & systems pharmacology*, 11(4):494–511, 2022. doi: 10.1002/psp4.12776.
- [70] S. Rüdeshiem, J.-G. Wojtyniak, D. Selzer, N. Hanke, F. Mahfoud, M. Schwab, and T. Lehr. Physiologically Based Pharmacokinetic Modeling of Metoprolol Enantiomers and α -Hydroxymetoprolol to Describe CYP2D6 Drug-Gene Interactions. *Pharmaceutics*, 12(12), 2020. doi: 10.3390/pharmaceutics12121200.
- [71] E. H. Jung, Y. J. Lee, D.-H. Kim, P. Kang, C. W. Lim, C.-K. Cho, C.-G. Jang, S.-Y. Lee, and J.-W. Bae. Effects of paroxetine on the pharmacokinetics of atomoxetine and its metabolites in different CYP2D6 genotypes. *Archives of pharmacol research*, 43(12):1356–1363, 2020. doi: 10.1007/s12272-020-01300-8.
- [72] S. H. Kim, J. Y. Byeon, Y. H. Kim, C. M. Lee, Y. J. Lee, C. G. Jang, and S. Y. Lee. Physiologically based pharmacokinetic modelling of atomoxetine with regard to CYP2D6 genotypes. *Scientific Reports*, 8(1):12405, 2018. ISSN 20452322. doi: 10.1038/s41598-018-30841-8. URL <http://dx.doi.org/10.1038/s41598-018-30841-8>.
- [73] J. M. Sauer, G. D. Ponsler, E. L. Mattiuz, A. J. Long, J. W. Witcher, H. R. Thomasson, and K. A. Desante. Disposition and metabolic fate of atomoxetine hydrochloride: The role of CYP2D6 in human disposition and metabolism. *Drug Metabolism and Disposition*, 31(1):98–107, 2003. ISSN 00909556. doi: 10.1124/dmd.31.1.98.

- [74] I. Todor, A. Popa, M. Neag, D. Muntean, C. Bocsan, A. Buzoianu, L. Vlase, A. M. Gheldiu, and C. Briciu. Evaluation of a potential metabolism-mediated drug-drug interaction between atomoxetine and bupropion in healthy volunteers. *Journal of Pharmacy and Pharmaceutical Sciences*, 19(2):198–207, 2016. doi: 10.18433/J3H03R.
- [75] J. Y. Byeon, Y. H. Kim, H. S. Na, J. H. Jang, S. H. Kim, Y. J. Lee, J. W. Bae, I. S. Kim, C. G. Jang, M. W. Chung, and S. Y. Lee. Effects of the CYP2-star allele on the pharmacokinetics of atomoxetine and its metabolites. *Archives of Pharmacol Research*, 38(11):2083–2091, 2015. ISSN 19763786. doi: 10.1007/s12272-015-0646-z.
- [76] T. Mürdter. Impact of CYP2D6 genotype and co-medication with paroxetine and clarithromycin on clomiphen metabolism in vivo. *Abstracts of the 82nd Annual Meeting of the German Society for Experimental and Clinical Pharmacology and Toxicology (DGPT) in Naunyn-Schmiedeberg's Archives of Pharmacology*, 2016.
- [77] F. Storelli, A. Matthey, S. Lenglet, A. Thomas, J. Desmeules, and Y. Daali. Impact of CYP2D6 Functional Allelic Variations on Phenoconversion and Drug–Drug Interactions. *Clinical Pharmacology and Therapeutics*, 104(1): 148–157, 2018. doi: 10.1002/cpt.889.
- [78] F. Qiu, S. Liu, P. Miao, J. Zeng, L. Zhu, T. F. Zhao, Y. Ye, and J. Jiang. Effects of the Chinese herbal formula “Zuojin Pill” on the pharmacokinetics of dextromethorphan in healthy Chinese volunteers with CYP2D6*10 genotype. *European Journal of Clinical Pharmacology*, 72(6):689–695, 2016. ISSN 14321041. doi: 10.1007/s00228-016-2048-7.
- [79] Pharmacokinetic effects of isavuconazole coadministration with the cytochrome P450 enzyme substrates bupropion, repaglinide, caffeine, dextromethorphan, and methadone in healthy subjects. *Clinical Pharmacology in Drug Development*, 6(1):54–65, 2017. ISSN 21607648. doi: 10.1002/cpdd.281.
- [80] D. A. Capon, F. Bochner, N. Kerry, G. Mikus, C. Danz, and A. A. Somogyi. The influence of CYP2D6 polymorphism and quinidine on the disposition and antitussive effect of dextromethorphan in humans. *Clinical Pharmacology and Therapeutics*, 60(3):295–307, 1996. doi: 10.1016/S0009-9236(96)90056-9.
- [81] J. C. Gorski, S. M. Huang, A. Pinto, M. A. Hamman, J. K. Hilligoss, N. A. Zaheer, M. Desai, M. Miller, and S. D. Hall. The effect of echinacea (*Echinacea purpurea* root) on cytochrome P450 activity in vivo. *Clinical Pharmacology and Therapeutics*, 75(1):89–100, 2004. ISSN 00099236. doi: 10.1016/j.clpt.2003.09.013.
- [82] T. D. Leemann, K. P. Devi, and P. Dayer. Similar effect of oxidation deficiency (debrisoquine polymorphism) and quinidine on the apparent volume of distribution of (+/-)-metoprolol. *European journal of clinical pharmacology*, 45(1):65–71, 1993. doi: 10.1007/BF00315352.
- [83] S. H. Bae, J. K. Lee, D. Y. Cho, and S. K. Bae. Simultaneous determination of metoprolol and its metabolites, α -hydroxymetoprolol and O-desmethylnmetoprolol, in human plasma by liquid chromatography with tandem mass spectrometry: Application to the pharmacokinetics of metoprolol associated with CYP2D6 genotypes. *Journal of Separation Science*, 37(11):1256–1264, 2014. ISSN 16159314. doi: 10.1002/jssc.201301353.
- [84] S. K. Jin, H. J. Chung, M. W. Chung, J. I. Kim, J. H. Kang, S. W. Woo, S. Bang, S. H. Lee, H. J. Lee, and J. Roh. Influence of CYP2D6*10 on the pharmacokinetics of metoprolol in healthy Korean volunteers. *Journal of Clinical Pharmacy and Therapeutics*, 33(5):567–573, 2008. ISSN 02694727. doi: 10.1111/j.1365-2710.2008.00945.x.
- [85] B. A. Hamelin, A. Bouayad, J. Méthot, J. Jobin, P. Desgagnés, P. Poirier, J. Allaire, J. Dumesnil, and J. Turgeon. Significant interaction between the nonprescription antihistamine diphenhydramine and the CYP2D6 substrate metoprolol in healthy men with high or low CYP2D6 activity. *Clinical Pharmacology and Therapeutics*, 67(5): 466–477, 2000. ISSN 00099236. doi: 10.1067/mcp.2000.106464.
- [86] A. Sharma, P. Pibarot, S. Pilote, J. G. Dumesnil, M. Arsenault, P. M. Bélanger, B. Meibohm, and B. A. Hamelin. Modulation of metoprolol pharmacokinetics and hemodynamics by diphenhydramine coadministration during exercise testing in healthy premenopausal women. *The Journal of pharmacology and experimental therapeutics*, 313(3):1172–1181, 2005. doi: 10.1124/jpet.104.081109.
- [87] J. D. Huang, S. K. Chuang, C. L. Cheng, and M. L. Lai. Pharmacokinetics of metoprolol enantiomers in Chinese subjects of major CYP2D6 genotypes. *Clinical Pharmacology and Therapeutics*, 65(4):402–407, 1999. ISSN 00099236. doi: 10.1016/S0009-9236(99)70134-7.

- [88] A. Seeringer, J. Brockmöller, S. Bauer, and J. Kirchheiner. Enantiospecific pharmacokinetics of metoprolol in CYP2D6 ultra-rapid metabolizers and correlation with exercise-induced heart rate. *European Journal of Clinical Pharmacology*, 64(9):883–888, 2008. ISSN 00316970. doi: 10.1007/s00228-008-0504-8.
- [89] L. Labbé, G. O'Hara, M. Lefebvre, É. Lessard, M. Gilbert, A. Adedoyin, J. Champagne, B. Hamelin, and J. Turgeon. Pharmacokinetic and pharmacodynamic interaction between mexiletine and propafenone in human beings. *Clinical Pharmacology and Therapeutics*, 68(1):44–57, 2000. ISSN 00099236. doi: 10.1067/mcp.2000.108023.
- [90] Z. Abolfathi, C. Fiset, M. Gilbert, K. Moerike, P. M. Belanger, and J. Turgeon. Role of polymorphic debrisoquin 4-hydroxylase activity in the stereoselective disposition of mexiletine in humans. *Journal of Pharmacology and Experimental Therapeutics*, 266(3):1196–1201, 1993.
- [91] R. Chen, H. Wang, J. Shi, K. Shen, and P. Hu. Cytochrome P450 2D6 genotype affects the pharmacokinetics of controlled-release paroxetine in healthy Chinese subjects: comparison of traditional phenotype and activity score systems. *European Journal of Clinical Pharmacology*, 71(7):835–841, 2015. doi: 10.1007/s00228-015-1855-6.
- [92] S. H. Sindrup, K. Brøsen, L. F. Gram, J. Hallas, E. Skjelbo, A. Allen, G. D. Allen, S. M. Cooper, G. Mellows, and T. C. Tasker. The relationship between paroxetine and the sparteine oxidation polymorphism. *Clinical Pharmacology & Therapeutics*, 51(3):278–287, 1992. doi: 10.1038/clpt.1992.23.
- [93] Y. R. Yoon, I. J. Cha, J. H. Shon, K. A. Kim, Y. N. Cha, I. J. Jang, C. W. Park, S. G. Shin, D. A. Flockhart, and J. G. Shin. Relationship of paroxetine disposition to metoprolol metabolic ratio and CYP2D6*10 genotype of Korean subjects. *Clinical Pharmacology & Therapeutics*, 67(5):567–576, 2000. doi: 10.1067/mcp.2000.106128.
- [94] J. Novalbos, R. López-Rodríguez, M. Román, S. Gallego-Sadín, D. Ochoa, and F. Abad-Santos. Effects of CYP2D6 genotype on the pharmacokinetics, pharmacodynamics, and safety of risperidone in healthy volunteers. *Journal of Clinical Psychopharmacology*, 30(5):504–511, 2010. doi: 10.1097/JCP.0b013e3181ee84c7.
- [95] G. Bondolfi, C. B. Eap, G. Bertschy, D. Zullino, A. Vermeulen, and P. Baumann. The effect of fluoxetine on the pharmacokinetics and safety of risperidone in psychotic patients. *Pharmacopsychiatry*, 35(2):50–56, 2002. doi: 10.1055/s-2002-25026.
- [96] G. Calvo, C. García-Gea, A. Luque, A. Morte, R. Dal-Ré, and M. Barbanoj. Lack of pharmacologic interaction between paroxetine and alprazolam at steady state in healthy volunteers. *Journal of clinical psychopharmacology*, 24(3):268–276, 2004. doi: 10.1097/01.jcp.0000125689.05091.c6.
- [97] I. Todor, A. Popa, M. Neag, D. Muntean, C. Bocsan, A. Buzoianu, L. Vlase, A. M. Gheldiu, and C. Briciu. Evaluation of the potential pharmacokinetic interaction between atomoxetine and fluvoxamine in healthy volunteers. *Pharmacology*, 99(1-2):84–88, 2017. doi: 10.1159/000452223.
- [98] Tanaka, G and Kawamura, H. Anatomical and physiological characteristics for Asian reference man: Male and female of different ages: Tanaka model. *Division of Radioecology. National Institute of Radiological Sciences. Hitachinaka 311-12 Japan. Report Number NIRS-M-115.*, 1996.
- [99] I. Todor, A. Popa, M. Neag, D. Muntean, C. Bocsan, A. Buzoianu, L. Vlase, A. M. Gheldiu, R. Chira, and C. Briciu. The influence of paroxetine on the pharmacokinetics of atomoxetine and its main metabolite. *Clujul Medical*, 88(4): 513–520, 2015. doi: 10.15386/cjmed-488.
- [100] D. J. Belle, C. S. Ernest, J.-M. Sauer, B. P. Smith, H. R. Thomasson, and J. W. Witcher. Effect of potent CYP2D6 inhibition by paroxetine on atomoxetine pharmacokinetics. *Journal of clinical pharmacology*, 42(11):1219–27, 2002. doi: 10.1177/009127002762491307.
- [101] K. A. Schoedel, L. E. Pope, and E. M. Sellers. Randomized Open-Label Drug-Drug Interaction Trial of Dextromethorphan/Quinidine and Paroxetine in Healthy Volunteers. *Clinical Drug Investigation*, 32(3):157–169, 2012. doi: 10.2165/11599870-000000000-00000.
- [102] M. Schadel, D. Wu, S. V. Otton, W. Kalow, and E. M. Sellers. Pharmacokinetics of Dextromethorphan and Metabolites in Humans. *Journal of Clinical Psychopharmacology*, 15(4):263–269, 1995. doi: 10.1097/00004714-199508000-00005.

- [103] E. Steiness, S. Waldorff, P. B. Hansen, H. Egeblad, J. Buch, and H. Egeblad. Reduction of digoxin-induced inotropism during quinidine administration. *Clinical Pharmacology and Therapeutics*, 27(6):791–795, 1980. doi: 10.1038/clpt.1980.112.
- [104] H. R. Ochs, G. Bodem, and D. J. Greenblatt. Impairment of digoxin clearance by coadministration of quinidine. *Journal of clinical pharmacology*, 21(10):396–400, 1981. doi: 10.1002/j.1552-4604.1981.tb01739.x.
- [105] M. C. Chellingsworth, S. Laughner, S. Akhlaghi, D. B. Jack, and M. J. Kendall. The effects of ranitidine and cimetidine on the pharmacokinetics and pharmacodynamics of metoprolol. *Alimentary pharmacology & therapeutics*, 2(6): 521–7, 1988. doi: 10.1111/j.1365-2036.1988.tb00726.x.
- [106] S. Toon, E. M. Davidson, F. M. Garstang, H. Batra, R. J. Bowes, and M. Rowland. The racemic metoprolol H₂-antagonist interaction. *Clinical pharmacology and therapeutics*, 43(3):283–9, 1988. doi: 10.1038/clpt.1988.34.
- [107] W. Kirch, H. Spahn, H. Köhler, E. E. Ohnhaus, and E. Mutschler. Interaction of metoprolol, propranolol and atenolol with concurrent administration of cimetidine. *Klinische Wochenschrift*, 60(22):1401–7, 1982. doi: 10.1007/BF01716245.
- [108] S. M. Stout, J. Nielsen, L. S. Welage, M. Shea, R. Brook, K. Kerber, and B. E. Bleske. Influence of metoprolol dosage release formulation on the pharmacokinetic drug interaction with paroxetine. *Journal of clinical pharmacology*, 51(3):389–96, 2011. doi: 10.1177/0091270010365559.
- [109] R. B. Parker and J. E. Soberman. Effects of paroxetine on the pharmacokinetics and pharmacodynamics of immediate-release and extended-release metoprolol. *Pharmacotherapy*, 31(7):630–41, 2011. doi: 10.1592/phco.31.7.630.
- [110] A. Hemeryck, R. A. Lefebvre, C. De Vriendt, and F. M. Belpaire. Paroxetine affects metoprolol pharmacokinetics and pharmacodynamics in healthy volunteers. *Clinical pharmacology and therapeutics*, 67(3):283–91, 2000. doi: 10.1067/mcp.2000.104788.
- [111] J. A. Johnson and B. S. Burlew. Metoprolol metabolism via cytochrome P4502D6 in ethnic populations. *Drug metabolism and disposition: the biological fate of chemicals*, 24(3):350–5, 1996.
- [112] P. N. Bennett, V. A. John, and V. B. Whitmarsh. Effect of rifampicin on metoprolol and antipyrine kinetics. *British journal of clinical pharmacology*, 13(3):387–91, 1982. doi: 10.1111/j.1365-2125.1982.tb01390.x.
- [113] Open Systems Pharmacology. Japanese Population Report, 2019. URL https://github.com/Open-Systems-Pharmacology/OSPSuite.Documentation/blob/master/Japanese_Population/Report.md.
- [114] N. Yasui-Furukori, M. Saito, T. Niioka, Y. Inoue, Y. Sato, and S. Kaneko. Effect of itraconazole on pharmacokinetics of paroxetine: the role of gut transporters. *Therapeutic drug monitoring*, 29(1):45–8, 2007. doi: 10.1097/FTD.0b013e31802bb20d.
- [115] A.-H. Andreasen, K. Brøsen, and P. Damkier. A Comparative Pharmacokinetic Study in Healthy Volunteers of the Effect of Carbamazepine and Oxcarbazepine on Cyp3a4. *Epilepsia*, 48(3):490–496, 2007. doi: 10.1111/j.1528-1167.2007.00924.x.
- [116] K. W. Kolb, W. R. Garnett, R. E. Small, G. W. Vetrovec, B. J. Kline, and T. Fox. Effect of Cimetidine on Quinidine Clearance. *Therapeutic Drug Monitoring*, 6(3):306–312, 1984. doi: 10.1097/00007691-198409000-00009.
- [117] B. G. Hardy and J. J. Schentag. Lack of effect of cimetidine on the metabolism of quinidine: effect on renal clearance. *International journal of clinical pharmacology, therapy, and toxicology*, 26(8):388–91, 1983.
- [118] P. Damkier, L. L. Hansen, and K. Brøsen. Effect of diclofenac, disulfiram, itraconazole, grapefruit juice and erythromycin on the pharmacokinetics of quinidine. *British Journal of Clinical Pharmacology*, 48(6):829–838, 1999. doi: 10.1046/j.1365-2125.1999.00099.x.
- [119] P. Damkier, L. L. Hansen, and K. Brøsen. Rifampicin treatment greatly increases the apparent oral clearance of quinidine. *Pharmacology and Toxicology*, 85(6):257–262, 1999. doi: 10.1111/j.1600-0773.1999.tb02019.x.
- [120] K. M. Kaukonen, K. T. Olkkola, and P. J. Neuvonen. Itraconazole increases plasma concentrations of quinidine. *Clinical pharmacology and therapeutics*, 62(5):510–7, 1997. doi: 10.1016/S0009-9236(97)90046-1.

- [121] M. S. Ching, S. L. Elliott, C. K. Stead, R. T. Murdoch, S. Devenish-Meares, D. J. Morgan, and R. A. Smallwood. Quinidine single dose pharmacokinetics and pharmacodynamics are unaltered by omeprazole. *Alimentary pharmacology & therapeutics*, 5(5):523–31, 1991. doi: 10.1111/j.1365-2036.1991.tb00521.x.
- [122] P. Damkier, L. L. Hansen, and K. Brøsen. Effect of fluvoxamine on the pharmacokinetics of quinidine. *European Journal of Clinical Pharmacology*, 55(6):451–456, 1999. doi: 10.1007/s002280050655.
- [123] D. J. Edwards, R. Lavoie, H. Beckman, R. Blevins, and M. Rubenfire. The effect of coadministration of verapamil on the pharmacokinetics and metabolism of quinidine. *Clinical Pharmacology and Therapeutics*, 41(1):68–73, 1987. doi: 10.1038/clpt.1987.11.
- [124] W. Mahatthanatrakul, S. Sriwiriyan, W. Ridditid, J. Boonleang, M. Wongnawa, N. Rujimamahasan, and W. Pipatratanaseree. Effect of cytochrome P450 3A4 inhibitor ketoconazole on risperidone pharmacokinetics in healthy volunteers. *Journal of clinical pharmacy and therapeutics*, 37(2):221–5, 2012. doi: 10.1111/j.1365-2710.2011.01271.x.
- [125] K.-A. Kim, P.-W. Park, K.-H. Liu, K.-B. Kim, H.-J. Lee, J.-G. Shin, and J.-Y. Park. Effect of rifampin, an inducer of CYP3A and P-glycoprotein, on the pharmacokinetics of risperidone. *Journal of clinical pharmacology*, 48(1):66–72, 2008. doi: 10.1177/0091270007309888.
- [126] W. Mahatthanatrakul, T. Nontaput, W. Ridditid, M. Wongnawa, and M. Sunbhanich. Rifampin, a cytochrome P450 3A inducer, decreases plasma concentrations of antipsychotic risperidone in healthy volunteers. *Journal of clinical pharmacy and therapeutics*, 32(2):161–7, 2007. doi: 10.1111/j.1365-2710.2007.00811.x.
- [127] T. Nakagami, N. Yasui-Furukori, M. Saito, T. Tateishi, and S. Kaneo. Effect of verapamil on pharmacokinetics and pharmacodynamics of risperidone: in vivo evidence of involvement of P-glycoprotein in risperidone disposition. *Clinical pharmacology and therapeutics*, 78(1):43–51, 2005. doi: 10.1016/j.clpt.2005.03.009.
- [128] FDA. Medication guide STRATTERA® (atomoxetine hydrochloride), 2007. URL https://www.accessdata.fda.gov/drugsatfda_docs/label/2007/021411s004s012s013s015s021lbl.pdf.
- [129] FDA. Highlights of prescribing information LOPRESSOR (metoprolol tartrate), 2023. URL https://www.accessdata.fda.gov/drugsatfda_docs/label/2023/017963s074lbl.pdf.
- [130] FDA. Outer packaging TAGAMET® HB (cimetidine), 2019. URL https://www.accessdata.fda.gov/drugsatfda_docs/label/2020/020238Orig1s024lbl.pdf.
- [131] FDA. Medication guide SPORANOX® (itraconazole), 2018. URL https://www.accessdata.fda.gov/drugsatfda_docs/label/2018/020083s062lbl.pdf.
- [132] FDA. Highlights of prescribing information PAXIL (paroxetine), 2021. URL https://www.accessdata.fda.gov/drugsatfda_docs/label/2021/020031s077lbl.pdf.
- [133] National Library of Medicine. Drug label information quinidine sulfate, 2023. URL <https://dailymed.nlm.nih.gov/dailymed/drugInfo.cfm?setid=b0d6341b-d880-4f0b-8844-bc788c03004a>.

ACKNOWLEDGMENTS

An dieser Stelle möchte ich die Gelegenheit nutzen, all denjenigen zu danken, die mich während meiner Doktorarbeit begleitet und unterstützt haben.

Mein besonderer Dank gilt meinem Doktorvater, Professor Thorsten Lehr, der mir die Promotion in seiner Arbeitsgruppe ermöglicht hat und mich mit seiner Expertise, seinen wertvollen Hinweisen und seiner stetigen Unterstützung auf diesem Weg gefördert hat. Des Weiteren möchte ich Professor Marc Schneider für die wissenschaftliche Begleitung dieser Arbeit und die Übernahme des Zweitgutachtens danken.

Ein großer Dank gilt ebenfalls meinen Kolleginnen und Kollegen des Arbeitskreises Klinische Pharmazie, insbesondere Dr. Denise Feick, Dr. Simeon Rüdesheim und Dr. Dominik Selzer. Zudem möchte ich allen Projektpartnern und Co-Autoren meinen Dank für die gute und erfolgreiche Zusammenarbeit aussprechen.

Darüber hinaus danke ich Professor Charlotte Kloft und Professor Wilhelm Huisinga für die Förderung im Rahmen des Graduate Research Training Program „PharMetrX – Pharmacometrics & Computational Disease Modelling“.

Abschließend möchte ich mich bei meiner Familie und meinen Freunden bedanken. Meiner besten Freundin Patricia danke ich für ihr stets offenes Ohr, ihre guten Ratschläge und ihre Unterstützung. Im Besonderen danke ich meinen Eltern, die mich immer meinen Weg gehen ließen, mir stets den Rücken freihielten und mit Rat und Tat zur Seite standen. Nicht zuletzt danke ich meinem Freund Quirin für seine unermüdliche Geduld, sein Verständnis und seine Unterstützung von Herzen.

COLOPHON

This document was typeset using the typographical look-and-feel `classicthesis` developed by André Miede and Ivo Pletikosić. The style was inspired by Robert Bringhurst's seminal book on typography "*The Elements of Typographic Style*". `classicthesis` is available for both \LaTeX and \LyX :

<https://bitbucket.org/amiede/classicthesis/>

Happy users of `classicthesis` usually send a real postcard to the author, a collection of postcards received so far is featured here:

<http://postcards.miede.de/>

Thank you very much for your feedback and contribution.